Experimental and Computational Studies of the Low Velocity Impact and Compression After Impact of Carbon Fiber Reinforced Polymer Composites

by

Shiyao Lin

A dissertation submitted in partial fulfillment
of the requirements for the degree of
Doctor of Philosophy
(Aerospace Engineering)
in The University of Michigan
2021

Doctoral Committee:

Professor Anthony M. Waas, Chair
Professor Pingsha Dong
Dr. Vipul Ranatunga
Professor Veera Sundararaghavan

Shiyao Lin

sylinae@umich.edu

ORCID iD: 0000-0002-8311-3531

To my family

ACKNOWLEDGEMENTS

I would like to extend my deepest gratitude to my Ph.D. advisor, Professor Anthony M. Waas, for his guidance, support, and wisdom. This thesis and the solution of many problems in the last five years would not be possible without him. He has set a great example for me as a knowledgeable and creative scientist, a problem-solving engineer, and an excellent educator. His instinct, enthusiasm, and good taste in research have cultivated my mind and skills. Many lessons I have learned from him will continue to benefit my future career and life.

My gratitude also goes to my master advisor, Professor De Xie, who was a postdoctoral researcher working with Professor Waas. Professor Xie guided me into the field of computational solid mechanics and has been encouraging me throughout the years. He suggested me to apply to be a Ph.D. student of Professor Waas and kindly wrote me a strong reference letter. To quote Professor Xie, "If you want to solve real and important problems, do your Ph.D. with Professor Waas."

I am grateful to my dissertation committee members, including Professor Anthony Waas, Professor Veera Sundararaghavan, Professor Pingsha Dong, and Dr. Vipul Ranatunga, for their reviews and suggestions for my thesis. I could not be more thankful to Dr. Vipul Ranatunga, who monitored the AFRL research project that provided me with financial support. He has inspired me with numerous insightful industry-based ideas and has always been tremendously supportive of my research and career.

I have had a great pleasure to work with the current and former members of

the Composite Structures Lab. Special thanks should go to Dr. Paul Davidson, Dr. Jiawen Xie, Dr. Kuo Tian, Dr. Solver Thorsson, Dr. Ashith Joseph, and Dr. Armanj Hasanyan. Dr. Davidson has offered me great suggestions regarding research and career choices, and has kindly helped me during my job search. Dr. Jiawen Xie was the first group member I met and helped me adjust to new life and work. Dr. Tian has always been a role model and a sincere friend to me, who has encouraged and inspired me to go through many difficult moments. Dr. Thorsson kindly shared his codes, knowledge, and experience with me on the subjects of this thesis. His excellent work has set a high bar for me to achieve. Dr. Joseph and Hasanyan have helped me over the years with research and life. I will always remember our discussions on Friday evenings in the AERB office of the University of Washington. And, of course, the time we spent together at the bars after the discussions. I would also like to thank the current group members including Dr. Royan D'Mello, Dr. Eugene Kheng, Andrew Seamone, James Finlay, Jose Fernando Rojas Sanchez, Alex Post, and Elisheva Phillips. Special thanks go out to my friends and comrades, Avinkrishnan Vijayachandran and Minh Hoang Nguyen. I have had the fortune to know these two great friends for five years and received tremendous help and encouragement from them. I will always remember the time we sat together in our office to finish homework and prepare for the preliminary exam, and those days that we helped each other with tests in the labs.

Thanks to my great friends: Dr. Yao Qiao, Dr. Yao Long, Mengyuan Wang, Dr. Guodong Chen, Dr. Shaowu Pan, Dr. Sicheng He, Dr. Linpeng (Peter) Wei, Yifan Bai, Shengyu Liu, Aaditya Lakshmanan, Dr. Hai Dong, Dr. Ting Xie and Dr. Siddhartha Srivastava. It is a pleasure for me to cross paths with you. I am sincerely grateful to my dearest friend, Bao-Tran Huynh, M.D., who has always been supportive, caring, considerate, and wise.

I am grateful for the support and assistance provided by the faculty and staff

of the University of Michigan (UM) Aerospace Engineering and the University of Washington (UW), Aero & Astro. Professor Marco Salviato has helped and inspired me with his outstanding knowledge and passion in both research and life. Denise Phelps, Ruthie Freemen, and Gwen Brown at UM; Ed Connery and Kim Maczko at UW have made my graduate study efficient and fruitful. Thomas Griffin, Chris Chartier, Aaron Borgman, David McLean, and Terry Larrow are the go-to people who have always been available and willing to help whenever I am troubled with technical issues.

I would like to express my gratitude to the Mitsubishi Heavy Industries and AFRL for their financial support. Furthermore, I wish to thank the AFRL-Israel project team members, including Professor Waas, Dr. Vipul Ranatunga, Profesor Rami Haj-Ali, Lt.Col. Noam Shemesh, Oleg Pery, and Yevheniia Kovalova for their valuable suggestions and positive feedback on my work.

Last but not least, I would like to thank my beloved parents, Dr. Jifu Lin and Mrs. Li Li, who have always been unconditionally encouraging and supporting me. The guidance I have received from them has led me through this long and exciting journey. I also wish to thank my little brother, Peiyu Lin, who has always been a source of happiness and love.

TABLE OF CONTENTS

LIST OF FIGURES

Figure

LIST OF TABLES

Table

LIST OF APPENDICES

Appendix

ABSTRACT

Carbon fiber reinforced polymer (CFRP) composites have been widely used in many industrial sectors because of their high strength-to-weight ratio, cost advantages, and the possibility of tailoring the design. During the lifetime of a composite structure, low velocity impact (LVI) tends to happen in many scenarios, including manufacturing, service, and maintenance operations. A small event such as a tool drop may cause barely visible impact damage (BVID) with extensive internal cracking while without any noticeable marks on the outer surface of a composite structure. LVI-induced damage can lead to a significant reduction in post-impact compressive strength. Therefore, the LVI and compression after impact (CAI) problems have received continued attention for decades. Considerable effort on experimental and numerical investigations persists. Generations of accurate, efficient, versatile, and robust numerical tools have been developed to tackle the LVI and CAI problems virtually to save experimental costs and accelerate the verification and validation (V&V) process. Experimental and computational studies on the LVI and CAI damage of CFRP laminated composites are presented in this dissertation. Effects of laminate stacking sequence, impact energy, and panel size on the LVI and CAI are investigated.

In the experimental part, LVI test results are reported. Non-destructive inspection (NDI) techniques, including ultrasound C-scanning and micro computed tomography (μCT), are conducted to characterize the impact damage. With the high-resolution μCT scanning, damage mechanisms are analyzed. Following the LVI tests and NDI

characterization, CAI tests are done to relate the impact energy to the degradation of compressive strength. CAI fixtures for standard-size composite panels are modified to customize to panels with increased sizes. Post-buckling responses during the CAI of panels with increased sizes are presented.

Parallel with the experimental results, computational results are obtained with the enhanced Schapery Theory (EST) model, which is a seamless combination of the Schapery theory (ST) and the crack band (CB) method. EST based on 2D plane stress is extended to a 3D stress state. A novel mixed-mode cohesive law is integrated to model the degradation of stress components progressively and simultaneously. The capability of EST to capture matrix inelasticity is implemented. 2D and 3D EST applied to LVI and CAI modeling are verified against the experimental results. A high-fidelity and high-efficiency LVI-CAI computational framework is established based on 2D EST to accurately predict the LVI damage and CAI strength with significantly improved efficiency. The computational results agree well with the experimental results in terms of the load responses, damage morphology, and CAI strength.

This dissertation provides detailed LVI and CAI results concerning the effects of stacking sequence, impact energy, and panel size. The EST model developed is validated and will be useful in the V&V process of aeronautical composite structures. Furthermore, the high-fidelity and high-efficiency LVI-CAI computational framework enables obtaining the CAI strength with significantly reduced computational time, which will help enlarge the design space of CFRP laminated composites with increased impact resistance.

CHAPTER I

Introduction

[1] Fiber reinforced polymer composite (FRPC) materials have been widely used in many industrial areas because of their high strength-to-weight ratio, cost advantages, and the possibility of tailoring the design. During the lifetime of a composite structure, low velocity impact (LVI) tends to happen in many scenarios, including manufacturing, service, and maintenance operations. Due to the fact that most composite materials are stiff and brittle, even a small event such as a tool drop may cause barely visible impact damage (BVID) with extensive internal damage, without leaving any obvious damage mark on the outer surface of a composite structure. Impact damage can lead to a significant reduction in post-impact structural strengths. Therefore, the LVI problems have received considerable attention and decades of effort in experimental and computational studies. The majority of the research is concentrated on developing novel experimental technologies, composite damage models, and numerical approaches for predicting, characterizing, and simulating LVI and compression after impact (CAI) responses.

[1]The introduction in this chapter is extended from the content published in:
Lin, Shiyao, Solver I. Thorsson, and Anthony M. Waas. "Predicting the low velocity impact damage of a quasi-isotropic laminate using EST." *Composite structures* 251 (2020): 112530.

1.1 Experimental Approaches

Impact testing apparatus include gas gun, pendulum, and drop weight systems. Gas gun is usually used for high-velocity impact with a small-mass impactor. Pendulum and drop weight tests are usually used for low-velocity impact with a relatively large-mass impactor [18]. Most of the LVI research has been carried out with drop tower systems. Industrial standards such as ASTM D7136 [19] has outlined standard LVI testing procedures for 6 inch $\times$ 4 inch (152.4 mm $\times$ 101.6 mm) samples with drop tower systems. Piezoelectric sensors and optical signal triggers are usually used to collect load and displacement data. LVI tests are sometimes accompanied by in-situ 3D digital image correlation (DIC) with high-speed cameras to capture the deformation on the non-impacted surface of the sample, as discussed in [20, 21, 22].

After the LVI tests, the dent depth of the impacted sample is usually measured with a dial indicator or optical profilometer. LVI-induced damage should also be detected and characterized. The damage inspecting methods can be categorized as destructive and non-destructive. Although destructive techniques are usually cheaper and allow for microscopic examination of samples, non-destructive inspection (NDI) is more favorable since attendant CAI tests still have to be performed. NDI techniques include ultrasound C-scanning and B-scanning, with which the overall size of the damage footprint can be measured. However, due to the overshadowing effect of C-scanning, interface-by-interface delamination cannot be characterized completely. Efforts have been made to deconstruct the overall C-scanning into more meaningful ply-by-ply damage data by using existing image processing algorithms [23]. X-ray μCT is sometimes used to acquire more details of LVI-induced damage. After μCT scanning, a 3D reconstruction step is usually performed to obtain a 3D model of the scanned damage [22, 24]. Other NDI techniques include thermography [25] and synchrotron radiation laminography. With high-resolution scans made possible by synchrotron radiation laminography, a comparison of impact damage in toughened

and untoughened material systems was reported in [26].

After the indentation depth measured and impact damage characterized, CAI tests are performed following the industrial standard ASTM D7137 [27]. Again, the sample size specified by ASTM D7137 is 6 inch $\times$ 4 inch (152.4 mm $\times$ 101.6 mm). CAI testing is performed by exerting axial quasi-static compressive loading. The speed of testing should be chosen such that the ultimate compressive failure would take place within 1 to 10 min. The recommended loading rate is 1.25 mm/min [27]. For 6 inch $\times$ 4 inch (152.4 mm $\times$ 101.6 mm) samples, usually, 2D DIC measurement of the deformation is sufficient since out-of-plane deformation of the sample is not expected. However, for samples with larger sizes, buckling and post-buckling behaviors might take place and therefore, 3D DIC is needed for measuring the out-of-plane deformation of the sample [28, 29].

1.2 Damage Mechanisms and Challenging Problems

To investigate the damage formation inside a composite laminate induced by LVI, it is critical to understand the in situ deformation of the laminated plate first. According to Olsson [1], the impact event of a composite laminate can be categorized into three types, as seen in Figure 1.1. The categorization is established upon elastic wave propagation inside the plate. If the impact duration is in the order of the transition time for through-the-thickness wave starting from the impacted point, the impact response is dominated by 3D wave propagation before reflection from the boundaries, as illustrated in Figure 1.1(a). This type of impact is highly local, typically associated with high-speed, ballistic loading. Since in most cases, ballistic impact damage is easily recognizable, it is not studied in this thesis. For an impact event with a longer duration, the response is initially governed by flexural waves and shear waves and then becomes global to the structure, as shown in Figure 1.1(b). For an impact duration much longer than the traveling time for these waves to reach the

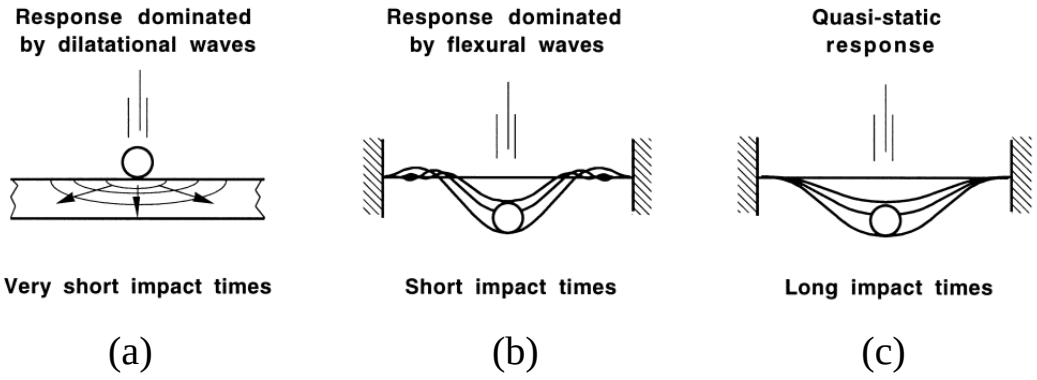

Figure 1.1: Three types of impact responses [1].

plate boundaries, the impact response is essentially quasi-static, global to the plate from the start of the impact. Hail impact and runway debris typically belong to the second type, as shown in Figure 1.1(b), while heavy tool drops belong to the third type, as shown in Figure 1.1(c). This thesis is focused on the second and third types of impact.

Next, it is important to understand the process of the impact damage initiation and growth to identify the governing parameters. This is critical for developing modeling tools for LVI problems. LVI-induced damage in composites has abundant modes. With minimal marks on the outer surface, internal damage might be extensive and show a coupling of various damage modes. For an impacted sample, on the impacted side, permanent indentation and cracking due to fiber kinking as well as matrix cracking are often observed, as shown in Figure 1.2(a). On the non-impacted side, fiber tensile rupture and matrix splitting are often seen, as shown in Figure 1.2(b). With NDI techniques, such as ultrasound C-scanning, internal delamination can be visualized, as shown in Figure 1.2(c). Interactions between damage modes, such as fiber-matrix damage interaction, fiber-delamination damage interaction, and matrix-delamination damage interaction can be detected by high-resolution μCT [22]

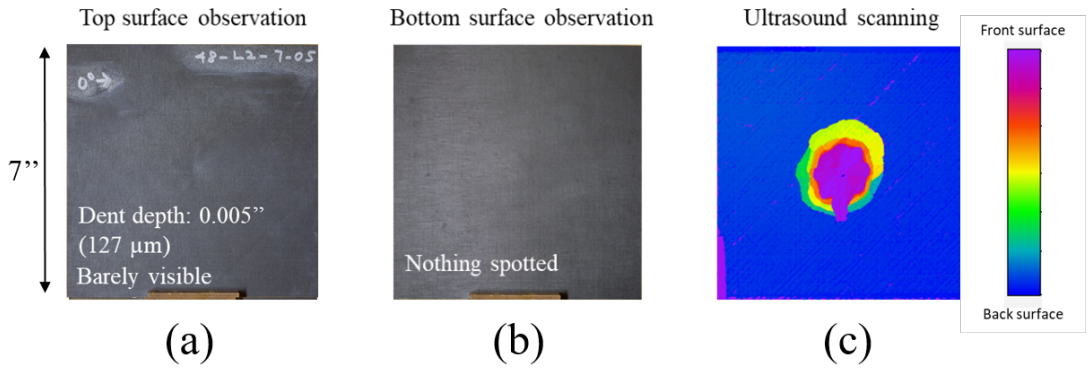

Figure 1.2: Typical damage observation: (a) the impacted side, (b) the non-impacted side, and (c) damage footprint characterized by ultrasound C-scanning.

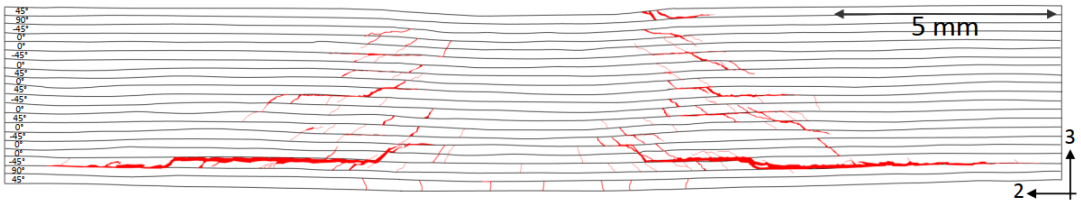

Figure 1.3: Sectional view of impact-induced damage [2].

assisted with dye penetrant. With damage interactions, LVI-induced damage is sometimes referred to as the “pine tree” shape [18], as shown in Figure 1.3.

As conventionally understood, the first damage to appear is matrix cracking. When the matrix crack density increases, delamination will quickly occur [30]. The interactions between matrix cracking and delamination typically have two types. When the laminate is thick, the matrix cracks would firstly take place in the top layers near the impacted side due to highly localized contact stresses. The development of damage is top-down, resulting in the “pine tree” shape. For thin laminates, tensile stresses due to bending on the non-impacted side of the laminate would cause matrix cracking and then delamination. A reversed “pine tree” pattern can be found in [18]. In conclusion, the most important damage modes in a composite laminate induced by LVI are:

1. **Matrix cracking:** matrix cracking happens in nearly every part (among the

top, middle, and bottom parts) of an impacted laminate. Usually, in an LVI event, matrix cracking occurs first and serves as an initiation for delamination. In the upper (close to the impacted side) and middle parts of the laminate, transverse shear matrix cracking predominates and in the lower part, tensile matrix splitting predominates because of the relatively high tensile stress induced by laminate bending.

2. **Fiber breakage:** fiber breakage appears as two types. When the impact energy is relatively low, such as under the BVID limit, fiber breakage will only happen in the top-most few plies, appearing as fiber kinking. When the impact energy is high enough, in the bottom-most few plies, tensile fiber rupture tends to happen. There is no clear definition of "high" energy in this context since the LVI response greatly varies according to the material systems, stress conditions, and boundary conditions.

3. **Delamination:** Delamination appears nearly in every part (among the top, middle, and bottom parts) of a laminate. It is defined as the separation between adjacent laminae which are bonded by resin. Delamination is usually considered initiated by matrix cracking and is the most important factor causing compressive strength reduction of an impacted laminate.

With the help of μCT, a closer observation can be made regarding the interaction between damage modes [22]. In [22], a quasi-isotropic laminate $[45/0/\text{-}45/90]_{3s}$ was studied experimentally and inspected with μCT scanning. The damage morphology in the upper, middle and lower parts of the laminate are shown in Figure 1.4, 1.6 and 1.8. The interaction between fiber kinking, delamination and matrix cracking is seen and illustrated in Figure 1.5 and 1.7. As shown in Figure 1.5, due to the highly compressive strain induced by the contact of the impactor, the top-most plies will undergo fiber kinking and the formation of the kink band will release a great amount

of energy, which would provoke large delamination at the top-most interfaces. This is the reason that in Figure 1.4, the CT scanned delamination footprint is larger and brighter than the others (and the μCT scanning was enhanced by dye penetrant). Figure 1.7 shows the interaction between matrix cracking and delamination, within which the matrix cracking serves as initiation and boundaries for the delamination. In the bottommost plies and interfaces, the delamination is not as salient but with larger sizes, as shown in Figure 1.6. This is partially due to that in the bottom-most plies, matrix splitting dominates due to high tensile stresses. Another highly cited work of Hull and Shi gives a detailed characterization and explanation for damage mechanisms [31]. Laminate deplying technology was applied for delamination inspection. Aside from μCT and deplying technologies, microscopy enables an even closer look into the damage modes and mechanisms in composite laminates subjected to LVI. All three damage failure modes can be seen in Figure 1.9.

With the most important damage modes and their interaction illustrated, several challenging topics are naturally brought up. For single or multiple damage modes, abundant damage models have been proposed to perform progressive damage analysis (PDA), to name a few, the NCYL model [32, 33, 34], the LaRC model [35, 36, 37], and the enhanced Schapery theory (EST) model [38, 39]. However, there are only a few methods taking a step forward to account for the interaction between the damage modes. The works include the enriched shell element developed by McElroy and Pankow [40, 41], which implants the interaction into the element formulation, and the intra-inter crack band model (I2CBM) developed by Joseph and Waas [42, 7, 6], which accounts for the interaction by a crack tracking algorithm. Both of these models will be illustrated in Section 1.4 as novel numerical methods.

One of the most important features of composite materials that is essential to successful modeling is the matrix shear nonlinearity. Matrix shear nonlinearity is due to micro-scale damage, including hackling, shear banding, and micro-fissures [43].

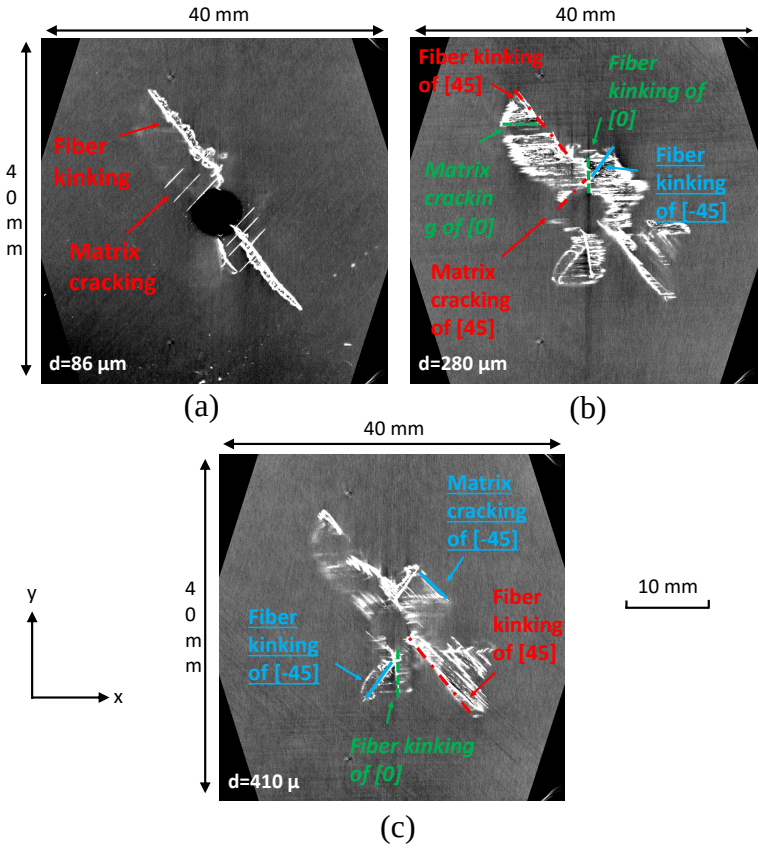

Figure 1.4: CT slices in the top part of the impacted specimen: (a) the top-most slice, (b) the slice 0.2 mm from the top and (c) the slice 0.26 mm below the top slice

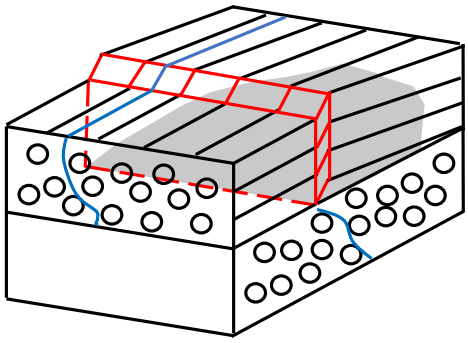

Figure 1.5: Interaction between fiber kinking and delamination in the top part of the laminate

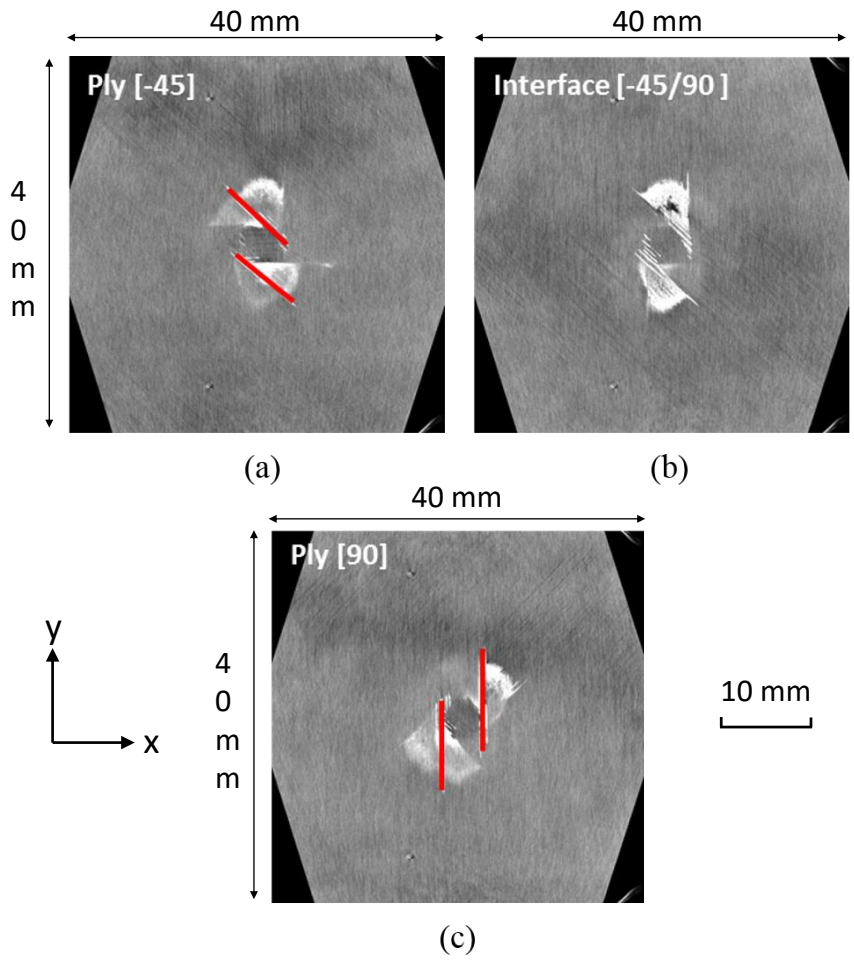

Figure 1.6: CT slices in the middle part of the impacted specimen: (a) the slice for ply [-45], (b) the slice for the interface [-45/90] (c) the slice for ply [90]

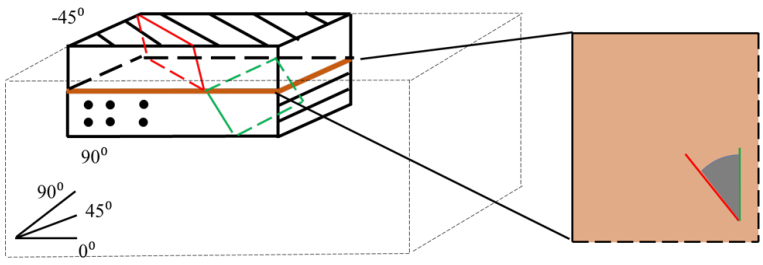

Figure 1.7: Interaction between matrix cracking and delamination in the top part of the laminate

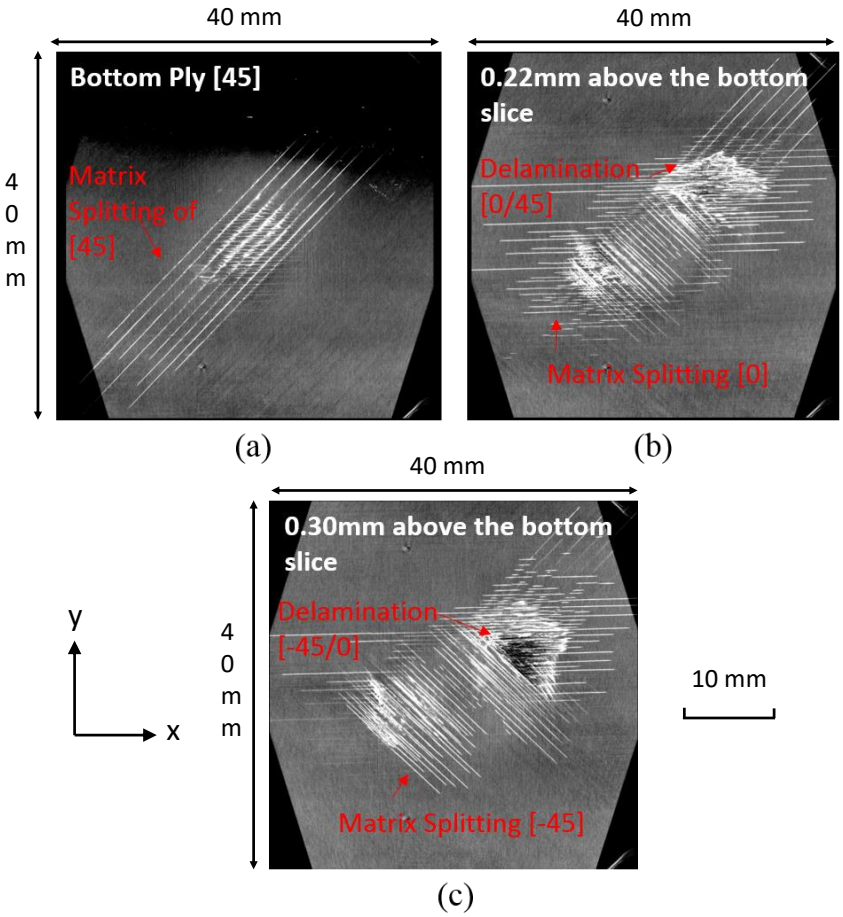

Figure 1.8: CT slices in the bottom part of the impacted specimen

Multiple models have been developed to characterize the nonlinearity, mostly based on curve fitting and plasticity theories. These models will be discussed in Section 1.3.

Another challenge to tackle is the permanent indentation on the impacted surface of the laminate. There are several reasons contributing to this phenomenon, including fiber entanglement, friction between damaged intra-ply parts and delaminated plies, matrix plasticity, fiber debris sticking into matrix cracks, and matrix debris [44, 45, 46]. There have been multiple models developed capable of capturing the permanent indentation and these model will be explained and compared in Section 1.3.

Finally, an effect that has been ignored by many is the strain rate dependency of the polymer matrix. The mode I fracture behavior of the interface with respect to an elevated strain rate was studied experimentally by Thorsson and Waas with a modified wedge-insert [47]. It was found that as the strain rate increases, the mode I fracture toughness G_{IC} of the interface decreased significantly. Koerber et al. studied the strain rate effect on transverse compression and in-plane shear moduli and strengths [48]. It was found that as the strain rate increases, the moduli and strengths increase correspondingly. There are only a few models that consider the strain rate effect in LVI, and will be illustrated in Section 1.3.

In conclusion, the challenging topics in LVI computational modeling are (but not limited to):

1. **Interaction between damage modes.**
2. **Shear nonlinearity of matrix.**
3. **Permanent indentation modeling.**
4. **Strain rate dependency of matrix and resin.**

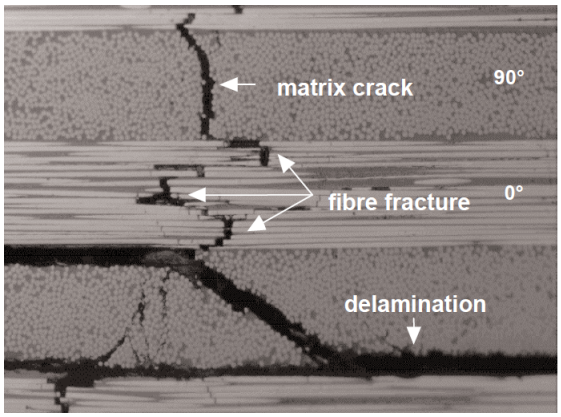

Figure 1.9: Damage modes in impacted laminate [3]

1.3 Literature Review on Computational Methods of LVI and CAI

Among many numerical methods used in the current research field, the finite element method (FEM) appears to be the most robust, efficient, and commercially available technique. Furthermore, for LVI and CAI simulations, which typically are costly in terms of time and computing resources, FEM seems to be the only option so far. With the advancement of computational power, there is no doubt that methods such as smoothed particle hydrodynamics (SPH) [49, 50] and Peridynamics [51, 52, 53] will become increasingly important. However, this section will only concentrate on FEM. Other novel computational approaches will be illustrated in Section 1.4.

1.3.1 Modeling Strategy

1.3.1.1 Length Scales of the Model

Various PDA models have been developed with different length scales of resolution. The length scales are as illustrated in Figure 1.10. In the macro-scale failure analyses, a composite laminate is treated as a general orthotropic material with effective mechanical properties. The crack angle and path are not presumed. The results of this scale are usually very coarse and can only yield a rough estimate of parameters

such as impact peak load and duration. Therefore, methods at this scale are usually applied when there is a low requirement on fidelity [54] and a high requirement on the efficiency of the analysis [10, 55]. In the meso-scale failure analyses, a composite laminate is usually treated as plies of transversely isotropic laminae adhered by resin-rich interfacial layers. Matrix cracking and fiber breakage can take place as intra-ply failure modes while delamination may occur as inter-ply failure. In this scale, for the intra-ply modeling, the crack angle is usually assumed parallel or perpendicular to the fiber orientation while the crack path is unknown. For the inter-ply crack (delamination) modeling, both the crack angle and crack path are fixed, since delamination can only take place at the interface. Meso-scale analysis is the mainstream method for LVI and CAI problems. In the micro-scale failure analyses, where matrix and fibers are explicitly modeled, a crack can initiate and propagate within the matrix with an arbitrary crack angle and location. In this case, the maximum principal stress/strain criterion (the Rankine criterion) is often used to determine the crack angle. This scale is highly involved with multiscale analysis and direct numerical analysis [56, 57, 58]. However, analyses at this length scale are not computationally efficient for LVI and CAI investigations.

1.3.1.2 Mesh Strategy

For the meso-scale analyses, all layers of the laminate are built explicitly and usually cohesively attached to the adjacent ones. For the modeling of intra-ply damage, planar shell elements [59], continuum shell elements [24, 21, 60] and 3D solid elements [61, 62, 63] are the most adopted element types. For the modeling of inter-ply damage (delamination), simulation can be performed with cohesive elements and cohesive contact. Cohesive element in the early stage was developed as nonlinear spring-based elements connecting coincident nodes of neighboring elements [45, 64]. Then, with the method gaining popularity, cohesive models have become commercially available in

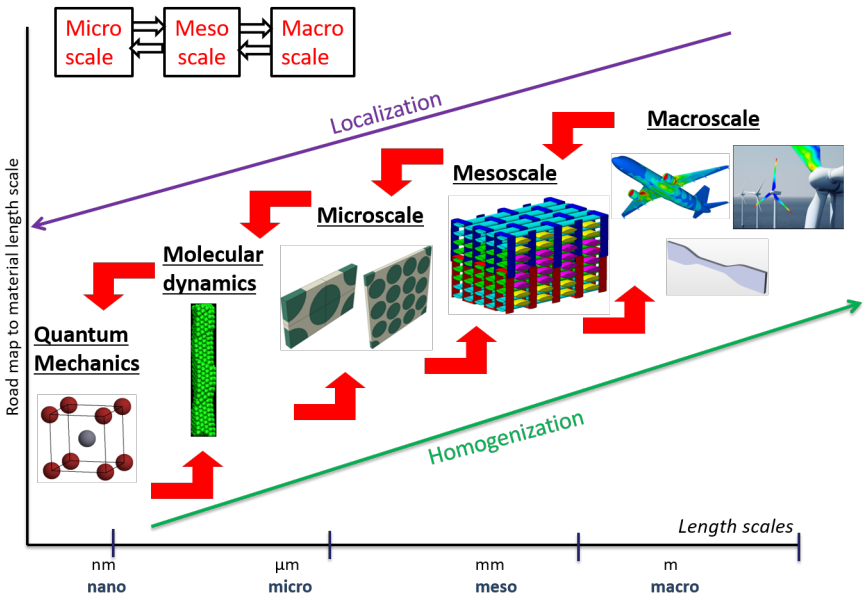

Figure 1.10: Micro, meso, and macro scales of computational models [4].

many commercial codes, such as element COH3D8 in Abaqus [65] and *MAT 138 in LS-DYNA [66]. A cohesive element can be defined with zero or finite small thickness. In addition to delamination modeling, cohesive elements have been inserted between strips of intra-ply elements to model matrix splitting [30, 63, 67]. Another way for interface modeling is using cohesive contact. For the cohesive contact definition in Abaqus [65], when two adjacent layers are in contact, the cohesive contact behave in the same way as the general contact option available in Abaqus [65]. When the layers are detached, the interaction will enter the cohesive zone dictated by predefined cohesive traction-separation laws. Several works have been reported using the cohesive contact model for interface modeling [68, 69, 70, 22].

There are different combinations of intra-ply modeling and inter-ply modeling. The most frequently used strategies were summarized and categorized by Gonzalez [5] as strategies I, II, and III, as shown in Figure 1.11. According to Figure 1.11 (a), strategy I uses uniform regular mesh for intra-ply damage modeling and finite/zero-thickness cohesive elements for inter-ply damage modeling. In Figure 1.11 (b), strategy II uses fiber-aligned mesh for intra-ply damage modeling and cohesive

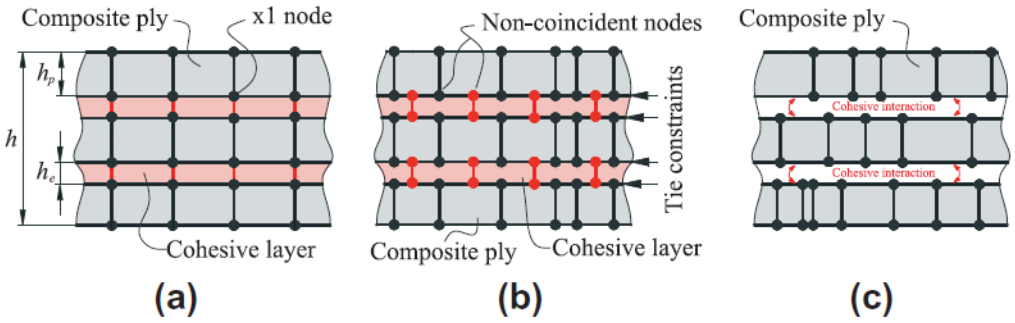

Figure 1.11: Three modeling strategies [5]: (a) using cohesive element and regular mesh, (b) using cohesive element and fiber-aligned mesh, and (c) using cohesive contact.

elements for inter-ply damage analysis. Strategy III, as shown in Figure 1.11 (c), technically should be divided into two strategies since the intra-ply mesh can be uniform or fiber-aligned. There are advantages and disadvantages of these three strategies. For strategy I, the advantage is the ease of building the model, since all the meshes are uniform. Also, compared with the cohesive contact modeling, cohesive element modeling is computationally more efficient, due to the complexity of the contact algorithm. Compared with strategy I, strategy II is believed to be able to give better predictions of matrix cracking since this damage mode is most likely to be along the fiber direction. However, fiber-aligned meshing is more complicated, especially for non-traditional fiber orientations, other than 0°, 45°, -45°, and 90° [42, 7, 6]. Strategy III is the easiest one to implement since no nodal coincidence or attachment is required due to the application of the cohesive contact model. Strategy III has been shown to generate the best results in terms of validation against test data [44] and be able to predict delamination very similar to the μCT scanning images [22]. The disadvantage of strategy III is its lower computational efficiency compared to strategy I and II.

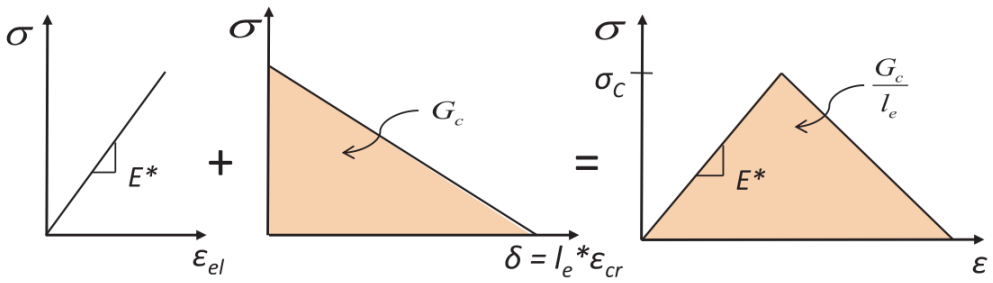

Figure 1.12: LVI-CAI modeling steps [6]

1.3.2 Damage Modeling

Most of the LVI and CAI computational models are based on the crack band (CB) method [71] and the smeared crack analysis (SCA) approach [72]. The CB method is an effective, element level approach to model the onset and propagation of macroscopic cracks in a mesh objective manner. For the CB model, the crack behavior is defined as the softening of the stress-strain relationship. The softening is dictated by cohesive traction-separation laws and at least two parameters for each damage mode are needed, including the crack strength and fracture toughness. Most computational models discussed in this section follow the same path. Crack initiation criteria are based on stresses or strains. A typical stress-strain relationship of the CB model is shown in Figure 1.12. In the model, the strain is decomposed into an elastic and crack component, as in Equation 1.1. E^* is the pristine elastic modulus, G_c is the fracture toughness, and σ_c is the fracture strength. For FEM implementation of the CB model, a characteristic length should be defined and the element size should be smaller than the Bazant's limit [71], as shown in Equation 1.2. The remaining part of this section focuses on various damage models considering all the damage modes following the CB method in the literature.

$$\epsilon = \epsilon_{el} + \epsilon_{cr} \tag{1.1}$$

$$l_e < \frac{2G_c E^*}{\sigma_c^2} \tag{1.2}$$

1.3.2.1 Fiber Failure

Fiber failure includes fiber tensile, compressive, and shear failure modes. Tensile failure is along the longitudinal direction of a lamina. Compressive failure of fiber is most likely in the form of fiber kinking involved with significant fiber rotation. Analyses of the kinking phenomena is usually based on the assumption of a local initial fiber misalignment [73, 74]. Fiber failure schemes are shown in Figure 1.13. In most of the fiber failure models, the fiber shear failure mode is not considered, but the shear stress in the 1-2 direction sometimes is accounted for in the fiber damage initiation criteria [8, 75, 76, 77]. In a series of studies by Soutis [8, 75, 76, 77], fiber tensile and compressive failure modes followed the Hashin criteria [78] for initiation and linear traction-separation laws for post-peak degradation. In Falzon's studies [68, 69, 79], with tensile loading, the initiation of fiber damage was determined by a strain-based criterion only involved with longitudinal strain values, and the post-peak degradation is assumed linear. With compressive loading, the initiation and degradation were the same as that in the tensile mode except that there was a residual strength simulating the effect of fiber crushing happening in the fiber kink band. In the works of Lopes, Gonzalez and Camanho [62, 44, 5, 80, 81, 82], the fiber damage model was one component of the LaRC model. In the LaRC model [35, 36, 37], the longitudinal compressive failure mode of fiber considered fiber misalignment [35]. In the works of Bouvet [30, 45, 83, 63], both the fiber tensile and compressive initiation criteria were based on strain and the post-peak degradation was linear. A residual compressive strength was defined according to [84] to simulate the crushing stress. In addition, plasticity was included to prevent the fiber compressive strain from returning to zero after unloading. The fiber failure mode defined by Bouvet is found to be the

most sophisticated in the literature [30]. In the work of Waas et al. [24, 21, 60, 22], no misalignment of fiber angle was considered because the compressive strength is computed using a micromechanics model that incorporate the fiber misalignment, and matrix shear nonlinearity. Both the tensile and compressive failure modes followed strain-based criteria and degraded linearly. It should be specifically noticed that in this model, once the fiber direction starts to degrade, the matrix components would degrade as well and the element was considered failed when the fiber direction failed.

1.3.2.2 Matrix Cracking

Matrix cracking includes tensile cracking (splitting), in-plane shear cracking. and out-of-plane shear cracking, as shown in Figure 1.14. Attention should be paid that matrix cracking is most likely with mode mixity, which means that the cracking phenomenon can be decomposed into both mode I and mode II damage. A mixed-mode PDA model accounting for intra-ply damage was developed by Joseph and Waas [42, 7, 6]. Another challenging issue of matrix cracking is the pre-peak nonlinearity, due to micro-scale damage, including hackling, shear banding, and micro-fissures [43]. Additionally, the matrix fracture behavior is highly rate-dependent. As shown in [48], the moduli and strengths of both mode I and mode II cracking are strongly affected by the loading rate. As the loading rate increases, the moduli and strength would increase significantly. Therefore, computational models describing matrix damage are usually more complex than that for fiber damage.

In the early works of Soutis [8], solid elements were used for the intra-ply modeling. Hashin criteria [78] were implemented for matrix tensile failure and the compressive failure followed the damage model developed by Puck and Schurmann [85, 86], in which the compressive failure of the matrix was modeled as the shear failure on a fracture plane, as shown in Figure 1.15. To account for the matrix crushing and fragment interaction effects within the damage zone, a finite stress value was kept

as a residual compressive strength. The pre-peak nonlinearity in shear cracking was accounted based on a semi-empirical expression developed by Soutis [87, 88]. In this expression, an inelastic strain was defined to model the permanent indentation. Then, in Soutis's later works [75, 76, 77], intra-ply zero-thickness cohesive elements were introduced between element strips to model matrix cracking.

In the works of Falzon and Donadon et al. [68, 69, 79], the stress-strain relationship of matrix tensile failure was linear in both pre-peak and post-peak parts and the compressive failure was again with respect to the fracture plane following Puck's criteria [85, 86]. The nonlinear shear matrix cracking was modeled with a fitted cubic law. The shear strain was decomposed into inelastic and elastic parts to capture the permanent indentation. Another work by Donadon et al. [89] enhanced the matrix shear cracking model with strain rate dependency.

In the works of Lopes, Gonzalez, Camanho et al. [62, 44, 5, 80, 81, 82], the matrix cracking model including matrix tensile, shear, and compressive failures followed the LaRC model [35, 36, 37]. Matrix shear nonlinearity and residual transverse strength were not implemented.

In Bouvet's early works, intra-ply matrix cracking was modeled by user-defined elements similar to cohesive spring elements [45]. Later, the intra-ply spring elements were substituted with zero-thickness cohesive elements available in Abaqus [30, 63, 83]. Pre-peak shear nonlinearity was not considered and the matrix debris effect was implemented with a finite compressive stiffness in both mode I and mode II cracking.

In the works of Waas et al. [24, 21, 60, 22], the matrix pre-peak nonlinearity was modeled with the Schapery theory [90, 38], which explained the micro-cracking effect on stiffness degradation using a thermodynamic scheme. The matrix crushing and debris effect were not modeled and therefore there was only a small residual stress kept after the failure of matrix damage modes, which was for better numerical stability. Also, no inelastic strain component was considered in the model. In [91], EST was

improved with the capability to capture material inelasticity and it was shown that the improved version of EST could successfully predict the permanent indentation.

1.3.2.3 Delamination

The delamination models can be divided into element-based and contact-based – both are available for implementation in the commercial software Abaqus. For both types of the models, initial penalty stiffness values need to be defined. The initiation and failure criteria can be selected within the built-in ones [65]. A mixed-mode cohesive formulation has been implanted in the cohesive element and contact of Abaqus following [92]. In the model, an effective separation was defined by a quadratic summation of crack separations of each damage mode. A novel mixed-mode cohesive formulation was developed by Nguyen and Waas [93], in which the definition of the effective separation was more physically rigorous. Lopes et al. [44] conducted a comparative study on interface model and compared the modeling results with experimental data. The conclusion was that the cohesive contact model generated the best results which were closest to the experimental data.

Soutis et al. [8, 75, 76, 77] simulated delamination using 3D finite-thickness cohesive elements. The initiation criterion was the second-order power law available in Abaqus and the failure criterion was the B-K criterion proposed by Benzeggagh and Kenane [94]. Falzon et al. [68, 69, 79] utilized the cohesive contact model and the initiation and failure criteria were also the second-order power law and B-K criterion. Camanho et al. utilized the cohesive elements with a small thickness [62, 5] and in their later work, results obtained with the cohesive elements and contact were compared [44]. In the works of Waas et al. [24, 21, 60], the interface model was based on the discrete cohesive zone method (DCZM), originally developed by Xie and Waas [64] and later improved by Gustafson and Waas [95]. Then, after comparative studies using DCZM, cohesive element and cohesive contact, the cohesive contact was used

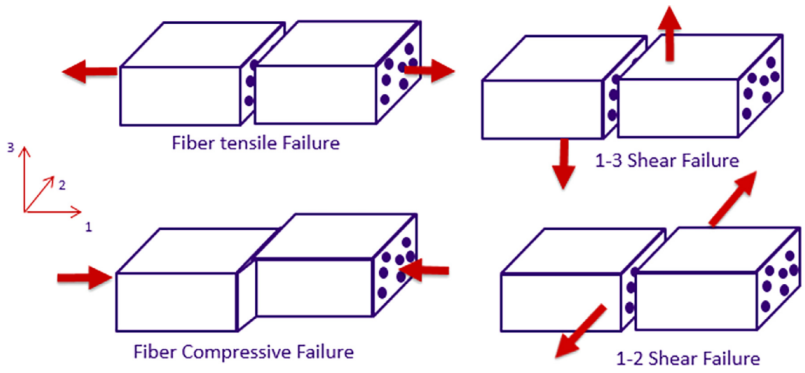

Figure 1.13: Fiber damage modes [7].

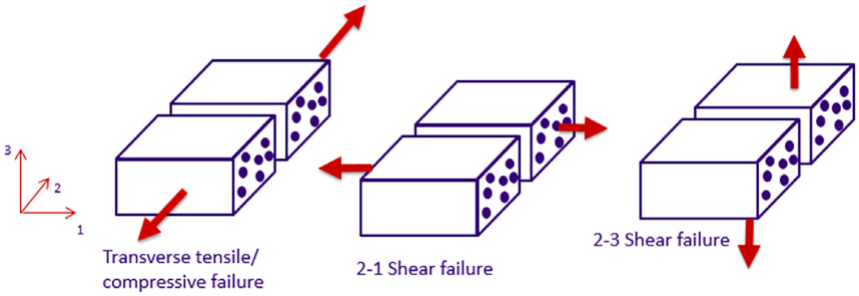

Figure 1.14: Matrix damage modes [7].

for delamination modeling due to its advantage in obtaining high-fidelity delamination patterns [22] using the post-processing viewer of Abaqus. When DCZM was used, it was realized that the built-in viewer of Abaqus could not directly visualize the predicted delamination.

1.4 Emerging Novel Computational Methods and Applications

In previous sections, modeling strategies and damage models based on FEM have been reviewed. In this section, some emerging novel methods – not necessarily based on FEM – for LVI and CAI analyses will be discussed.

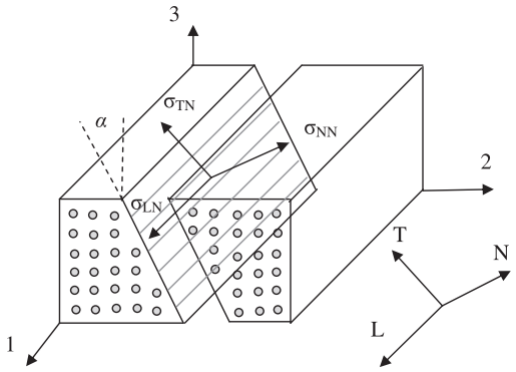

Figure 1.15: Matrix compressive failure on a slanted fracture plane [8]

1.4.1 Enriched Shell Element

The enriched shell element (ESE) has been developed by McElroy and Pankow [40, 41]. The basic idea of the method was the seamless transition from one single layer of elements for the laminate to multiple layers of elements when delamination was activated. Floating nodes were attached with degrees of freedom (DOFs) in the method from the start and remain dormant. The DOFs of the floating nodes would be attached to the delamination modeling after damage onset. In this way, the computational time could be greatly saved. Another advantage was the explicit interaction of intra-ply and inter-ply damage implemented in the ESE, which was claimed as "delamination migration" due to the introduction of floating nodes. Such interaction is difficult to model with standard FEM. A similar partition-of-unity (POU) method was developed by Waas et al. [96, 97, 98, 99] as the continuum decohesive finite element (CDFE) and can be reformed into a scheme similar to ESE for LVI and CAI modeling.

1.4.2 Peridynamics

Peridynamics was originally proposed by Silling [51] and then applied to the LVI analysis of composites [9]. In the results shown in [9], high-fidelity patterns of delamination were obtained as a comparison to test results, as shown in Figure 1.16. As

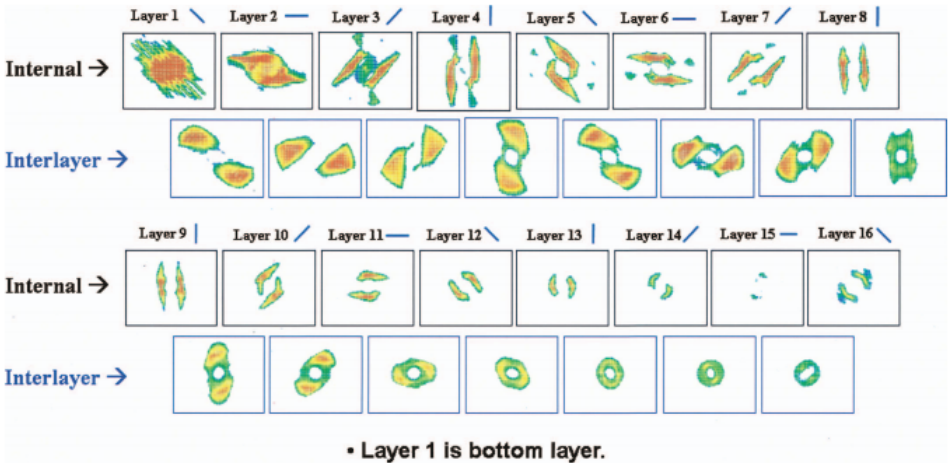

Figure 1.16: Damage results obtained with Peridynamics [9].

shown in the figure, fan-shape delamination was reproduced and the crack spacing of matrix cracking was captured. This should be due to the nature of the method, which directly models the interaction of a particle with every other particle within a finite neighborhood. In this way, sharp crack in terms of displacement continuity can be modeled. In addition, efforts were made to bridge Peridynamics with commercially available FEM software [100] and related studies have has been done for impact modeling [101]. By examining wave-dispersion effects, the limitation and drawbacks of Peridynamics modeling has recently been studied by Bazant et al. [102].

1.4.3 Semi-discrete Damage Model (SD2M)

SD2M was developed for PDA of composites [67]. The method utilized a separation of fiber and matrix failure modes and introduced randomness in the distribution of material strength. Thin strips of matrix-splitting elements were built within plies of laminae to capture the progression of transverse matrix cracking. A novel mixed-mode law was proposed and implemented into the scheme of SD2M. So far, SD2M has been applied to problems including single edge notched tension (SENT) and open hole tension (OHT) of composites [103]. It is promising for SD2M to address LVI and

CAI problems with high-fidelity.

1.4.3.1 Data Driven Models

Data-driven models have gained popularity within physics due to the ever-increasing computational power and accumulating data. One application of the data-driven methods is model reduction, which appear in the work of Metoui et al. recently [104]. Proper generalized decomposition (PGD) was used to significantly reduce the number of DOFs involved in the analysis. However, to utilize such methods requires a user-developed code, which, in the paper, has features including the cohesive zone model, a modified nonlinear Hertzian contact law and an implicit Newmark time integration algorithm. Also, a great deal of simplification was applied. However, model reduction has been proved highly efficient in the field of shell buckling [105]. There are many reasons to look forward to the combination of traditional LVI and model reduction methods.

Another application of data-driven methods is the development of efficient methods for prediction. Surrogate models can be established based on many models including artificial neural network (ANN), Kriging analysis and support vector machine (SVM) [106]. ANN has been primarily combined with LVI data acquired with numerical modeling by Lin et al. and some physical-sound trends have been discovered [107]. However, the database was not sufficiently large and the sampling method still need to be improved to smartly design the sampling space. Other studies have also utilized ANN but the numerical method was over simplified which cannot reveal the progressive damage process during LVI [108, 109].

1.5 Objective and Organization of the Thesis

This thesis is mainly focused on experimental and computational studies of the LVI and CAI of laminated fiber reinforced polymer matrix composites. Experimen-

tal work aims at understanding the stacking sequence effects and size effects of the LVI and CAI behavior. Computational work aims at refining and extending the EST model to achieve better computational fidelity, versatility, and efficiency. Through the high-fidelity computational analyses, complex damage mechanisms, as well as the stacking sequence and size effects, have been accurately illustrated. Additionally, with the proposed and developed high-fidelity and high-efficiency computational framework for LVI-CAI analysis, the computational time has been significantly reduced (by 67%) while preserving the computational fidelity. The work conducted in this thesis endeavors to lay the foundation for the future development and application of data-driven models.

The organization of this thesis is as follows. Chapter II will focus on experimental studies of the LVI experimental work accounting for the stacking sequence effects and size effects. Experimental results in terms of load responses, high-speed 3D DIC measurement of in-situ deformation, and high-resolution damage characterization with ultrasound C-scanning as well as X-ray μCT will be presented. Chapter III will provide results of the CAI experimental work, including load responses, in-situ 2D and 3D DIC measurement of the deformation of samples, and post-CAI observation of the damage patterns. Chapter IV will illustrate the theoretical and computational background of the 2D and 3D EST model with inelasticity captured (EST-InELA). Benchmark element patch test will be presented as a validation of the developed 2D and 3D EST-InELA models.

Chapter V will provide computational results for the LVI tests conducted in Chapter II using both 2D and 3D EST-InELA models. Damage predictions for the LVI of a quasi-isotropic laminate and a highly anisotropic laminate will be illustrated in detail due to the challenge of capturing their unique damage pattern. 2D and 3D EST-InELA will also be applied and compared in terms of computational accuracy and efficiency.

In Chapter VI, a high-fidelity and high-efficiency computational framework for consecutive LVI-CAI analysis will be proposed and implemented. Three methods, including a smart mesh paradigm, a damage transferring algorithm, and an efficient modeling strategy, will be illustrated in detail. A benchmark LVI-CAI example will be studied to evaluate the efficiency improvement brought by the high-fidelity and high-efficiency framework.

Chapter VII will provide computational results for the CAI tests conducted in Chapter III. Detailed analyses of the damage patterns as well as the effects of the stacking sequence, impact energy, and sample size will be presented.

Finally, Chapter VIII will conclude the thesis by pinpointing critical research findings, existing challenging issues, and suggestions for future work.

1.6 Unique Contributions in the Thesis

The unique contributions of this thesis are as follows:

1. *Detailed LVI and CAI experimental results*, including real-time DIC measurement of the deformation of samples and high-resolution damage characterization.

2. *Stacking sequence effects and panel size effects of the LVI and CAI.* A systematic study of the effects from the stacking sequence with elevating impact energy and from the sample size is rare in the research field. This thesis will provide comprehensive experimental and computational results focusing on the stacking sequence effects and panel size effects.

3. *High-fidelity computational predictions of damage patterns.* Featured damage patterns such as the "rotating-fan" pattern and "kidney" pattern are highly challenging to be numerically predicted. These damage patterns have been re-

solved by high-fidelity EST predictions in this thesis, with their damage mechanisms investigated and illustrated.

4. *Refinement and development of the 2D and 3D EST models with inelasticity.* With the improvement of the EST models in terms of the capability to capture material inelasticity and a novel mixed-mode cohesive law [7], the computational fidelity with respect to capturing damage morphology, permanent indentation, and energy absorption has been enhanced.

5. *The high-fidelity and high-efficiency computational framework.* This original framework helps significantly reducing the computational time by 67% while preserving the computational fidelity. Based on the high-fidelity and high-efficiency framework, the possibility for LVI and CAI studies to embrace advanced data-driven models has been increased.

CHAPTER II

Experimental Studies of the Low Velocity Impact (LVI) of Laminated Composites

2.1 Introduction

[1] In this chapter, experimental results for the LVI of CFRP composites are reported. Two major topics have been studied: i) the effects of stacking sequence on the LVI behavior and ii) the effects of panel size on the LVI behavior. Two material systems have been tested, including T800s/3900-2B and IM7/977-3. LVI tests were performed with an Instron drop tower. In situ deformation of the samples was characterized by high-speed 3D digital image correlation (DIC). Post-impact non-destructive inspection (NDI) was conducted with ultrasound C-scanning and X-ray

[1] The results presented in this chapter have been published in:

- Lin, Shiyao, and Anthony M. Waas. "The effect of stacking sequence on the LVI damage of laminated composites; experiments and analysis." *Composites Part A: Applied Science and Manufacturing* 145 (2021): 106377.
- Lin, Shiyao, Solver I. Thorsson, and Anthony M. Waas. "Predicting the low velocity impact damage of a quasi-isotropic laminate using EST." *Composite structures* 251 (2020): 112530.
- Lin, Shiyao, and Anthony M. Waas. "An Experimental and Computational Study on the Low Velocity Impact-Induced Damage of a Highly Anisotropic Laminated Composite Panel." *Journal of Applied Mechanics* 88.8 (2021): 081001.
- Lin, Shiyao, Vipul Ranatunga, and Anthony M. Waas. "A Comprehensive Experimental and Computational Study on LVI Induced Damage of Laminated Composites." *AIAA Scitech 2021 Forum*. 2021.

micro computed tomography (μCT). Through the acquired load responses, captured deformation field, and characterized impact damage, damage mechanisms and effects of stacking sequence and panel size have been investigated.

Stacking sequence effect studies have been performed with respect to T800s/3900-2B laminates including $[0/45/0/90/0/\text{-}45/0/45/0/\text{-}45]_{s}$, $[45/0/\text{-}45/90]_{3s}$, and $[45/\text{-}45/0/45/\text{-}45/90/45/\text{-}45/45/\text{-}45]_{s}$, which are [50/40/10], [25/50/25], and [10/80/10] layups where each number indicates the percentage of 0°, 45° and 90° plies. Additionally, detailed experimental analysis has been carried out for a "sandwich-like" $[0/90/0/90_{9}]_{s}$ laminate, whose impact damage is unique due to the strong interaction between matrix cracking and delamination. Through this study, the physics of the LVI-induced damage with various stacking sequences and as a function of impact energy has been examined.

Panel size effect studies have been performed with respect to IM7/977-3 laminates including two stacking sequences: $[45/\text{-}45/0/90/0/0]_{ns}$ and $[45/0/\text{-}45/90]_{ns}$; two total thicknesses: 24-ply and 48-ply; and three in-plane sizes: 152.4 mm × 101.6 mm, 177.8 mm × 177.8 mm, and 330.2 mm × 330.2 mm. The panel size effects on the load response, damage morphology, and damage size have been investigated.

With the presented experimental results in this chapter, mechanisms of LVI-induced damage will be illustrated. The effects on the damage from stacking sequence, panel size, impact energy, and the material system will be discussed, summarized, and explained. The experimental findings will be compared with computational results reported in Chapter V for the validation and verification (V&V) of the developed computational model - EST. In this chapter, Section 2.2 will outline the experimental procedure. Section 2.3 will focus on the effects of stacking sequence on the LVI. Section 2.4 will present and discuss the effects of panel size on the LVI. Discussions will be provided in Section 2.5.

2.2 Experimental Procedure

LVI tests were performed on T800s/3900-2B and IM7/977-3 laminates using the CEAST 9350 Drop Tower Impact System. The impact tests were carried out according to ASTM D7136 standard [19]. During the tests, the samples were placed upon steel roller plates, as shown in Figures 2.1 and 2.2. The supports shown in Figure 2.1 were used for the impact study of the 152.4 mm $\times$ 101.6 mm samples. The supports shown in Figure 2.2 were used for the 177.8 mm $\times$ 177.8 mm samples. The roller plates for the 330.2 mm $\times$ 330.2 mm samples are very similar to that in Figure 2.2 and therefore not shown. The fixtures were composed of two steel plates. The upper plates and lower plates were used for sandwiching the samples, using hex screws. The diameters of the rollers of all the fixtures was 6.35 mm.

A 45 $^\circ$ mirror was placed underneath the roller supports to reflect the deformation of the bottom surfaces of the samples to two Photron SA-X high-speed cameras. The two cameras were synchronized and activated on the triggering mode. The triggering signal was from the photocell triggering system of the drop tower. The recording rate ranged from 20,000 frames/second to 25,000 frames/second. The bottom surfaces of the samples were speckled with black and white paints and the pictures taken by the cameras were processed with 3D DIC using Aramis v6.1. The experimental setup, including the drop tower, high-speed cameras, mirror, and light source are demonstrated in Figure 2.3

After LVI and before CAI, NDI was performed for the impacted samples. Ultrasound C-scanning was conducted for to characterize overall damage footprints induced by impact, using a Mistras UPK-T36 immersion ultrasound system and a Dolphicam 2 handheld scanner. 5 MHz ultrasound transducers were used and the scanning pixel size was 0.1 mm $\times$ 0.1 mm. To gain more detailed damage morphology, μCT was performed using an NSI X5000 CT system and a Zeiss Xradia Versa 520 system. The μCT scans were performed via absorption contrast tomography (ACT) on a labo-

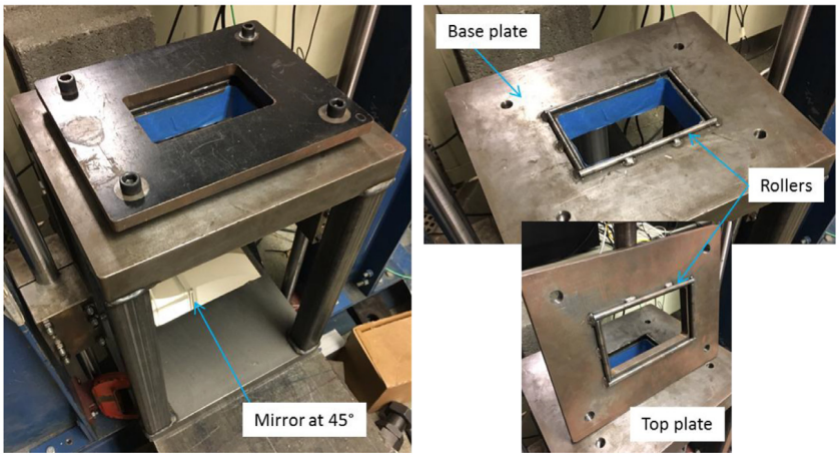

Figure 2.1: The LVI fixture used for 152.4 mm × 101.6 mm samples.

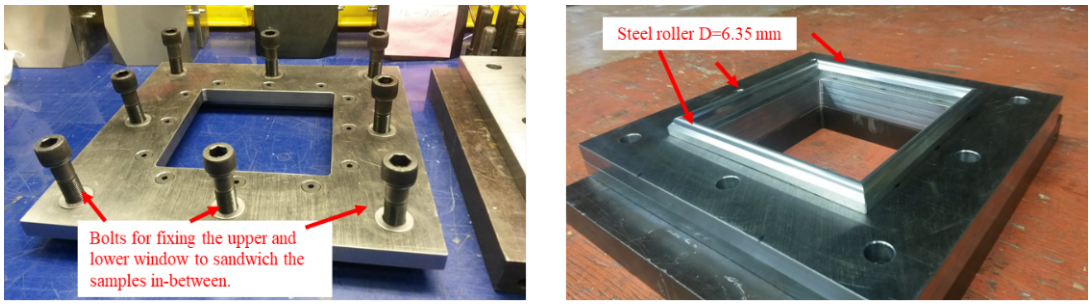

Figure 2.2: The LVI fixture used for 177.8 mm × 177.8 mm samples.

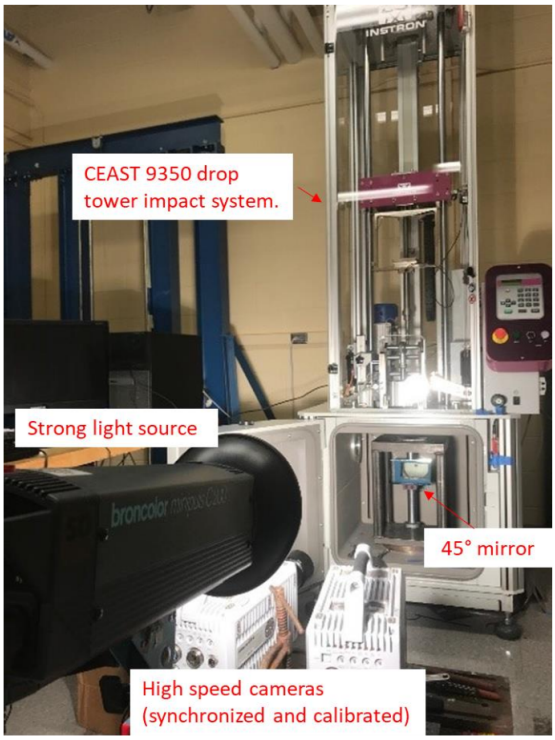

Figure 2.3: The Instron drop tower with high-speed cameras.

ratory X-ray microscope. The impacted sample was imaged using a polychromatic X-ray beam centered at 120 kV and 83.57 μA. Due to the high-volume density of the sample, an exposure time of 6s and a total of 1601 projections were taken over 360° to ensure a high signal-to-noise ratio in the images. The x-ray projection images were magnified by 0.4X objective lens and coupled to a 2k X 2k CCD detector operating in binning 2. The scanning voxel sizes ranged from 21.6 μm $\times$ 21.6 μm $\times$ 21.6 μm to 50.0 μm $\times$ 50.0 μm $\times$ 50.0 μm . Before the μCT scanning, the sample was immersed in dye penetrant fluid containing Zinc Iodide for 12 hours. The formula of the dye penetrant can be found in [110, 111].

(a) (b)

Figure 2.4: NDI instruments: (a) a Dolphicam 2 handheld ultrasound scanner, and (b) a Zeiss Xradia Versa 520 μCT system.

2.3 Experimental LVI Study with the Effects of Stacking Sequence

In this section, LVI tests of 150 mm $\times$ 100 mm T800s/3900-2B samples are presented. The impactor mass was 7.5 kg. The shape of the impactor was hemispherical, with a diameter of 20 mm. The roller support size was 139.7 mm $\times$ 88.9 mm. Averaged layer thickness of the samples was 0.19 mm. It should be noted that one of the sample sizes in the panel size effect study was 152.4 mm $\times$ 101.6 mm, which is slightly different from the size in this section. This slight difference is due to requirements by various research projects. Samples of both sizes were tested using the same LVI fixture, so there was essentially no physical difference.

2.3.1 A Comprehensive Report of the LVI Experimental Results

LVI tests were performed for T800s/3900-2B laminates of three stacking sequences, including $[0/45/0/90/0/\text{-}45/0/45/0/\text{-}45]_s$ (named as A), $[45/0/\text{-}45/90]_{3s}$ (named as B), and $[45/\text{-}45/0/45/\text{-}45/90/45/\text{-}45/45/\text{-}45]_s$ (named as C). Layup A, B, C are [50/40/10], [25/50/25], and [10/80/10] stacking sequences, where each number in-

Table 2.1: LVI testing parameters.

Stacking sequence	E1 (J)	E2 (J)	E3 (J)
A: $[0/45/0/90/0/-45/0/45/0/-45]_s$	15	20	25
B: $[45/0/-45/90]_{3s}$	25	30	35
C: $[45/-45/0/45/-45/90/45/-45/45/-45]_s$	20	25	30

dicates the percentage of 0°, 45°, and 90° plies. These three layups have also been studied regarding their open-hole tension (OHT) and open-hole compression (OHC) behavior in [112]. In addition, detailed LVI results of layup A with a different material system IM7/8552 have been reported in [21]. By comparing the results of layup A in this paper and that in [21], the effect of the material system on the LVI behavior can be investigated.

Three impact energies were tested for each layup. For each layup, one of the three energy levels was determined according to the recommendation from the ASTM D7136 standard [19] that the ratio of impact energy to sample thickness should be 6.7 J/mm. Then, the other two energy levels were selected to be one higher and the other lower. The highest energy was determined such that fiber tensile rupture took place and large load oscillations were observed on the load curves. The impact energy levels are summarized in Table 2.1.

2.3.1.1 Load Responses

The load-time, load-displacement, and kinetic energy-time curves of all the tested samples are demonstrated in Figures 2.5 to 2.7. In each figure, the three rows correspond to the three energy levels. The three columns correspond to the load-time, load-displacement, and kinetic energy-time responses. The kinetic energy is calculated based on the mass and velocity of the impactor. It is seen that the test results are highly repetitive, demonstrating the validity of the experiments. In the first two rows, the load curves are smooth, except for one layup A sample, sample 03, impacted

with 20 J. The reason for the load responses of sample 03 of layup A being more oscillatory than the other two samples may be attributed to the randomness in material property distribution and manufacturing defects in the samples. Additionally, the impact energy of 20 J may be the transitioning energy which is just enough to cause a certain extent of bottom-ply fiber tensile rupture. The third rows of Figures 2.5 to 2.7 contain the the experimental results of the three layups with the highest impact energies, which are 25 J, 35 J, and 30 J. In the third rows, the curves are more oscillatory, corresponding to the fiber tensile rupture and splitting on the bottom surfaces of the samples, which can be visualized from 3D DIC characterization, as presented in Figures 2.9 to 2.11. It is also observed that the LVI load responses of layup B are less oscillatory than that of layup A and C. This might be caused by the thickness of layup B (24-ply) being thicker than that of layup A (20-ply) and C (20-ply). When impacted with the same energy, layup B samples would deform less due to their higher bending rigidity, which would lead to less microscale and macroscale damage. With less induced damage, the load responses of layup B samples would be smoother.

Critical parameters of the test data, including peak load, maximum displacement of the impactor, residual displacement at which load returns back to zero, and energy absorption are collected from the test curves and presented in Figure 2.8. The results of stacking sequence A, B, and C are colored blue, orange, and yellow. The energy absorption is calculated by the impactor's initial kinetic energy after subtracting the kinetic energy at the end of LVI. From Figures 2.8 (a) and (b), the peak load and maximum impactor displacement of all the layups grow monotonically with the impact energies. When the three layups are impacted with the same energy, 25 J, the peak loads of layup B, C, and A are in ascending order while the corresponding maximum impactor displacement values are in descending order. This is due to the fact that layup B is thicker than the other two layups, hence the bending rigidity is the highest. The bending rigidity of layup A is the lowest. From Figure 2.8 (c), it

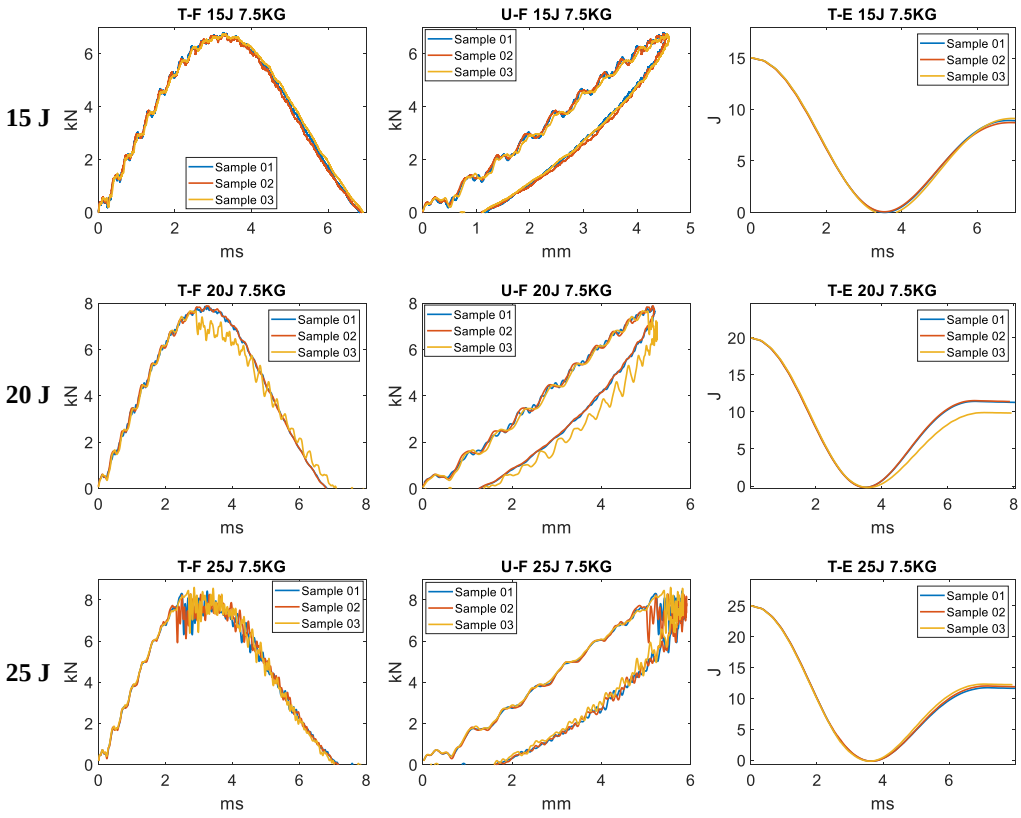

Figure 2.5: Load responses of all the tested layup A samples.

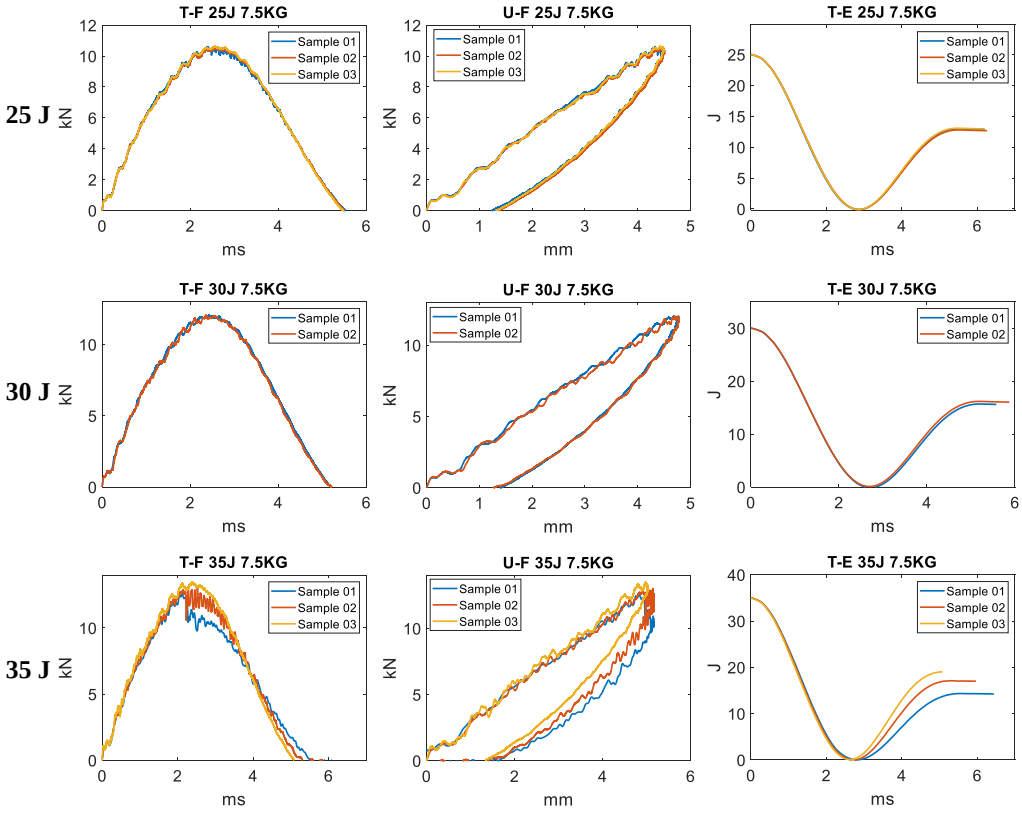

Figure 2.6: Load responses of all the tested layup B samples.

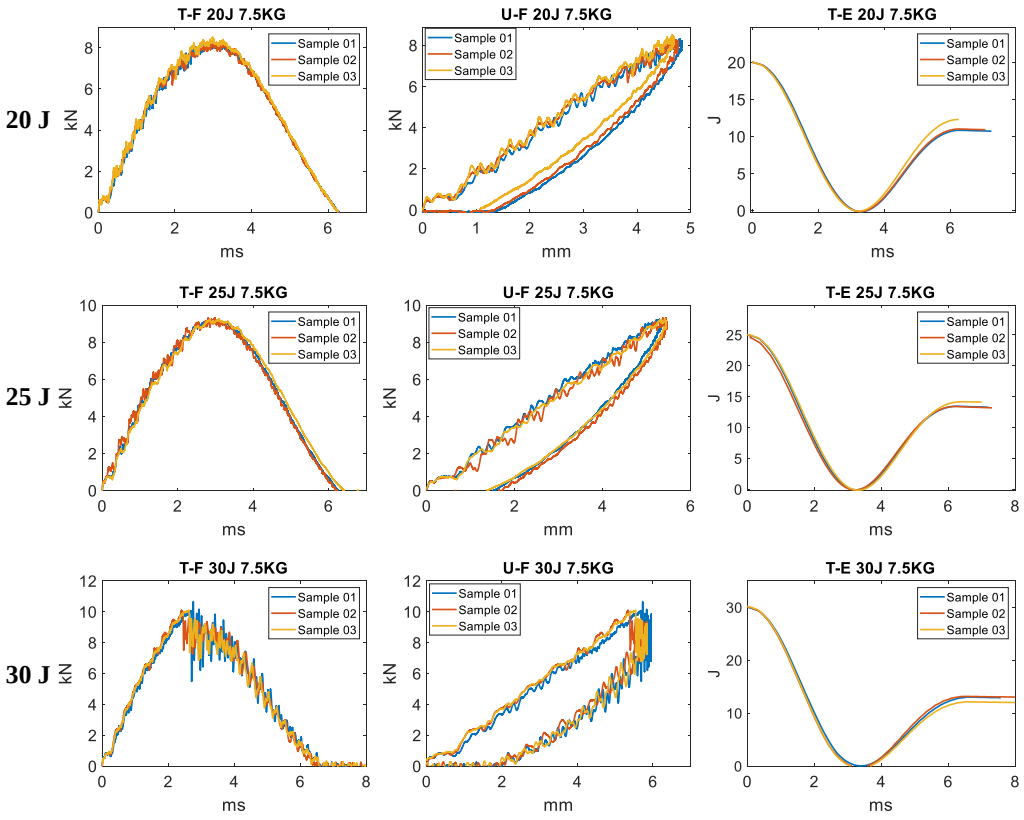

Figure 2.7: Load responses of all the tested layup C samples.

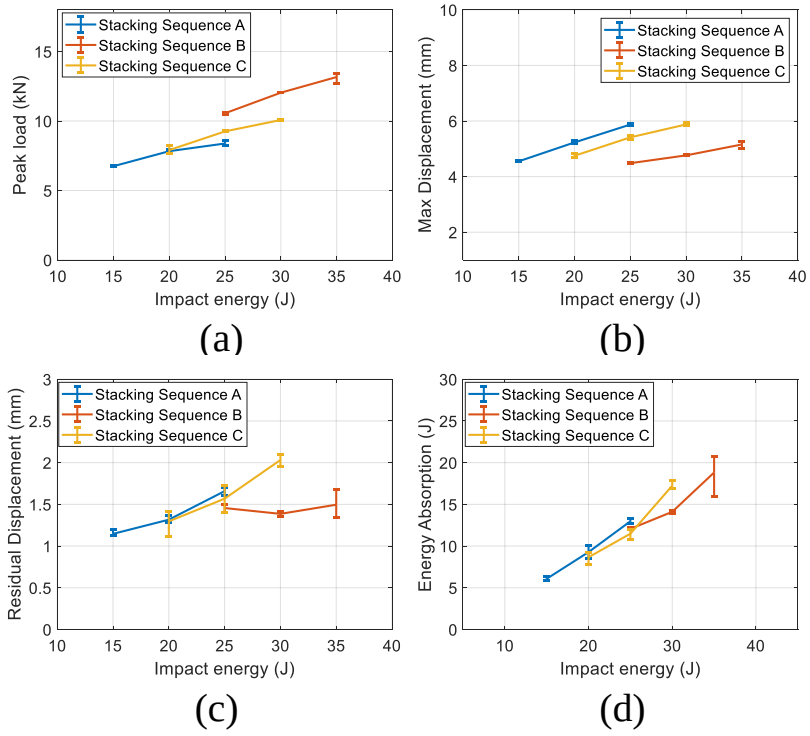

Figure 2.8: Statistics of the critical parameters: (a) peak load, (b) maximum displacement, (c) residual displacement, and (d) energy absorption.

is observed that the residual displacement grows with the increasing impact energy, except for layup B samples impacted with 30 J energy. According to Figure 2.8 (d), the energy absorption increases with the escalation of impact energies. The energy absorption is made of energy dissipated by material damage, material inelasticity, heat release, and friction.

Accompanying the drop tower impact tests, the in situ out-of-plane deformation of the samples was characterized with high-speed 3D DIC. The deformation history of the three layups are displayed in Figures 2.9, 2.10 and 2.11. In Figures 2.9 (a), 2.10(a), and 2.11(a), the center displacement histories of the three layups impacted with three energies are plotted. The blue and orange curves seem to be smooth, indicating that there was no decorrelation of the DIC characterization. The decorrelation of DIC is usually due to excessive deformation of the inspected surface, which is frequently

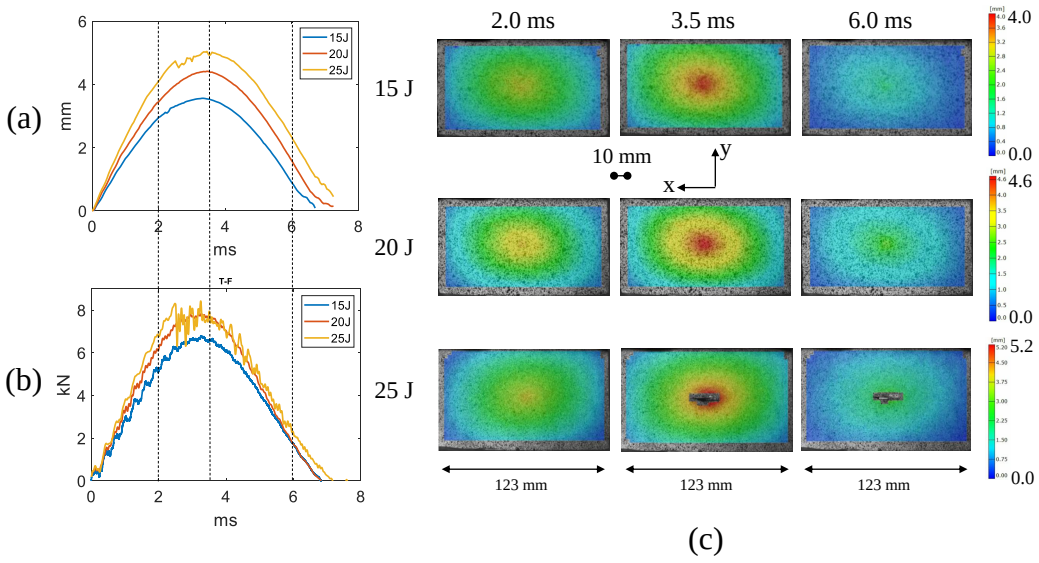

Figure 2.9: 3D DIC results of the layup A LVI tests: (a) out-of-plane center displacement histories, (b) impact load histories, and (c) out-of-plane deformation fields.

caused by damage. Oscillations are seen on the yellow curves in Figures 2.9(a), 2.10(a) and 2.11(a), implying that the deformation discontinuities have been captured by 3D DIC for the LVI tests with the highest impact energy levels, which are 25 J for layup A; 35 J for layup B; and 30 J for layup C. The decorrelation of the DIC is seen in the third rows of Figures 2.9(c), 2.10(c) and 2.11(c). Load-time curves exported from the drop tower are plotted in Figures 2.9(b), 2.10(b) and 2.11(b). Comparing with the center displacement history curves, the oscillation on the load curves correlate well with the oscillations on the out-of-plane displacement curves. This implies that the LVI-induced damage affects both the load and deformation collected from the testing system. Out-of-plane deformation fields are presented in Figures 2.9(c), 2.10(c) and 2.11(c), where the three rows correspond to the three impact energy levels and the three columns correspond to three time points. The three time points are also indicated by the black dashed lines in Subfigures (a) and (b).

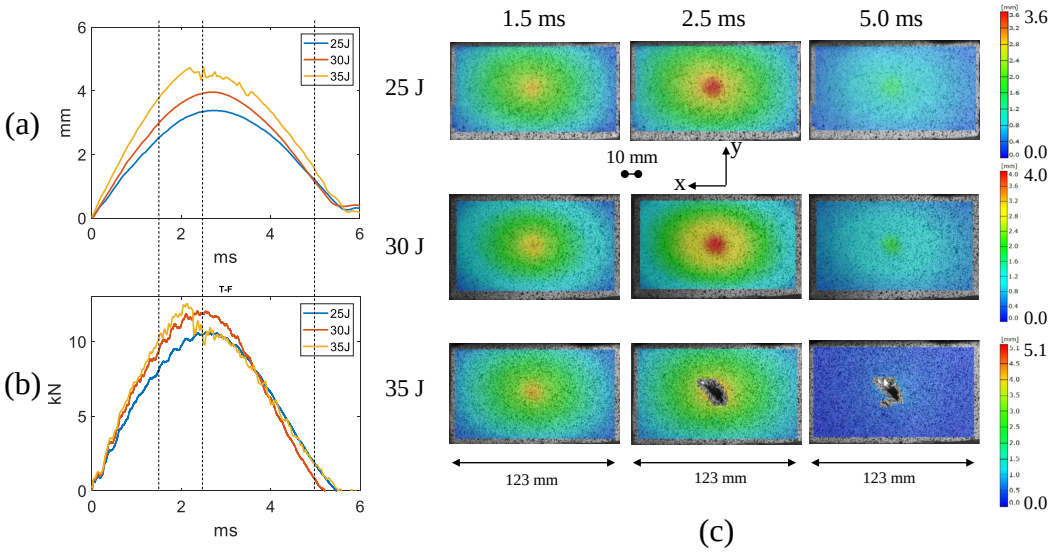

Figure 2.10: 3D DIC results of the layup B LVI tests: (a) out-of-plane center displacement histories, (b) impact load histories, and (c) out-of-plane deformation fields.

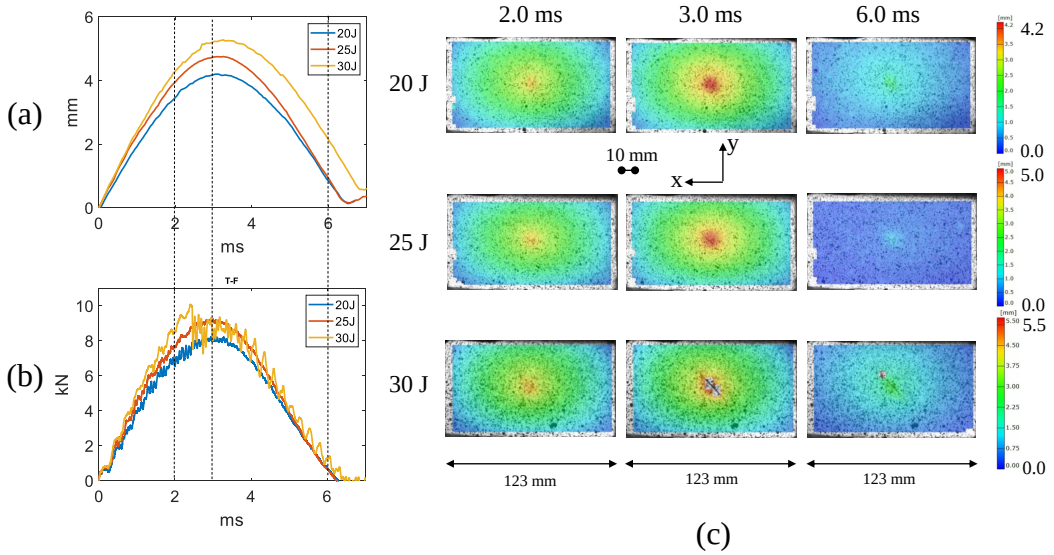

Figure 2.11: 3D DIC results of the layup C LVI tests: (a) out-of-plane center displacement histories, (b) impact load histories, and (c) out-of-plane deformation fields.

2.3.1.2 LVI-induced Damage

Ultrasound C-scanning was conducted for the impacted samples, as shown in Figures 2.12 to 2.14. The time-of-flight (TOF) data was used for plotted, where the TOF value indicated the distance of detected damage to the top surfaces of the samples. The color code varying from black to red means that the characterized damage gets further from the top surface. Figure 2.12 shows that the overall size of LVI-induced damage grows as the impact energy increases. The damage footprints in Figure 2.12 are similar in shape, being longer along the x-axis. This shape is due to the relatively high percentage of 0° plies of this [50/40/10] layup. A laminate panel with a high number of 0° plies under impact loading would have many matrix cracks along the 0° degree direction, which would facility the delamination to form along the 0° degree direction. The areas of the damage footprints as a function of impact energies are presented in Figure 2.12 (d).

The damage footprints of layup B samples are shown in Figure 2.13. The damage sizes are observed to increase with the escalating impact energies. The shape of damage footprints are almost circular, due to the fact that the stacking sequence of layup B is quasi-isotropic. The reason for the formation this type of circular impact damage footprints is similar to that explained for layup A: the direction of the matrix cracks of layup B samples are evenly distributed, and therefore the delamination bounded by the matrix cracks at all the interfaces, after overlapped together, would form an almost circular shape. The damage shape in Figure 2.13 (c) is various from that in Subfigures (a) and (b), in the sense that a black sticking-out part is seen, which correspond to delamination induced by the fiber kinking near the top surface of the sample. This pattern can be observed better in the μCT slices displayed in the latter part of this section.

The damage footprints of layup C samples are shown in Figure 2.14. The overall damage size is observed to increase as the impact energy increases. The damage

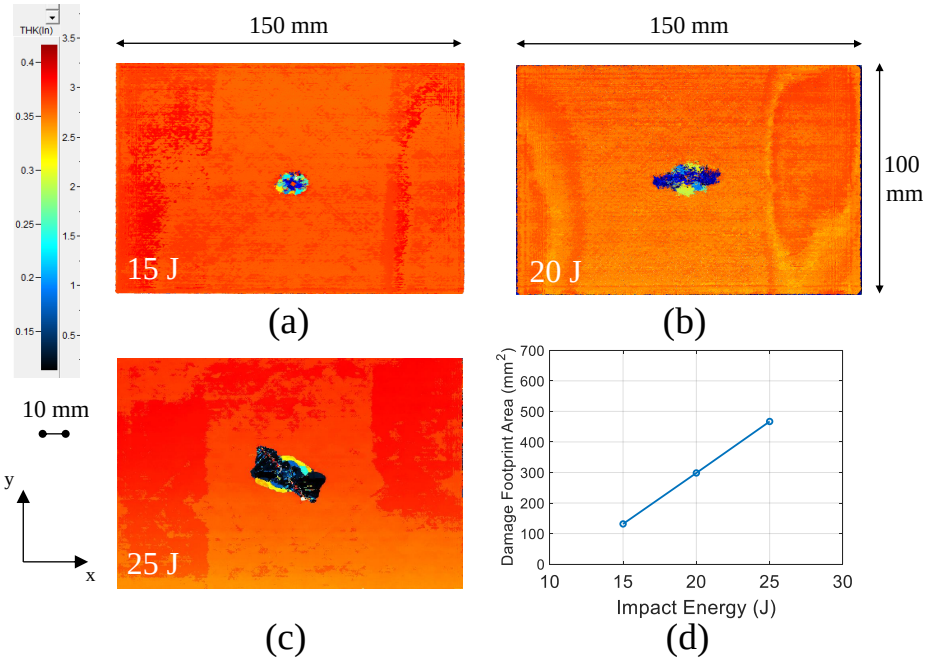

Figure 2.12: Ultrasound C-scans of layup A samples: (a) impacted with 15 J, (b) impacted with 20 J, and (c) impacted with 25 J.

shapes are similar to each other. The damage areas are plotted as a function of impact energies in Figure 2.14 (d).

The overall areas of LVI-induced damage footprints of the three layups are plotted collectively in Figure 2.15. The blue, orange, and yellow curves represent data of layup A, B, and C samples. Overall, the upward trend of the damage areas with the increasing impact energies is obvious. At the same energy level, 25 J, the damage footprint areas of layup B, A, and C are in ascending order. The reason for layup B having the smallest damage footprint is that layup B is the thickest stacking sequence, hence being more impact resistant.

X-ray μCT scanning was performed for each layup with two impact energy levels. Since the samples impacted with the higher energy levels usually have more enriched damage modes and patterns, the μCT slices of a layup A sample impacted with 25 J, a layup B sample impacted with 35 J, and a layup C sample impacted with 30 J are presented in Figures 2.16 to 2.18. The μCT slices normal to the thickness direction

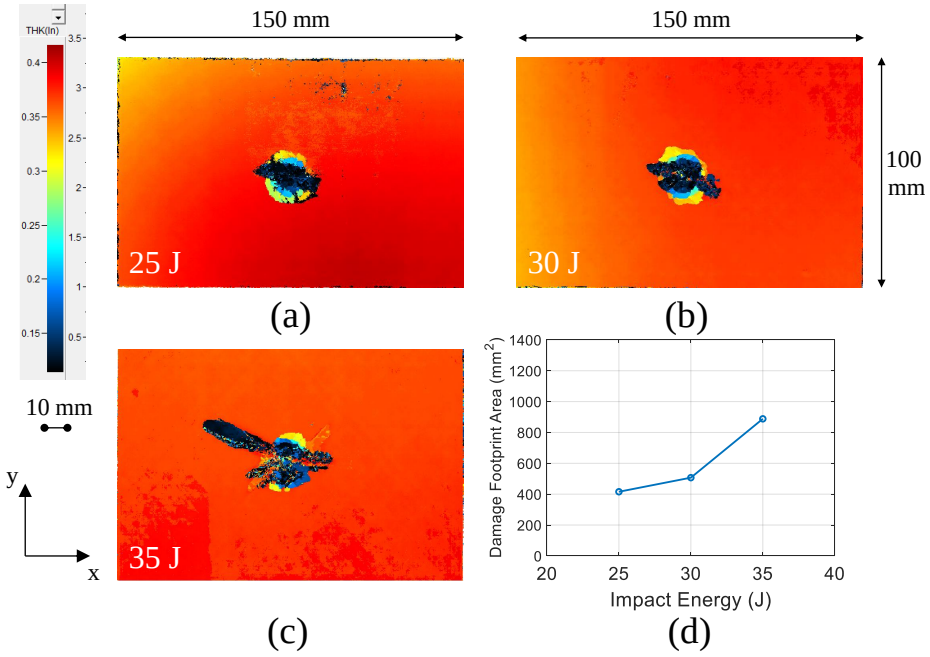

Figure 2.13: Ultrasound C-scans of layup B samples: (a) impacted with 25 J, (b) impacted with 30 J, and (c) impacted with 35 J.

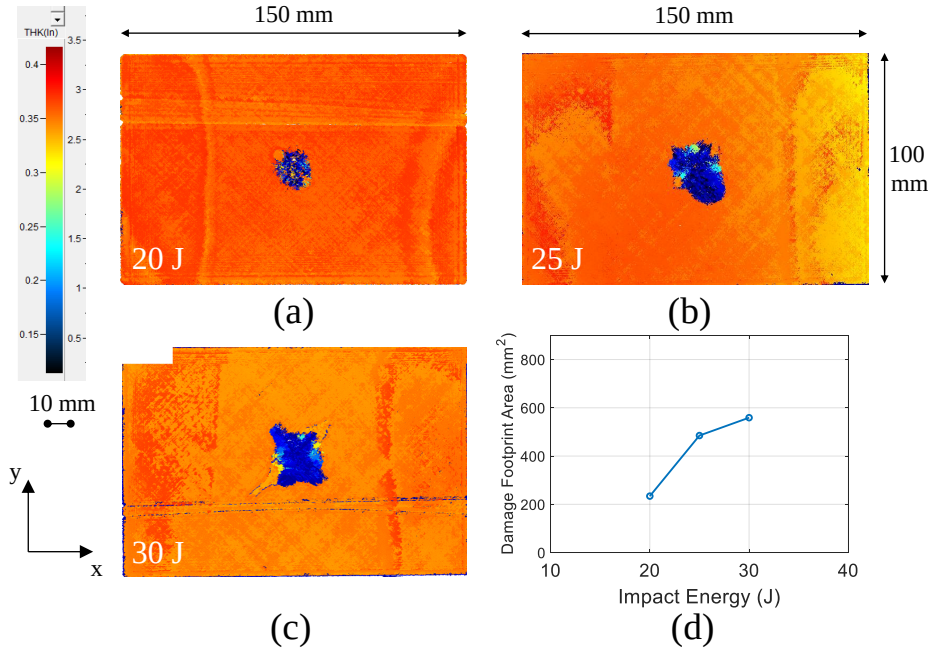

Figure 2.14: Ultrasound C-scans of layup C samples: (a) impacted with 20 J, (b) impacted with 25 J, and (c) impacted with 30 J.

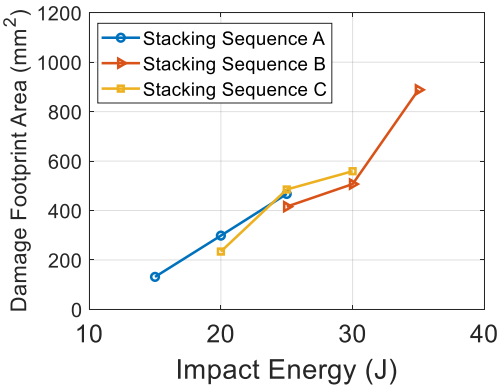

Figure 2.15: Areas of the C-scans.

(face-on) of the layup A sample are shown in Figure 2.16. The voxel size of the μCT scanning was 33 μm $\times$ 33 μm $\times$ 33 μm. The top surface of the scanned sample corresponds to slice no. 47. The bottom surface corresponds to slice no. 148. 17 slices are presented in the figure with the interval of the slice number being 5 or 6, such that these slices would relate to the interfaces of the sample. As seen in the figure, in slices no. 47 to 67, fiber kinking and delamination are observed. The damage pattern observed in slice no. 52 correlates well with the damage displayed in Figure 2.12(c). In slices no. 73 to 108, fan-shaped delamination is observed, bounded by matrix cracks. In slices no. 114 to 148, delamination together with extensive matrix cracking are observed. The damage near the sample bottom, as displayed in slices no. 142 and 148 is observed to be extensive, correlating well with the loss of correlation due to fiber tensile rupture in the 3D DIC image shown in figure 2.9(c).

The face-on slices of the layup B sample impacted with 35 J are presented in Figure 2.17. The top surface of the sample is shown in slice no. 113 and the bottom surface is shown in slice no. 248. From slices no. 113 to 143, fiber kinking and delamination are observed. The delamination with an extensive sticking-out pattern found in slice no. 120 correlates well with the C-scan shown in Figure 2.13 (c). Fan-shaped delamination together with matrix cracking are seen in slices no. 148 to 208. Near the sample bottom, in slices no. 214 to 248, delamination with large-scale

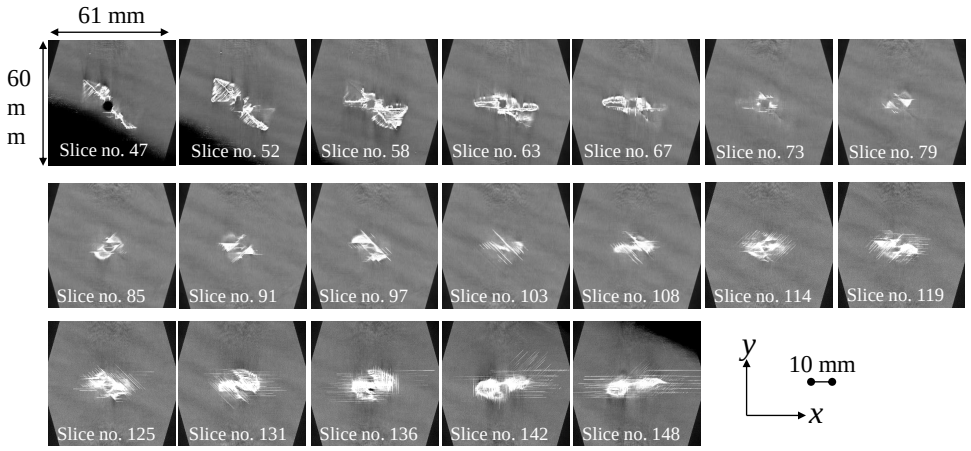

Figure 2.16: X-ray μCT slices of a layup A sample impacted with 25J.

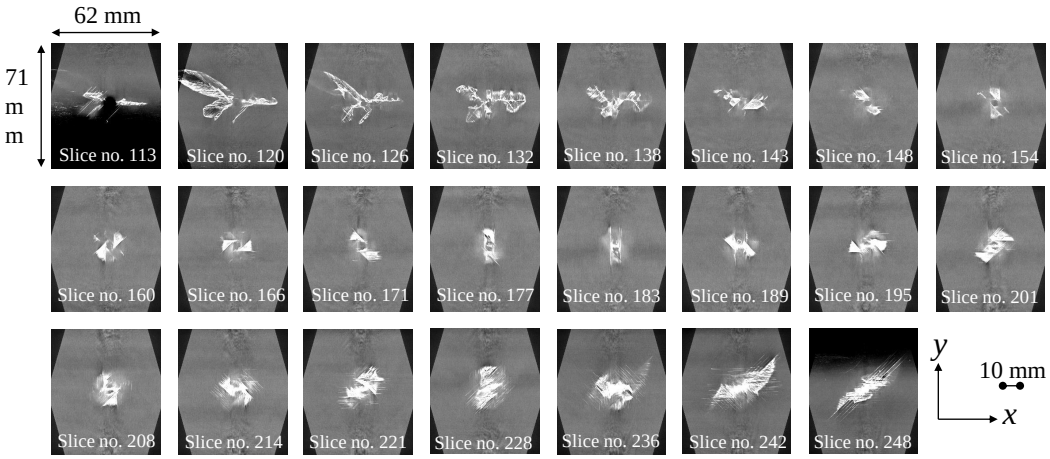

Figure 2.17: X-ray μCT slices of a layup B sample impacted with 35J.

matrix cracking are observed. In the last two slices, fiber tensile rupture is seen, highly similar to the area with the loss of 3D DIC correlation shown in Figure 2.10 (c).

The face-on slices of the layup C sample impacted with 30 J are displayed in Figure 2.18. The slices correspond to the the sample top and bottom surfaces are no. 72 and 172. Fiber kinking and delamination are seen in slices no. 72 to 93. Fan-shaped delamination is observed in slices no. 98 to 147. Peanut-shaped delamination is spotted in slices no. 109, 115, 125, and 132. Starting from slice no. 132, extensive

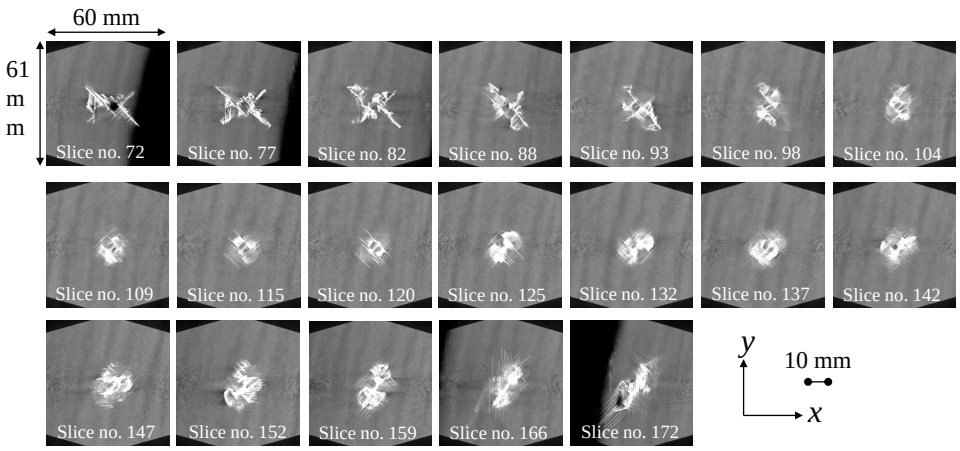

Figure 2.18: X-ray μCT slices of a layup C sample impacted with 30J.

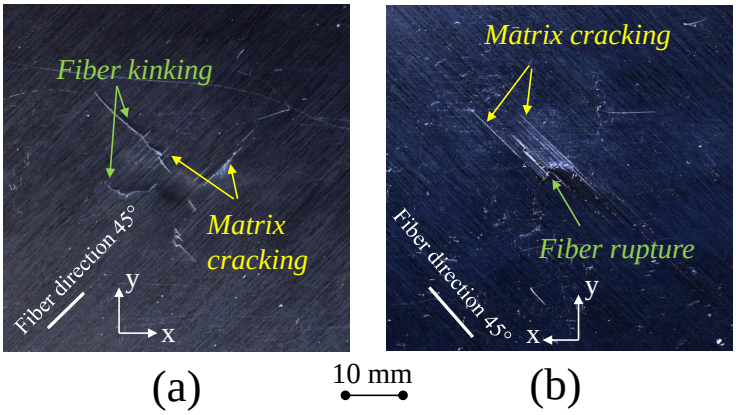

Figure 2.19: Post-impact observation of a layup B sample impacted with 35 J: (a) the impacted side, and (b) the non-impacted side.

matrix cracking is seen. Severe damage is observed in the last two slices, correlating well with that shown in Figure 2.11 (c).

Representative photos of LVI-induced damage on the top and bottom surfaces of a layup B sample impacted with 35 J energy are shown in Figure 2.19. Fiber compressive kinking, matrix cracking, and fiber tensile rupture can be found in the figure. The surface damage correlates well with the μCT slices in Figure 2.17.

In this section, LVI experimental results of three stacking sequences of the T800s/3900-2B material system have been presented. The sample in-plane size is 150 mm $\times$ 100 mm. For each layup, three impacted energy levels have been tested. The test results

are highly repeatable, demonstrating the validity of the tests. At the two lower energy levels, the load responses are smooth while at the highest energy level, large-scale load oscillations are seen, which are caused by bottom-ply fiber tensile rupture and ply-splitting. The out-of-plane deformation of the samples have been captured by high-speed 3D DIC, from which the fiber rupture and ply splitting can be observed. Critical LVI parameters such as the peak load, maximum impactor displacement, residual displacement, and energy absorption have been summarized.

LVI-induced damage has been characterized with ultrasound C-scanning and X-ray μCT scanning. The damage footprints of layup A, B, and C samples are different in shape. When impacted at the same energy level of 25 J, the damage footprint of the layup B sample is the smallest, mainly due to the fact that layup B (24-ply) is thicker than layup A (20-ply) and C (20-ply). The difference between the overall damage of the three layups is relatively small. High-resolution μCT scanning has revealed many details of the LVI-induced damage, including fiber kinking, fan-shaped and peanut-shaped delamination, and fiber tensile rupture and ply-splitting near the sample bottom surfaces. The interaction between damage modes and the damage mechanisms will be discussed in detail in Section 2.3.2.

2.3.2 Mechanisms of LVI-induced Damage

In this section, mechanisms of LVI-induced damage will be illustrated in detail with the high-resolution μCT scanning of a layup B sample impacted with 25 J energy. The reason for choosing this layup with this impact energy is that the damage pattern of this layup is unique, in the sense that the fan-shaped delamination keeps rotating as the μCT slice approaches the sample bottom surface from the top surface. This pattern is referred to as the "rotating-fan" damage. In order to demonstrate the "rotating-fan" damage to the best extent, the μCT slices of the layup B sample impacted with 35 J energy, as shown in Figure 2.17 are not discussed in this section

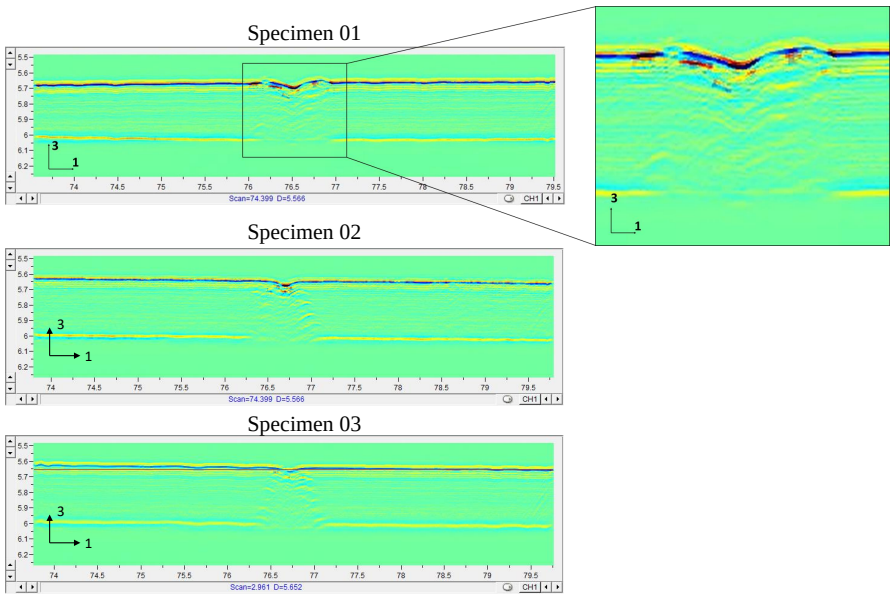

Figure 2.20: B-scanning results of three layup B samples impacted with 25 J energy.

due to the severe damage modes taking place near the sample's top and bottom surfaces. Instead, a layup B sample impacted with 25 J is studied.

Along with the ultrasound C-scanning presented in Figure 2.13, ultrasound B-scanning was performed for three layup B samples impacted with 25 J. The B-scanning results are shown in Figure 2.20. B-scanning provides an edge-on views cutting through the centers of the samples. As seen in Figure 2.20, most parts of the impacted samples still remain flat while the impacted central areas, as magnified in Subfigure (a), show curved layers. These curved layers correspond to permanent indentations on the samples caused by LVI.

Due to the permanent indentation on the μCT scanned sample, the μCT slices near the top surface (impacted side) of the sample might cut through multiple layers of the laminate, as illustrated in Figure 2.21. Therefore, it is only strict to claim that a face-on slice represents the ply-by-ply and interface-by-interface damage when it is away from the top and bottom surfaces. For each slice presented in this section, the distance d from the current slice to the very top of the plate is measured and only in this way can a slice be attached to a ply or an interface. The displacement d is

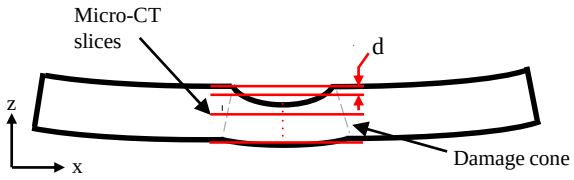

Figure 2.21: The definition of the distance d attached to a slice

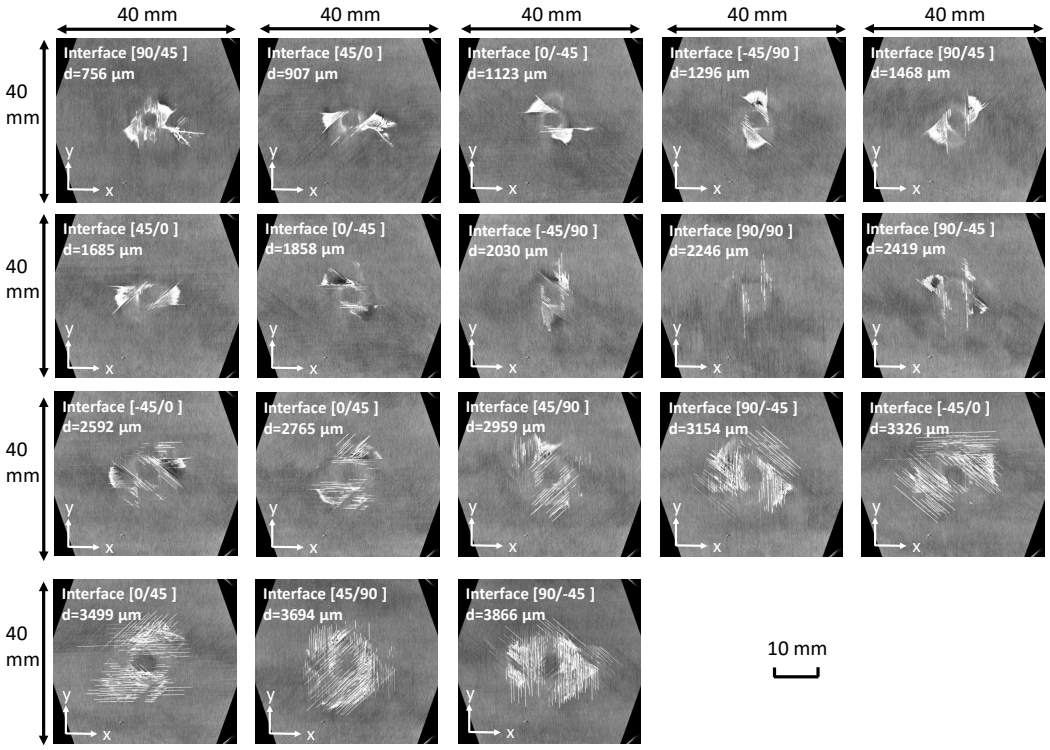

Figure 2.22: Delamination slices of the μCT scanning.

illustrated in Figure 2.21.

The face-on slices with clear fan-shaped delamination are presented in Figure 2.22. The "rotating fan" is due to the stacking sequence of layup B being quasi-isotropic. As seen in Figure 2.22, the "fan" keeps rotating as d increases. With $d = 2246\mu m$, no delamination is seen, due to the neighboring plies of this interface are of the same fiber angles of 90°, and the interfacial shear stress at this interface is minimal compared to that at the other interfaces.

In Figure 2.23, the slices demonstrating matrix cracking are provided. To enhance

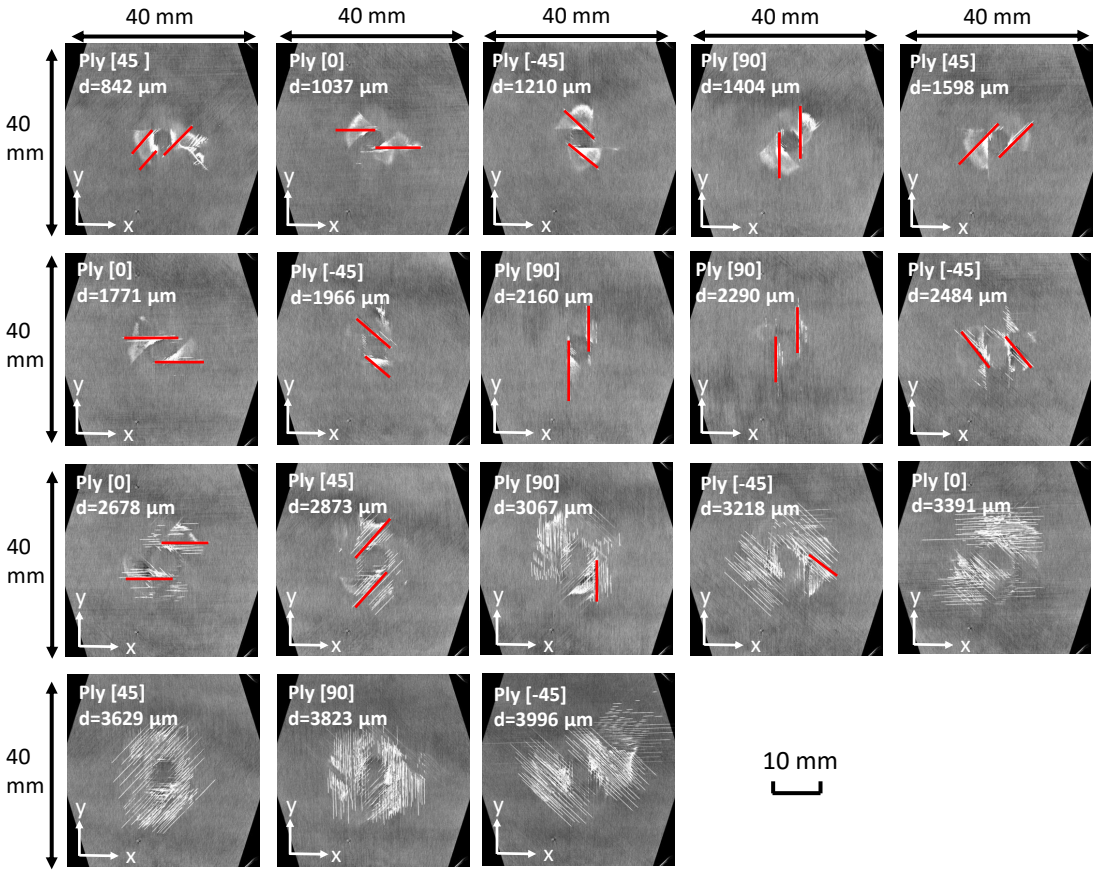

Figure 2.23: Matrix cracking slices of the μCT scanning.

the visualization, in some slices the matrix cracking is noted with red solid lines. When d becomes greater than 2873 μm, the number of matrix cracks significantly increases. Similar to the delamination, the matrix cracking is along the fiber direction and keeps rotating.

Besides the slices in the middle of the sample clearly showing the ply-by-ply and interface-by-interface damage, slices near the top surface of the sample are presented in Figure 2.24. Subfigure (a) shows the slice 86 μm below the top surface, corresponding to the first 45° ply of the laminate. The two bold lines indicate the fiber kinking perpendicular to the fiber direction and the thin lines represent the matrix cracking parallel with the fiber direction. The reason for correlating these two bold lines with

fiber kinking is three-fold. First, the two lines are perpendicular to the fiber direction of the current 45° ply. Second, since it is the topmost ply, naked-eye observation shows that these two bold lines are fiber kinking. Third, as explained later in Figure 2.25, fiber kinking tends to induce out-of-plane deformation, which would facilitate the penetration of the dye, rendering fiber kinking more salient than matrix cracking in μCT scans. In Figure 2.24 (a), it is also observed that the matrix cracking is well spaced, along the fiber direction. Enriched damage modes can be found in Figure 2.24 (b). The red dotted lines with normal-font words indicate the fiber kinking and matrix cracking from the topmost 45° ply. The green dashed lines with italic words indicate the fiber kinking and matrix cracking on the second 0° ply. The blue solid lines together with underlined words indicate the fiber kinking on the third -45° ply. Large-scale delamination is found in Figure 2.24 (b). The delamination is enclosed by the fiber kinking and matrix cracking. In Figure 2.24 (c), fiber kinking from the first 45° ply, second 0° ply and the -45° ply is observed. Matrix cracking on the third ply is seen as well. The delamination is again found to be enclosed by fiber kinking and matrix cracking.

The damage mechanisms close to the top surface of the sample are disclosed by Figure 2.25. In the figure, the red solid lines represent fiber kink band, the blue dashed lines represent transverse matrix cracking and the grey area indicate delamination induced by fiber kinking and matrix cracking. These three damage modes, including fiber kinking, matrix cracking, and delamination, interact with each other, as reflected by Figure 2.24. As shown in Figure 2.25, the fiber compressive kink band deforms out-of-plane, hence it is favorable for delamination to initiate and grow. This explains that the delamination in Figure 2.24 (b) is significantly larger than that in Figure 2.22, which is only induced by matrix cracking.

Damage mechanism in the middle part of the plate can be explained by carefully reviewing the slices shown in Figure 2.26. In Figure 2.26 (a) and (c), matrix cracking

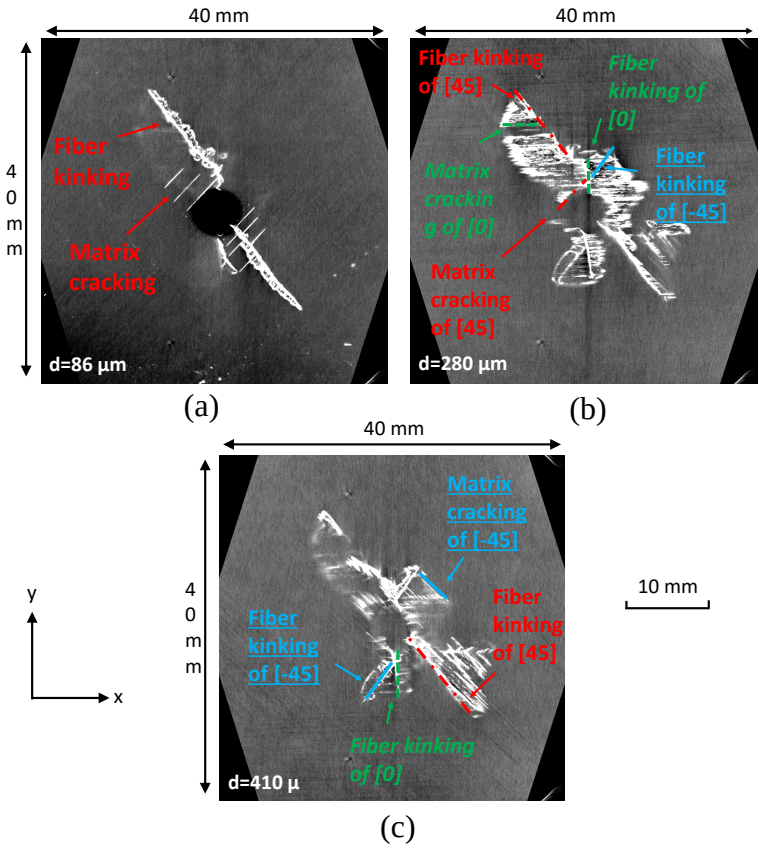

Figure 2.24: Slices of the top part of the specimen: (a) the topmost slice, (b) the slice 0.2 mm under the top slice, and (c) the slice 0.26 mm under the top slice.

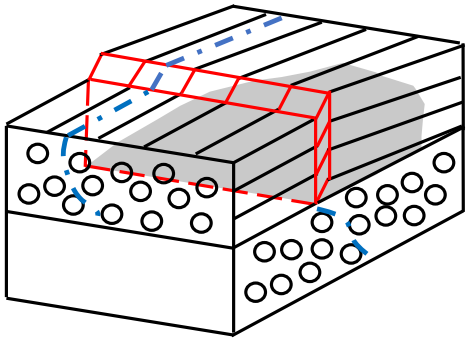

Figure 2.25: A sketch of the mechanism of damage modes interaction in the top part of the specimen.

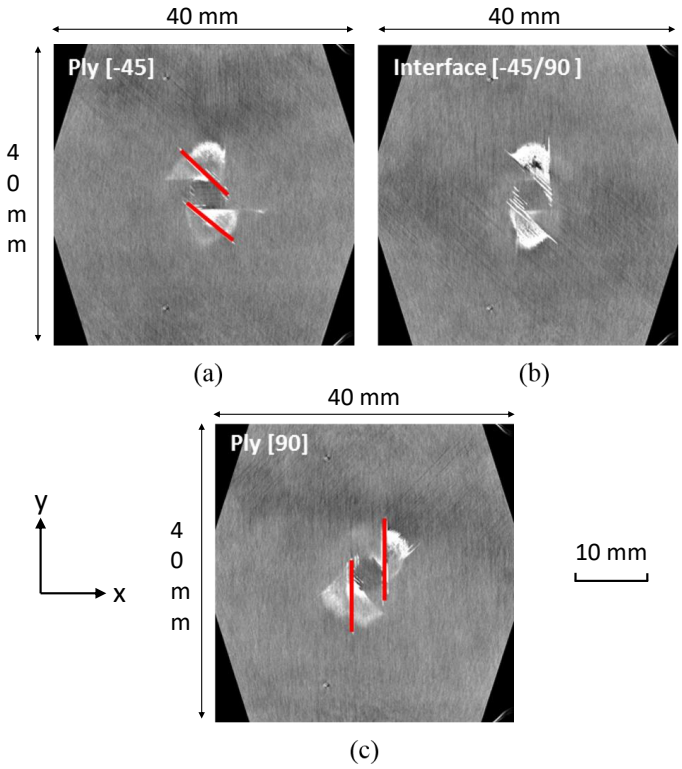

Figure 2.26: Slices of the middle part of the specimen: (a) the slice for the -45° ply, (b) the slice for the interface [-45/90], and (c) the slice for the 90° ply.

is denoted with red solid lines and the delamination between these two layers is shown Figure 2.26 (b). From the subfigures, it is clear that the delamination is enclosed by the matrix cracking in the adjacent plies. Since no fiber kinking is seen in the middle part of the sample, the damage pattern is less complicated than that in Figure 2.24. The interaction between damage modes only take place between matrix cracking and delamination. The mechanism of the interaction is illustrated in Figure 2.27. Only a quarter of the sample is drawn to reveal the internal damage. In Figure 2.27, the red double-compound lines represent the matrix cracking of the -45° ply. The green bold lines represent the matrix cracking of the 90° ply. The grey fan-shaped area represents the delamination triggered and enclosed by the matrix cracking happening in the adjacent layers.

Damage patterns near the bottom surface of the sample are shown in Figure

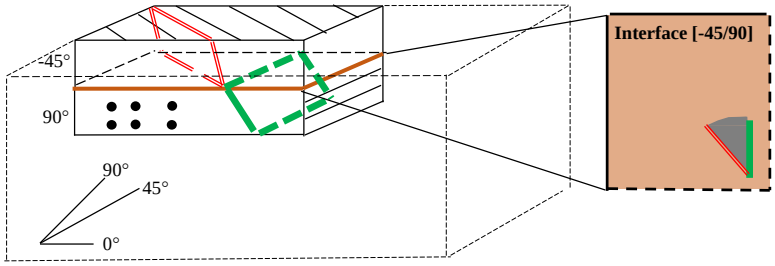

Figure 2.27: Sketch of the mechanism of damage modes interaction in the middle part of the specimen

2.28. It is observed that the matrix cracking is well spaced and extensive. When the sample bends, the bottom plies experience relatively high tensile stress and therefore, extensive matrix cracks open. In Figure 2.28 (b), the delamination between the bottommost 45° and the adjacent 0° ply is seen. The delamination has less clear boundaries than the fan-shaped delamination in Figure 2.26. The reason is that, in the middle part of the plate, only one matrix cracking of each ply serves as the boundary for the delamination, while for the bottom part, multiple matrix cracks in one ply can initiate the delamination. Therefore, the "fan" in Figure 2.28 is not as well-bounded as that in Figure 2.26. The damage mechanism of the bottom part of the plate is similar to that in the middle part, and therefore is not drawn but is referred to Figure 2.27.

The edge-on μCT slice cutting through the center of the sample is shown in Figure 2.29. The "pine tree" damage pattern as mentioned in Section I is observed with a central damage-free cone. The face-on slices are correlated with the edge-on slice in Figure 2.29 at several locations. In Figures 2.29 (b) and (d), the delamination corresponds to the horizontal lines in the edge-on view. In Figure 2.29 (c), the extensive matrix cracking is found as spaced dots in the sectional view. A bright area in the edge-on slice near the top correlates to the top-ply fiber kinking as shown in Figure 2.29 (e). Since the fiber kink band deforms out-of-plane, it is easier for the

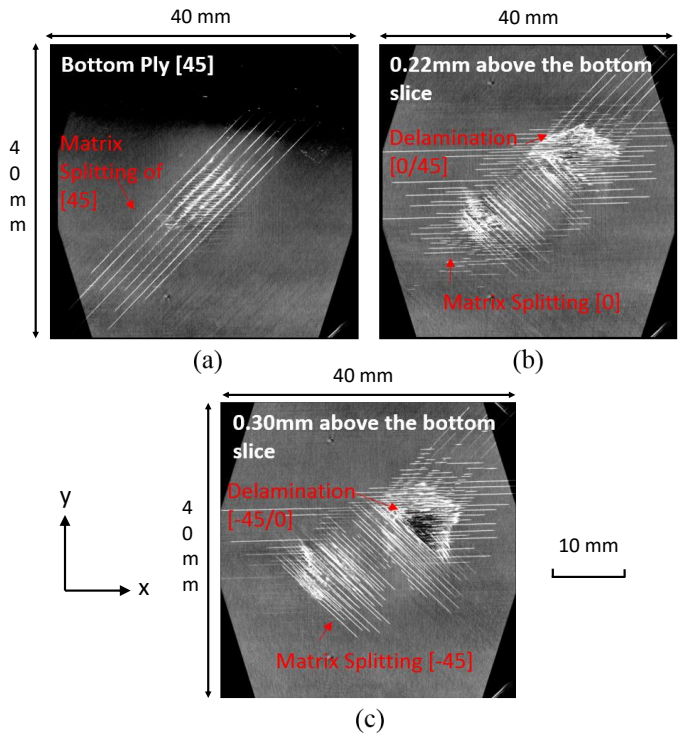

Figure 2.28: Slices of the bottom part of the specimen

dye to penetrate into the panel, and therefore the area is excessively bright.

In this section, μCT slices of a layup B sample impacted with 25 J have been analyzed in detail to reveal the LVI-induced damage mechanisms. The damage interaction patterns in the top, middle, and bottom parts of the sample have been presented. The featured "rotating-fan" damage pattern has been illustrated, which is caused by the interaction between matrix cracking and delamination. Illustrative sketches of the damage mechanisms are provided.

2.3.3 LVI-induced Damage of a highly-anisotropic laminate

In this section, experimental of the LVI on a highly anisotropic laminate with the material system T800s/3900-2B are presented. The stacking sequence is $[0/90/0/90_9]_s$. Other than the stacking sequence, the experimental conditions are identical to that described in Section 2.3.1. Three samples were tested to gain repeatable results. The

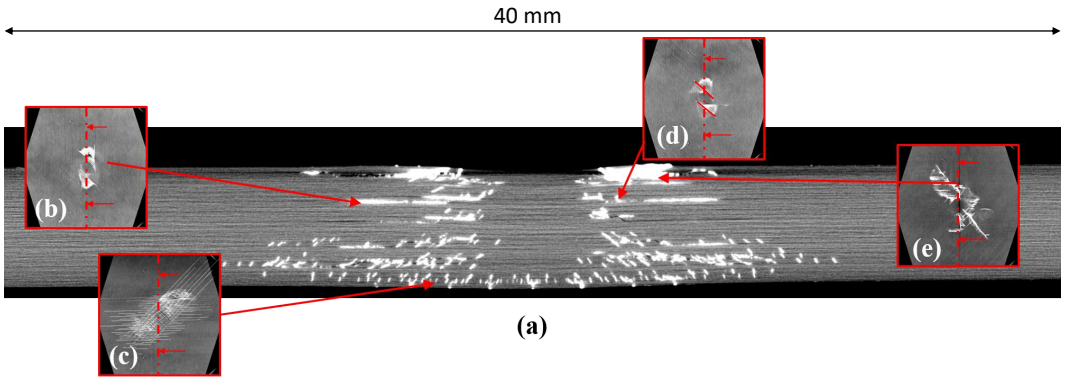

Figure 2.29: μCT slices illustrating the "pine tree" damage pattern: (a) the edge-on μCT slice providing a sectional view of the "pine tree" pattern, (b) the face-on slice showing the corresponding delamination on the "pine tree", (c) the face-on slice showing the corresponding delamination on the "pine tree", (d) the face-on slice showing the corresponding fiber kinking on the "pine tree", and (e) the face-on slice showing the corresponding matrix cracking on the "pine tree".

reason to present the test results of this layup alone in this section is that this stacking sequence is unique, in the sense that the layup resembles a sandwich composite panel. The [0/90/0] outer layers serve as the "face sheet" while the inner 18 plies of 90° layers serve as the "core". The LVI-induced damage pattern is special and significantly different than that demonstrated in Section 2.3.1. The experimental results in this section, especially the characterized damage pattern, can be regarded as a challenging LVI case to examine and calibrate computational models.

It should be pointed out that similar previous investigations were conducted for laminated and sandwich composite beams. Topac et al. performed an experimental and computational study of the damage process in CFRP beams under LVI loading [113]. The stacking sequence studied was $[0_5/90_3]_s$. Thorsson et al. studied three-point bending (3PB) induced damage of sandwich composite beams [114]. However, experimental study on this "sandwich-like" composite panel has not been performed yet.

The load-time and load-displacement curves of the three samples are shown in Figure 2.30. The test results are highly repeatable, demonstrating the validity of

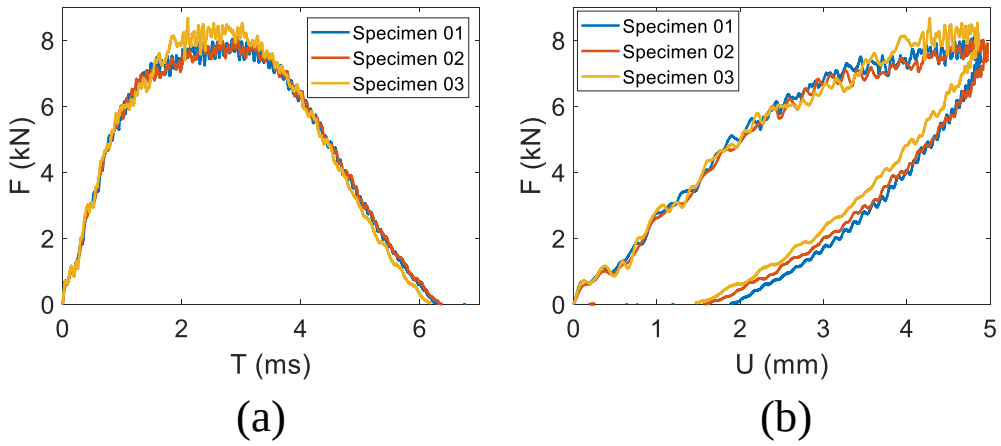

Figure 2.30: Load responses of the LVI tests: (a) load-time curves, and (b) load-displacement curves.

the tests. The test curves are smooth, without any large-amplitude oscillations. As explained in Section 2.3.1, the smoothness of the load curves implies that severe damage modes such as fiber tensile rupture did not take place during the LVI tests.

After the LVI tests, the three samples were inspected firstly with Nikon cameras. On the top surfaces (impacted side) of the samples, damage features such as fiber kinking and matrix cracking are observed, as shown in Figure 2.31 (a)-(c). In the subfigures, compressive fiber kinking perpendicular to the fiber direction of the topmost 0 ° ply is marked with yellow dashed lines. Matrix cracking along the fiber direction is denoted with blue dashed lines. At the non-impacted sides of the samples, bulging out areas were spotted. Light sources were placed at an angle to demonstrate the bulging out areas on the samples clearly, as shown in Figure 2.31 (d)-(f).

The three samples were subjected to ultrasound C-scanning using a Dolphicam 2 handheld scanner. The 5 MHz transducer was placed on the impacted and non-impacted sides of the samples to detect LVI-induced damage. The TOF data was used for plotting the overall damage footprints with information about the depth of damage. The characterized damage footprints are shown in Figure 2.32. The first row of the figure are the scanning results from the impacted sides. The second

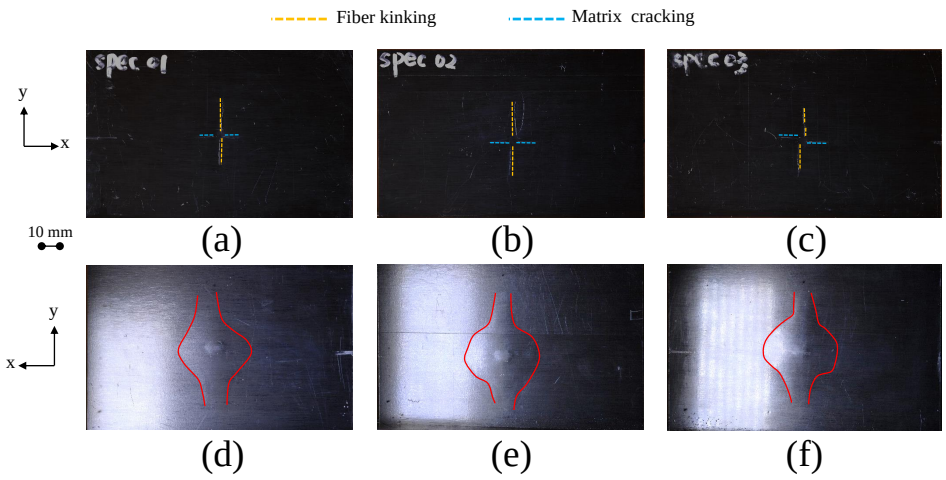

Figure 2.31: Inspection on the impacted and non-impacted sides of the samples.

row include results scanned from the non-impacted sides. The LVI-induced damage footprints are very similar in terms of shape and size among the three samples. The color code varying from red to blue represents the distance of the scanned damage to the transducer varying from small to large. From the first row, close to the samples' impacted sides, the red parts are in the shape of a cross, longer along the y-axis and shorter along the x-axis. As the location of damage approaches the non-impacted sides, the damage is similar to the shape of a kidney. This "kidney" shaped damage pattern is observed more clearly in the second row of Figure 2.32. Due to the damage closer to the non-impacted side being larger than that closer to the impacted side, the "cross" damage is hidden by the "kidney" damage in the second row of images. This is usually described as the "overshadowing" effect of ultrasound C-scanning.

X-ray μCT was performed for one of the three impacted samples using a Zeiss Xradia Versa 520 system. The face-on μCT slices are shown in Figure 2.33. In the figure, as the slice number decreases, the location of the slice approaches the bottom surface of the sample from the top surface. The parameter d represents the distance from a slice to the top surface of the sample. The slices in Figure 2.33 were chosen such that they correspond to the interfaces. The "cross" damage observed in Figure 2.32 is found to be composed of matrix cracking and fiber kinking, as shown in slice

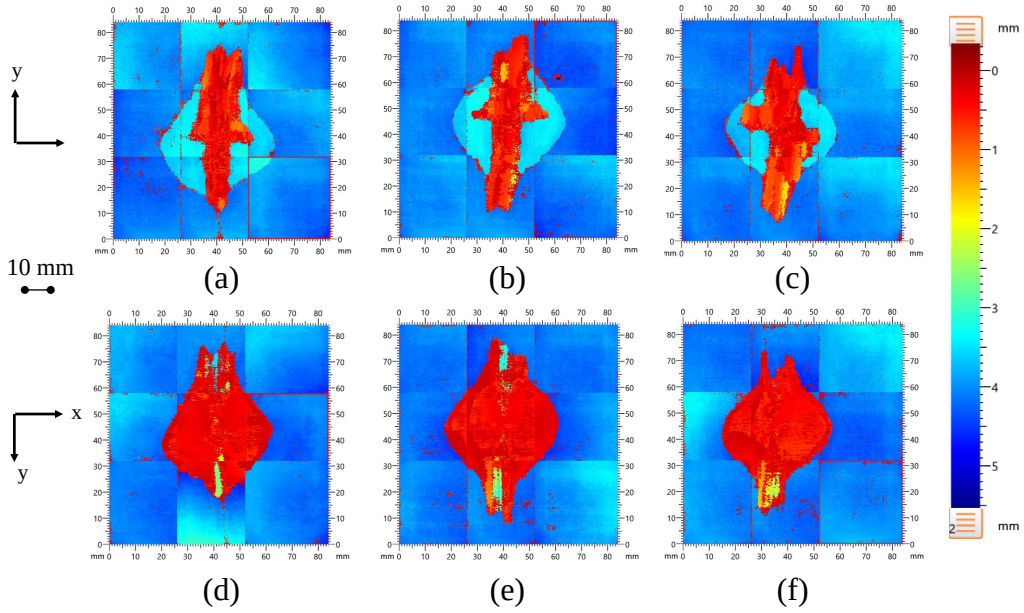

Figure 2.32: Ultrasound C-scanning of the three impacted samples, scanned from: (a) the impacted side of sample 01, (b) the impacted side of sample 02, (c) the impacted side of sample 03, (d) the non-impacted side of sample 01, (e) the non-impacted side of sample 02, and (f) the non-impacted side of sample 03.

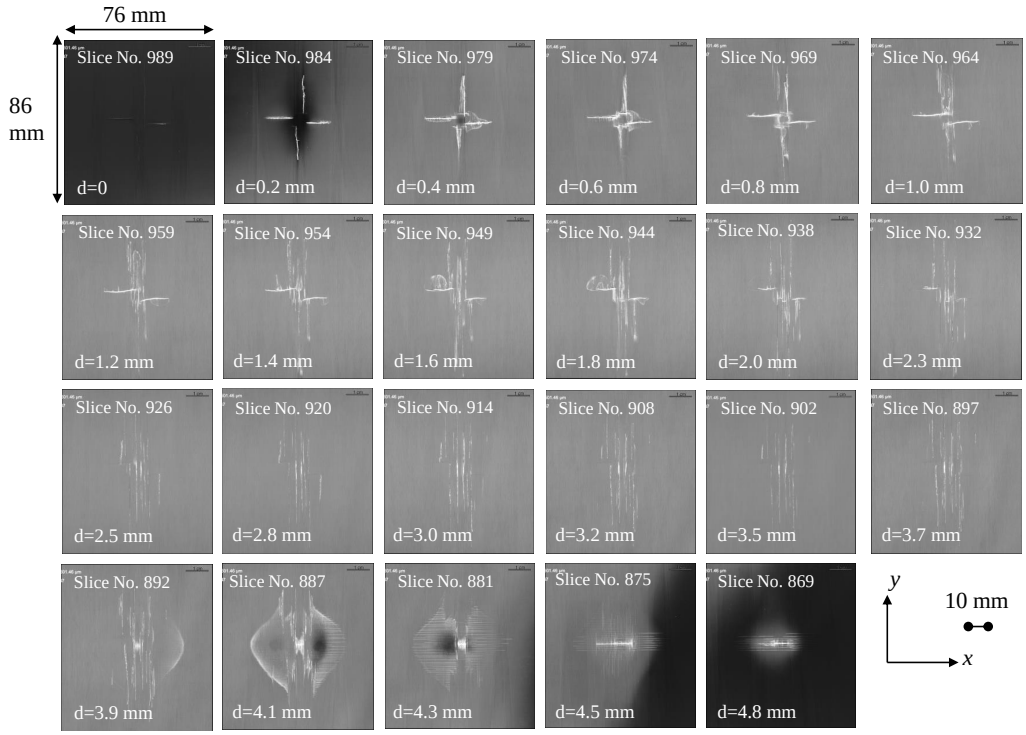

Figure 2.33: Face-on μCT slices of specimen 03.

no. 984 to 944. Only matrix cracking along the y-axis can be seen in slices no. 938 to 897. These correspond to the matrix cracking in the "core" of this sandwich-like $[0/90/0/90_9]_s$ laminate. In slices no. 892 to 881, the "kidney" damage pattern is observed. The "kidney" delamination seems to be darker in its center. This is due to the fact that the dye penetrant containing Zinc Iodide could not penetrate sufficiently into the center of this large delamination. Near the bottom surface of the sample, in slices no. 881 to 869, matrix cracking is found with a clear spacing. The well-spaced matrix cracking is similar to that in Figure 2.23, caused by relatively high transverse tensile stress near the bottom of the sample during the LVI.

Edge-on μCT slices of sample 03 are shown in Figure 2.34. The parameters d is the distance of a slice to the mid-section of the sample. Seven representative slices are presented in Figure 2.34. In slice no. 917, which cut through the center of the sample, slanted matrix cracks are observed. A damage-free cone is seen at

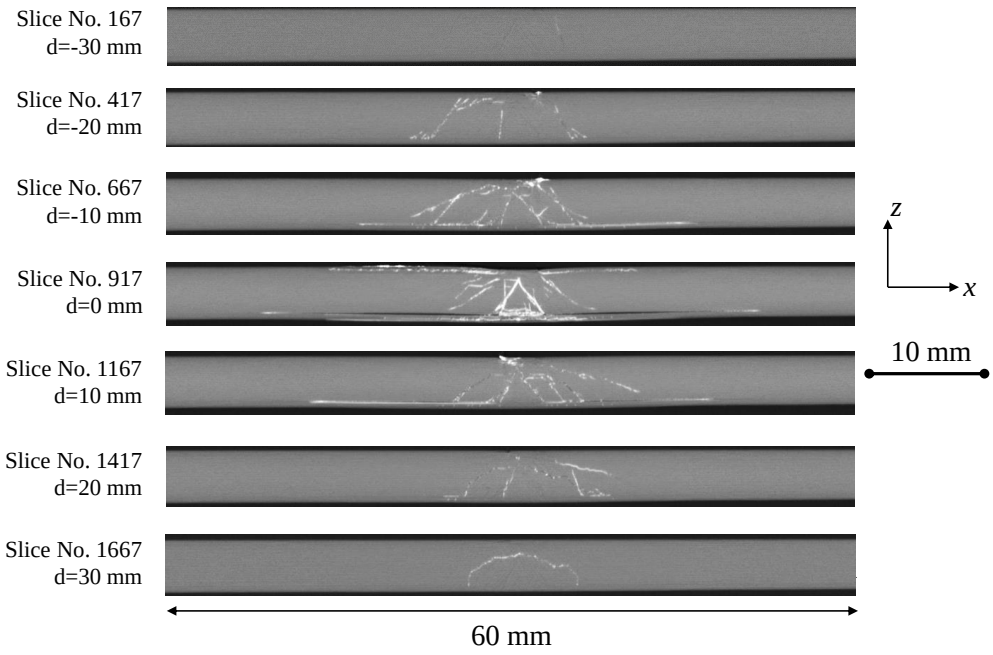

Figure 2.34: Edge-on μCT slices of specimen 03.

the center of the slice. Near the bottom surface, extensive black voids are spotted, corresponding to the "kidney" delamination, as shown in Figure 2.33. This damage structure was also reported in laminated and sandwich composite beams under 3PB loading [113, 114, 115]. The similar damage structure can also be seen in slices no. 417, 667, 1167, and 1414 in Figure 2.34. As the absolute value of d increases, the damage-free cone becomes smaller, shorter along the x-direction, corresponding well with the damage footprints shown in Figure 2.32.

To better visualize the LVI-induced damage, voxels in the μCT reconstructed 3D model with relatively high gray-scale values were segmented out using the software Dragonfly. A higher gray-scale value corresponds to a better penetration of Zinc Iodide. The segmented damage morphology is shown in Figure 2.35. The "kidney" damage is shown with high-resolution details. Figure 2.35 (b) correlates very well with the C-scanning in Figure 2.32 (c). From Figure 2.35 (c), the "cross" shaped damage near the top surface of the sample and the "kidney" damage pattern near the bottom surface of the sample are revealed clearly.

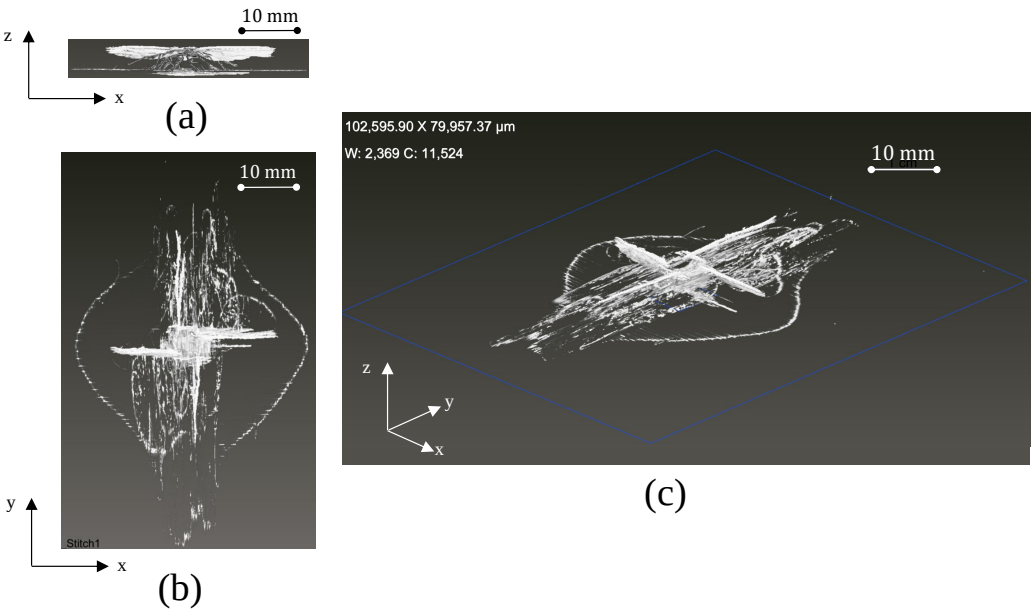

Figure 2.35: μCT scanned damage after segmentation observed: (a) in the x-z plane, (b) in the x-y plane, and (c) with a 3D view.

In this section, experimental LVI results of a "sandwich-like" layup have been presented. The damage is unique, referred to as the "kidney" damage. This section poses a challenging LVI case to examine and calibrate computational models.

2.4 Experimental LVI Study with the Effects of Panel Size

In this section, experimental results of the investigations on the panel size effects of the LVI behavior are presented. The material system is IM7/977-3. Two stacking sequences have been tested, each with three sample in-plane sizes and two thicknesses (number of plies). The stacking sequences are $[45/\text{-}45/0/90/0/0]_{ns}$ and $[45/0/\text{-}45/90]_{ns}$, where n is decided by the total number of plies of the layup. For example, if $[45/\text{-}45/0/90/0/0]_{ns}$ is a 24-ply laminate, n is equal to 2. The two layups are named as L1 and L2, corresponding to $[45/\text{-}45/0/90/0/0]_{ns}$ and $[45/0/\text{-}45/90]_{ns}$. The sample in-plane sizes are named as S, M and L corresponding to 152.4 mm x 101.6 mm, 177.8 mm x 177.8 mm, and 330.2 mm x 330.2 mm. The two thicknesses of the samples correspond to 24-ply and 48-ply. The average layer thickness is 0.13 mm.

For the conciseness of this section, a sample according to its layup, in-plane size, and thickness is referred to as L1/L2-S/M/L-24/48. The samples were tested with a drop tower system as described in Section 2.2. The impactor mass was 8.53 kg. The shape of the impactor was hemispherical, with a diameter of 25.4 mm. The roller support sizes for the S, M, and L samples were 139.7 mm $\times$ 88.9 mm, 152.4 mm $\times$ 152.4 mm, and 304.8 mm $\times$ 304.8 mm. The diameter of the rollers was 6.4 mm. Impact energy levels for the test cases were determined based on the recommendation from the ASTM standard that the ratio of impact energy to thickness should be 6.7 J/mm [19] and preliminary numerical predictions. The critical parameters for the test cases can be found in table 2.2. LVI tests of each case described in Table 2.2 were performed with at least three samples to gain repeatable experimental results. After the LVI tests and before the CAI tests, the samples were subjected to ultrasound C-scanning and representative samples were chosen for μCT scanning.

Table 2.2: LVI testing parameters of the panel size effects study.

Sample in-plane size (mm x mm)		S: 152.4 x 101.6		M: 177.8 x 177.8		L: 330.2 x 330.2	
Impactor diameter (mm)		25.4		25.4		25.4	
Impactor mass (kg)		8.53		8.53		8.53	
Support size (mm x mm)		139.7 x 88.9		152.4 x 152.4		304.8 x 304.8	
L1 [45/-45/0/90/0/0]ns	No. of plies	24	48	24	48	24	48
	Impact energy (J)	25	40	30	60	50	80
L2 [45/0/-45/90]ns	No. of plies	24	48	24	48	24	48
	Impact energy (J)	25	40	30	60	50	80

2.4.1 Load Responses

The load-time and load-displacement responses of all the tested cases are reported in Figures 2.36 and 2.37. Figure 2.36 contains the tests results of the 24-ply samples and Figure 2.37 shows results of the 48-ply samples. In each figure, the two columns separated by the black dashed line are results from two stacking sequences – L1 and L2. The three rows of each figure correspond to three in-plane sizes – S, M, and L. The meaning of these names can be found in Table 2.2. As seen in Figures 2.36 and 2.37, curves of different colors are from various samples. It is observed in Figure 2.36 that the test results are highly repeatable, demonstrating the validity of the LVI tests. Some samples have data of the first few milliseconds (0.5 to 1.5 ms) missing due to data acquisition issues of the Instron data exporting module, such as samples 01 and 03 of L1-M-24, and samples 02 and 03 of L1-L-24. The load curves presented in Figure 2.37 are highly repeatable. Most of the curves are on top of each other, except that sample 04 of L1-S-48 seems to have a lower peak load compared to the other three samples of the same case. This might caused by the random distribution of the material properties and manufacturing defects.

Figures 2.36 and 2.37 show highly repeatable experimental results. More physical insights can be gained by regrouping the plots to study the effects of the stacking sequence, panel in-plane size, and laminate thickness on the LVI behavior.

Effects of the Stacking Sequence

The effects of the stacking sequence can be observed in Figure 2.38. The three columns of the figure correspond to the three in-plane sizes. The two rows correspond to the two thicknesses. Only load-displacement curves are plotted in Figure 2.38. The blue curves are obtained from L1 samples and the orange curves are from the L2 samples. It is observed from all the plots that the blue curves are almost on top of the orange curves, implying that the difference of the current two layups, L1 and

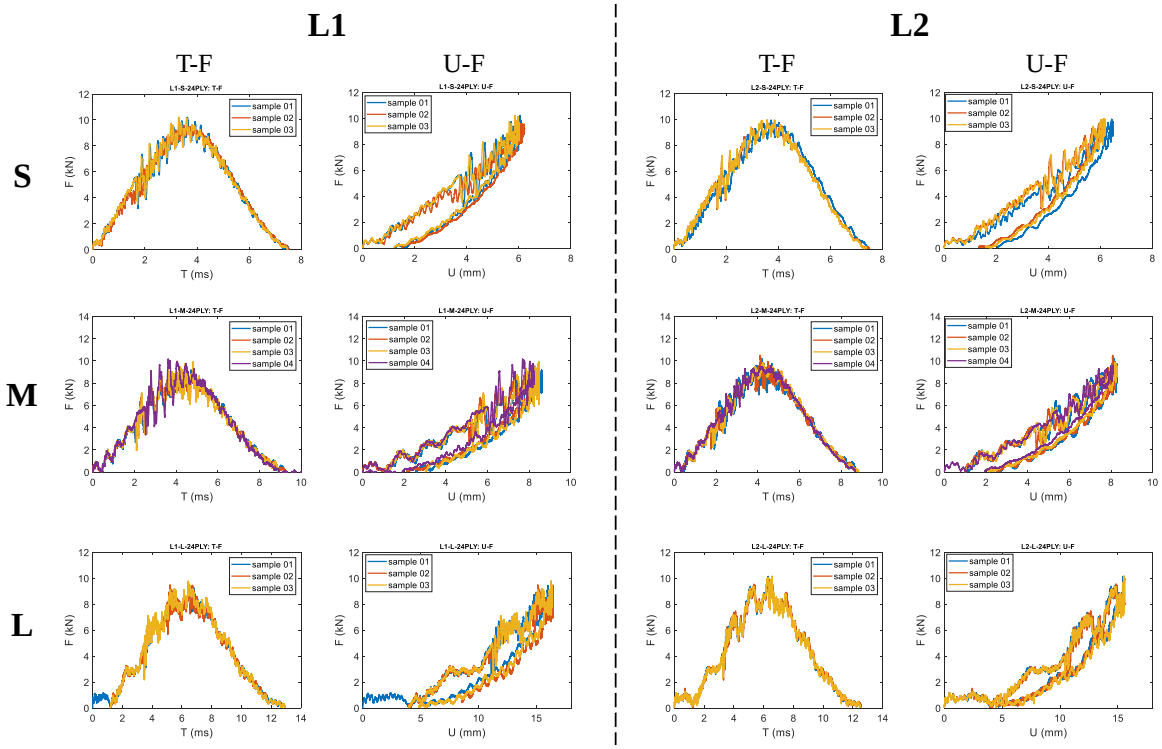

Figure 2.36: Load responses of all the 24-ply LVI tests.

L2, almost generates no effect on the LVI load responses. From the studies in Section 2.3, the stacking sequences affect the impact load responses strongly, which is not the case for the current two layups studied in this section. Preliminary numerical analyses were performed to calculated the bending of an L1-S-24 laminate and an L2-S-24 laminate with central loading. It was found that the bending rigidity values of the two layups obtained numerically were almost identical, therefore resulting in the highly similar LVI load responses of the L1 and L2 results, as show in Figure 2.38.

Effects of the In-plane Size

The effects of the panel in-plane size are shown in Figure 2.39. The load-displacement curves are colored blue, orange, and yellow, corresponding to the three in-plane sizes S, M, and L. Figure 2.39 (a) includes representative results of L1-S/M/L-24 cases and subfigure (b) contains representative results of L1-S/M/L-48 cases. It is seen that

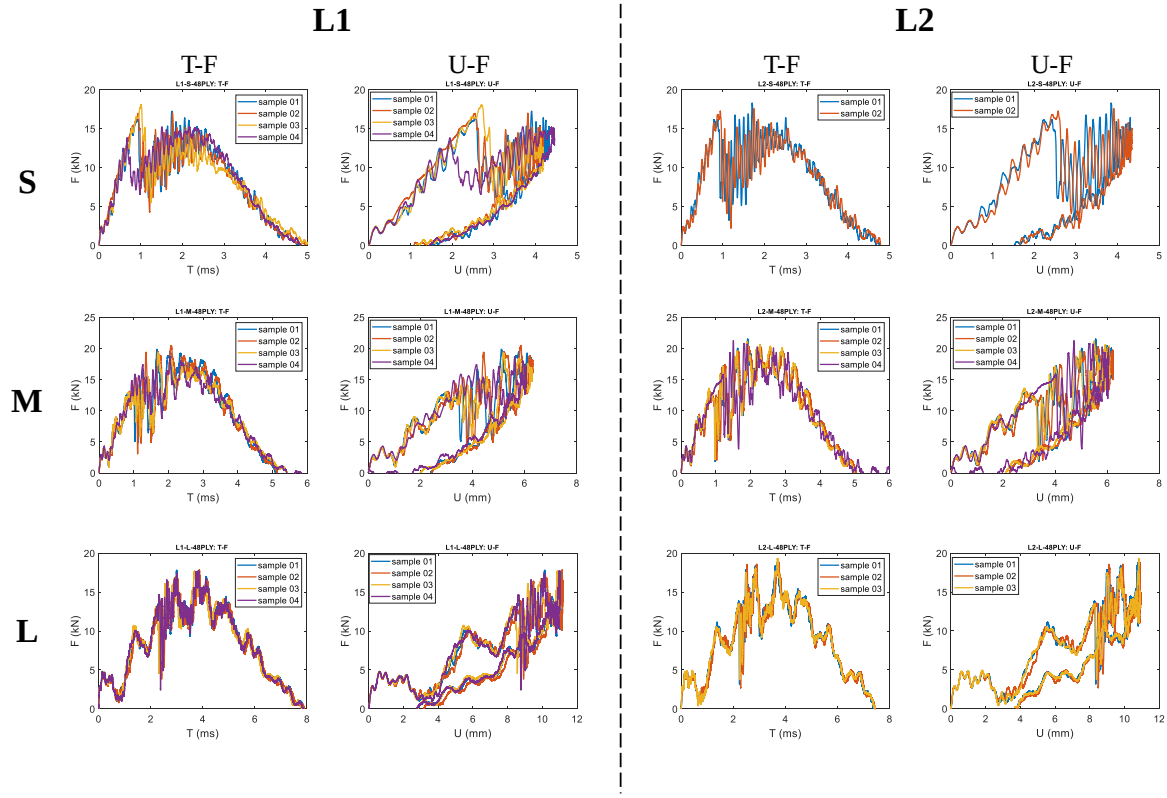

Figure 2.37: Load responses of all the 48-ply LVI tests.

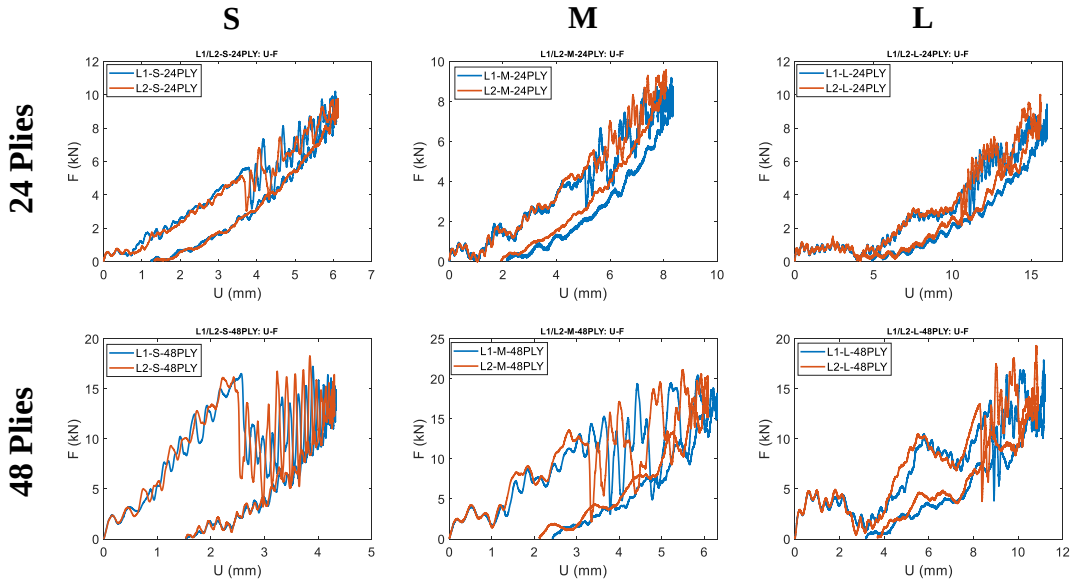

Figure 2.38: Effects of the stacking sequence on the LVI responses.

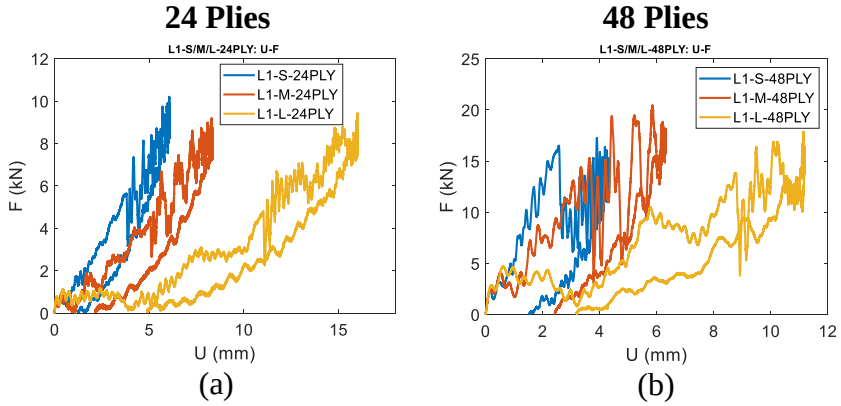

Figure 2.39: Effects of the in-plane size on the LVI responses: (a) 24-ply samples, and (b) 48-ply samples.

the peak load of the three in-plane sizes are very close. The bending rigidity (initial load-displacement stiffness) is found to decrease as the in-plane size increases. In addition, the residual displacement, at which the load returns back to zero, increases with the increase of in-plane size.

Effects of the Thickness

The effects of the laminate thickness (the number of plies) are shown in Figure 2.40. Load-displacement curves colored blue and orange correspond to two sample thicknesses with 24 plies and 48 plies of laminae. The three columns of the figure represent three in-plane sizes: S, M, and L. As shown in Figure 2.40, with greater thickness, the bending rigidity of the samples increase. The effects of the thickness is the most salient in Figure 2.40 (a). On the L1-S-24 curve, load oscillation due to matrix cracking and delamination onset and propagation slightly reduce the bending rigidity of the sample, However, on the L1-S-48 curve, the LVI-induced damage severely knocks down the bending rigidity. The significant bending rigidity degradation is denoted with two dashed straight lines in Figure 2.40 (a). As the in-plane size increases, this reduction of the bending rigidity becomes less significant. It is believed that the cause of the severe degradation of the bending rigidity is the high thickness-

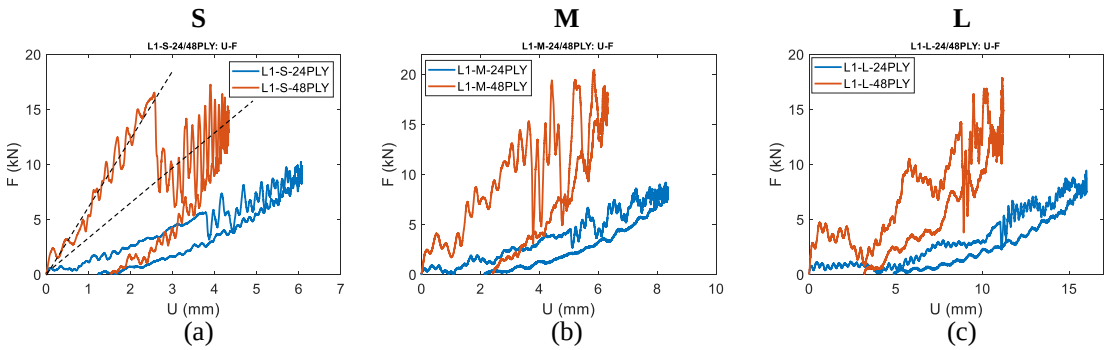

Figure 2.40: Effects of the sample thickness on LVI responses: (a) 152.4 mm × 101.6 mm samples, (b) 177.8 mm × 177.8 mm samples, and (c) 330.2 mm × 330.2 mm samples

to-length/width ratio of the samples. When two plates are bent with the same amount of out-of-plane deformation, the one with a higher thickness-to-length/width ratio would have higher transverse shear stresses τ_{31} and τ_{32}, which drive the initiation and propagation of the delamination. In addition, before the delamination onset, the strain energy has gathered much greater momentum in a thicker 48-ply sample than a 24-ply sample, which is the reason for the knocking down of the bending rigidity being drastic and significant in Figure 2.40(a).

In this section, the LVI load responses of the panel size effect study have been presented. The test results are highly repeatable, demonstrating the validity of the experimental study. Through comparing the load-displacement curves by regrouping according to the layup, panel in-plane size, and panel thickness, the thickness-to-length/width ratio of the samples has been identified to be the most important geometric parameter affecting the LVI load responses.

2.4.2 LVI-induced Damage

After the LVI tests, the samples were inspected with a high-resolution Nikon camera. The indentations on the sample top surfaces (impacted side) were measured with a dial indicator. The lengths of the ply-splitting on the bottom surfaces (non-impacted side) were measured with a caliper. The top and bottom surfaces of representative

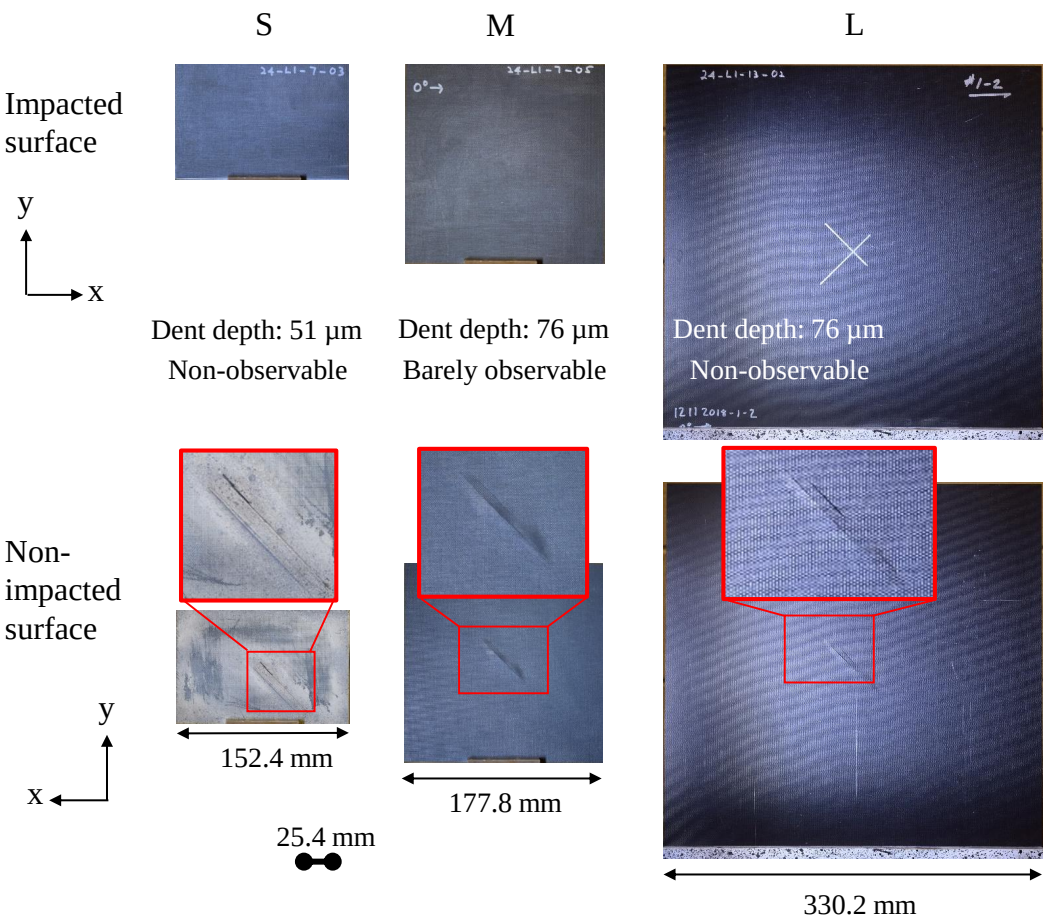

Figure 2.41: Inspections on the impacted L1-S/M/L-24 samples.

samples are displayed in Figures 2.41 to 2.44. Impacted L1-S/M/L-24 samples are shown in Figure 2.41. According to the observation of the top surfaces shown in the first row of the figure, the impact-induced dents are barely visible, meaning that the damage of the these samples can be categorized as BVID. According to the second row, various extents of back-ply splittings are observed. The back-ply splittings are along the fiber direction, caused by relatively high transverse tensile stress σ_{22} on the bottom surfaces during the LVI tests.

Impacted L2-S/M/L-24 samples are displayed in Figure 2.42. According to the first row, again, the LVI-induced dents are barely visible or non-visible at all. No back-ply splitting is seen on the back surface of the L2-S-24 sample, but visible on

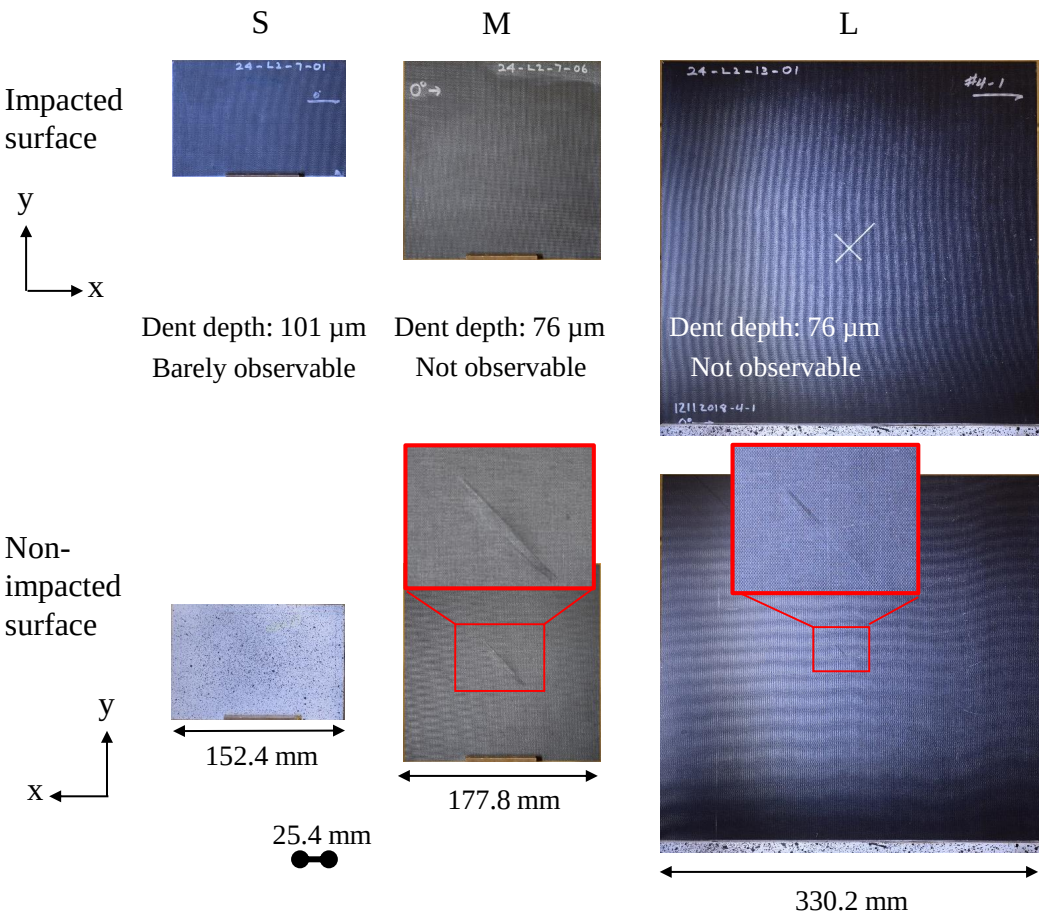

Figure 2.42: Inspections on the impacted L2-S/M/L-24 samples.

the L2-M/L-24 samples.

Inspected L1-S/M/L-48 samples are presented in Figure 2.43. The surface dents are barely visible. No back-ply splitting is seen on the L1-S-48 sample but observed on the L1-M/L-48 samples.

Impacted L2-S/M/L-48 samples are demonstrated in Figure 2.44. From the first row, the indentations are barely visible. From the second row, on all the samples, no back-ply splitting is seen.

A summary of the surface damage features including the dent depth and back-ply splitting lengths measured from the dial indicator and caliper can be found in Tables 2.3 and 2.4 .

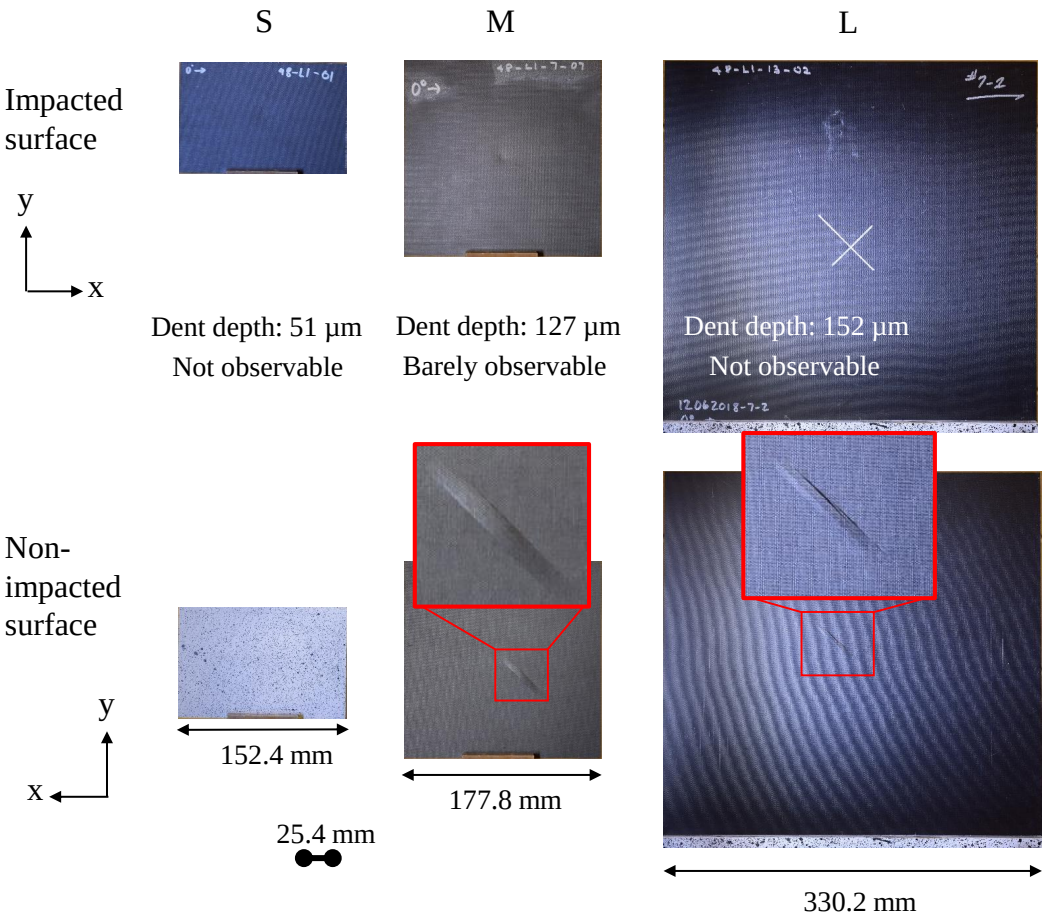

Figure 2.43: Inspections on the impacted L1-S/M/L-48 samples.

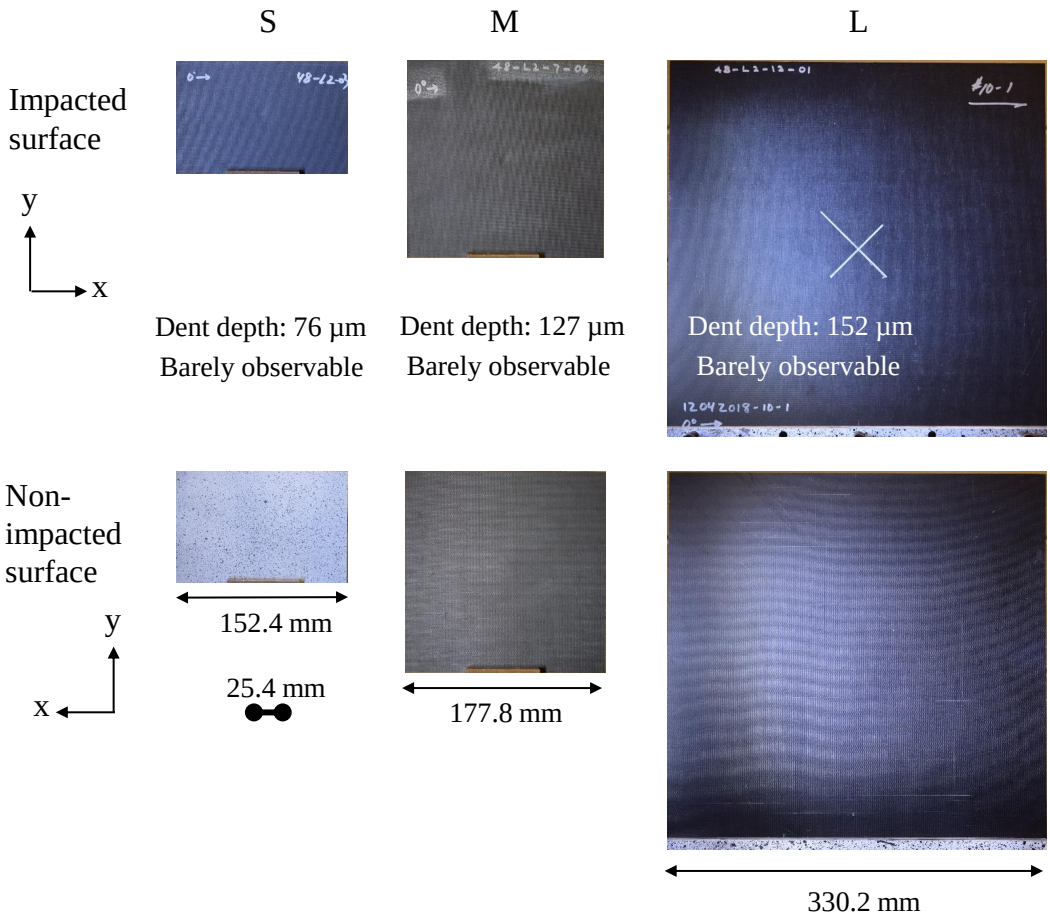

Figure 2.44: Inspections on the impacted L2-S/M/L-48 samples.

Ultrasound C-scanning was performed for all the impacted sample using a Dolphicam 2 handheld 5 MHz scanner. The characterized damage footprints are highly repeatable. Therefore, C-scans of only one sample of each test case are shown in Figures 2.45 and 2.46. In both figures, the three columns correspond to the three panel in-plane sizes – S, M, and L. The two rows correspond to the two stacking sequences – L1 and L2. From Figure 2.45, it is seen that the LVI-induced damage footprints of L1 samples are longer along the x-axis while the damage footprints of L2 samples are almost circular. The reason for the damage footprints of L1 samples being longer along the x-axis is the relatively high percentage (50%) 0° plies, which has been explained in Section 2.3. L2 is a quasi-isotropic layup. This type of circular damage footprints has also been presented in Section 2.3. According to Figure 2.38 and the comparison between Figure 2.45 (a) and (b), although the load responses are not significantly affected by the difference between the stacking sequences L1 and L2, the LVI-induced damage is greatly influenced by the stacking sequence.

The damage footprints of the 48-ply samples are shown in Figure 2.46. The shapes of the damage are similar to that in Figure 2.45. However, the overall damage sizes of the 48-ply samples are significantly larger than the 24-ply samples. For example, for L1/L2-S samples, the impact energy for L1/L2-S-24 samples is 25 J, while the impact energy for L1/L2-S-48 samples is 40 J. Although 40 J is less than twice of 25 J, the damage footprints of L1/L2-S-48 samples are more than twice the sizes of the damage footprints of L1/L2-S-24 samples. This finding means that the LVI-induced damage size does not increase proportionally with the impact energy and thickness. With a greater thickness-to-length/width ratio, as explained previously, the sample becomes more vulnerable to delamination due to higher transverse shear stresses at the interfaces. A summary of the overall damage footprint areas can be found in Tables 2.3 and 2.4 .

Detailed damage morphology has been characterized by μCT scanning using a

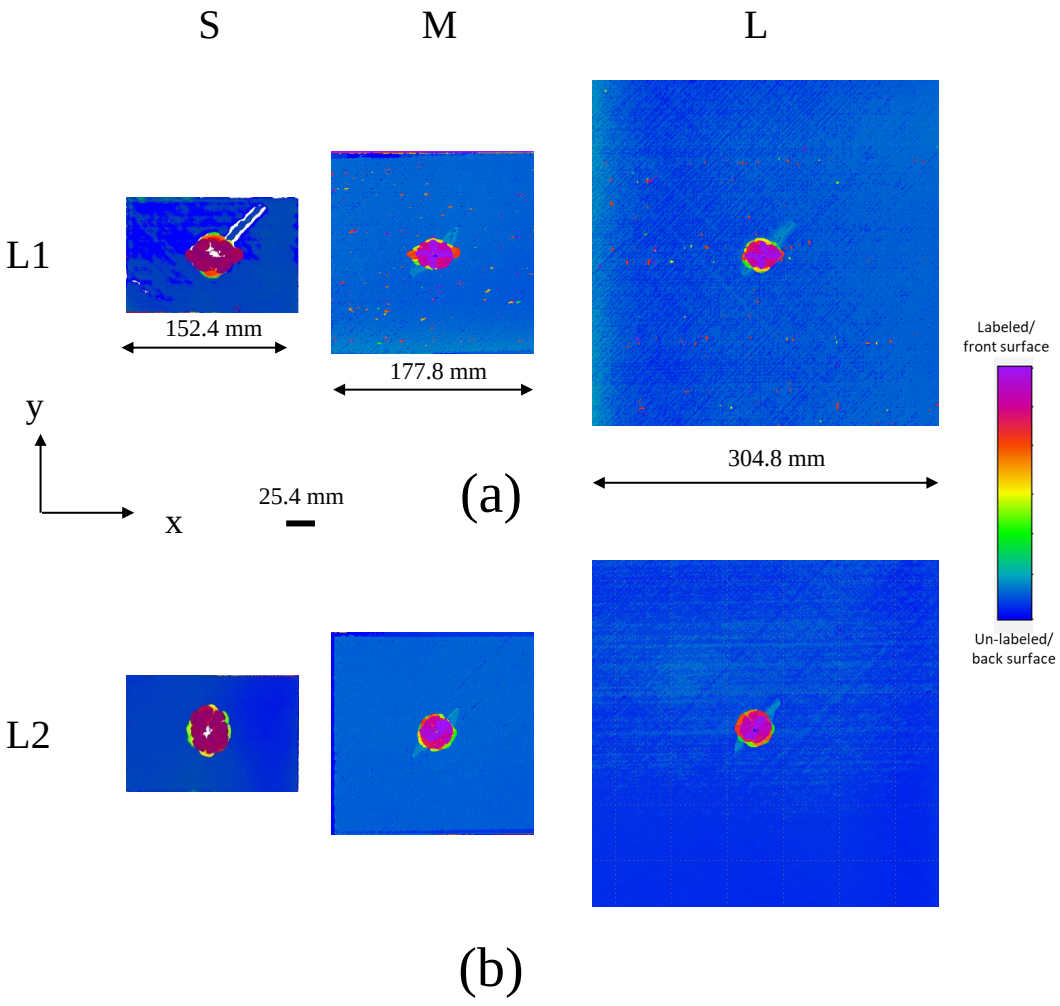

Figure 2.45: Ultrasound C-scanning of the 24-ply samples .

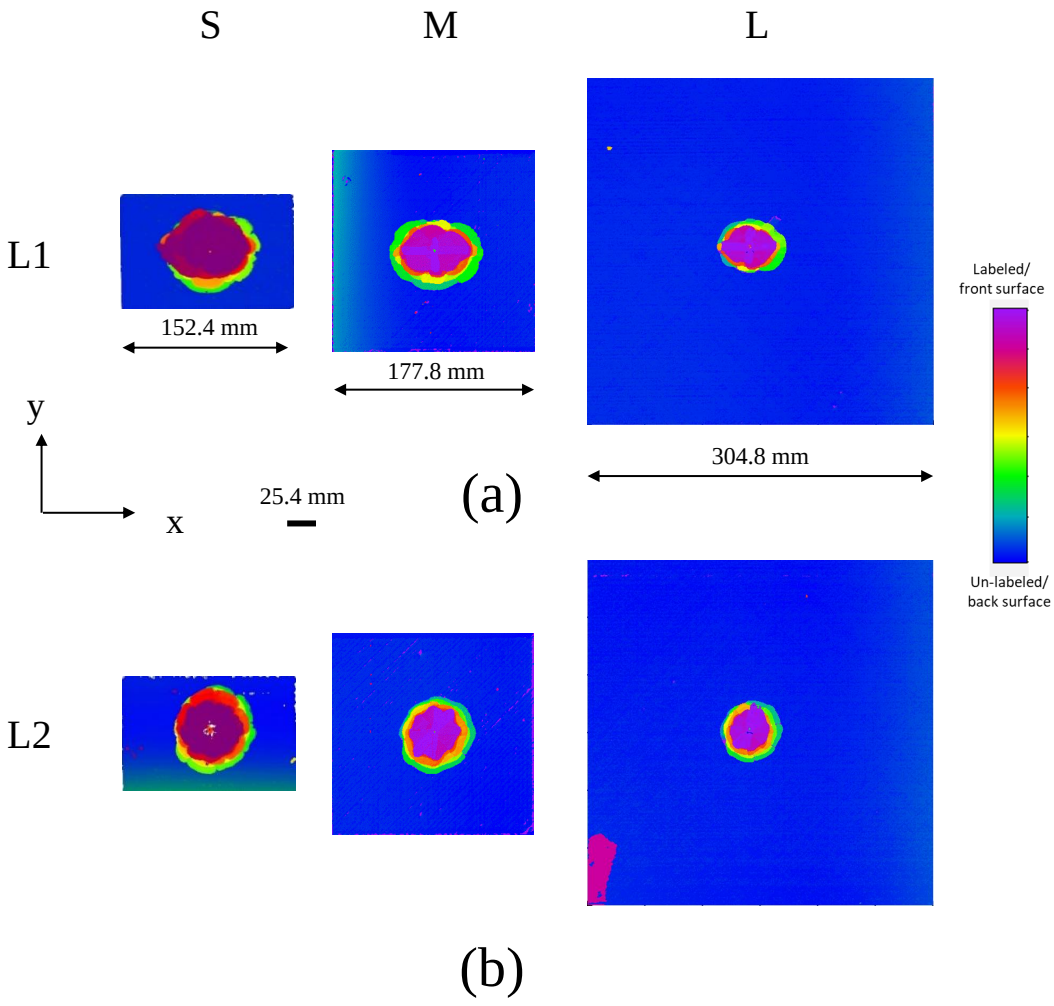

Figure 2.46: Ultrasound C-scanning of the 48-ply samples .

Zeiss Xradia Versa 520 system. Five samples including L1-S-24, L2-S-24, L1-S-48, L2-S-48, and L1-L-48 were subjected to μCT. In order to perform μCT scanning for the L1-L-48 sample, the sample was trimmed by waterjet cutting such that a central 152.4 mm $\times$ 101.6 mm area could fit inside the scanning chamber of the scanner. The purpose of scanning the L1-L-48 and L1-S-48 samples is to investigate the panel in-plane size effects on detailed LVI-induced damage morphology. It was found that except for the damage size, the damage geometrical details of L1-L-48 and L1-S-48 are almost identical. In addition, the damage patterns of L1-S-24 are highly similar to that of L1-S-48, and the damage patterns of L2-S-24 are highly similar to that of L2-S-48. Therefore, in this section, only the μCT slices of the L1-S-24 and L2-S-24 samples are demonstrated in Figures 2.47 and 2.48.

The voxel size of the μCT scanning of the L1-S-24 sample is 25 μm $\times$ 25 μm $\times$ 25 μm. The voxel size of the L2-S-24 sample scanning is 35 μm $\times$ 35 μm $\times$ 35 μm. Featured delamination pattern such as the "peanut" shape and "fan" shape are observed in Figure 2.47, such as that in slices no. 301 and 321. The "peanu" shaped delamination usually happens between two adjacent plies having an angle difference of 90 °. The angle difference of the "fan" shaped delamination is usually 45 °. Back-ply splitting is observed in slices no. 341 and 347. The damage mechanism of these featured LVI-induced delamination patterns have been illustrated in Section 2.3.2. In Figure 2.48, the "rotating-fan" pattern of this quasi-isotropic L2 layup is seen, which has been illustrated in detail in Section 2.3.2. Compared to the μCT scanning presented in Sections 2.3, the μCT scans as shown in Figures 2.47 and 2.48 do not show fiber compressive kinking near the top surfaces of the impacted samples. In addition, the bottom-ply splitting shown in Figures 2.47 and 2.48 are more extensive than that in Section 2.3. The reason for these differences is three-fold. First, in Section 2.3, the material system studied is T800s/3900-2B, which is a material system toughened at layer interfaces. The material system studied in this

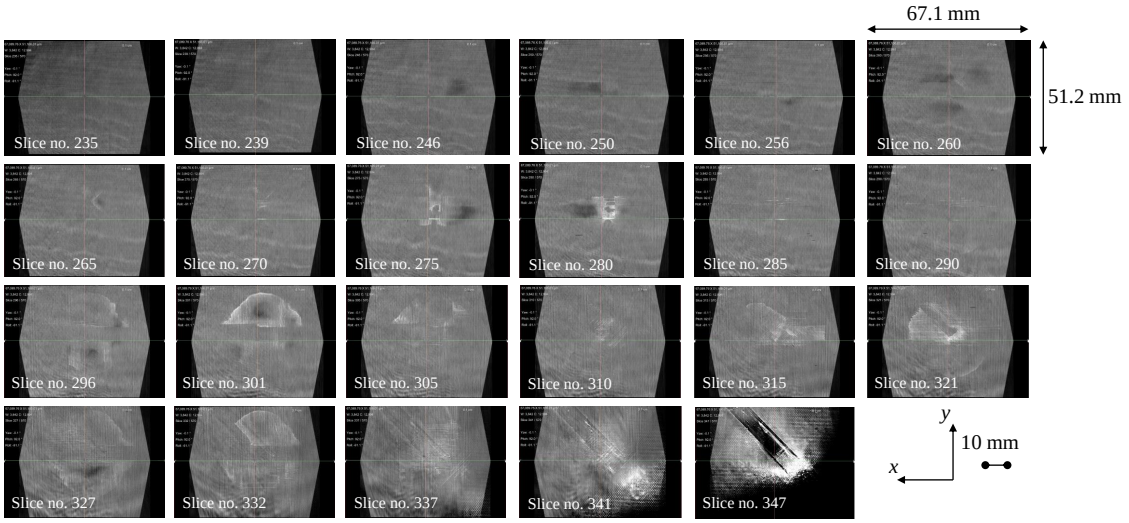

Figure 2.47: Face-on μCT slices of an impacted L1-S-24 sample.

section, IM7/977-3, is not interfacially toughened. As LVI-induced delamination is reduced by the interfacial toughening of T800s/3900-2B, the impact energy would be dissipated more favorably by other damage modes, such as fiber compressive kinking near the top sample surface. Second, the impactor diameter of the tests in Section 2.3 is 20 mm, while the diameter in this section is 25.4 mm. A smaller impactor diameter would induce a greater extent of local bending at the impacted area, which would lead to higher compressive stresses near the top surfaces of the samples. Therefore, the T800s/3900-2B samples have more fiber kinking near their top surfaces. Third, the average layer thickness of T800s/3900-2B is 0.19 mm, while the average layer thickness of IM7/977-3 is 0.13 mm. With the same panel in-plane size, the IM7/977-3 samples are thinner; thus when impacted with the same amount of energy of 25 J, the IM7/977-3 samples would undergo a higher out-of-plane deformation. Correspondingly, tensile stresses on the bottom surfaces of the IM7/977-3 samples are higher than that of the T800s/3900-2B samples. This explains that the back-ply splitting extent of the IM7/977-3 samples is more severe than that of the T800s/3900-2B samples.

Damage features including the overall damage footprint area measured from ultra-

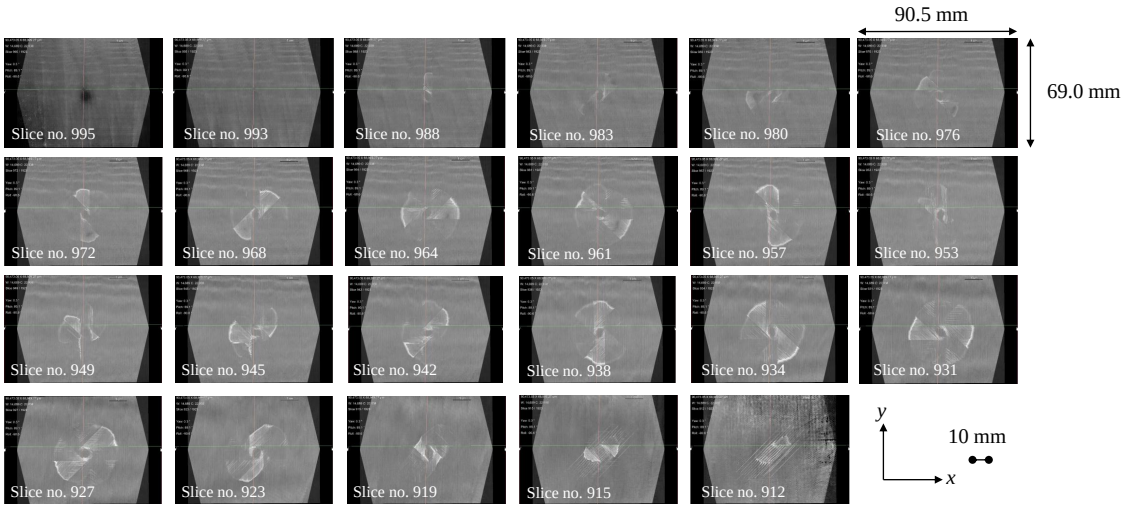

Figure 2.48: Face-on μCT slices of an impacted L2-S-24 sample.

sound C-scans, back-ply splitting length, and dent depth are summarized in Tables 2.3 and 2.4. The dent depth was measured using an dial indicator. The back-ply splitting length was measured by a caliper. The charted values in Tables 2.3 and 2.4 are averaged values of all the tested samples. Two uniform trends can be found from the tables. First, the areas of the damage footprints have a general descending trend with the increase of the in-plane size. However, the impact peak forces of the three in-plane sizes are close to each other, as can be observed in in Figure 2.39. This trend implies that, with the same impact peak force, samples with lower thickness-to-length/width ratios tend to have smaller LVI-induced damage footprints.

The second general trend found from Tables 2.3 and 2.4 is that the 48-ply samples tend to have smaller back-ply splitting lengths compared to the 24-ply samples, although the damage areas of the 48-ply samples are much greater (more than 200%) than that of the 24-ply samples. LVI-induced back-ply splitting is due to high tensile stresses on the bottom surfaces of the samples. As can be found in Figure 2.40, the maximum displacement of 48-ply samples are uniformly smaller than that of the 24-ply samples. Therefore, tensile stresses on the bottom surfaces of the 48-ply samples

Table 2.3: LVI-induced damage features of the 24-ply samples.

		S (25 J)	M (30 J)	L (50 J)
L1-24Ply	Damage area (mm^2)	1548	1161	968
	Back-ply splitting length (mm)	73.7	63.5	61.0
	Dent depth (mm)	0.08	0.08	0.09
L2-24Ply	Damage area (mm^2)	1226	968	839
	Back-ply splitting length (mm)	NA	48.3	45.7
	Dent depth (mm)	0.10	0.08	0.08

Table 2.4: LVI-induced damage features of the 48-ply samples.

		S (40 J)	M (60 J)	L (80 J)
L1-48Ply	Damage area (mm^2)	4258	5226	2323
	Back-ply splitting length (mm)	NA	45.7	35.6
	Dent depth (mm)	0.05	0.13	0.15
L2-48Ply	Damage area (mm^2)	4452	3419	2065
	Back-ply splitting length (mm)	NA	NA	NA
	Dent depth (mm)	0.13	0.15	0.15

would be smaller than that of the 24-ply samples. As a result, the back-ply splitting on the 48-ply samples are uniformly shorter than the 24-ply samples.

In this section, the LVI-induced damage of the panel size effect study have been presented. The discussed damage includes permanent indentation, back-ply splitting, and internal damage characterized by surface inspection, ultrasound C-scanning, and μCT scanning. By comparing the C-scans of 24-ply samples and 48-ply samples, the thickness-to-length/width ratio again has been identified as as the most important geometric parameter affecting the LVI-induced damage.

2.5 Summary and Conclusions

This chapter presents the experimental results of the LVI studies concerning the stacking sequence effects and panel size effects. In Section 2.3 which discusses about the stacking sequence effects, four stacking sequences have been studied, including $[0/45/0/90/0/\text{-}45/0/45/0/\text{-}45]_s$ (layup A), $[45/0/\text{-}45/90]_{3s}$ (layup B), [45/-45/0/45/-

$45/90/45/\text{-}45/45/\text{-}45]_s$ (layup C), and $[0/90/0/90_9]_s$ (the "sandwich-like" layup). The sample in-plane size is 150 mm × 100 mm. The material system is T800s/3900-2B. For each layup, at least three samples have been tested, with highly repeatable experimental results gained. The test results of layup A, B, and C are compared in order to investigate the stacking sequence effects. For each layup, three impact energies have been tested. It is shown that the stacking sequence strongly affects the shape of the LVI-induced damage footprint. The damage footprint of the layup containing a higher percentage of 0° plies would be longer along the 0° axis. However, the discrepancy between the damage sizes of different layups is relatively small. When impacted at the same energy level of 25 J, the damage footprint of the layup B sample is the smallest, possibly due to layup B (24-ply) being thicker than the other two layups (20-ply). High-resolution μCT slices of an impacted layup B sample have been analyzed in detail to understand the damage mechanism of the interaction between damage modes, including fiber kinking, matrix cracking, and delamination. The interaction between damage modes is the key to the formation of the featured LVI-induced "fan-shape" and "peanut-shape" delamination and the "rotating-fan" pattern of damage. LVI-induced damage of the highly anisotropic "sandwich-like" sample is unique in the sense that the damage is similar to the shape of a kidney. The ultrasound C-scanning and μCT scanning have revealed the mechanism of the "kidney" damage – a strong interaction between transverse matrix cracking and delamination.

Section 2.4 reports the experimental LVI results of the panel size effect study. Two layups have been studied, each with three sample in-plane sizes and two thicknesses (number of plies). The layups are L1: $[45/\text{-}45/0/90/0/0]_{ns}$ and L2: $[45/0/\text{-}45/90]_{ns}$. The sample in-plane sizes are named S, M, and L, corresponding to 152.4 mm x 101.6 mm, 177.8 mm x 177.8 mm, and 330.2 mm x 330.2 mm. The two thicknesses of the samples correspond to 24-ply and 48-ply. The material system tested is IM7/977-3. The impact energy levels of the testing were determined according to ASTM D7136

[19] and preliminary blind predictions. At least three samples have been tested for each case, with highly repetitive load responses obtained. Surface inspections, including measurements of the dent depth and back-splitting length, have been conducted. High-resolution ultrasound C-scanning and μCT scanning have been performed for the impacted samples. By comparing the load responses and damage morphology of different test cases, the effects of stacking sequence, panel in-plane size, and panel thickness have been investigated. It is found that the difference between the layups of L1 and L2 has little effect on the load responses but significantly influences the overall shape of the damage footprint. The thickness-to-length/width ratio of the samples has been identified as the most important geometrical parameter affecting the LVI behavior. With a higher thickness-to-length/width ratio, a sample is more vulnerable to impact loading and can have severe bending rigidity reduction as well as extensive LVI-induced damage.

The experimental work presented in this chapter contributes to the understanding of the damage mechanisms of LVI-induced damage and the effects of stacking sequence and panel size on the LVI behavior. The experimental results can be used to challenge the fidelity and versatility of computational models to check if the unique damage patterns, such as the "rotating-fan" and "kidney" patterns, and the panel size effects can be numerically captured.

CHAPTER III

Experimental Studies of the Compression After Impact (CAI) of Laminated Composites

3.1 Introduction

In this chapter, experimental results for the CAI of CFRP composites are reported. Similar to Chapter II, effects of stacking sequence and panel sizes are investigated. The CAI experiments were carried out for the impacted and inspected samples described in Chapter II. CAI tests were performed with an MTS 809 Axial/Torsional load frame with the maximum load capacity being 444 kN. The loading rate for the tests ranged from 0.01 mm/s to 0.018 mm/s, all satisfying the quasi-static loading speed requirement by ASTM D7137 [27]. For the 150 mm $\times$ 100 mm and 152.4 mm $\times$ 101.6 mm impacted samples (size S, see Table 2.2), the CAI fixture was fabricated according to [27]. For the larger 177.8 mm $\times$ 177.8 mm (size M, see Table 2.2) and 330.2 mm $\times$ 330.2 mm (size L, see Table 2.2) samples, the CAI fixture was properly scaled up as described in [27]. During the CAI tests, 2D DIC was performed for all the size S samples. For the size M samples, 2D DIC was performed for the non-impacted surfaces while 3D DIC was performed for the impacted surfaces. For the size L samples, 3D DIC was performed for both surfaces. After the CAI tests, damage features on the outer surfaces of the samples were inspected. Several repre-

sentative samples were subjected to NDI techniques including ultrasound C-scanning and high-resolution μCT.

Following Chapter II, the stacking sequence effect studies have been performed for T800s/3900-2B laminates with stacking sequences being $[0/45/0/90/0/-45/0/45/0/-45]_s$ (layup A), $[45/0/-45/90]_{3s}$ (layup B), and $[45/-45/0/45/-45/90/45/-45/45/-45]_s$ (layup C). The physics of CAI induced damage as a function of the stacking sequence and impact energy has been investigated. CAI behavior with the panel size effects has been studied with respect to IM7/977-3 laminates including two stacking sequences: $[45/-45/0/90/0/0]_{ns}$ (layup L1) and $[45/0/-45/90]_{ns}$ (layup L2); two total thicknesses: 24-ply and 48-ply; and three in-plane sizes: S, M, and L. There are three major goals of the experimental studies in this chapter:

1. Understanding the damage mechanisms of impacted samples subjected to compressive loading.

2. Examining the effects of stacking sequence on the CAI behavior.

3. Investigating the effects of panel size on the CAI behavior.

Section 3.2 will describe the experimental setups. Section 3.3 will present experimental results of the stacking sequence effect studies. Section 3.4 will report the effects of panel size on the CAI behavior. A brief summary and discussions will be provided in Section 3.5

3.2 Experimental Procedure

CAI tests were performed for T800s/3900-2B and IM7/977-3 laminates using an MTS 809 Axial/Torsional test system. The CAI tests were conducted according to ASTM D7137 standard [27]. For brevity, the size S samples are simply referred to as S samples and similarly for M and L samples. For the S samples, the experimental

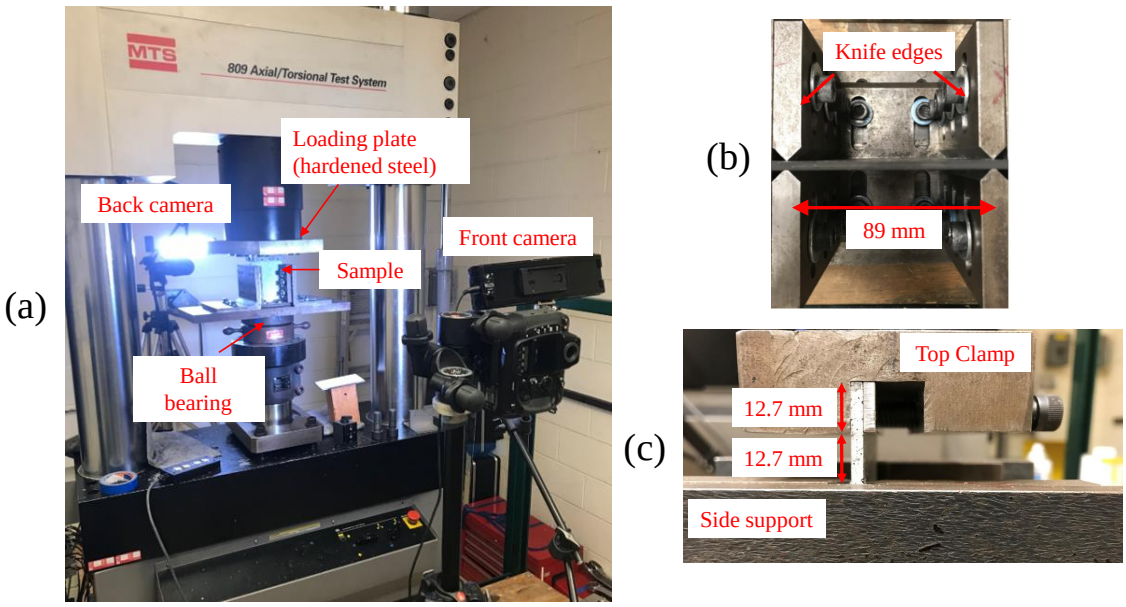

Figure 3.1: CAI test setup of S samples: (a) arrangement of samples, cameras, and MTS, (b) top view of the CAI fixture, and (c) side view of the CAI fixture.

setup is shown in Figure 3.1. As shown in Figure 3.1 (a), the sample together with the CAI fixture were placed on a ball bearing and under a hardened steel loading plate. The use of the ball bearing was to avoid load eccentricity. Two Nikon cameras were placed in front of and behind the sample to record its deformation during the CAI tests. 2D DIC was performed for both the front and back surfaces of the sample. The recording rate was 1 frame per second. Figure 3.1 (b) and (c) show the top view and side view of the CAI fixture. The lateral sides of the sample were sandwiched by knife edges as shown in Figure 3.1 (b). The top and bottom of the sample were clamped by 12.7 mm wide steel plates, as shown in Figure 3.1 (c). A 12.7 mm wide part of the sample was free to deform without restraint.

The CAI setup of M samples is demonstrated in Figure 3.2. From Figure 3.2 (b), the sample with the CAI fixture were placed on the lower loading head of MTS and under the hardened steel loading plate. The reason for omitting the ball bearing was due to the calibration process of 3D DIC. One Nikon camera was placed behind the

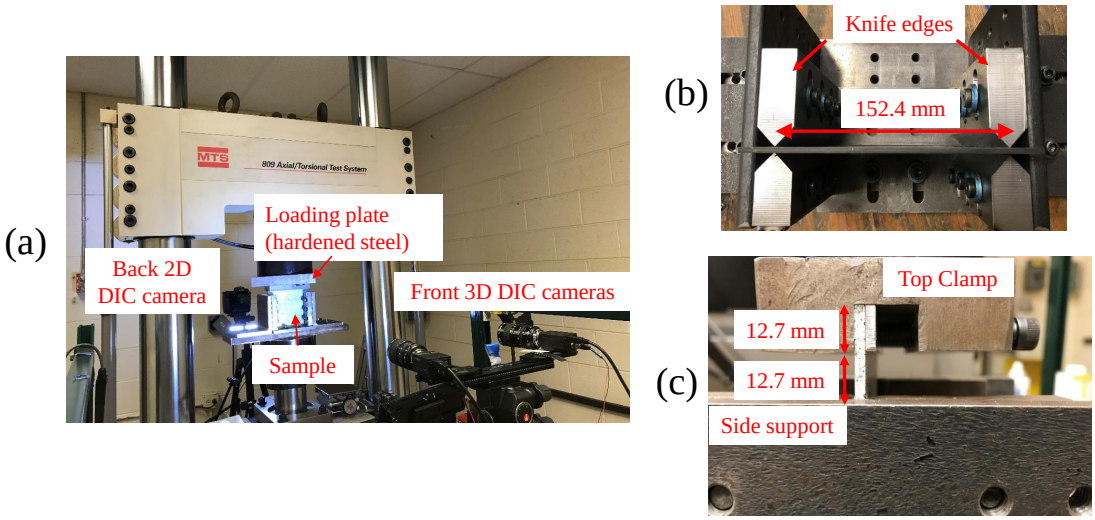

Figure 3.2: CAI test setup of M samples: (a) arrangement of samples, cameras, and MTS, (b) top view of the CAI fixture, and (c) side view of the CAI fixture.

sample to capture the deformation of the non-impacted side of the sample with 2D DIC. Two Grasshopper cameras were placed in front of the sample to capture the deformation with 3D DIC. The CAI fixture of the M samples is shown in Figure 3.2 (b) and (c). The widths of the top and bottom clamps were 12.7 mm. The distances from the lateral edges of the sample to the locations supported by the knife supports were 12.7 mm. The width of the free-to-deform area was 12.7 mm.

The CAI setup of L samples is displayed in Figure 3.3. From Figure 3.3 (b), the L sample was placed between the lower loading head and the hardened steel loading plate. Two groups of Grasshopper cameras were placed in front of and behind the sample to capture the deformation with 3D DIC. The CAI fixture of the L samples is shown in Figure 3.3 (b) and (c). The widths of the top and bottom clamps were 12.7 mm. The support distances from the knife supports to the lateral edges of the sample were 12.7 mm. The width of the free-to-deform area was 12.7 mm.

After CAI tests, both the impacted and non-impacted sides of the samples were

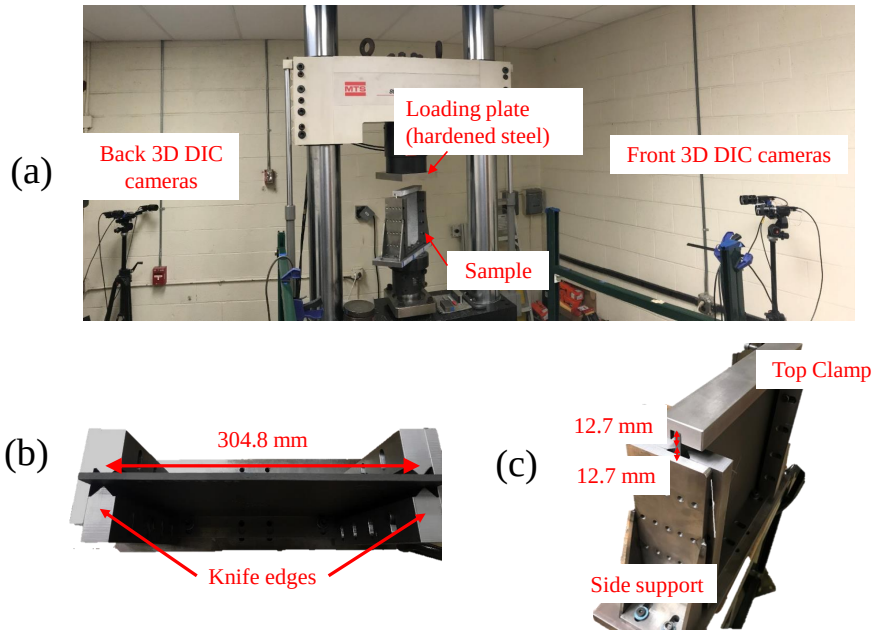

Figure 3.3: CAI test setup of L samples: (a) arrangement of samples, cameras, and MTS, (b) top view of the CAI fixture, and (c) side view of the CAI fixture.

inspected to capture damage features on the outer surfaces. Ultrasound C-scanning was performed selectively for representative samples using a Dolphicam 2 handheld scanner. μCT scanning was performed for one layup C size S sample to characterize the CAI damage patterns.

3.3 Experimental CAI Study with the Effects of Stacking Sequence

The samples studied in this section have the in-plane size of 150 mm $\times$ 100 mm, categorized as S samples. The material system is T800s/3900-2B. The average layer thickness is 0.19 mm. The layup and impact energy information can be found in Table 2.1. The LVI behavior of the samples tested in this section has been reported in Section 2.3. After the NDI characterization of the LVI-induced damage, the top and bottom edges of the samples were sanded down to provide smooth, flat, and

parallel surfaces for compression, as recommended by ASTM D7137 [27]. For each test case in Table 2.1, the deformation of one sample was measured with 2D DIC from both the impacted and non-impacted surfaces. For the other two samples, 2D DIC was only performed for the non-impacted surface, where the speckling used for LVI 3D DIC was existent.

3.3.1 Load Responses

The load data was collected from the load cell of MTS. The displacement data was collected from the deformation field characterized by DIC, as shown in Figure 3.4. In Figure 3.4, two gauge areas from which average axial displacement values were taken are highlighted. The width of the gauge areas was the length of one DIC facet. The averaged displacement values from the top and bottom gauge areas are plotted in Figure 3.4 (b) against the frame number. From Figure 3.4 (b), it is seen that before frame no. 22, the average top and bottom displacement values are identical. This is because that at the beginning of the CAI test, the compression had to close the gap existing in the testing system known as machine compliance. After frame no. 22, the bottom displacement starts to grow faster than the top displacement. The reason is that the MTS's actuator loaded the sample using the lower loading head, while the upper loading head was fixed. At frame no. 102, the bottom displacement increases drastically while the top displacement has no value. This indicates the failure of the sample and would usually correspond to a drastic load drop. The displacement data used for plotting the CAI load (F)-displacement (U) responses was obtained by subtracting the top displacement from the bottom displacement, as illustrated in Figure 3.5. This can be regarded as the end shortening of the sample. In this case, the DIC serves as a "virtual extensometer".

Load-displacement curves of the impacted layup A samples are plotted in Figure 3.6. It is seen that the curves of the same impact energy agree well with each other.

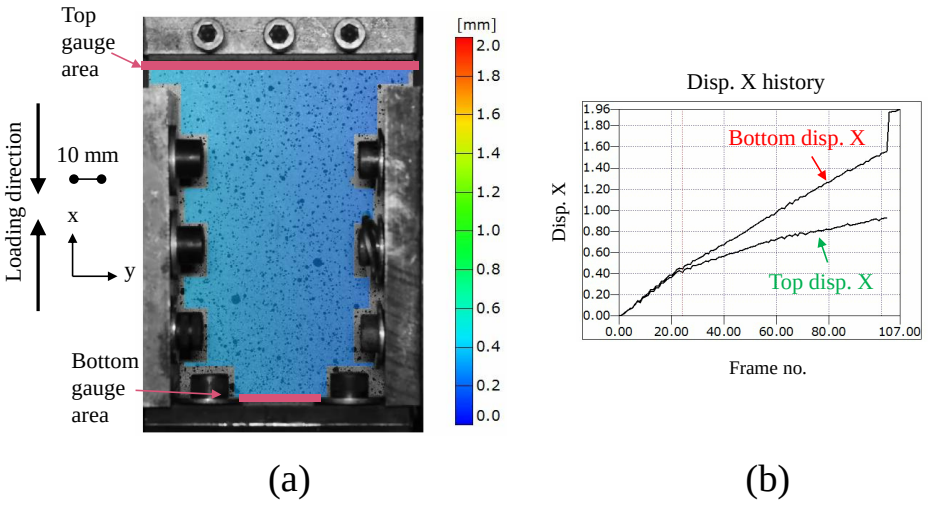

Figure 3.4: Displacement acquisition from the axial deformation field characterized by DIC: (a) deformation field, and (b) axial displacement history.

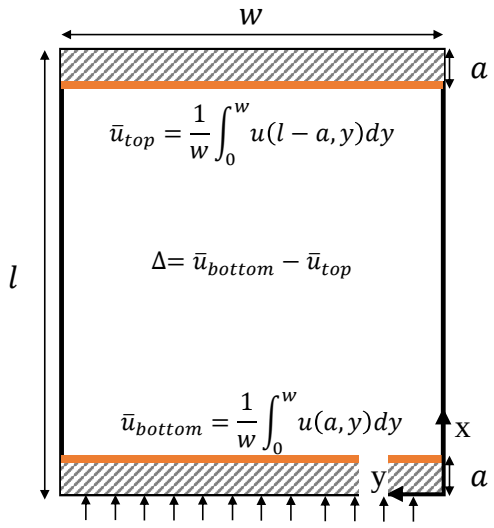

Figure 3.5: An illustration of the acquisition of the displacement value of the CAI test.

Two out of three impacted samples were tested for the 25 J case. The third sample was preserved for future trimming and microscopic observation of the damage features to draw a direct comparison with an IM7/8552 sample with the same layup and impact energy [60]. The curves are plotted together in Figure 3.6 (d). The black curve corresponds to the CAI test of a pristine (non-impacted) layup A sample. Due to the limited total number of samples, only one pristine CAI test was performed. From Figure 3.6 (d), it is seen that the CAI peak loads degrade with the increasing impact energy marginally. There is no significant difference between the initial stiffnesses of the samples impacted by different energies.

Load-displacement responses of the impacted layup B samples are plotted in Figure 3.7. For the 25 J and 30 J cases, the curves of the three samples of each case are very repeatable. For the 35 J case, the peak load of sample 02 (137 kN) is 18% higher than the averaged peak load of sample 01 and 03 (116 kN). The reason for this difference may be due to the randomness in the distribution of material properties and manufacturing defects in samples. Comparing the curves in Figure 3.7 (d), with the energy escalating from 25 J to 30 J, the CAI peak loads seem to decrease marginally. However, both the load-displacement stiffnesses and CAI peak loads of the 35 J case seem to be obviously lower than that of the 25 J and 30 J cases.

Load-displacement curves of the impacted layup C samples are plotted in Figure 3.8. Again, for all three impact energy levels, the curves of the three samples are highly repetitive. It should be noted that in one of the three tests (sample 02) of the 25 J case, near the beginning of CAI, the camera frame rate was not stable. Therefore, the corresponding load-displacement curve seems to behave nonlinearly at first and then return to linear. The load data collected from the load cell is still accurate. Therefore, the nonlinear part of the curve is colored gray to avoid confusion. From Figure 3.8 (d), the CAI peak load seems to decrease gradually with the growing impact energy. There is no obvious stiffness degradation.

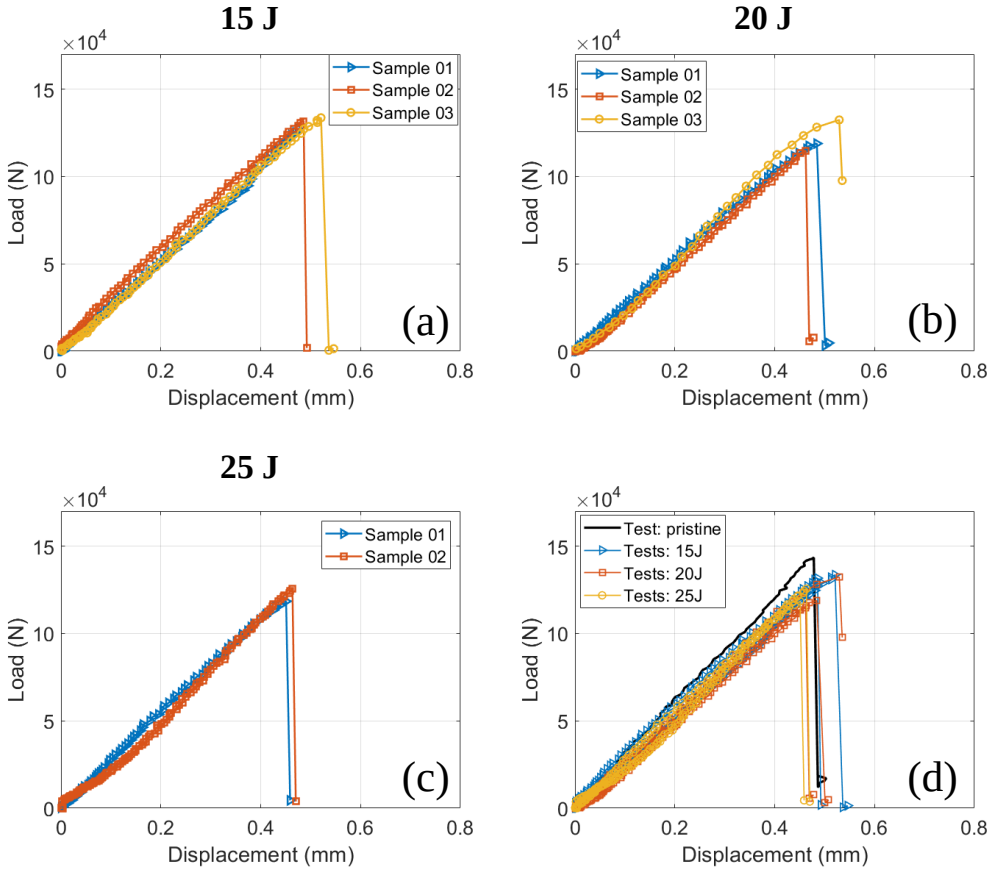

Figure 3.6: Load-displacement curves of the CAI tests of layup A samples: (a) samples impacted with 15 J, (b) samples impacted with 20 J, (c) samples impacted with 25 J, and (d) curves plotted together.

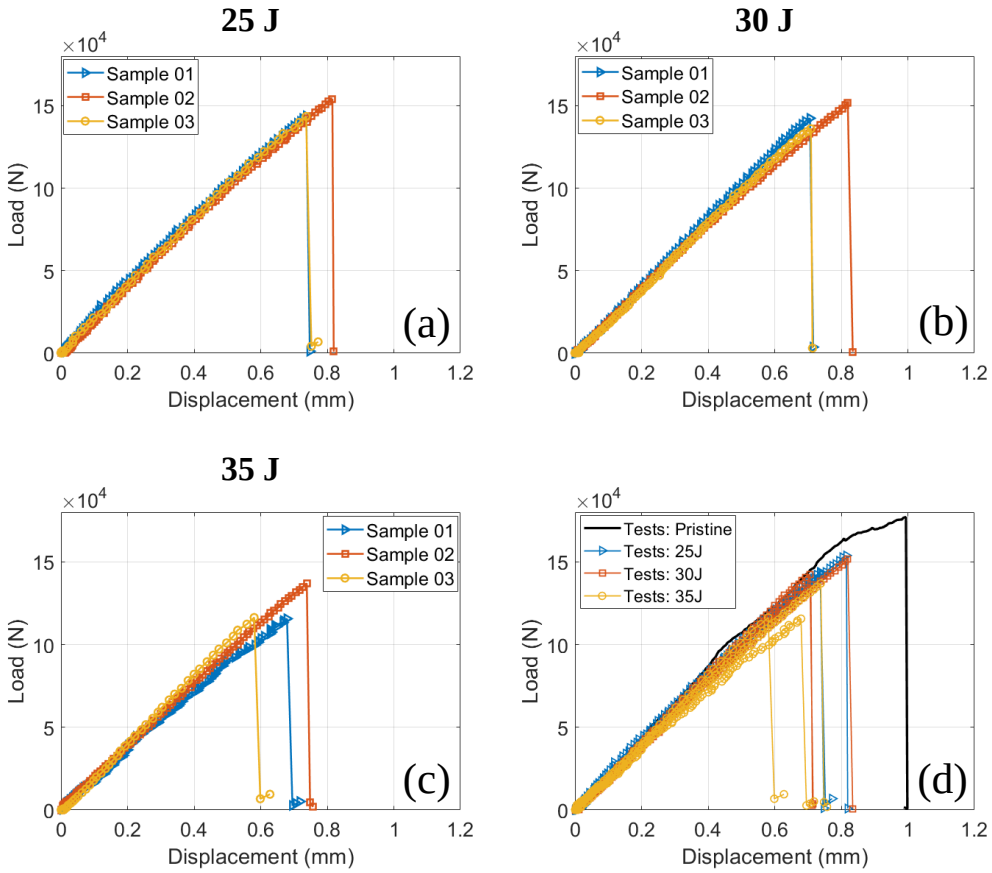

Figure 3.7: Load-displacement curves of the CAI tests of layup B samples: (a) samples impacted with 25 J, (b) samples impacted with 30 J, (c) samples impacted with 35 J, and (d) curves plotted together.

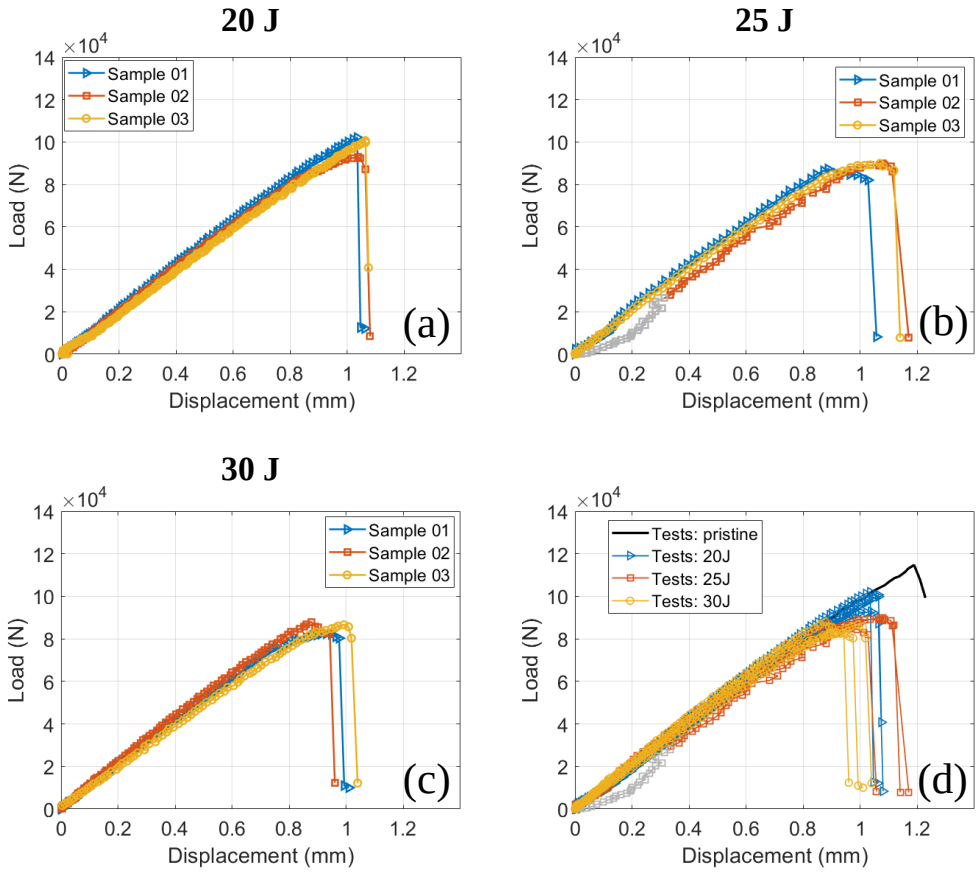

Figure 3.8: Load-displacement curves of the CAI tests of layup C samples: (a) samples impacted with 20 J, (b) samples impacted with 25 J, (c) samples impacted with 30 J, and (d) curves plotted together.

The CAI peak forces and stresses of all the samples are plotted in Figure 3.9. The stresses are simply calculated by dividing the peak forces with corresponding sectional areas. The data of layup A, B, and C is denoted with blue circles, orange triangles, and yellow squares. The decreasing trend of the CAI peak load with the increasing impact energy is clearly seen. According to Figure 3.9 (a), overall, layup B samples have higher peak loads than layup A, and C, which is most likely due to the thickness of the layup (24-ply) being greater than that of layup A, and C (20-ply). The peak loads of layup A are greater than that of layup B, due to the fact that layup A ([50/40/10]) has a higher percentage of 0° plies than layup C ([10/80/10]). According to Figure 3.9 (b), at 25 J, layup A samples and layup B samples have very similar peak stresses. The peak stresses of layup C samples are uniformly lower than that of layup A and B samples, due to the low percentage of 0° plies of layup C.

The peak loads and stresses are also plotted as a function of the overall damage area obtained by ultrasound C-scanning in Figure 3.10. The degrading trend of the peak loads and stresses of layups A and B is unique in the sense that the degradation seems to slow down as the damage area grows. This trend resembles a notch sensitivity study carried out in [116], where effects of the sizes of circular holes on the compressive strengths of laminates were studied by open-hole compression (OHC) tests.

3.3.2 CAI-induced Damage

After removing the failed samples from the testing system, CAI-induced damage on the outer surfaces of representative samples was photographed. The images are displayed in Figures 3.11 to 3.13. In Figures 3.11 (a) and (b), failure bands of a layup A sample along the y-axis can be observed on both the impacted and non-impacted surfaces. The failure bands are found to be composed of fiber breaking and matrix cracking perpendicular to and along the fiber direction. More information can be gained from the side view in Figure 3.11 (c). Matrix cracking, fiber breaking, and

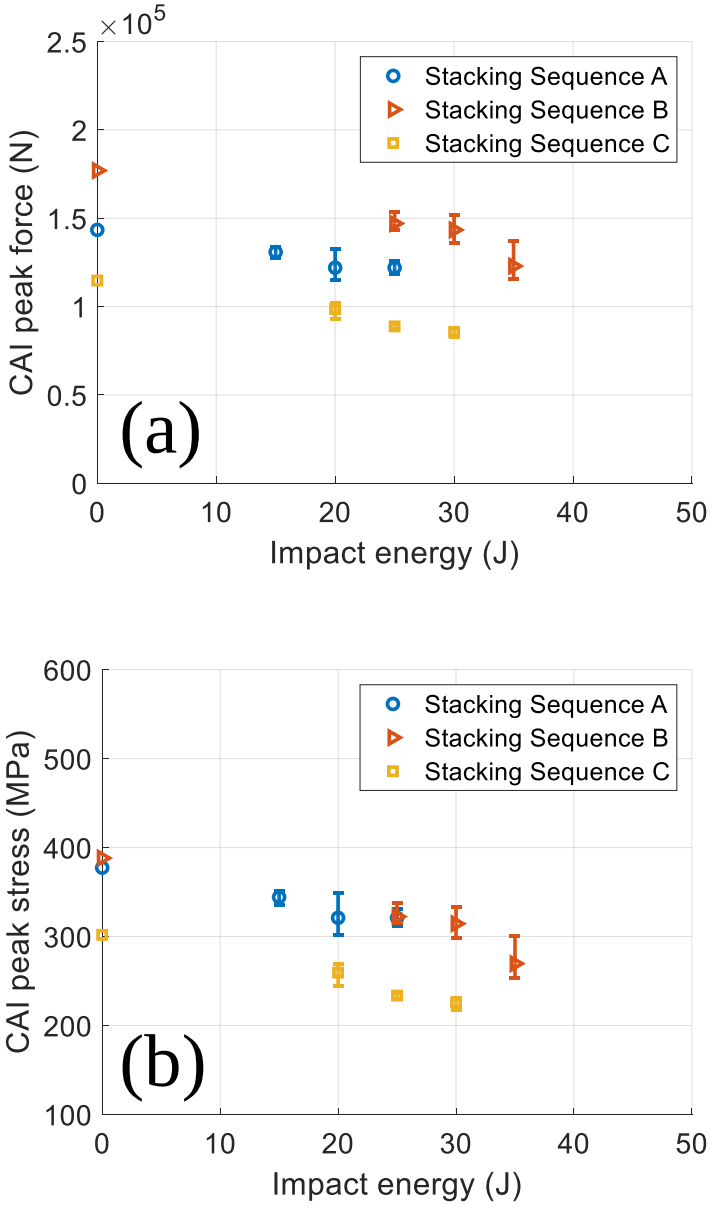

Figure 3.9: (a) CAI peak loads vs. impact energies, and (b) CAI peak stresses vs. impact energies.

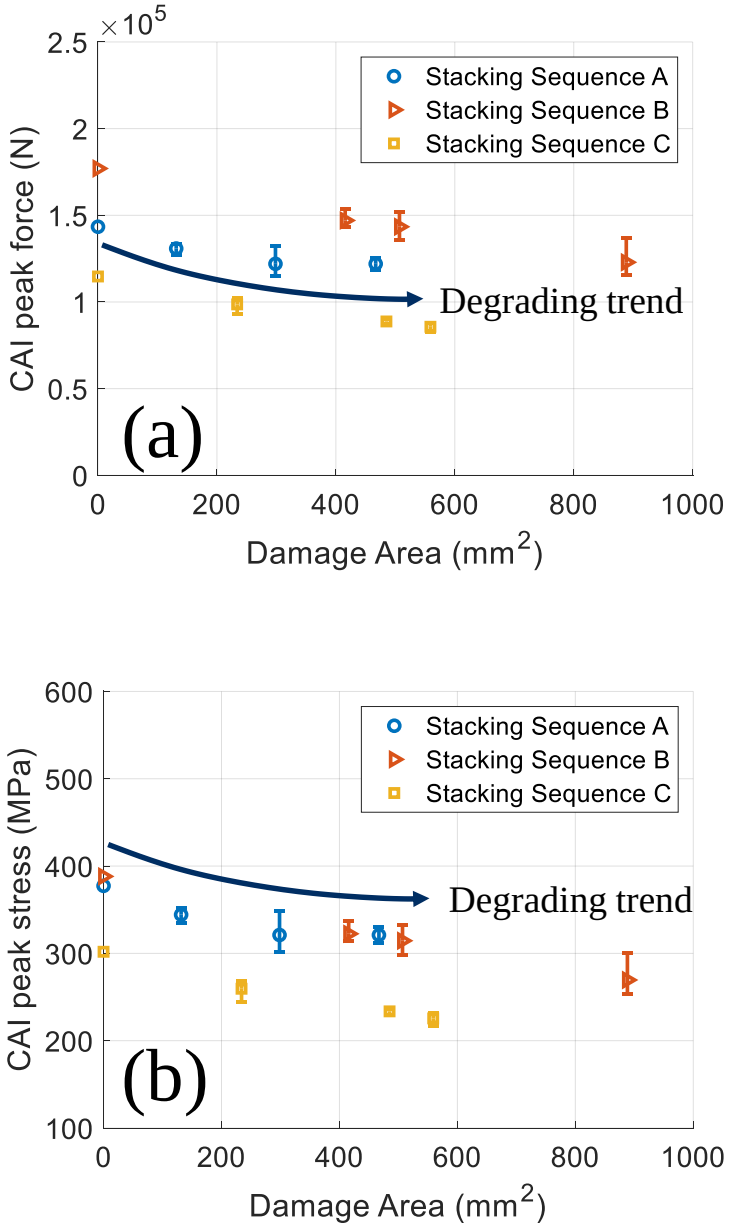

Figure 3.10: (a) CAI peak loads vs. overall damage footprint areas, and (b) CAI peak stresses vs. overall damage footprint areas.

delamination are indicated by orange dashed lines, green solid lines, and blue filled areas. However, not every damaged location is indicated for clarity. Fiber kink bands on the outer surfaces, matrix cracking within layers, and delamination between layers can be clearly seen. It is hypothesized that kind bands, which lead to large fiber rotation, cause the fiber breaks that are seen.

Surface damage of a layup B sample is displayed in Figure 3.12. Again, failure bands along the y-axis are found in Figure 3.12 (a) and (b), composed of matrix cracking and fiber breaking. A major matrix cracking along the 45 ° direction is seen in Figure 3.12 (b), which was caused by the LVI. From the side view in Figure 3.7 (c), enriched damage modes can be observed. Near the surfaces, large out-of-plane deformation is found, caused by fiber compressive kinking.

Surface damage of a layup C sample is shown in Figure 3.8. The failure band on the non-impacted surface, as shown in Figure 3.8 (a) is made of many small-scale matrix cracking and one major fiber breaking, therefore, the failure band is no longer only along the y-axis. In addition, a bulging-out part caused by delamination is identified in Figure 3.8 (a). The failure band on the impacted surface is not as salient as that in Figures 3.6 (b) and 3.7 (b). From the side view, damage modes including matrix cracking, fiber breaking, and their interaction with delamination can be observed.

As presented, the tested load-displacement curves are very repetitive, demonstrating the validity of the tests. Layup B has the highest peak loads, due to the thickness of layup B being greater than that of layup A and C. The peak loads of layup A is higher than that of layup C, due the fact that there are more 0° plies in layup A. When plotting the peak loads as a function of impact energies, the degrading trend is found similar to a notched sensitivity study reported in [116]. The surface damage of layup A seems to have more salient failure bands along the width direction of the samples than that of layup B and C, most likely due to the high percentage of 0° plies

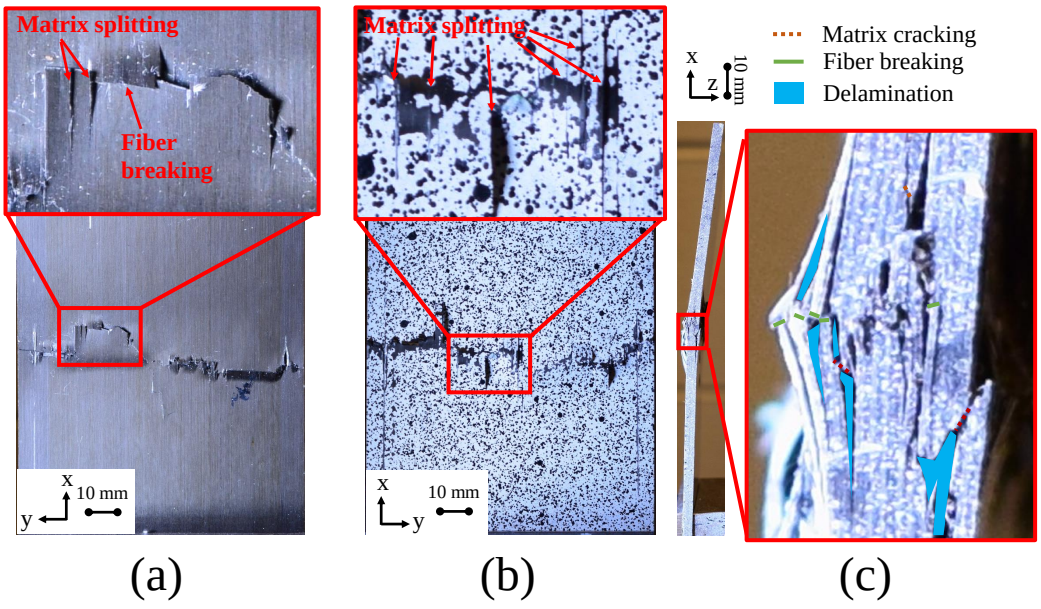

Figure 3.11: Surface inspections of the CAI-induced damage of a layup A sample: (a) non-impacted surface, (b) impacted surface, and (c) side view.

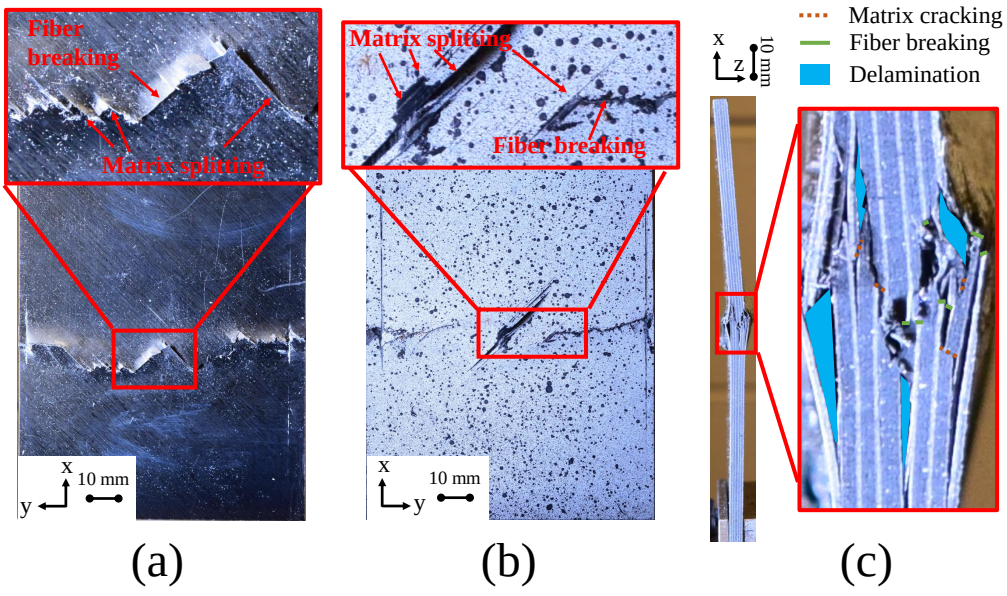

Figure 3.12: Surface inspections of the CAI-induced damage of a layup B sample: (a) non-impacted surface, (b) impacted surface, and (c) side view.

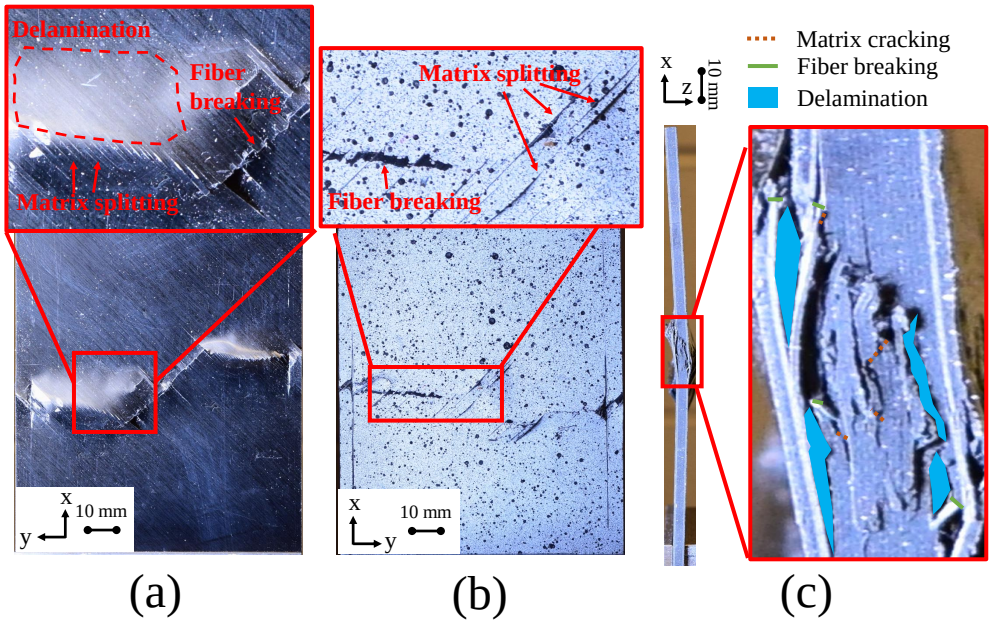

Figure 3.13: Surface inspections of the CAI-induced damage of a layup C sample: (a) non-impacted surface, (b) impacted surface, and (c) side view.

in layup A. The CAI failure of layup A seems to be dominated by fiber compressive damage, while less fiber compressive kinking but more delamination can be found in a CAI failed layup C sample, where there are only 10% 0° plies.

3.4 Experimental CAI Study with the Effects of Panel Size

In this section, experimental results of the investigations on the panel size effects of the CAI behavior are presented. The material system is IM7/977-3. Two stacking sequences have been tested, each with three sample in-plane sizes and two thicknesses (number of plies). The stacking sequences are $[45/\text{-}45/0/90/0/0]_{ns}$ and $[45/0/\text{-}45/90]_{ns}$, named as L1 and L2, where n is decided by the total number of plies of the layup. The sample in-plane sizes are named as S, M and L corresponding to 152.4 mm x 101.6 mm, 177.8 mm x 177.8 mm and 330.2 mm x 330.2 mm. The two thicknesses of the samples correspond to 24-ply and 48-ply. The averaged ply thickness is 0.13 mm. The samples subjected to CAI testing in this section were impacted

with the test parameters charted in Table 2.2. More details of the LVI test results can be found in Chapter II. The CAI test setups for the three in-plane sizes are shown in Figures 3.1 to 3.3. The loading speed was uni formally 1 mm/min for all the tested samples.

3.4.1 Load Responses

The load and displacement data was obtained with the same methodology explained in Section 3.3. The load-displacement curves of all the 24-ply samples and 48-ply samples are plotting in Figures 3.14 and 3.15. In each figure, the three columns represent three in-planes sizes – S, M, and L. The two columns correspond to two stacking sequences – L1 and L2.

From Figure 3.14, it is seen that the test results of the three samples of L1-S-24 and L2-S-24 cases are very repeatable. The response is linear, very similar to the results in Section 3.3. However, for the L1/L2-M/L-24 cases, the load-displacement curves are bi-linear, meaning that after the transitioning points, the stiffnesses of the curves are lower than the initial stiffnesses. This salient bi-linear behavior is caused by the post-buckling of the samples, which will be illustrated in detail with 3D DIC characterization. In Figure 3.14, the three curves of the L1-M-24 case agree well with the post-buckling stiffness of sample 01 being slightly higher than that of sample 02 and sample 03. For the L2-M-24 case, the post-buckling stiffness of sample 03 is higher than that of the other two samples. For sample 01 and sample 02 of L2-M-24, the post-buckling parts of the curves are jagged, implying damage growth during the post-buckling phase. The load-displacement curves of the L1-L-24 and L2-L-24 cases agree very well in terms of the initial stiffnesses and the transitioning points. The CAI peak loads of the L1-L-24 samples are also very repeatable. However, the peak load together with the corresponding displacement values of the L2-L-24 samples do not agree as well as the other cases. This might be due to the randomness in ma-

terial properties, manufacturing-induced defects, or slight deviation in the boundary conditions between tests.

The load-displacement results of the 48-ply samples are presented in Figure 3.15. The behavior of the L1/L2-S/M-48 cases is almost linear, meaning that the samples' deformation with the compressive loading was mostly in-plane. Post-buckling behavior is seen from the L1/L2-L-48 results. The test results of the L1/L2-S-48 and the L2-M-48 results are very repeatable, For the L1-M-48 case, the difference between sample 01 from sample 02, 03, and 04 is obvious, with the stiffness of sample 01 being higher and the peak load being lower. For the L1/L2-L-48 cases, before the transitioning points, the curves of the samples agree well. The post-peak parts of the curves are jagged, implying that progressive damage took place along with the post-buckling of the samples. As the jaggedness starts to appear on the curves, the curves become divergent.

Deformation of the L1/L2-S-24 samples

2D DIC was performed for both the impacted and non-impacted surfaces of the samples during the CAI testing. Deformation fields characterized on both sides are highly similar, and therefore only that from the impacted sides are displayed, as shown in Figure 3.16 and Figure 3.17. The deformation fields are uniform along the y-axis in stages (i) to (iii), while the load-displacement curves are mostly linear except for some local jaggedness. From stage (iii) to (iv), the change is drastic, as can be seen in the deformation fields. Sharp discontinuity of the deformation fields can be observed in stage (iv), implying that the CAI-induced failure mostly concentrates around the discontinuities. The formation of the failure band correlates with the drastic load drop between stages (iii) and (iv).

Deformation of the L1/L2-S-48 samples

The CAI experimental setup of the L1/L2-S-48 samples is identical to that of the

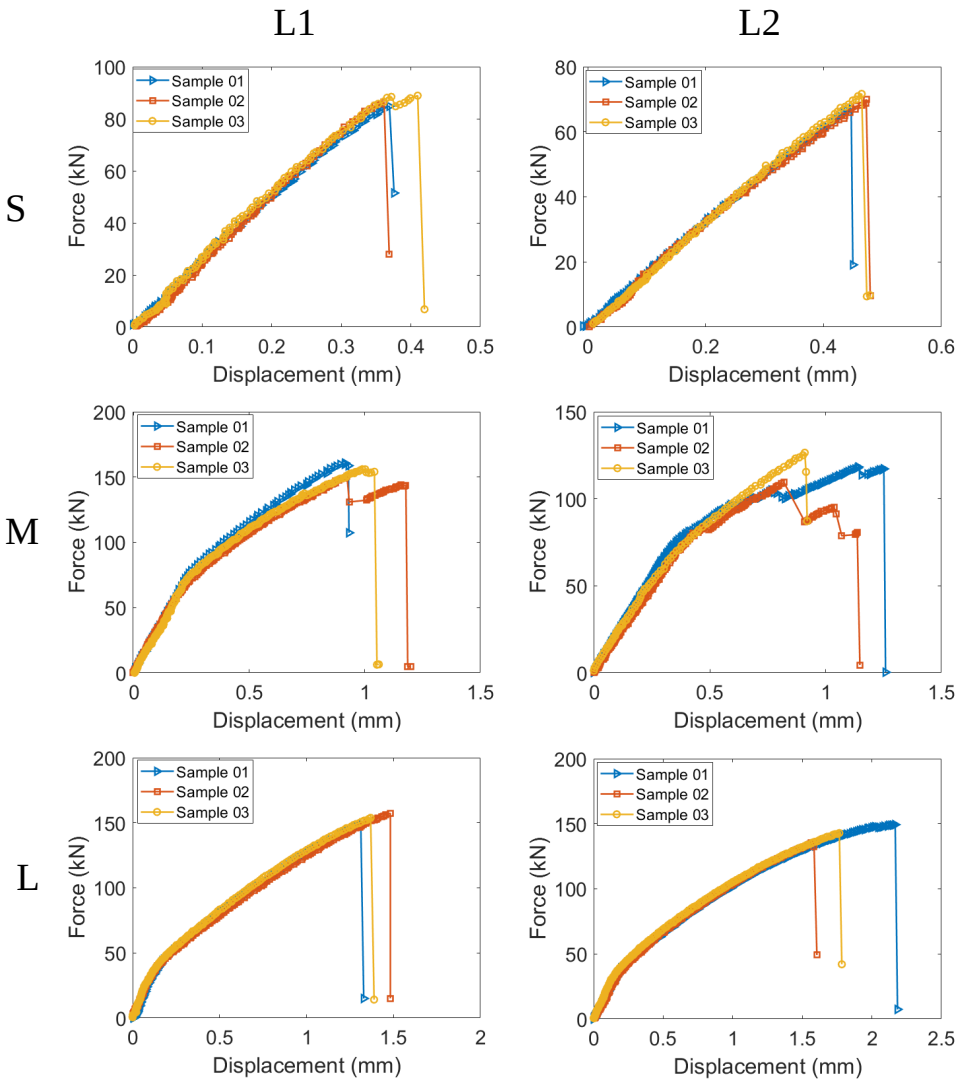

Figure 3.14: CAI load-displacement responses of all the 24-ply impacted samples.

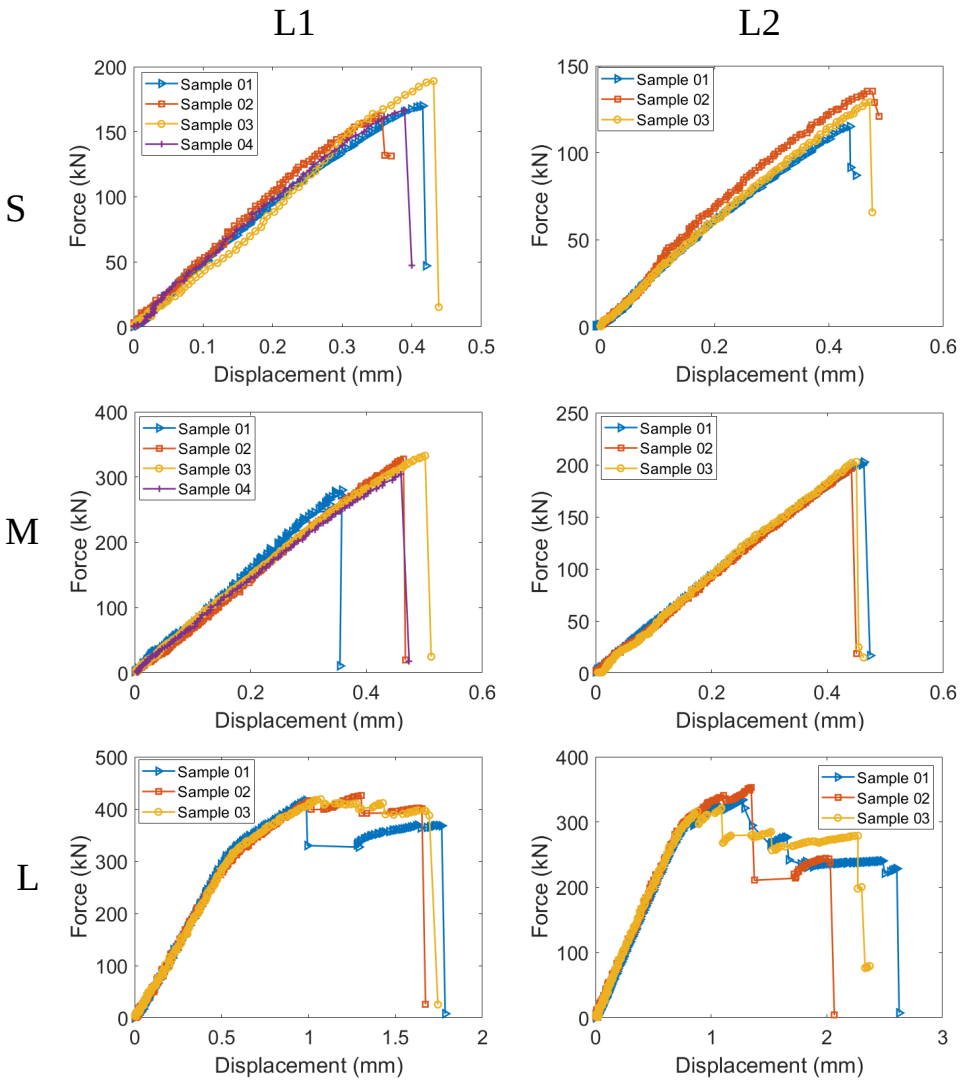

Figure 3.15: CAI load-displacement responses of all the 48-ply impacted samples.

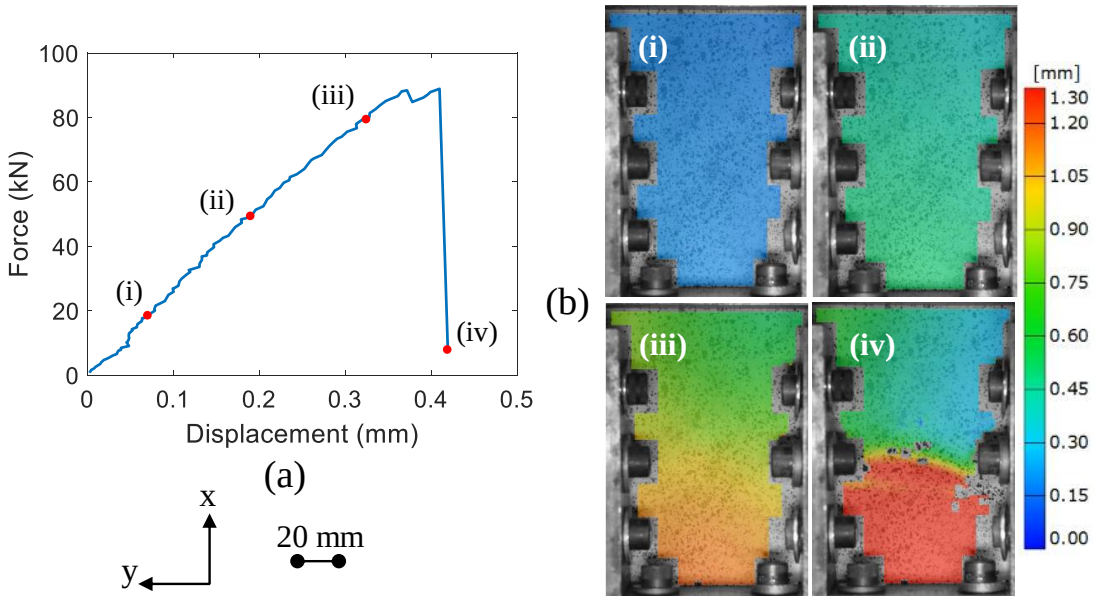

Figure 3.16: Load history vs. deformation history of an impacted L1-S-24 sample: (a) load-displacement response, and (b) axial deformation history.

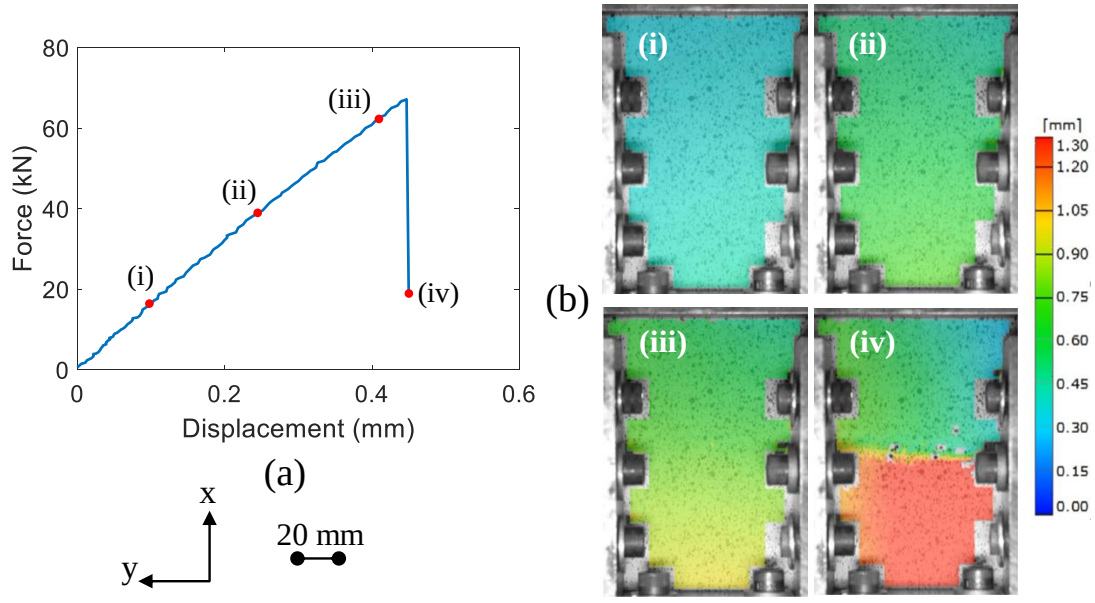

Figure 3.17: Load history vs. deformation history of an impacted L2-S-24 sample: (a) load-displacement response, and (b) axial deformation history.

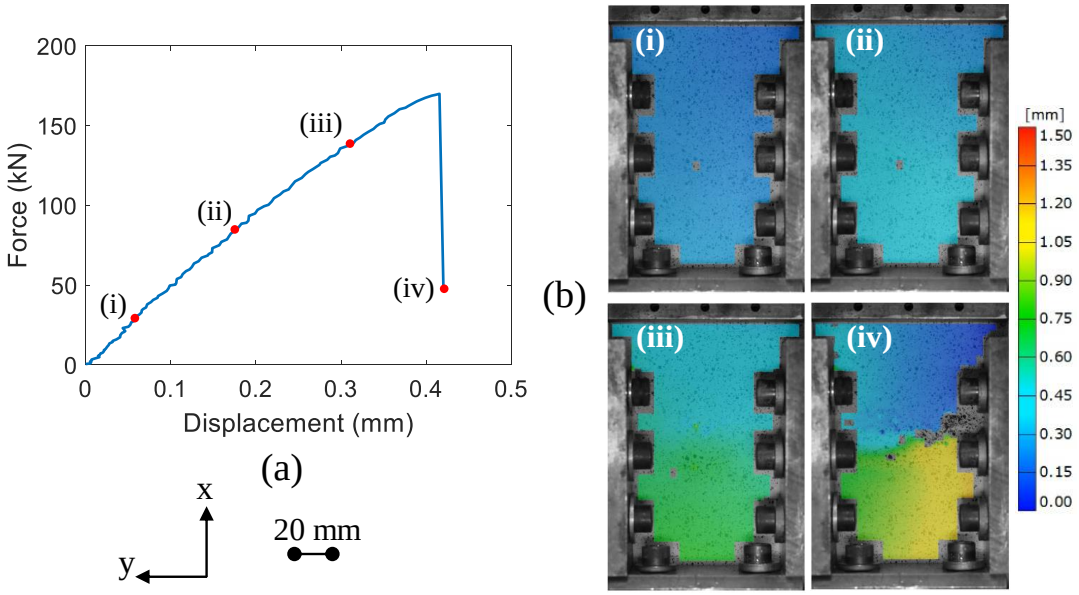

Figure 3.18: Load history vs. deformation history of an impacted L1-S-48 sample: (a) load-displacement response, and (b) axial deformation history.

L1/L2-S-24 samples, with 2D DIC characterizing deformation fields on both sides of the samples. The load-displacement curves with the deformation history are plotted in Figures 3.18 and 3.19. The CAI behavior displayed in Figures 3.18 and 3.19 is almost identical to that in Figures 3.16 and 3.17: the load-displacement curves are linear followed by sharp load drops, while the deformation fields are uniform along the y-axis until the final failure stage where strong axial deformation discontinuities can be seen.

Deformation of the L1/L2-M-24 samples

For the L1/L2-M-24 samples, 3D DIC characterization was performed for the impacted side while 2D DIC was performed for the non-impacted side. 3D DIC results are shown in Figures 3.20 and 3.21. Since the post-buckling behavior is seen from Figure 3.14, the load-out-of-plane-displacement responses are also plotted in Figures 3.20 and 3.21. The out-of-plane displacement was obtained from the 3D DIC characterization as the max deformation of the whole deformation field. After the drastic final CAI failure, the location where the maximum out-of-plane deformation

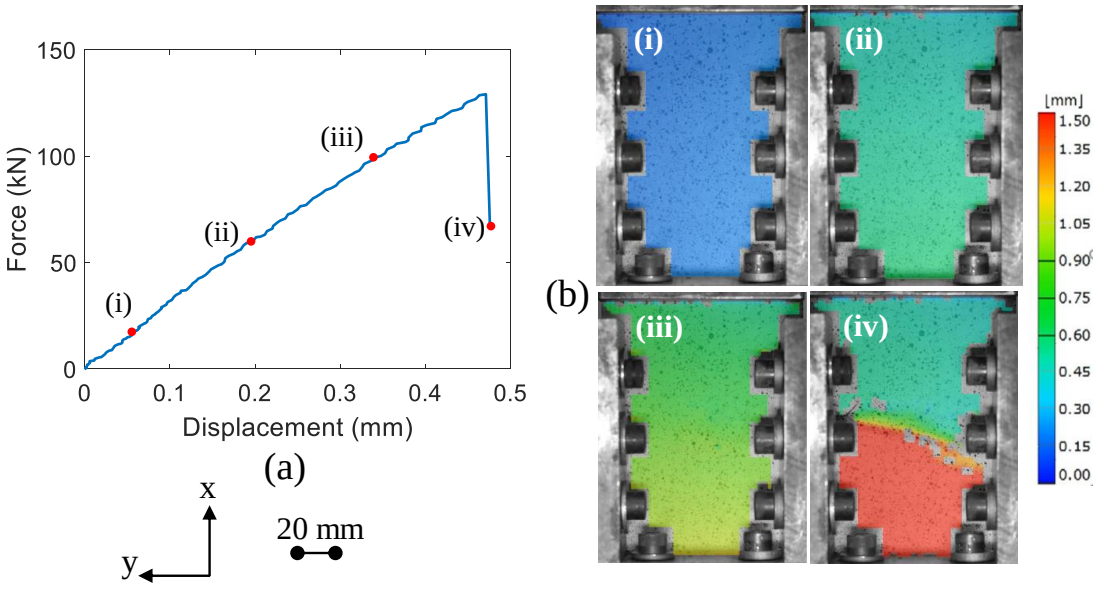

Figure 3.19: Load history vs. deformation history of an impacted L2-S-48 sample: (a) load-displacement response, and (b) axial deformation history.

takes place might change, so the load-out-of-plane-displacement responses are only plotted until the stage right before the final drastic failure. From Figures 3.20 (b) and 3.21 (b), at stages (i) and (ii), the out-of-plane displacement of the samples is small, implying that the sample at these two stages were still in the pre-buckling state. Between stage (ii) and (iii), post-buckling took place, as also seen in the out-of-plane deformation fields in Figures 3.20 (c) and 3.21 (c). At the final failure, the deformation field of the L1-M-24 sample is different than that of the L2-M-24 sample. The sharp out-of-plane deformation discontinuity in Figure 3.20 (c), stage (vi) seems to be closer to the top clamp, while the discontinuity of the L2-M-24 sample concentrates around the center of the sample, similar to that in Figures 3.16 to 3.19.

Deformation of the L1/L2-M-48 samples

The load-axial-displacement response and out-of-plane deformation history of the L1/L2-M-48 samples are displayed in Figures 3.22 and 3.23. Since the post-buckling behavior is not seen in the load-axial-displacement curves, the load-out-of-plane-displacement response is not plotted. The load-axial-displacement curves in the

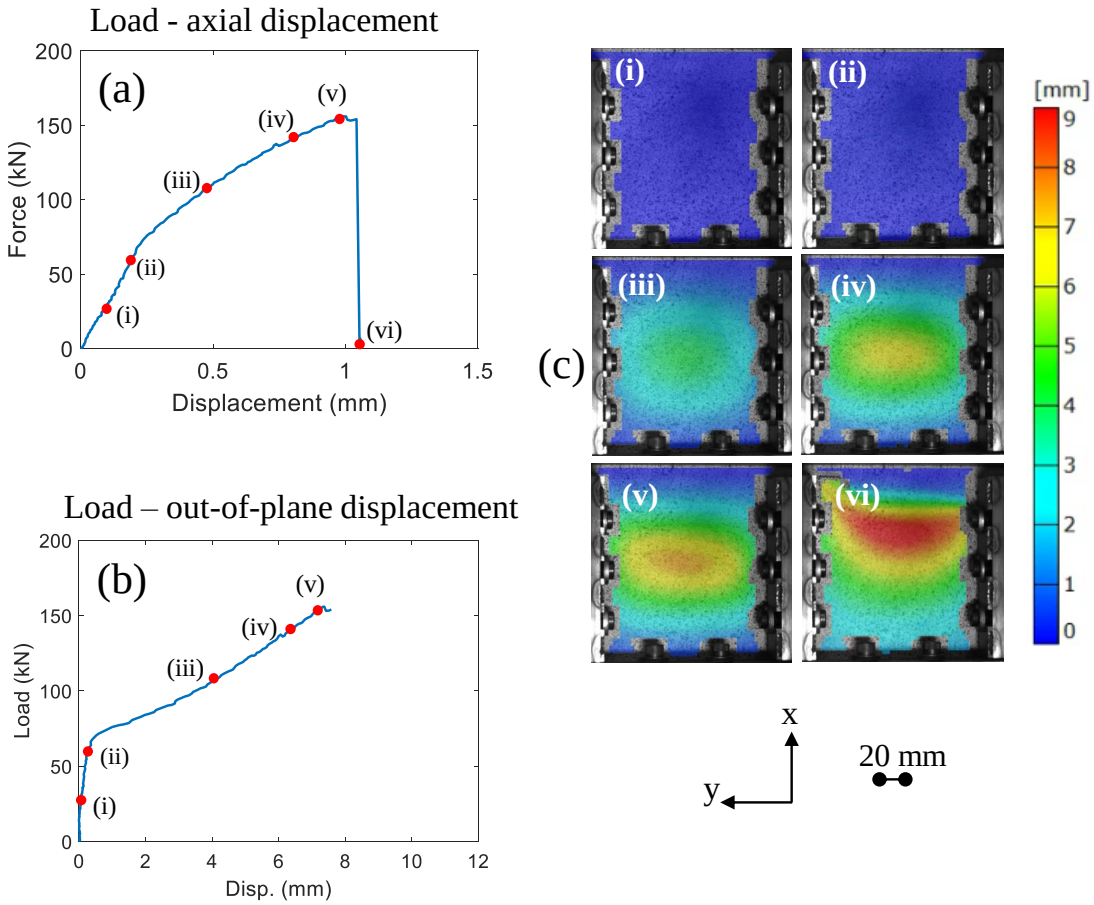

Figure 3.20: Load history vs. deformation history of an impacted L1-M-24 sample: (a) load-axial-displacement response, (b) load-out-of-plane-displacement response, and (c) out-of-plane deformation history.

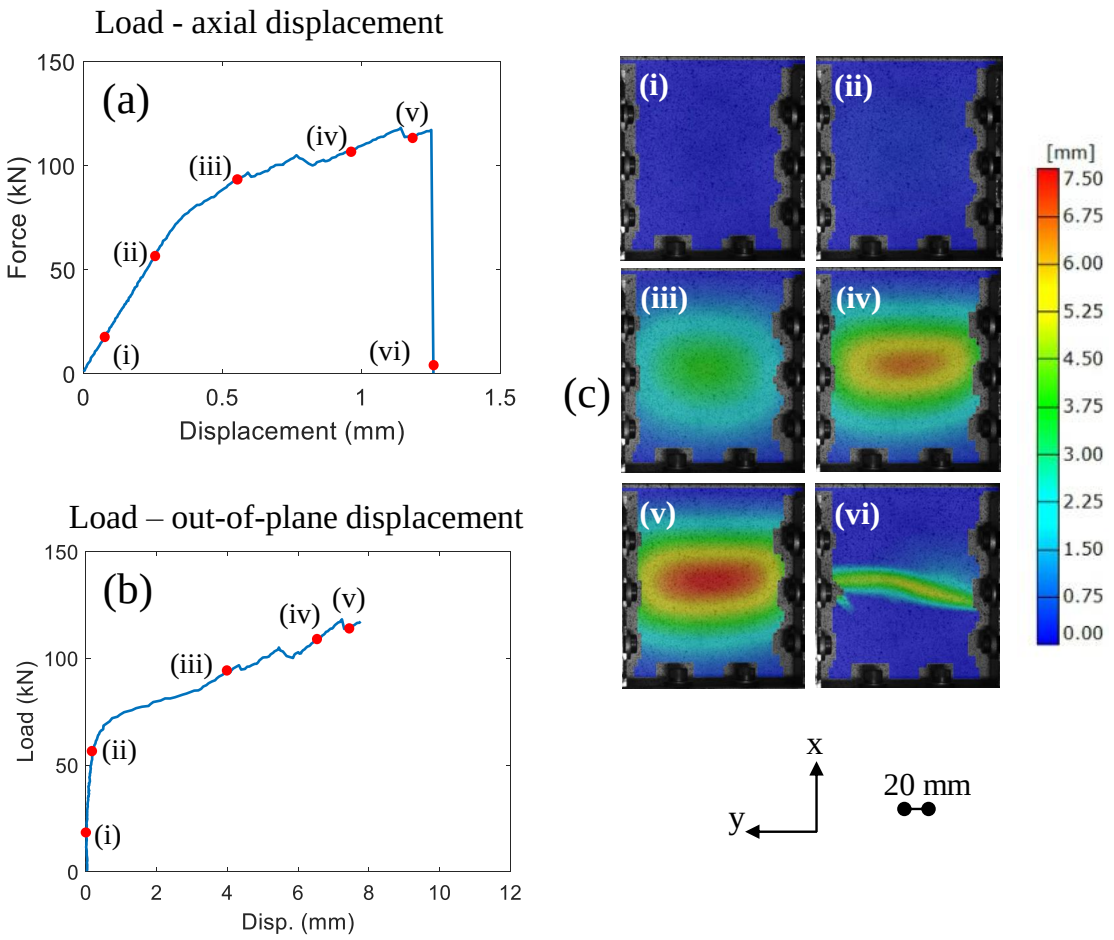

Figure 3.21: Load history vs. deformation history of an impacted L2-M-24 sample: (a) load-displacement response, (b) load-out-of-plane-displacement response, and (c) out-of-plane deformation history.

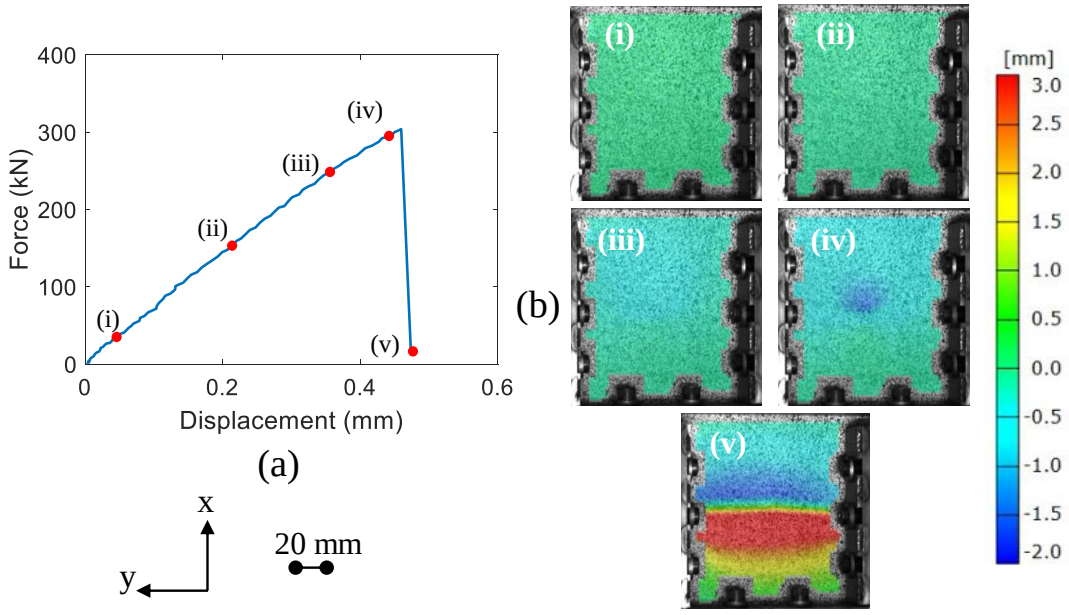

Figure 3.22: Load history vs. deformation history of an impacted L1-M-48 sample: (a) load-displacement response, and (b) out-of-plane deformation history.

figures are linear, similar to that in Figures 3.16 to 3.19, implying that there was no global post-buckling of the samples. However, a small amount of local out-of-plane deformation can be visualized around the impacted areas in Figures 3.22 (b) and 3.23 (b), starting from stage (iii). Although with the local out-of-plane deformation, the load-displacement curves seem unaffected. This out-of-plane deformation is most likely to be caused by the local buckling of the LVI-induced delaminated areas. At stage (v), after the drastic load drops, sharp discontinuities in the out-of-plane deformation fields are seen.

Deformation of the L1/L2-L-24 samples

The load-axial-displacement, load-out-of-plane-displacement, and deformation fields of L1/L2-L-24 samples are plotted in Figures 3.24 and 3.25. The behavior seen in the figures is very similar to that in Figure 3.20. At stages (i) and (ii), the out-of-plane deformation is very small, meaning that the deformation of the sample during the test was mostly in-plane. Between stages (ii) and (iii), transitioning happened and

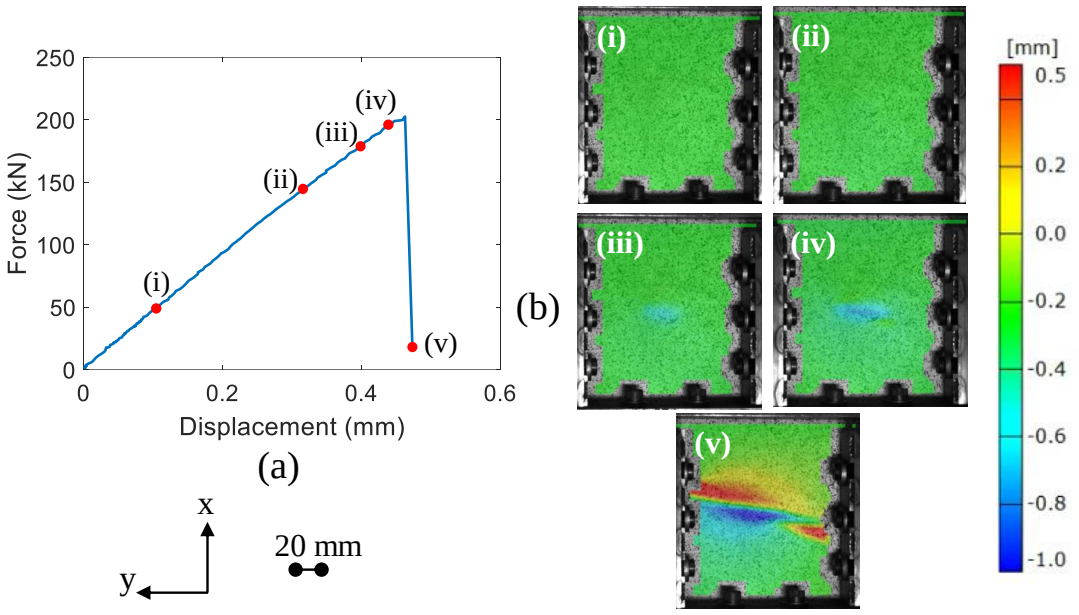

Figure 3.23: Load history vs. deformation history of an impacted L2-M-48 sample: (a) load-displacement response, and (b) out-of-plane deformation history.

the samples changed to the post-buckling state. The post-buckling parts of the load-axial-displacement and load-out-of-plane-displacement curves are smooth, meaning that no damage happened along with the post-buckling. Between stages (iv) and (v), sharp load drops are seen. The failure bands with deformation discontinuities at stage (vi) in Figures 3.24 and 3.25 are closer to the top clamp of the CAI fixture. According to Figures 3.24 and 3.25, for the L1/L2-L-24 samples, the post-buckling happened very early and the final CAI failure took place in the deep post-buckled state.

Deformation of the L1/L2-L-48 samples

The post-buckling behavior is also observed for the L1/L2-L-48 samples from Figures 3.26 and 3.27. At stages (i) and (ii), the behavior of the samples was in-plane. After the transitioning points between stages (ii) and (iii), the curves are found jagged, indicating that progressive damage grew along with the post-buckling of the samples. From stage (iii) to stage (vi), the damage growth can be visualized clearly

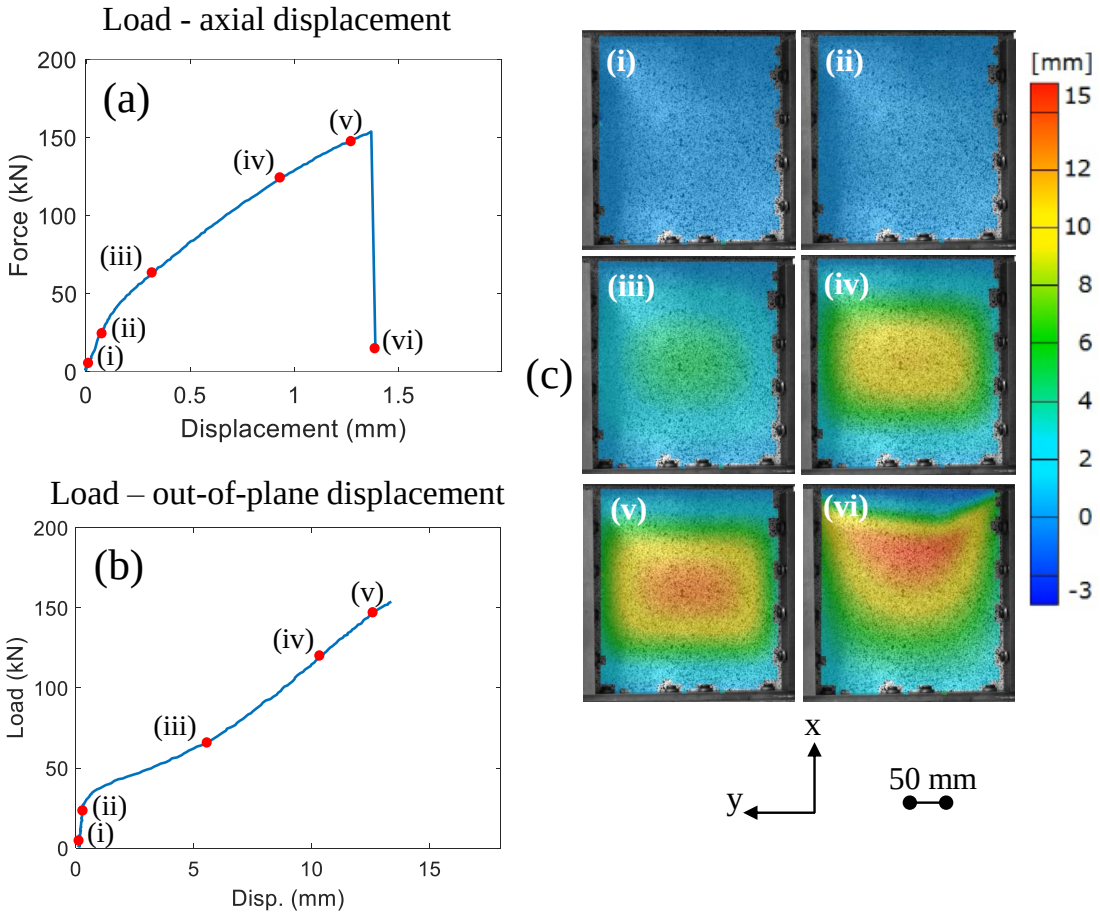

Figure 3.24: Load history vs. deformation history of an impacted L1-L-24 sample: (a) load-axial-displacement response, (b) load-out-of-plane-displacement response, and (c) out-of-plane deformation history.

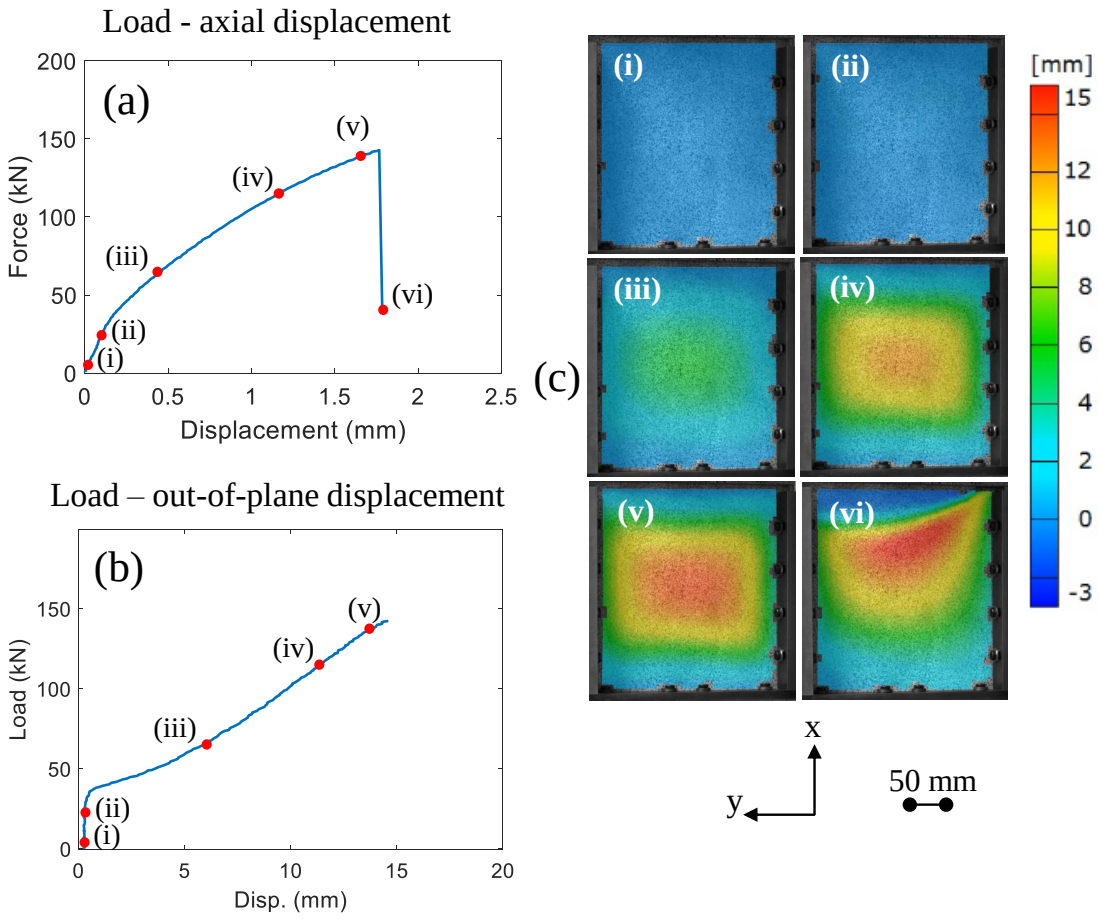

Figure 3.25: Load history vs. deformation history of an impacted L2-L-24 sample: (a) load-axial-displacement response, (b) load-out-of-plane-displacement response, and (c) out-of-plane deformation history.

in Figure 3.26. Unlike the L1/L2-L-24 samples, the transitioning of the L1/L2-L-48 samples happened much later. In addition, the final failure bands seem to concentrate near the centers of the samples. Comparing Figure 3.26 with 3.27, it is noticed that the out-of-plane deformation directions of the displayed two samples are different. For the L1-L-48 sample, the deformation was from the impacted side to the non-impacted side. The out-of-plane deformation of the L2-L-48 sample was reversed. After checking the 3D DIC characterization of all the L1/L2-L-48 samples, it is found that all the L1-L-48 samples bent in the same direction, while two of the L2-L-48 samples bent reversely compared to that shown in Figure 3.27. It should also be pointed out that the out-of-plane displacement value plotted in Figure 3.26 (b) is the absolute value.

3.4.2 CAI-induced Damage

CAI-induced damage on the outer surfaces of representative samples is displayed in Figures 3.28 to 3.33. Only L1 samples of different panel sizes are demonstrated, since the damage modes of L1 and L2 samples are highly similar. The non-impacted side of a failed L1-S-24 sample due to the CAI loading is shown in Figure 3.28. Back-ply splitting along the 45° direction caused by LVI is marked with orange dashed lines. Not too much damage can be seen on the non-impacted surface shown in Figure 3.28(a). However, from the side views shown in Figure 3.28 (b) and (c), damage modes including delamination, matrix cracking, and fiber kinking are observed. The damage patterns observed from the non-impacted surface in Figure 3.28 (a) is significantly less obvious than the T800s/3900-2B samples studied in Section 3.3. This might be due to the fact that T800s/3900-2B is an interface-toughened material system. Under compressive loading, interface delamination is suppressed, hence more fiber damage and matrix cracking appear on the surfaces of the T800s/3900-2B samples.

The inspected surface damage of the L1-S-48 sample has a damage pattern similar

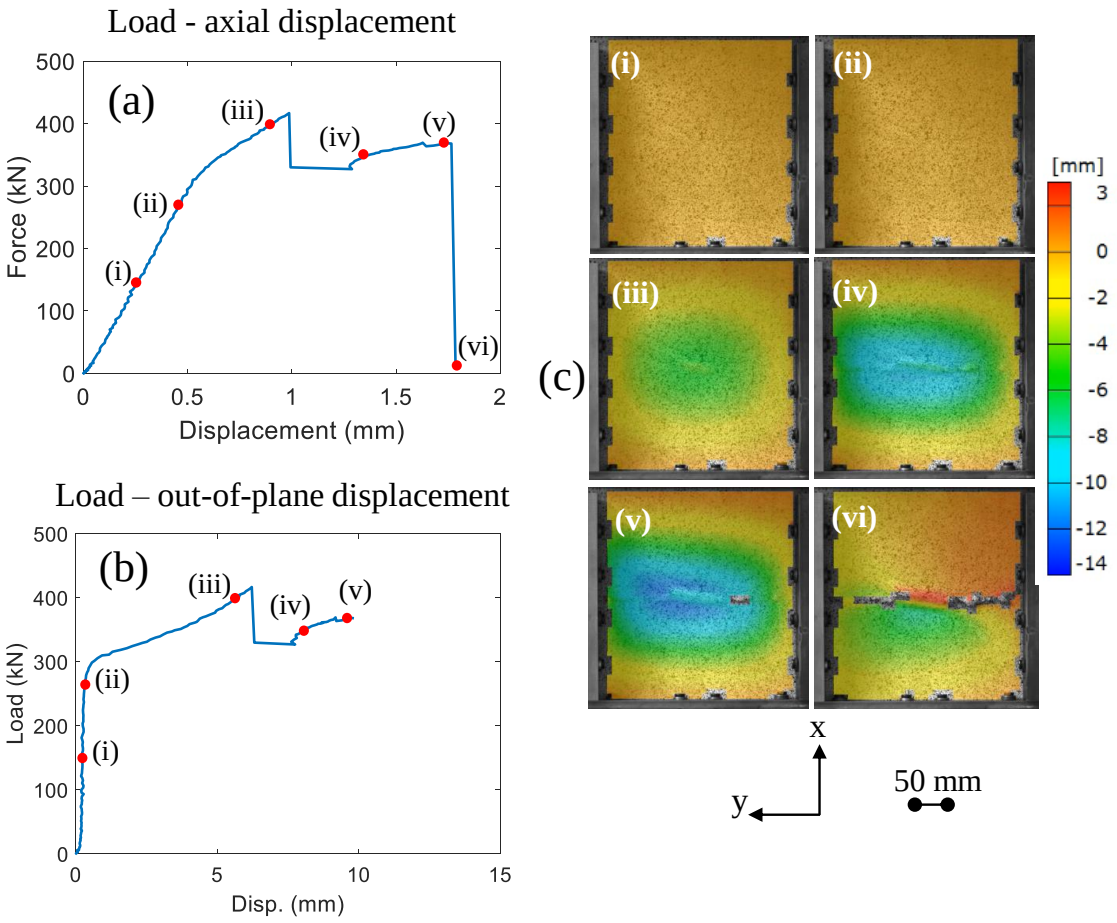

Figure 3.26: Load history vs. deformation history of an impacted L1-L-48 sample: (a) load-axial-displacement response, (b) load-out-of-plane-displacement response, and (c) out-of-plane deformation history.

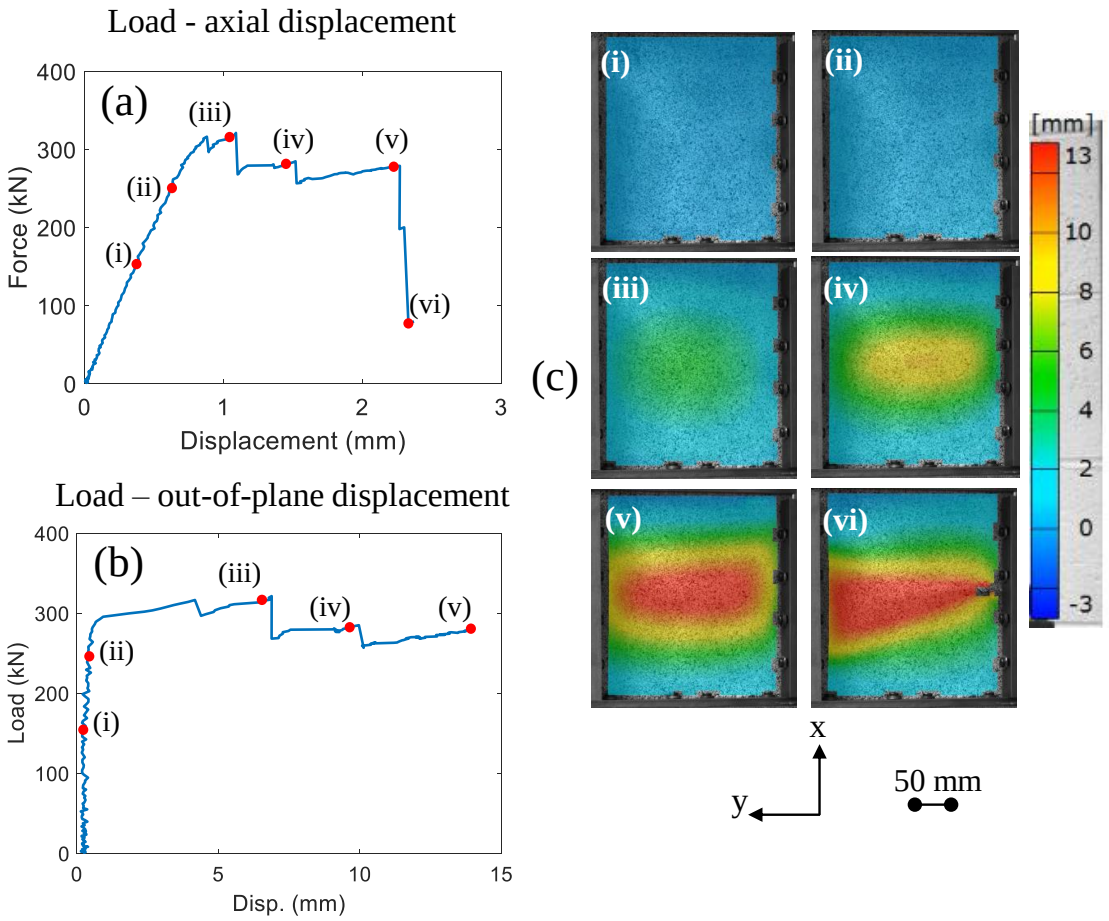

Figure 3.27: Load history vs. deformation history of an impacted L2-L-48 sample: (a) load-axial-displacement response, (b) load-out-of-plane-displacement response, and (c) out-of-plane deformation history.

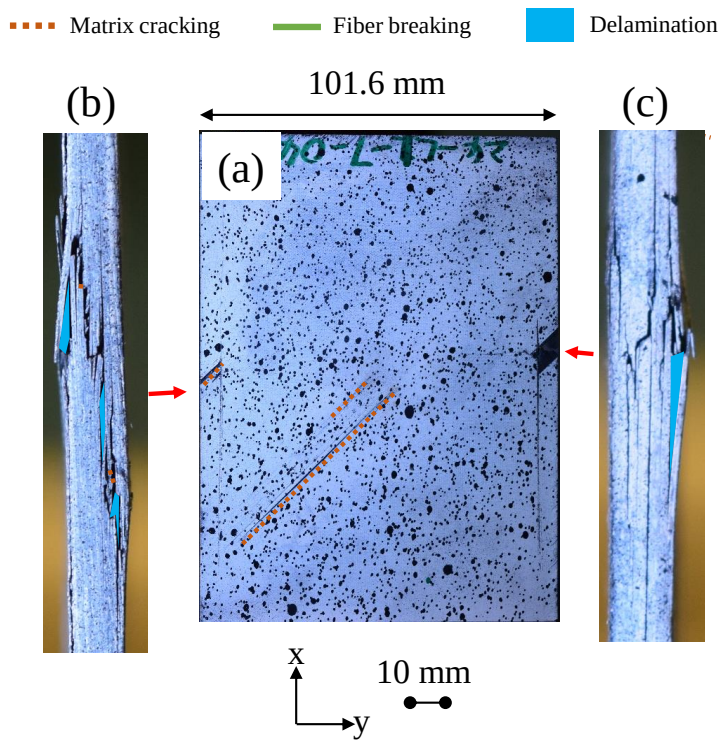

Figure 3.28: Surface inspections of the CAI-induced damage of an L1-S-24 sample: (a) non-impacted surface, (b) left side view, and (c) right side view.

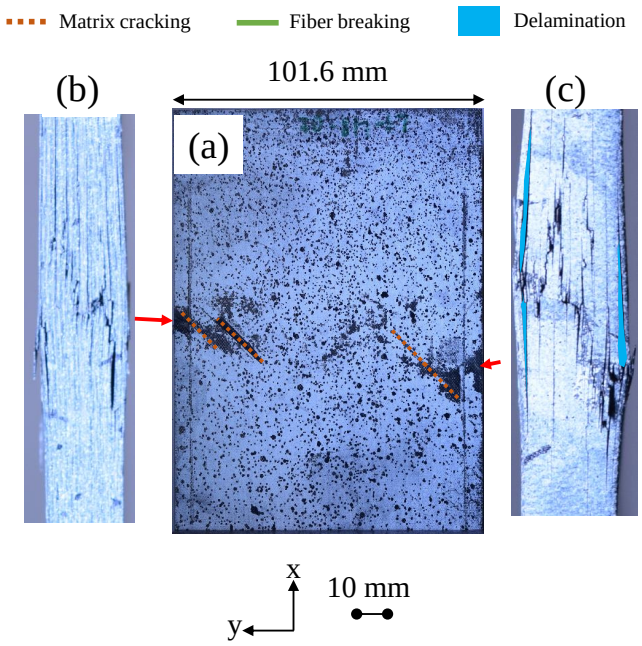

Figure 3.29: Surface inspections of the CAI-induced damage of an L1-S-48 sample: (a) non-impacted surface, (b) left side view, and (c) right side view.

to that shown in Figure 3.29. The surface damage is quite limited and not easily visible. From the side views, a great extent of delamination at many interfaces is seen, together with matrix cracking and fiber breaking.

Damage patterns of the L1-M-24 sample inspected from the outer surfaces are displayed in Figure 3.30. From the non-impacted surface, Figure 3.30 (a), a long matrix cracking can be seen, denoted by an orange dashed line, along the 45° direction. Damage on the rest of the surface seems relatively small. From the side views, large-scale delamination is seen. In Figure 3.30 (c), delamination is found close to the top clamp, connecting with the long matrix crack observed in Figure 3.30. The overall damage pattern is similar to the out-of-plane deformation field of the sample after the CAI failure.

The damage modes of the L1-M-48 sample are similar to that of the L1-S-24 and L1-S-48 samples. Damage patterns can be clearly visualized only from the side views, as shown in Figure 3.31. Different from Figure 3.30, the damage seems to be closer to

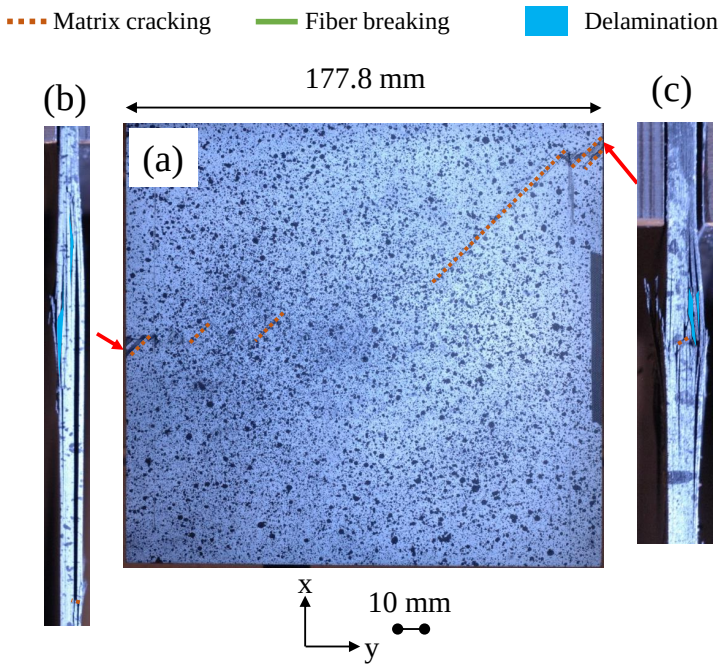

Figure 3.30: Surface inspections of the CAI-induced damage of an L1-M-24 sample: (a) non-impacted surface, (b) left side view, and (c) right side view.

the impacted area for the L1-M-48 sample, while the damage of the L1-M-24 sample seems to be closer to the top clamp.

The damage pattern of the L1-L-24 sample is similar to that of the L1-M-24 sample, meaning that the CAI-induced damage is barely visible from the impacted and non-impacted sides. After a careful check, fiber compressive breaking is found on the impacted side, as marked by the green solid lines in Figure 3.32. Again, the damage is remote from the impacted center of the sample.

The damage pattern of the L1-L-48 sample is similar to that of the L1-M-48 sample. A small amount of surface damage can be seen in Figure 3.33 (a), mostly matrix crack. From the side view, extensive delamination can be observed. The CAI-induced damage seems to form a failure band going across the impacted sample center.

CAI-induced damage of selected samples are presented in Figure 3.34. The selected samples include L2-S-24, L2-S-48, L1-M-24, L1-M-48, L2-L-24, and L2-L-48

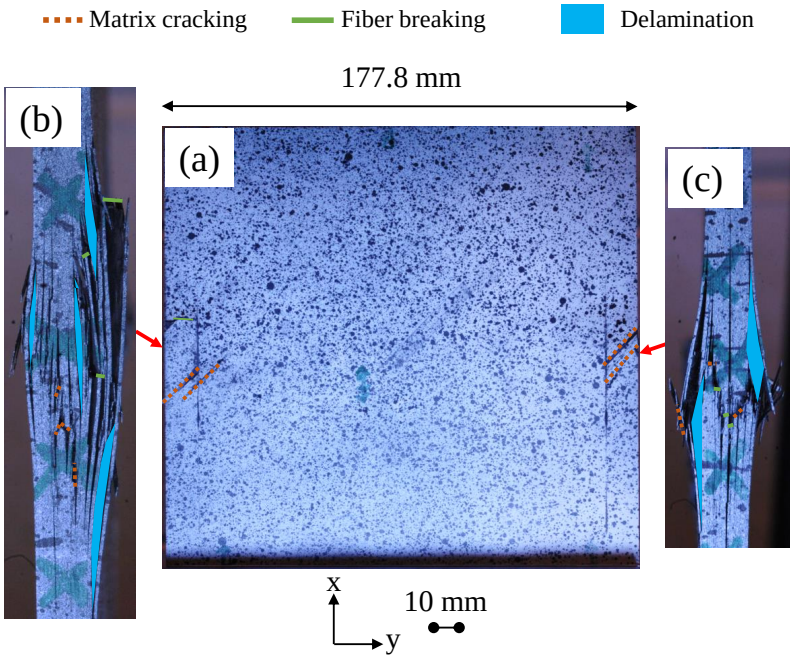

Figure 3.31: Surface inspections of the CAI-induced damage of an L1-M-48 sample: (a) non-impacted surface, (b) left side view, and (c) right side view.

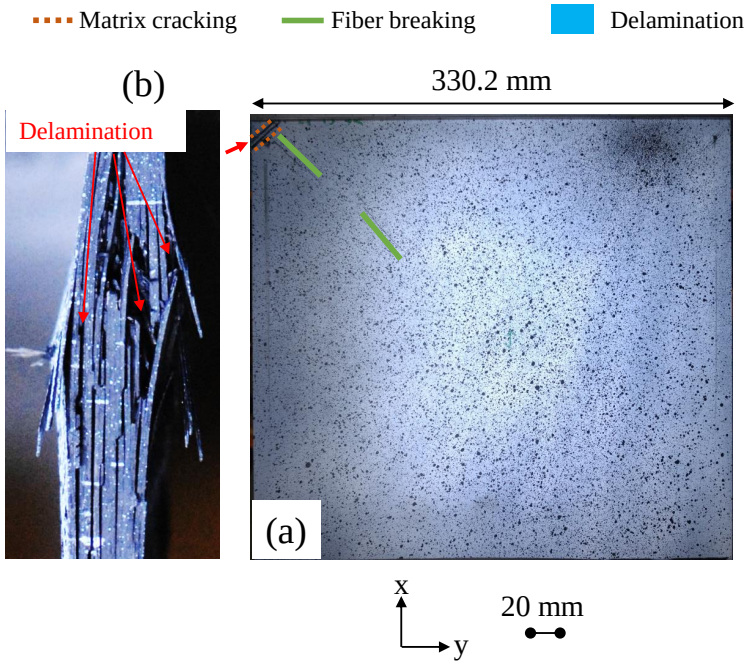

Figure 3.32: Surface inspections of the CAI-induced damage of an L1-L-24 sample: (a) non-impacted surface, and (b) left side view.

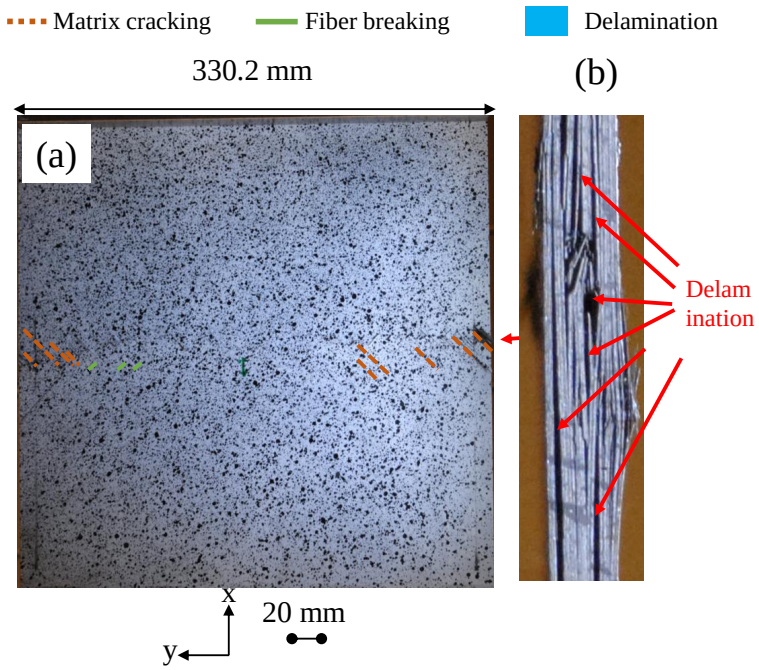

Figure 3.33: Surface inspections of the CAI-induced damage of an L1-L-48 sample: (a) non-impacted surface, and (b) left side view.

samples. It is seen in Figure 3.34 that on the left side of the dashed lines, the CAI-induced damage is in the form of a band going across the LVI-induced damage. These are the samples whose CAI behavior was mostly in-plane. On the right side of the dashed line, the damage seems to be not majorly caused by LVI-induced damage, especially for the L2-L-24 sample, where the failure band is not connected with the LVI-induced damage. For the L2-L-48 sample, the damage near the lateral edges is significantly larger than that near the LVI-induced damage. Post-buckling occurred for the three samples on the right side of the dashed line.

The tested peak loads and transitioning loads for the cases with post-buckling are summarized in Table 3.1. As displayed in the table, the loads of the samples with and without post-buckling are colored yellow and purple.

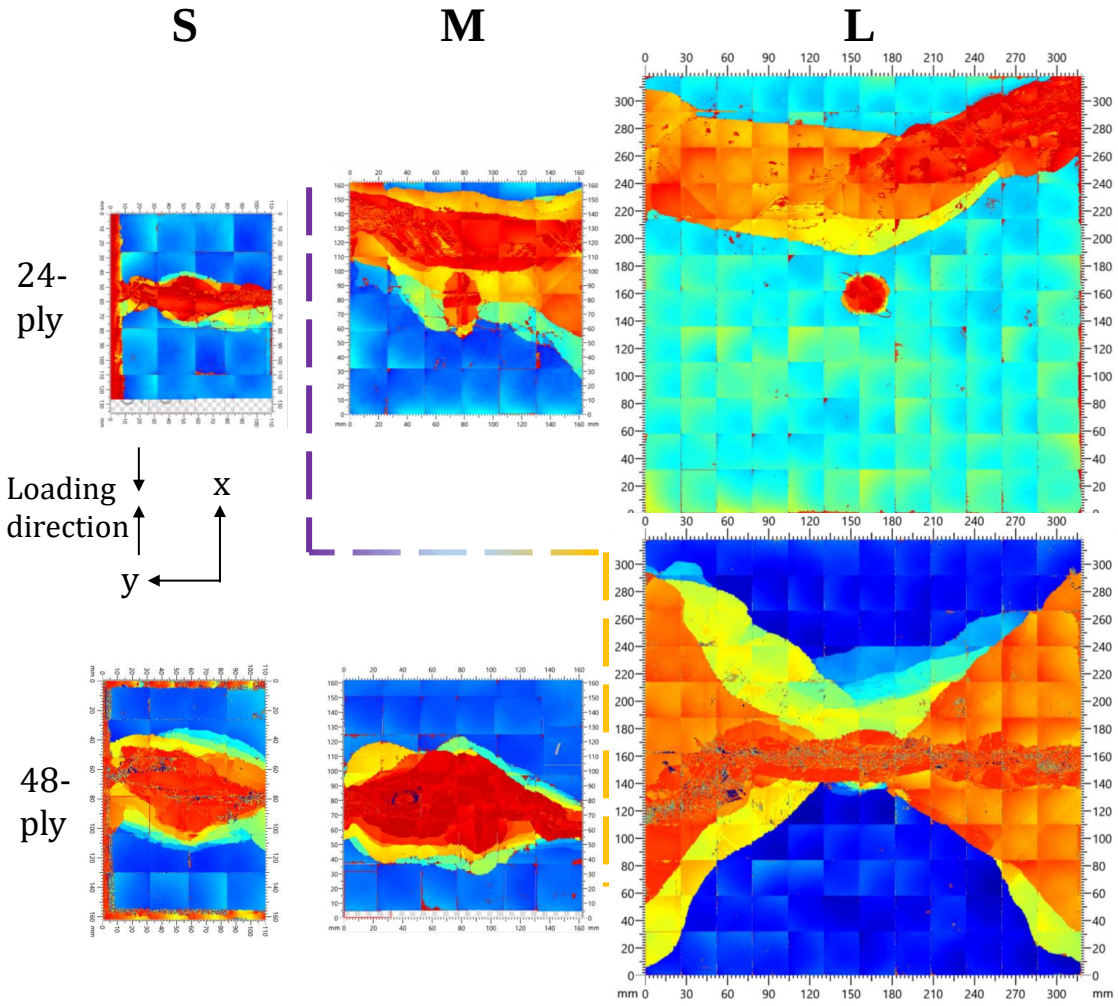

Figure 3.34: CAI-induced damage characterized by ultrasound C-scanning.

Table 3.1: A summary of the tested peak loads and transitioning loads.

L1

	S		M		L	
24-ply	Ultimate peak load (kN)	Transitioning load (kN)	Ultimate peak load (kN)	Transitioning load (kN)	Ultimate peak load (kN)	Transitioning load (kN)
	86.7	NA	155.8	71.7	153.2	39.8
48-ply	Ultimate peak load (kN)	Transitioning load (kN)	Ultimate peak load (kN)	Transitioning load (kN)	Ultimate peak load (kN)	Transitioning load (kN)
	172.0	NA	311.1	NA	420.6	315.7

Linear

Bi-linear

L2

	S		M		L	
24-ply	Ultimate peak load (kN)	Transitioning load (kN)	Ultimate peak load (kN)	Transitioning load (kN)	Ultimate peak load (kN)	Transitioning load (kN)
	69.6	NA	118.1	72.5	142.6	38.2
48-ply	Ultimate peak load (kN)	Transitioning load (kN)	Ultimate peak load (kN)	Transitioning load (kN)	Ultimate peak load (kN)	Transitioning load (kN)
	126.5	NA	200.6	NA	334.5	294.1

In this section, the CAI-induced damage of the panel size effect studies have been presented. The tested load-displacement curves are mostly very repetitive. The overall CAI behavior of the L1/L2-S-24/48 samples and L1/L2-M-48 samples is in-plane, with the load-axial-displacement responses being linear. Post-buckling responses are observed for the L1/L2-M-24 and L1/L2-L-24/48 samples, with the load-axial-displacement curves being bi-linear. The panel size has a significant influence on the deformation of samples during CAI. The CAI-induced damage of the L1-M-24 and L1/L2-L-24 samples is remote from the impacted areas, while the CAI damage of the other samples took place near the impacted areas.

3.5 Summary and Conclusions

In this chapter, experimental results of the CAI studies concerning the stacking sequence effects and the panel size effects have been presented. In Section 3.3 which discusses about the stacking sequence effects, three stacking sequences have been studied, including $[0/45/0/90/0/\text{-}45/0/45/0/\text{-}45]_s$ (layup A), $[45/0/\text{-}45/90]_{3s}$ (layup B), and $[45/\text{-}45/0/45/\text{-}45/90/45/\text{-}45/45/\text{-}45]_s$ (layup C). The sample in-plane size is 150 mm $\times$ 100 mm. The material system is T800s/3900-2B. For each layup, three impact energies were examined, and the impacted sample were subjected to the CAI loading. For each test case as described in Table 2.1, three impacted samples were compressed, with repeatable results observed. Layup B samples have the highest CAI peak loads when impacted with the same amount of impact energy compared to layup A and layup C samples. The reason is that layup B (24-ply) is thicker than layup A (20-ply) and layup C (20-ply). The CAI peak loads of layup A are uniformly higher than that of layup C, due to the fact that layup A has 50% of 0° plies while layup C only has 10% of 0° plies. The degrading trend of the CAI peak loads with the overall areas of the LVI-induced damage resembles the trend reported in a notch sensitivity study through OHC tests [116]. In general, the CAI induced failure patterns of the

three layups are similar. A higher extent of fiber damage is observed on the surfaces of a failed layup A sample, possibly due to the higher percentage of 0° plies.

Section 3.4 reports the experimental CAI results of the panel size effect study. Two layups have been studied, each with three in-plane sizes and two thicknesses (number of plies). The layups are L1: $[45/\text{-}45/0/90/0/0]_{ns}$ and L2: $[45/0/\text{-}45/90]_{ns}$. The sample in-plane sizes are named S, M, and L, corresponding to 152.4 mm x 101.6 mm, 177.8 mm x 177.8 mm, and 330.2 mm x 330.2 mm. The two thicknesses of the samples correspond to 24-ply and 48-ply. The material system tested is IM7/977-3. The impact energy levels can be found in Table 2.2. For each test case, three samples were tested. For most cases, highly repeatable load-axial-displacement responses have been observed, except for the L1-M-48 and L2-L-24 samples. The difference among the test results is believed to be caused by manufacturing-induced defects and randomness in the distribution of material properties. According to the experimental study, the panel size has a strong influence on the CAI behavior of the samples. With a relatively large thickness-to-length/width ratio, the CAI behavior of a sample is most likely to be in-plane, except for a small amount of local out-of-plane deformation due to the local buckling of LVI-induced delaminated plies. As the thickness-to-length/width ratio decreases, such as that for the L1/L2-M-24 and L1/L2-L-24/48 samples, post-buckling took place during the CAI loading. The CAI-induced damage pattern is significantly affected by the post-buckling response. Without post-buckling, the CAI damage is concentrated around the impacted areas. However, for some cases with post-buckling, such as for the L1-M-24 and L1/L2-L-24 samples, the CAI damage is remote from the impacted areas.

The experimental work presented in this chapter contributes to the understanding of the effects of stacking sequence and panel size on the CAI behavior and CAI-induced damage patterns. The experimental results can be used to examine the fidelity and versatility of computational models in predicting the CAI peak loads and if the the

failure modes and post-buckling response are accurately captured.

CHAPTER IV

2D and 3D Enhanced Schapery Theory with Material Inelasticity (EST-InELA)

4.1 Introduction

EST is a thermodynamically based work potential model seamlessly combining the Schapery theory (ST) [90] and Bazant's crack band (CB) approach [71]. EST was firstly developed in [39] and latter applied to various problems including open-hole tension/compression (OHT/OHC) [112], unnotched tension (UNT) [67], bolted joints [6], LVI [21], and CAI [60]. In this thesis, EST serves as the intra-ply constitutive model of composites. The inter-ply damage (delamination) is captured by Abaqus built-in cohesive contact model. 2D plane-stress and 3D versions of EST have been developed. Since 2D EST has been outlined in detail in [21] and can be regarded as a subset of 3D EST, in this thesis, only 3D EST and its implementation will be introduced.

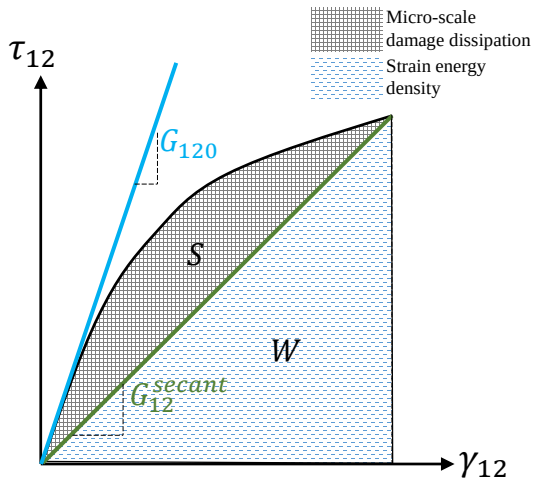

Figure 4.1: Pre-peak nonlinear behavior in the shear 12 direction.

4.2 3D Enhanced Schapery Theory (EST) Model

4.2.1 Pre-peak Nonlinearity: ST

The term "pre-peak" represents the part on the stress-strain curve before the tangent stiffness decreasing to zero. Nonlinear pre-peak behavior happens in matrix shear and tensile cracking. In EST, the nonlinear pre-peak behavior is governed by ST. The typical pre-peak nonlinear behavior in the in-plane shear 12 direction is as shown in Figure 4.1. In the pre-peak region, the total work potential W_T is composed of the strain energy density W and energy dissipation S due to microscale cracking of composites. W and S are as illustrated in Figure 4.1. The work potential balance is Equation 4.1.

$$W_T = W + S \tag{4.1}$$

According to [90], the total work potential is stationary to the energy dissipation

$$\frac{dW_T}{dS} = 0 \tag{4.2}$$

Substituting Equation 4.1 into Equation 4.2

$$\frac{dW}{dS} = -1 \tag{4.3}$$

According to the second law of thermodynamics, it follows that

$$\dot{S} \geq 0 \tag{4.4}$$

The strain energy density W for a full 3D stress state is

$$\begin{aligned} W =& \frac{1}{2}(C_{11}^{sec}\epsilon_{11}^2 + C_{22}^{sec}\epsilon_{22}^2 + C_{33}^{sec}\epsilon_{33}^2) + \\ & (C_{12}^{sec}\epsilon_{11}\epsilon_{22} + C_{13}^{sec}\epsilon_{11}\epsilon_{33} + C_{23}^{sec}\epsilon_{33}\epsilon_{22}) + \\ & \frac{1}{2}(C_{44}^{sec}\gamma_{23}^2 + C_{55}^{sec}\gamma_{13}^2 + C_{66}^{sec}\gamma_{12}^2) \end{aligned} \tag{4.5}$$

In Equation 4.5, the superscript "sec" means for the secant stiffness terms. The terms of the secant stiffness matrix C^{sec} are

$$C_{11}^{sec} = \frac{1 - \nu_{23}\nu_{32}}{E_{22}^{sec}E_{33}^{sec}\Delta} \tag{4.6a}$$

$$C_{22}^{sec} = \frac{1 - \nu_{13}\nu_{31}}{E_{11}^{sec}E_{33}^{sec}\Delta} \tag{4.6b}$$

$$C_{33}^{sec} = \frac{1 - \nu_{12}\nu_{21}}{E_{11}^{sec}E_{22}^{sec}\Delta} \tag{4.6c}$$

$$C_{23}^{sec} = \frac{\nu_{23} + \nu_{21}\nu_{13}}{E_{11}^{sec}E_{22}^{sec}\Delta} \tag{4.6d}$$

$$C_{13}^{sec} = \frac{\nu_{13} + \nu_{12}\nu_{23}}{E_{11}^{sec}E_{22}^{sec}\Delta} \tag{4.6e}$$

$$C_{12}^{sec} = \frac{\nu_{12} + \nu_{32}\nu_{13}}{E_{11}^{sec}E_{33}^{sec}\Delta} \tag{4.6f}$$

$$C_{44}^{sec} = G_{23}^{sec} \tag{4.6g}$$

$$C_{55}^{sec} = G_{13}^{sec} \tag{4.6h}$$

$$C_{66}^{sec} = G_{12}^{sec} \tag{4.6i}$$

$$\Delta = \frac{1 - \nu_{12}\nu_{21} - \nu_{23}\nu_{32} - \nu_{13}\nu_{31} - 2\nu_{21}\nu_{32}\nu_{13}}{E_{11}^{sec}E_{22}^{sec}E_{33}^{sec}} \tag{4.6j}$$

According to ST, secant stiffness values are calculated from the pristine values with Schapery micro-damage functions $e_s(S)$ and $g_s(S)$

$$E_{22}^{sec} = E_{220}e_s(S) \tag{4.7a}$$

$$E_{33}^{sec} = E_{220}e_s(S) \tag{4.7b}$$

$$G_{12}^{sec} = G_{120}g_s(S) \tag{4.7c}$$

$$G_{13}^{sec} = G_{120}g_s(S) \tag{4.7d}$$

$$G_{23}^{sec} = G_{230}e_s(S) \tag{4.7e}$$

where, E_{220}, G_{120}, and G_{230} are pristine material moduliIn this thesis, $e_s(S)$ is assumed identical to $g_s(s)$. It should be noted that the material transverse isotropy has been assumed such that E_{330}=E_{220} and G_{130}=G_{120} to simplify the equations. Substitute Equation 4.5 into Equation 4.3, and introduce a reduced damage variable S_r defined as $S_r = \sqrt[3]{S}$ [39]

$$\begin{aligned}[2(\nu_{12} + \nu_{12}\nu_{23})\epsilon_{11}\epsilon_{22} + 2(\nu_{23} + \nu_{12}\nu_{21})\epsilon_{22}\epsilon_{33} + 2(\nu_{12} + \nu_{12}\nu_{23})\epsilon_{11}\epsilon_{33} + (1 - \nu_{12}\nu_{21})\epsilon_{22}^2 \\ + (1 - \nu_{12}\nu_{21})\epsilon_{33}^2]\frac{E_{220}}{\Lambda}\frac{de_s}{dS_r} + G_{230}\gamma_{23}^2\frac{de_s}{dS_r} + G_{120}(\gamma_{12}^2 + \gamma_{13}^2)\frac{dg_s}{dS_r} = -6{S_r}^2\end{aligned} \tag{4.8}$$

$$\Lambda = (1 - 2\nu_{12}\nu_{21} - \nu_{23}\nu_{32} - 2\nu_{12}\nu_{21}\nu_{23}) \tag{4.9}$$

Equation 4.8 is an ordinary differential equation (ODE) and referred to as the microscale damage evolution function. In EST, Equation 4.8 is constantly being solved to obtain the microscale damage dissipation and induced degradation of the secant moduli. The instantaneous secant moduli are calculated according to Equations 4.7a to 4.7e.

Finally, in the pre-peak region, the stress-strain relationship is

$$\begin{bmatrix} \sigma_{11} \\ \sigma_{22} \\ \sigma_{33} \\ \tau_{23} \\ \tau_{13} \\ \tau_{12} \end{bmatrix} = \begin{bmatrix} C_{11}^{sec} & C_{12}^{sec} & C_{13}^{sec} & 0 & 0 & 0 \\ C_{12}^{sec} & C_{22}^{sec} & C_{23}^{sec} & 0 & 0 & 0 \\ C_{13}^{sec} & C_{23}^{sec} & C_{33}^{sec} & 0 & 0 & 0 \\ 0 & 0 & 0 & C_{44}^{sec} & 0 & 0 \\ 0 & 0 & 0 & 0 & C_{55}^{sec} & 0 \\ 0 & 0 & 0 & 0 & 0 & C_{66}^{sec} \end{bmatrix} \begin{bmatrix} \epsilon_{11} \\ \epsilon_{22} \\ \epsilon_{33} \\ \gamma_{23} \\ \gamma_{13} \\ \gamma_{12} \end{bmatrix} \tag{4.10}$$

where, the secant stiffness terms can be calculated according to Equations 4.6.

Characterization of the Schapery Function $g_s(S_r)$

In-plane shear coupon-level tests of $\pm 45^\circ$ samples are performed for the characterization of $g_s(S_r)$. The characterization procedure of the IM7/977-3 material system is illustrated here for an example.

The in-plane shear tests follow the ASTM D3518 [117]. The sample's layup was $[45/\text{-}45/45/\text{-}45]_s$. The gauge area of the dogbone specimen was 82.6 mm $\times$ 25.4 mm, as shown in Figure 4.2 (a). The thickness of the sample was 965.2 μm. Quasi-static tensile tests were performed with the loading rating being 1 mm/min. 2D DIC was performed with the tests to capture the stain field. With the load data and DIC information, the nonlinear τ_{12} - γ_{12} relationship can be obtained. τ_{12} is calculated by

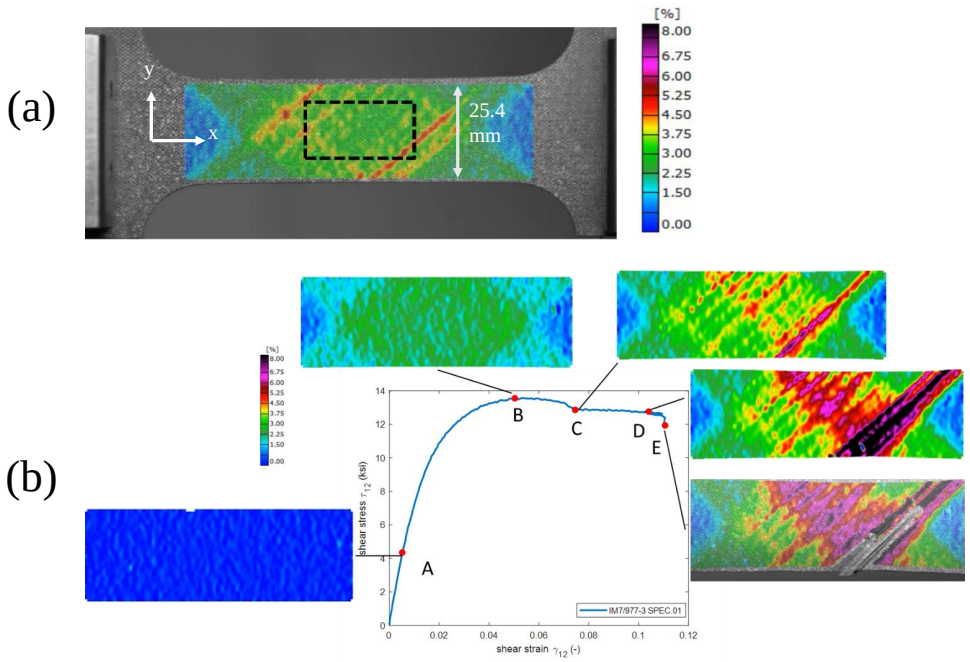

Figure 4.2: Strain field history of a ±45° test of IM7/977-3.

$$\tau_{12} = \sigma_x/2 \tag{4.11}$$

where, σ_x is calculated by dividing the load by the area of the cross section. γ_{12} is calculated by

$$\gamma_{12} = \epsilon_x - \epsilon_y \tag{4.12}$$

where, ϵ_x and ϵ_y are average values obtained inside the black dashed box shown in Figure 4.2 (a).

With obtained σ_{12}-γ_{12} data, the characterization of the Schapery function is as illustrated in Figure 4.3.

The shear nonlinearity induced by matrix microscale damage also affects the transverse stiffness. The nonlinearity in the 22, 33, and 23 directions are characterized by another Schapery function $e_s(S_r)$. The characterization of $e_s(S_r)$ can be achieved by

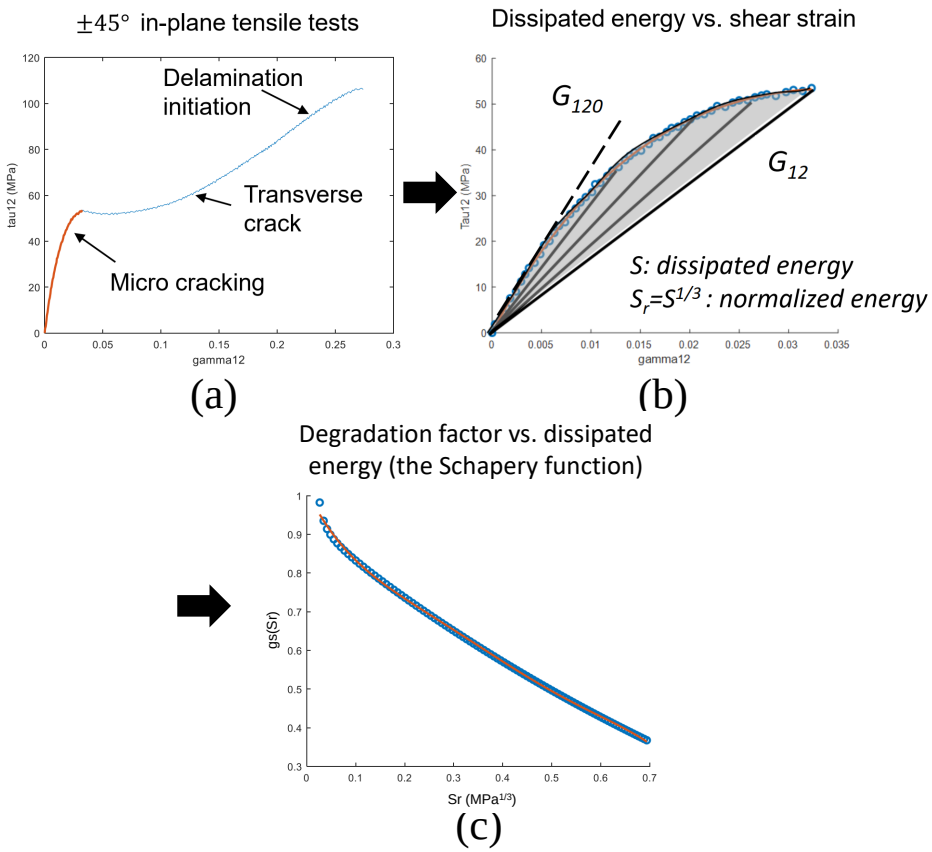

Figure 4.3: The characterization of the Schapery function: (a) identifying the non-linear response due to matrix micro-cracking, (b) calculating dissipated energy S and normalized energy S_r, and (c) obtain g_s as a function of S_r

doing coupon-level tensile tests of $\pm 30^\circ$ samples or micromechanical analyses of composites, as illustrated in [2]. In this thesis, for the material systems T800S/3900-2B and IM7/977-3, $e_s(S_r)$ is assumed identical to $g_s(S_r)$, since it is believed that matrix micro-cracking in the shear 12 direction, such as matrix shear cracks and powdering between fibers, is the driving force for the pre-peak nonlinearity in the transverse 22, 33, and 23 directions.

4.2.2 Macroscale Damage Modes, Initiation, and Rescaling

4.2.2.1 Macroscale Damage Modes and Initiation

There are two major categories of the damage modes – fiber damage and matrix damage. Along the fiber direction, there is fiber tensile and compressive damage (kinking), as illustrated in Figure 4.4. The fracture plane is the 2-3 plane in the local coordinate system shown in the figure. In Figure 4.4, $\epsilon_{11}^{ini,T}$ and $\epsilon_{11}^{ini,C}$ are the strain values corresponding to the initiation of fiber tensile and compressive damage. G_{IF}^{T} and G_{IF}^{C} are the fracture toughness values corresponding to fiber tensile and compressive damage. L_{el} is the elemental characteristic length along the fiber direction.

The matrix damage modes are illustrated in Figure 4.5. As shown, the fracture plane is the 1-3 plane in the local coordinate system. $\epsilon_{22}^{ini,T}$ and $\epsilon_{22}^{ini,C}$ are strain values corresponding to the initiation of matrix transverse tensile and compressive damage. G_{IM}^{T} and G_{IM}^{C} are matrix mode I tensile and compressive fracture toughness values. γ_{12}^{ini} and γ_{23}^{ini} are the strain values corresponding to the initiation of matrix in-plane and out-of-plane shear damage. G_{IIM} and G_{IIIM} are the fracture toughness values corresponding to the matrix mode II and III damage. L_{el}^{90} is the elemental characteristic length perpendicular to the fiber direction.

It should be noted that, in some other progressive failure analysis (PFA) codes, macroscale damage modes on the 1-2 fracture plane normal are also captured [7, 67].

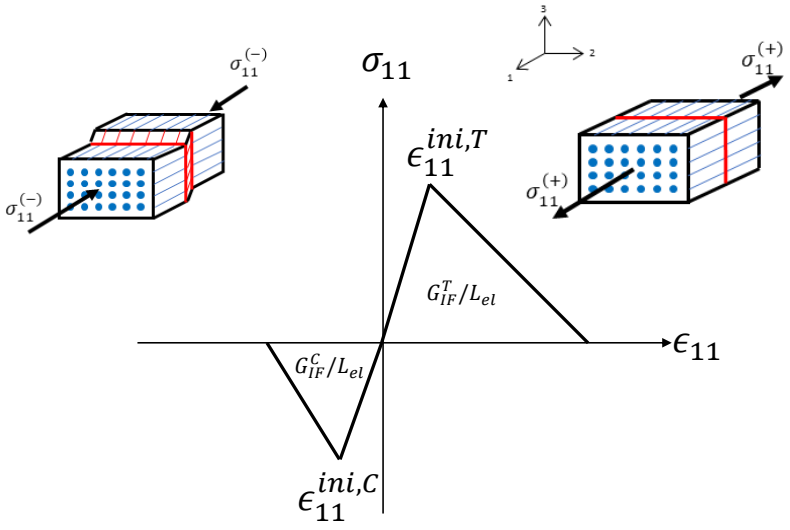

Figure 4.4: Illustration of the fiber damage modes.

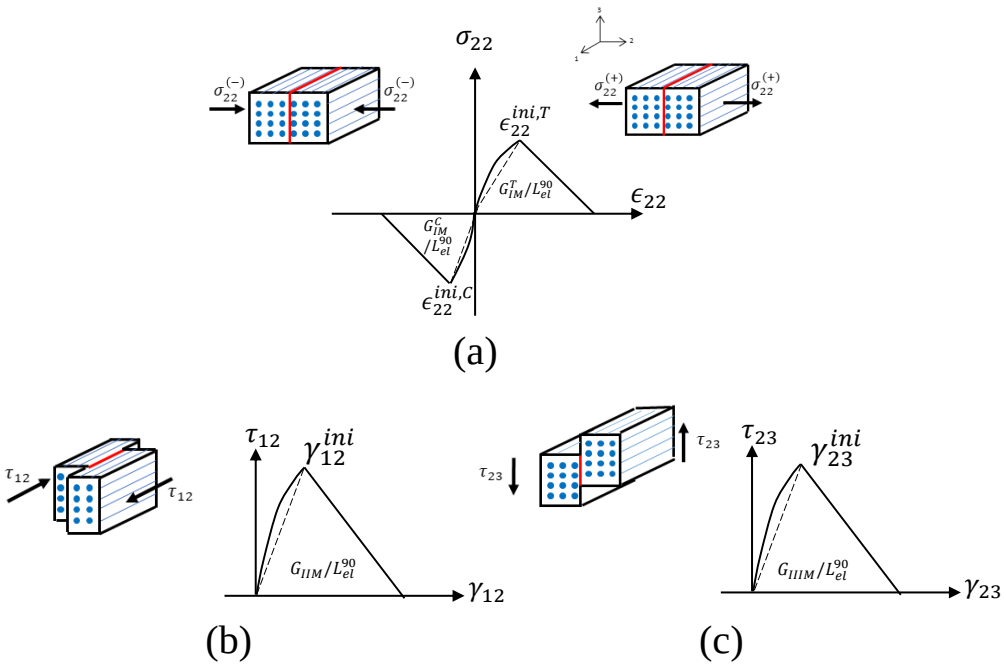

Figure 4.5: Illustration of the matrix damage modes: (a) matrix transverse tensile/compressive damage, (b) matrix in-plane shear damage, and (c) matrix out-of-plane shear damage.

This fracture plane is referred to as the "delamination failure plane" in [7]. In this thesis, since delamination is mainly captured by the cohesive contact model of Abaqus, the damage modes on the 1-2 fracture plane are not accounted for in 3D EST.

Damage modes captured by 2D EST is a subset of that of 3D EST. Fiber tensile/compressive damage (Figure 4.4), matrix transverse tensile/compressive damage (Figure 4.5(a)), and matrix in-plane shear damage (Figure 4.5(b)) are accounted for in 2D EST.

The elemental characteristic lengths along and perpendicular to the fiber direction L_{el} and L_{el}^{90} are illustrated in Figure 4.6. The lengths are calculated by straight lines going across the in-plane centroid of an element along and perpendicular to the fiber direction. Elemental characteristic lengths are used in the CB to ensure mesh objectivity and correct fracture energy dissipation.

Fiber tensile/compressive damage initiation on the 2-3 fracture plane is governed by Equations 4.13 and 4.14.

$$\left(\frac{\epsilon_{11}}{\epsilon_{11}^{ini,T}}\right)^2 \geq 1 \quad (\epsilon_{11} \geq 0) \tag{4.13}$$

$$\left(\frac{\epsilon_{11}}{\epsilon_{11}^{ini,C}}\right)^2 \geq 1 (\epsilon_{11} < 0) \tag{4.14}$$

Matrix damage initiation on the 1-3 fracture plane is governed by Equations 4.15 and 4.16.

$$\left(\frac{\epsilon_{22}}{\epsilon_{22}^{ini,T}}\right)^2 + \left(\frac{\gamma_{12}}{\gamma_{12}^{ini}}\right)^2 + \left(\frac{\gamma_{23}}{\gamma_{23}^{ini}}\right)^2 \geq 1 \quad (\epsilon_{22} \geq 0) \tag{4.15}$$

$$\left(\frac{\epsilon_{22}}{\epsilon_{22}^{ini,C}}\right)^2 + \left(\frac{\gamma_{12}}{\gamma_{12}^{ini}}\right)^2 + \left(\frac{\gamma_{23}}{\gamma_{23}^{ini}}\right)^2 \geq 1 \quad (\epsilon_{22} < 0) \tag{4.16}$$

For 2D EST, the fiber damage initiation criteria are identical to Equations 4.13

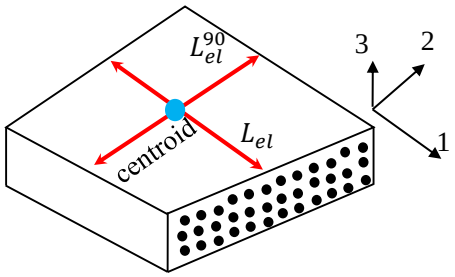

Figure 4.6: Illustration of the elemental characteristic length.

and 4.14. Since 2D EST is based on the assumption of plane stress, the terms relative to γ_{23} and γ_{23}^{ini} are omitted from Equations 4.15 and 4.16.

4.2.2.2 Rescaling of the Traction-separation Laws

As seen in Equations 4.15 and 4.16, when the matrix damage initiation criteria become satisfied, the absolute values of ϵ_{22}, γ_{12}, and γ_{23} are smaller than $\epsilon_{22}^{ini,T/C}$, γ_{12}^{ini}, and γ_{23}^{ini}, as shown in Figure 4.7. In Figure 4.7, the circular dots represent the stress-strain values when matrix damage initiation criteria get satisfied.

The rescaling of the traction-separation laws in terms of stress-strain relationships is to prevent further growth of stress components after the initiation of matrix macroscale damage. To be more specific, in Figure 4.7, after the circular dots, σ_{22}, τ_{12}, and τ_{23} can only decrease. The values of ϵ_{22}, γ_{12}, γ_{23}, σ_{22}, τ_{12}, and τ_{23} at the moment when Equation 4.15 or 4.16 become satisfied are recorded as $\epsilon_{22}^{ini,*,T/C}$, $\gamma_{12}^{ini,*}$, $\gamma_{23}^{ini,*}$, $\sigma_{22}^{ini,*,T/C}$, $\tau_{12}^{ini,*}$, and $\tau_{23}^{ini,*}$. The superscript "*" means the rescaled values at damage initiation. "T/C" corresponds to the situation where Equation 4.15 or 4.16 becomes satisfied. $(\epsilon_{22}^{ini,*,T/C}, \sigma_{22}^{ini,*,T/C})$, $(\gamma_{12}^{ini,*}, \tau_{12}^{ini,*})$, and $(\gamma_{23}^{ini,*}, \tau_{23}^{ini,*})$ are used as the initiation strain and stress values of the rescaled traction-separation laws, as shown in Figure 4.7. The rescaling step does not change the fracture toughness of the updated traction-separation laws. The strain values corresponding to damage propagation are calculated as Equations 4.17 to 4.19. $\epsilon_{22}^{fail,T/C}$, ϵ_{12}^{fail}, and ϵ_{23}^{fail} are denoted by solid square dots in Figure 4.7.

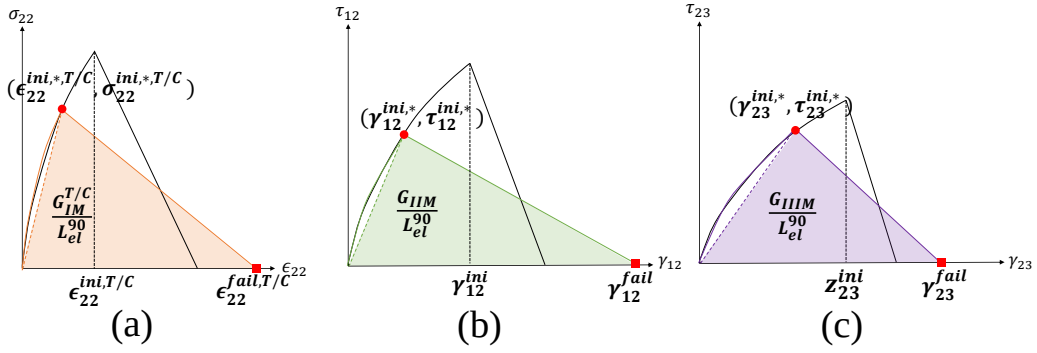

Figure 4.7: Rescaling of the traction-separation laws of matrix macroscale damage: (a) transverse tensile/compressive damage, (b) in-plane shear damage, and (c) out-of-plane shear damage.

$$\epsilon_{22}^{fail,T/C} = \frac{2G_{IM}^{T/C}}{\sigma_{22}^{ini,T/C} L_{el}^{90}} \tag{4.17}$$

$$\epsilon_{12}^{fail} = \frac{2G_{IIM}}{\tau_{12}^{ini} L_{el}^{90}} \tag{4.18}$$

$$\epsilon_{23}^{fail} = \frac{2G_{IIIM}}{\tau_{23}^{ini} L_{el}^{90}} \tag{4.19}$$

Rescaling is also performed for 2D EST with respect to traction-separations laws of matrix transverse tensile/compressive damage and in-plane shear damage, as shown in Figure 4.7(a) and (b).

It should be noted that the rescaling is not needed for fiber tensile/compressive damage, since it is assumed that there is no mode mixity in fiber damage.

4.2.3 Post-peak Degradation: a Novel Mixed-mode Cohesive Formulation

The post-peak degradation of fiber and matrix damage is governed by the CB model. Since there is no mode mixity in the fiber damage, the post-peak behavior of

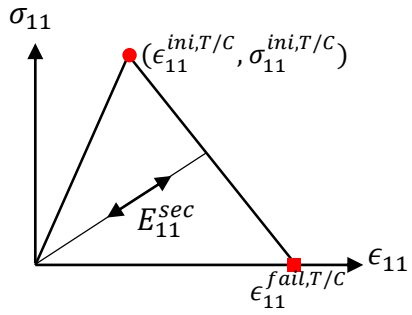

Figure 4.8: Post-peak degradation of the fiber damage.

σ_{11} - ϵ_{11} is dictated by Figure 4.8. In Figure 4.8, $\epsilon_{11}^{fail,T/C}$ is the strain corresponding to fiber tensile/compressive failure, calculated by Equation 4.20. E_{11}^{sec} is the post-peak secant stiffness, calculated by Equation 4.21.

$$\epsilon_{11}^{fail,T/C} = \frac{2G_{IF}^{T/C}}{\sigma_{11}^{ini,T/C} L_{el}} \tag{4.20}$$

$$E_{11}^{sec,T/C} = \frac{(\epsilon_{11}^{fail,T/C} - \epsilon_{11})}{\epsilon_{11}^{fail,T/C} - \epsilon_{11}^{ini,T/C}} \times \frac{\sigma_{11}^{ini,T/C}}{\epsilon_{11}} \tag{4.21}$$

In previous works [21, 60], the post-peak degradation of the moduli were linear, following the straight downslopes as shown in Figure 4.7. The failure criterion in the previously implemented 2D EST model was Equation 4.22.

$$\frac{G_{IM}^{diss,T/C}}{G_{IM}^{T/C}} + \frac{G_{IIM}^{diss}}{G_{IIM}} \geq 1 \tag{4.22}$$

where, $G_{IM}^{diss,T/C}$ and G_{IIM}^{diss} were the dissipated energy values. Once Equation 4.22 was satisfied, the stress components were forced to be zero instantaneously, which would lead to stress jumps. Those stress jumps were physically incorrect and numerically unstable.

In this thesis, the post-peak degradation of mixed-mode matrix damage is governed by the novel mixed-mode cohesive law proposed by Joseph and Waas in [7].

The major purpose of this novel mixed-mode law is to degrade the stress components σ_{22}, τ_{12}, and τ_{23} simultaneously and progressively. In the novel mixed-mode cohesive law, three energy ratios are defined in Equations 4.23.

$$g_1 = \frac{G_{IM}^{diss,T/C}}{G_{IM}^{T/C}} \tag{4.23a}$$

$$g_2 = \frac{G_{IIM}^{diss}}{G_{IIM}} \tag{4.23b}$$

$$g_3 = \frac{G_{IIIM}^{diss}}{G_{IIIM}} \tag{4.23c}$$

where, G_{IIIM}^{diss} is the dissipated energy of matrix mode III damage (out-of-plane shear).

The residual energy values to be dissipated for all the matrix damage modes are calculated according to Equations 4.24.

$$G_{IM}^{R,T/C} = \frac{g_1 G_{IM}^{T/C}}{g_1 + g_2 + g_3} - G_{IM}^{diss,T/C} \tag{4.24a}$$

$$G_{IIM}^{R} = \frac{g_2 G_{IIM}}{g_1 + g_2 + g_3} - G_{IIM}^{diss} \tag{4.24b}$$

$$G_{IIIM}^{R} = \frac{g_3 G_{IIIM}}{g_1 + g_2 + g_3} - G_{IIIM}^{diss} \tag{4.24c}$$

At a certain time increment i, the stress-strain states $(\sigma_{22}^i, \epsilon_{22}^i)$, $(\tau_{12}^i, \gamma_{12}^i)$, $(\tau_{23}^i, \gamma_{23}^i)$, dissipated energy values, and residual energy values are known. Correspondingly, instantaneous traction-separation laws in terms of stress-strain relationships are known, as illustrated in Figure 4.9. In Figure 4.5, the solid square dots represent instantaneous strains corresponding to failure of each mode, which are calculated as Equations 4.25.

$$\epsilon_{22}^{fail,T/C} = \frac{2G_{IM}^{R,T/C}}{L_{el}^{90}\sigma_{22}^i} + \epsilon_{22}^i \tag{4.25a}$$

$$\gamma_{12}^{fail} = \frac{2G_{IIM}^{R}}{L_{el}^{90}\tau_{12}^i} + \gamma_{12}^i \tag{4.25b}$$

$$\gamma_{23}^{fail} = \frac{2G_{IIIM}^{R}}{L_{el}^{90}\tau_{23}^{i}} + \gamma_{23}^{i} \tag{4.25c}$$

At time increment i, the strain increment is known and therefore the strain values at the next time increment $i+1$ ϵ_{22}^{i+1}, γ_{12}^{i+1}, and γ_{23}^{i+1} are obtained. The instantaneous secant moduli E_{22}^{sec}, G_{12}^{sec}, and G_{23}^{sec} are calculated as Equations 4.26.

$$E_{22}^{sec,T/C} = \frac{\epsilon_{22}^{fail,T/C} - \epsilon_{22}^{i+1}}{\epsilon_{22}^{fail,T/C} - \epsilon_{22}^{i}} \times \frac{\sigma_{22}^{i}}{\epsilon_{22}^{i+1}} \tag{4.26a}$$

$$G_{12}^{sec} = \frac{\gamma_{12}^{fail} - \gamma_{12}^{i+1}}{\gamma_{12}^{fail} - \gamma_{12}^{i}} \times \frac{\tau_{12}^{i}}{\gamma_{12}^{i+1}} \tag{4.26b}$$

$$G_{23}^{sec} = \frac{\gamma_{23}^{fail} - \gamma_{23}^{i+1}}{\gamma_{23}^{fail} - \gamma_{23}^{i}} \times \frac{\tau_{23}^{i}}{\gamma_{23}^{i+1}} \tag{4.26c}$$

The matrix failure criterion is Equation 4.27, which is equivalent to Equation 4.28

$$\frac{G_{IM}^{diss,T/C}}{G_{IM}^{T/C}} + \frac{G_{IIM}^{diss}}{G_{IIM}} + \frac{G_{IIIM}^{diss}}{G_{IIIM}} \geq 1 \tag{4.27}$$

$$g_1 + g_2 + g_3 \geq 1 \tag{4.28}$$

Substituting Equation 4.28 and Equations 4.23 into Equations 4.24, it is easily obtained that $G_{IM}^{R,T/C} = 0$, $G_{IIM}^{R} = 0$, and $G_{IIIM}^{R} = 0$. According to Equations 4.26 and 4.25, E_{22}^{sec}, G_{12}^{sec}, and G_{23}^{sec} are calculated as zeros simultaneously. This shows that the novel mixed-mode cohesive law degrades stress components progressively and simultaneously.

Damage indicators are calculated to indicate the damage extent of fiber and matrix damage modes, as in Equations 4.29

$$D_{IF}^{T/C} = E_{11}^{sec,T/C}/E_{110} \tag{4.29a}$$

$$D_{IM}^{T/C} = E_{22}^{sec,T/C}/E_{220} \tag{4.29b}$$

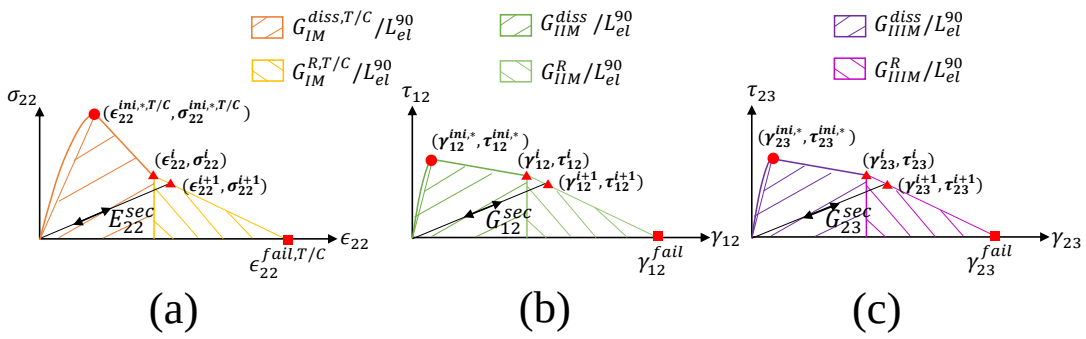

Figure 4.9: Post-peak degradation of the matrix mixed-mode damage: (a) mode I, (b) mode II, and (c) mode III.

$$D_{IIM} = G_{12}^{sec}/G_{120} \tag{4.29c}$$

$$D_{IIIM} = G_{23}^{sec}/G_{230} \tag{4.29d}$$

After the fiber and matrix failure criteria become satisfied, instead of using zero secant moduli values, small finite values used for E_{11}^{sec}, E_{22}^{sec}, G_{23}^{sec}, and G_{13}^{sec}. The small finite values are referred to as the residual stiffness. The values of the residual stiffness are 1% of the pristine material moduli.

Based on the assumption that there is no post-peak degradation for the secant moduli E_{33}^{sec} and G_{13}^{sec}, E_{33}^{sec} and G_{13}^{sec} are still calculated according to Equations 4.7(b) and 4.7(d). It should be pointed out that S_r ceases growing after the macroscale matrix damage initiation.

With post-peak secant moduli obtained according to Equations 4.21, 4.26, 4.7(b), and 4.7(d), the stiffness matrix can be calculated by substituting the post-peak secant moduli into Equations 4.6 and 4.10.

In 2D EST, the post-peak matrix mixed-mode degradation is captured for σ_{22} and τ_{12}, as shown in Figure 4.9(a) and (b). The fiber post-peak degradation is identical that illustrated in Figure 4.8.

4.3 EST with Inelasticity (EST-InELA)

Schapery correlated inelastic behavior of composite materials with the phenomenon of fiber debris sticking into matrix cracks and stopping complete closure of the cracks [46]. It was demonstrated that if the solved S_r increased with time ($\dot{S}_r > 0$), the material was being loaded. Otherwise ($\dot{S}_r = 0$), the material was at the state of unloading/reloading. It should be pointed out that according to the second law of thermodynamics, S_r should only increase or stay constant with time marching, namely, $\dot{S}_r \geq 0$.

Simply solving Equation 4.8 might lead to $\dot{S}_r < 0$, which is physically incorrect. In this chapter, the solved S_r value is changed to be identical to that obtained at the previous time increment, such that $\dot{S}_r = 0$. The material status in this case is unloading/reloading. The pre-peak nonlinear in-plane shear response considering loading/unloading/reloading is illustrated in Figure 4.10. In the figure, γ_{12}^{in} and γ_{12}^{ela} are the inelastic and elastic components of the total strain γ_{12}. G_{12}^{ela} is the elastic modulus. In EST-InELA, inelasticity in the 22, 23, and 33 directions are also considered, similar to the illustration in Figure 4.10.

In EST-InELA, when the material is at the loading status ($\dot{S}_r > 0$), the secant moduli are still calculated according to Equation 4.7. The elastic moduli are correlated with the pristine moduli through two proposed functions $\alpha(S_r)$ and $\beta(S_r)$, as in Equations 4.30.

$$E_{22}^{ela} = E_{220}(1 - \alpha(S_r)) \tag{4.30a}$$

$$E_{33}^{ela} = E_{220}(1 - \alpha(S_r)) \tag{4.30b}$$

$$G_{12}^{ela} = G_{120}(1 - \beta(S_r)) \tag{4.30c}$$

$$G_{13}^{ela} = G_{120}(1 - \beta(S_r)) \tag{4.30d}$$

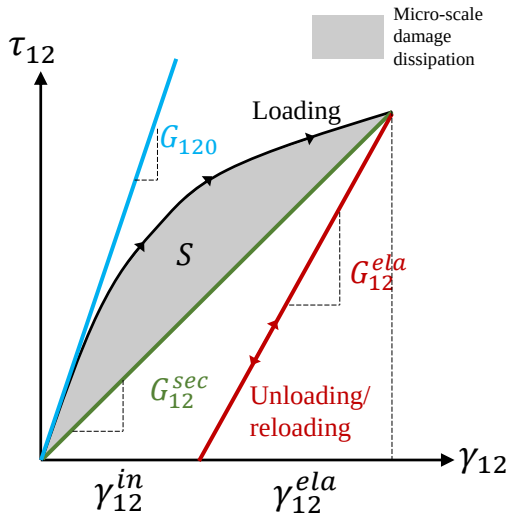

Figure 4.10: Pre-peak stress-strain relationship considering loading / unloading / reloading.

$$G_{23}^{ela} = G_{230}(1 - \alpha(S_r)) \tag{4.30e}$$

At the loading status, the inelastic strain components are updated as in Equations 4.31. When the material is at the unloading/reloading status ($\dot{S}_r = 0$) are not updated. It should be pointed out that, as seen in Equations 4.31, $\epsilon_{11}^{in} = 0$. It is because that fiber damage is not the cause for the inelasticity in laminated composites.

$$\epsilon_{11}^{in} = 0 \tag{4.31a}$$

$$\epsilon_{22}^{in} = \epsilon_{22} - \frac{E_{22}^{sec}\epsilon_{22}}{E_{22}^{ela}} \tag{4.31b}$$

$$\epsilon_{33}^{in} = \epsilon_{33} - \frac{E_{33}^{sec}\epsilon_{33}}{E_{33}^{ela}} \tag{4.31c}$$

$$\gamma_{12}^{in} = \gamma_{12} - \frac{G_{12}^{sec}\gamma_{12}}{G_{12}^{ela}} \tag{4.31d}$$

$$\gamma_{13}^{in} = \gamma_{13} - \frac{G_{13}^{sec}\gamma_{13}}{G_{13}^{ela}} \tag{4.31e}$$

$$\gamma_{23}^{in} = \gamma_{23} - \frac{G_{23}^{sec}\gamma_{23}}{G_{23}^{ela}} \tag{4.31f}$$

The terms of the elastic stiffness matrix can be calculated by Equations 4.32.

$$C_{11}^{ela} = \frac{1 - \nu_{23}\nu_{32}}{E_{22}^{ela} E_{33}^{ela} \Delta^{ela}} \tag{4.32a}$$

$$C_{22}^{ela} = \frac{1 - \nu_{13}\nu_{31}}{E_{11}^{sec} E_{33}^{ela} \Delta^{ela}} \tag{4.32b}$$

$$C_{33}^{ela} = \frac{1 - \nu_{12}\nu_{21}}{E_{11}^{sec} E_{22}^{ela} \Delta^{ela}} \tag{4.32c}$$

$$C_{23}^{ela} = \frac{\nu_{23} + \nu_{21}\nu_{13}}{E_{11}^{sec} E_{22}^{ela} \Delta^{ela}} \tag{4.32d}$$

$$C_{13}^{ela} = \frac{\nu_{13} + \nu_{12}\nu_{23}}{E_{11}^{sec} E_{22}^{ela} \Delta^{ela}} \tag{4.32e}$$

$$C_{12}^{ela} = \frac{\nu_{12} + \nu_{32}\nu_{13}}{E_{11}^{sec} E_{33}^{ela} \Delta^{ela}} \tag{4.32f}$$

$$C_{44}^{ela} = G_{23}^{ela} \tag{4.32g}$$

$$C_{55}^{ela} = G_{13}^{ela} \tag{4.32h}$$

$$C_{66}^{ela} = G_{12}^{ela} \tag{4.32i}$$

$$\Delta^{ela} = \frac{1 - \nu_{12}\nu_{21} - \nu_{23}\nu_{32} - \nu_{13}\nu_{31} - 2\nu_{21}\nu_{32}\nu_{13}}{E_{11}^{sec} E_{22}^{ela} E_{33}^{ela}} \tag{4.32j}$$

In the pre-peak region of EST-InELA, the stress-strain relationship is calculated by Equation 4.33.

$$\begin{bmatrix} \sigma_{11} \\ \sigma_{22} \\ \sigma_{33} \\ \tau_{23} \\ \tau_{13} \\ \tau_{12} \end{bmatrix} = \begin{bmatrix} C_{11}^{ela} & C_{12}^{ela} & C_{13}^{ela} & 0 & 0 & 0 \\ C_{12}^{ela} & C_{22}^{ela} & C_{23}^{ela} & 0 & 0 & 0 \\ C_{13}^{ela} & C_{23}^{ela} & C_{33}^{ela} & 0 & 0 & 0 \\ 0 & 0 & 0 & C_{44}^{ela} & 0 & 0 \\ 0 & 0 & 0 & 0 & C_{55}^{ela} & 0 \\ 0 & 0 & 0 & 0 & 0 & C_{66}^{ela} \end{bmatrix} \begin{bmatrix} \epsilon_{11} \\ \epsilon_{22} - \epsilon_{22}^{in} \\ \epsilon_{33} - \epsilon_{33}^{in} \\ \gamma_{23} - \gamma_{23}^{in} \\ \gamma_{13} - \gamma_{13}^{in} \\ \gamma_{12} - \gamma_{12}^{in} \end{bmatrix} \tag{4.33}$$

The damage initiation criteria in the 3D EST-InELA model are identical to that in

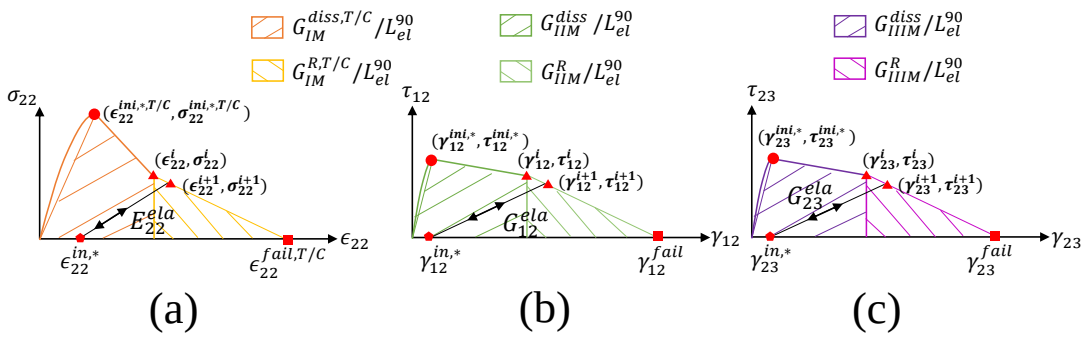

Figure 4.11: Post-peak degradation of the matrix mixed-mode damage with inelasticity: (a) mode I, (b) mode II, and (c) mode III.

the EST model without considering material inelasticity, as in Equations 4.13 to 4.16. Once the matrix initiation criteria get satisfied, the rescaling step will be performed following Equations 4.17 to 4.19 and Figure 4.7.

In the post-peak region of the 3D EST-InELA, the novel mixed-mode law is followed, as illustrated by Equations 4.23 to 4.25, and Figure 4.11. In Figure 4.11, $\epsilon_{22}^{in,*}$, $\gamma_{12}^{in,*}$, $\gamma_{23}^{in,*}$ represent inelastic strain components at the moment of matrix macroscale damage initiation. Similarly, $\epsilon_{33}^{in,*}$ and $\gamma_{13}^{in,*}$ values are recorded. There is no further growth of inelastic strain components after the initiation of matrix damage.

The only difference between the mixed-mode post-peak degradation of EST-InELA and EST is that in EST-InELA, the unloading/reloading follows the elastic moduli, as shown in Figure 4.11; while in EST, the unloading/reloading follows the secant stiffness without considering the inelastic strain components, as shown in Figure 4.5. The elastic moduli in 3D EST-InELA are calculated according to Equations 4.34.

$$E_{22}^{ela,T/C} = \frac{\epsilon_{22}^{fail,T/C} - \epsilon_{22}^{i+1}}{\epsilon_{22}^{fail,T/C} - \epsilon_{22}^{i}} \times \frac{\sigma_{22}^{i}}{\epsilon_{22}^{i+1} - \epsilon_{22}^{in,*}} \tag{4.34a}$$

$$G_{12}^{ela} = \frac{\gamma_{12}^{fail} - \gamma_{12}^{i+1}}{\gamma_{12}^{fail} - \gamma_{12}^{i}} \times \frac{\tau_{12}^{i}}{\gamma_{12}^{i+1} - \gamma_{12}^{in,*}} \tag{4.34b}$$

$$G_{23}^{ela} = \frac{\gamma_{23}^{fail} - \gamma_{23}^{i+1}}{\gamma_{23}^{fail} - \gamma_{23}^{i}} \times \frac{\tau_{23}^{i}}{\gamma_{23}^{i+1} - \gamma_{23}^{in,*}} \tag{4.34c}$$

Same as EST, elastic moduli E_{33}^{ela} and G_{13}^{ela} are not degraded in the post-peak region of EST-InELA. E_{33}^{ela} and G_{13}^{ela} are calculated according to Equations 4.30(b) and 4.30(d). Since there is no inelasticity accounted for in the fiber direction, secant stiffness $E_{11}^{fail,T/C}$ is calculated as Equation 4.21.

The damage indicators $D_{IF}^{T/C}$, $D_{IM}^{T/C}$, D_{IIM}, and D_{IIIM} of EST-InELA can be calculated as Equations 4.35.

$$D_{IF}^{T/C} = E_{11}^{sec,T/C}/E_{110} \tag{4.35a}$$

$$D_{IM}^{T/C} = E_{22}^{ela,T/C}/E_{220} \tag{4.35b}$$

$$D_{IIM} = G_{12}^{ela}/G_{120} \tag{4.35c}$$

$$D_{IIIM} = G_{23}^{ela}/G_{230} \tag{4.35d}$$

With all the secant and elastic moduli obtained according to Equations 4.21, 4.34, 4.30(b), and 4.30(d), the post-peak stress-strain relationship of 3D EST-InELA is

$$\begin{bmatrix} \sigma_{11} \\ \sigma_{22} \\ \sigma_{33} \\ \tau_{23} \\ \tau_{13} \\ \tau_{12} \end{bmatrix} = \begin{bmatrix} C_{11}^{ela} & C_{12}^{ela} & C_{13}^{ela} & 0 & 0 & 0 \\ C_{12}^{ela} & C_{22}^{ela} & C_{23}^{ela} & 0 & 0 & 0 \\ C_{13}^{ela} & C_{23}^{ela} & C_{33}^{ela} & 0 & 0 & 0 \\ 0 & 0 & 0 & C_{44}^{ela} & 0 & 0 \\ 0 & 0 & 0 & 0 & C_{55}^{ela} & 0 \\ 0 & 0 & 0 & 0 & 0 & C_{66}^{ela} \end{bmatrix} \begin{bmatrix} \epsilon_{11} \\ \epsilon_{22} - \epsilon_{22}^{in,*} \\ \epsilon_{33} - \epsilon_{33}^{in,*} \\ \gamma_{23} - \gamma_{23}^{in,*} \\ \gamma_{13} - \gamma_{13}^{in,*} \\ \gamma_{12} - \gamma_{12}^{in,*} \end{bmatrix} \tag{4.36}$$

where, the stiffness terms C_{ij} can be calculated according to Equations 4.32.

In 2D EST-InELA, the material inelasticity and post-peak matrix mixed-mode degradation are captured for σ_{22} and τ_{12}, as shown in Figure 4.11(a) and (b). The fiber post-peak degradation is identical that illustrated in Figure 4.8.

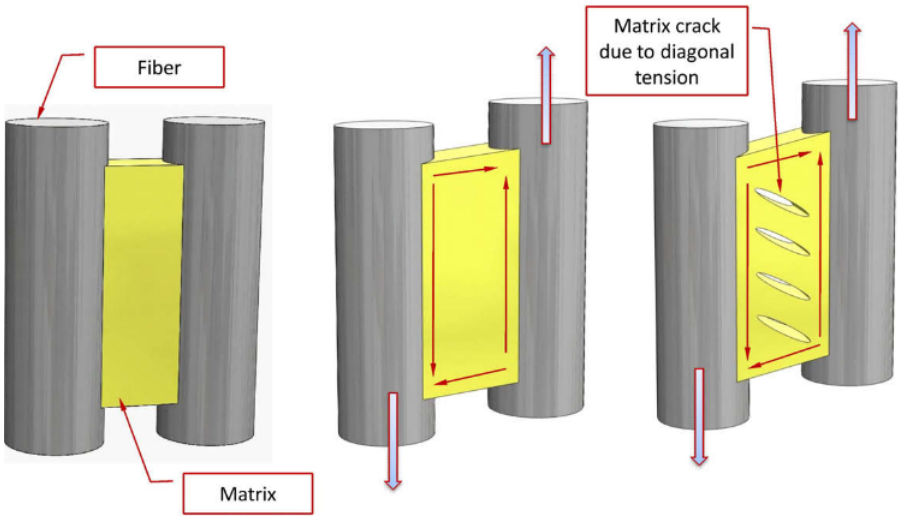

Figure 4.12: Formation of matrix shear cracks between adjacent fibers [10].

4.4 Element Patch Test

Element patch tests are performed to validate the successful implementation of EST. In this thesis, only the patch tests of 3D EST are presented. Single-element patch tests are conducted w.r.t. a 0.1 mm $\times$ 0.1 mm $\times$ 0.1 mm 3D reduced-order element (C3D8R). Tensile, compressive, shear, and multi-axial loading is applied to the element. The predicted stress-strain responses are recorded and demonstrated in Figures 4.13-4.17.

Single-mode responses are shown in Figures 4.13-4.16, in terms of $\sigma_{11}-\epsilon_{11}$, $\sigma_{22}-\epsilon_{22}$, $\tau_{12}-\gamma_{12}$, $\tau_{23}-\gamma_{23}$. As shown in the figures, pre-peak nonlinearity only exists in the $\tau_{12}-\gamma_{12}$ case. For $\sigma_{22}-\epsilon_{22}$ and $\tau_{23}-\gamma_{23}$, with with the Schapery function $e_s(S_r)$ defined, pre-peak nonlinearity is not seen. The reason is that microscale shear cracking in the 12 and 13 directions are the driving force for the nonlinearity in the 22, 33, and 23 directions. Therefore, when the element is under single-mode loading in the 22, 33, and 23 directions, without microscale 12 and 13 shear cracking, the nonlinearity governed by $e_s(S_r)$ is not triggered. The formation of micro-scale shear cracking is illustrated in Figure 4.12 and discussed in detail in [43].

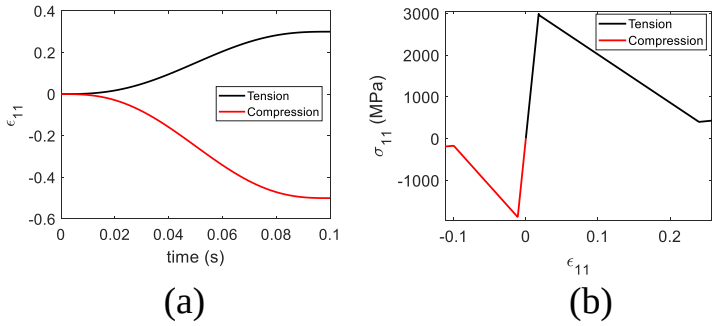

Figure 4.13: Single-element patch test σ_{11}-ϵ_{11}: (a) strain history, and (b) stress-strain relationship.

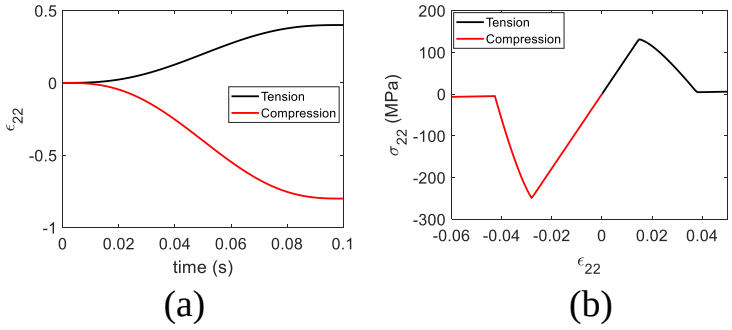

Figure 4.14: Single-element patch test σ_{22}-ϵ_{22}: (a) strain history, and (b) stress-strain relationship.

Mixed-mode loading responses are shown in Figure 4.17. The element is loaded in the 22, 12, and 23 directions. As seen from Figure 4.17 (b), with monotonic growth of strains, corresponding stress components degrade simultaneously and progressively until the final failure of the element, after which residual stiffness values are assigned to the element to avoid numerical instability. From Figure 4.17 (b), pre-peak nonlinearity is seen in all the 22, 12, and 23 directions. Due to the existence of shear 12 loading, the nonlinearity in the 22 and 23 directions are triggered.

Mesh objectivity of 3D EST is verified by a simple uniaxial tension test as shown in Figure 4.18. A 1 mm $\times$ 1 mm $\times$ 0.13 mm lamina is discretized with the element size being 0.5 mm, 0.3 mm, and 0.2 mm. Tensile loading is applied along the fiber direction. The fiber damage indicator is shown in Figure 4.19 for the three meshes.

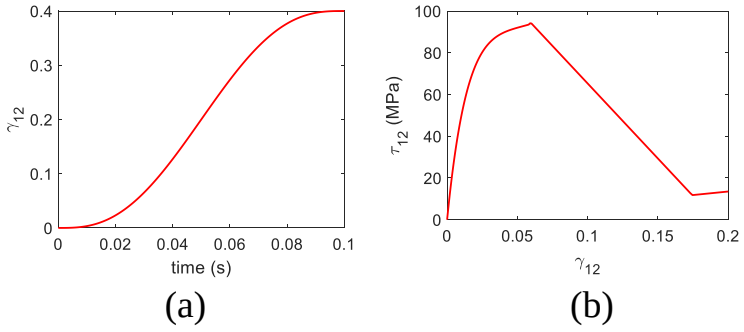

Figure 4.15: Single-element patch test τ_{12}-γ_{12}: (a) strain history, and (b) stress-strain relationship.

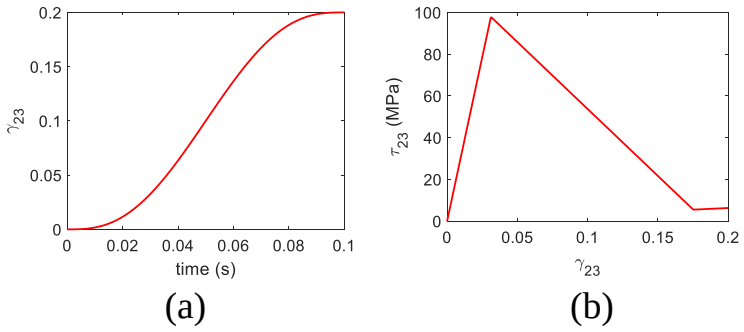

Figure 4.16: Single-element patch test τ_{23}-γ_{23}: (a) strain history, and (b) stress-strain relationship.

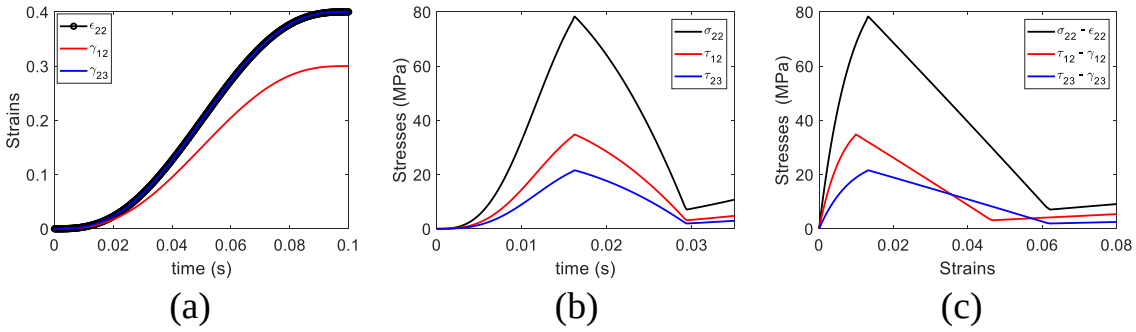

Figure 4.17: Single-element patch test triaxial loading: (a) strain history, (b) stress history, and (c) stress-strain relationship.

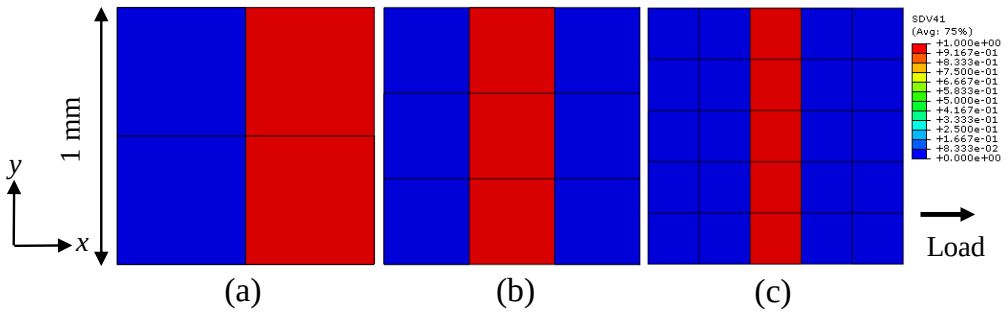

Figure 4.18: Mesh objectivity study: fiber damage.

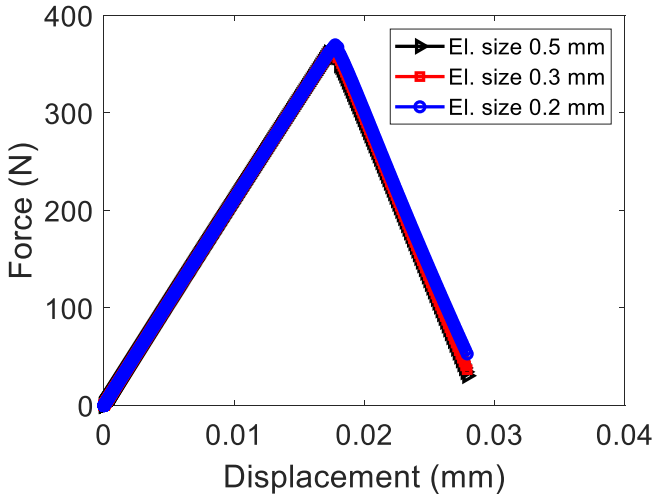

Figure 4.19: Mesh objectivity study: load-displacement responses of a lamina under uniaxial tension.

The force-displacement curves are shown in Figure 4.18. The force-displacement curves of the three meshes are identical, demonstrating the mesh objectivity of EST.

4.5 Inter-laminar Damage Model: Cohesive Contact

The Abaqus built-in cohesive contact model is used in this thesis to capture the delamination damage of laminated composites. With the cohesive contact model, interfaces of composites are modeled as of zero thickness. In Abaqus, cohesive elements are sometimes also used for PFA of composites. However, a finite mass property has to be attached to the cohesive elements in explicit analyses. If used with zero thickness, cohesive elements with a finite mass property is unphysical. Another reason for

using the cohesive contact model rather than the cohesive elements is based on the research presented in [44], where it was state that the cohesive contact was superior over the cohesive element model in terms of numerical stability. Additionally, when used with fiber-aligned meshes, establishing an FEM model with cohesive contact is more straightforward than that with cohesive elements.

Cohesive contact is defined between adjacent layers of composites. When the two neighboring interfaces contact (with negative normal tractions), the cohesive contact model would automatically follow the general contact model. When the two interfaces separate, the traction between the interfaces will be governed by specified traction-separation laws. For the cohesive contact model used in this thesis, nine parameters are needed, which are the normal, first shear, and second shear penalty stiffnesses K_{nn}, K_{ns}, K_{nt}; fracture strengths t_{nn}^{ini}, t_{ns}^{ini}, t_{nt}^{ini}; and mode I, II, and III fracture toughnesses G_I, G_{II}, G_{III}. The quadratic stress criterion is used for determining the initiation of delamination, as expressed in Equation 4.37.

$$(\frac{t_{nn}}{t_{nn}^{ini}})^2 + (\frac{t_{ns}}{t_{ns}^{ini}})^2 + (\frac{t_{nt}}{t_{nt}^{ini}})^2 \geq 1 \tag{4.37}$$

In Equation 4.37, t stands for the traction between adjacent interfaces. Subscripts nn, ns, and nt represent traction components in the normal, first shear and second shear directions. Superscript ini means for the values corresponding to the initiation of delamination. The normal, first shear, and second shear directions are illustrated in Figure 4.20(a).

The failure criterion of delamination used in this thesis is Equation 4.38, where G_{nn}, G_{ns}, G_{nt} are the energy dissipated of mode I, II, and III delamination.

$$\frac{G_{nn}}{G_I} + \frac{G_{ns}}{G_{II}} + \frac{G_{nt}}{G_{III}} \geq 1 \tag{4.38}$$

The delamination initiation and failure criteria follow the work presented in [21].

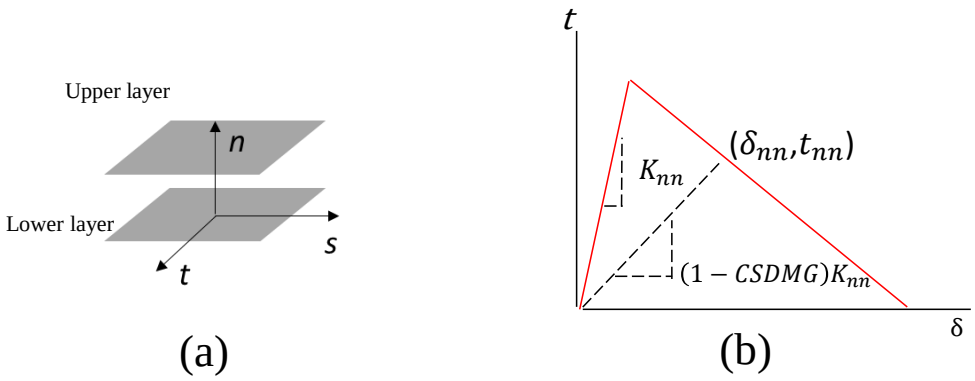

Figure 4.20: The cohesive contact model: (a) the three directions, and (b) the specified traction-separation law.

Similar delamination initiation criteria were also used by [70, 30, 68, 69, 79]. Similar delamination failure criteria were adopted by [70].

The damage variable indicating the delamination extent is referred to as $CSDMG$ in the cohesive contact model. $CSDMG$ relates the traction and separation according to Equations 4.39 to 4.41. δ_{nn}, δ_{ns}, and δ_{nt} are the separation values between adjacent interfaces along the normal, first shear, and second shear directions. The illustration of Equation 4.39 is as shown in Figure 4.20(b).

$$t_{nn} = (1 - CSDMG)K_{nn}\delta_{nn} \tag{4.39}$$

$$t_{ns} = (1 - CSDMG)K_{ns}\delta_{ns} \tag{4.40}$$

$$t_{nt} = (1 - CSDMG)K_{nt}\delta_{nt} \tag{4.41}$$

More implementation details and methodology of the cohesive contact model can be found in the user documentation of Abaqus [65] and [92].

4.6 Summary and Conclusions

In this chapter, the theoretical background of 2D and 3D EST with material inelasticity has been outlined. 2D plane stress EST can be regarded as a subset of 3D EST. Therefore, this chapter focuses on illustrating 3D EST and 3D EST-InELA.

In EST, the pre-peak nonlinearity of composites is captured by ST [90]. The post-peak degradation is captured by Bazant's CB model [71]. A novel mixed-mode cohesive formulation has been integrated to the EST model which guarantees that stress components degrade to zeros progressively and simultaneously in mixed-mode scenarios. The capability of EST to capture material inelasticity has been implemented by relating the degradation of elastic moduli to the reduced energy dissipation S_r.

Simple tests including element patch tests and mesh objectivity tests have been performed and reported to validate the correct implementation of the EST models. Computational studies in this thesis are mostly based on EST models, as discussed later in Chapters V to VII.

CHAPTER V

Computational Studies of the LVI of Laminated Composites

5.1 Introduction

[1] In this chapter, computational results for the LVI of CFRP composites are reported. The computational models used are 2D plane stress EST and 3D EST, as illustrated in Chapter IV. Corresponding to Chapter II, two topics are of major concern: the effects of stacking sequence on the LVI behavior and the effects of panel size on the LVI behavior. Every section in this chapter can find its counterpart in Chapter II. The material system used for the stacking sequence effect studies is T800s/3900-2B. IM7/977-3 is used for the panel size effect studies. For the stacking

[1] The results presented in this chapter have been published in:

- Lin, Shiyao, and Anthony M. Waas. "The effect of stacking sequence on the LVI damage of laminated composites; experiments and analysis." *Composites Part A: Applied Science and Manufacturing* 145 (2021): 106377.
- Lin, Shiyao, Solver I. Thorsson, and Anthony M. Waas. "Predicting the low velocity impact damage of a quasi-isotropic laminate using EST." *Composite structures* 251 (2020): 112530.
- Lin, Shiyao, and Anthony M. Waas. "An Experimental and Computational Study on the Low Velocity Impact-Induced Damage of a Highly Anisotropic Laminated Composite Panel." *Journal of Applied Mechanics* 88.8 (2021): 081001.
- Lin, Shiyao, Vipul Ranatunga, and Anthony M. Waas. "A Comprehensive Experimental and Computational Study on LVI Induced Damage of Laminated Composites." *AIAA Scitech 2021 Forum*. 2021.

sequence effect studies, the panel size is 150 mm × 100 mm. The stacking sequences are $[0/45/0/90/0/\text{-}45/0/45/0/\text{-}45]_s$ (layup A), $[45/0/\text{-}45/90]_{3s}$ (layup B), and $[45/\text{-}45/0/45/\text{-}45/90/45/\text{-}45/45/\text{-}45]_s$ (layup C), which are [50/40/10], [25/50/25], and [10/80/10] layups. The naming pattern and test parameters can be found in Table 2.1. Additionally, the LVI of the "sandwich-like" stacking sequence has been numerically studied to challenge the accuracy of the computational model.

The panel size effect studies include two stacking sequences: $[45/\text{-}45/0/90/0/0]_{ns}$ (L1) and $[45/0/\text{-}45/90]_{ns}$ (L2); two total thicknesses: 24-ply and 48-ply; and three in-plane sizes: 152.4 mm × 101.6 mm, 177.8 mm × 177.8 mm, and 330.2 mm × 330.2 mm. Both 2D plane stress EST-InELA (with material inelasticity) and 3D EST-InELA (with material inelasticity) have been applied to the LVI modeling of the panel size effect studies.

With the presented computational results in this chapter, LVI-induced damage mechanisms have been investigated numerically. The fidelity, efficiency, and versatility of 2D plane stress EST and 3D EST have been evaluated and compared. In this chapter, Section 5.2 will focus on the computational stacking sequence effect studies. Section 5.3 will present the computational results of the panel size effect studies. Discussions and conclusions will be provided in Section 5.4.

5.2 Computational LVI Study with the Effects of Stacking Sequence

In this section, computational LVI results of the stacking sequence effect studies are presented. As illustrated in Chapter II, the diameter of the impactor is 20 mm. The impactor's mass is 7.5 kg. Averaged layer thickness is 0.19 mm. The total thicknesses of the panels depend on the number of plies. The in-plane size of the panels is 150 mm × 100 mm. Detailed test parameters can be found in Table 2.1. In

this section, the modeling of layup A, B, and C samples was performed using 2D EST due to its relatively high computational efficiency. The modeling of the "sandwich-like" layup used 2D EST and 2D EST with inelasticity (EST-InELA). 2D EST used in this section was originally developed and reported in [38]. 2D EST-InELA was redeveloped based on the theory of EST. The novel mixed-mode cohesive law [7] and the capability to capture material inelasticity reported Chapter IV were integrated into the redeveloped model.

5.2.1 A Comprehensive Report of the LVI Computational Results

Computational results of all the cases studied in Section 5.2 are presented in this section. The meshes were uniform, without fiber alignment. Continuum shell elements were used. Modeling strategies such as element deletion or mass scaling were not used.

The material parameters of T800s/3900-2B used for 2D EST modeling are listed in Table 5.1.

5.2.1.1 Load Responses

The predicted load-time, load-impactor displacement, and impactor kinetic energy-time responses of the layup A, B, and C samples are displayed in Figures 5.1 to 5.3. In the figures, the black curves are the test results and the red curves are the computational results. For layup A cases, as shown in Figure 5.1, the predicted curves are found agreeing well with the test curves, except for the samples impacted with 25 J impact energy. Large oscillations which are seen on the experimental curves are not reproduced by 2D EST. In Figure 5.1, the middle column contains the load-displacement results. From the load-displacement responses, it is seen that the residual displacement values have been underpredicted. The residual displacement value of LVI, as illustrated in Chapter II indicates the impactor's displacement when the

Table 5.1: Material properties of T800S/3900-2B used in numerical predictions

ρ	Density	1.5×10^{-9} t/mm^3	measured
E_{11}	1-direction modulus	167,542 MPa	[118]
E_{22}	2-direction modulus	8,480 MPa	[118]
G_{12}	Shear modulus	4,481 MPa	[118]
ν_{12}	Poisson's ratio	0.3	[118]
$\epsilon_{11}^{ini,T}$	1-direction initiation strain (tension)	0.0176	[118]
$\epsilon_{11}^{ini,C}$	1-direction initiation strain (compression)	0.0106	[118]
$\epsilon_{22}^{ini,T}$	2-direction initiation strain (tension)	0.007	Toray tests
$\epsilon_{22}^{ini,C}$	2-direction initiation strain (compression)	0.0251	Toray tests
γ_{12}^{ini}	Shear initiation strain	0.0323	[118]
$G_{IC}^{f,T}$	Fiber mode I toughness in tension	40 N/mm	[21]
$G_{IC}^{f,C}$	Fiber mode I toughness in compression	10 N/mm	[21]
G_{IC}^{m}	Matrix mode I toughness	0.54 N/mm	Assumed identical to G_I
G_{IIC}^{m}	Matrix mode II toughness	1.40 N/mm	Assumed identical to G_{II}
σ_C	Interface normal strength	66.9 MPa	[70]
τ_C	Interface shear strength	100 MPa	[70]
G_I	Interface mode I toughness	0.54 N/mm	[70]
G_{II}	Interface mode II toughness	1.40 N/mm	[22]
G_{III}	Interface mode III toughness	1.40 N/mm	[22]

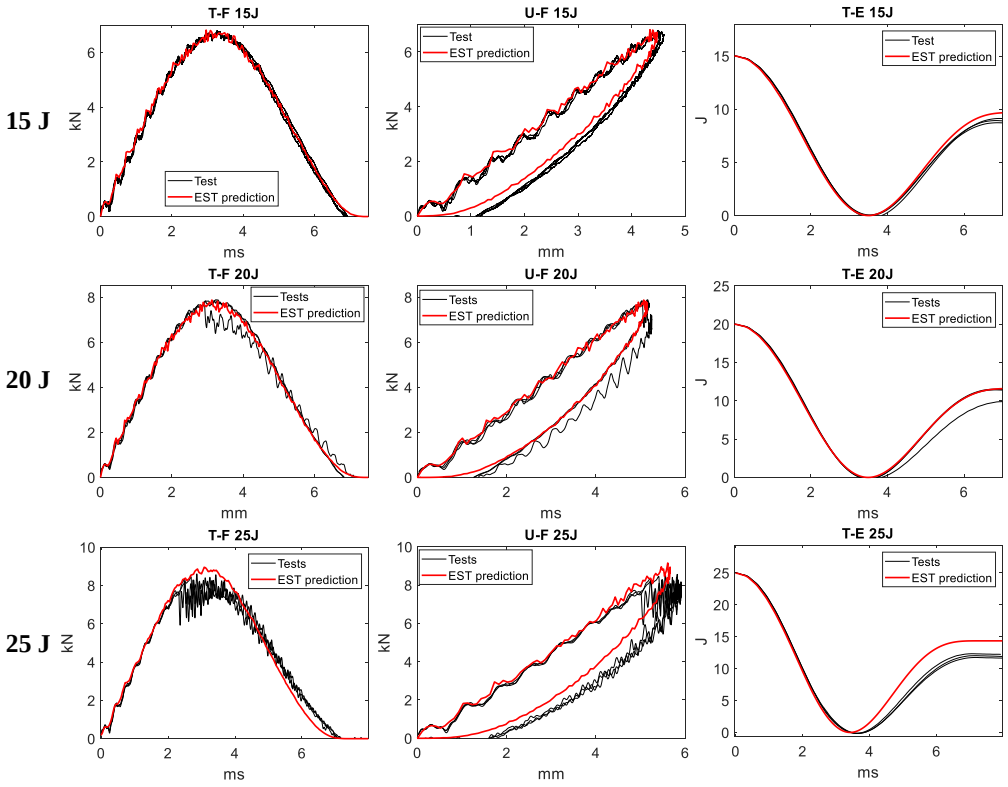

Figure 5.1: Predicted mechanical responses of the layup A samples.

impactor detach with the impacted panel. In the rightmost column of Figure 5.1, the energy absorption values are found to be underpredicted.

The computational LVI results of layup B samples are displayed in Figure 5.2. From the leftmost and middle columns, the predicted results agree well with the test data in terms of both the load-time and load-displacement responses, except for the fact that the residual displacement values are underpredicted. For the 35 J impact case, it is seen that the large oscillations on experimental curves are captured by 2D EST. Again, from the rightmost column, the energy absorption values are underpredicted.

The computational results of layup C samples are shown in Figure 5.3. It seems that the predicted load-time curves are almost on top of the experimental load-time curves. In the middle column, for the loading part of the load-displacement curves, the computational results agree well with the experimental results. However, for the

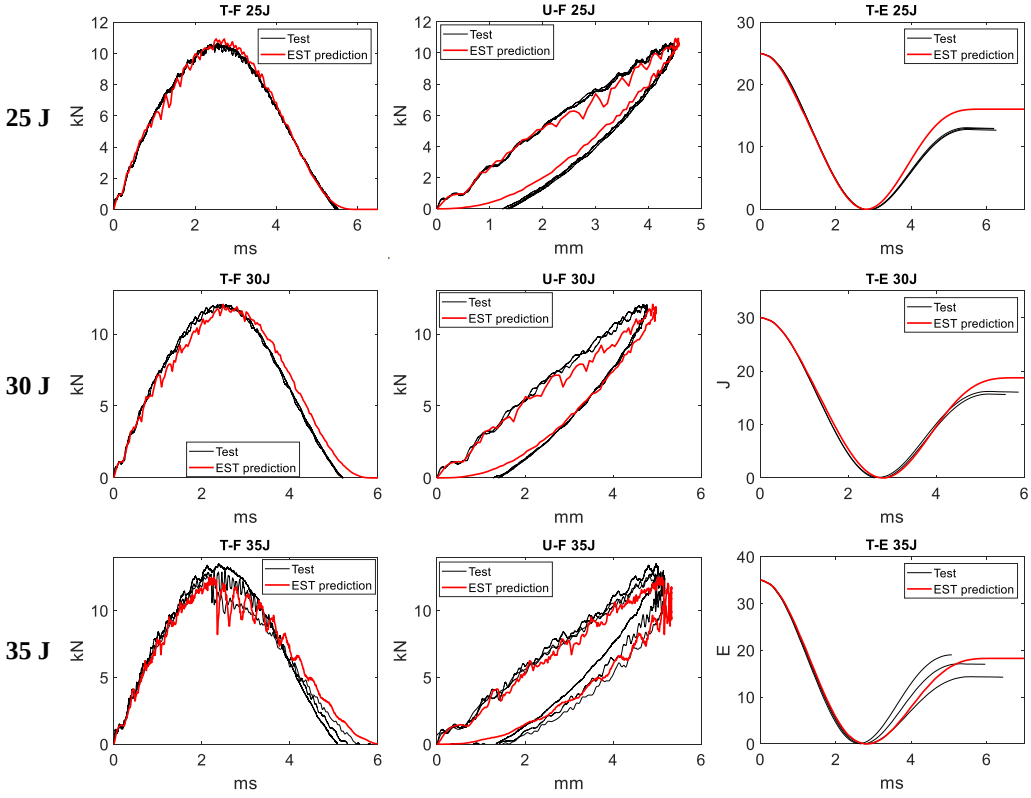

Figure 5.2: Predicted mechanical responses of the layup B samples.

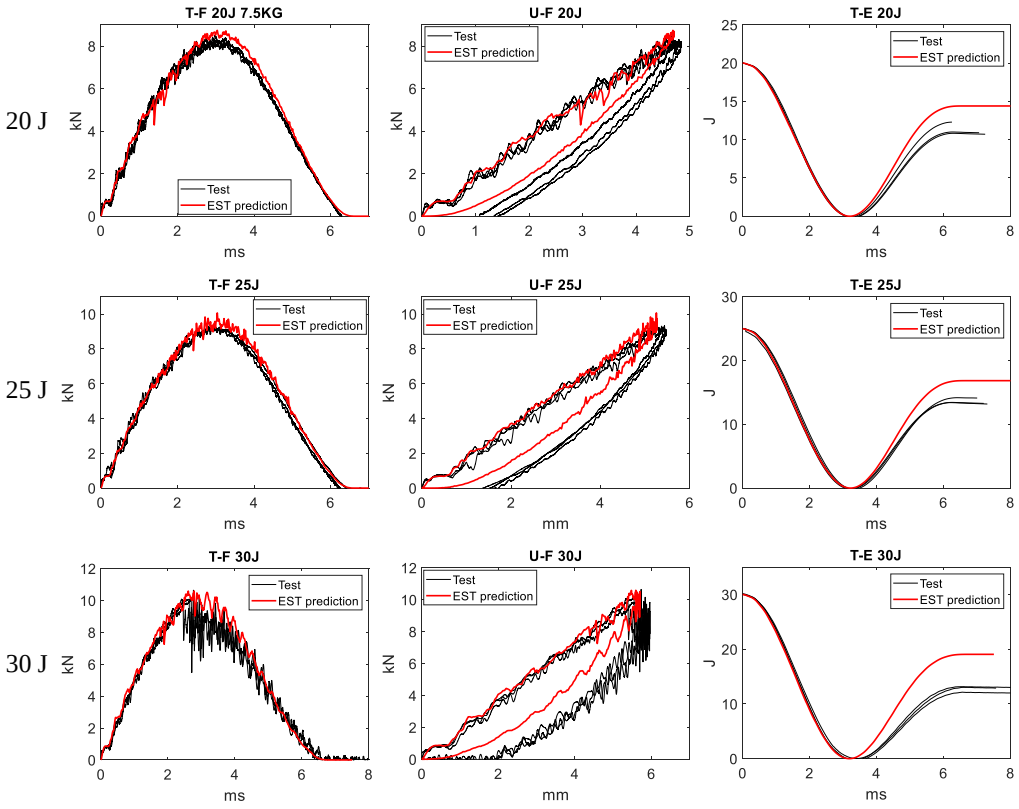

Figure 5.3: Predicted mechanical responses of the layup C samples.

unloading part, where the loads return from the maximum values to zeros, the difference between the predictions and the experiments is pronounced. This phenomenon might be due to the fact that layup C has a higher percentage of $\pm 45°$ plies, whose pre-peak damage is dominated by shear nonlinearity induced by matrix micro-cracking. Micro-cracking of matrix contributes to material inelasticity. However, 2D EST does not have the capability to capture inelasticity of composites. As observed in the rightmost column, the energy absorption values are underpredicted.

The important parameters obtained from the test data and predicted data are listed compared in Figures 5.4 to 5.6. The critical parameters include peak load, maximum displacement, residual displacement, and energy absorption. In Figures 5.4 to 5.6, numerical results correspond to orange dashed curves while the experimental results correspond to the solid blue curves. In Figures 5.4 (a), 5.5 (a), and 5.6 (a), the computationally obtained peak loads are very close to the test values.

The errors are under 9% (mostly under 5%). In Figures 5.4 (b), 5.5 (b), and 5.6 (b), the predicted maximum impactor displacement values agree very well with the experimental results, with all the errors being under 5%. From subfigures (c) and (d) of Figures 5.4 to 5.2, the residual displacement and energy absorption values are uniformly underpredicted. The cause of the underprediction is believed to be the lack of the capability to capture material inelasticity in 2D EST. In addition, the discrepancy between the computational and test results may be due to the randomness in material property distribution, and rate dependency of critical material properties such as interfacial strengths, which greatly affect the impact-induced delamination size. Also, another possible cause is unintended manufacturing defects in the samples.

The predicted deformation history of the bottom centers of the samples are compared with the experimental results characterized by 3D DIC in Figure 5.7. In the figure, the solid curves are the 3D DIC results while the dotted curves are the numerical results. The blue, orange, and yellow colors correspond to 15 J, 20 J, and 25 J for layup A; 25 J, 30 J, and 35 J for layup B; 20 J, 25 J, and 30 J for layup C. For layup A samples, as shown in Figure 5.7 (a), the predicted out-of-plane displacement values are smaller than the experimental results. As the energy gets higher, the discrepancy gets larger. This difference is also observed in Figures 5.7 (b) and (c). However, in Figures 5.4 (b), 5.5 (b), and 5.6 (b), the predictions of the impactor displacement agrees well with the test values. This means that the thickness reduction of the samples predicted is more significant than that actually happened during the tests. This might be due to the continuum shell elements near the impactor having sever thickness reduction due to high compressive stresses. Using solid elements might help reduce this effect and obtain computational results agreeing better to the 3D DIC characterization.

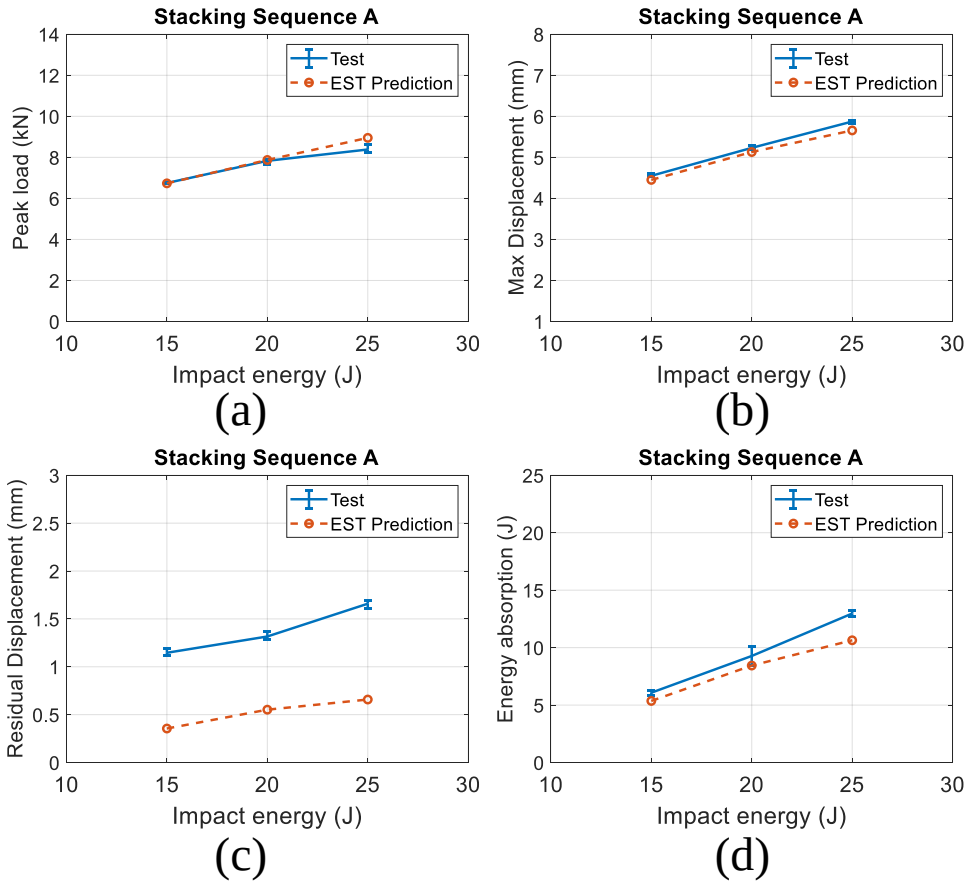

Figure 5.4: Statistics of the predicted critical parameters of layup A: (a) peak load, (b) maximum displacement, (c) residual displacement, and (d) energy absorption.

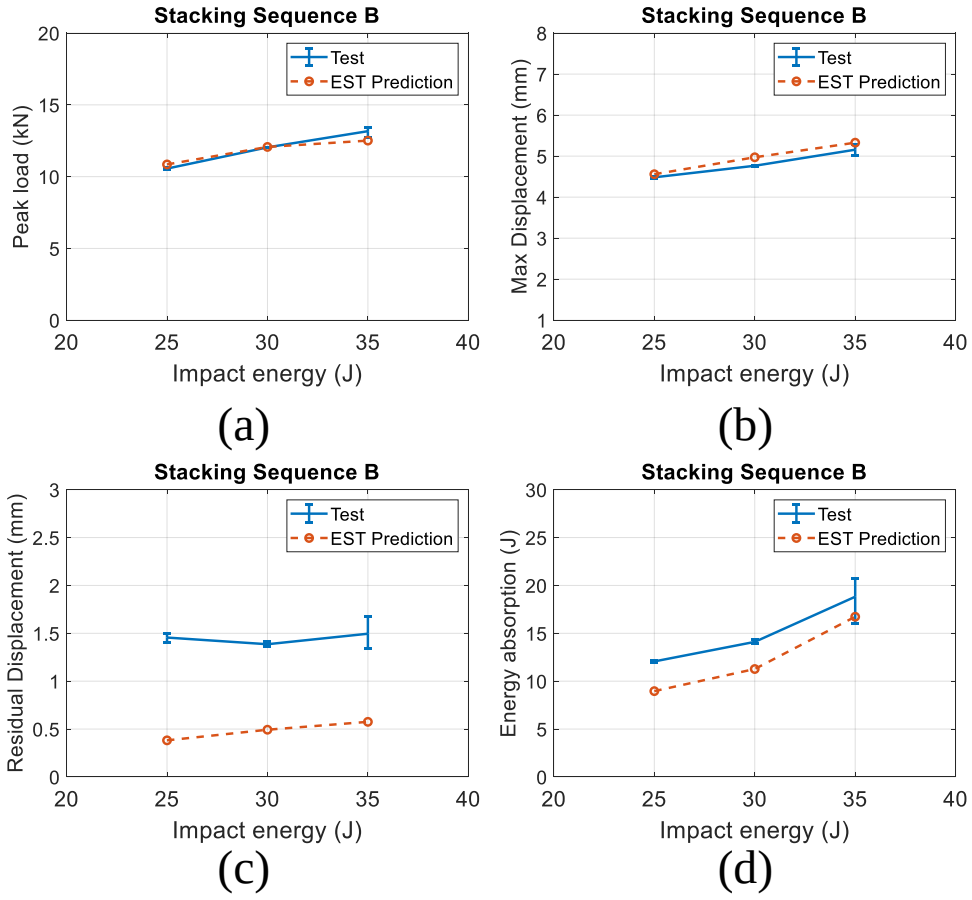

Figure 5.5: Statistics of the predicted critical parameters of layup B: (a) peak load, (b) maximum displacement, (c) residual displacement, and (d) energy absorption.

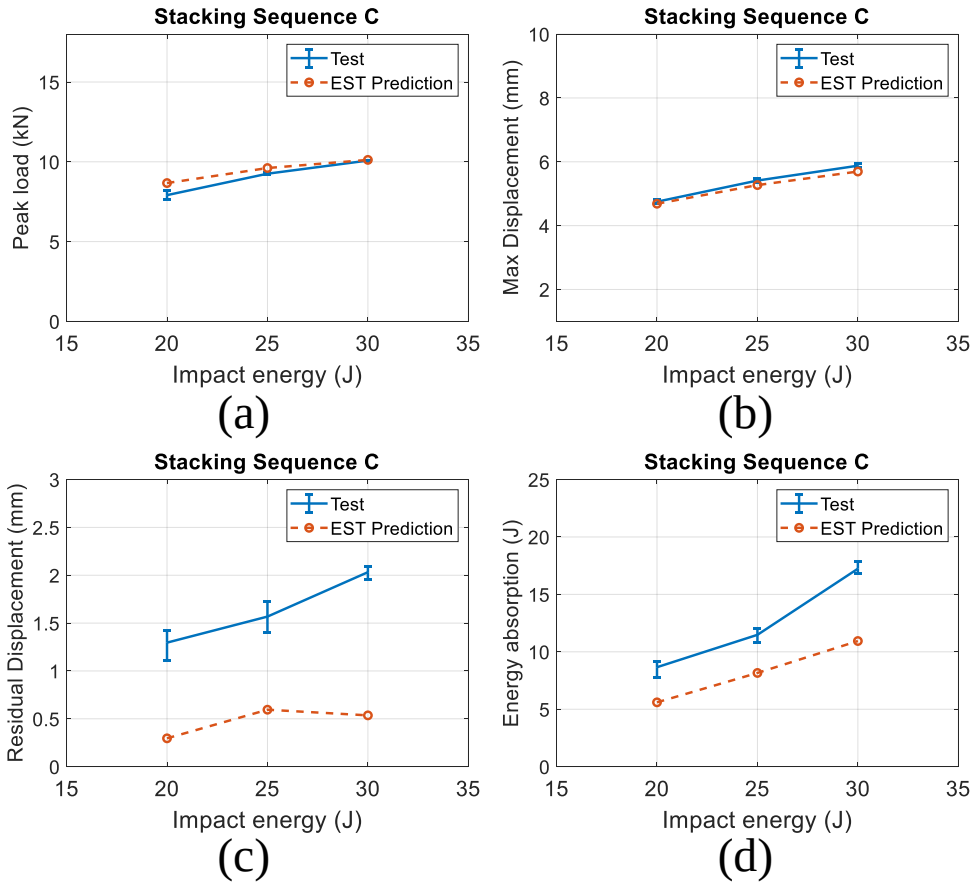

Figure 5.6: Statistics of the predicted critical parameters of layup C: (a) peak load, (b) maximum displacement, (c) residual displacement, and (d) energy absorption.

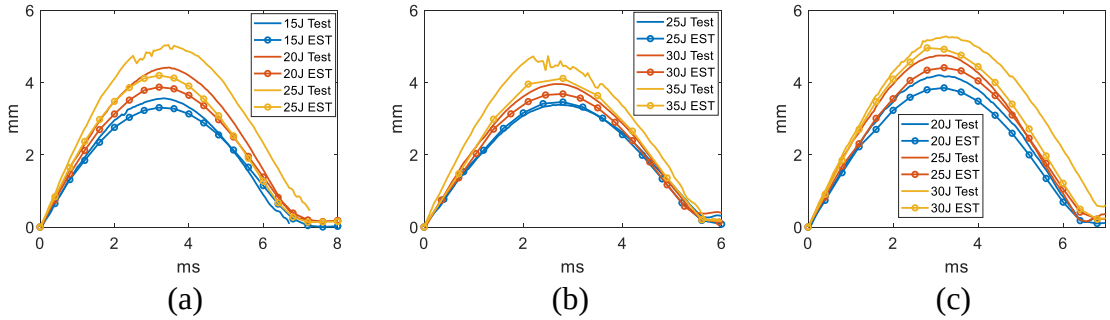

Figure 5.7: Predicted bottom center displacement histories: (a) layup A samples impacted with various impact energies, (b) layup B samples impacted with various impact energies, and (c) layup C samples impacted with various impact energies.

5.2.1.2 LVI-induced Damage

The damage footprints predicted by 2D EST of all the test cases are displayed in Figures 5.8 to 5.10. The delamination indicator CSDMG defined in Chapter IV is used for plotting the damage footprints. In Figures 5.8 to 5.10, the color bar ranging from blue to red means that the delamination state ranging from pristine to completely delaminated (with zero traction). The white solid contours represent damage footprints characterized by ultrasound C-scanning, as demonstrated in Chapter II. In general, the predicted damage footprints agree well with the C-scans in terms of shape and size. However, as seen in Figures 5.9 (c) and 5.10 (c), the some local differences are seen. In Figure 5.9 (c), the sticking-out pattern along the -45° direction is not captured by 2D EST. This sticking-out pattern corresponds to fiber kinking near the impacted surface of the sample. In Figure 5.10 (c), the sticking-out pattern along the 45° direction is not predicted by 2D EST. This pattern is caused by matrix splitting happening close to the non-impacted side of the sample. The overall damage areas predicted and characterized by C-scanning are summarized in Figures 5.8 (d) to 5.10 (d). For all the cases, the predicted damage footprints are larger than the C-scanning results. This is due to several reasons. First, the delamination indicator CSDMG is based on the traction value between interfaces. If the traction is zero, the void is not necessarily large enough for the dye penetrant to get in. However, when a void large enough, there is absolutely zero traction between the interfaces. Therefore, the predicted damage footprints should be larger than the characterized ones by definition. In addition, the interfacial properties might be rate dependent, as reported in [47]. The material properties used for 2D EST predictions in Table 5.1 were obtained from quasi-static tests, but used for LVI modeling with intermediate strain rates. Therefore, discrepancies between numerical and experimental results are expected. Finer tuning of material properties could be done to improve the computational accuracy. However, this is not the major purpose of this dissertation.

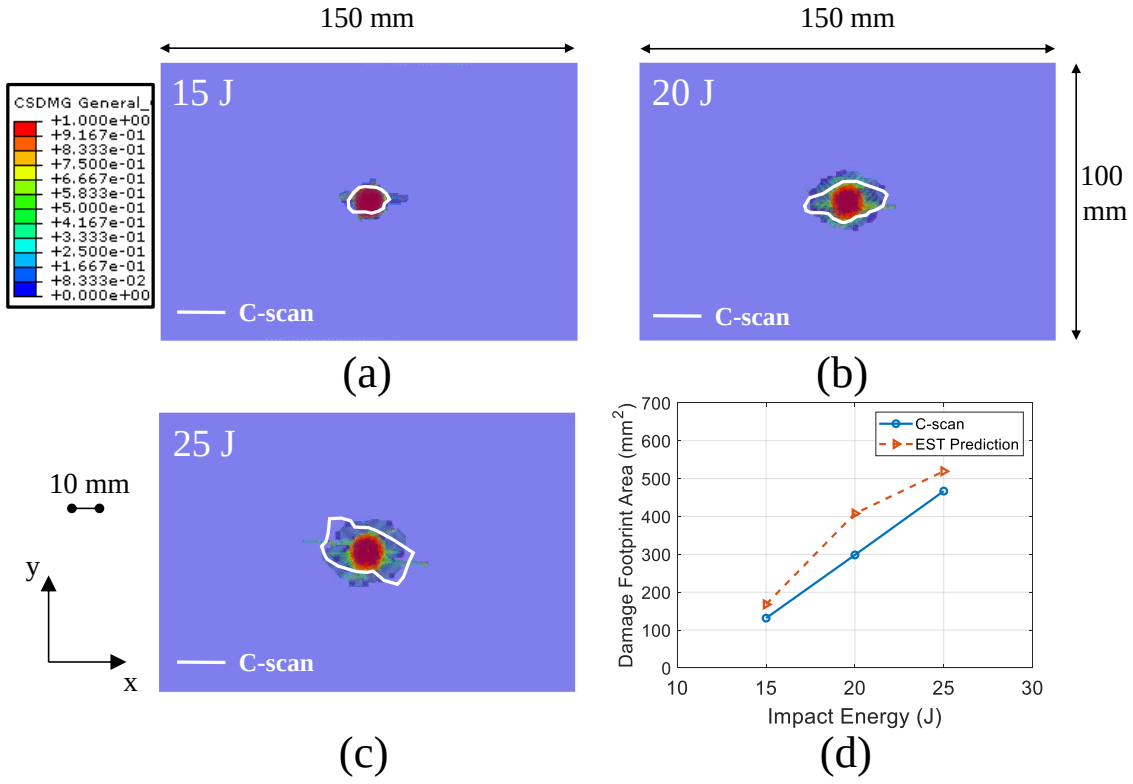

Figure 5.8: Predicted damage footprints of layup A samples: (a) impacted with 15 J, (b) impacted with 20 J and (c) impacted with 25 J, and (d) predicted overall damage areas compared with the C-scanned values.

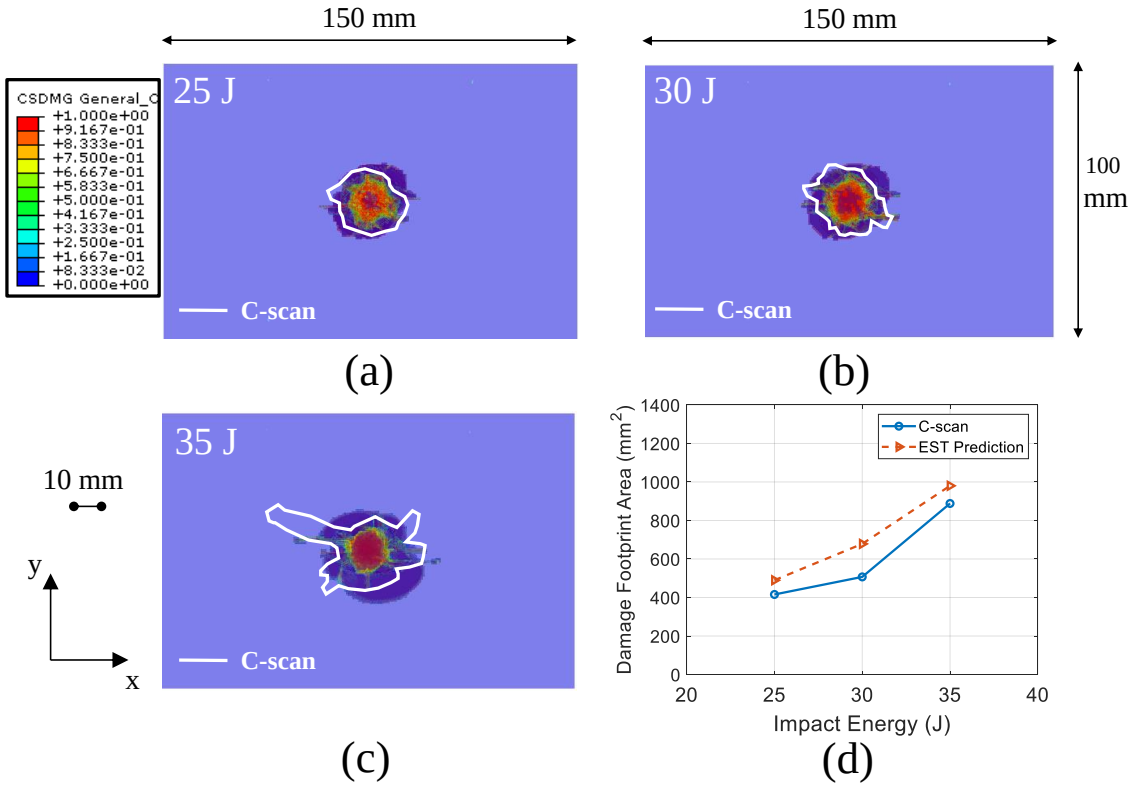

Figure 5.9: Predicted damage footprints of layup B samples: (a) impacted with 25 J, (b) impacted with 30 J and (c) impacted with 35 J, and (d) predicted overall damage areas compared with the C-scanned values.

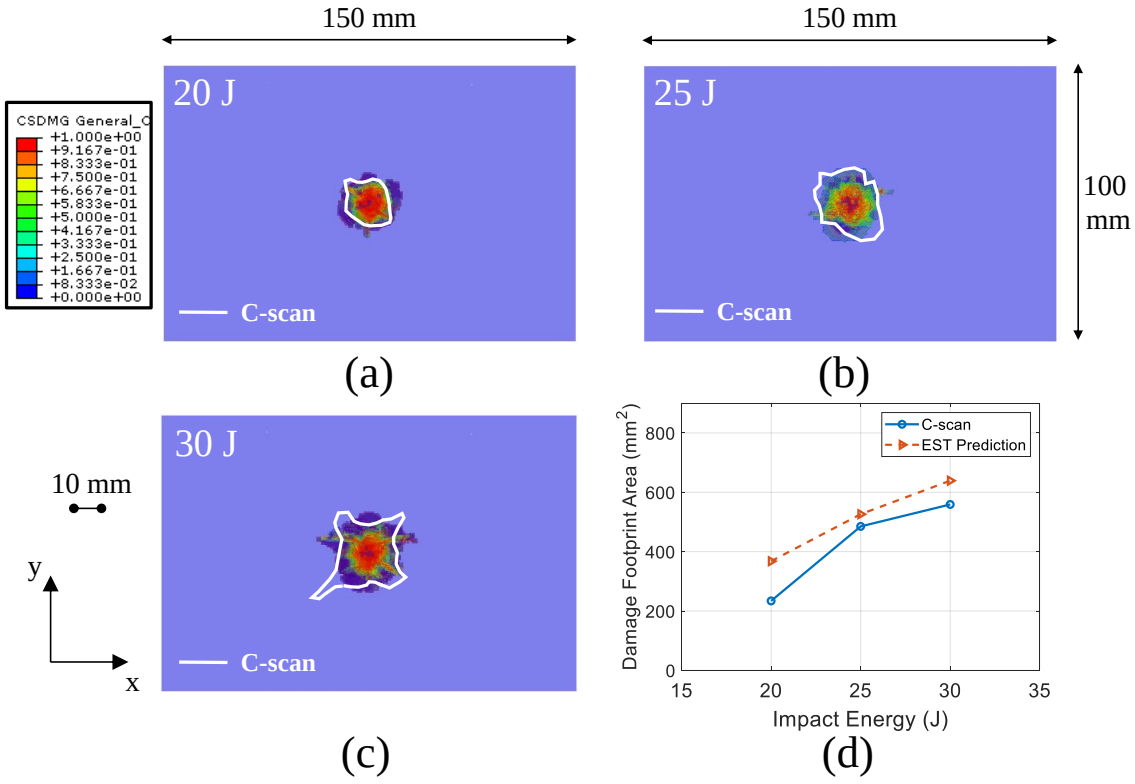

Figure 5.10: Predicted damage footprints of layup C samples: (a) impacted with 20 J, (b) impacted with 25 J and (c) impacted with 30 J, and (d) predicted overall damage areas compared with the C-scanned values.

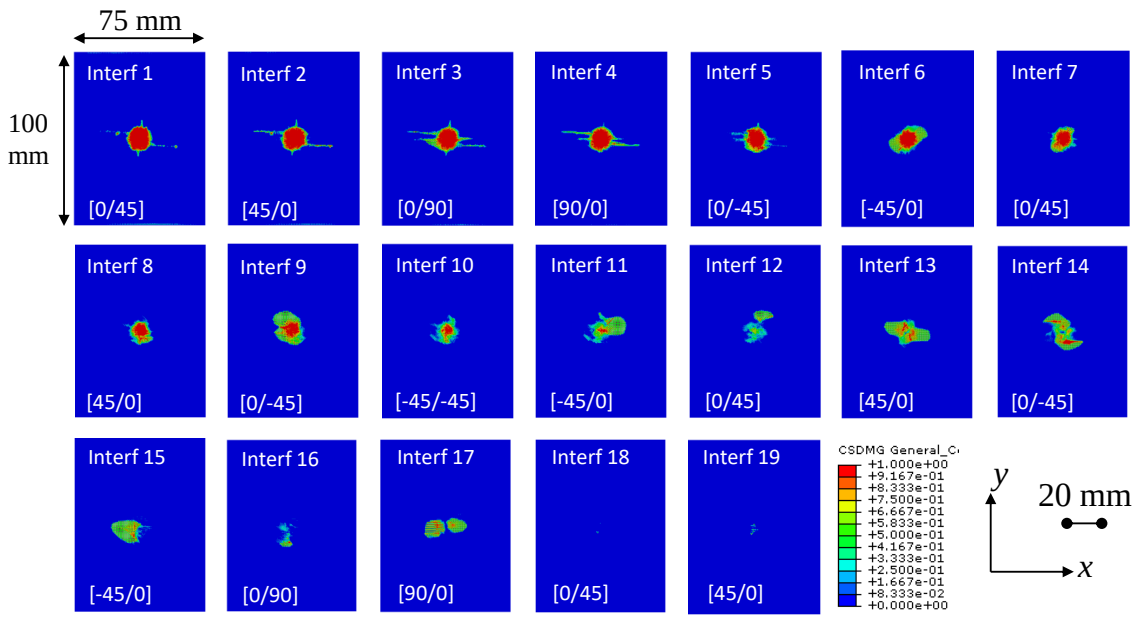

Figure 5.11: Predictions of delamination of the layup A sample impacted with 25 J.

Predicted delamination at all the interfaces of a layup A sample impacted with 25 J is displayed in Figure 5.11. The reason for choosing this impact energy is that the LVI-induced damage has the most enriched patterns for the cases with the highest impact energies, namely 25 J for layup A, 35 J for layup B, and 30 J for layup C. In Figure 5.11, delamination induced by fiber kinking is seen at interfaces 2 to 4 as the sticking-out patterns. Fan-shaped delamination is seen at interfaces 6, 13, and 14. Peanut-shape delamination is seen at interface 17. No significant damage is seen at interfaces 17-19 which are close to the non-impacted side of the sample. This does not agree well with μCT slices in Figure 2.16. In addition, the lack of predicted damage near the non-impacted side of the sample explains the smoothness of the predicted load curves, while there are oscillations on the test curves of relatively large amplitudes.

Predicted delamination of a layup B impacted with 35 J is displayed in Figure 5.12. Delamination induced by fiber kinking is seen at interfaces 1 to 5. Fan-shape

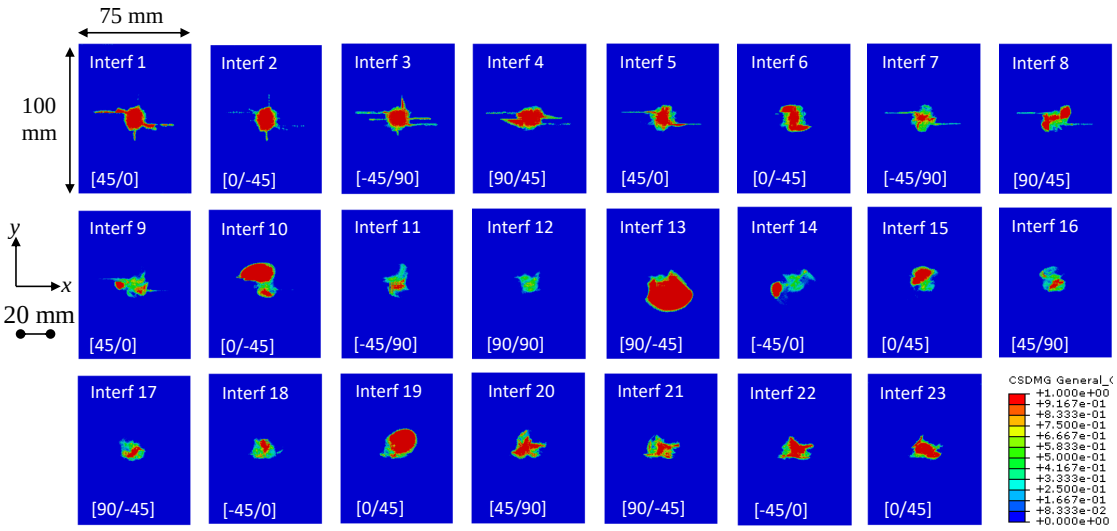

Figure 5.12: Predictions of delamination of the layup B sample impacted with 35 J.

delamination is seen at interfaces 6, 8, 10, and 13. Near the non-impacted side, at interfaces 20 to 23, delamination induced by fiber tensile rupture is seen. At some interfaces, such as interfaces 10, 13, and 19, the predicted delamination is significantly larger than that at the other interfaces. This is quite different from the μCT scanning in Figure 2.17, where in the middle part of the sample, the delamination at every interface is of equivalent size. This difference might be caused by spurious numerical oscillations induced by severe damage modes, such as fiber tensile rupture near the non-impacted side.

The predicted delamination of a layup C sample impacted with 30 J is demonstrated in Figure 5.13. Near the impacted side, at interfaces 1 to 5, delamination induced by fiber kinking is observed. Fan-shape delamination is observed at interfaces 5, 6, 14, and 15. Peanut-shape delamination is observed at interfaces 9, 12, 13, and 16. Delamination induced by fiber tensile rupture near the non-impacted side of the sample can be found at interfaces 17 to 19.

The history of LVI-induced damage growth of a layup C sample impacted with 30 J is illustrated in Figure 5.14. Delamination at interface 6, matrix cracking at plies 6

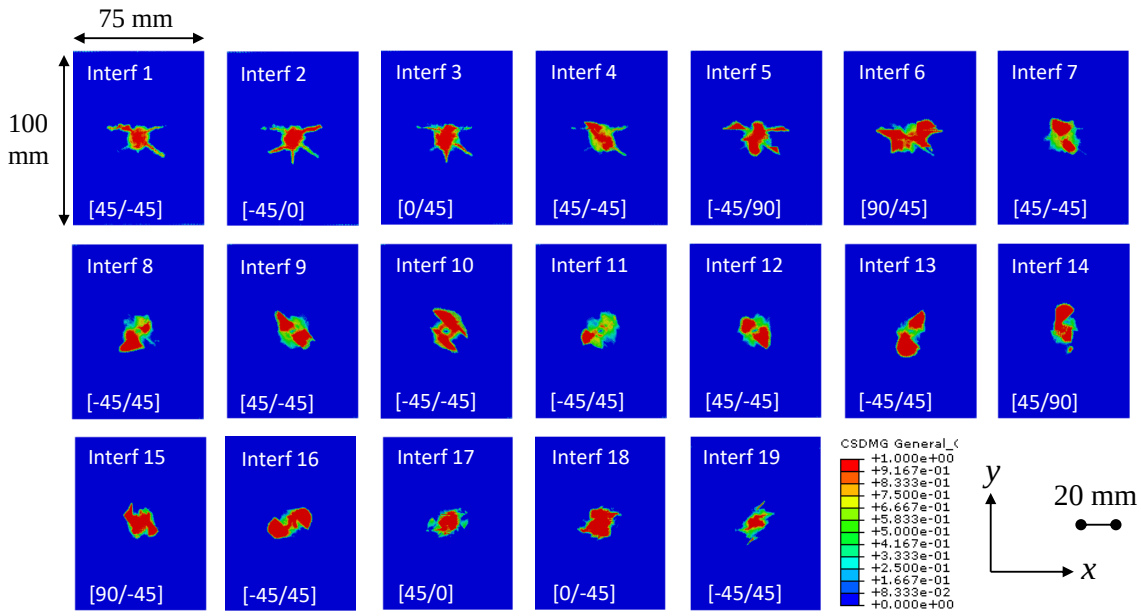

Figure 5.13: Predictions of delamination of the layup C sample impacted with 30 J.

and 7, and fiber breaking at plies 6 and 7 are displayed for an example. Figures 5.14 (a), (b), and (c) show the matrix cracking, fiber breaking, and delamination at 2.0 ms, 3.6 ms, and 6.8 ms. Different color codes are applied to the plotting of different damage modes. Fiber compressive kinking is observed in ply 6 starting from 2.0 ms. Matrix damage is seen at plies 6 and 7 along with the 90 ° and 45 ° directions. The matrix cracking in ply 6 seems to be affected by the fiber damage at the same ply. The delamination at interface 6 is fan-shape, but also reflecting the fiber damage. This directly shows the interaction between damage modes including matrix cracking, fiber kinking, and delamination. The growth of the damage size is continuous from 2.0 ms to 3.6 ms, and stops after 3.6 ms. In Figure 5.14 (d), the three time points are marked as green solid dots on the load-time curve.

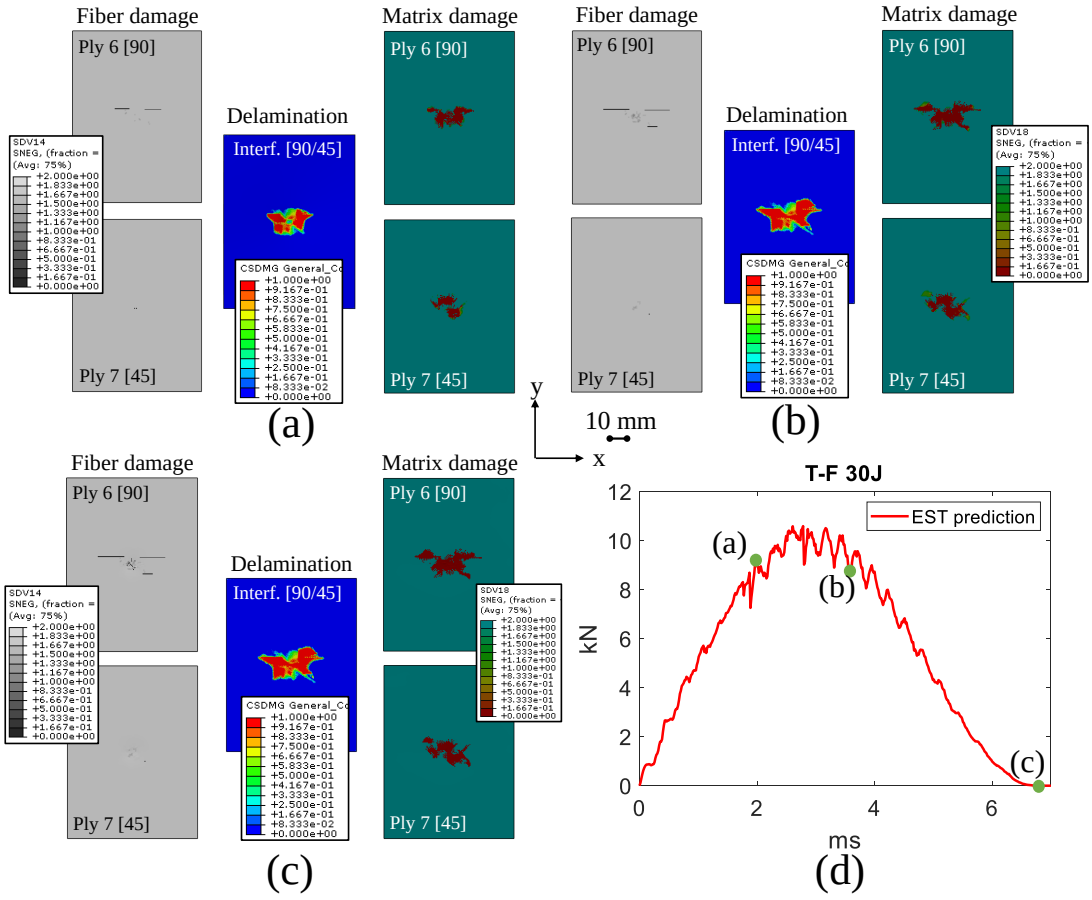

Figure 5.14: Damage modes interaction of the layup C sample impacted with 30 J: (a) at 2.0 ms, (b) at 3.6 ms, (c) at 6.8 ms, and (d) the predicted force-time curve.

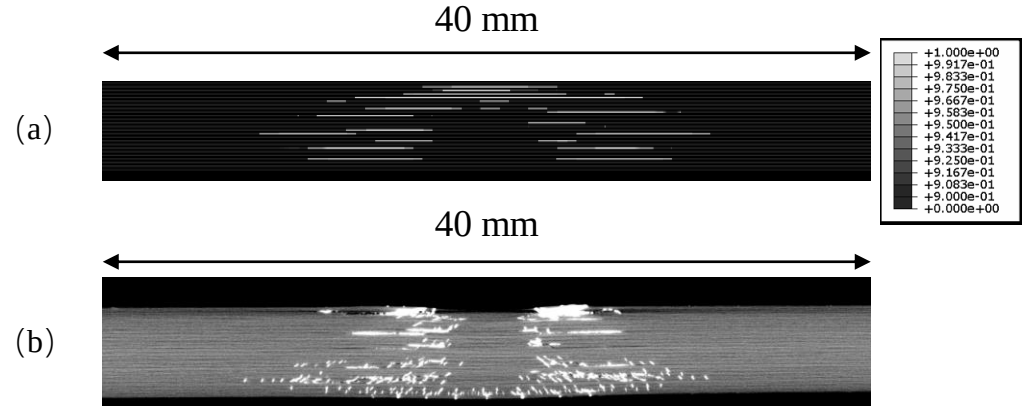

Figure 5.15: Comparison of the sectional views of damage: (a) predicted, and (b) μCT scanned

5.2.2 Mechanisms of LVI-induced Damage

This section focuses on the LVI-induced damage mechanisms revealed by computational studies. A layup B sample impacted with 25 J is used as an example. This section directly correspond to Section 2.3.2. The goal of this section is to investigate if the featured "rotating-fan" delamination can be captured numerically, and if the interaction between damage modes can be modeled.

First, side views of the layup B sample impacted with 25 J at the location going across the panel's center are provided in Figure 5.15. Figure 5.15 (a) contains the numerical results while (b) show the μCT slice at the corresponding location. Damage variable CSDMG is used to display the delamination at the interfaces. As seen in Figure 5.15 (a), the damage-free cone at the center of the side view is numerically predicted, which is also seen in the μCT slice. The predicted distribution of the delamination through the thickness of the panel is in general correct. Delamination at the top few interfaces seems to be overpredicted, which might be due to that the top plies tend to have more severe local bending and compression, where the damage patterns are more challenging to be computationally captured.

Face-on views of the delamination at all the interfaces are displayed in Figure

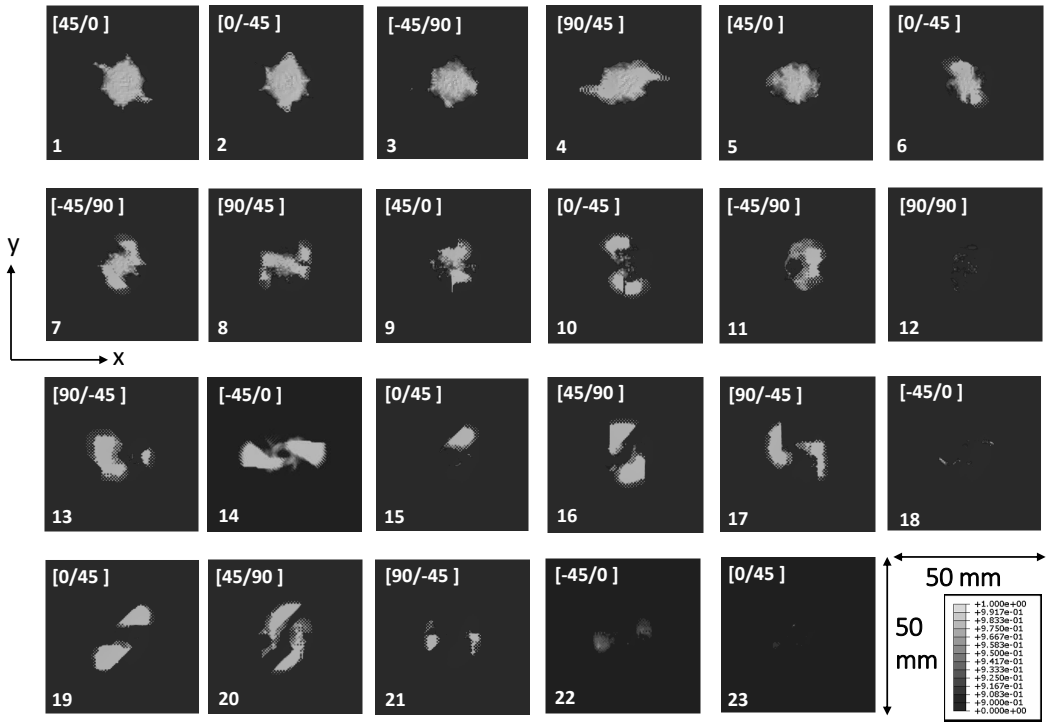

Figure 5.16: Prediction of the interface-by-interface delamination

5.16. This figure can be directly compared to the μCT slices displayed in Figure 2.22. In Figure 5.16, at interfaces 1 to 5, the delamination seems to be heavily influenced by the fiber kinking near the impacted side. Starting from interface 7, the fan-shaped delamination is clearly observed, especially at interfaces 7, 10, 13, 14-17, 19 and 20. It seems that as the interface number increases, the size of the "fan" has a growing trend. This is believed to be caused by the fact that tensile and in-plane shear stresses σ_{22} and τ_{12} in laminae closer to the non-impacted side is higher than that closer to the impacted side. With higher σ_{22} and τ_{12}, matrix cracking tend to be longer. Therefore, delamination bounded by longer matrix cracking tends to be larger. However, at interfaces 21 to 23, the predicted delamination is very small. This is due to that near the very bottom of the sample, interfacial shear stresses τ_{13} and τ_{23} are relatively small to induce delamination. If the delamination patterns at interface 7 to 20 are displayed consecutively, the "rotating-fan" feature will be observed.

Matrix cracking at all the plies is displayed in Figure 5.17. The state variable

of 2D EST SDV18 was used for plotting the matrix damage. The value of SDV18 ranges from 0 to 2. If SDV18 is equal to 2, the state of matrix is pristine. SDV18=1 means that matrix damage has initiated but not propagated. SDV18=0 indicates matrix failure. In Figure 5.17, in plies 1 to 5, the predicted matrix cracking is significantly influenced by fiber kinking. 2D EST has been implemented such that when an element has fiber tensile/compressive failure, the matrix is automatically failed. In plies 8 to 21, the predicted matrix cracking is observed to align well with the fiber directions. In plies 11 to 21, damage-free zones near the center of the observed areas are seen. In plies 22 to 24, relatively large areas are found to have matrix cracking. This is due to the relatively high σ_{22} and τ_{12} values near the non-impacted side of the sample. Compared to the μCT slices shown in Figure 2.22, well-spaced matrix cracking is not predicted. This is believe to be due to the fact that the current used mesh is not fine enough to capture the shear transfer phenomenon, which is the major cause for the well spaced matrix cracking. In addition, the nature of the crack band (CB) method [71] implemented in EST is to smear crack separations into finite characteristic lengths. Therefore, the modeled matrix cracks are not sharp as that in the μCT slices.

Predicted fiber kinking is shown in Figure 5.18. Only plies 1 to 5 near the impacted side of the sample have fiber kinking. The state variable SDV14 ranging from 0 to 2 is used for plotting fiber damage. SDV14=2 implies that there is no fiber damage. SDV14=1 means for fiber tensile/compressive damage initiation. SDV14=0 indicates fiber failure. In Figure 5.18, in plies 1, 2, and 4, the directions of the predicted fiber kinking are perpendicular to the corresponding fiber orientations, which are physically correct. However, in ply 3, the fiber kinking is not perpendicular to the fiber direction. This might be due to spurious numerical errors. Except for ply 3, the predicted fiber kinking in the other plies in Figure 5.18 correlates well with the μCT slices shown in Figure 2.24.

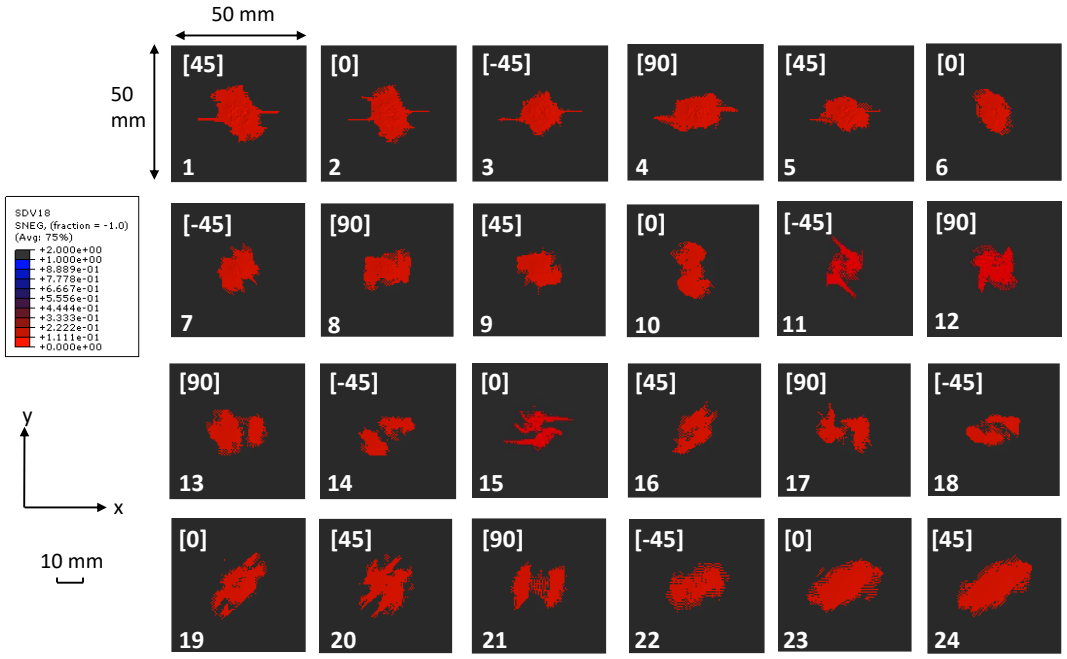

Figure 5.17: Prediction of the ply-by-ply matrix cracking

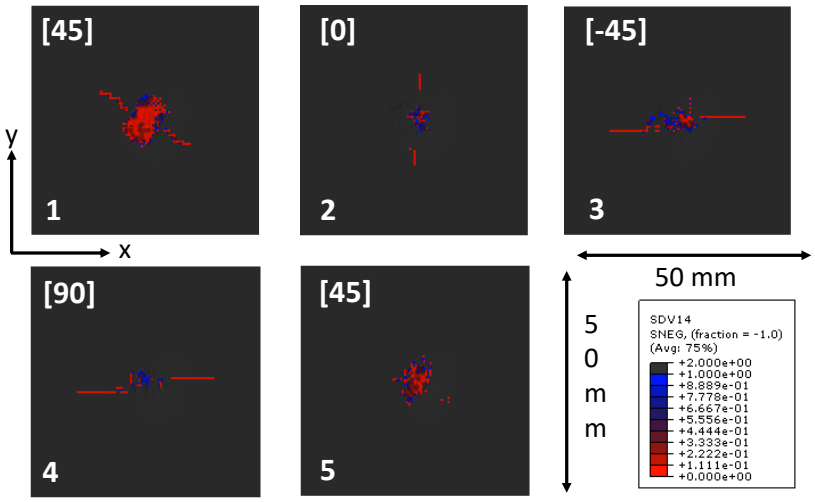

Figure 5.18: Prediction of the fiber kinking

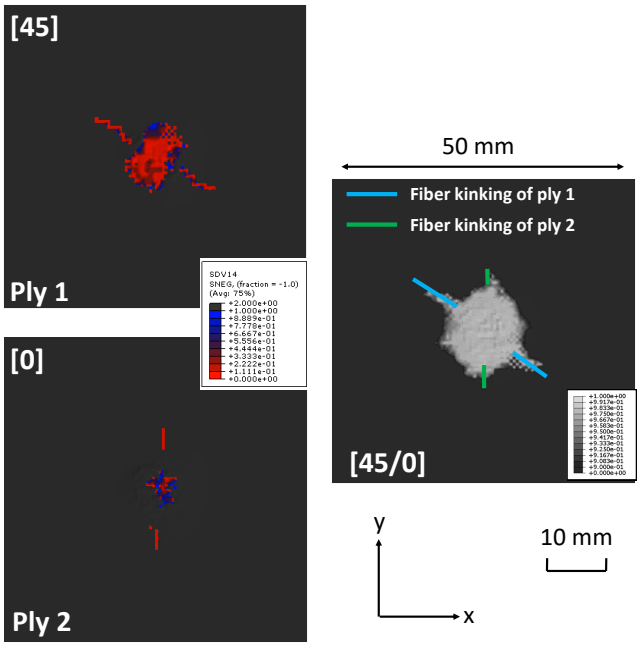

Figure 5.19: Interaction between the fiber kinking and delamination

As illustrated in Chapter II, the interaction between the damage modes including matrix cracking, fiber breaking, and delamination is the key to the LVI-induced damage patterns. The interaction is also captured by the numerical predictions. For example, the predicted fiber kinking in the first and second plies and the delamination between these two plies are displayed together in Figure 5.19. From the figure, the delamination shape seems to be affected significantly by the fiber kinking morphology. The interaction between matrix cracking and delamination is demonstrated in Figure 5.20 which groups the predicted matrix cracking in plies 20 and 21, and the predicted delamination at the interface between these two plies. The delamination in Figure 5.20 is found to be bounded by matrix cracking in the neighboring plies. From Figures 5.19 and 5.20, it can be concluded that the capturing of the damage mode interaction is the gist for predicting the "rotating-fan" delamination pattern.

The history of the predicted matrix damage in plies 20 and 21, and the predicted delamination in between is displayed in Figure 5.21. Four time points including 1.2

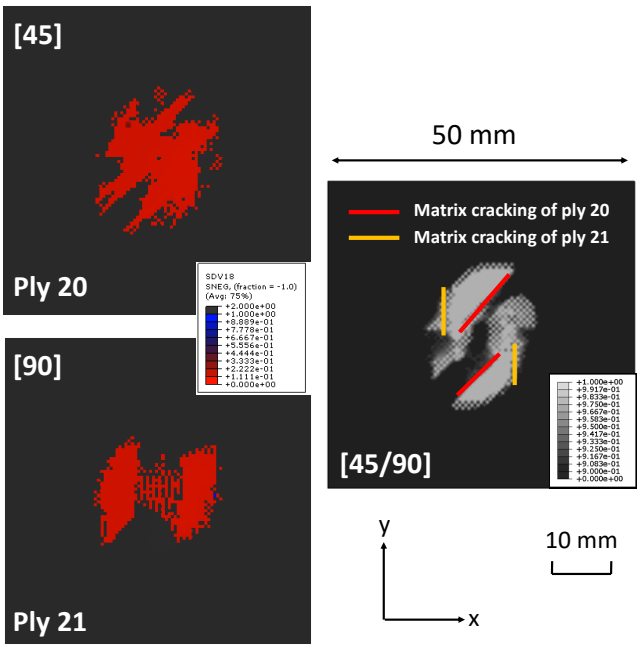

Figure 5.20: Interaction between the matrix cracking and delamination

ms, 2.0 ms, 4.0 ms, and 6.0 ms are chosen for plotting the damage. At 1.2 ms, as seen in Figure 5.21 (a), a small amount of matrix cracking in the centers of the observed area is seen. However, no delamination is observed at the interface. Figure 5.21 (a) numerically demonstrates that matrix cracking serves as the precursor for delamination. The interaction between matrix cracking and delamination is seen in Figures 5.21 (b) to (d). From 2.0 ms to 4.0 ms, the size of the damage increases. From 4.0 ms to 6.0 ms, the damage stops enlarging. This is because that the peak load happens before 4.0 ms. After the peak load, the impactor would start to rebound with the contact load starting to decrease. With the decreasing contact load, damage is not likely to have further growth.

5.2.3 LVI Damage of the Highly-anisotropic Laminate

The experimental results of the LVI-induced damage of the high-anisotropic laminate have been reported in Section 2.3.3. The stacking sequence is $[0/90/0/90_9]_s$. The

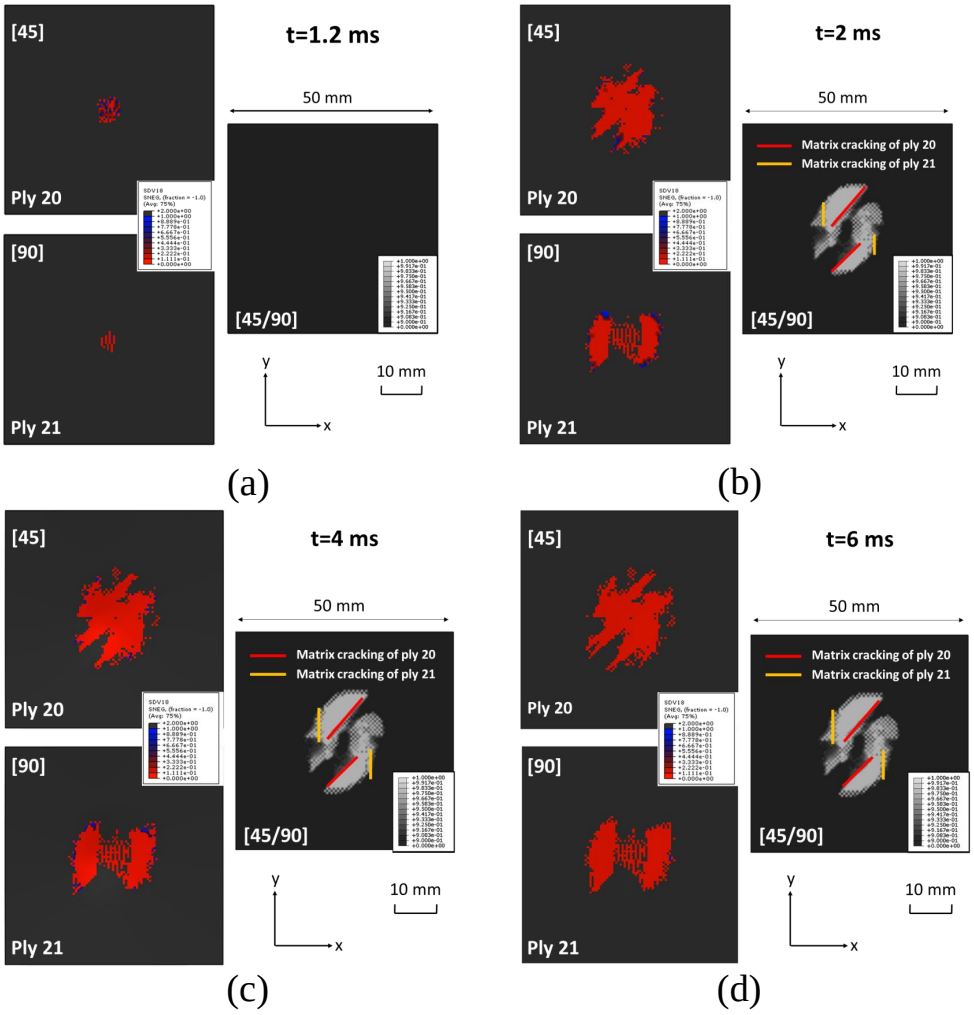

Figure 5.21: History of the interaction between the matrix cracking and delamination: (a) 1.2 ms, (b) 2.0 ms, (c) 4.0 ms, and (d) 6.0 ms

[0/90/0] outer layers serve as the "face sheet" while the inner 18 plies of 90° layers serve as the "core". The LVI-induced damage pattern is referred to as the "kidney" pattern. In this section, both 2D EST and 2D EST-InELA are applied to the modeling of the LVI of this high-anisotropic layup with 25 J impact energy. The difference between 2D EST and 2D EST-InELA is that in 2D EST-InELA, a mixed-mode cohesive law [7] has been integrated and the capability to capture material inelasticity has been implemented. The material properties used by the computational model are listed in Table 5.1.

The predicted load responses are plotted in Figure 5.22 in comparison with the experimental results. The black curves correspond to the test results. The red curves are the 2D EST-InELA results and the green curves are the 2D EST results. Overall, the predictions agree well with the test results. Critical parameters including the peak load and displacement values are captured accurately. There are two major differences. First, sharp load drops are seen in the computationally obtained curves but not observed in the test curves. It is suspected that the cutoff frequency of the load cell of the drop tower tester was not high enough to record these sharp load drop in the experimental results. In addition, parameters used in numerical predictions such as frictional coefficients and fracture toughness values might need further calibration to achieve a better computational fidelity. The second major difference is seen in Figure 5.22 (b) as the residual displacement being underpredicted by both 2D EST and 2D EST-InELA. Material inelasticity is the major reason for the residual displacement. 2D EST-InELA seems better than 2D EST in terms of capturing the effect of inelasticity, but still not sufficient to obtain the correct residual displacement value. The reason is that 2D EST-InELA only captures inelasticity in the 22 and 12 directions. Inelasticity in other components including 33, 13, and 23 also need to be accounted for to predict the residual displacement better.

Damage footprints predicted by 2D EST-InELA and 2D EST are demonstrated

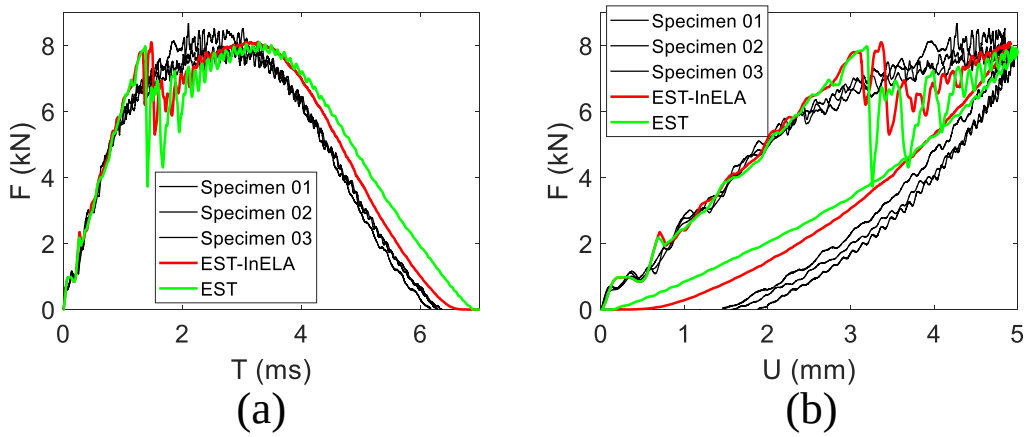

Figure 5.22: Predicted load responses compared to the experimental results: (a) load-time curves, and (b) load displacement curves.

in Figure 5.23. In the figure, the solid curves correspond to damage footprints characterized by ultrasound C-scanning, as displayed in Figure 2.32. CSDMG is used for plotting the predicted damage footprints. The damage footprints demonstrated in the first row are predicted by 2D EST-InELA, observed from the impacted and non-impacted side. The second row corresponds to the predictions using 2D EST. It is observed from Figure 5.23 that the 2D EST-InELA prediction agrees much better with the C-scanning than the 2D EST prediction. The "kidney" damage seems to be captured by 2D EST-InELA. For the rest of this section, only the damage predicted by 2D EST-InELA will be illustrated in detail.

The evolution history of the damage footprint predicted by 2D EST-InELA is plotted in Figure 5.24, accompanied by the load-time curve. From time point (a) to (b), the growth of the damage footprint is rapid and pronounced. This rapid growth correlates well with the load drops on the load-time curve. Then, from time point (b) to (d), the damage footprint grows progressively. After time point (d), after the peak load, the damage stops growing.

The predicted delamination at all the interfaces are displayed in Figure 5.25. As the interface number increase, the location gets closer to the non-impacted side of

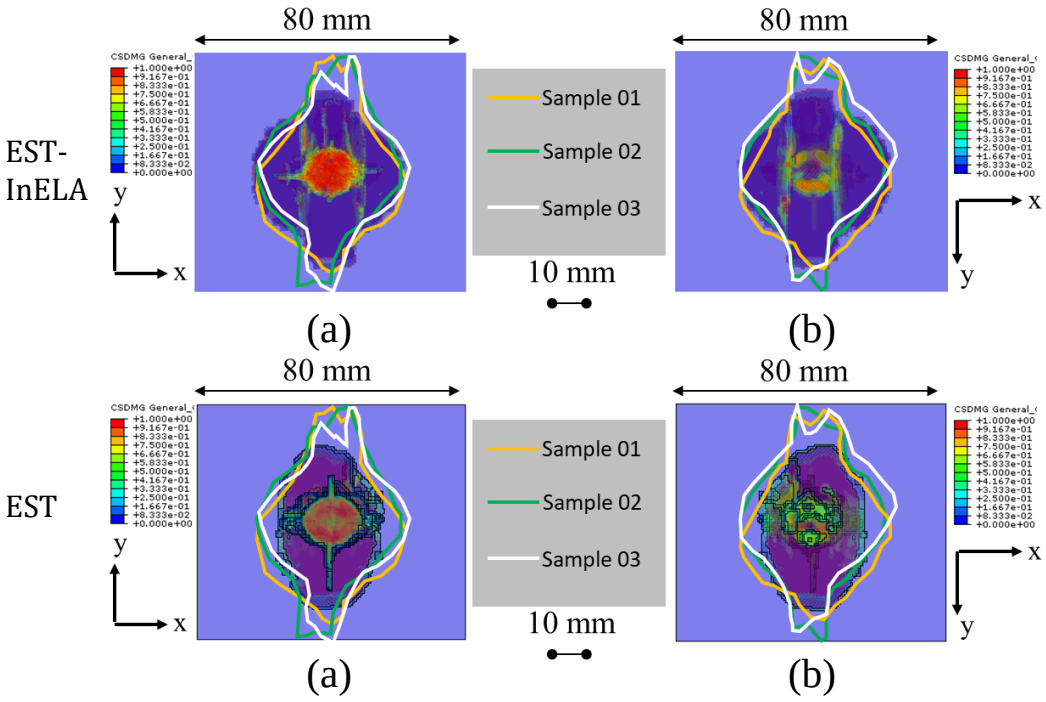

Figure 5.23: Predicted damage footprints: (a) by 2D EST-InELA, observed from the impacted side, (b) by 2D EST-InELA, observed from the non-impacted side, (c) by 2D EST, observed from the impacted side, and (d) by 2D EST, observed from the non-impacted side.

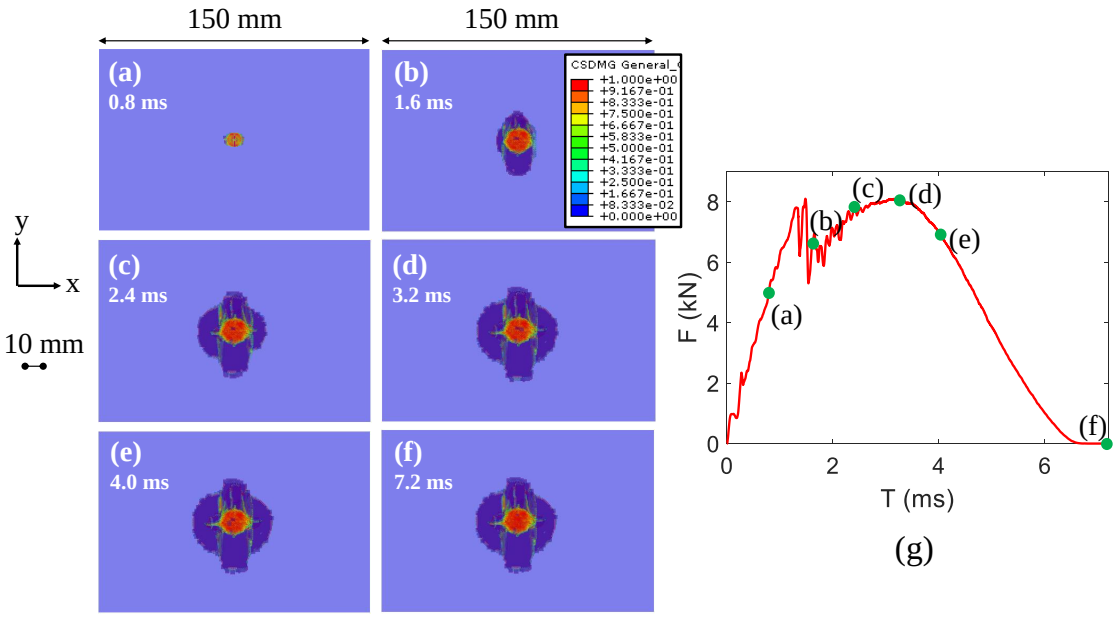

Figure 5.24: Predicted damage footprints by 2D EST-InELA at: (a) 0.8 ms, (b) 1.6 ms, (c) 2.4 ms, (d) 3.2 ms, (e) 4.0 ms, (f) 7.2 ms, and (g) the load-time response.

the sample. At interfaces 1 to 6, sticking out patterns are seen, which should be induced by fiber kinking near the impacted side of the sample. At interfaces 9 to 20, 22, and 23, delamination along the 90° direction is seen. The delamination at these interfaces is similar to that observed in face-on μCT slices, as shown in Figure 2.33. Large delamination at interfaces 13 and 17 is seen, which is not observed from the μCT slices. The highlight of the prediction is that the "kidney" delamination is successfully predicted at interface 21, which is between a 90° and a 0° ply.

The predicted fiber kinking is seen in plies 1 to 3 in Figure 5.26. The directions of the fiber kinking are observed to be perpendicular to the corresponding fiber orientations. The predicted fiber kinking correlates well with the sticking-out patterns of delamination displayed in Figure 5.25.

The predicted matrix cracking can be found in most of the plies, as shown in Figure 5.27. Matrix cracking along the 90° direction can be observed in plies 10 to 21. In plies

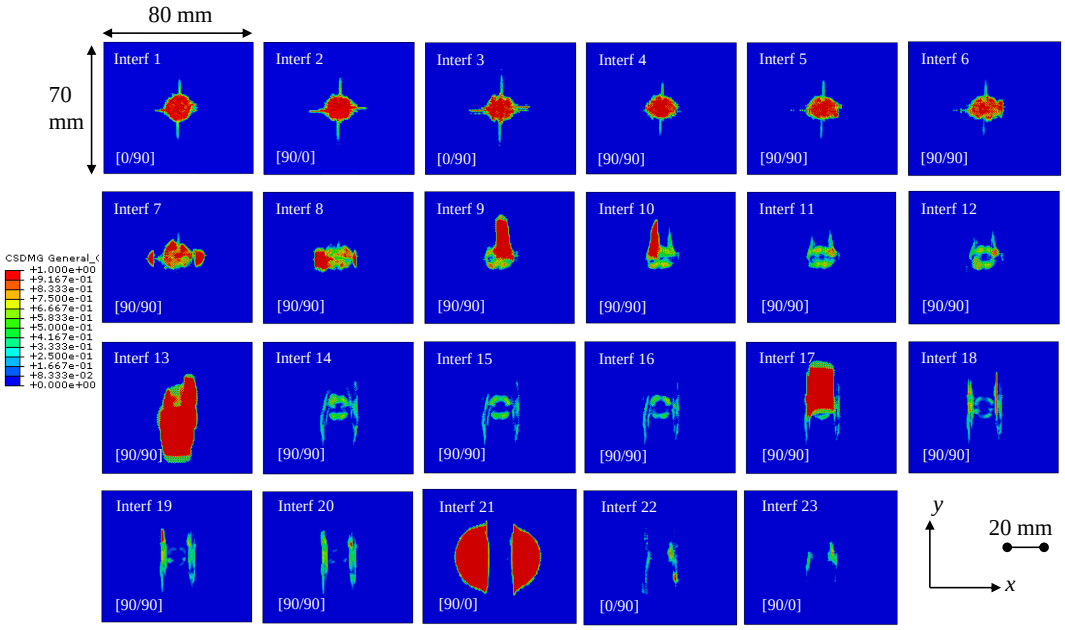

Figure 5.25: Delamination predicted by 2D EST-InELA at all the interfaces.

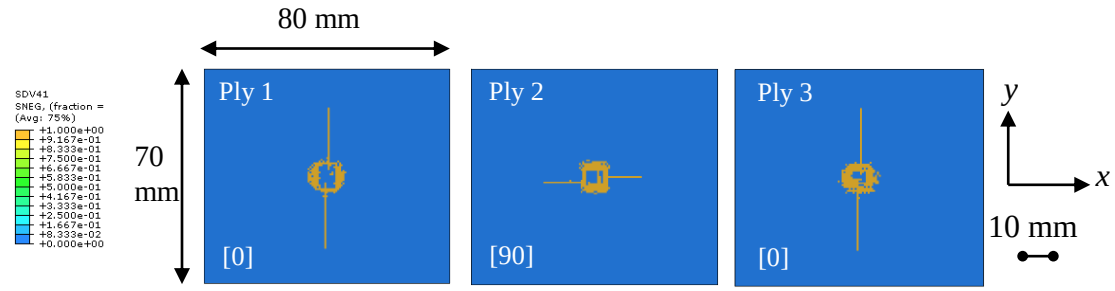

Figure 5.26: Fiber damage predicted by 2D EST-InELA.

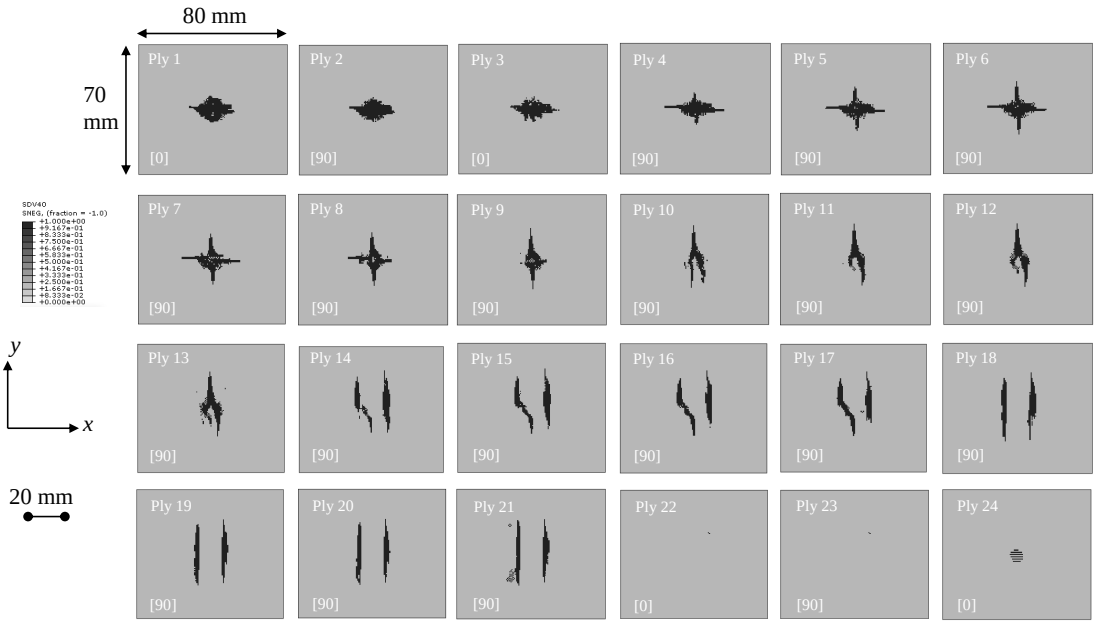

Figure 5.27: Matrix damage predicted by 2D EST-InELA in all the plies.

14 to 21, parallel matrix cracks and damage-free zone at the centers of the observed areas are seen. This agrees well with the μCT slices in Figure 2.33. However, in plies 22 to 24, barely any matrix cracking is predicted, which is significantly different from the corresponding μCT slices in Figure 2.33. This difference is believed to be due to the matrix transverse tensile strength used in EST-InELA prediction being higher than the actual value.

The predicted damage by 2D EST-InELA is visualized with edge-on views. Cross-sectional views at 7 locations are displayed in Figure 5.28, directly compared with edge-on μCT slices at the corresponding locations. In Figure 5.28, elements with fiber failure, matrix failure, and delamination are colored yellow, black, and red. d in the figure represents the distance of the cross-section to the center of the panel. Slanted matrix cracking is seen in Figure 5.28 (a) at $d = 0$. However, the slant angle seems to be smaller that that characterized by μCT. It is believed that adding more layers of continuum shell elements to the model would help capture the stress state more accurately, and hence the slanted matrix cracking with higher fidelity. Extensive de-

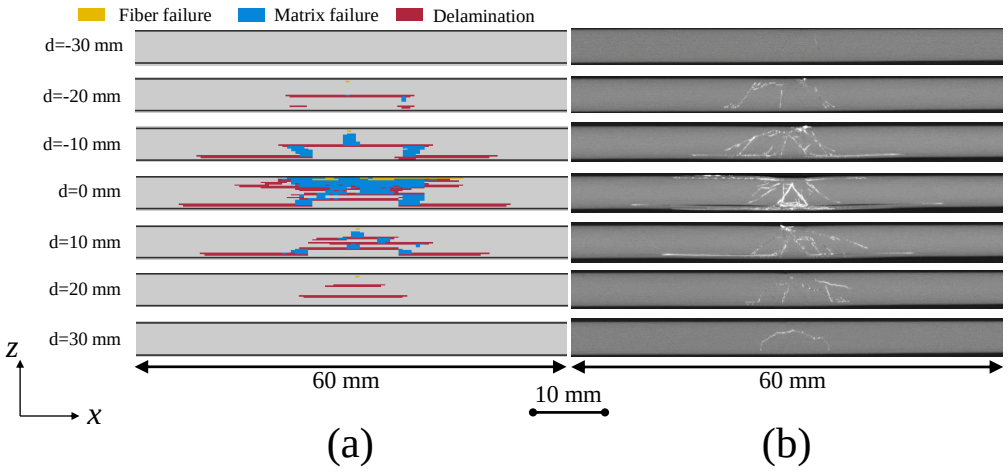

Figure 5.28: Damage with edge-on views: (a) predicted, and (b) μCT.

lamination is seen near the bottom of the panel, happening at the interface between the 90° and 0° plies. Comparing Figure 5.28 (a) with 5.28 (b), delamination seems to be predicted at more interfaces. This might be caused by spurious numerical oscillations and the usage of inappropriate material properties, especially the interfacial strengths and toughnesses.

Similar to Figure 2.35, elements with fiber failure, matrix failure, and delamination are segmented out and displayed in Figure 5.29. Fiber failure, matrix failure, and delamination are colored yellow, blue, and red. The three subfigures of Figure 5.29 are arranged with the same pattern of Figure 2.35 such that a direct comparison can be made. It is seen that the predicted LVI-induced damage morphology highly resembles the μCT characterization.

5.3 Computational LVI Study with the Effects of Panel Size

In this section, computational results of the LVI studies considering the panel size effects are reported. The material system studied is IM7/977-3. Two stacking sequences are analyzed, with three in-plane sizes and two laminate thicknesses. The stacking sequences are L1 $[45/\text{-}45/0/90/0/0]_{ns}$ and L2 $[45/0/\text{-}45/90]_{ns}$. The in-plane

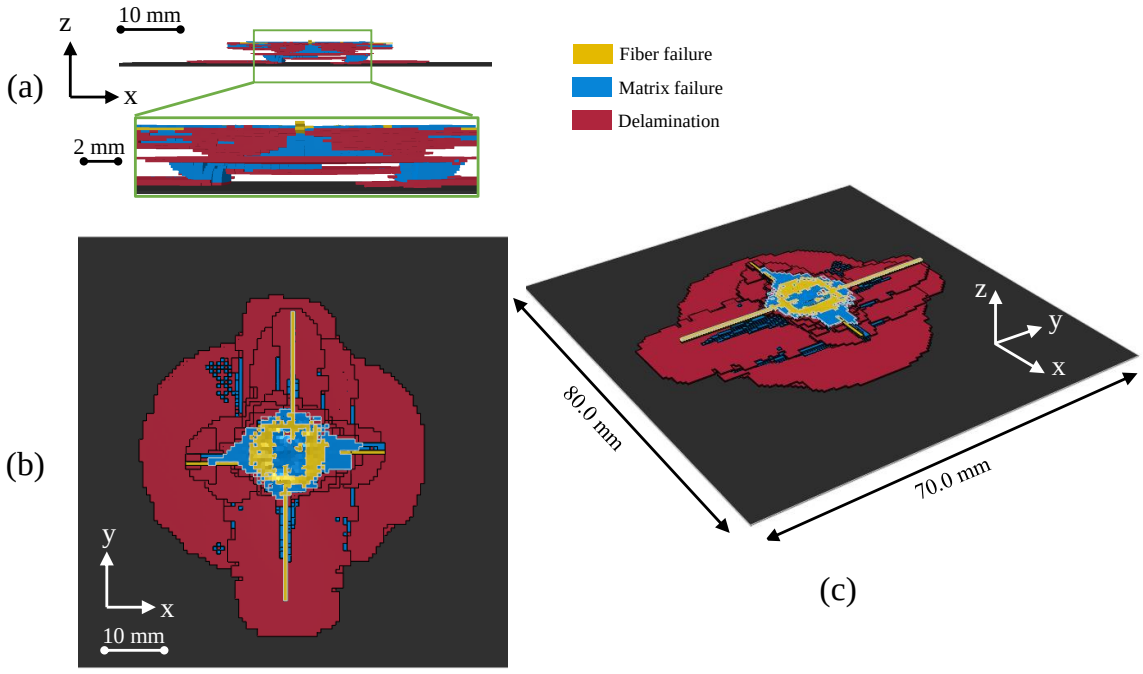

Figure 5.29: Predicted damage after segmentation observed: (a) in the x-z plane, (b) in the x-y plane, and (c) with a 3D view.

sizes are S (152.4 mm x 101.6 mm), M (177.8 mm x 177.8 mm), and L (330.2 mm x 330.2 mm). The two thicknesses correspond to 24-ply and 48-ply. Impact energy levels and other test parameters can be found in Table 2.2. 2D EST-InELA and 3D EST-InELA are applied to perform the computational analyses. The material properties used for the modeling are listed in Table 5.2. Some of the parameters in the table should be explained. Fiber compressive failure was suppressed. The reason for doing so is that no fiber compressive failure was observed on the impacted samples by naked-eye inspection, C-scanning, or μCT characterization. In addition, the transverse shear initiation strain Z_{23} is suppressed. The reason is that in preliminary predictions, when Z_{23} was set to be 0.031 (tested by AFRL), the matrix damage was found to be too large to agree with the experimental findings. After setting Z_{23} as a high value, such as 1000, the predicted damage agreed much better with the test results. It should be specifically pointed out that setting Z_{23} as a high value does not mean that

there is no damage in the 23 direction. The initiation and degradation of the matrix mixed-mode damage still follow the theoretical procedure outlined in Chapter IV. In addition, the interfacial shear strength was calibrated. In the preliminary analyses, when the interfacial shear strength $\sigma_t = 121$ MPa [119] was used, the predicted damage footprints were significantly smaller than the actual LVI-induced damage. Therefore, the interfacial shear strength was calibrated to be 79 MPa.

The primary reason for these calibrations might be due to the effects of strain rate on the material behavior. In addition, more damage initiation criteria might need to be investigated. The current initiation criteria are strain-based. Adopting stress-based damage initiation criteria may help obtain better computational results.

5.3.1 Load Responses

The predicted load responses of the 24-ply samples are presented in Figure 5.30. Results of the L1 samples are on the left of the dashed line, and the results of the L2 samples are on the right of the dashed line. The three rows correspond to in-plane sizes S, M, and L. In the subfigures, the black curves are the experimental results. The red curves are numerical results obtained by 2D EST-InELA. The green curves are obtained by 3D EST-InELA. In Figure 5.30, according to the load-displacement curves (U-F), the loading parts predicted by 2D and 3D EST-InELA agree very well with the test results. For the unloading parts, where the loads return from the maximum values to zeros, the agreement between the experimental and computational results gets worse as the in-plane size increases. In terms of the prediction of the residual displacement values, 3D EST-InELA performs better. As for the kinetic energy - time plots, the loading parts, where the kinetic energies degrade from the impact energies to zeros, are also captured well by 2D and 3D EST-InELA. Both the models underpredict the energy absorption values. 3D EST-InELA is demonstrated to be more accurate in terms of predicting the energy absorption. Again, as the in-plane

Table 5.2: Material properties of IM7/9773-3 used in numerical predictions

ρ	Density	$1.5 \times 10^{-9}\ t/mm^3$	measured
E_{11}	1-direction modulus	164,300 MPa	[120]
E_{22}	2-direction modulus	8,850 MPa	[120]
G_{12}	Shear modulus	6753 MPa	in-house tests
G_{23}	Shear modulus	3142 MPa	AFRL tests
ν_{12}	Poisson's ratio	0.32	[120]
ν_{23}	Poisson's ratio	0.46	AFRL tests
$\epsilon_{11}^{ini,T}$	1-direction initiation strain (tension)	0.0177	[120]
$\epsilon_{11}^{ini,C}$	1-direction initiation strain (compression)	suppressed	Preliminary modeling
$\epsilon_{22}^{ini,T}$	2-direction initiation strain (tension)	0.0147	[120]
$\epsilon_{22}^{ini,C}$	2-direction initiation strain (compression)	0.0279	[120]
γ_{12}^{ini}	Longitudinal shear ini. strain	0.059	in-house tests
γ_{23}^{ini}	Transverse Shear ini. strain	suppressed	Preliminary modeling
G_{IF}^{T}	Fiber mode I toughness in tension	40 N/mm	[21]
G_{IF}^{C}	Fiber mode I toughness in compression	10 N/mm	[21]
G_{IM}	Matrix mode I toughness	0.255 N/mm	Assumed identical to G_I
G_{IIM}	Matrix mode II toughness	0.896 N/mm	Assumed identical to G_{II}
σ_C	Interface normal strength	64 MPa	[119]
τ_C	Interface shear strength	79 MPa	Calibrated
G_I	Interface mode I toughness	0.255 N/mm	AFRL tests
G_{II}	Interface mode II toughness	0.896 N/mm	AFRL tests
G_{III}	Interface mode III toughness	0.896 N/mm	AFRL tests

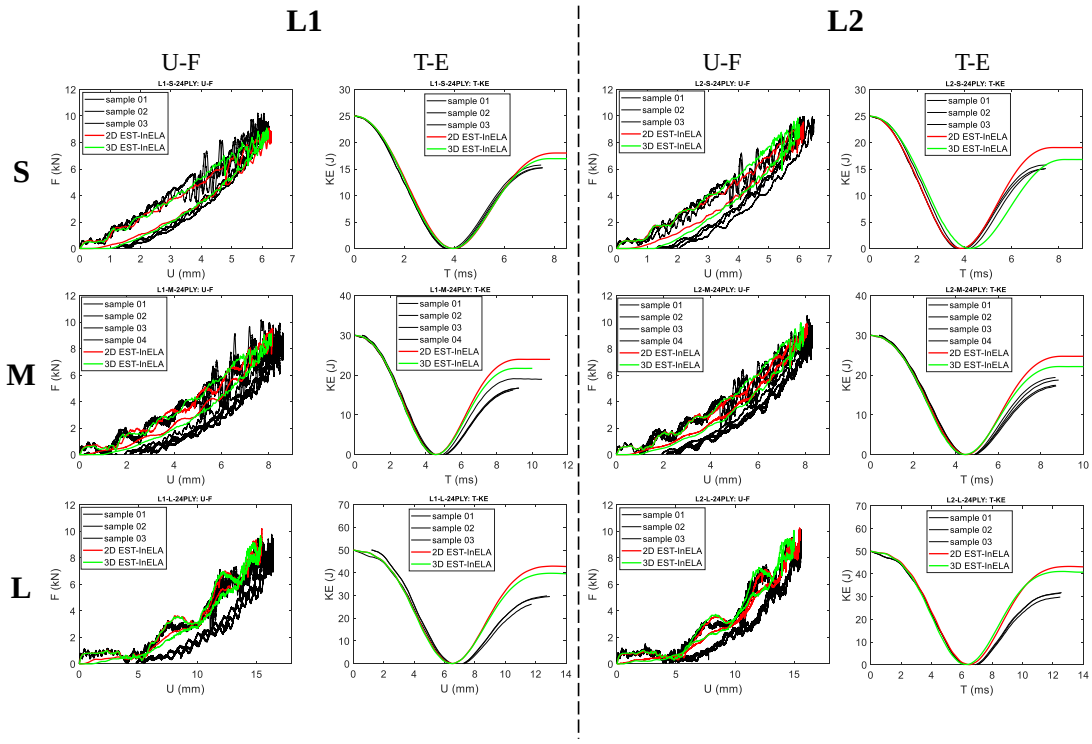

Figure 5.30: Load-displacement and kinetic-energy-time predictions by the 2D and 3D EST-InELA models for the 24-ply samples

size of the samples increases, the prediction of the energy absorption gets worse. The energy absorption of LVI is calculated by subtracting the kinetic energy of the impactor from its initial kinetic energy (impact energy).

The load response of the 48-ply samples predicted by 2D and 3D EST-InELA are displayed in Figure 5.31. In the loading parts, the computational results agree better with the experimental results for the M and L samples. For the S samples, the major difference between the predictions and tests is that the drastic bending rigidity knockdown is not captured well. To be more specific, from the first row of Figure 5.31, 2D EST-InELA is capable of predicting the knockdown of the bending rigidity. However, the loads where the knockdowns happen are underpredicted. A small extent of bending rigidity reduction is predicted by 3D EST-InELA, whereas the reduction is progressive. Aside from the bending rigidity knockdown, the peak loads and maximum displacements are captured well by both 2D EST-InELA and

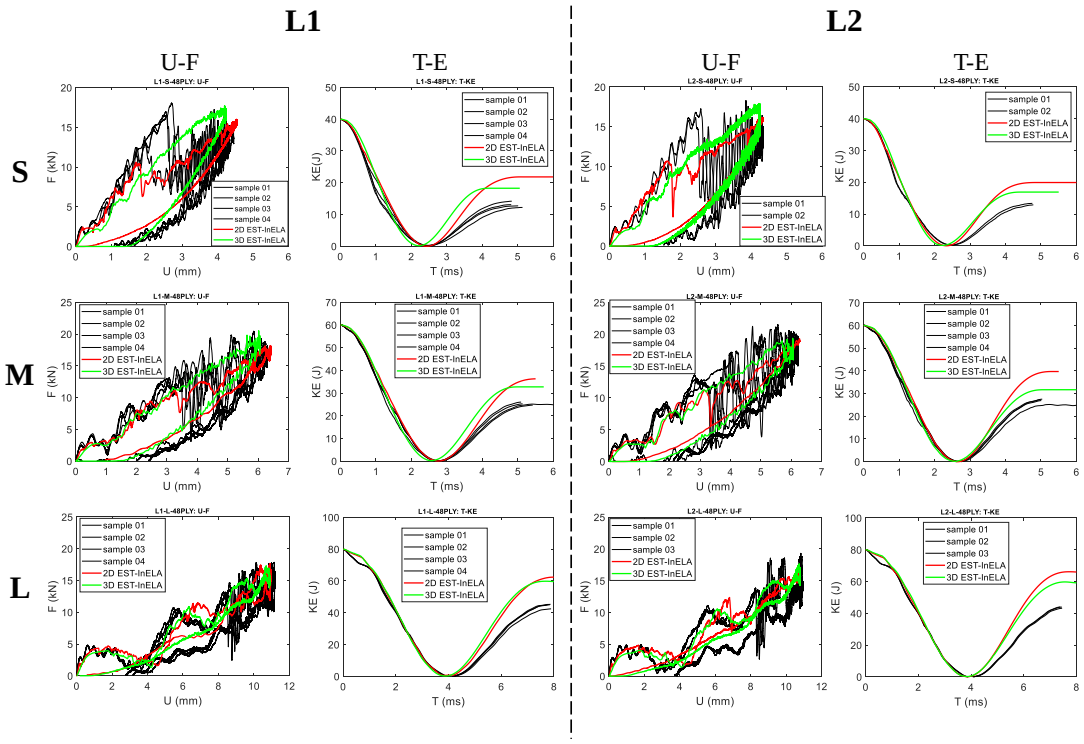

Figure 5.31: Load-displacement and kinetic-energy-time predictions by the 2D and 3D EST-InELA models for the 48-ply samples

3D EST-InELA. Similar to the results of 24-ply samples, 3D EST-InELA performs better in terms of capturing the residual displacement and energy absorption values. As the in-plane size increases, the prediction of the loading part gets better, while the prediction of the residual displacement and energy absorption gets worse.

5.3.2 LVI-induced Damage

LVI-induced damage footprints predicted by 2D and 3D EST-InELA are displayed in Figure 5.32. Figures 5.32 (a) and 5.32 (b) contain damage footprints of L1-S/M/L-24 and L2-S/M/L-24 samples. The three rows correspond to 2D EST-InELA modeling, 3D EST-InELA results, and ultrasound C-scanning. The shapes of the damage footprints are captured well by both the 2D and 3D models. The sizes of the predicted damage footprints are smaller than that of the scanned ones. In general, damage footprints predicted by 2D EST-InELA are larger than that predicted by 3D

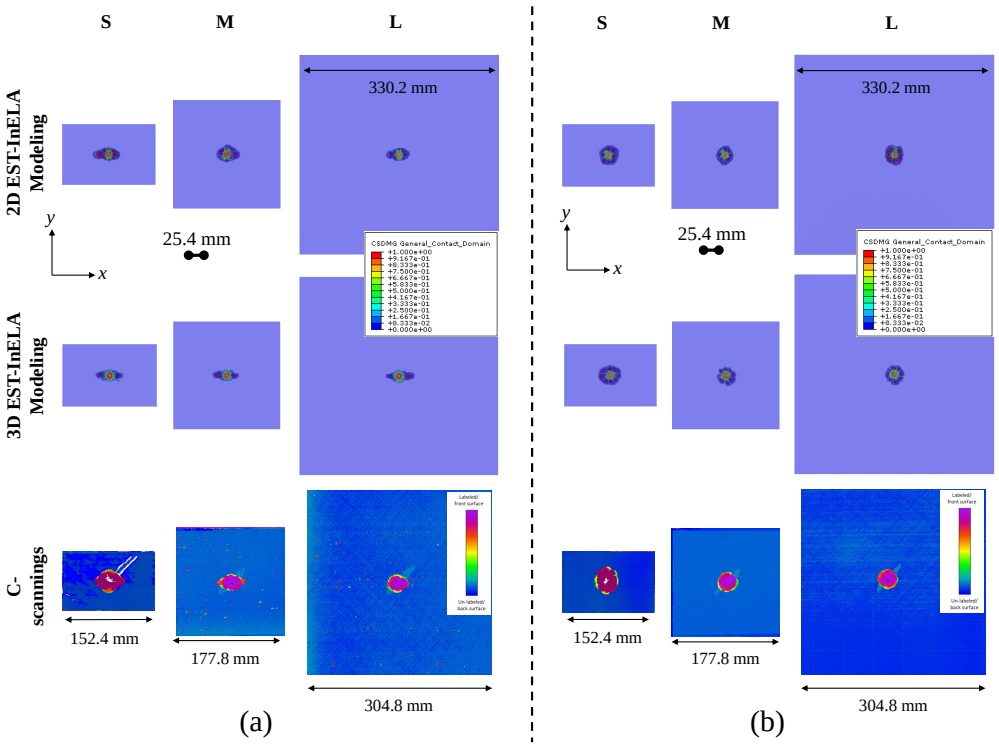

Figure 5.32: Damage footprints predicted by the 2D and 3D EST models: (a) L1-S/M/L-24 samples, and (b) L2-S/M/L-24 samples.

EST-InELA.

The predicted damage footprints of the 48-ply samples are shown in Figure 5.33. Damage morphology predicted by 2D EST-InELA is observed to be of higher quality than that obtained by 3D EST-InELA, in terms of both shape and size. The 3D EST-InELA damage predictions of the L1-S/M/L-48 cases are the poorest among all the cases, as sizes of the predicted damage footprints being significantly smaller than the C-scanning characterization. This relatively low-quality predictions might be due to the excessive prediction fiber damage of the L1-S/M/L-48 cases by 3D EST-InELA. With too much fiber damage predicted, spurious numerical oscillations are induced excessively, because of the high fracture energy released by fiber failure.

Cross sections going across the plate centers predicted by 2D and 3D EST-InELA are shown in Figures 5.34 and 5.35. The color map corresponds the out-of-plane

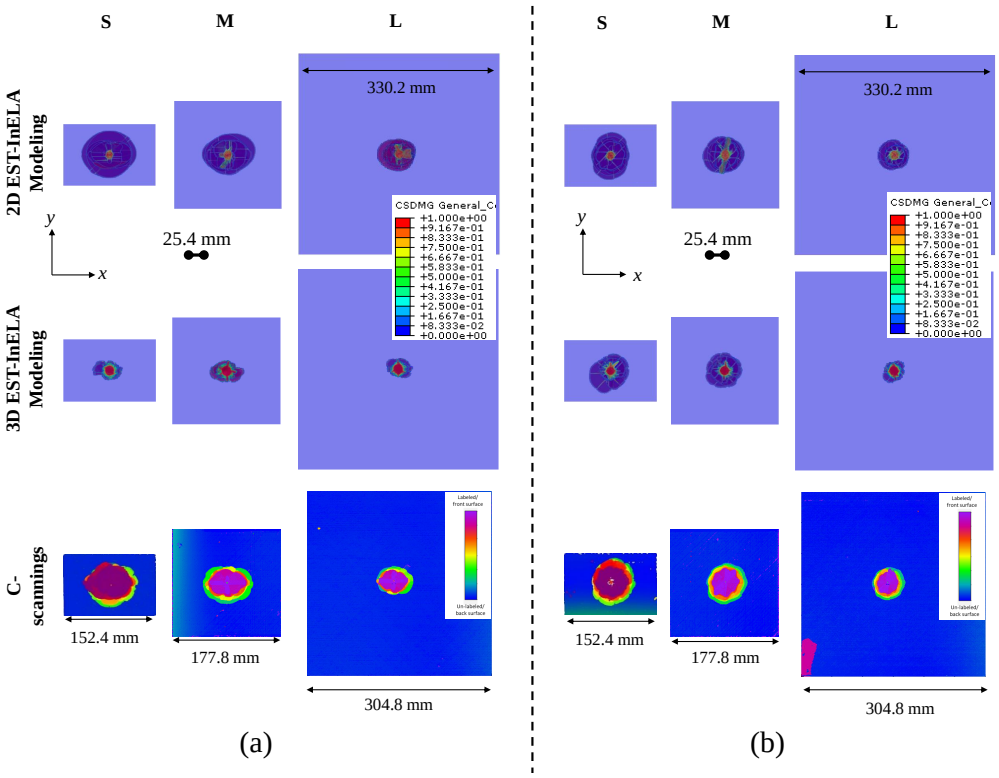

Figure 5.33: Damage footprints predicted by the 2D and 3D EST-InELA models: (a) L1-S/M/L-48 samples, and (b) L2-S/M/L-48 samples.

displacement. The images of the cross-sections are captured at the end of the LVI events, with the load being zero. As seen in Figures 5.34 and 5.35, the central dents predicted by 2D EST-InELA are much smaller than that obtained by 3D EST-InELA. The reason is believed to be that in the 2D EST-InELA model, inelasticity in the 22 and 12 directions are captured since it is based on the 2D plane stress assumption. However, in the 3D EST-InELA model, in addition to the 22 and 12 directions, inelasticity in the 13, 23, and 33 directions is also captured. The 23, 13 and 33 directions are critical for capturing dent depth.

Another important observation from Figures 5.34 and 5.35 is that the dent depths predicted by 3D EST-InELA are uniformly larger than the dent depths measured by the dial indicator shown in Tables 2.3 and 2.4. Nevertheless, from the predicted load response curves as displayed in Figures 5.30 and 5.31, the predicted residual displacement values are uniformly smaller than the test values. This implies that, during the impact event, the 3D EST-InELA model captures the material inelasticity well. However, after the event (with the load returning to zero), the predicted dent would not decrease anymore since 3D EST-InELA does not capture any time-related effect, such as viscoplasticity for composites. It is believed that in the tests, after the separation of the impactors and the panels, the dent depths would keep decreasing to the values displayed in Tables 2.3 and 2.4. To resolve this difference, a viscoplastic model might have to be implemented in the future.

The predicted delamination at all the interfaces of the L2-S-24 sample is presented in Figures 5.36 and 5.37. Comparing to the μCT slices demonstrated in Figure 2.48, the predictive quality of both 2D and 3D EST-InELA is very high. The "rotating-fan" delamination pattern has been captured by both the models.

The computation time of the modeled L2 cases using 2D and 3D EST-InELA are summarized in Table 5.3. The total CPU time of each computing job was calculated by multiplying the number of computing cores used and the CPU time used

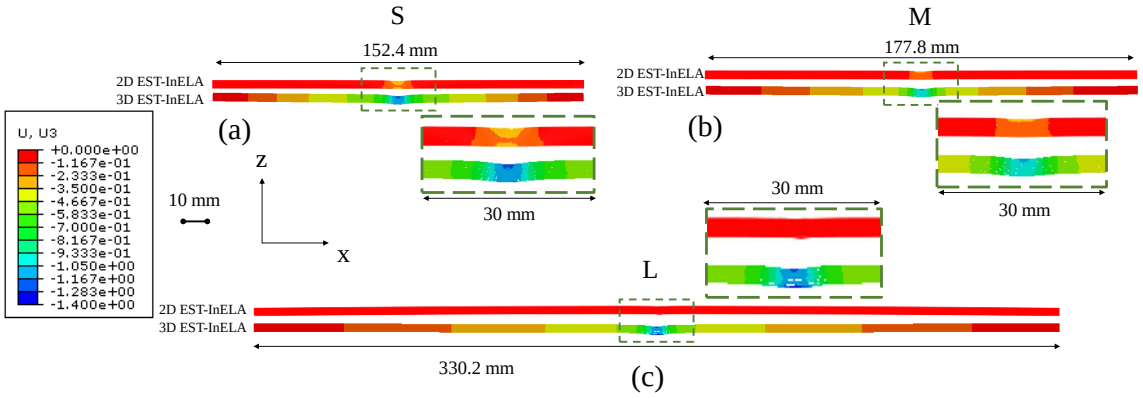

Figure 5.34: Cross sections of the predicted samples: (a) L2-S-24, (b) L2-M-24, and (c) L2-L-24.

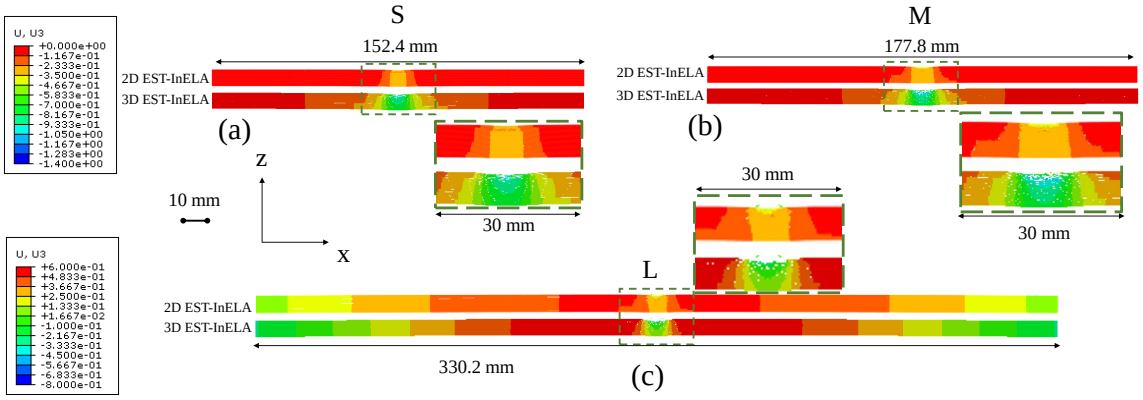

Figure 5.35: Cross sections of the predicted samples: (a) L2-S-48, and (b) L2-M-48, and (c) L2-L-48.

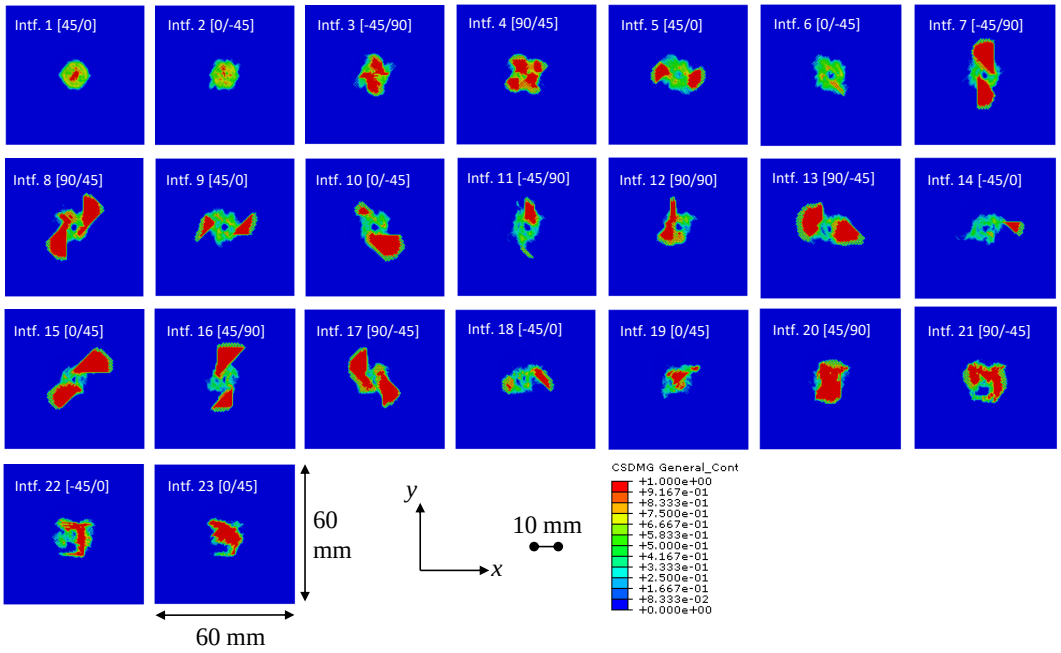

Figure 5.36: Interface-by-interface delamination predicted by 2D EST-InELA of a L2-S-24 sample.

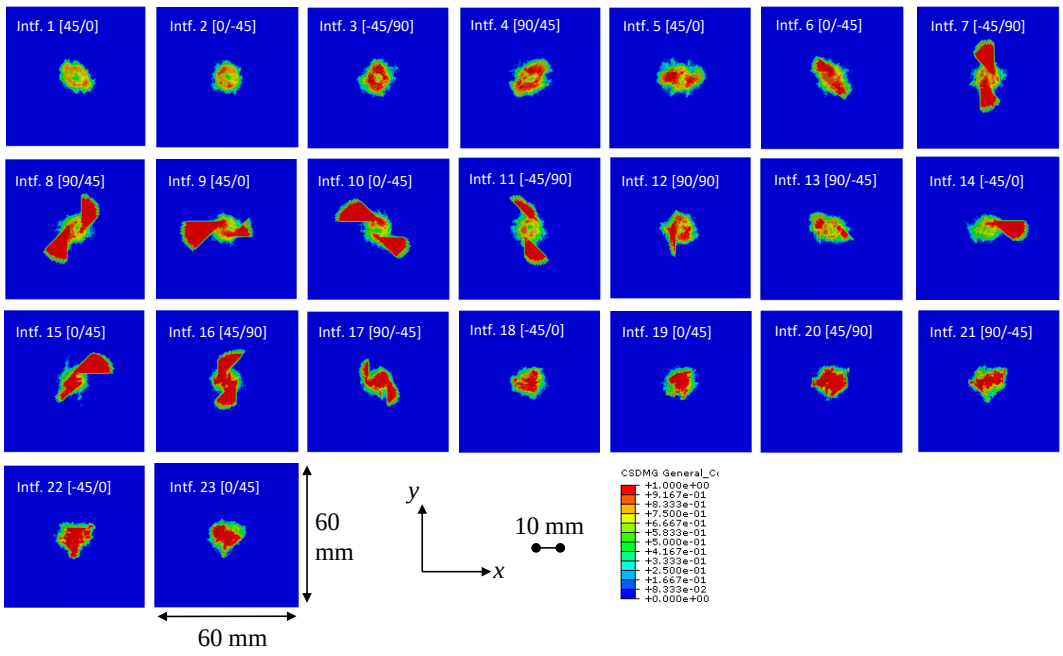

Figure 5.37: Interface-by-interface delamination predicted by 3D EST-InELA of a L2-S-24 sample.

Table 5.3: Computational time of the 2D and 3D EST-InELA models.

	2D EST-InELA (Core number x CPU time hrs)	3D EST-InELA (Core number x CPU time hrs)
L2-S-24	561	2128
L2-S-48	1267	4590
L2-M-24	648	2462
L2-M-48	2707	11970
L2-L-24	1021	3062
L2-L-48	2050	9507

to complete the job. In Table 5.3, it is seen that the computation hours of the 3D EST-InELA modeling is significantly (almost 300%) higher than that of the 2D EST-InELA modeling.

To evaluate the computational efficiency and fidelity of 2D and 3D EST-InELA, a qualitative radar plot has been generated as shown in Figure 5.38. From the figure, both the models are equivalently good at predicting the peak impact load and displacement. 2D EST-InELA performs better in terms of capturing the bending rigidity knockdown of the samples with relatively high thickness-to-length/width ratios. In addition, LVI-induced damage footprints are predicted better by 2D EST-InELA. 3D EST-InELA performs better in terms of capturing the impact energy absorption and the residual displacement values. 2D EST-InELA is significantly more efficient than 3D EST-InELA.

5.3.3 Parameter Study on the Interfacial Properties

From Figures 5.32 and 5.33, it is seen that LVI-induced damage of the 24-ply samples is under-predicted while that of the 48-ply samples is correctly predicted. Note that for all the predictions presented in this section, identical material properties from Table 5.2 are used. However, this might be inappropriate. Material properties are highly dependent on loading rate which may vary significantly for different test cases in Table 2.2 considering samples with various panel sizes impacted with different

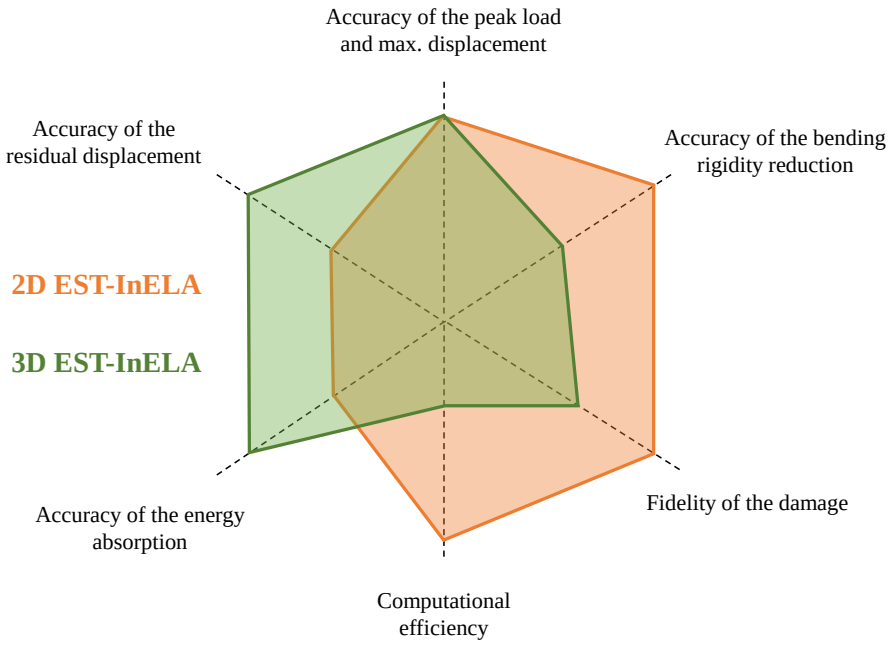

Figure 5.38: Strengths and weaknesses of the 2D and 3D EST models.

impact energies. Therefore, parameter studies for the interfacial material properties of the 24-ply samples need to be performed.

From previous analyses [22], interfacial strength τ_C and mode II/III toughness G_{II}/G_{III} affect the delamination prediction significantly. Therefore, in this section, parameter studies will be concentrated on these two parameters. Figure 5.39 shows the effects of the interfacial shear strength on the LVI responses with respect to a L1-S-24 sample. From Figure 5.39 (a), it is observed that the changing of τ_C seems to change the load response minimally. From Figure 5.39 (b), the trend of the overall area of the predicted damage footprint varying with τ_C is displayed. The trend is nonlinear. From $\tau_C = 79$ MPa to $\tau_C = 40$ MPa, the growth in the area is 57%. From From $\tau_C = 40$ MPa to $\tau_C = 20$ MPa, the growth is 112%. Predicted damage footprints are demonstrated in Figure 5.39 (c). It is seen that with τ_C being greater than 20 MPa, the predicted damage footprints resemble the ultrasound C-scanning in shape. However, for $\tau_C = 20$ MPa, A sticking-out pattern near the impacted side of the

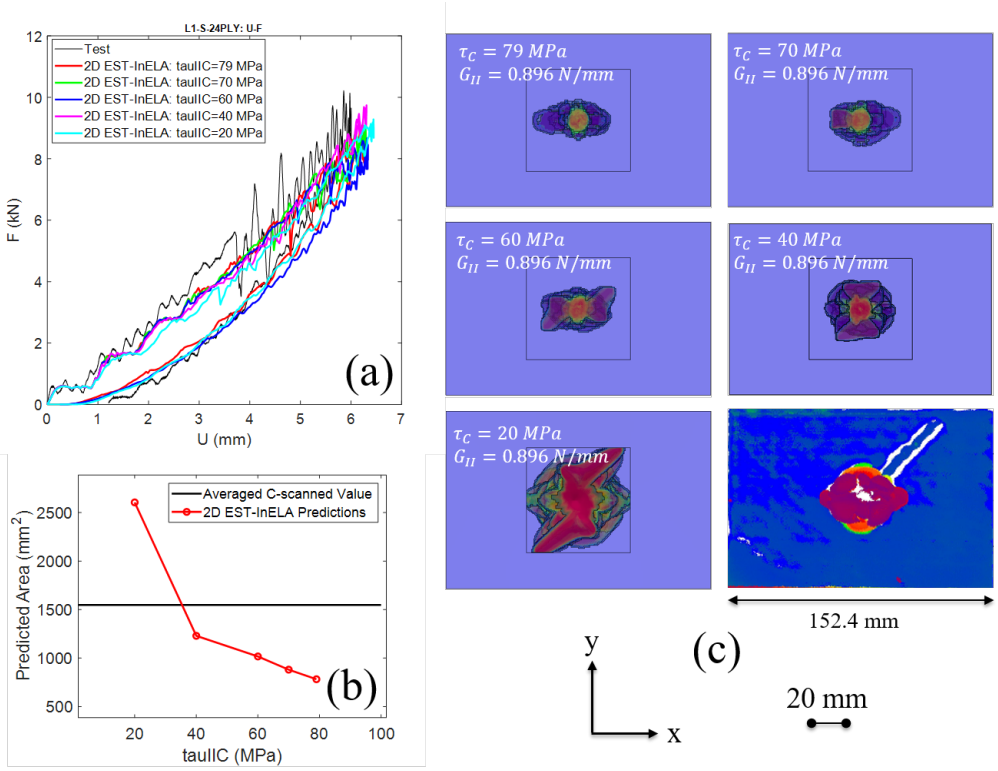

Figure 5.39: Parameter study of the effects of interfacial shear strength on the LVI responses of a L1-S-24 sample: (a) load-displacement curves, (b) predicted overall damage area as a function of the interfacial shear strength, and (c) predicted damage footprints.

sample is seen. This pattern is not observed in the scanned damage. This incorrectly predicted pattern is believed to be caused by the interfacial strength τ_C being too low. Due to the excessively low shear strength, the impact energy is mostly absorbed by delamination rather than other damage modes including matrix cracking and fiber breaking. Without sufficient matrix cracking, the shape of the predicted delamination might be erroneous since matrix cracking bounds delamination, as illustrated in Chapter II.

The effects of interfacial mode II/III toughness $G_{II/III}$ on the LVI responses are presented in Figure 5.40. From Figure 5.40 (a), similar to the effects of τ_C, it is seen that $G_{II/III}$ has no significant effect on the load responses. From Figure 5.40 (b), with the decreasing of toughness, the increase of the overall damage area is salient.

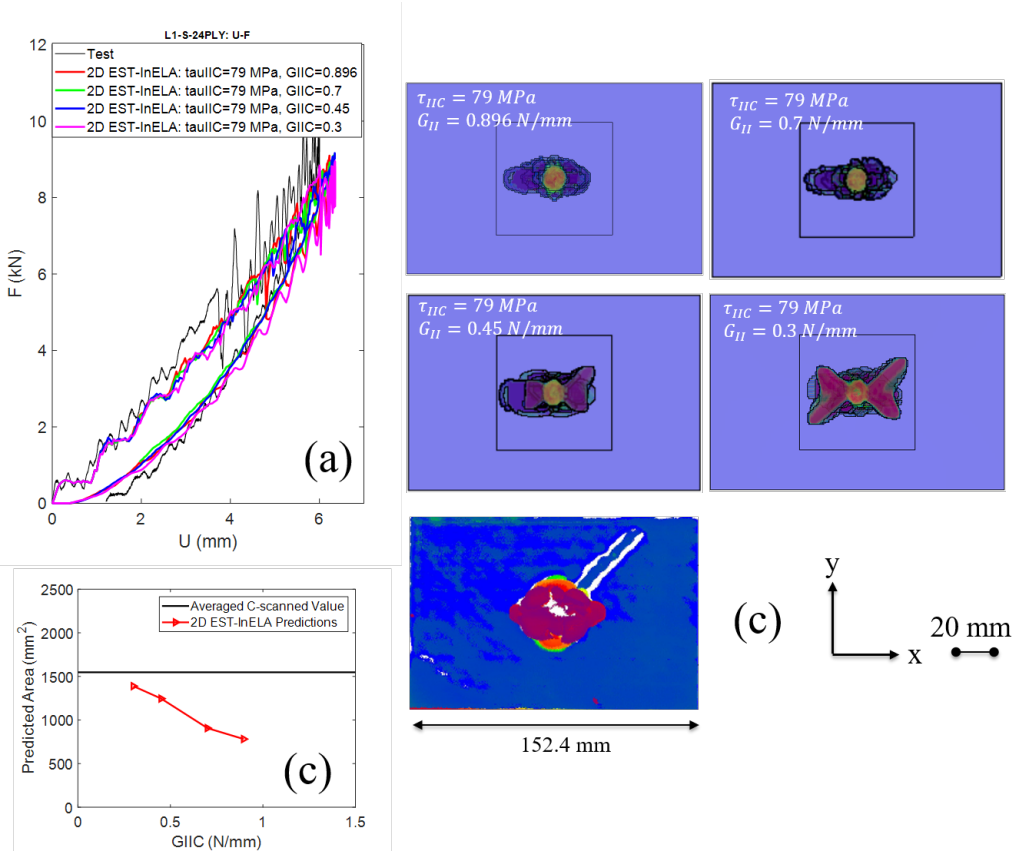

Figure 5.40: Parameter study of the effects of interfacial mode II/III fracture toughness on the LVI responses of a L1-S-24 sample: (a) load-displacement curves, (b) predicted overall damage area as a function of the fracture toughness, and (c) predicted damage footprints.

The predicted damage footprints are shown in Figure 5.40 (c). With $G_{II/III} = 0.896$ N/mm, 0.7 N/mm, and 0.45 N/mm, the predicted damage resembles the scanned damage in terms of shape. However, with $G_{II/III} = 0.3$ N/mm, the sticking-out pattern as seen in Figure 5.39 (c) is observed. This is believed to be due to the interfacial mode II/III toughness being excessively small, which may lead excessive delamination predicted and a lack of matrix damage predicted. Insufficiently predicted matrix damage may cause a poor delamination prediction.

With the strength and toughnesses of a traction-separation fixed, the shape of the traction-separation law may also affect the predicted results. Computational results presented in this chapter so far are based on triangular traction-separation laws.

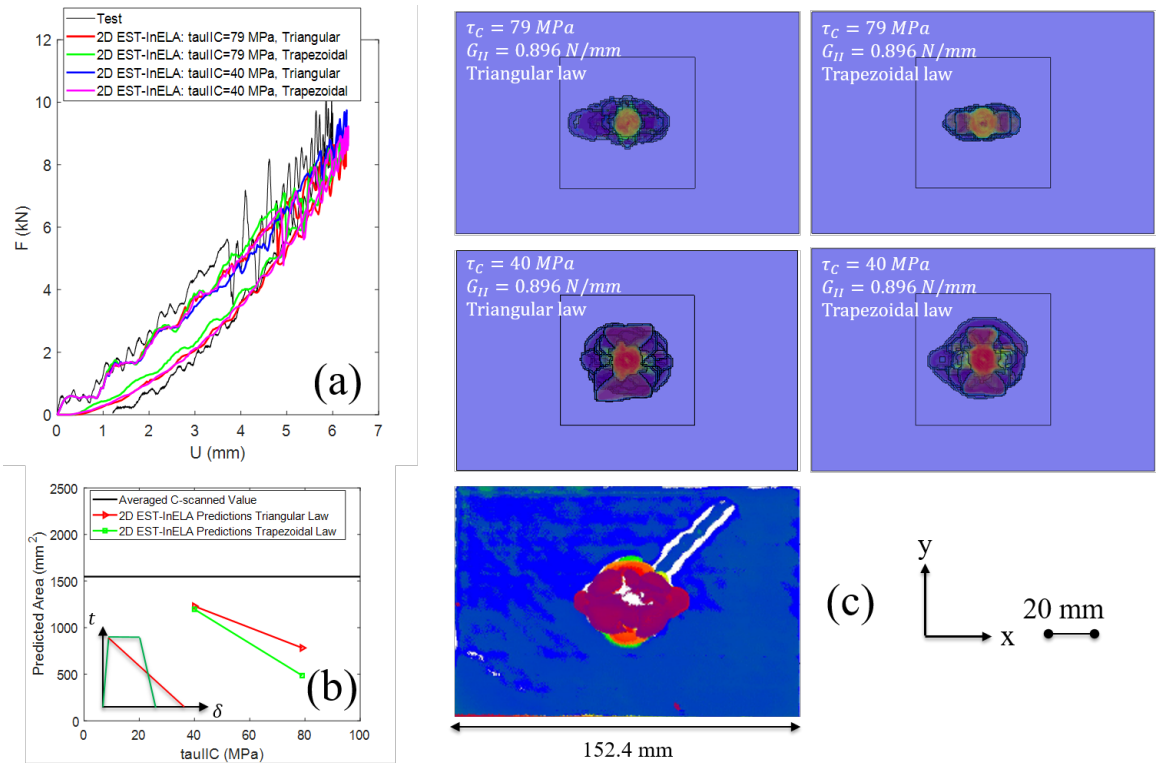

Figure 5.41: Parameter study of the effects of traction-separation law's shape on the LVI responses of a L1-S-24 sample: (a) load-displacement curves, (b) predicted overall damage area as a function of interfacial shear strength, and (c) predicted damage footprints.

Here, a trapezoidal traction-separation law is also investigated. Figure 5.41 shows LVI-induced damage footprints predicted using triangular and trapezoidal traction-separation laws. The shapes of the laws are sketched in Figure 5.41 (b). From Figure 5.41 (a), it is seen that the shape of the traction-separation affect the load responses minimally. From Figure 5.41 (b), it is seen that the predicted damage footprints using the trapezoidal laws seem slightly smaller than the that using the triangular laws. In Figure 5.41 (c), the predicted damage footprints are found correct in shape. With τ_C=40 MPa and $G_{II/III}$=0.896 N/mm, the size of the predicted damage footprints are slightly smaller than the scanned damage.

From the parameter studies, it is realized that reducing interfacial shear strength and mode II/III fracture toughness helps improving the computational accuracy in

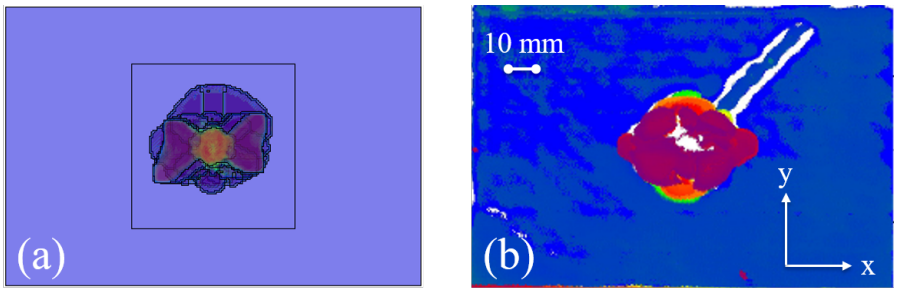

Figure 5.42: Predicted LVI-induced damage footprint with calibrated interfacial properties τ_C=60 MPa, and $G_{II/III}$=0.7 N/mm: (a) predicted damage, and (b) scanned damage.

terms of damage area. In addition, it is found that using excessively small τ_C and $G_{II/III}$ values may lead to erroneous local damage prediction near the impacted side of the sample. Therefore, both τ_C and $G_{II/III}$ should be lowered properly while a triangular shape of the traction-separation law should be maintained. After a few iterations, the calibrated interfacial properties are τ_C=60 MPa, and $G_{II/III}$=0.7 N/mm. The predicted LVI-induced damage footprint is compared with the scanned damage in Figure 5.42. As seen in Figure 5.42, the predicted damage is highly similar to the scanned damage in terms of both shape and size. It should be pointed out that for the damage prediction in Figure 5.42 (a), except for the calibrated τ_C and $G_{II/III}$ values, other used material properties are from Table 5.2. This does not mean that other material properties are insensitive to loading rates and need no calibration. Considering the scope of this dissertation, only the two most important material parameters τ_C and $G_{II/III}$ are studied. More material parameter sensitivity studies will significantly benefit the computational accuracy and is suggested as a future direction in Chapter VIII.

5.4 Summary and Conclusions

In this chapter, computational results of the LVI studies have been presented. The computational analyses of the stacking sequence effect studies were performed

by using 2D EST, while that of the panel size effect studies were conducted with 2D and 3D EST-InELA.

For the stacking sequence effect studies, in general, most of the LVI predictions are accurate in terms load responses and LVI-induced damage. However, the residual displacement and energy absorption are significantly underpredicted. Interaction between damage modes including fiber breaking, matrix cracking, and delamination has been captured computationally. As a result of the accurate predictions, the featured damage patterns such as the "rotating fan" and the "kidney" damage have been captured.

For the panel size effect studies, both 2D EST-InELA and 3D EST-InELA have been applied. The loading parts of the load-displacement responses are predicted better by 2D EST-InELA. The sharp load drops and bending rigidity reduction are captured well by 2D EST-InELA but not by 3D EST-InELA. The unloading parts regarding the residual displacement and impact energy absorption are predicted better by 3D EST-InELA. For most cases, the shapes and sizes of the damage footprints are predicted better by 2D EST-InELA than by 3D EST-InELA. The computational efficiency of 2D EST-InELA is significantly higher than that of 3D EST-InELA.

CHAPTER VI

A High-Fidelity and High-Efficiency LVI-CAI Computational Framework

6.1 Introduction

[1] CAI predictions are based on the numerical results of the LVI analyses. In this chapter, a high-fidelity and high-efficiency LVI-CAI computational framework will be introduced and implemented. The discussed framework serves the purpose of connecting the LVI analysis and the CAI analysis. Conventionally, the connection of analyses is based on the *Import and *Restart functions of Abaqus or similar functions of other commercial codes. In this chapter, first, the shortages of the *Import and *Restart functions will be provided in Section 6.2. Then, the high-fidelity and high-efficiency computational framework will be illustrated. The framework is based on three methods, including a smart mesh paradigm, a damage transferring algorithm, and an efficient modeling strategy. which will be outlined in Sections 6.3, 6.4, 6.5. LVI-CAI analyses have been performed based on the conventional method using the *Restart function and the proposed high-fidelity and high-efficiency compu-

[1] The results presented in this chapter have been published in:

- Lin, Shiyao, and Anthony M. Waas. "Accelerating computational analyses of low velocity impact and compression after impact of laminated composite materials." *Composite Structures* 260 (2021): 113456.

tational framework. The results will be reported in Section 6.6. The computational accuracy and the efficiency improvement of of the computational framework will also be evaluated in Section 6.6. Discussions and conclusions will be provided in Section 6.7.

6.2 LVI-CAI Analyses

LVI analyses with EST and cohesive contact have been introduced in Chapter V. CAI analysis is usually based on computationally predicted LVI damage. There are two major approaches of utilizing the LVI results, enumerated as follows.

1. Approach 1: Step 01: LVI modeling → *import → Step 02: CAI modeling (2-step modeling in two consecutive jobs)

2. Approach 2: Step 01: LVI modeling → *restart → Step 02: stabilization modeling → Step 03: CAI modeling (3-step modeling in two consecutive jobs)

Approach 1 is to finish the LVI modeling first and then import the numerical data into the CAI model based on the *import function of Abaqus. This approach was used by [5, 80, 60]. However, a large-memory node is required to perform the *import function. After trials, it was suggested that 8 computing cores should be used with 64 GB random accessory memory (RAM). In this case, the computational time of the CAI analysis was more than three times of that of the LVI analysis using 48 computing cores [2]. Another shortcoming of approach 1 is that the LVI-induced damage (delamination) obtained by the cohesive contact model or user-defined cohesive elements such as the discrete cohesive zone model (DCZM) elements [21, 64] can not be directly imported into the CAI model. Element filtering had to be performed for the DCZM elements in [2].

Approach 2 is to restart the CAI analysis from the end of the LVI analysis using the *restart function of Abaqus. With this approach, the initial state of the CAI analysis

is identical to the end of the LVI analysis. Therefore, the kinetic energy at the end of LVI is inherited by the CAI analysis. The kinetic energy, though small, needs to be damped out with a stabilizing step to prevent the dynamic effect in the quasi-static CAI loading. After the damping step, the panel with LVI-induced damage is loaded with controlled displacement. Approach 2 was adopted by [83, 79]. The greatest advantage of approach 2 over approach 1 is that the delamination predicted by the cohesive contact model or the user-defined cohesive elements can be transferred from the LVI analysis to the CAI analysis smoothly. In addition, the *restart function does not demand a high-memory node, but requires that the configuration of the computing resources of the CAI analysis be identical to that of the LVI analysis. Therefore, CAI analyses with approach 2 are much faster than that using approach 1, even after considering the initial damping step.

The two approaches are illustrated and compared in Figure 6.1. In the figure, the dark green part in the middle of the plate is with a fine mesh and the shallow green part is with a coarse mesh. It should be mentioned that the these two approaches are purely numerical considerations. The CAI analysis performed either way is physically equivalent. However, it is still important to have a through evaluation of the two approaches since computational efficiency is of vital importance for a computational model. In this thesis, benchmark analyses are performed using approach 2 based on *restart.

Computational LVI-CAI analyses of a 24-ply, 150 mm $\times$ 100 mm composite laminate based on approach 2 usually take about 20 hours to run even with 72 computing cores. The scope of this thesis also contains the analyses for significantly larger and thicker samples (330.2 mm $\times$ 330.2 mm, 48-ply). Therefore, the computational burden would be formidable. In this chapter, a high-fidelity and high-efficiency LVI-CAI computational framework is proposed to carry out the analyses to save the computational time while preserve the accuracy. Three methods for accelerating the LVI-CAI

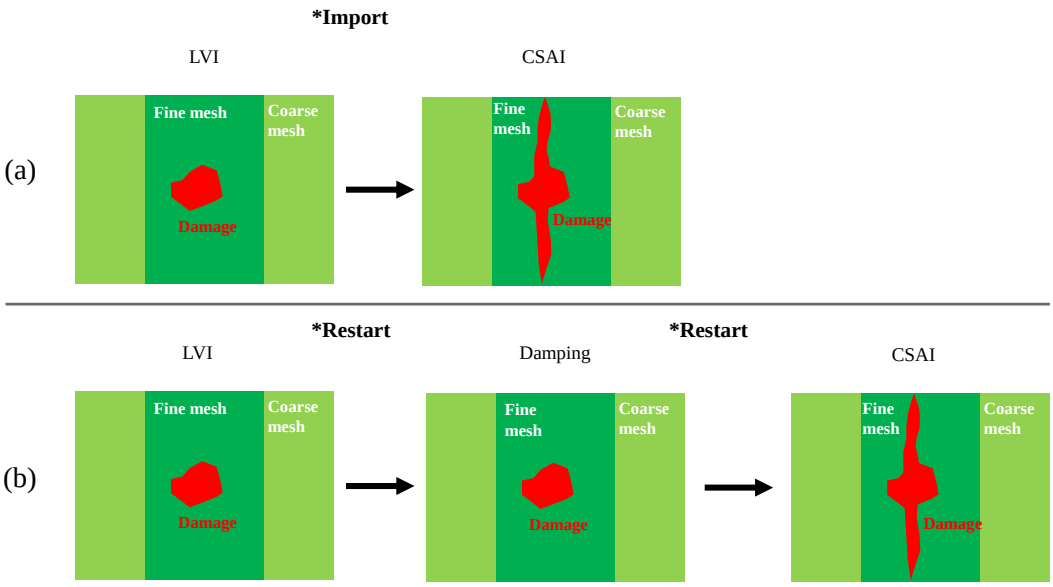

Figure 6.1: Illustration of the transition between LVI and CAI analyses: (a) approach 1 based on *import, and (b) approach 2 based on *restart.

analyses without any loss of the fidelity have been implemented to establish this high-fidelity and high-efficiency framework. The three methods include a smart mesh paradigm, an efficient modeling strategy, and a damage state transferring algorithm.

6.3 The Smart Mesh Paradigm

For LVI analyses according to the industrial standard [19], impact-induced damage is most likely to be concentrated near the center of the sample, as shown in Figure 6.2 (a). The CAI-induced, which is usually drastic and extensive, is most likely to span through the width direction (along the y axis in Figure 6.2) of the sample, as shown in Figure 6.2 (b). For the LVI analyses in Figure 6.2 (a), a fine mesh is only needed around the impacted area, while for the CAI analyses, a fine mesh is needed for the area spanning through the whole width of the sample. With the conventional approach 1 and 2 as described in Section 6.2, the meshes of that in Figure 6.2 (a)

and (b) should be identical. Therefore, for the LVI analysis, the yellow region as shown in Figure 6.2 (c) is unnecessarily fine. This is considered wasteful in terms of computational resources.

A smart mesh paradigm is proposed as shown in Figure 6.2 (d), where the fine-mesh region shrinks from 75 mm × 100 mm as shown in Figure 6.2 (a-c) to 60 mm × 50 mm. With keeping the elemental sizes of the fine (0.6 mm × 0.6 mm) and coarse (2.0 mm × 2.0 mm) mesh the same, the size shrinkage of the fine-mesh region leads to a reduction of the total degrees of freedom (DOFs) from 2,982,726 to 1,431,852, by 52%, which would significantly reduce the computing time of the LVI analysis. It should be noted that the fine-mesh region should be sufficiently larger than the impact damage footprint. The size of the region can be determined from NDI characterization or preliminary LVI numerical predictions with a coarser mesh.

With the LVI mesh being different from the CAI mesh, the transition from LVI to CAI analyses can no longer be based on the Abaqus built-in *import or *restart function. An algorithm transferring the impact-induced damage between various meshes needs to be adopted.

6.4 The Damage Transferring Algorithm

The proposed damage transferring algorithm is the gist of the high-fidelity and high-efficiency LVI-CAI framework. The other two accelerating methods, including the smart mesh paradigm and the efficient modeling strategy are established upon the damage transferring algorithm. The states of fiber damage, matrix micro-cracking and macro-cracking , and delamination are transferred between different LVI meshes and CAI meshes. The LVI meshes follow the smart mesh paradigm as shown in Figure 6.2 (d), while the CAI meshes follow the pattern as shown in Figure 6.2 (b). The versatility brought by the damage transferring algorithm to connect the LVI and CAI analyses enables the efficiency improvement induced by the smart mesh paradigm

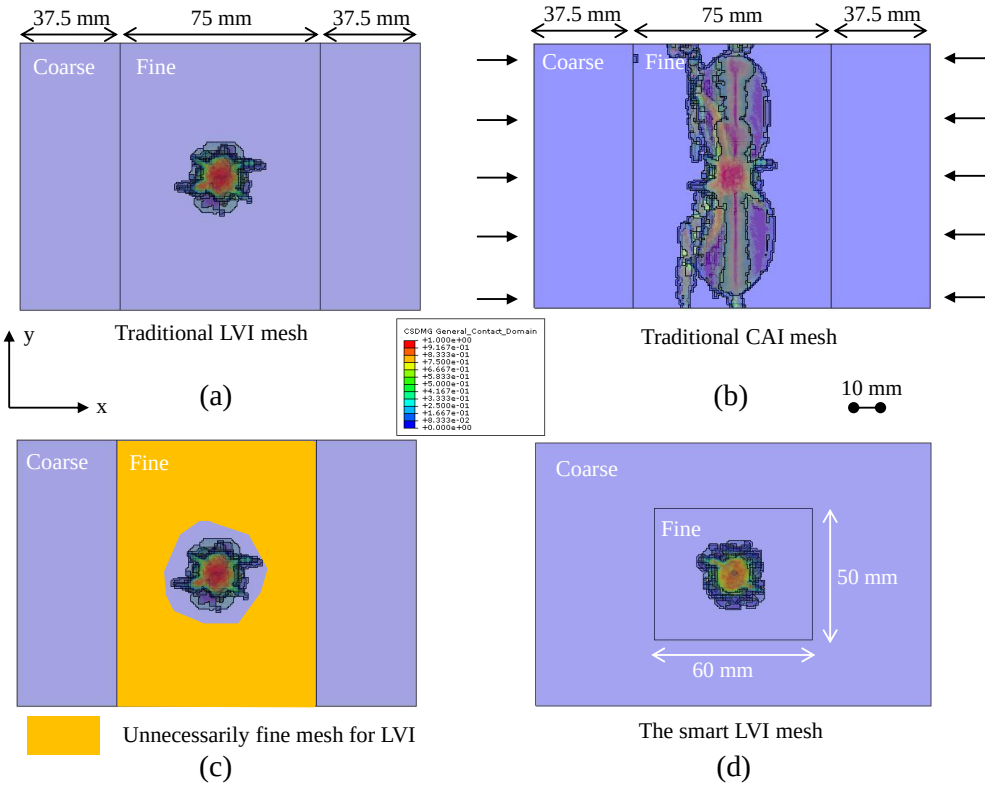

Figure 6.2: LVI and CAI meshing strategies: (a) traditional LVI mesh, (b) traditional CAI mesh, (c) traditional LVI mesh with unnecessarily fine mesh part marked as yellow, and (d) the smart mesh paradigm.

and the efficient modeling strategy, which could not be achieved by the *import or *restart function of Abaqus.

6.4.1 The Framework of the Damage Transferring Algorithm

There are in total four major steps to perform damage between an LVI mesh and a CAI mesh. The four steps are as follows.

1. Step 01: Automated extraction of damage state variables from the LVI results.
2. Step 02: Calculating elemental averaged damage state variables for the CAI mesh.
3. Step 03: CAI elements grouping based on averaged damage state variables.
4. Step 04: Assigning degraded material properties to CAI elements.

Step 01

The damage transferring of the LVI-induced delamination at a [-45/90] interface is taken for an illustrative example. The delamination is as shown in Figure 6.3. In Figure 6.3, the Abaqus built-in delamination indicator $CSDMG$ is used for plotting. The calculation of $CSDMG$ has been illustrated in Chapter IV. $CSDMG = 0$ implies there is no delamination initiated while $CSDMG = 1$ means the interface is completely delaminated such that there is no traction between interfaces. In step 01, the nodal $CSDMG$ values at the interface are extracted at a certain user-specified time point of the LVI results. The automated extraction process is implemented with a Python-based script. The automated extraction is also performed for the intra-ply damage variables including the reduced microscale damage dissipation S_r, damage indicators for fiber macroscale damage and matrix macroscale damage.

Step 02

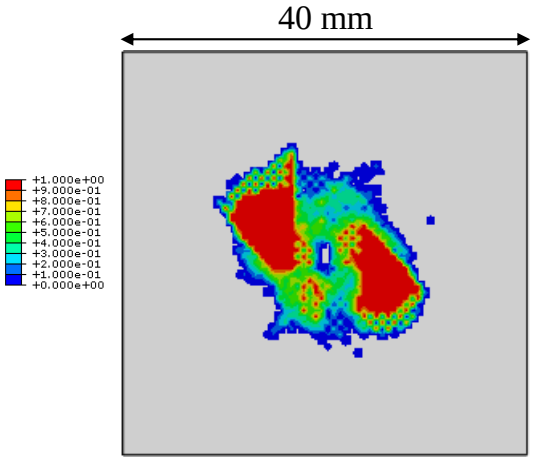

Figure 6.3: Step 01 of the damage transferring algorithm: automated extraction of the damage state variables.

Step 02 is to calculate elemental averaged CSDMG values of the CAI mesh. The calculation is performed in a loop going over all the CAI elements. The looping process is illustrated in Figure 6.4. In the figure, the solid dots represent nodes of the LVI mesh. The rainbow color code indicates the LVI CSDMG nodal value varying from 0 to 1. The blue grid represents the CAI mesh. N is the total number of elements of the CAI mesh at the [-45/90] interface. As shown in Figure 6.4 (a), for the shadowed element that is being looped, a circle with the diameter of elemental characteristic length is drawn with the center being at the centroid of the element. The CSDMG values of the LVI nodes inside the circle are averaged and assigned to the CAI element being looped. The same process continues element by element for the whole CAI mesh, as shown in Figure 6.4 (b) to (c). The damage state assignment is also conducted for the intra-ply damage variables indicating the fiber macroscale damage, matrix microscale, and macroscale damage.

Step 03

Step 03 is to group the elements of the CAI mesh according to the averaged damage state variable assigned to them in Step 02. For the transferred delamination, ten fractions are used for the CSDMG values varying from 0 to 1. Therefore, for a

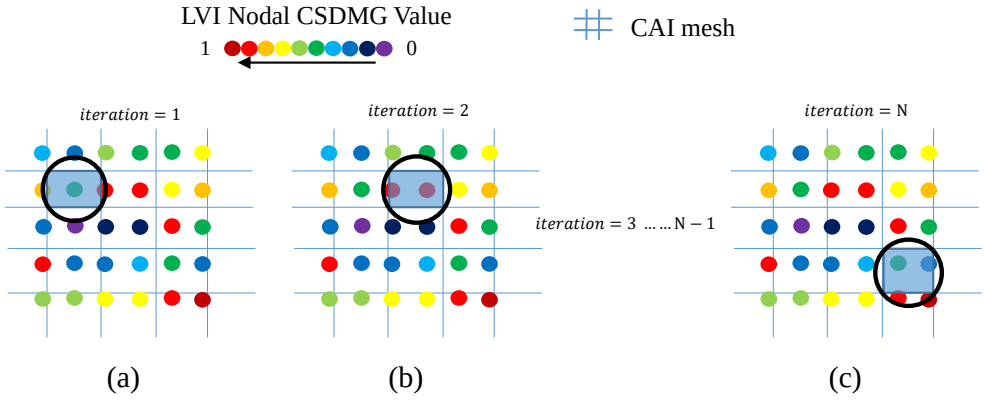

Figure 6.4: Step 02 of the damage transferring algorithm: calculating CAI elemental averaged values: (a) $iteration = 1$, (b) $iteration = 2$, and (c) $iteration = N$.

certain interface, there are in total of 10 groups of the CAI elements. The grouped elements are shown in Figure 6.5. It is obvious that the transferred and grouped damage replicates the delamination pattern in the LVI modeling as shown in Figure 6.3. It should be pointed out that in Figure 6.3, the LVI nodal CSDMG values vary smoothly from 0 to 1, while in Figure 6.5, the CAI elemental CSDMG values only vary among the grouped values. The grouped values are taken as the medians of the groups. For example, for a group of CAI elements with $0.1 < CSDMG < 0.2$, the $CSDMG$ value assigned to the group is 0.15. The element grouping process is also performed for the intra-ply damage variables indicating the fiber macroscale damage, matrix microscale damage, and matrix macroscale damage.

Step 04

Step 04 is to calculate and assign degraded material properties to the CAI elements. The degraded material properties are determined according to the transferred damage state variables including D_{IF} indicating fiber damage, S_r indicating matrix microscale damage, D_{IM} indicating matrix macroscale mode I damage, D_{IIM} indicating matrix macroscale mode II damage. In Chapter IV, it was illustrated that the mode I macroscale damage of matrix and fiber can be either tensile or compressive.

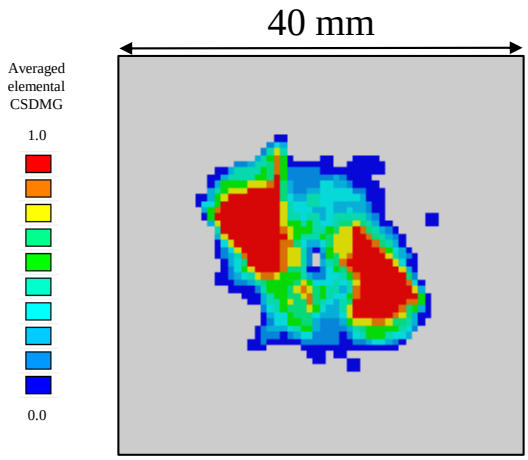

Figure 6.5: Step 03 of the damage transferring algorithm: CAI elements grouping based on averaged damage state variables.

However, in the damage transferring algorithm, for the mode I macroscale fiber and matrix damage, only two damage indicators D_{IF} and D_{IM} are transferred, calculated as in Equations 6.1 and 6.2.

$$D_{IF} = max\{D_{IF}^{T}, D_{IF}^{C}\} \tag{6.1}$$

$$D_{IM} = max\{D_{IM}^{T}, D_{IM}^{C}\} \tag{6.2}$$

Determination of the degraded fiber properties is the simplest case since there is no mode mixity. With transferred D_{IF}, the degraded properties defining the updated modulus and traction-separation law are calculated according to Equations 6.3 to 6.7.

$$\epsilon_{11}^{fail,T/C,d} = \epsilon_{11}^{fail,T/C} = \frac{2G_{IF}^{T/C}}{\sigma_{11}^{ini,T/C} L_{el}} \tag{6.3}$$

$$\epsilon_{11}^{ini,T/C,d} = \frac{\epsilon_{11}^{ini,T/C}\epsilon_{11}^{fail,T/C}}{(\epsilon_{11}^{fail,T/C} - \epsilon_{11}^{ini,T/C})(1 - D_{IF}) + \epsilon_{11}^{ini,T/C}} \tag{6.4}$$

$$E_{11}^{d} = E_{110}(1 - D_{IF}) \tag{6.5}$$

$$\sigma_{11}^{ini,T/C,d} = E_{11}^{d}\epsilon_{11}^{ini,T/C,d} \tag{6.6}$$

$$G_{IF}^{T/C,d} = \frac{\epsilon_{11}^{ini,T/C,d}(1-D_{IF})}{\epsilon_{11}^{ini,T/C}} G_{IF}^{T/C} \tag{6.7}$$

$\epsilon_{11}^{ini,T/C,d}$ and $\sigma_{11}^{ini,T/C,d}$ are the strain and stress corresponding to fiber tensile or compressive damage initiation while $\epsilon_{11}^{fail,T/C,d}$ is the strain at fiber tensile/compressive failure. E_{11}^{d} is the degraded fiber modulus. $G_{IF}^{T/C,d}$ is the degraded fiber mode I toughness with tensile/compressive loading. In the superscripts, "ini" represents damage initiation, "T/C" represents tensile/compressive, and "d" represents degraded material properties. All these parameters are attached with the degraded traction-separation law of the fiber damage mode to be assigned to CAI elements. The pristine traction-separation law used in the LVI analysis and the degraded traction-separation law to be used in the CAI analysis are as illustrated in figure 6.6. The calculation and determination of the pristine traction-separation law can be found in Chapter IV.

The determination of the degraded matrix properties is more complicated due to mode mixity in both microscale and macroscale damage. For an element without macroscale matrix damage initiation, only the effects of matrix microscale damage need to be considered. Assume a CAI element has been assigned with the reduced microscale damage dissipation S_r, indicated by point 2 in Figure 6.7 (a). The pre-peak nonlinear response transferred to the CAI element is as shown in Figure 6.7 (b), following the loading-unloading line 1-2 and nonlinear curve 2-3. The determination of the degraded Schapery function $g_S^d(S_r)$ still follows the procedure outlined in Figure 4.3 and described in Chapter IV.

For the matrix macroscale damage transferring, with damage state variables D_{IM} and D_{IIM} obtained from step 03, the degraded parameters defining the updated

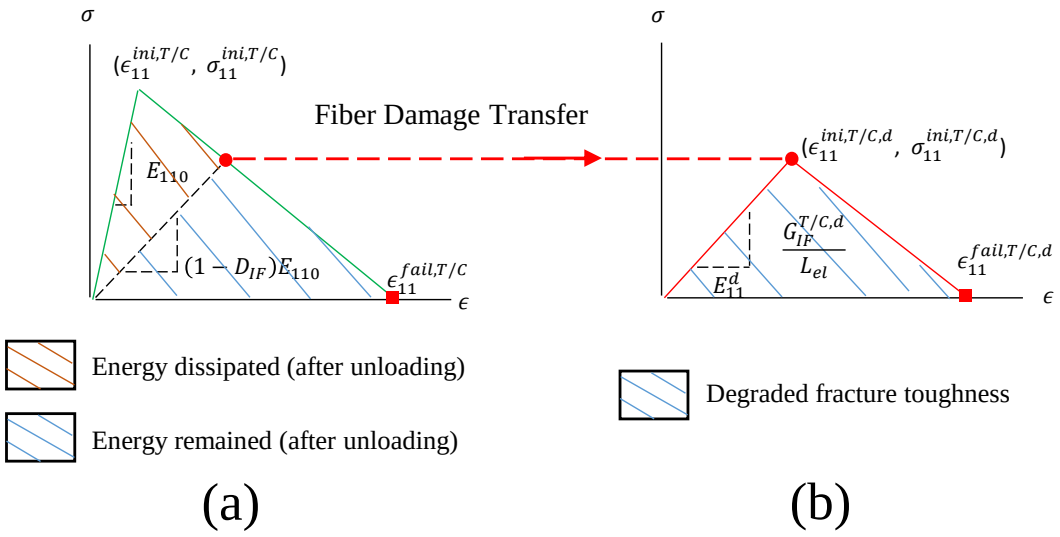

Figure 6.6: Traction-separation laws of the fiber damage mode: (a) pristine law assigned to LVI, and (b) degraded law assigned to CAI.

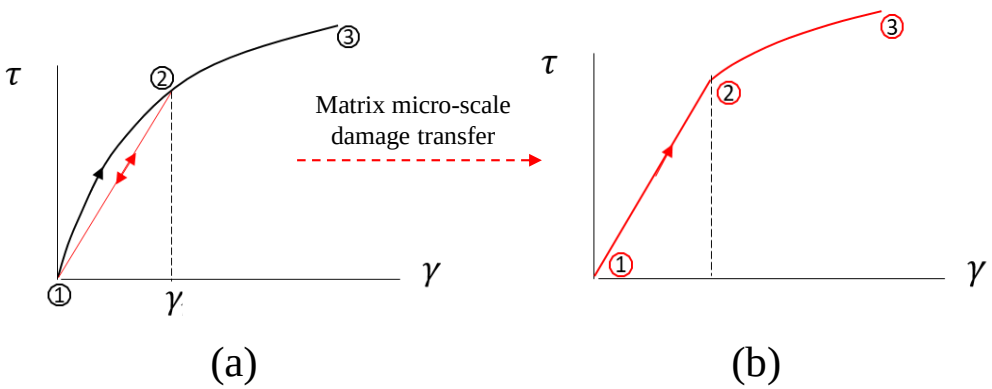

Figure 6.7: Matrix pre-peak nonlinear responses: (a) pristine response assigned to LVI, and (b) degraded response assigned to CAI.

traction-separation laws are calculated by Equations 6.8 to 6.17.

$$\epsilon_{22}^{fail,T/C,d} = \epsilon_{22}^{fail,T/C} = \frac{2G_{IM}^{T/C}}{L_{el}^{90}\sigma_{22}^{ini,*,T/C}} \tag{6.8}$$

$$\epsilon_{22}^{ini,T/C,d} = \frac{\epsilon_{22}^{ini,*,T/C}\epsilon_{22}^{fail,T/C}}{(\epsilon_{22}^{fail,T/C} - \epsilon_{22}^{ini,*,T/C})(1 - D_{IM}) + \epsilon_{22}^{ini,*,T/C}} \tag{6.9}$$

$$E_{22}^{d} = E_{220}(1 - D_{IM}) \tag{6.10}$$

$$\sigma_{22}^{ini,T/C,d} = E_{22}^{d}\epsilon_{22}^{ini,T/C,d} \tag{6.11}$$

$$G_{IM}^{T/C,d} = \frac{\epsilon_{22}^{ini,T/C,d}(1 - D_{IM})}{\epsilon_{22}^{ini,*,T/C}}G_{IM} \tag{6.12}$$

$$\gamma_{12}^{fail,d} = \gamma_{12}^{fail} = \frac{2G_{IIM}}{L_{el}^{90}\tau_{12}^{ini,*}} \tag{6.13}$$

$$\gamma_{12}^{ini,d} = \frac{\gamma_{12}^{ini,*}\gamma_{12}^{fail}}{(\gamma_{12}^{fail} - \gamma_{12}^{ini,*})(1 - D_{IIM}) + \gamma_{12}^{ini,*}} \tag{6.14}$$

$$G_{12}^{d} = G_{120}(1 - D_{IIM}) \tag{6.15}$$

$$\tau_{12}^{ini,d} = G_{12}^{d}\gamma_{12}^{ini,d} \tag{6.16}$$

$$G_{IIM}^{d} = \frac{\gamma_{12}^{ini,d}(1 - D_{IIM})}{\gamma_{12}^{ini,*}}G_{IIM} \tag{6.17}$$

$\epsilon_{22}^{ini,T/C,d}$, $\sigma_{22}^{ini,T/C,d}$, $\gamma_{12}^{ini,d}$ and $\tau_{12}^{ini,d}$ are the strains and stresses corresponding to matrix mode I and II damage initiation of the degraded traction-separation laws.

$\epsilon_{22}^{fail,T/C,d}$ and $\gamma_{12}^{fail,d}$ are the strains at matrix mode I and II failure of the degraded traction -separation laws. E_{22}^{d} and G_{12}^{d} are the degraded matrix moduli. $G_{IM}^{T/C,d}$ and G_{IIM}^{d} are the degraded matrix mode I and II toughnesses. All these parameters are attached to the degraded traction-separation laws to be assigned to the CAI elements. The rescaled traction-separation laws used in the LVI analysis and the degraded traction-separation laws used in the CAI analysis are illustrated in Figure 6.8. The calculation and determination of the rescaled traction-separation laws can be found in Chapter IV.

The degradation of the delamination properties using the $CSDMG$ value is highly similar to the degradation processes of fiber and matrix macroscale damage as in Equations 6.8 to 6.17. Therefore, for the conciseness of this thesis, the equations of the delamination degradation are not explicitly written out. The degradation is illustrated in Figure 6.9. In the figure, $\delta_{nn}^{ini,d}$, $\delta_{nt}^{ini,d}$, $\delta_{ns}^{ini,d}$, $t_{nn}^{ini,d}$, $t_{ns}^{ini,d}$ and $t_{nt}^{ini,d}$ are the separations and tractions corresponding to mode I, II and III delamination initiation of the degraded traction-separation laws. $\delta_{nn}^{fail,d}$, $\delta_{nt}^{fail,d}$ and $\delta_{ns}^{fail,d}$ are the separations at complete delamination of the degraded traction-separation laws. K_{nn}^{d}, K_{ns}^{d} and K_{nt}^{d} are the degraded penalty stiffness values. G_{I}^{d}, G_{II}^{d} and G_{III}^{d} are the degraded matrix mode I, II and III toughnesses.

6.5 The Efficient Modeling Strategy

When using the conventional way to perform LVI-CAI analyses with the *restart function of Abaqus, the CAI analysis is based on the LVI results at the end of the LVI event, where the impacted sample is detached from the impactor. According to [11, 121], the overall damage footprint stops growing once the impact load reaches its maximum point. The impact force history and the overall damage area history are displayed in Figure 6.10. According to Figure 6.10, in the sense of LVI-induced damage prediction and transferring, the LVI prediction for the second half of the

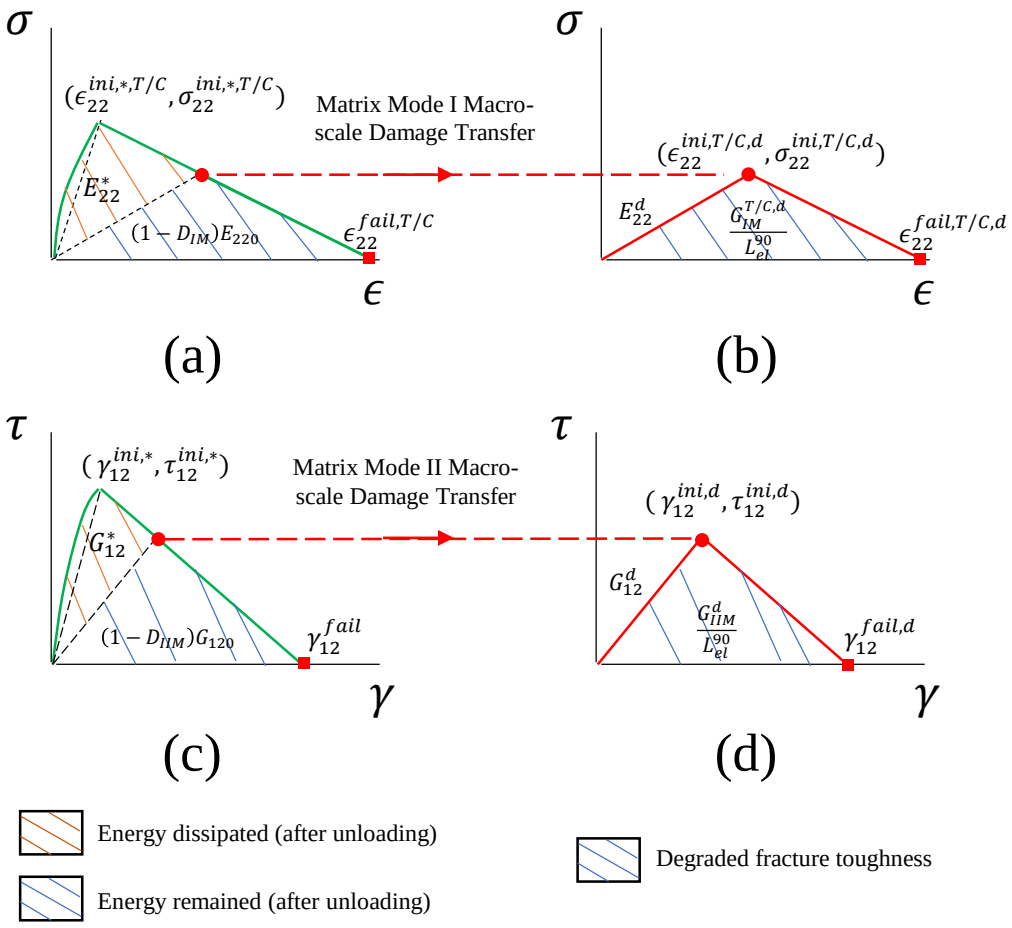

Figure 6.8: Traction-separation laws of the matrix damage modes: (a) pristine mode I law assigned to LVI, (b) degraded mode I law assigned to CAI, (c) pristine mode II law assigned to LVI, and (d) degraded mode II law assigned to CAI.

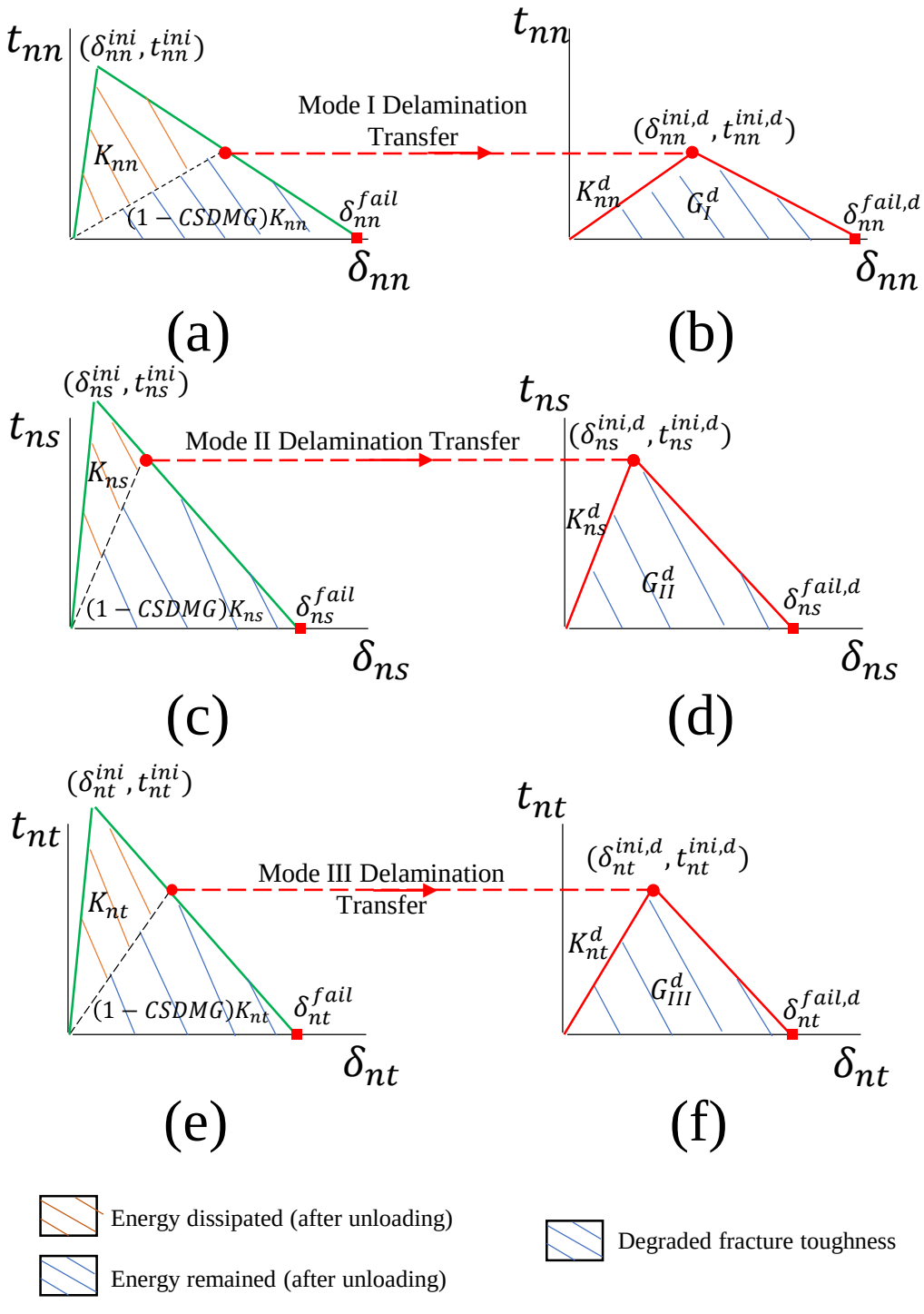

Figure 6.9: Traction separation laws of the delamination modes: (a) pristine mode I law assigned to LVI, (b) degraded mode I law assigned to CAI, (c) pristine mode II law assigned to LVI, (d) degraded mode II law assigned to CAI, (e) pristine mode III law assigned to LVI, and (f) degraded mode III law assigned to CAI.

impact event (after stage (v)) is unnecessary. Accordingly, with stopping the LVI computational analysis at stage v, the computational time for the LVI prediction can be reduced by about 50%.

However, if the conventional method based on the *restart function is used, the second half of the LVI prediction can not be omitted. The reason is that at stage (v) in Figure 6.10, the deformation of the sample is at about the maximum extent, which can not be directly set as the initial state of the CAI analysis. Therefore, in order to implement the efficient modeling strategy introduced by this section, the damage transferring algorithm introduced in Section 6.4 must be used together to transfer the LVI-induced damage on a deformed mesh at the middle of the LVI analysis to the start of the CAI analysis when the CAI mesh is undeformed.

It should be noted that an assumption being made here is that the permanent indentation caused by the LVI does not heavily influence the CAI strength, considering the LVI-induced damage extent studied in this dissertation is under the BVID limit. The effects of local permanent indentation on the CAI strength will be studied in the future.

So far, the three methods to accelerate the LVI-CAI analyses have been developed. These three methods are mutually independent as illustrated in Figure 6.11. The optimal way to conduct LVI-CAI analyses is by using the three methods collectively. The smart mesh paradigm which minimizes the element number for the LVI should be used and the LVI analysis should be run up to half of the LVI event, following the efficient modeling strategy. Then, the predicted fiber damage, matrix micro- and macro-scale damage, and delamination are extracted and implanted into the CAI mesh based on the developed damage transferring algorithm to carry out the CAI analysis.

In summary, compared to conventional LVI-CAI analyses based on the *restart function or the *import function of Abaqus, the proposed computational framework

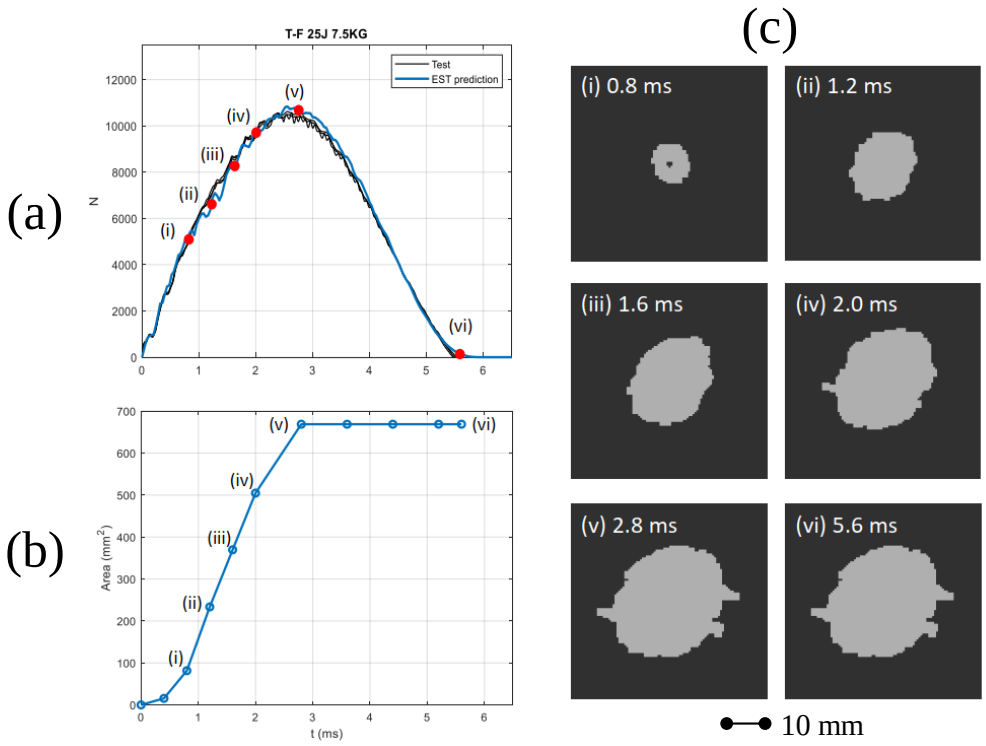

Figure 6.10: (a) Load history of LVI, (b) overall damage area history of LVI, and (c) damage footprint growth over time [11].

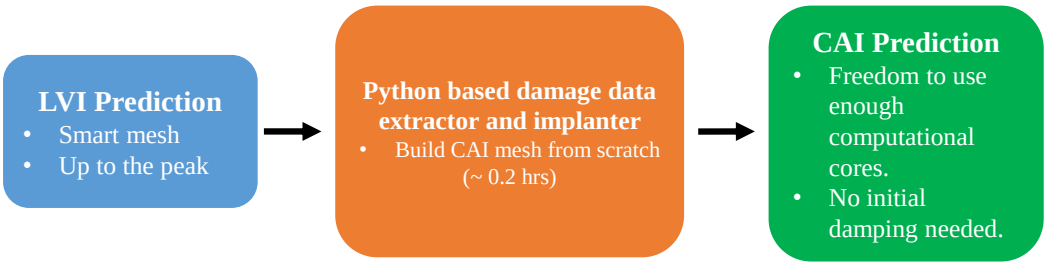

Figure 6.11: The high-efficiency and high-fidelity LVI-CAI analysis framework.

improves the computational efficiency in three major aspects:

1. DOFs of the LVI analysis reduced by the smart mesh paradigm.

2. Time to be analyzed for the LVI event reduced by about 50% by the efficient modeling strategy.

3. Avoidance of the initial damping step in CAI analysis due to the damage transferring algorithm.

6.6 Application of the High-fidelity and High-efficiency Framework

The high-fidelity and high-efficiency LVI-CAI computational framework will be applied to the analyses of a $[45/-45/0/45/-45/90/45/-45/45/-45]_s$ T800s/3900-2B laminate. This laminate is named as layup C in Chapters II, III, and V. The reason for studying this laminate is that its LVI induced damage patterns are enriched, including the "fan" shaped and "peanut" shaped delamination. The LVI prediction of this layup is more challenging due to the existence of various featured damage patterns. In addition, as reported in Chapter III, due to the existence of the high percentage of $\pm 45^\circ$ plies and low percentage of 0° plies, the CAI failure process tends to be more progressive compared to layup A and layup B, whose definition can be found in Table 2.1. Capturing a relatively more progressive failure process is usually more demanding for the accuracy of computational models. Therefore, the major purpose of choosing to study this $[45/-45/0/45/-45/90/45/-45/45/-45]_s$ laminate is to challenge the LVI-CAI computational framework.

The boundary conditions of the LVI-CAI models are shown in Figure 6.12. From Figure 6.12 (a), it is seen that for the LVI analysis, the laminate is sandwiched between two picture roller frames, as illustrated in Chapter II. Two reference points are defined

for the lower and upper roller frames and the six DOFs of these two reference points are fixed during the LVI and CAI analyses. The two roller frames are meshed with rigid planar elements R3D4, so is the impactor. A reference point is assigned to the hemispherical impactor with the diameter of 20 mm. Initial velocity along the z-axis is specified for the impactor's reference point. The initial velocity is calculated from the impact energy and the impactor's mass. All the three rotational DOFs of the impactor's reference point are fixed. The laminate is modeled using continuum shell elements SC8R. General contact is defined between the laminate, the impactor, and the roller frames. The frictional coefficient is set as 0.3. The boundary conditions of the LVI analysis is identical to that illustrated in Chapter II.

The boundary conditions of the CAI analysis is demonstrated in Figure 6.12 (b). As pointed out in [60], the CAI model was imported from the LVI results and the roller frames were inherited from the LVI model. As discussed in [60], compared with the knife edge supports shown in Figure 3.1, the locations of the roller-to-laminate contact in Figure 6.12 (b). The only difference between the CAI computational model illustrated in Figure 6.12 (b) and the actual experimental setup is that the radius of the roller support is larger than that of the knife support. However, this difference has negligible effect on the CAI results. As shown in Figure 6.12 (b), two regions at the longitudinal ends of the laminate are clamped, corresponding to the top and bottom clamping of the experimental setup, as illustrated in Figure 3.1. The width of the clamped region is 12.7 mm. Displacement-controlled compressive loading along the x-axis is applied to the two ends of the panel and all the other five DOFs are constrained.

In section 3, the results obtained with the conventional method utilizing the *restart function will be presented first as the benchmark case. Then, the LVI-CAI results obtained with the high-fidelity and high-efficiency framework will be reported and compared with that acquire by the conventional method. The computational

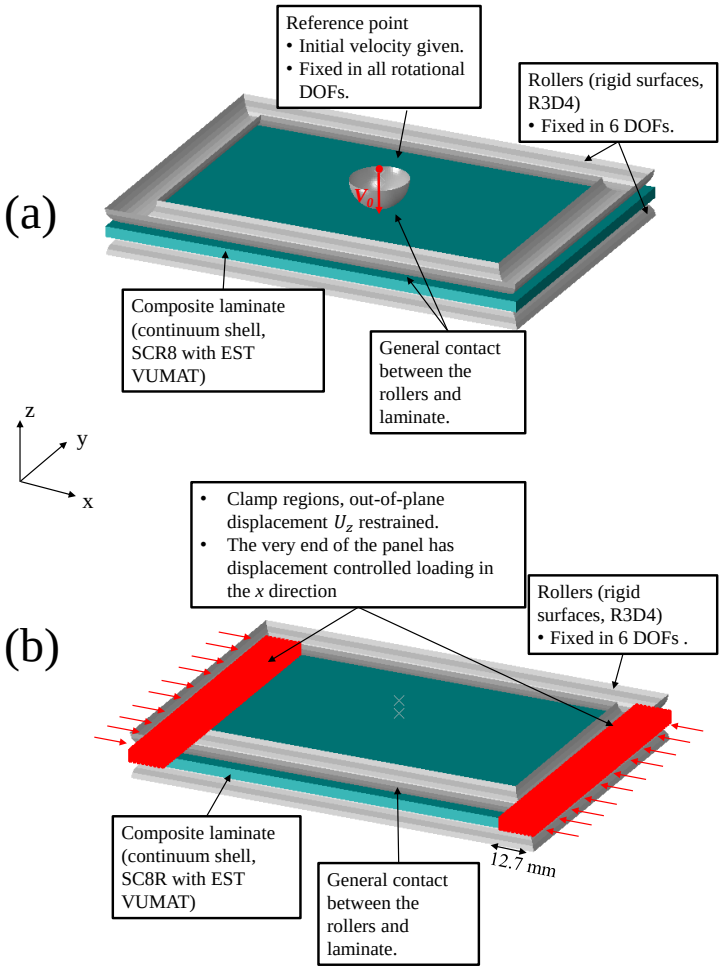

Figure 6.12: Boundary conditions of (a) LVI, and (b) CAI.

accuracy will measured according to the corresponding experimental results reported in Chapters II and III. The improvement of the computational efficiency by the three accelerating methods discussed in Sections 6.3 to 6.5 will be quantified.

6.6.1 LVI Results

LVI Results Obtained with the Traditional Approach

LVI results obtained with the traditional approach using the mesh pattern shown in Figure 6.2 (a) are presented and compared with the test results. The comparison is demonstrated in Figure 6.13. In Figures 6.13 (a) and (b), the load-time and load-displacement responses are compared. In both the Figures, the black curves correspond to the test results, while the red curves correspond to the numerical results obtained with the traditional approach. Generally speaking, the agreement between the computationally predicted and experimentally obtained load responses is good. Some discrepancy is seen. In the unloading phase (from stage (iii) to (iv) in Figures 6.13 (a) and (b)), at the same load level, the predicted displacement is smaller than the experimental data. The major reason for this difference is the lack of 2D EST's capability to capture the inelasticity in laminated composite materials [21, 22]. This difference is believed to be noneffective to the prediction of the LVI-induced damage morphology, since the initiation and formation of the damage footprint mostly take place in the loading phase, as illustrated by Figure 6.10.

Four time points are taken to investigate the deformation and damage growth history of the layup C sample impacted with 25 J. The predicted damage footprint at the four time points is displayed in Figure 6.13 (c). The LVI-induced damage footprint characterized by ultrasound C-scanning is shown in Figure 6.13 (c). It is seen that the predicted damage footprint agrees well with the C-scanned footprint in terms of both size and morphology. It is observed in Figure 6.13 (e) that the predicted out-of-plane deformation agrees very well with the deformation field characterized by

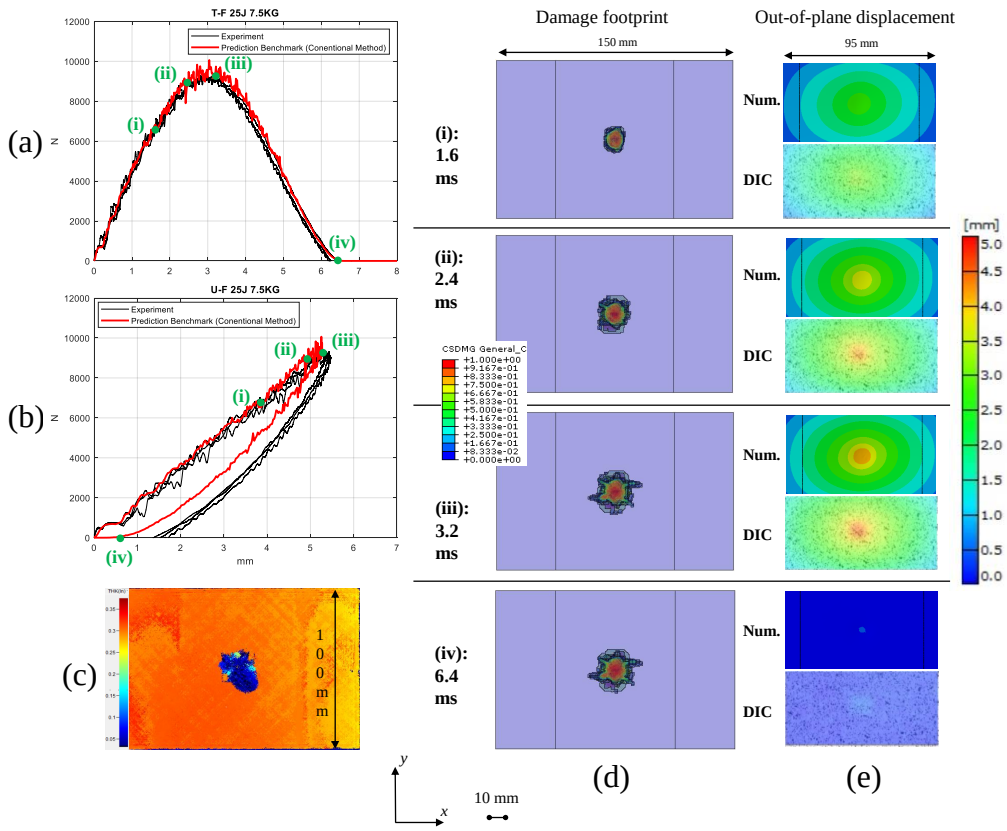

Figure 6.13: LVI experimental results vs. computational results: (a) load-time curves, (b) load-displacement curves, (c) C-scanned damage footprint, (d) predicted damage footprint at four time points, and (d) predicted and 3D DIC out-of-plane displacement field at four time points.

high-speed 3D DIC throughout the entire impact event.

μCT scanning of a layup C sample impacted with 25J is compared with the predicted delamination in Figure 6.14. The chosen μCT slices in Figure 6.14 are based on the locations of the slices such that the delamination can be visualized. The delamination at the [45/-45] interface is shown in Figure 6.14 (a). The sticking-out part caused by fiber kinking near the impacted surface is seen in both the μCT slice and 2D EST prediction. Figures 6.14 (b) and (d) show the delamination at the [45/-45] and [-45/45] interfaces. This "peanut-shape" delamination has been illustrated in Chapters II and V. The delamination at the [90/-45] interface is shown in Figure 6.14 (b). This "fan-shape" pattern has been illustrated in Chapters II and V. As seen

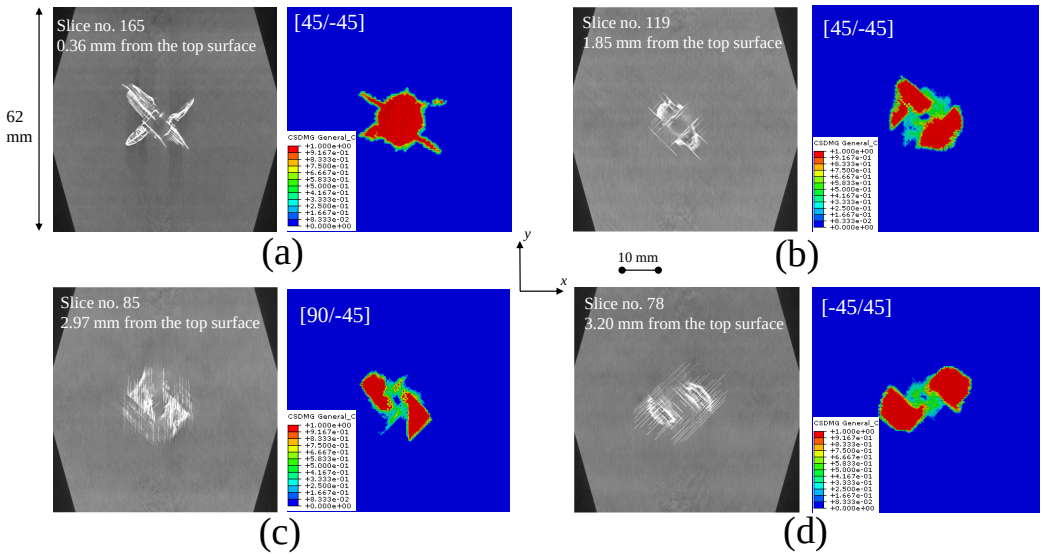

Figure 6.14: (a) Delamination at the interface between the 1st and 2nd ply, (b) delamination at the interface between the 7th and 8th ply, (c) delamination at the interface between the 15th and 16th ply, and (d) delamination at the interface between the 19th and 20th ply.

in Figure 6.14, the predictive quality of the damage morphology is high. This high fidelity is due to the correct capturing of the interaction between different damage modes, including matrix cracking, fiber breaking, and delamination. More detailed LVI-induced damage mechanisms can be found in Chapter II.

LVI Results Obtained with the Smart Mesh Paradigm

The accuracy of LVI predictions using meshes following the smart mesh paradigm as illustrated in Section 6.3 is evaluated in Figure 6.15. The three smart mesh patterns are shown in Figures 6.15 (d) to (f). The sizes of the center fine-mesh region are 75 mm × 60 mm, 60 mm × 50 mm, and 40 mm × 40 mm. The elemental sizes of fine and coarse elements are 0.6 mm × 0.6 mm and 2.0 mm × 2.0 mm. Besides the difference in the mesh patterns, all the parameters defining the numerical models are identical for the displayed cases in Figures 6.15 (c-f).

As seen in Figures 6.15 (a) and (b), the predicted load responses agree well with the benchmark numerical results and the test results. In other words, the results

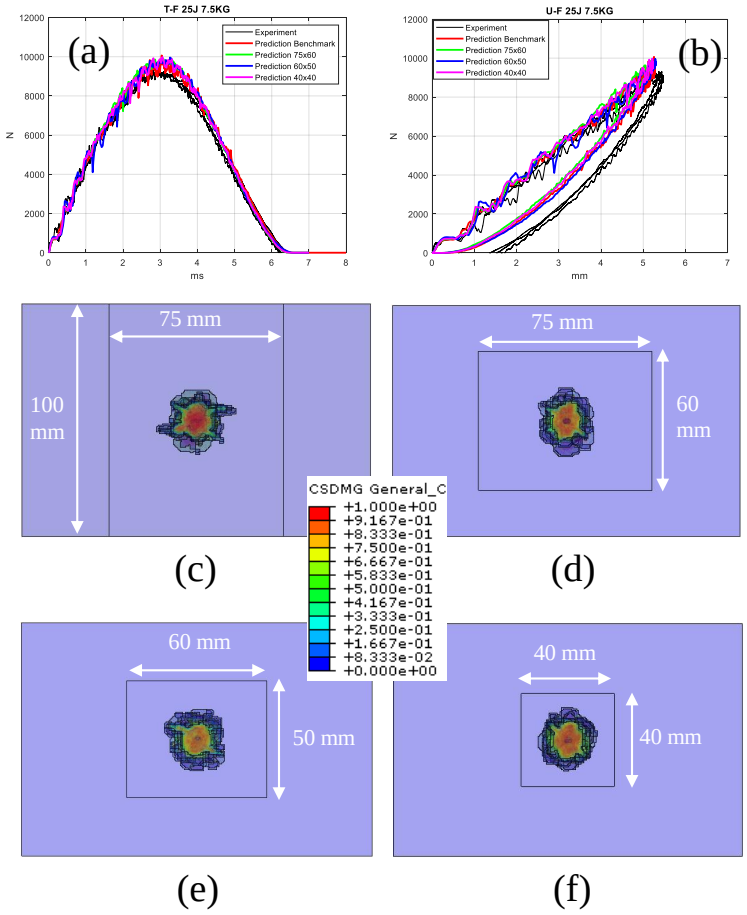

Figure 6.15: (a) Load-time response, (b) load-displacement response, (c) damage predicted with the benchmark case, (d) damage predicted with the smart mesh (75 mm × 60 mm), (e) damage predicted with the smart mesh (60 mm × 50 mm), and (f) damage predicted with the smart mesh (40 mm × 40 mm.)

obtained using the smart meshes are essentially identical to the results obtained using the conventional mesh. The predicted damage footprints using the smart meshes are shown in Figures 6.15 (d) to (f). Again, in terms of the LVI-induced damage prediction, the damage footprints obtained with the smart meshes agree well with the benchmark results displayed in Figure 6.15 (c). Some local difference is seen but is most likely due to numerical effects existing in computational analyses.

Critical LVI parameters obtained experimentally and numerically are compared in Table 6.1. Data smoothening based on the simple moving average (SMA) method

Table 6.1: Comparison of predicted critical LVI parameters and computational time.

	Peak load (N) (error)	Max disp. (mm) (error)	CPU time (hrs)
Experiment	9222	5.46	NA
Benchmark	9609 (4.2%)	5.27 (3.5%)	8.7
Smart mesh (75 mm x 60 mm)	9665 (4.8%)	5.21 (4.6%)	5.9
Smart mesh (60 mm x 50 mm)	9643 (4.6%)	5.22 (4.4%)	4.7
Smart mesh (40 mm x 40 mm)	9634 (4.5%)	5.28 (3.3%)	3.4

[122] was performed to filter out the high-frequency oscillations caused by numerical effects in order to correctly record the predicted LVI parameters. From table 6.1, it is seen that the predicted LVI parameters including peak load and max impactor displacement are within 5% difference from the averaged experimental values. From the last column of Table 6.1, the smart mesh with the fine-mesh region being 40 mm $\times$ 40 mm can help save the computational time by 61% compared to the benchmark case.

6.6.2 CAI Results

The CAI experimental and numerical results obtained with the conventional method are presented in Figure 6.16. In Figure 6.16 (a), the predicted load-displacement response (red curve) agrees well with the experimental results (black dotted curves). The load and displacement data of the experimental results is collected from the load cell of the MTS system and the 2D DIC characterization. These test results have been discussed in Chapter III. The averaged experimental compressive strength after impact (CSAI) values is 89.0 kN, while the predicted CSAI is 93.3 kN. The difference is 4.8%.

Figures 6.16 (b) and (c) display the computationally predicted and experimentally characterized axial deformation field after the CAI failure. Bands of deformation

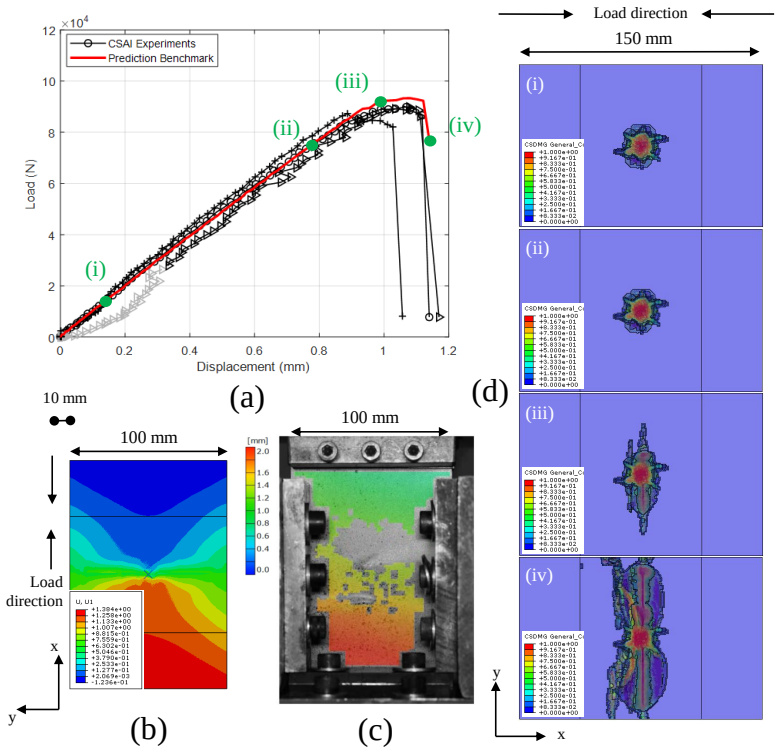

Figure 6.16: (a) Load-displacement responses, (b) predicted displacement field after the CAI failure, (c) 2D DIC displacement field after the CAI failure, and (d) the damage growth history.

discontinuity are found in both the subfigures. This type of discontinuity near the impacted area has been illustrated in Chapter III. Four time points are noted on the computational curve in Figure 6.16 (a) and the corresponding damage footprints are shown in Figure 6.16 (d). As seen, from time stage (i) to (ii), no damage growth due to CAI loading is observed. From (ii) to (iii). damage growth along the y-axis in the forms of fiber kinking and delamination is seen. From (iii) to (iv), the load drop is drastic, accompanied with the significant damage growth.

The predicted sample's geometry after the failure is compared with the experimental observation before in Figure 6.17. Figures 6.17 (a) and (b) demonstrate the impacted side of the failed specimen. The non-impacted surface is displayed in Figures 6.17 (c) and (d). Elements with fiber failure are removed from the computational model to visualize the damage more clearly. The green level being various in Figures

6.17 (b) and (d) is due to the 3D visual effect rendered by the viewer of Abaqus. From Figure 6.17, a direct comparison is drawn between the deformed sample in the lab and the predicted deformed sample to demonstrate the fidelity of the computational model.

One of the failed CAI samples was removed from the testing system and subjected to μCT scanning to characterize its internal damage patterns. The voxel size was 35 μm $\times$ 35 μm $\times$ 35 μm. Since the sample was severely deformed, the face-on slices are not very useful since one slice may contain damage data from multiple layers. Therefore, only the edge-on slices are displayed in Figure 6.18. The μCT slices that are 20 mm, 10 mm, and 0 mm from the center-line of the sample are demonstrated in Figure 6.18. The computationally predicted cross-sections at the corresponding locations are shown under the μCT slices in each of the subfigures. Similar to Figure 6.17, elements undergoing fiber failure are removed from the plots. From Figure 6.18, the CAI-induced delamination, matrix cracking, and fiber compressive failure are clearly seen. The computationally predicted sample resembles the μCT characterized sample very well. The numerical results have larger out-of-plane deformation values than the μCT slices because the cross-sectional views of the numerical results were taken at the end of CAI modeling without the displacement-controlled loading being removed. However, the μCT scanning for the failed sample was performed after the removal of the loading.

It should be noted that in Figures 6.17 and 6.18 the elements with fiber failure are removed from plotting simply for the purpose of illustrating the CAI-induced damage patterns more clearly. Element deletion was not applied during the numerical analyses.

.

CAI Results Obtained with the Transferred Damage

Instead of the conventional approach, CAI analyses were performed based on the

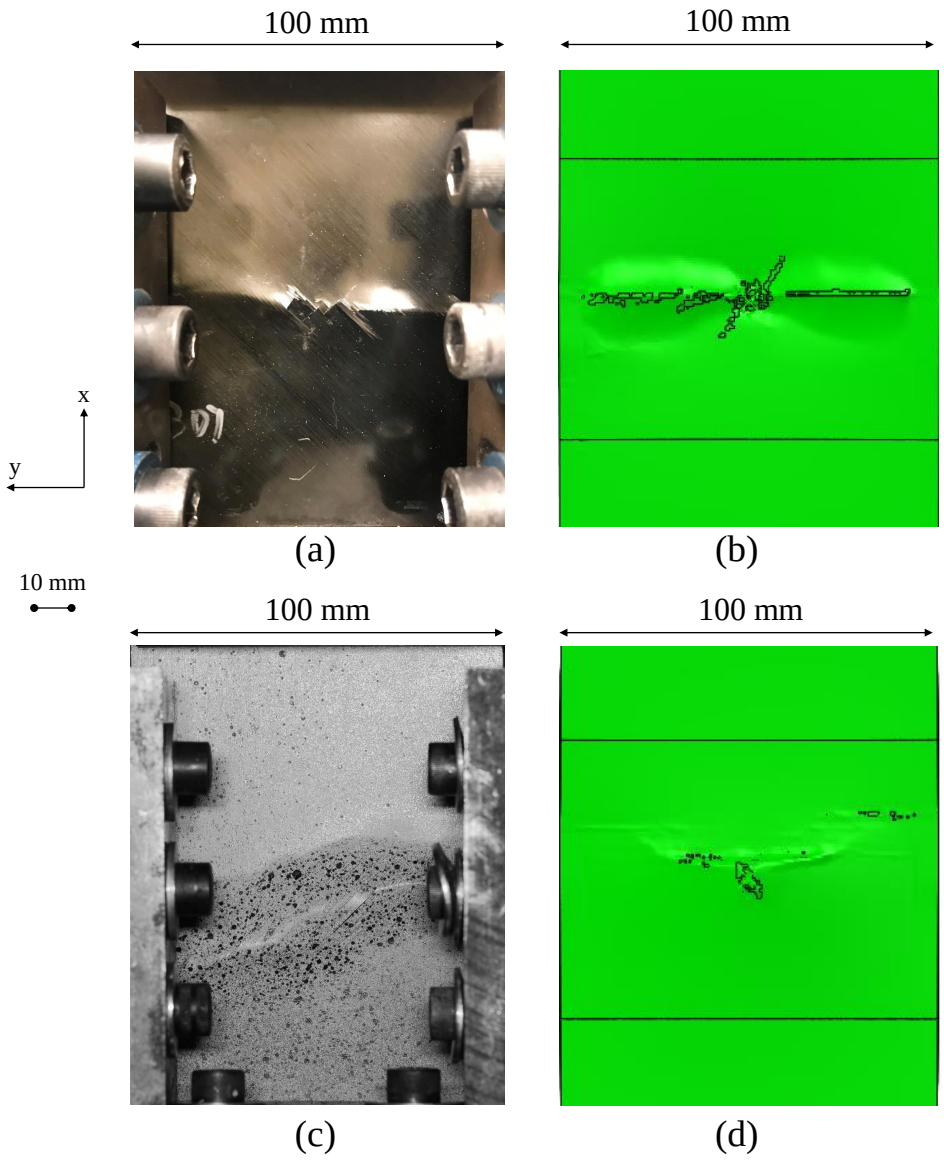

Figure 6.17: (a) Impacted surface of the failed sample (experimental), (b) impacted surface of the failed sample (numerical), (c) non-impacted surface of the failed sample (experimental), and (d) non-impacted surface of the failed sample (numerical).

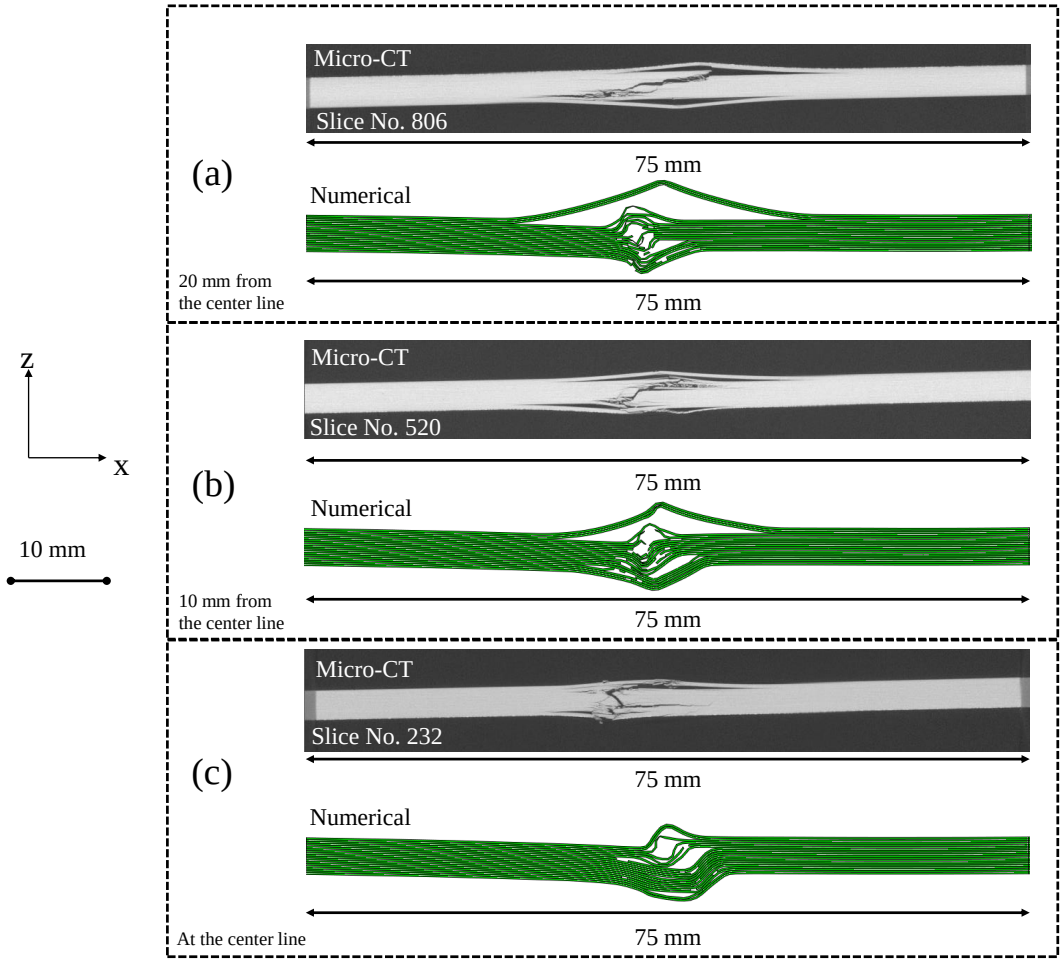

Figure 6.18: μCT characterization and numerical predictions of the cross-sectional views: (a) 20 mm from the centerline of the sample, (b) 10 mm from the centerline of the sample, and (c) at the centerline of the sample.

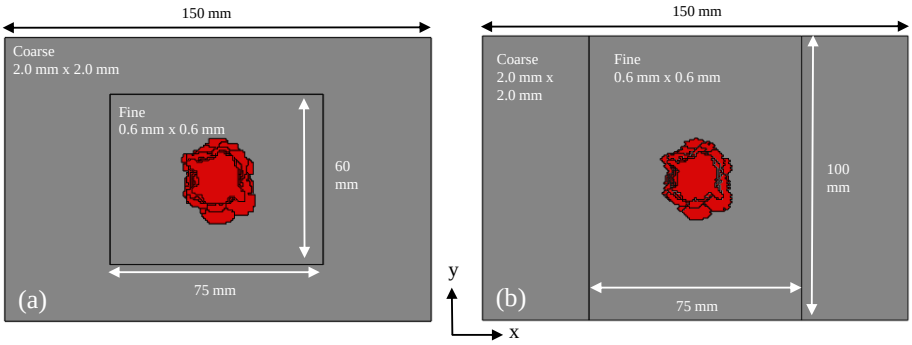

Figure 6.19: (a) Damage footprint predicted with the smart LVI mesh, and (b) damage footprint transferred to the CAI mesh.

damage transferring algorithm illustrated in Section 6.4. The damage transferring was performed using the numerical results at the end of the LVI analyses. Figure 6.19 shows the damage footprint transferred from a smart LVI mesh to a CAI mesh. The smart LVI mesh has a 75 mm $\times$ 60 mm fine-mesh region, as shown in Figure 6.19 (a). The CAI mesh is identical to the mesh used with the conventional approach, as shown in Figure 6.19 (b). In Figure 6.19 (a), the predicted LVI-induced damage is displayed. In Figure 6.19 (b), transferred LVI-induced damage on the CAI mesh is displayed. The damage in both the subfigures is essentially identical, with some trivial local differences. The transferred damage from the other smart LVI meshes with the fine-mesh region being 60 mm $\times$ 50 mm and 40 mm $\times$ 40 mm is also identical to that predicted at the end of the LVI analyses. The purpose of Figure 6.19 is to demonstrate that the damage transferring algorithm has been successfully implemented.

With the LVI-induced damage transferred from the end of the LVI analyses presented in Figure 6.15, CAI predictions were performed and the numerical results are presented in Figure 6.20. As shown in Figure 6.20 (a), the predicted load-displacement curve using the conventional approach (benchmark) and the results based on the damage transferring algorithm are almost on top of each other. The benchmark prediction of the CAI-induced failure is displayed in Figure 6.20 (b), while the predicted CAI-

Table 6.2: Comparison of predicted critical CSAI values and computational time (smart mesh + damage transfer).

	CSAI (kN) (error)	CPU Time (hrs, running with 72 cores)		
		LVI	Damping + CAI	
Experiment	89.0	NA	NA	
Benchmark	93.3 (4.8%)	8.7	5.3	
		LVI	Damage transfer	CAI
Transfer from smart mesh (75 mm x 60 mm)	93.4 (4.9%)	5.9	0.2	2.5
Transfer from smart mesh (60 mm x 50 mm)	92.1 (3.5%)	4.7	0.2	2.7
Transfer from smart mesh (40 mm x 40 mm)	94.3 (5.9%)	3.4	0.2	2.7

induced damage using the damage transferred from the three smart LVI meshes is shown in Figures 6.20 (c) to (e). Generally speaking, the predicted damage patterns are similar to each other. The damage footprints in Figures 6.20 (c) and (e) seem smaller than that in (b) and (d). This is not due to the predicted CAI-induced damage being less, but due to the fact that the numerical predictions corresponding to (c) and (e) got aborted earlier than that corresponding to (b) and (d). Analysis abortion usually happens when some elements are severely distorted during the analyses, especially for the analyses involving damage initiation and propagation.

The error of the computational results from the averaged test results in terms of the CSAI value and the CPU time consumption are summarized and compared in Table 6.2.

CAI Results Obtained with the Transferred Damage + the Efficient Modeling Strategy

The CAI predictions based on the LVI-induced damage transferred from the middle of the LVI analyses using the smart meshes as shown in Figure 6.15 are presented in Figure 6.21. The damage transferring algorithm and the efficient modeling strategy have been illustrated in detail in Sections 6.4 and 6.5. The middle of the LVI analyses

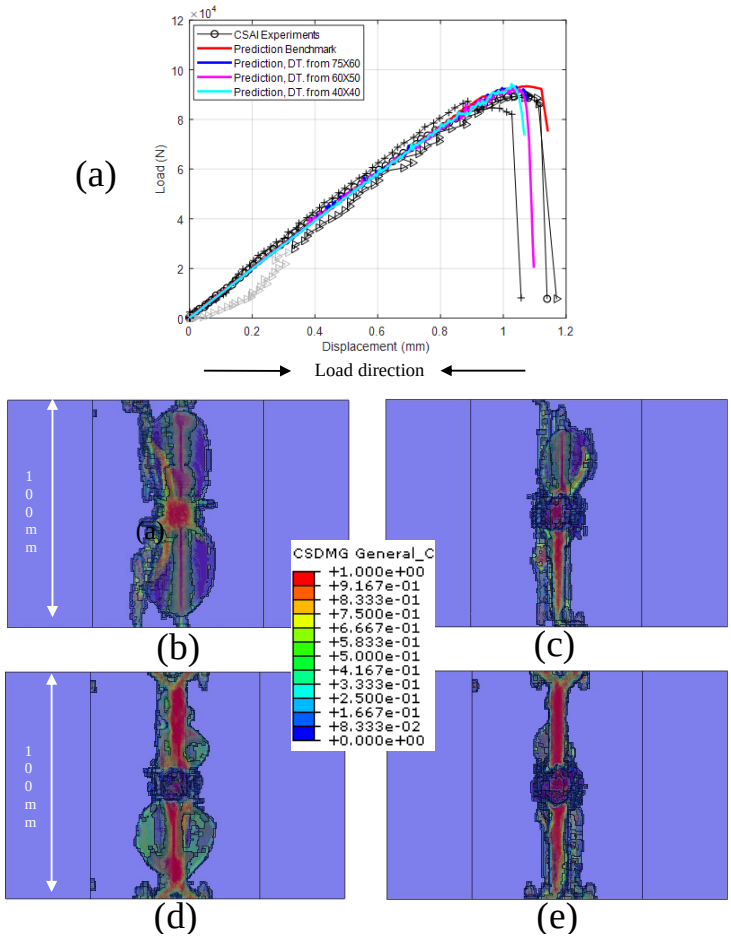

Figure 6.20: (a) Load-displacement response, (b) CAI damage predicted with the conventional method using *restart, (c) CAI damage predicted with LVI damage transferred from the smart mesh (75 mm × 60 mm), (d) CAI damage predicted with LVI damage transferred from the smart mesh (60 mm × 50 mm), and (e) CAI damage predicted with LVI damage transferred from the smart mesh (40 mm × 40 mm)

Table 6.3: Comparison of predicted critical CSAI values and computational time (smart mesh + damage transfer from the middle of LVI).

	CSAI (kN) (error)	CPU Time (hrs, running with 72 cores) LVI	Damping + CAI	
Experiment	89.0	NA	NA	
Benchmark	93.3 (4.8%)	8.7	5.3	
		LVI	Damage transfer	CAI
Transfer from mid. smart mesh (75 mm x 60 mm)	91.6 (2.9%)	3.0	0.2	2.6
Transfer from mid. smart mesh (60 mm x 50 mm)	93.5 (5.1%)	2.3	0.2	2.7
Transfer from mid. smart mesh (40 mm x 40 mm)	87.5 (1.7%)	1.7	0.2	2.7

can be illustrated as point (v) in Figure 6.10. The predicted CAI load-displacement curves are shown in Figure 6.21 (a). It is seen that the numerical results are highly similar to each other and agree well with the experimental results. The predicted damage is shown in Figures 6.21 (b) to (e). Again, the damage in Figure 6.21 (c) and (e) seems smaller than that in (b) and (d). The reason is the early analysis abortion due to the excessive elemental distortion. The computational errors and time are summarized in Table 6.3.

6.6.3 Evaluation on the Computational Accuracy and Efficiency

A comprehensive evaluation of the computational fidelity and efficiency of all the cases presented in Figures 6.20 and 6.21 are summarized in Figure 6.22. The fidelity is measured by calculating the errors of the predicted CSAI values from the averaged experimental CSAI value. The computational efficiency is quantified by the CPU time. In Figure 6.22, the red dot and line represent the benchmark LVI-CAI analysis based on the conventional approach. The results based on the smart LVI meshes and damage transferring from the end and middle of LVI analyses correspond to the squares and triangles. The cases based on the 75 mm $\times$ 60 mm, 60 mm $\times$ 50 mm, and

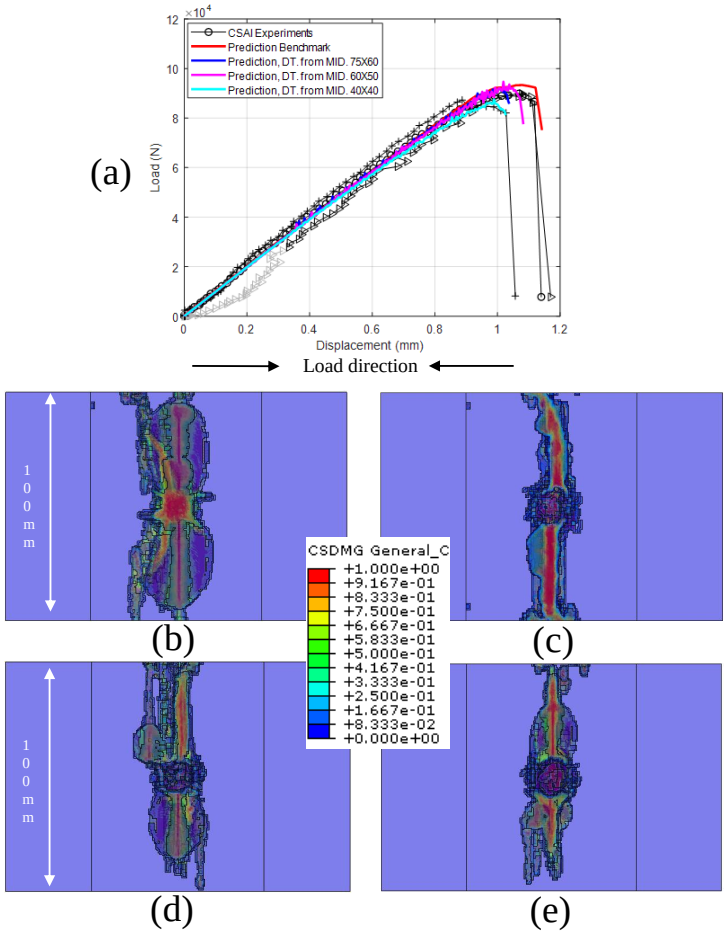

Figure 6.21: (a) Load-displacement response, (b) CAI damage predicted with the conventional method using *restart, (c) CAI damage predicted with damage transferred from the middle of LVI using smart mesh (75 mm × 60 mm), (d) CAI damage predicted with damage transferred from the middle of LVI using smart mesh (60 mm × 50 mm), and (e) CAI damage predicted with damage transferred from the middle of LVI using smart mesh (40 mm × 40 mm).

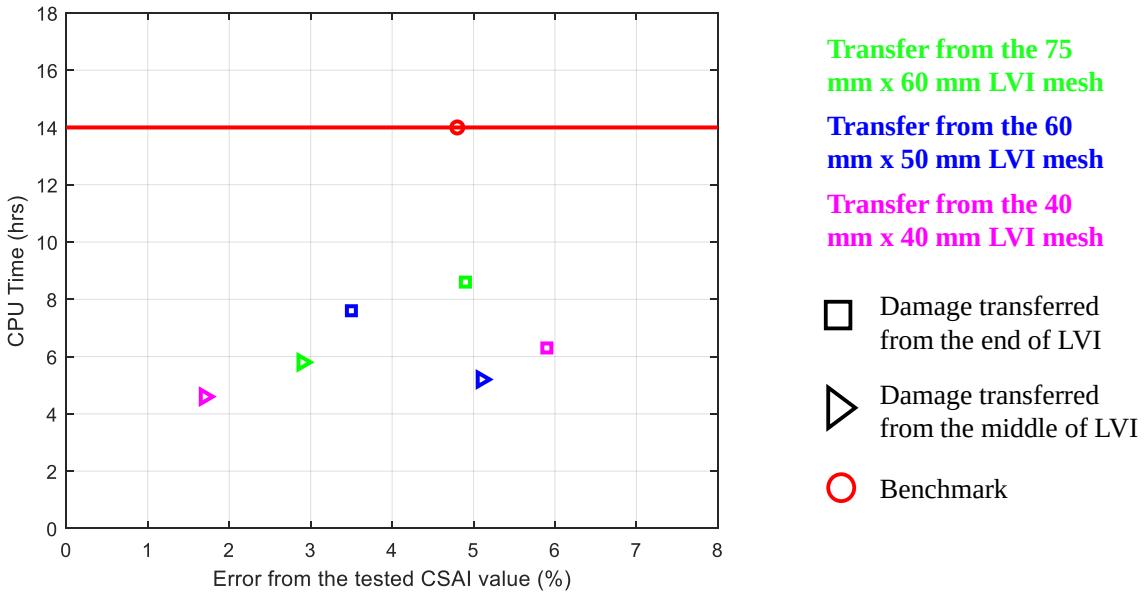

Figure 6.22: A comprehensive evaluation of the computational fidelity and efficiency.

40 mm $\times$ 40 mm smart meshes are colored green, blue, and magenta. It is seen that all the predicted CSAI values stay within 6% difference from the averaged experimental value. With the proposed high-fidelity and high-efficiency computational framework, the most efficiency LVI-CAI analysis can predict the CSAI value with 4.6 hrs using 72 computing cores. Compared to the benchmark case using the conventional approach, the computational time has been saved by 67%.

6.7 Summary and Conclusions

In this section, the high-fidelity and high-efficiency LVI-CAI computational framework has been illustrated. The major goal of this framework is to accelerate the computational analyses without sacrificing the computational fidelity. This frame work is composed of three accelerating phases, including a smart LVI mesh paradigm, an efficient modeling strategy, and a damage transferring algorithm. The damage trans-

ferring algorithm is the gist of the developed computational framework. With the framework, the computational time for LVI-CAI analyses to obtain the the CSAI values has been reduced by 67% with the error of predicted CSAI values staying within 6% different from the experimentally obtained averaged value.

In addition to the major task of boosting the computational efficiency, the high-fidelity and high-efficiency computational framework can also predict the LVI-induced damage and CAI-induced failure patterns accurately. The predicted critical LVI parameters stay within 5% error from the averaged test values. The damage features such as the "fan" and "peanut" delamination, and the interaction between matrix cracking, fiber breaking, and delamination have been correctly captured.

Compared with the conventional approach, the high-fidelity and high-efficiency computational framework helps to significantly improve the computational efficiency. Furthermore, the framework can be used to numerically generate large databases of the LVI and CAI analyses. Based on the databases, data-driven models can be trained, based upon which optimization algorithms can run for better impact resistance and damage tolerance of composites.

CHAPTER VII

Computational Studies of the CAI of Laminated Composites

7.1 Introduction

In this chapter, computational results of the CAI analyses that consider the stacking sequence effects and panel size effects are reported. For the stacking sequence effect studies, the modeling was performed based on the *Restart function of Abaqus, as described in Chapter VI. The CAI step was started from the end of the LVI analysis. Both the CAI and LVI modeling used 2D EST. For the panel size effect studies, the modeling was conducted based on the high-fidelity and high-efficiency LVI-CAI framework outlined in Chapter VI. The CAI step started with the LVI-induced damage transferred from the middle point of the LVI analysis. 2D EST-InELA was used for the LVI analysis, as reported in Section 5.3. 2D EST was used for the CAI modeling. The reason for using 2D EST instead of 2D EST-InELA for the CAI predictions is twofold. First, the CAI loading is monotonic. Therefore, accounting for the inelasticity effect is not as important as modeling the progressive damage. Second, 2D EST is computationally more efficient than 2D EST-InELA.

For the stacking sequence effect studies, T800s/3900-2B material was investigated. The studied stacking sequences include $[0/45/0/90/0/\text{-}45/0/45/0/\text{-}45]_s$ (layup A),

$[45/0/\text{-}45/90]_{3s}$ (layup B), and $[45/\text{-}45/0/45/\text{-}45/90/45/\text{-}45/45/\text{-}45]_{s}$ (layup C). The LVI test parameters can be found in Table 2.1. For the panel size effect studies, IM7/977-3 material was used. The studied cases include two stacking sequences: $[45/\text{-}45/0/90/0/0]_{ns}$ (L1) and $[45/0/\text{-}45/90]_{ns}$ (L2); two laminate thicknesses: 24-ply and 48-ply; and three in-plane sizes: 152.4 mm × 101.6 mm (S), 177.8 mm × 177.8 mm (M), and 330.2 mm × 330.2 mm (L). The LVI test parameters can be found in Table 2.2.

From the computational results presented in this chapter, the capability of the EST model to accurately predict the residual strengths of impacted panels is demonstrated. The damage mechanisms of the CAI process are investigated numerically. In this chapter, Section 7.2 will illustrate the boundary conditions and modeling procedures of the CAI analyses. Section 7.3 will present the computational results of the stacking sequence studies. Section 7.4 will report the results of the panel size effect studies. Discussions and conclusions will be provided in Section 7.5.

7.2 Modeling Strategy

For the stacking sequence effect studies, the CAI analyses were based on the *Restart function of Abaqus. The modeling strategy and boundary conditions have been illustrated in detail in Section 6.6. For the panel size effect studies, the CAI analyses were based on the high-fidelity and high-efficiency framework. The initial damage in the CAI models was implanted from that predicted by the LVI models using the damage transferring algorithm developed in Chapter VI. For the L1/L2-S-24/48 cases, the boundary conditions of the CAI analyses were identical to those used for the stacking sequence effect studies since the in-plane sizes of the panels are identical. The boundary conditions are illustrated in Figure 6.12 (b). For the L1/L2-M/L-24/48 cases, the boundary conditions of the CAI analyses are illustrated in Figure 7.1. Consider the CAI analysis of an impacted L1-M-24 sample as an example.

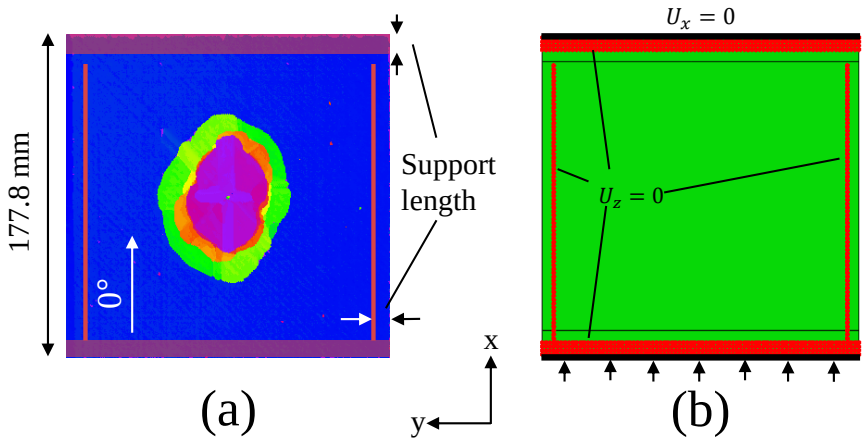

Figure 7.1: Boundary conditions of the CAI analysis: (a) an impacted L1-M-24 sample with supports illustrated, (b) the FEM model with boundary conditions noted.

The restrained areas and the damage are shown in Figure 7.1 (a). The compressive loading is along the 0° direction. More details regarding the FEM implementation can be found in Figure 7.1 (b). The out-of-displacement (U_z) at the highlighted nodes (red) is restrained as zero. The axial displacement (U_x) of the very top of the panel, as noted by the bold black line, is restrained as zero. The very bottom of the sample is subjected to controlled displacement. The support length shown in Figure 7.1 (a) is determined according to the experimental conditions and preliminary numerical analyses. The support length represents the widths of the top and bottom clamps, and the distances from the knife edges to the lateral edges. The reason to perform preliminary analyses will be provided in Section 7.4. The boundary conditions used for the L1/L2-M/L-24/48 cases essentially follow the same pattern as that used for the L1/L2-S-24/48 cases, except that for the L1/L2-S-24/48 cases, the roller supports are inherited from the LVI analyses. However, for the L1/L2-M/L-24/48 cases, the nodes at the corresponding locations are restrained instead of explicitly modeling the supports. The latter method is computationally more efficient since the contact between the supports and the panels is not modeled.

7.3 Computational CAI Study with the Effects of Stacking Sequence

In this section, the numerical results of the CAI of the impacted samples of the stacking sequence effect studies are reported. 2D EST was used to perform the CAI analyses based on the *Restart function of Abaqus. The corresponding numerical LVI results have been presented in Section 5.2.

7.3.1 Load Responses

The predicted load-displacement results of the CAI of the impacted layup A samples are shown in Figure 7.2. In Figure 7.2, the black curves are the test results; the red curves are the computational results predicted by 2D EST. The predicted curves agree well with the test data. It should be noted that for the case with 25 J impact, the CAI analysis got aborted due to excessive element distortion since the modeling strategy of element deletion was not used. However, based on the damage prediction displayed in Figure 7.6 (c), it can be concluded that CAI failure has been achieved. By plotting the CAI predictions together, it is seen that according to the predictions, with increasing impact energies, the CAI peak load decreases. However, the peak loads of the 20 J and 25 J impact cases have minimal difference. In addition, the load-displacement stiffness seems to be unaffected by the increasing impact energy. This finding agrees well with the experimental results.

The predicted load-displacement responses of the impacted layup B samples are shown in Figure 7.3. Overall, the predicted curves agree well with the experimental curves. Similarly to Figure 7.2 (c), the prediction shown in Figure 7.3 (a) also got aborted due to element excessive distortion. In Figure 7.3 (c), it is seen that the predicted load-displacement stiffness for the case with 35 J impact seems to be higher than the experimental value. By plotting the predicted curves together in Figure 7.3

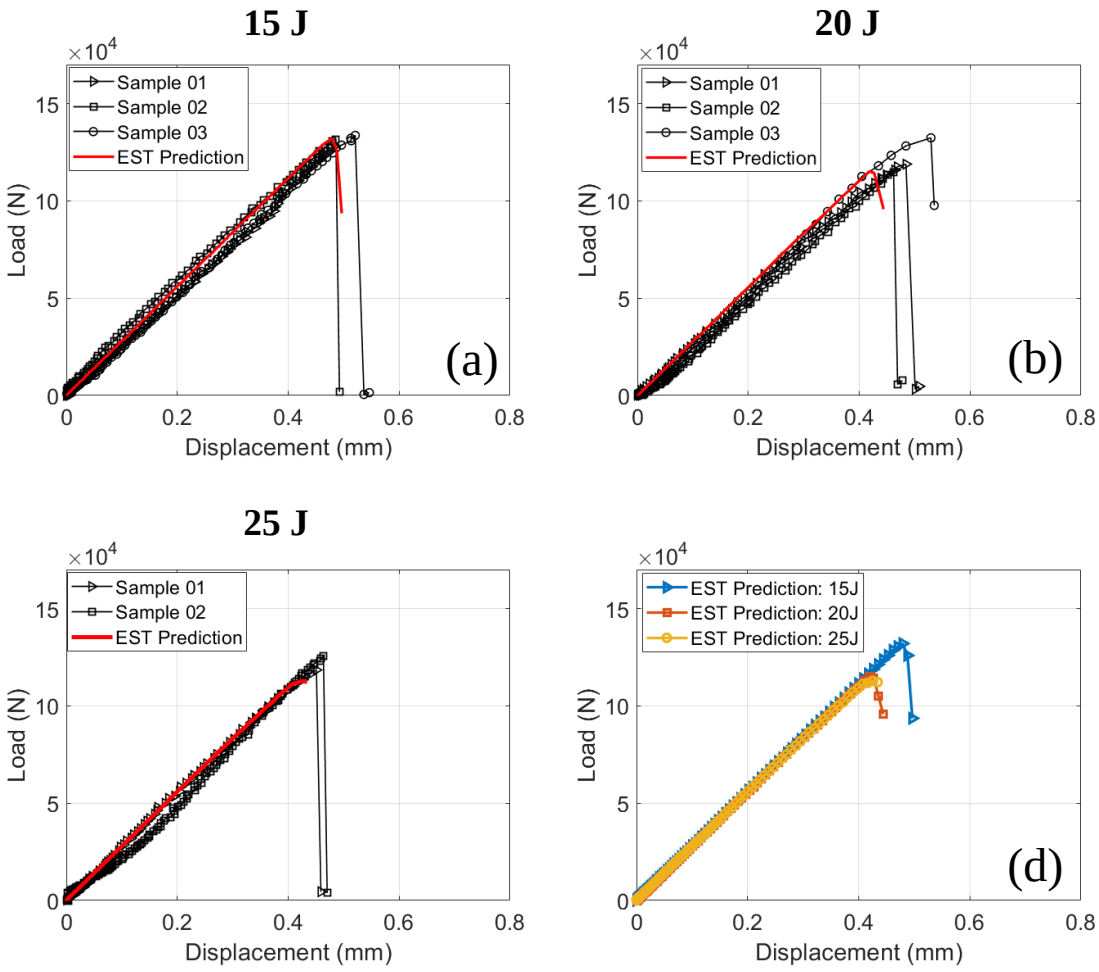

Figure 7.2: CAI load-displacement curves of the impacted layup A samples: (a) impacted with 15 J, (b) impacted with 20 J, (c) impacted with 25 J, and (d) predicted curves plotted together.

Table 7.1: The predicted CAI peak load vs. the test peak loads.

Layup	Impact energy (J)	Prediction error
A	15	1.0%
	20	5.7%
	25	7.5%
B	25	6.0%
	30	5.4%
	35	3.4%
C	20	2.5%
	25	4.8%
	30	1.7%

(d), the degradation of the peak load with the increase of impact energy is clearly seen. However, unlike Figure 3.7 (d) the degradation of the load-displacement stiffness is not numerically captured. The reason might be that for the 35 J impact case, the fiber tensile and compressive damage is underpredicted, as illustrated in Figure 5.9 (c).

The predicted load-displacement curves of the impacted layup C samples are shown in Figure 7.4. The predicted curves agree very well with the test curves in terms of both the peak loads and load-displacement stiffness values. Early abortion of the analysis also occurred for the 30 J impact case. However, according to the damage shown in Figure 7.8 (c), the CAI failure had taken place before the analysis got aborted. According to Figure 7.8 (c), from 20 J to 25 J, the reduction of the peak load is seen. However, from 25 J to 30 J, the reduction is marginal. In addition, the predicted load-displacement values are identical.

The CAI peak loads as a function of impact energies of the three layups are presented in Figure 7.5. As seen, the degrading trends of the three layups have been captured accurately. The predicted peak load values agree well with the test data, as summarized in Table 7.1.

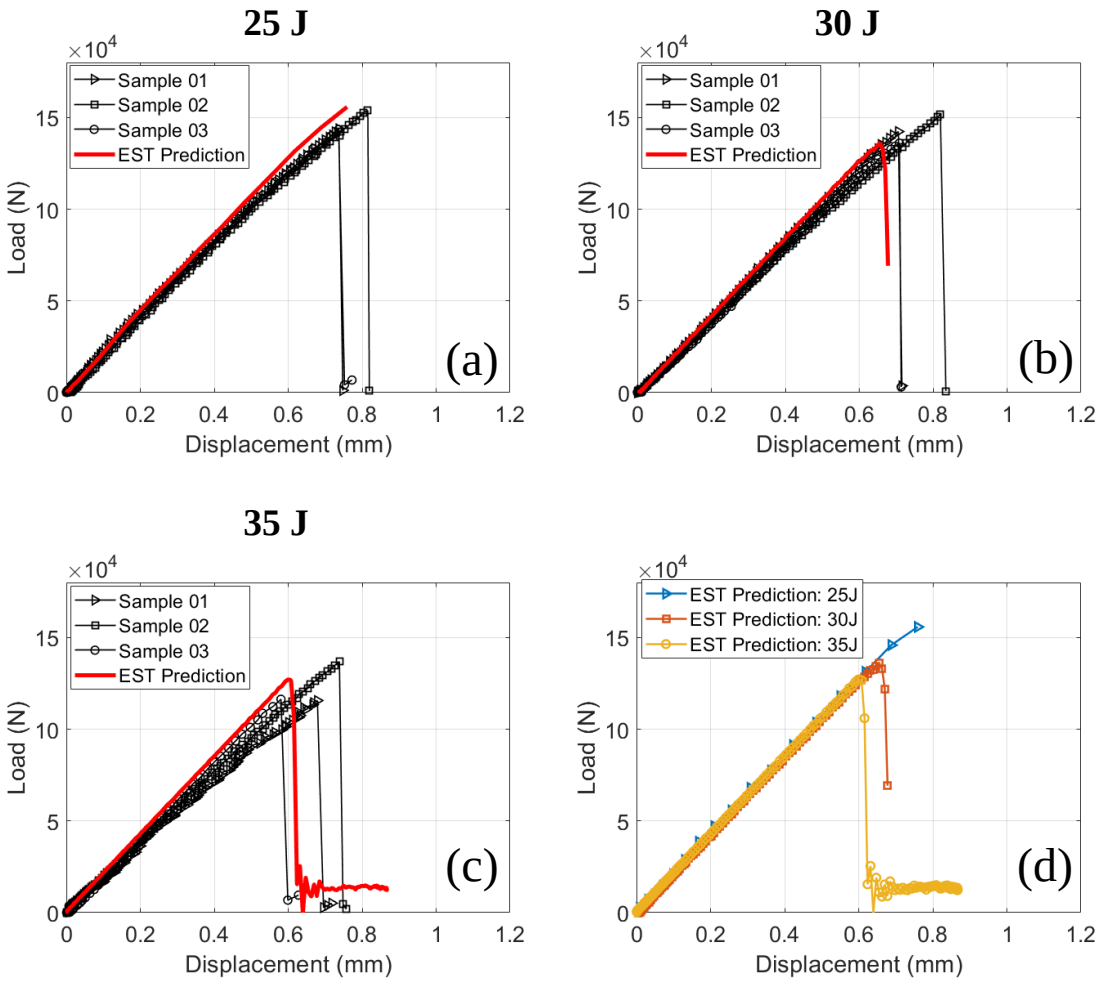

Figure 7.3: CAI load-displacement curves of the impacted layup B samples: (a) impacted with 25 J, (b) impacted with 30 J, (c) impacted with 35 J, and (d) predicted curves plotted together.

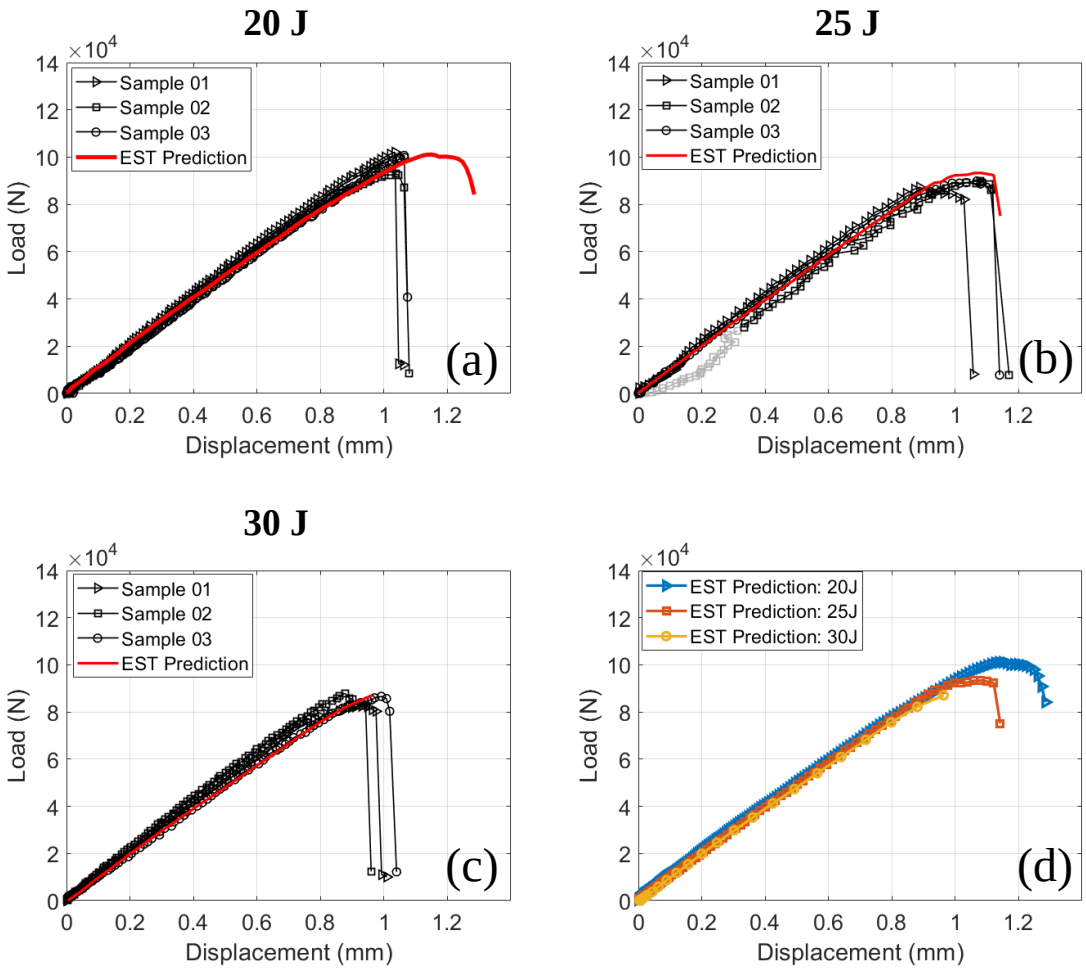

Figure 7.4: CAI load-displacement curves of the impacted layup C samples: (a) impacted with 20 J, (b) impacted with 25 J, (c) impacted with 30 J, and (d) predicted curves plotted together.

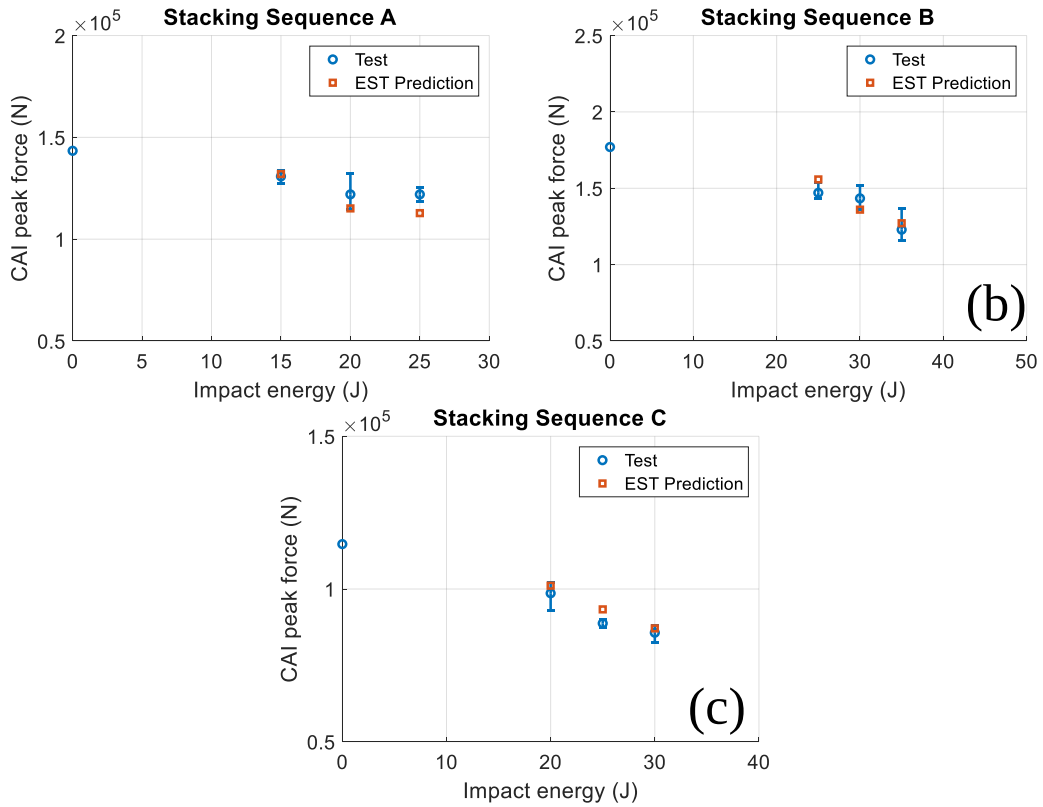

Figure 7.5: Variation of the CAI peak loads with the impact energies: (a) layup A, (b) layup B, and (c) layup C.

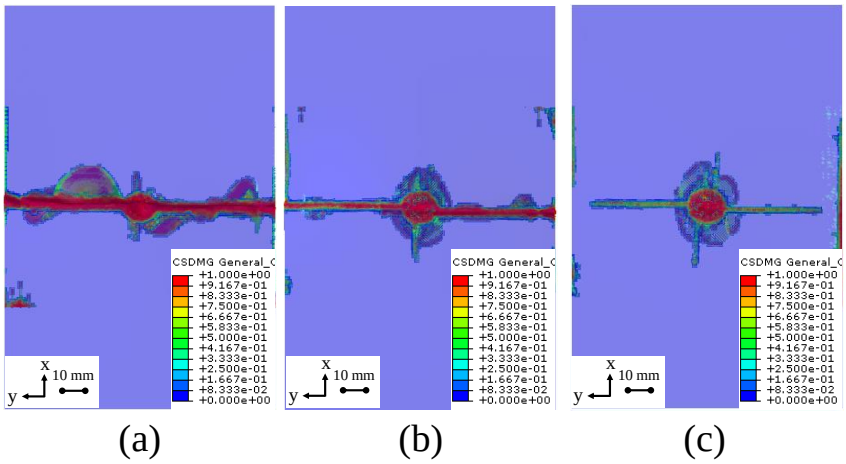

Figure 7.6: Predicted CAI-induced damage footprints of layup A samples impacted with (a) 15 J, (b) 20 J, and (c) 25 J.

7.3.2 CAI-induced Damage

CAI-induced damage footprints at the end of the analyses of layup A samples are presented in Figure 7.6. From all the subfigures, it is seen that the damage is in the form of a relatively narrow band that forms through the width direction (along the y-axis) of the samples. This narrow failure band indicates that the CAI-induced damage of layup A samples seems to be dominated by fiber compressive failure. In Figure 7.6 (c), the failure band does not reach the edges of the panel. This is due to the early abortion of the CAI analysis of this case. However, since the CAI failure of this layup is drastic, it is safe to conclude that the sample shown in Figure 7.6 (c) has failed.

The predicted damage footprints of layup B samples after the CAI failure are shown in Figure 7.7. Again, the reason for the damage not reaching the edges of the sample in Figure 7.7 (a) is the analysis aborting early. As shown in Figure 7.7 (b), the damage seems to be dominated by fiber compressive breaking, as the shape of the failure band is narrow. Fiber breaking is governed by the fiber direction critical strain $\epsilon_{11}^{ini,C}$, which is 0.0106. In Figure 7.7 (c), the damage modes are more enriched. Fiber breaking and large delamination are seen. The delamination is believed to be induced

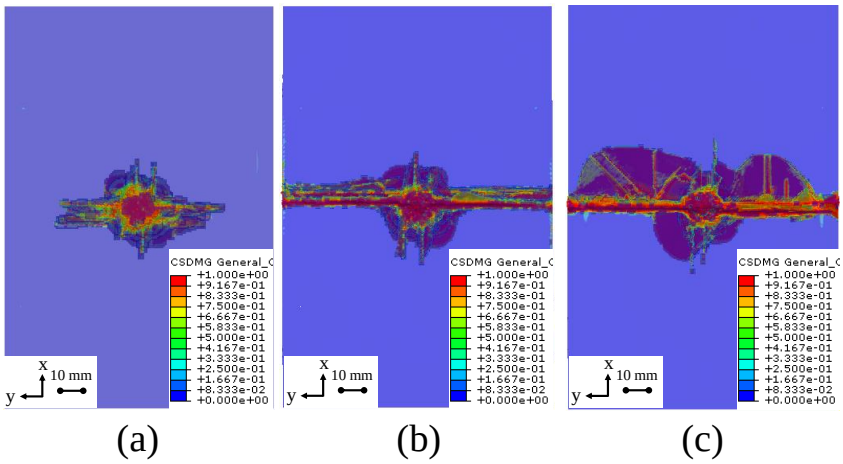

Figure 7.7: Predicted CAI-induced damage footprints of layup B samples impacted with (a) 25 J, (b) 30 J, and (c) 35 J.

by fiber compressive breaking. As the fiber breaks, severe out-of-plane deformation of the sample occurs, and hence large interfacial stresses are caused, which will facilitate the growth of LVI-induced delamination.

CAI-induced damage footprints of the layup C samples as shown in Figure 7.8 seem to have more delamination than that of layups A and B. Comparing Figure 7.8 to Figures 7.6 and 7.7, the damage footprints of layup C samples are significantly larger. In addition, the fiber compressive breaking in Figure 7.8 is no longer simply one band across the width direction but is made of several parts of fiber breaking parallel to the width direction. The reason for the differences in shape and size of the CAI-induced damage footprints of layup A, B, and C samples is most likely to be the effects of stacking sequence. As 80% of layup A's plies are 0°, the CAI damage is more likely to be very drastic and dominated by fiber kinking. For layup C, which has only 10% 0° plies, but 80% ±45° plies, the CAI damage is more progressive and involves delamination, as a mode of energy dissipation.

The CAI-induced damage growth history of a layup B sample impacted with 35 J is demonstrated in Figure 7.9. The load-displacement responses are plotted in Figure 7.9 (a) along with the damage footprints at various stages. From stages (i) to (ii),

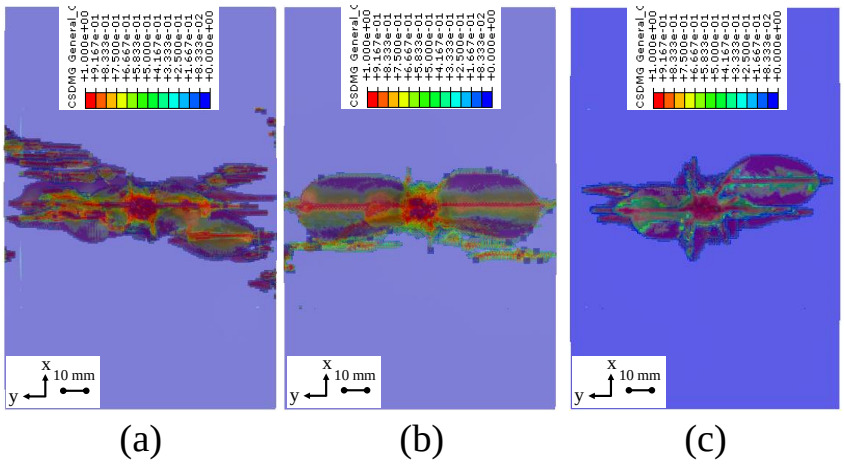

Figure 7.8: Predicted CAI-induced damage footprints of layup C samples impacted with (a) 20 J, (b) 25 J, and (c) 30 J.

there is no growth of the LVI-induced damage as the compressive load increases. The damage footprint grows drastically between stages (v) and (vi) with the load drop. Edge-on views of the cross-section going across the sample's center along the x-axis at the noted stages are shown in Figure 7.10. Elements undergoing fiber failure and matrix failure are colored red and blue. In Figure 7.10, from stages (i) to (iv), no damage growth is observed. Comparing stage (i) to (iv), near the top and bottom of the sample, minimal deformation along the z-axis is observed at the delaminated areas. Stages (iv) and (v) show a drastic change from the previous stages, with clear separation between the delaminated plies and the sample no longer being planar. μCT scanning of a layup C sample presented in Figure 6.18 also shows similar patterns of CAI-induced damage.

7.4 Computational CAI Study with the Effects of Panel Size

As reported in Chapter III, the CAI behavior of the L1/L2-M-24 and L1/L2-L-24/48 cases is involved with post-buckling. In order to numerically capture the post-buckling behavior, linear buckling analyses (eigenvalue problems) were conducted first to obtain the buckling modes. The buckling analyses were performed using Abaqus

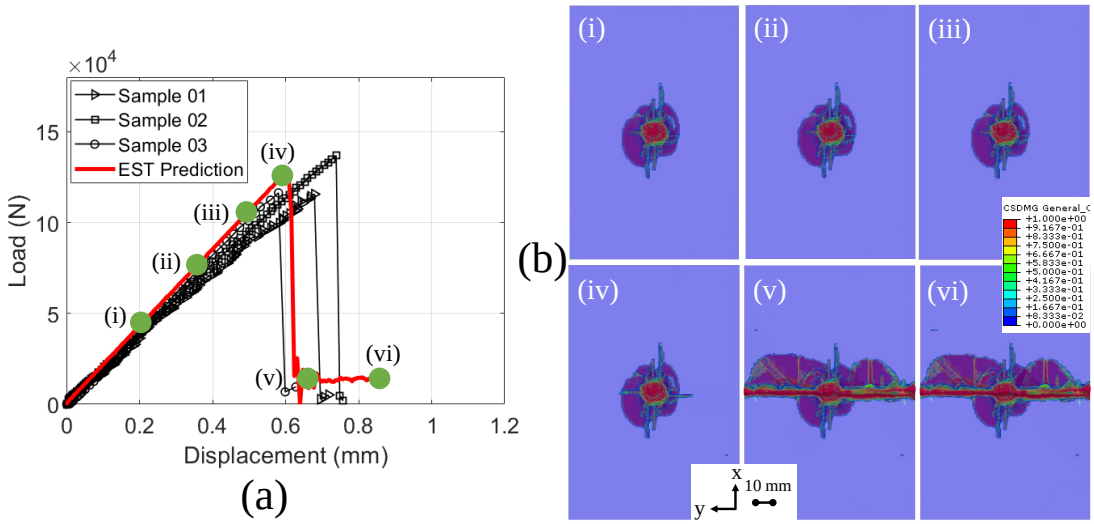

Figure 7.9: CAI-induced damage growth history of a layup B sample impacted with 35 J.

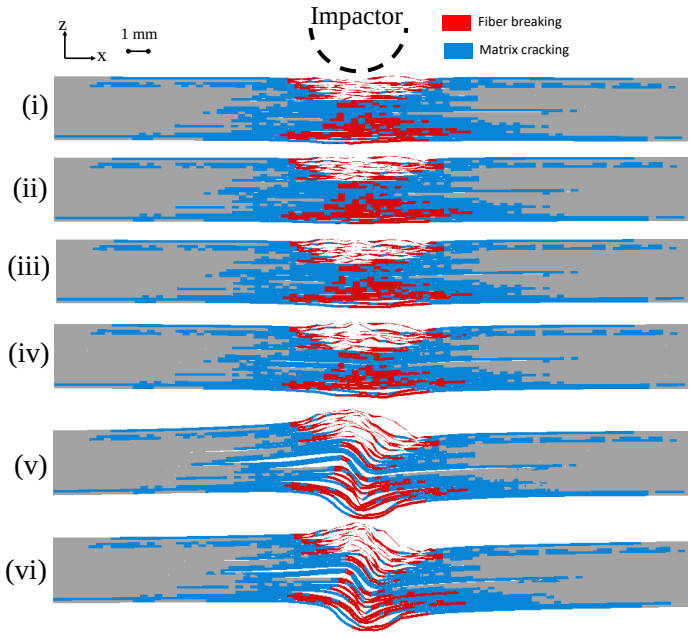

Figure 7.10: Cross-sectional views of a layup B sample impacted with 35 J during the CAI loading with the stages corresponding to Figure 7.9 (a)

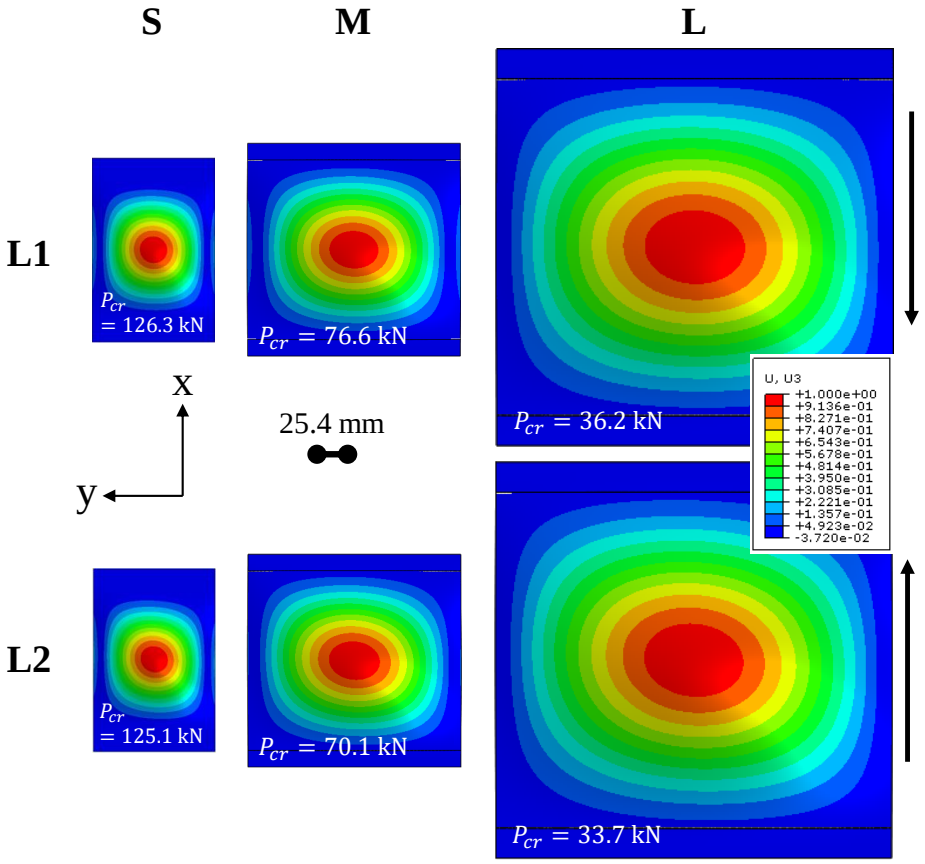

Figure 7.11: Results of the buckling analyses for the 24-ply samples.

built-in *Buckle option. For the L1/L2-M-24 and L1/L2-L-24/48 cases, the meshes of the buckling analyses and CAI analyses were identical.

The lowest buckling modes (corresponding to the lowest buckling loads) of the 24-ply samples and the 48-ply samples are shown in Figures 7.11 and 7.12. The compressive loading direction is along the x-axis, as noted in the figures. The buckling modes resemble half-sinusoidal-wave shapes. The critical buckling loads are also displayed in Figures 7.11 and 7.12.

CAI analyses were performed using 2D EST with Abaqus's explicit solver. For the L1/L2-M-24 and L1/L2-L-24/48 cases, geometric imperfections were seeded as geometric perturbation based on the lowest buckling mode shapes using the *Imperfection function of Abaqus. The magnitudes of the half-sinusoidal-wave imperfections

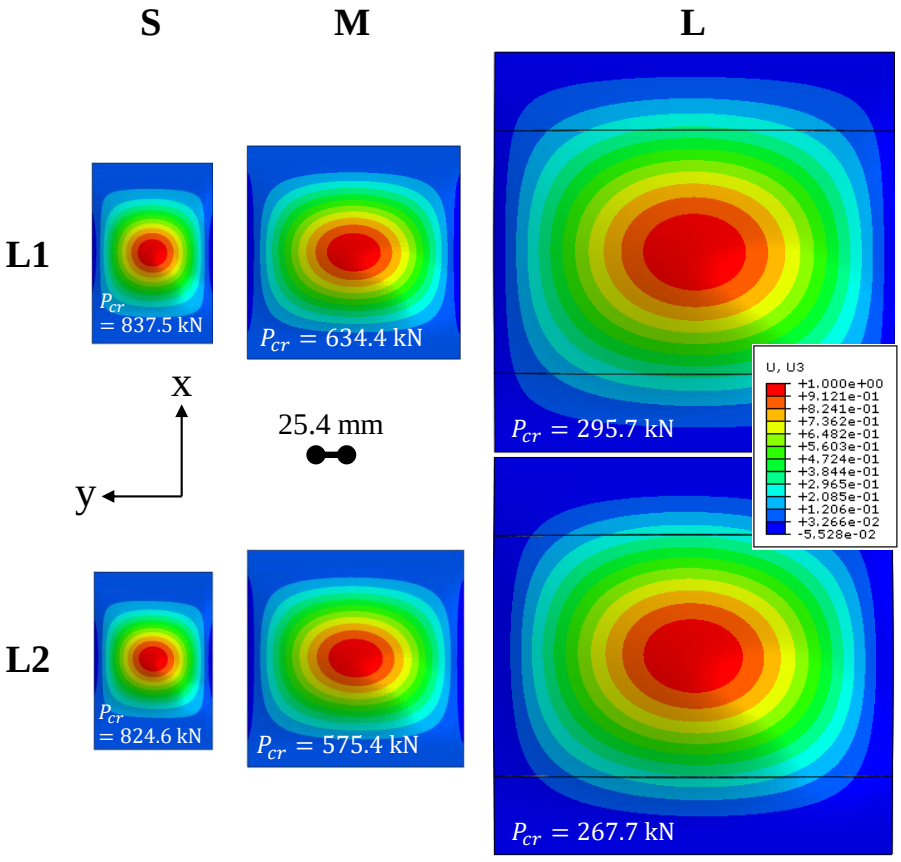

Figure 7.12: Results of the buckling analyses for the 48-ply samples.

were 3% of the total laminate thicknesses. For the L1/L2-S-24/48 and L1/L2-M-48 cases, where the CAI behavior was mostly in-plane, the analyses were carried out without initial geometric imperfections.

During the CAI tests for the cases with post-buckling, the supports were observed to be deformed by the samples due to their out-of-plane deformation. The supports were fixed by hex-head bolts. However, after the CAI studies, it is believed that this way of supporting is sufficient only for samples without significant out-of-plane deformation but might not be sufficiently rigid for samples undergoing post-buckling deformation during CAI tests. For CAI tests involved with the post-buckling behavior, it is strongly suggested that Devcon steel putty be used to fix the samples' top and bottom edges entirely.

To account for the insufficiency of the CAI supports, the effects of the support lengths were analyzed first. The support length is illustrated in Figure 7.1 (a). According to the tests, the length should be 12.7 mm. However, as shown in Figure 7.14, the post-buckling stiffness with the support length being 12.7 mm is much higher than the experimental values. The support length is indicated in Figure 7.1 (a). The predicted post-buckling stiffness matches the test values by reducing the support length from 12.7 mm to 3 mm. The support length being changed from 12.7 mm to 3 mm is illustrated in Figure 7.13. Another way to compensate for the effects of the support lengths is to use translational and rotational springs at the supported locations of the samples. Then, the stiffnesses of the springs need to be calibrated to predict the post-buckling stiffness accurately. After the preliminary studies, the support lengths for L1/L2-M-24, L1/L2-L-24, and L1/L2-L-48 cases have been determined to be 3 mm, 3 mm, and 6 mm.

The material properties of the IM7/977-3 material system used for the CAI predictions are listed in Table 7.2. The only difference between Tables 7.2 and 5.2 is that the compressive damage mode in the fiber direction is activated for the CAI analy-

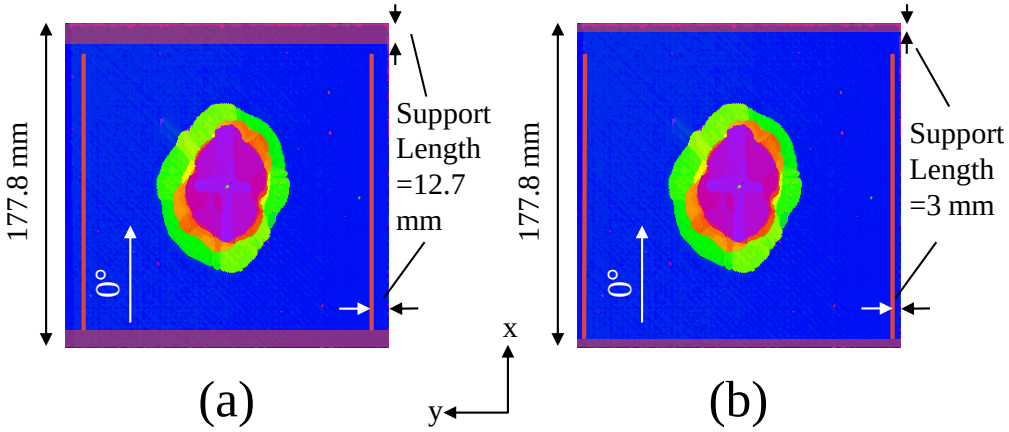

Figure 7.13: (a) The original support length of 12.7 mm, and (b) the calibrated support length of 3 mm.

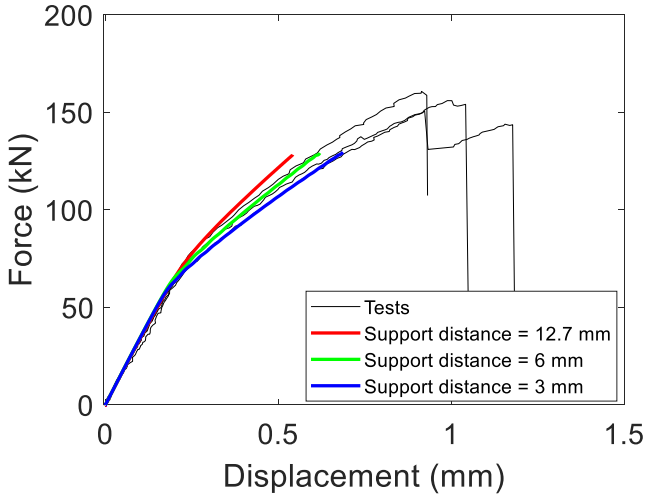

Figure 7.14: Study of the effects of the support lengths.

Table 7.2: Material properties of IM7/9773-3 used for CAI predictions

ρ	Density	$1.5 \times 10^{-9}\ t/mm^3$	measured
E_{11}	1-direction modulus	164,300 MPa	[120]
E_{22}	2-direction modulus	8,850 MPa	[120]
G_{12}	Shear modulus	6753 MPa	in-house tests
ν_{12}	Poisson's ratio	0.32	[120]
X_T	1-direction initiation strain (tension)	0.0177	[120]
X_C	1-direction initiation strain (compression)	0.0112	AFRL tests
Y_T	2-direction initiation strain (tension)	0.0147	[120]
Y_C	2-direction initiation strain (compression)	0.0279	[120]
Z_{12}	Longitudinal shear ini. strain	0.059	in-house tests
G_{IF}^T	Fiber mode I toughness in tension	40 N/mm	[21]
G_{IF}^C	Fiber mode I toughness in compression	10 N/mm	[21]
G_{IM}	Matrix mode I toughness	0.255 N/mm	Assumed identical to G_I
G_{IIM}	Matrix mode II toughness	0.896 N/mm	Assumed identical to G_{II}
σ_C	Interface normal strength	64 MPa	[119]
τ_C	Interface shear strength	79 MPa	Calibrated
G_I	Interface mode I toughness	0.255 N/mm	AFRL tests
G_{II}	Interface mode II toughness	0.896 N/mm	AFRL tests
G_{III}	Interface mode III toughness	0.896 N/mm	AFRL tests

ses. Previously, for the LVI analyses, the compressive strength of fiber was set to an arbitrary high value to avoid the initiation of fiber compressive damage since such damage was not seen in either the ultrasound C-scanning or μCT characterization.

7.4.1 Load Responses

The predicted CAI load-displacement responses are shown in Figure 7.15. The black curves are the experimental results. The red curves are predicted by 2D EST. For the L1/L2-S-24 cases, the predictions agree very well with the test data regarding the load-displacement stiffness and the peak load. For the L1/L2-M-24 cases, the transition loads, pre-buckling stiffnesses, and post-buckling stiffnesses are pre-

dicted well. The peak load of the L1-M-24 case is also predicted accurately. The predicted peak load of the L2-M-24 case seems to be slightly lower than the test results. In addition, the displacement value at which the CAI failure occurs is significantly underpredicted. Some jaggedness is seen on the experimental curves of the L2-M-24 samples, which indicate progressive damage. The jaggedness tends to lower the post-buckling stiffness. Therefore, the displacement values corresponding to the final failure are quite large in the test results. However, such a jaggedness is not seen on the predicted curve. Hence the predicted post-buckling stiffness remains the same until the final CAI failure. According to the out-of-plane deformation characterization by 3D DIC displayed in Figure 3.21, the CAI-induced damage go across the LVI-induced the damage. The jaggedness on the experimental curves is believed to be associated with delamination growth from the impacted area to the lateral edges. However, the progressive growth of the CAI-induced damage is not captured by 2D EST. This explains why the predicted displacement at which CAI failure occurs is significantly lower than the experimental values.

For the L1/L2-L-24 cases, the predicted curves agree very well with the test data in terms of the initial stiffness, post-buckling stiffness, transition loads, and peak loads. There seems to be some small-scale oscillations on the curves after the transition points. It should be pointed out that data smoothening was performed for the L1/L2-L-24 cases. The reason for the smoothening was that relatively high oscillations were seen on the curves. This is the nature of post-buckling analysis using an explicit solver. After the CAI failure, the predicted curves of the L1/L2-L-24 samples do not drop to low load values, similar to that for the L1/L2-S/M-24 cases. The reason is believed to be that the predicted damage does not completely go across the width direction of the samples, as shown in Figure 7.17.

The predicted load-displacement curves of the 48-ply samples are shown in Figure 7.16. For the L1-S-48 sample, the prediction agrees very well with the test results. For

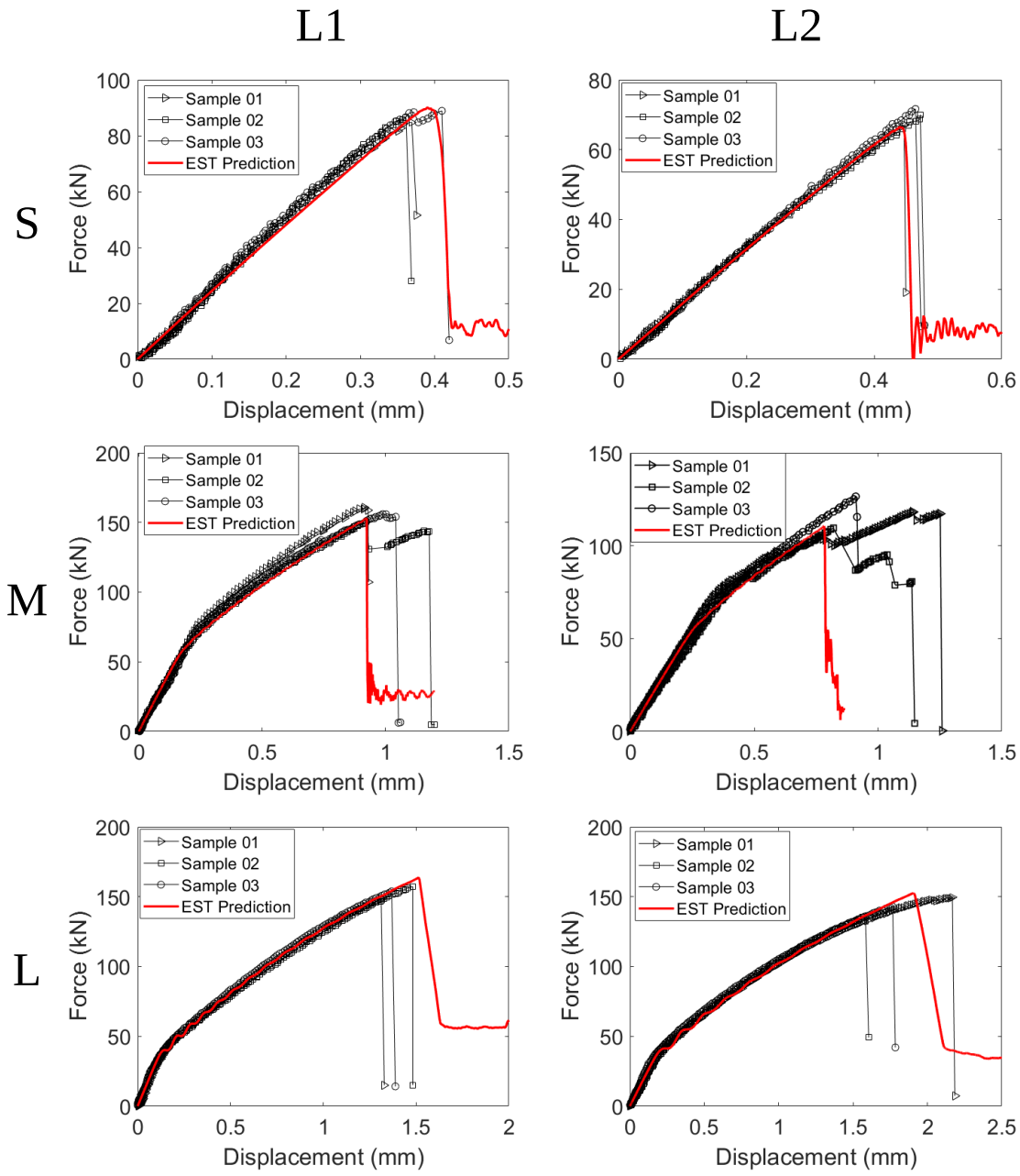

Figure 7.15: Predicted CAI load-displacement responses of the 24-ply samples.

the L2-S-48 case, the peak load is underpredicted. For the L1-M-48 sample, the initial stiffness seems to be slightly underpredicted. The peak load is predicted well. For the L2-M-48 case, the initial stiffness is captured accurately. However, after 0.2 mm, the predicted stiffness degrades slightly, which is not observed in the experimental curves. After 0.5 mm, the load grows very slowly. The slow increase of the load is believed to be due to the predicted damage growth being too progressive. Due to this effect, the predicted displacement at which the CAI failure occurs is significantly higher than the test values. For the L1-L-48 case, the initial stiffness is slightly overpredicted. The peak load is captured very well. However, the predicted damage growth is not as progressive as the test results. Accordingly, the predicted load drops too fast compared to the test results. For the L2-L-48 case, the initial stiffness and the peak load are predicted well. Again, the predicted load drops too soon compared to the test curves, meaning that the predicted CAI damage is not progressive enough.

7.4.2 CAI-induced Damage

The predicted CAI-induced damage footprints of the 24-ply samples are shown in Figure 7.17. The blue part represents LVI-induced damage transferred from the middle of the corresponding LVI analysis in each subfigure. The red part indicates the newly developed damage induced by the CAI loading. For the L1/L2-S-24 samples, the new CAI-induced damage forms a narrow band going across the width direction of the samples along the y-axis. For the L1-M-24 sample, the damage pattern is quite different. The major damage seems to take place away from the LVI-induced damage footprint. The damage footprint of the L2-M-24 sample is similar to that of the L1/L2-S-24 samples. For the L1/L2-L-24 samples, the damage pattern is similar to that of the L1-M-24 case, while the predicted damage seems to be not fully developed. For the L1/L2-L-24 samples, it is observed that the predicted damage does not go across the width direction completely. This correlates well with the fact that the predicted

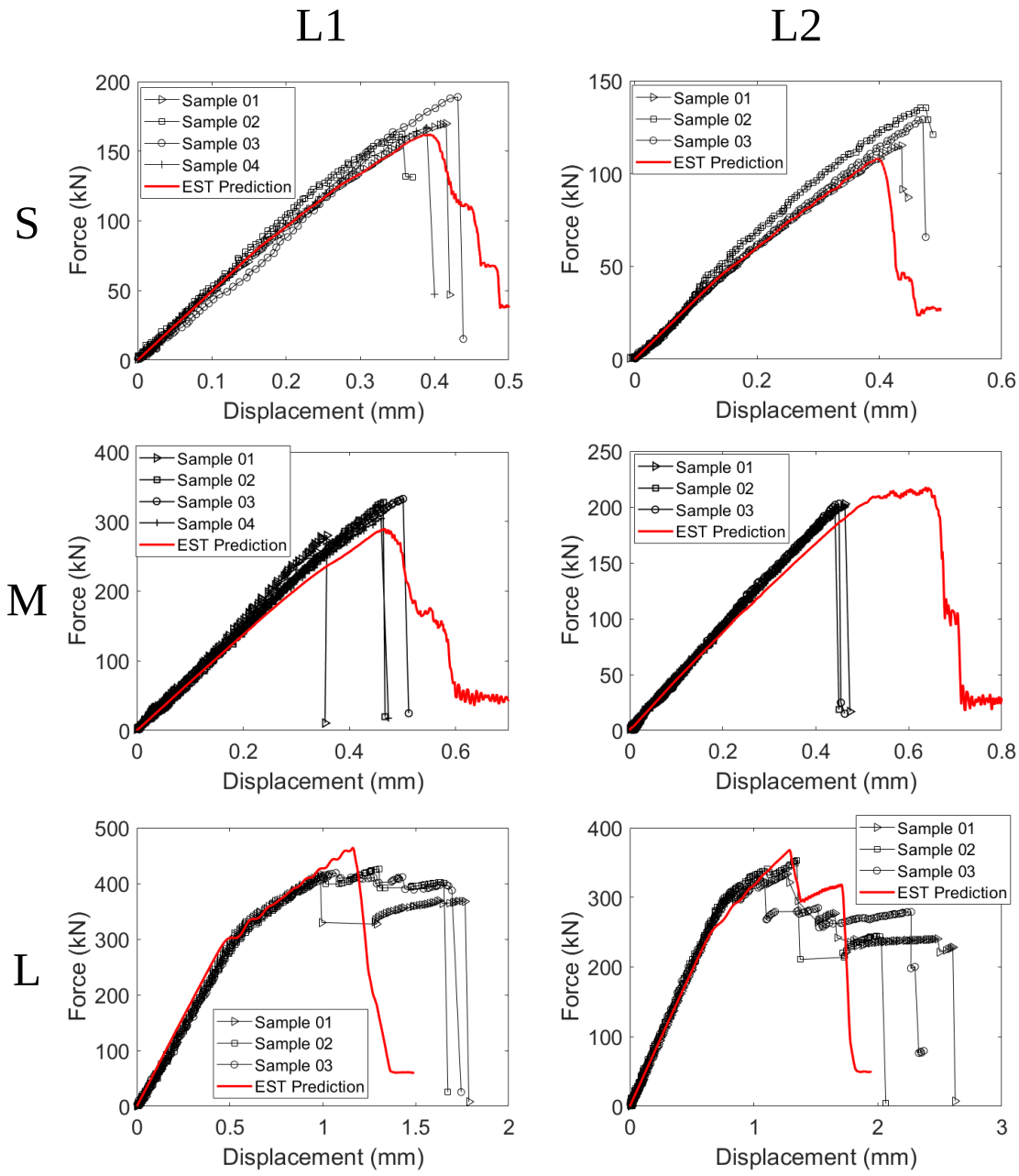

Figure 7.16: Predicted CAI load-displacement responses of the 48-ply samples.

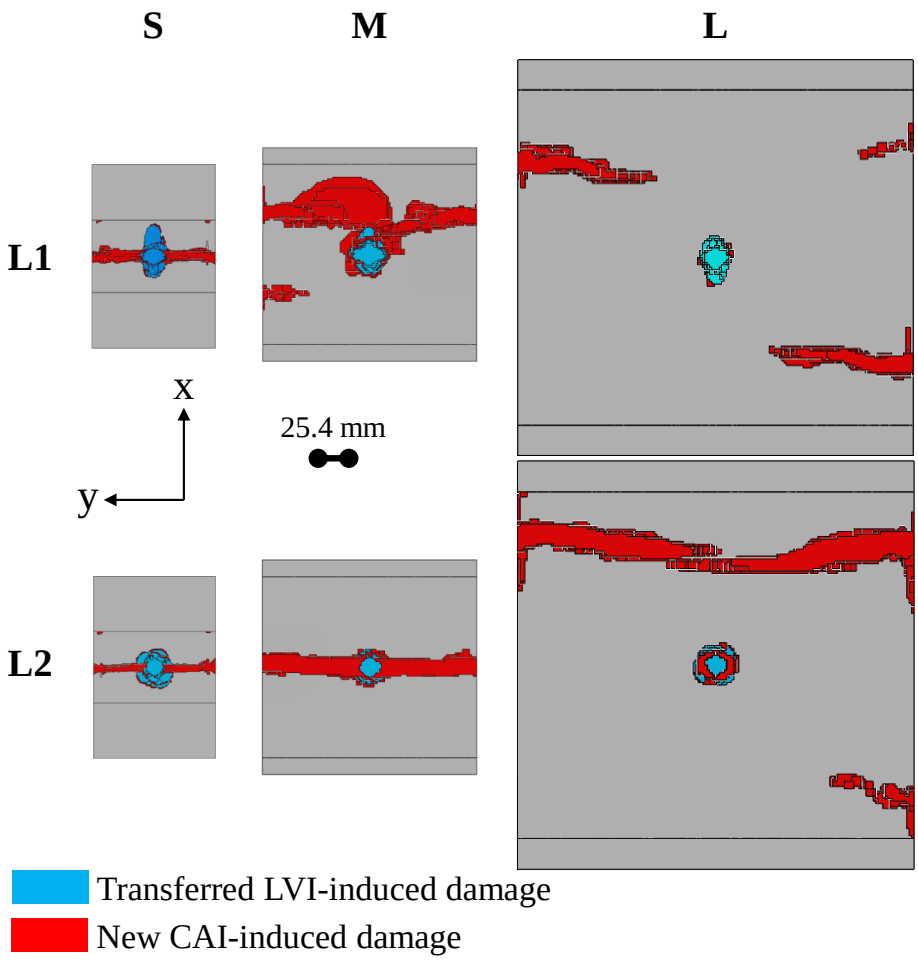

Figure 7.17: Predicted CAI-induced damage footprints of the 24-ply samples.

loads did not drop to small values, as shown in Figure 7.15. In Figure 7.17, the CAI-induced damage footprints of the L1/L2-L-24 cases clearly show that the newly developed damage does not originate from the LVI-induced damage footprints. This might be explained by the stress analysis presented in Figure 7.18. In Figure 7.18, the σ_{11} field of a L1-M-24 sample under CAI loading is shown. The bending direction is noted in the figure with the dashed arrow. It is seen that hot spots of compressive σ_{11} (minimum value) take place far from the plate center due to the post-buckling induced out-of-plane deformation. The hot spots of compressive σ_{11} correlate well with the locations of CAI-induced damage of the L1-M-24 and L1/L2-L-24 cases.

The CAI-induced damage footprints of the 48-ply samples predicted by 2D EST

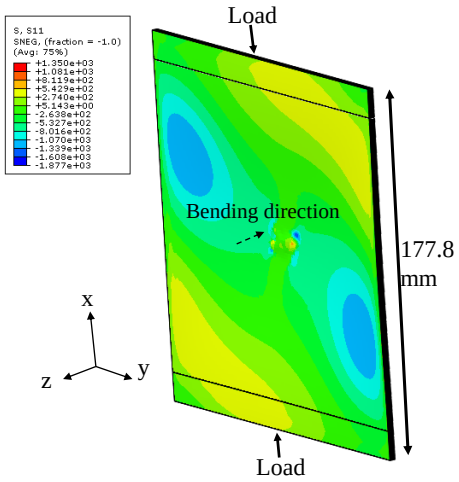

Figure 7.18: Stress contour of a compressed L1-M-24 sample.

are displayed in Figure 7.19. The damage patterns shown in all the subfigures are uniform: the newly developed CAI-induced damage forms failure bands going across the samples' width direction (along the y-axis). The failure bands are not obvious for the L1/L2-S-48 samples since the LVI-induced damage is already large and close to the samples' edges. For the L1/L2-M/L-48 samples, the failure bands are narrow and spanning across the LVI-induced damage footprints.

The damage growth histories of the L1/L2-S-24 samples are shown in Figures 7.20 and 7.21. In both figures, the damage growth is minimal from stage (i) to (ii). After the load drops, the failure bands are seen. This trend agrees well with that shown in Figure 7.9.

The predicted damage growth histories of the L1/L2-S-48 samples are shown in Figure 7.22 and 7.23. Again, the damage growth is minimal for both samples from the origins to the stages immediately before the peak CAI loads. Accompanying the load drops, from stage (i) to (ii) for the L1-S-48 sample and from stage (ii) to (iii) for the L2-S-48 sample, the damage develops progressively, but not to the edges of the samples. For the L1-S-48 sample, after stage (ii), it seems that every time load decreases significantly, damage develops. For the L2-S-48 sample, the damage also grows progressively and finally connects to the edges, as shown in stage (iv).

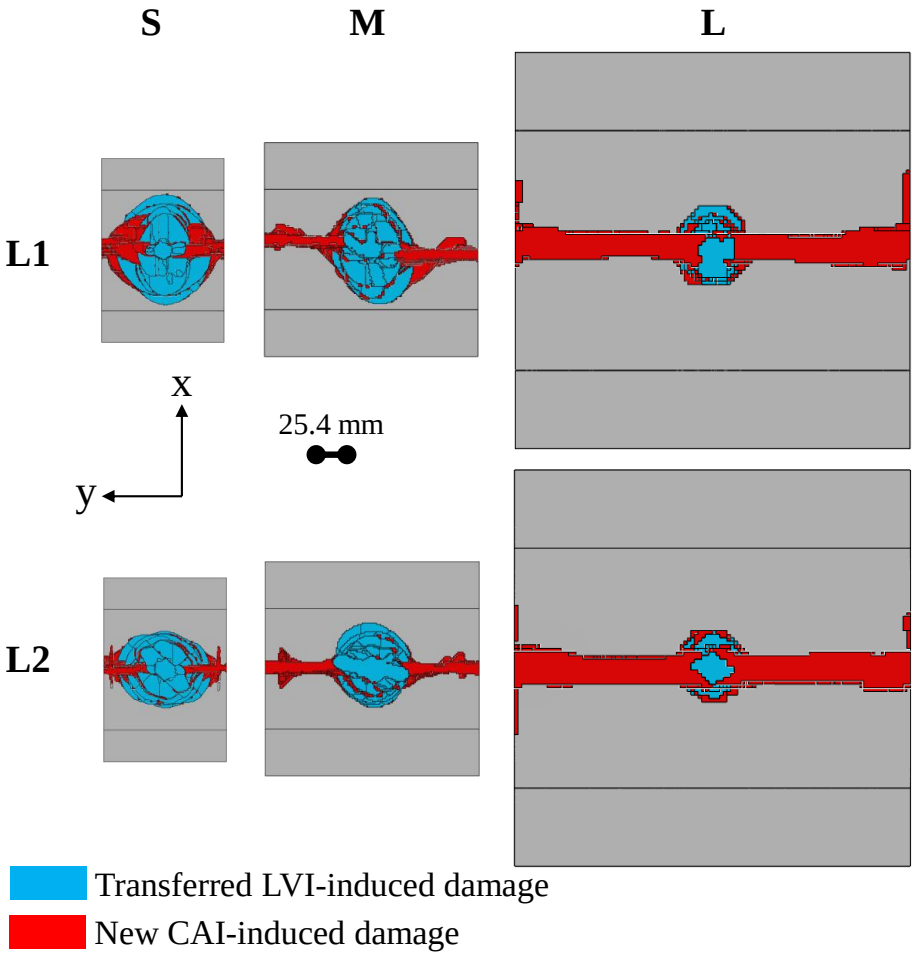

Figure 7.19: Predicted CAI-induced damage footprints of the 48-ply samples.

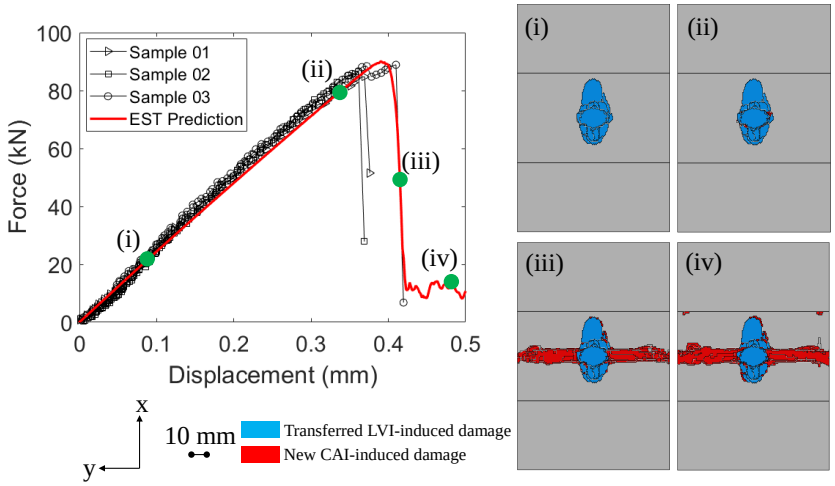

Figure 7.20: Predicted CAI-induced damage growth history of an impacted L1-S-24 sample.

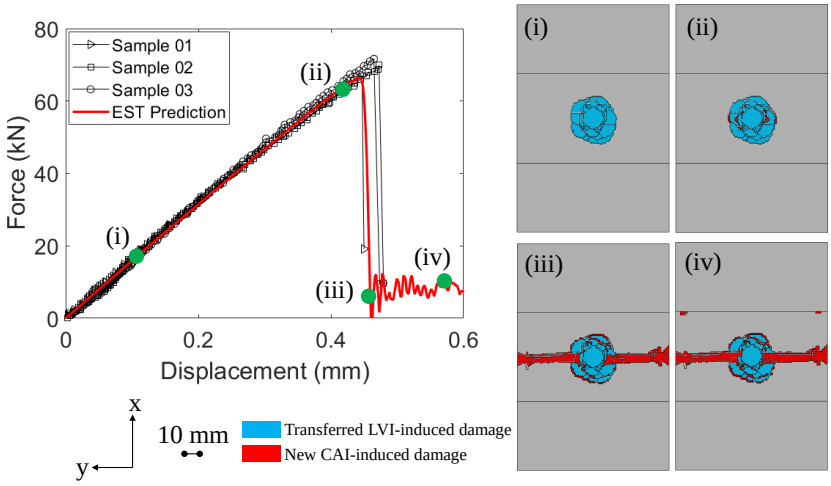

Figure 7.21: Predicted CAI-induced damage growth history of an impacted L2-S-24 sample.

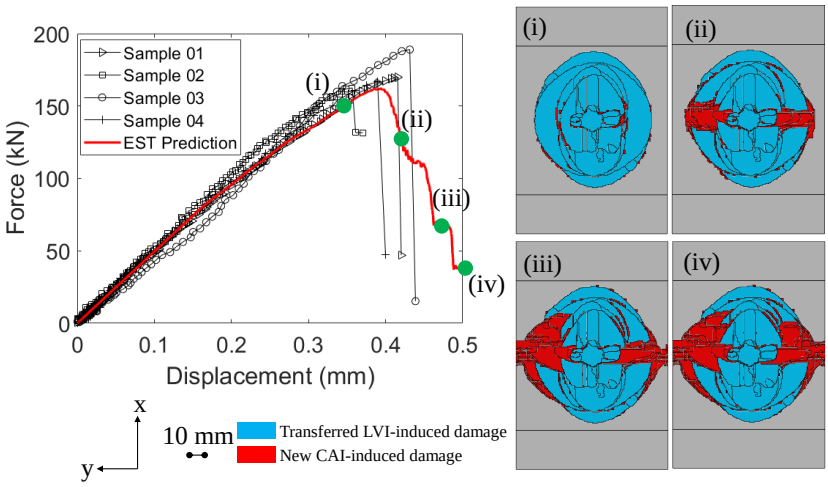

Figure 7.22: Predicted CAI-induced damage growth history of an impacted L1-S-48 sample.

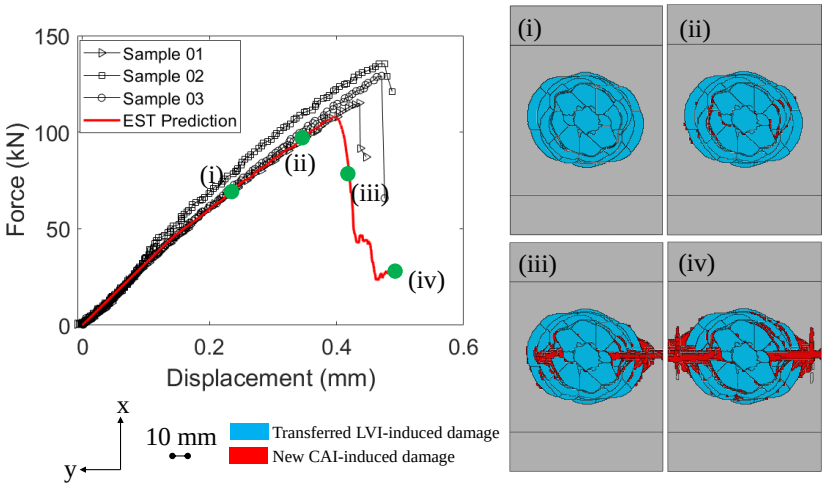

Figure 7.23: Predicted CAI-induced damage growth history of an impacted L2-S-48 sample.

The predicted damage growth history of the L1-M-24 sample is illustrated in Figure 7.24. As shown in Figure 7.24, from stage (i) to (ii), there is no damage growth although with out-of-plane deformation due to post-buckling. The damage growth is drastic from stage (ii) to (iii), associated with the load drop on the predicted load-displacement curve.

The evolution of the out-of-plane deformation field of the L1-M-24 sample is displayed in Figure 7.25. Initially, from stage (i) to (ii), the deformation stays in-plane. Then, as buckling and post-buckling takes place, the out-of-plane deformation is seen and keeps growing. At stage (v), the deformation field similar to the first mode shape is disturbed after the load drop due to the failure band. Comparing the deformation field at stage (v) with the 3D DIC characterization, it is seen that the sharp deformation discontinuities do not go across the samples' centers. This implies that for the experimental and computational analyses, the CAI-induced damage is not primarily caused by the LVI-induced damage, but by the stress hot spots of σ_{11}, as shown in Figure 7.18.

The damage growth history of the L2-M-24 sample is highly similar to that of the L1/L2-S-24 samples. The damage growth is drastic, from stage (iii) to (iv) in

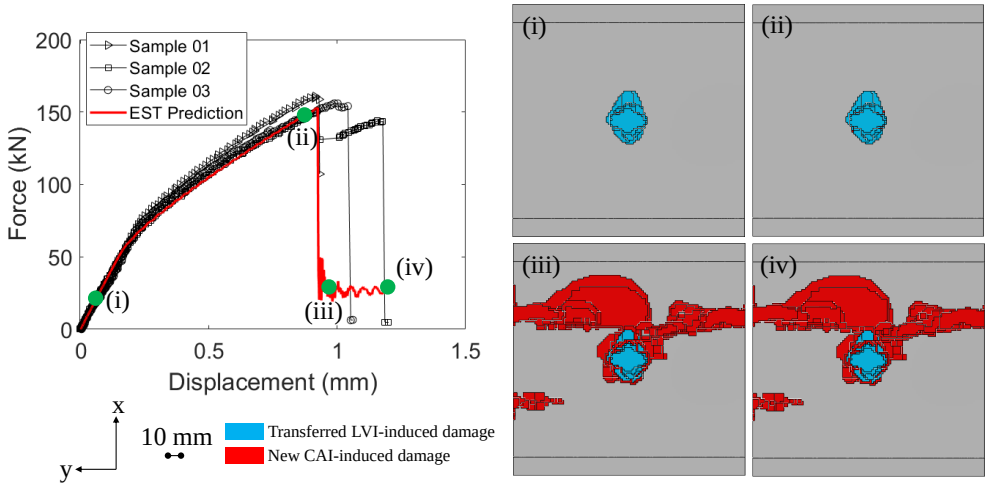

Figure 7.24: Predicted CAI-induced damage growth history of an impacted L1-M-24 sample.

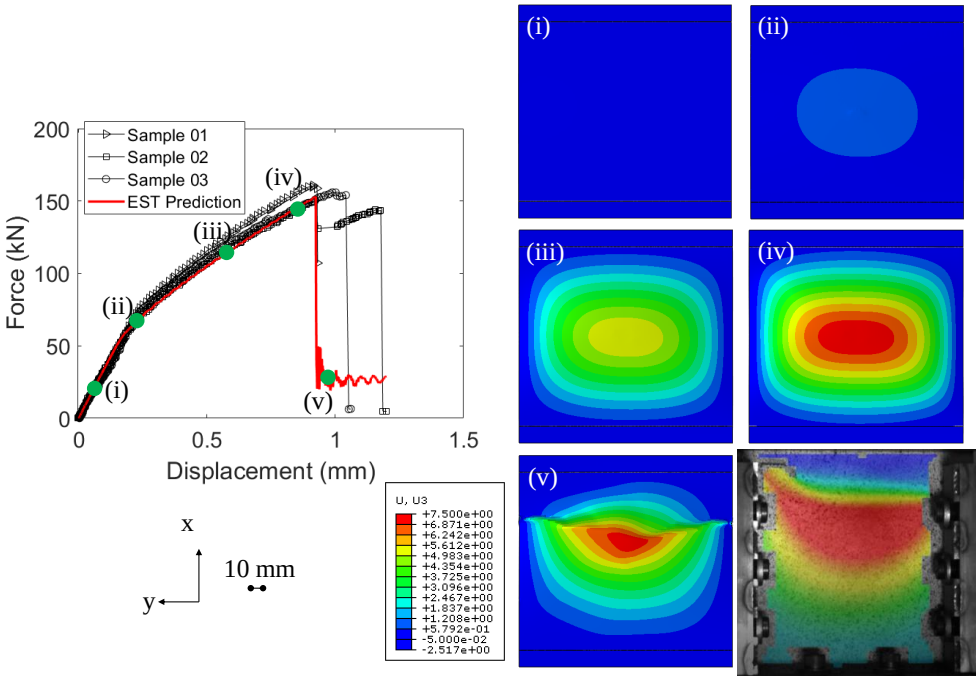

Figure 7.25: Predicted CAI out-of-plane deformation history of an impacted L1-M-24 sample.

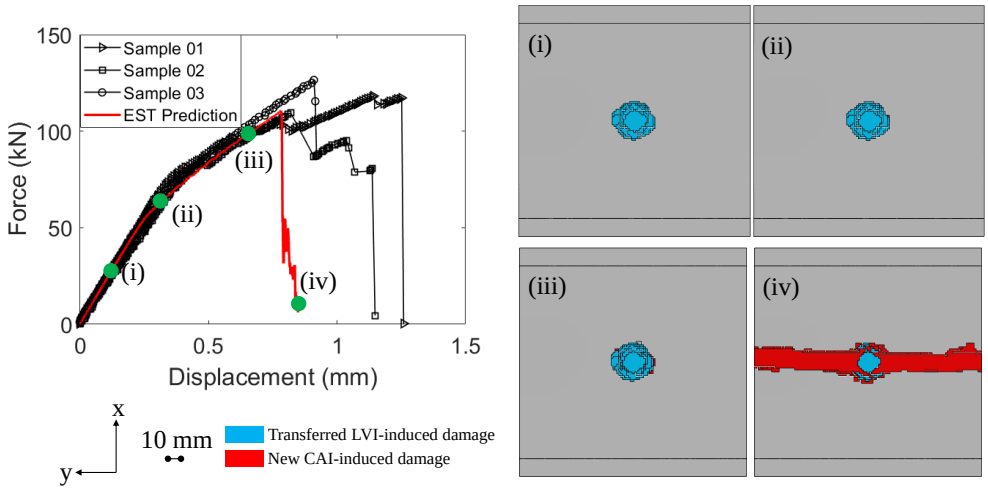

Figure 7.26: Predicted CAI-induced damage growth history of an impacted L2-M-24 sample.

Figure 7.26, along with the sharp load drop. The deformation field is shown in Figure 7.27. Similar to Figure 7.25, in Figure 7.27, the out-of-plane deformation starts and develops after stage (ii), after the transition load. The deformation discontinuities in both the predicted and experimentally characterized deformation fields imply that the CAI-induced failure goes across the center of the sample, as shown in Figure 7.26.

The predicted damage growth of the L1-M-48 sample is shown in Figure 7.28. Similar to that of the L1/L2-S-48 samples, before the peak load, the damage grows marginally from stage (i) to (ii). Stages (iii) and (iv) show the development of the damage towards the sample's lateral edges.

The predicted damage growth of the L2-M-48 sample is displayed in Figure 7.29. Similar to the L1-M-48 sample, at stages (i) and (ii), there is barely any damage growth. From stages (ii) to (iii), the damage grows by a small amount, which seems not sufficient to cause a load drop, but significantly degrades the stiffness. After the load drop, the failure band is formed across the sample's center.

The damage growth of the L1-L-24 sample is seen in Figure 7.30. From the figure, it is clear that the damage initiates close to the edges and the stress hot spots of the sample. Contrary to the damage growth histories of the samples without

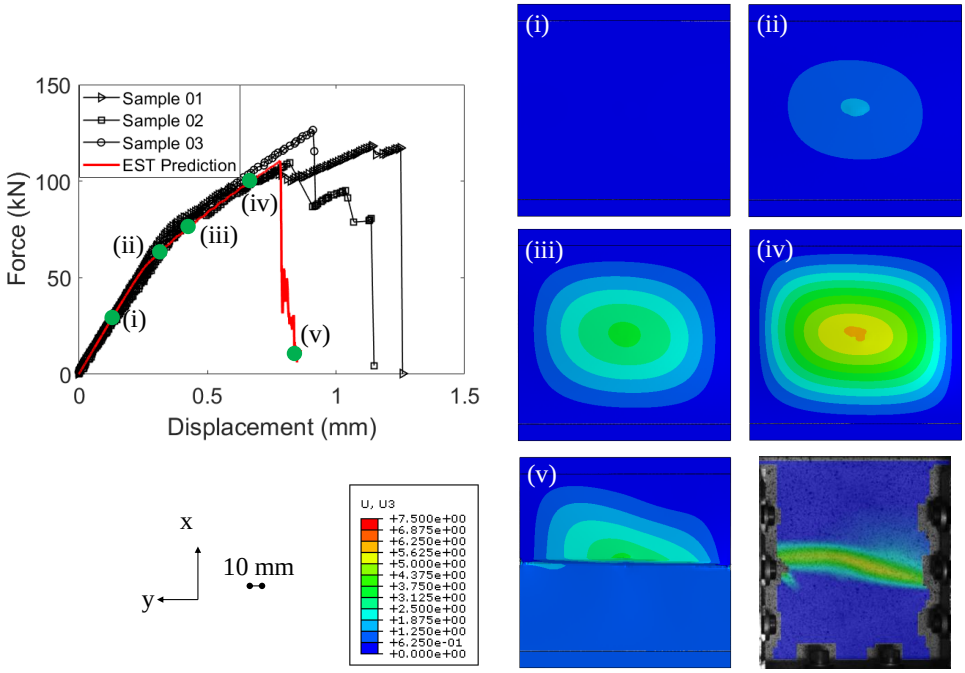

Figure 7.27: Predicted CAI out-of-plane deformation history of an impacted L2-M-24 sample.

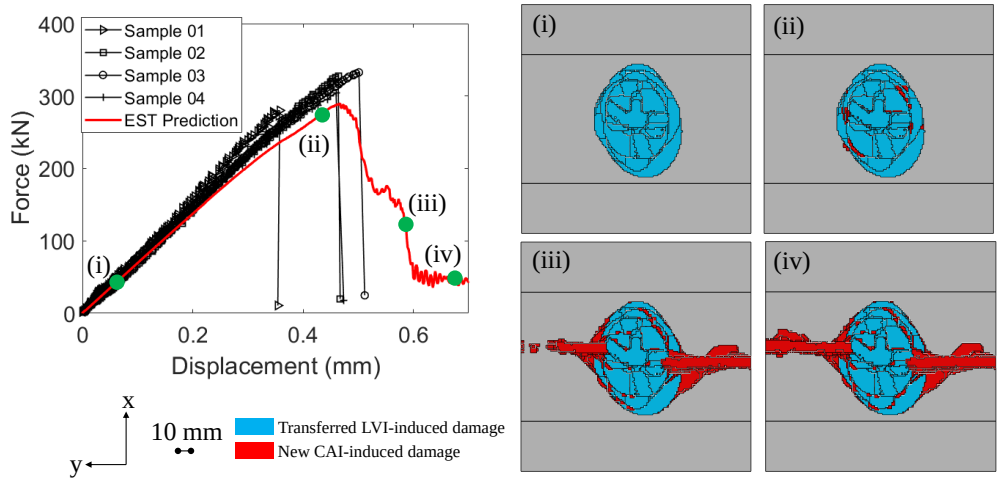

Figure 7.28: Predicted CAI-induced damage growth history of an impacted L1-M-48 sample.

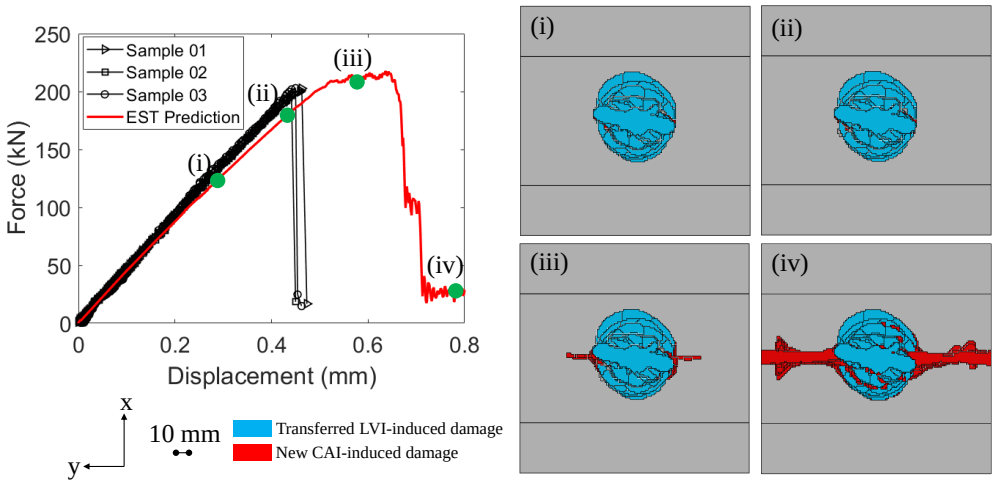

Figure 7.29: Predicted CAI-induced damage growth history of an impacted L2-M-48 sample.

post-buckling (L1/L2-S-24/48 and L1/L2-M-48), the damage of the L1-L-24 sample develops from the edges towards the middle of the sample. The predicted out-of-plane deformation is displayed in Figure 7.31. After the initiation of damage (after the load drop), the buckling mode is disturbed. From stage (iv) to (v), with the growth of damage, the magnitude of the deformation increases with the shape staying still. The predicted out-of-plane deformation field is different from the experimentally characterized field. This might be due to the different locations where damage initiates and develops. It should be pointed out that four stages are shown in Figure 7.30 while Figure 7.31 contains five stages. The additional stage corresponds to stage (ii) in Figure 7.31. The reason for not showing the corresponding stage in Figure 7.30 is that there is no damage growth from stage (i) to stage (ii).

The predicted damage growth history and out-of-plane deformation field of the L2-L-24 sample (displayed in Figures 7.32 and 7.33) are very similar to that of the L1-L-24 sample. The deformation field at stage (v) in Figure 7.33 seems to be various from the 3D DIC characterization. Again, this might be due to the different locations where damage initiates and develops. The incorrect prediction of the damage initiation location might be due to manufacturing-induced defects, randomness in the

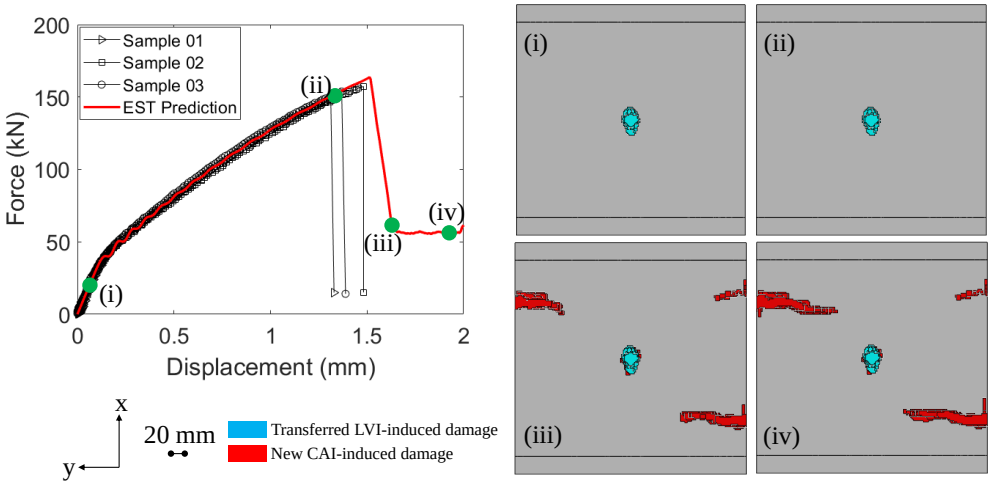

Figure 7.30: Predicted CAI-induced damage growth history of an impacted L1-L-24 sample.

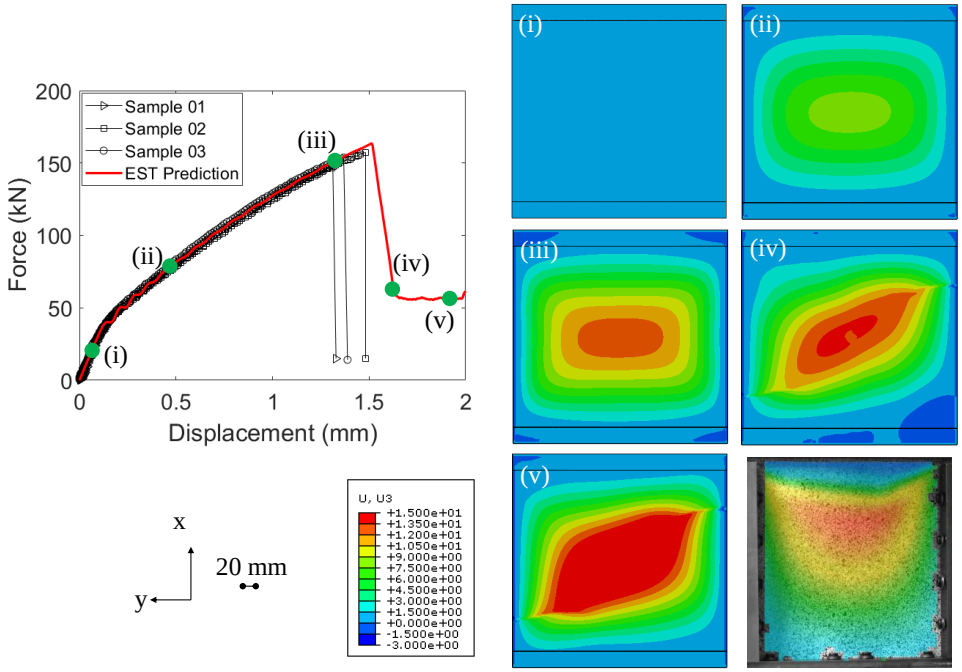

Figure 7.31: Predicted CAI out-of-plane deformation history of an impacted L1-L-24 sample.

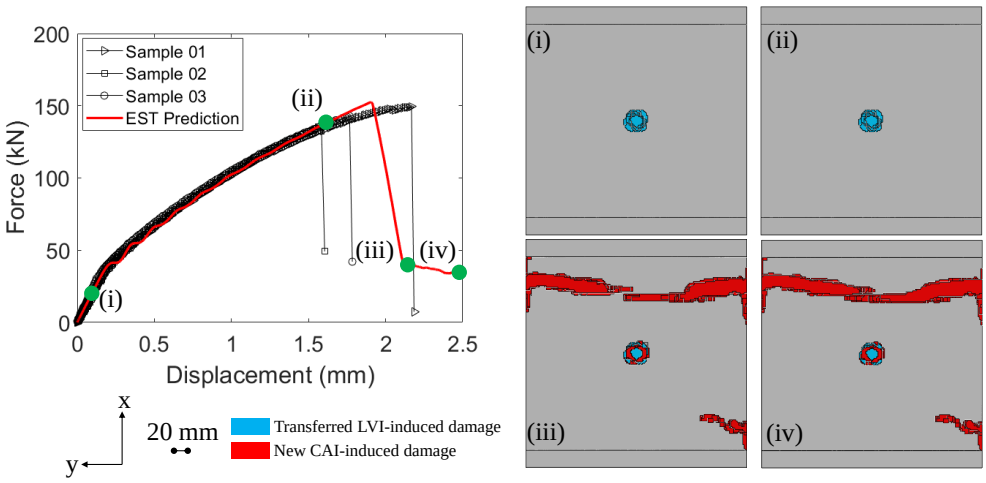

Figure 7.32: Predicted CAI-induced damage growth history of an impacted L2-L-24 sample.

distribution of material properties, and imperfect alignment of the CAI fixtures.

The damage growth history of the L1-L-48 sample is shown in Figure 7.34. The damage growth is minimal from stage (i) to (ii), although with post-buckling. A sudden load drop happens after stage (ii). At stage (iii), a failure band cutting across the sample is formed. From stage (iii) to (iv), the damage gets slightly larger near the lateral edges of the sample. The out-of-plane deformation field is displayed in Figure 7.35. It should be noted that the out-of-plane deformation direction characterized by 3D DIC is in the reverse direction of the prediction. Therefore, the color code of the numerical results has been adjusted to use the "reverse rainbow" pattern to acquire a better visual comparison. The predicted deformation field at stage (v) agrees well with that characterized by 3D DIC.

The damage growth history of the L2-L-48 sample is very similar to that of the L1-L-48 sample, as shown in Figure 7.36. After the peak load, the damage initiates at both the impacted center and the lateral edges. The growth of the damage areas and their connectivity indicate the final CAI failure. The predicted out-of-plane deformation field in Figure 7.37 shows that after stage (ii), the buckling mode is affected by the damage growth. At stage (v), the deformation discontinuity is in the

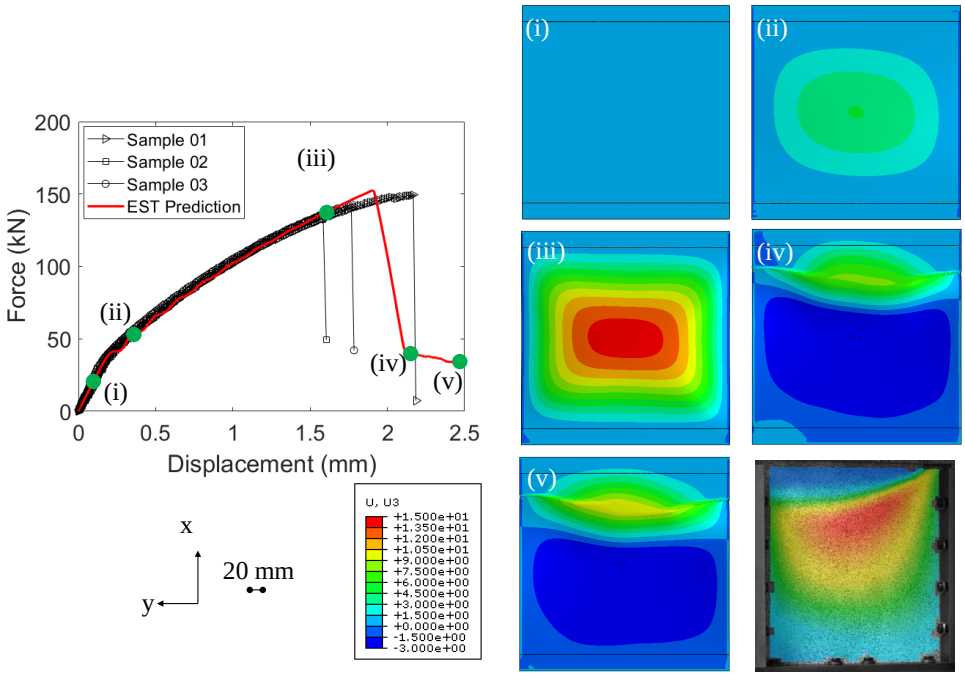

Figure 7.33: Predicted CAI out-of-plane deformation history of an impacted L2-L-24 sample.

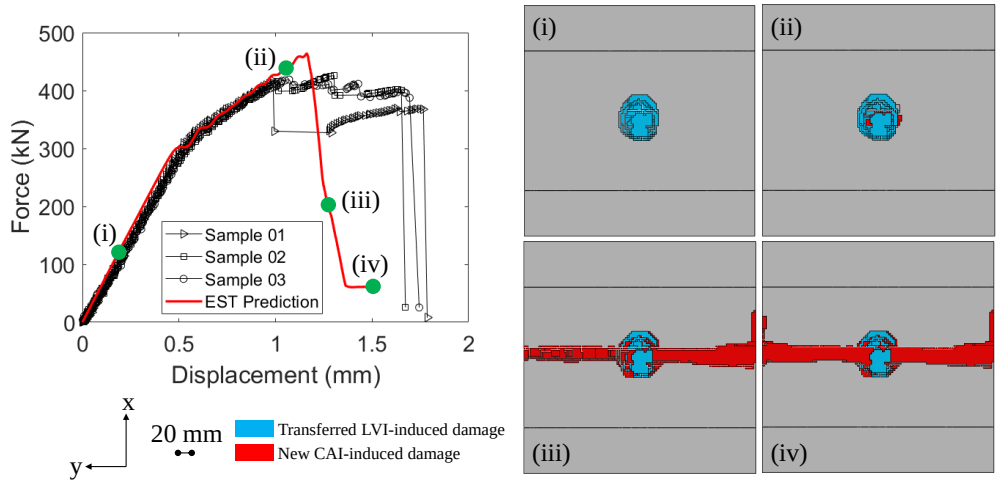

Figure 7.34: Predicted CAI-induced damage growth history of an impacted L1-L-48 sample.

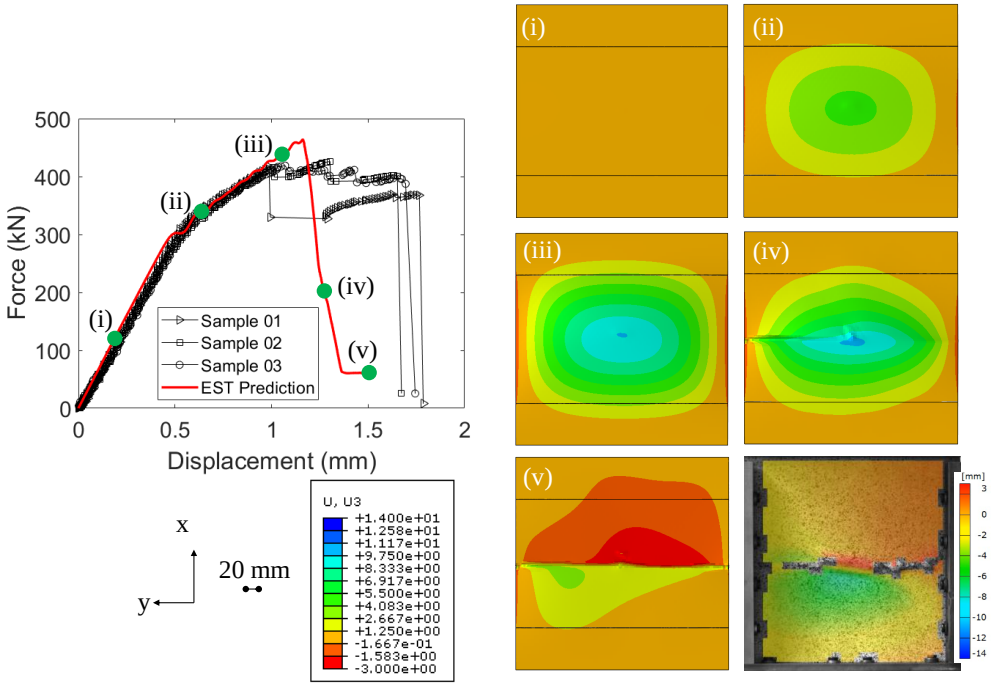

Figure 7.35: Predicted CAI out-of-plane deformation history of an impacted L1-L-48 sample.

form of a band going across the width direction of the sample. However, the out-of-plane deformation field characterized by 3D DIC is much larger than the prediction. This is believed to be the extensive delamination occurring in the actual samples not being predicted.

The predicted CAI-induced damage footprints are compared to the ultrasound C-scanning of the L2-S-24, L2-S-48, L1-M-24, L1-M-48, L2-L-24, and L2-L-48 samples in Figures 7.38 to 7.43. From the figures, in general, the location of CAI-induced damage is captured correctly. However, the sizes of the damage footprints are underpredicted. As seen in Figures 7.40 and 7.42, the CAI-induced damage seems to be not concentrated around the impacted area, which has been predicted well. As demonstrated in Figures 7.15 and 7.16, the load-displacement curves are predicted well until the peak loads. The pre-transition stiffness and post-buckling behavior are captured accurately. However, the damage growth reflected on the load-displacement curves seems to be excessively progressive or insufficiently progressive for some cases.

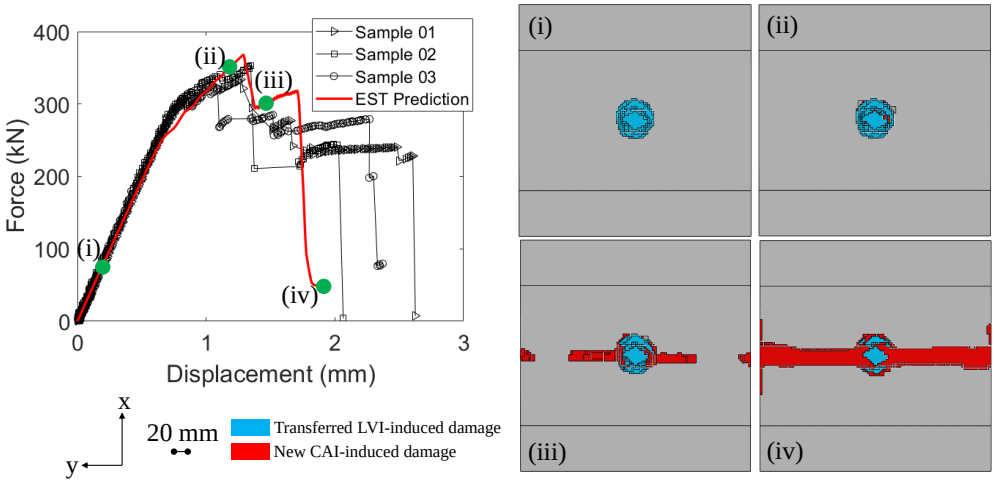

Figure 7.36: Predicted CAI-induced damage growth history of an impacted L2-L-48 sample.

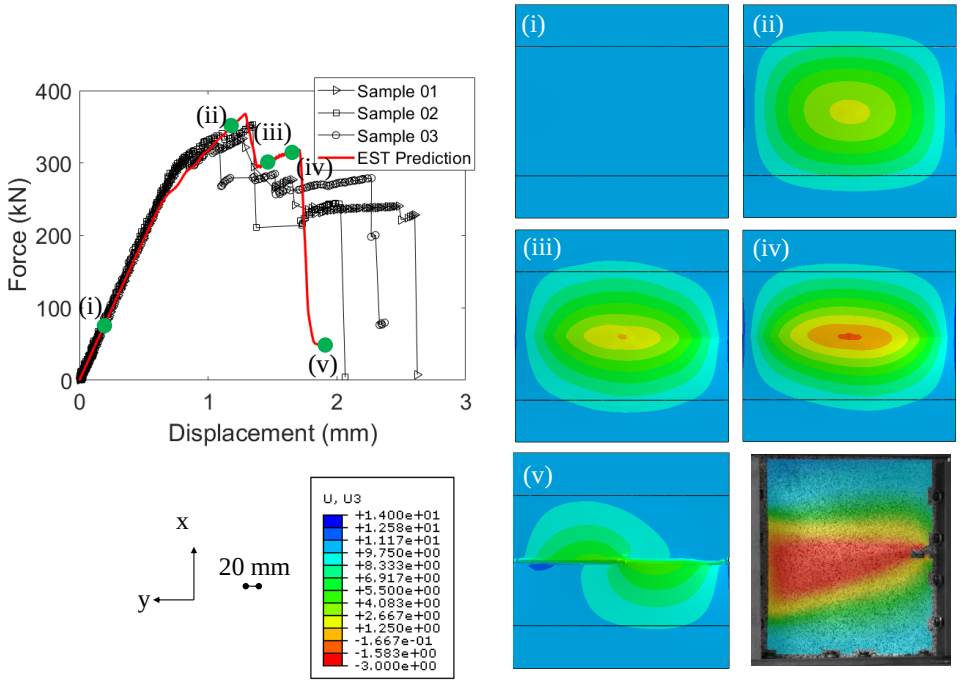

Figure 7.37: Predicted CAI out-of-plane deformation history of an impacted L2-L-48 sample.

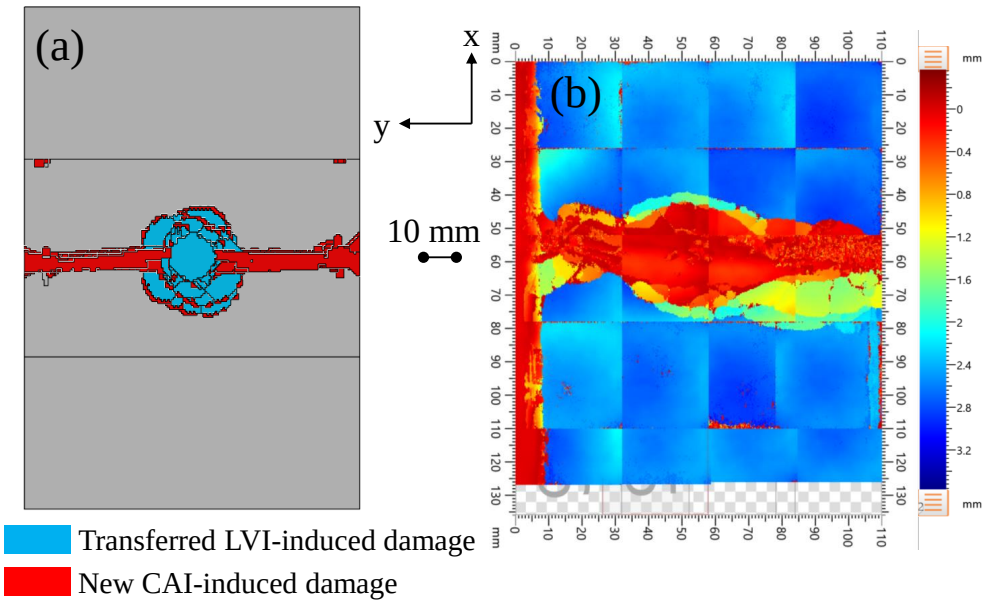

Figure 7.38: Predicted CAI-induced damage vs. ultrasound scanning of the L2-S-24 sample.

This difference might be caused by the underprediction of CAI-induced damage as shown in Figures 7.38 to 7.43. More investigation needs to be done to improve the damage development prediction of the CAI analysis.

7.4.3 Parameter Study on the Interfacial Properties

As shown in Figures 7.38 to 7.43, overall, the predicted CAI-induced damage is smaller than the scanned damage, especially for the L1/L2-L-48 samples. In this section, parameter studies with respect to interfacial shear strength and mode II/III toughness will be performed to investigate their effects on the CAI responses. Interfacial material properties including shear strength τ_C and mode II/III toughness $G_{II/III}$ are studied with respect to a L1-L-48 sample.

The effects of τ_C on the CAI responses are demonstrated in Figure 7.44. From the figure, with τ_C decreasing from 79 MPa to 20 MPa, the CAI-induced damage footprint

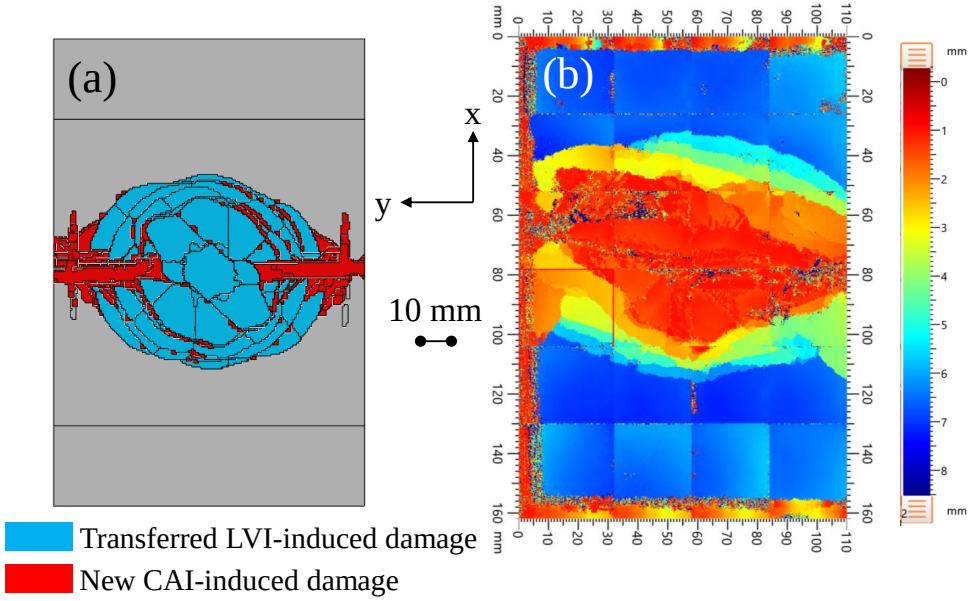

Figure 7.39: Predicted CAI-induced damage vs. ultrasound scanning of the L2-S-48 sample.

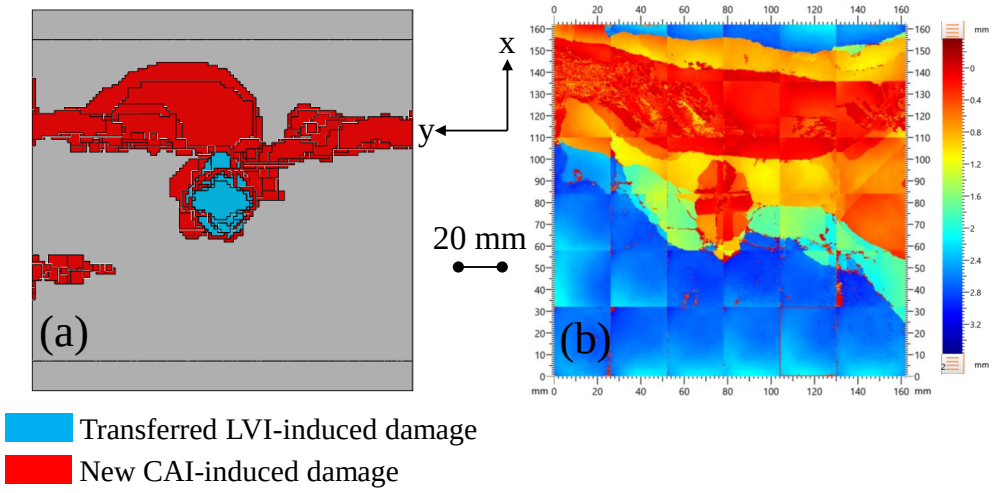

Figure 7.40: Predicted CAI-induced damage vs. ultrasound scanning of the L1-M-24 sample.

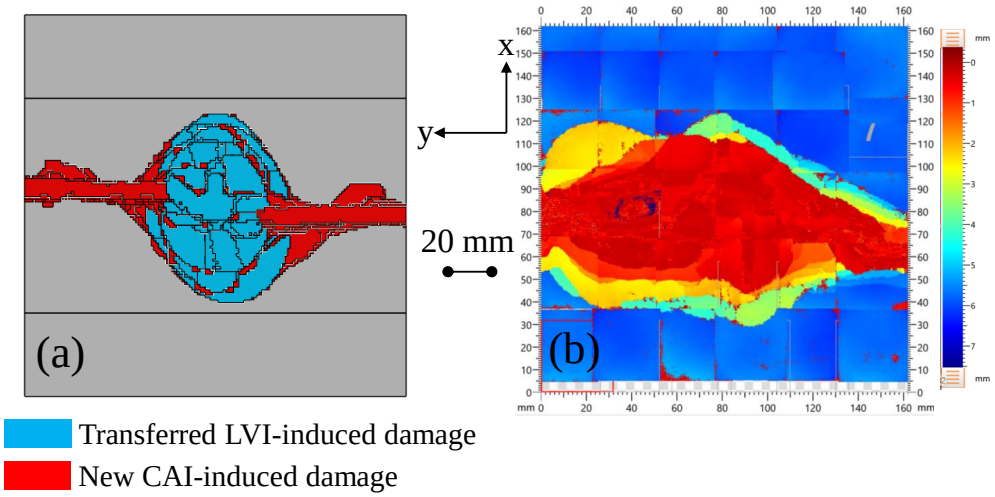

Figure 7.41: Predicted CAI-induced damage vs. ultrasound scanning of the L1-M-48 sample.

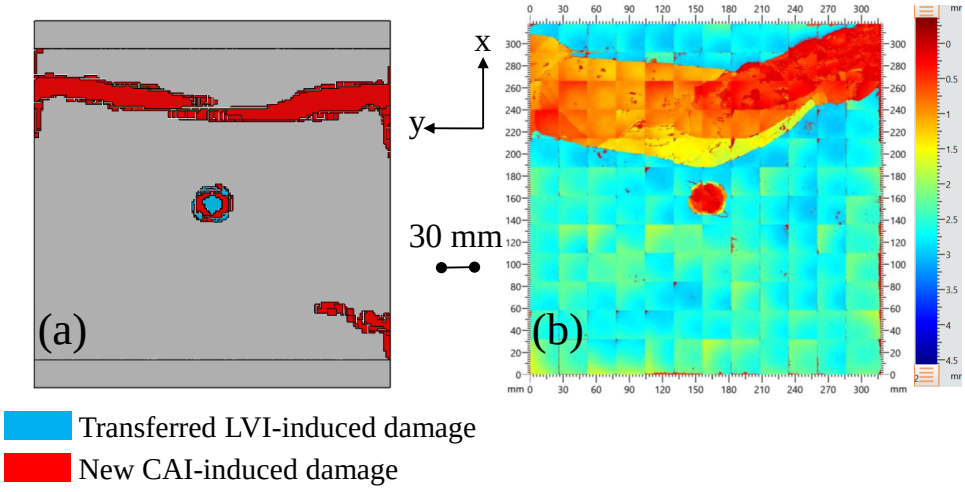

Figure 7.42: Predicted CAI-induced damage vs. ultrasound scanning of the L2-L-24 sample.

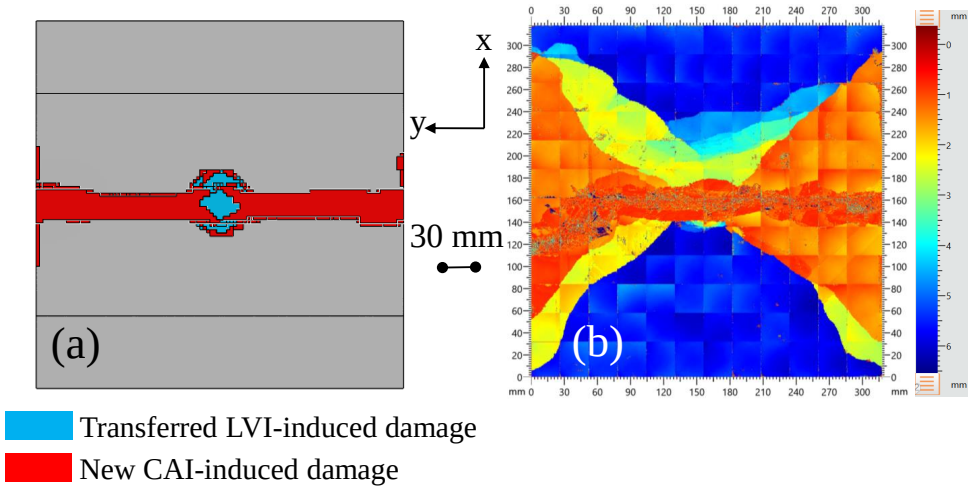

Figure 7.43: Predicted CAI-induced damage vs. ultrasound scanning of the L2-L-48 sample.

gets closer to the scanned damage in Figure 7.44 (b) but still smaller than the scanned damage. In Figure 7.44 (c), the predicted load displacement curves show that with the decrease of τ_C, the predicted peak CAI load decreases, but not significantly. However, all the predicted curves are not as progressive as the experimental curves. After the peak loads, the experimental curves still have plateaus indicating the propagation of CAI-induced damage, which have not been captured computationally.

The effects of interfacial mode II/III fracture toughness $G_{II/III}$ are illustrated in Figure 7.45. With $G_{II/III}$ increasing from 0.45 N/mm to 8.96 N/mm, according to Figure 7.45 (a), the predicted CAI-induced damage footprints have little difference. According to 7.45 (b), the predicted peak loads have little difference with the varying fracture toughness. However, with $G_{II/III}$ being 8.96 N/mm (10 times of the previously used value), after the peak load, the predicted load-displacement curve seems to be more progressive.

The effects of the shape of the interfacial traction-separation law are demonstrated in Figure 7.46. From Figure 7.46 (a), it seems that changing the law shape from triangular to trapezoidal does not affect the CAI-induced damage significantly. The damage predicted with the trapezoidal law is slightly smaller than that obtained with

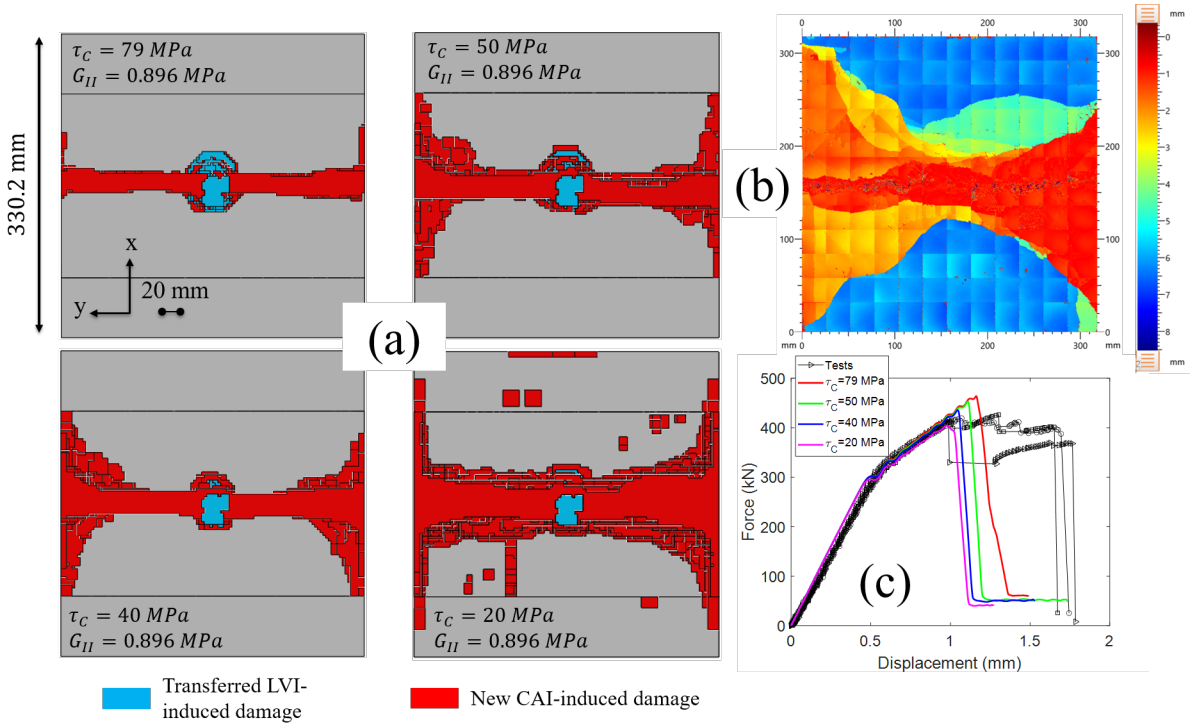

Figure 7.44: Effects of interfacial shear strength τ_C on the CAI responses of a L1-L-48 sample: (a) predicted damage, (b) scanned damage, and (c) load-displacement curves.

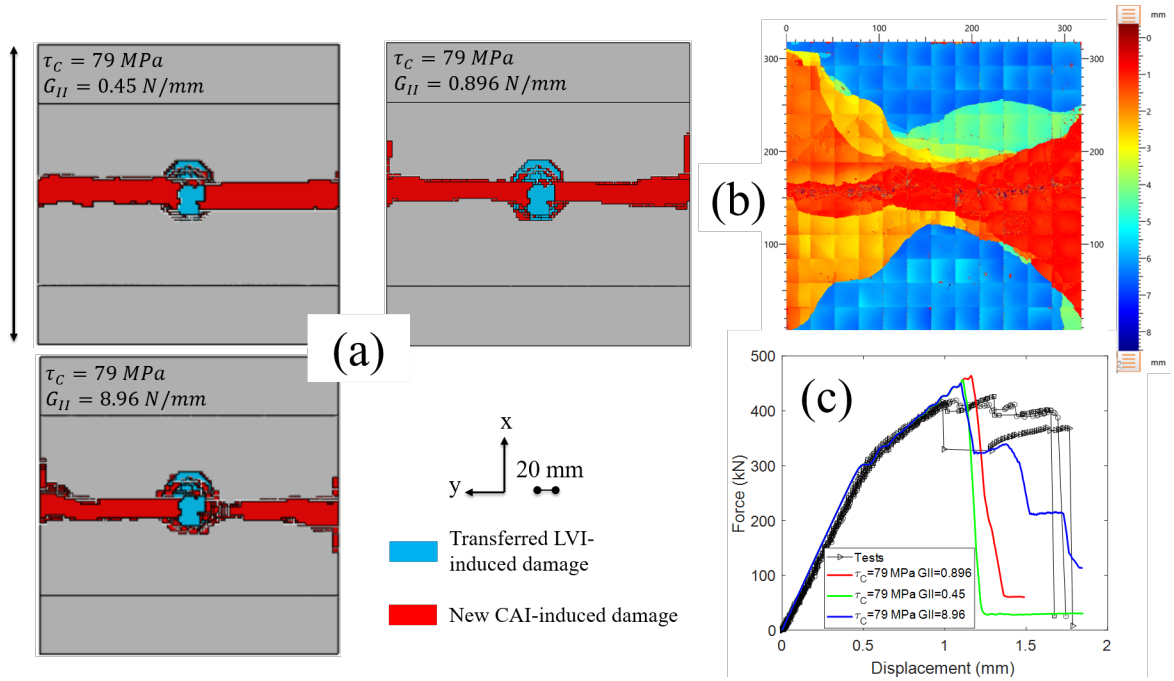

Figure 7.45: Effects of interfacial mode II/III fracture toughness $G_{II/III}$ on the CAI responses of a L1-L-48 sample: (a) predicted damage, (b) scanned damage, and (c) load-displacement curves.

the triangular traction-separation law. For the case with τ_C=20 MPa and $G_{II/III}$=4.5 N/mm, whose trapezoidal traction-separation law has a relatively long plateau, the predicted CAI-induced damage is still significantly smaller than the scanned damage. From Figure 7.46 (c), the predicted peak CAI loads are still close to the experimental values but the progressiveness of the curve is not captured computationally,

The three tested L1-L-48 samples are scanned with ultrasound C-scanning, as displayed in Figure 7.47. As seen in the figure, the damage shapes of the three samples are similar. However, the sizes of the scanned damage footprints vary significantly. The reason for the large variation is twofold. First, there are material randomness and possible manufacturing-induced defects distributed in the three samples, which might lead to the divergence of the CAI-induced damage. Second, slight deviation in the boundary conditions may exist among the three CAI tests. The tightening and alignment of the CAI fixtures, especially the side knife edges is believed to strongly

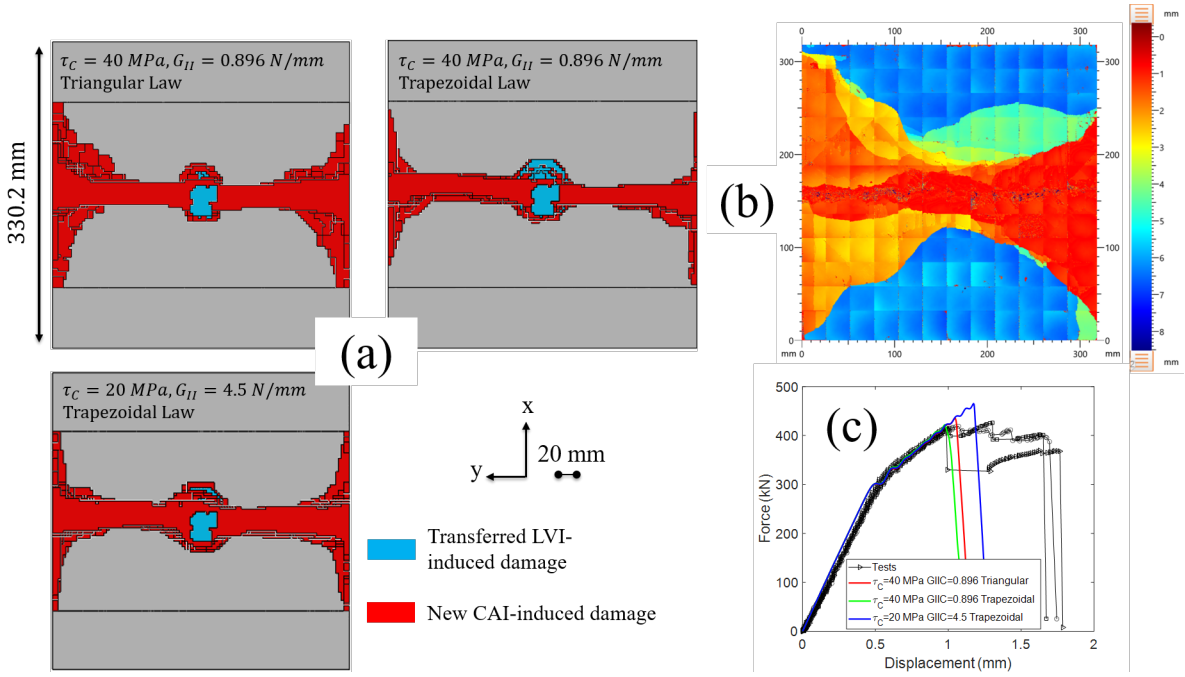

Figure 7.46: Parameter study of the effects of traction-separation law's shape on the CAI responses of a L1-L-48 sample: (a) predicted damage, (b) scanned damage, and (c) load-displacement curves.

affect the CAI-induced damage, since the delamination near the lateral edges is extensive, as seen in Figure 7.47. This finding also helps explain the difference between the computational results and CAI results. In the computational model, the boundary conditions are applied by restraining the displacement of nodes corresponding to the supported locations. However, the slight misalignment and the movement of the CAI fixtures during testing are not modeled. As a panel gets larger and thicker, the CAI load gets higher and the possibility for the CAI fixture to be deformed and displaced is higher, therefore leading to the disagreement between the predicted and tested CAI-induced damage.

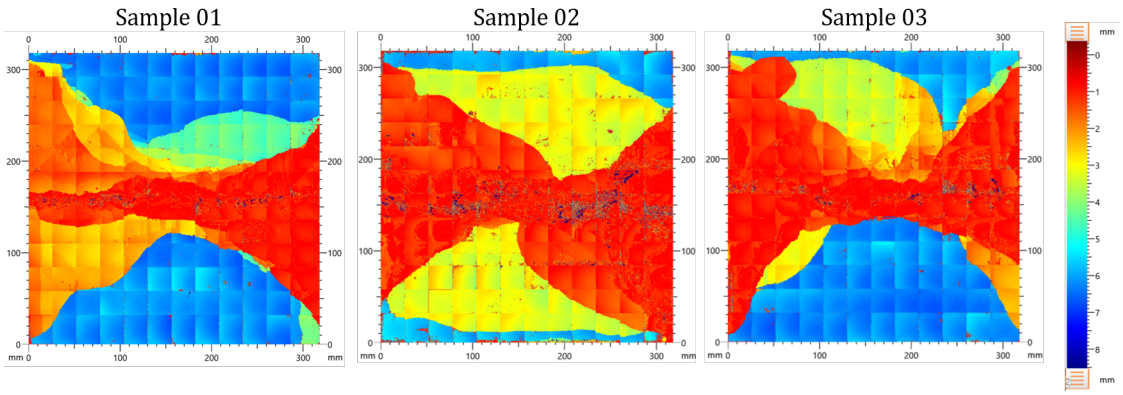

Figure 7.47: CAI-induced damage of the three tested L1-L-48 samples characterized by ultrasound C-scanning.

7.5 Summary and Conclusions

CAI analyses based on the *Restart function of Abaqus have been performed for the stacking sequence effect studies. In general, the predicted load responses agree very well with the test results. The predicted CAI-induced damage footprints are smallest for the layup A samples and largest for the layup C samples. Due to the high percentage of 0° plies in layup A, the CAI failure of layup A seems to be more dominated by fiber compressive failure. On the contrary, the CAI-induced damage of the layup C samples with 10% of 0° plies contains more delamination. These results are in agreement with the experimental results reported in Chapter III.

With the high-fidelity and high-efficiency LVI-CAI framework illustrated in Chapter VI, analyses of the panel size effect studies have been performed using 2D EST. In most cases, the predicted load-displacement curves agree very well with the test results. Critical parameters, including the transition loads and peak loads, are predicted accurately. For some cases, the damage growth seems to be predicted excessively progressive or insufficiently progressive, leading to incorrect predictions of the displacement values at which CAI final failure takes place. The locations of the CAI-induced damage are predicted correctly for all the cases. However, compared to the ultrasound C-scanning, the predicted damage footprints are underpredicted. Through

parameter studies with respect to interfacial material properties, the interfacial shear strength τ_C is found to have the strongest effect on the size of the predicted damage. With the reduction of τ_C, the predicted CAI-induced damage footprint gets closer to the scanned damage. It is also found that increasing the mode II/III fracture toughness $G_{II/III}$ helps obtain more progressive load-displacement curves, but does not increase the damage size. By comparing the C-scanning of three L1-L-48 samples, it is believed that the discrepancy between the predicted and tested CAI-induced damage is also caused by the CAI fixture not being entirely rigid and fixed during CAI testing. Accounting for this effect will be performed in the future.

CHAPTER VIII

Summary and Concluding Remarks

8.1 Summary

In this thesis, the responses of CFRP laminates subjected to LVI and CAI have been investigated experimentally and computationally. The effects of stacking sequences and panel sizes on the LVI and CAI behavior have been studied. For the stacking sequence effect studies, T800s/3900-2B material has been used. Samples of three stacking sequences have been tested and analyzed. The three layups contain 80%, 25%, and 10% of 0° plies. Each layup has been impacted with three energy levels which have caused various extents of LVI-induced damage. In addition, a "sandwich-like" layup has been impacted. This layup is special in the sense that the laminate resembles a sandwich structure. The [0/90/0] plies near the top and bottom sample surfaces serve as the "face sheet" while the $[90]_{18}$ plies serve as the "core". For the panel size effect studies, IM7/977-3 material has been used. Two stacking sequences with three in-plane sizes and two laminate thicknesses have been investigated.

The experimental LVI studies were performed using a drop tower testing system. High-speed 3D DIC was conducted to capture the in-situ deformation of the impacted samples. After the LVI tests, the impacted samples were subjected to NDI characterization including ultrasound C-scanning and X-ray μCT. μCT was enhanced with dye penetrant containing Zinc Iodide. CAI tests were performed using a uniaxial

tension/compression testing system. 2D and 3D DIC was performed to capture the in-plane and out-of-plane deformation of the compressed samples.

2D and 3D EST models with the capability to capture material inelasticity have been developed and applied to the computational analyses of the LVI and CAI responses. LVI predictions have been done using both 2D EST-InELA and 3D EST-InELA. A comprehensive evaluation of the two models has been carried out and reported. A high-fidelity and high-efficiency computational framework has been proposed and developed to connect the numerical LVI analysis and CAI analysis. The major goal of the developed framework is to reduce the computation time without sacrificing the computational accuracy. Based on the high-fidelity and high-efficiency framework, the CAI analyses have been conducted to predict the residual strengths of impacted composites.

8.2 Concluding Remarks

Experimental Studies

LVI

- In the stacking sequence effect studies, the damage events characterized by high-speed 3D DIC correlate very well with sharp load oscillations on the load response curves. The characterized damage events include fiber tensile rupture and back-ply splitting, which seem to serve as the indicators for the load drops on the LVI response curves.

- The damage footprints of the layup A (80% of 0° plies) T800s/3900-2B samples the L1 (50% of 0° plies) IM7/977-3 samples are of the elliptical shapes whose major axes are along the 0° direction. This is believed to be caused by the fact that delamination is bounded by matrix cracking in its neighboring plies. For the layup B (25% of 0° plies) and layup C (10% of 0° plies) T800s/3900-2B

samples, and the L2 (25% of 0° plies) IM7/977-3 samples, the damage footprints are of circular shapes since the number of 0°, ±45°, and 90° plies are more evenly distributed. For the "sandwich-like" samples, the damage footprints is very unique, referred to as the "kidney" shape in this thesis.

- The featured "kidney" and "rotating-fan" LVI-induced damage patterns have been characterized with high-resolution μCT scanning. With damage details revealed by the reconstructed 3D μCT models, the damage mechanisms have been disclosed. The interaction between three major damage modes, including fiber breaking, matrix cracking, and delamination is the key reason for the formation of the featured damage patterns.

- For the investigated two layups of the panel size effect studies, the stacking sequences seem to affect the LVI load responses marginally but influence the LVI-induced damage morphology significantly. The key geometry parameter affecting the LVI load responses and induced damage is the thickness-to-length/width ratios of the studied panels. With a relatively high thickness-to-length/width ratio, drastic bending rigidity reduction takes place in the loading phase of the LVI behavior (L1/L2-S-48 samples). In addition, a high thickness-to-length/width ratio seems to facilitate the LVI-induced delamination due to induced high interfacial shear stresses.

CAI

- In the stacking sequence effect studies, the layup B (24-ply) samples have the highest CAI peak loads compared to layup A (20-ply) and layup C (20-ply) samples. This is due to the thickness of layup B being higher than that of layup A and C. The CAI peak loads of layup A samples are higher than layup C samples. This is due to the percentage of 0° plies of layup A being higher than that of layup C.

- The thickness-to-length/width ratio is again found to be the key factor affecting the CAI behavior in the panel size effect studies. For the L1/L2-S-24/48 and L1/L2-M-48 samples, whose thickness-to-length/width ratios are relatively high, the CAI deformation is mostly in-plane, until the stages very close to the final failure, where local buckling of delaminated plies takes place. For the L1/L2-M-24 and L1/L2-L-24/48 samples, post-buckling happens during the CAI process. For the layups with the lowest thickness-to-length/width ratio (L1/L2-L-24), the CAI induced damage seems to be not affected by the LVI-induced damage. In other words, LVI-induced damage does not contribute to the CAI failure for these layups due to the post-buckling behavior. The most complicated CAI behavior is associated with the L1/L2-L-48 samples, where the post-buckling and damage development are coupled.

Computational studies

LVI

- In the stacking sequence effect analyses, the load responses are predicted well by 2D EST, in terms of the peak loads and maximum impactor displacement. The residual displacement and energy absorption are underpredicted. The reason is believed to be the lack of the capability to capture material inelasticity of the 2D EST. The damage footprints are predicted well, in terms of both shape and size.

- From the detailed analyses of the LVI-induced damage predictions of a layup B sample impacted with 25 J and a "sandwich-like" layup sample impacted with 25 J, the interaction between different damage modes, including fiber breaking, matrix cracking, and delamination has been captured. Therefore, the predictions of the featured damage patterns such as the "rotating-fan" and the "kidney" shape damage are successful.

- 2D EST-InELA and 3D EST-InELA have been used for the LVI predictions of the panel size effect studies. In general, the predicted load responses agree well with the test results. In the loading phase, the oscillations due to damage initiation and bending rigidity reduction due to drastic delamination growth are predicted well by 2D EST-InELA. The bending rigidity reduction is not sufficiently captured by 3D EST-InELA. In the unloading phase, the residual displacement and energy absorption values are predicted better by 3D EST-InELA. As the in-plane sizes of the samples increase, the accuracy of the residual displacement and energy absorption predictions gets worse.

- 2D EST-InELA performs better in terms of predicting the LVI-induced damage. The predicted damage shapes agree very well with the damage footprints characterized by ultrasound C-scanning. The sizes of the damage footprints of the 24-ply samples are underpredicted by the 2D EST-InELA. The damage footprints of the 48-ply samples are predicted very well by 2D EST-InELA but underpredicted by 3D EST-InELA.

- 2D EST-InELA performs better in terms of capturing the damage-induced load drops and bending rigidity reduction. In addition, 2D EST-InELA is better at predicting LVI-induced damage. 3D EST-InELA performs better at predicting the residual displacement and energy absorption. 2D EST-InELA is much more efficient than 3D EST-InELA.

CAI

- In the stacking sequence effect analyses, the load-displacement responses and the CAI peak loads are predicted accurately by 2D EST. The CAI-induced damage footprints seem to become more involved with delamination and less dominated by fiber compressive damage as layups' percentages of 0° plies increases.

- A high-fidelity and high-efficiency LVI-CAI computational framework has been proposed, developed, and applied. Compared to conventional analyses based on the *Restart function of Abaqus, the computational analyses performed with the newly introduced framework have resulted in a 67% faster computational time without without any loss of the computational accuracy.

- In the panel size effect studies, the load-displacement responses are predicted well by 2D EST in most cases. For all the cases, the load responses are accurately predicted until the drastic drop caused by CAI failure. After the drastic drop, the predicted damage growth seems to be excessively or insufficiently progressive, leading to incorrect predictions of the displacement values at which the final load drops happen.

- The CAI-induced damage locations are predicted well. For the cases involved with post-buckling, the out-of-plane deformation fields are captured well. Compared to the CAI-induced damage footprints characterized by ultrasound C-scanning, the predicted damage footprints are too small.

8.3 Unique Contributions in this Thesis

1. Comprehensive and systematic experimental results of the LVI and CAI responses of CFRP laminated composites have been reported. The results can be used for the calibration and V&V of computational models.

2. The effects of panel sizes on the LVI and CAI behavior have been investigated, which have not been presented before. The panel size effect studies can be a supplement to the existing industrial standards such as ASTM D7136 [19] and D7137 [27].

3. CAI responses associated with interdependent post-buckling and damage pro-

gression have been experimentally and computationally studied, which have not been reported before.

4. Based on 2D plane stress EST proposed and developed in [39], a novel mixed-mode cohesive law has been integrated. In addition, the capability to capture material inelasticity has been implemented. The newly developed version is referred to as 2D EST-InELA. 3D EST-InELA has also been implemented and applied. A comprehensive evaluation of 2D EST-InELA and 3D EST-InELA in terms of computational accuracy and efficiency has been performed with respect to the LVI analyses.

5. A high-fidelity and high-efficiency computational LVI-CAI framework has been established. This type of acceleration method has rarely been developed and reported. The computation time to acquire the ultimate CAI peak load has been reduced by 67%. As the panel size increases, the reduction of the computation time will be more significant.

8.4 Future Work

1. Effects of strain rates on the material behavior should be investigated. Currently, the material parameters used for the LVI and CAI predictions are obtained from quasi-static tests. Therefore, some material properties need to be calibrated to acquire better predictions. Implementing the strain rate effects in the EST models will benefit computational accuracy.

2. The current EST models utilize strain-based damage initiation criteria. A comprehensive parameter study should be performed to evaluate the effects of the damage initiation criteria on the damage prediction. Stress-based damage initiation criteria may be used to improve computational accuracy.

3. Fiber aligned meshes with intra-ply matrix cracking elements [103] can be used for both LVI and CAI predictions. Damage features such as ply splitting happening on the non-impacted surfaces of the impacted samples may be captured.

4. More parameter studies need to be performed for the CAI analyses to investigate the reason for the underprediction of the CAI-induced damage.

5. Based on the significant efficiency improvement enabled by the high-fidelity and high-efficiency computational framework, data-driven models can be developed, based on which optimizations can be performed to improve the impact resistance of CFRP laminated composites.

6. LVI and CAI analyses may be performed for novel composites enabled by advanced manufacturing such as automated fiber placement (AFP) and multi-material additive manufacturing to evaluate the improvement in the LVI and CAI behavior of these architected materials and structures.

APPENDICES

APPENDIX A

Continuum Decohesive Finite Element (CDFE) for Progressive Failure Analyses of Composites

A.1 Introduction

[1] Continuum decohesive finite element (CDFE) is a novel finite element scheme seamlessly bridging continuum and cohesive crack modeling. In the CDFE scheme, the transition from a continuum element to a system of continuum sub-elements and a cohesive element is by introducing pairs of dummy nodes to account for the crack separation. A static condensation step is performed to calculate the separation of the crack and enable the implementation of CDFE in the computational framework of the commercial software Abaqus.

FEA based progressive failure analysis (PFA) models usually fall under two categories, namely continuum damage model and discrete damage model. In the continuum damage model, the crack separation is usually smeared over a finite characteristic

[1] The results presented in this appendix have been published in:

- Lin, Shiyao, Nhung Nguyen, and Anthony M. Waas. "Application of continuum decohesive finite element to progressive failure analysis of composite materials." *Composite Structures* 212 (2019): 365-380.

length and the degradation of material properties is dictated according to stress-strain relationships transferred from traction-separation laws. EST as introduced in Chapter IV belongs to the continuum damage model. Other representative works of the continuum damage model include [71, 72, 7, 36].

For the discrete damage model, if the crack angle and path are known beforehand, such as the modeling of delamination and adhesively bonded structures, PFA is usually carried out using cohesive interfacial elements [64] or cohesive contact model [65]. For the cases where the crack orientation and angle is not known until the crack initiation, more advanced PFA methods have been developed. Nodal enrichment or elemental enrichment is performed and advanced FEM schemes have been implemented, such as the eXtended FEM (XFEM) [123, 124], phantom node method (PNM) [125], the variational multiscale cohesive method (VMCM) [126, 127], the augmented FEM (A-FEM) [128, 129, 130], and the floating node method (FNM) [131, 132, 133].

Inspired by VMCM, where a sharp crack is modeled by enriched elemental shape functions and static condensation, CDFE has been developed as a novel FEM scheme to seamlessly bridge the continuum damage model and the discrete damage model [134, 98]. In CDFE, a crack is modeled as a physical discontinuity inside an element by the introduction of pairs of dummy nodes. Before the crack initiation, the CDFE element follows the classical elastic FEM scheme. At the crack initiation, the continuum element is split along a line cutting through the centroid of the element into two sub-elements. These two sub-elements are connected by an element following the discrete cohesive zone model (DCZM) [64]. After the splitting of the element, at each time increment, the equivalent elemental stiffness matrix of the CDFE element is obtained by statically condensing the stiffness matrix of the DCZM element and the stiffness matrices of the two sub-elements. Detailed methodology can be found in Sections A.2 and A.3.

In this appendix, the background of CDFE is introduced first in Section A.1. Then the methodology of CDFE will be provided in Sections A.2 and A.3. Computational results obtained with CDFE will be presented in Section A.4.

A.2 CDFE for Arbitrary Crack Analysis

In this section, the methodology of CDFE capturing the initiation and growth of an arbitrary crack is introduced. This type of CDFE can be used for the cases where the crack orientation and path are not known a priori, such as the micromechanical PFA of matrix cracking between fibers, which will be illustrated in Section A.4.1.

Mathematical Formulation

Before crack initiation, the CDFE element is identical to the formulation of a classical elastic finite element. Its principal of virtual work (PVW) is,

$$\int_{\Omega} \nabla \mathbf{w} : \boldsymbol{\sigma} \mathrm{dV} = \int_{\Omega} \nabla \mathbf{w} \cdot \mathbf{b} dV + \int_{\Gamma_t} \mathbf{w} \cdot \mathbf{f} dS \tag{A.1}$$

where $\mathbf{w}$ is the virtual displacement vector, $\boldsymbol{\sigma}$ is the actual stress tensor, $\mathbf{b}$ is the body force vector, $\mathbf{f}$ is the external surface force vector, Γ_t is the normal boundary, Γ_k is the kinematic boundary, and Ω is the continuum domain. An illustrating diagram is shown in Figure A.1 (a).

As shown in Figure A.1 (b), at and after the crack initiation, a cohesive crack following the DCZM model is inserted into the continuum body through the centroid with a certain crack angle. In Figure A.1 (b), the CDFE system can be regarded as two continuum bodies connected by a DCZM cohesive zone. The crack angle is determined using the maximum principle stress criterion, as in Equation A.2. In the equation, σ_n is the normal component of the principal stress, the local principal coordinate system is as shown in Figure A.1 (a). σ_C is the critical strength for mode I

cracking, which is one of the material properties. After the crack initiation, the crack angle will stay fixed.

$$\sigma_n \geq \sigma_C \tag{A.2}$$

The PVW of the CDFE element at and after crack initiation is expressed as Equation A.3.

$$\int_{\Omega_1} \nabla \mathbf{w} : \boldsymbol{\sigma} \mathrm{dV} + \int_{\Omega_2} \nabla \mathbf{w} : \boldsymbol{\sigma} \mathrm{dV} = \int_{\Omega_1} \mathbf{w} \cdot \mathbf{b} \mathrm{dV} + \int_{\Omega_2} \mathbf{w} \cdot \mathbf{b} \mathrm{dV} + \int_{\Gamma_{t_1}} \mathbf{w} \cdot \mathbf{f} \mathrm{dV} + \int_{\Gamma_{t_2}} \mathbf{w} \cdot \mathbf{f} \mathrm{dS} + \int_{\Gamma_{c_1}} \mathbf{w} \cdot \mathbf{t}(\langle \mathbf{w} \rangle) \mathrm{dS} + \int_{\Gamma_{c_2}} \mathbf{w} \cdot \mathbf{t}(\langle \mathbf{w} \rangle) \mathrm{dS} \tag{A.3}$$

In Equation A.3, Ω_1 and Ω_2 stand for two sub-domains. Γ_{t1}, Γ_{t_2}, Γ_{k1} and Γ_{k_2} are normal and kinematic boundaries on the corresponding sub-domains. Γ_{c_1} and Γ_{t_2} represent two crack faces, on which crack traction $\mathbf{t}$ is distributed. $\mathbf{t}$ is determined according to designated traction-separation law and the crack separation $\langle \mathbf{w} \rangle$, where $\langle \cdot \rangle$ represents the determination of separation from the displacement field. The calculation of $\mathbf{t}$ will be explained in detail in the latter part of this section.

Damage Initiation and Evolution

The damage evolution is governed by the cohesive laws. In this appendix, the bi-linear cohesive law is adopted, but it should be noted that any type of cohesive law can be implemented with CDFE. The mode I and II traction-separation laws are shown in Figure A.2. To fully describe these laws, five input parameters are needed, including mode I crack strength σ_C and fracture toughness G_{IC}, mode II crack strength τ_C and fracture toughness G_{IIC} and the ratio between the initiation separation δ_{n0}, δ_{t0} and the critical separation δ_{nC}, δ_{tC}, which is denoted as η. The

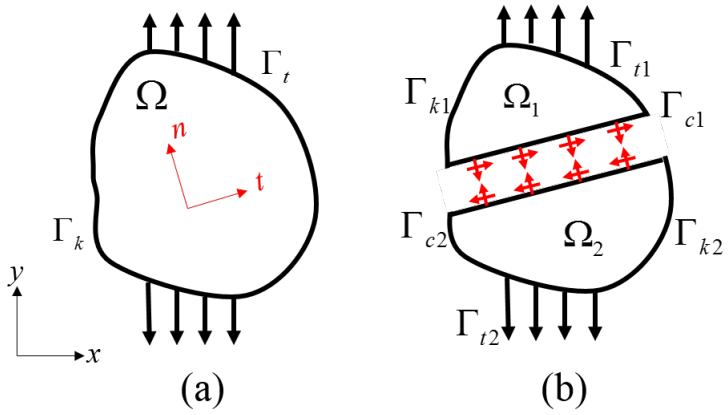

Figure A.1: CDFE mathematical scheme: (a) before initiation, and (b) after initiation

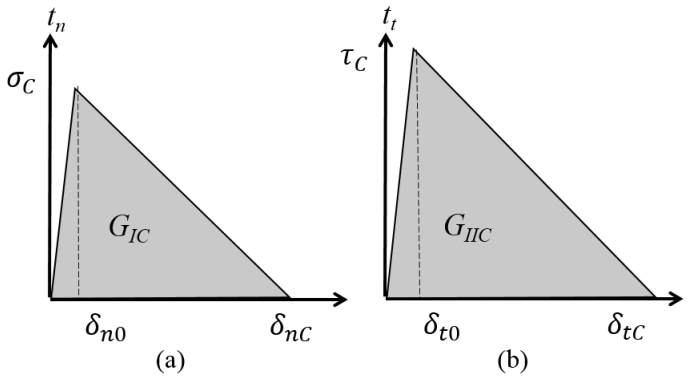

Figure A.2: Cohesive laws (a) mode I and, (b) mode II

critical mode I and II separations are calculated according to Equation A.4. The separations corresponding to the crack initiation, δ_{n0} and δ_{t0}, are determined as in Equation A.5.

$$\delta_{nC} = \frac{2G_{IC}}{\sigma_C}, \tag{A.4a}$$

$$\delta_{tC} = \frac{2G_{IIC}}{\tau_C} \tag{A.4b}$$

$$\delta_{n0} = \eta\delta_{nC}, \tag{A.5a}$$

$$\delta_{t0} = \eta\delta_{tC} \tag{A.5b}$$

The traction laws for mode I and mode II are,

$$t_n(\delta_n) = \frac{\sigma_C}{\delta_{n0}}\delta_n \ (\delta_n \leq \delta_{n0}), \tag{A.6a}$$

$$t_n(\delta_n) = \frac{\delta_n - \delta_{n0}}{\delta_{nC} - \delta_{n0}}\sigma_C \ (\delta_{n0} \leq \delta_n < \delta_{nC}), \tag{A.6b}$$

$$t_n(\delta_n) = 0 \ (\delta_{nC} \leq \delta_n) \tag{A.6c}$$

$$t_t(\delta_t) = \frac{\tau_C}{\delta_{t0}}\delta_t \ (\delta_t \leq \delta_{t0}), \tag{A.7a}$$

$$t_t(\delta_t) = \frac{\delta_t - \delta_{t0}}{\delta_{tC} - \delta_{t0}}\tau_C \ (\delta_{t0} \leq \delta_t < \delta_{tC}), \tag{A.7b}$$

$$t_t(\delta_t) = 0 \ (\delta_{tC} \leq \delta_t) \tag{A.7c}$$

where, δ_n, δ_t and t_n, t_t are normal and tangential components of separation and traction vectors.

It should be pointed out that, for the case where CDFE is used for arbitrary crack analysis, only mode I cracking is accounted for. Mode II damage evolution is illustrated here for the completeness and the next section.

For CDFE capable of capturing arbitrary cracking, the crack initiation criterion is the maximum principal stress criterion, as in Equation A.2. After the initiation, the crack angle is fixed, being perpendicular to the maximum principal tensile stress.

Since only mode I cracking is involved in the arbitrary crack problems, the failure criterion is simply the mode I energy dissipated G_I being greater than mode I critical

energy G_{IC}, as in Equation A.8. Since no tangential traction is involved, this is essentially equivalent to normal separation δ_n being greater than the normal critical separation δ_{nC}, which is shown in Equation A.9. Equation A.9 is implemented in the CDFE method.

$$G_I \geq G_{IC} \tag{A.8}$$

$$\delta_n \geq \delta_{nC} \tag{A.9}$$

FEM Formultation

Before crack initiation, the CDFE element is identical to an elastic finite element. A quadrilateral element is taken for an example in Figure A.3. The elemental equations are,

$$\mathbf{RHS} = \mathbf{K_e U_e} - \mathbf{F_e^{ext}}, \tag{A.10a}$$

$$\mathbf{K_e} = \int_{\Omega} \mathbf{B^T D B} \mathrm{dV}, \tag{A.10b}$$

$$\mathbf{F_e^{ext}} = \int_{\Omega} \mathbf{N^T} \cdot \mathbf{b} \mathrm{dV} + \int_{\Gamma_t} \mathbf{N^T} \cdot \mathbf{f} \mathrm{dS} + \sum \mathbf{N^T} \cdot \mathbf{F_n} \tag{A.10c}$$

where $\mathbf{K_e}$ is the elemental stiffness matrix, $\mathbf{U_e}$ is the nodal displacement vector, $\mathbf{F_e^{ext}}$ is the elemental external force vector, $\mathbf{B}$ is the matrix relating displacement and strain. $\mathbf{D}$ is the material stiffness matrix, $\mathbf{N}$ is the matrix of interpolation functions and $\mathbf{F_n}$ is the nodal force vector.

At and after crack initiation, the continuum element as shown in Figure A.3 (a) is split into two sub-elements connected by one DCZM element, as shown in Figure

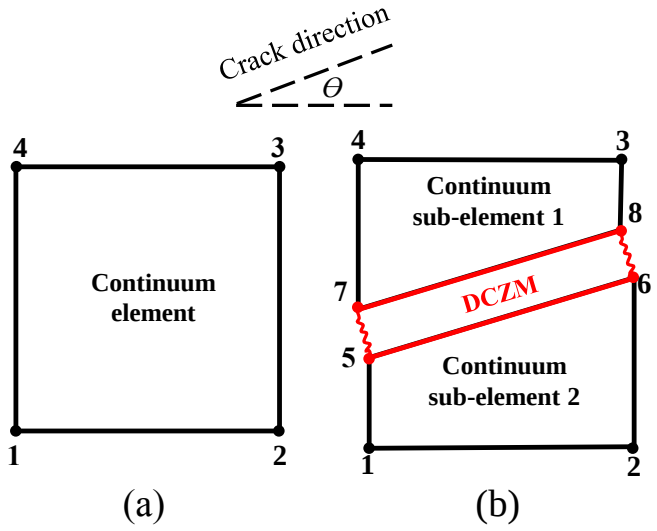

Figure A.3: CDFE FEM scheme for arbitrary crack problems: (a) before initiation, (b) after initiation

A.3 (b). The elemental stiffness matrices for the sub-elements are

$$\mathbf{K_i} = \int_{\Omega_i} \mathbf{B_i^T D B_i} \mathrm{dV} \quad (i = 1, 2) \tag{A.11}$$

where, i denotes sub-element domain 1 and 2.

The DCZM element is a node-based cohesive element. The stiffness matrix of the DCZM element is in Equation A.12.

$$\mathbf{K_{DCZM}} = \mathbf{R^T} \begin{bmatrix} K_{57t} & 0 & 0 & 0 & -K_{57t} & 0 & 0 & 0 \\ 0 & K_{57n} & 0 & 0 & 0 & -K_{57n} & 0 & 0 \\ 0 & 0 & K_{68t} & 0 & 0 & 0 & -K_{68t} & 0 \\ 0 & 0 & 0 & K_{68n} & 0 & 0 & 0 & -K_{68n} \\ -K_{57t} & 0 & 0 & 0 & K_{57t} & 0 & 0 & 0 \\ 0 & -K_{57n} & 0 & 0 & 0 & K_{57n} & 0 & 0 \\ 0 & 0 & -K_{68t} & 0 & 0 & 0 & K_{68t} & 0 \\ 0 & 0 & 0 & -K_{68n} & 0 & 0 & 0 & K_{68n} \end{bmatrix} \mathbf{R} \tag{A.12}$$

In Equation A.12, $\mathbf{R}$ is the rotation matrix transforming the stiffness matrix in the local coordinates of the principal direction to the global coordinates. $\mathbf{R}$ is written in Equation A.13 in detail, in which θ is the crack angle. $K_{ab\alpha}$ means the α component of the stiffness of the spring connecting node a and b. The t and n components of the stiffness are local tangential and normal secant stiffness on the corresponding traction-separation laws, which are calculated in Equation A.14, where t_t and t_n are determined from Equations A.6 and A.7. It should be noted that, since arbitrary crack problem is mode I dominated, the tangential traction is automatically zero, hence the secant stiffness K_{abt} is also zero. However, Equations (A.11) – (A.14) are still written in full for the structure of this appendix.

$$\mathbf{R} = \begin{bmatrix} \cos\theta & \sin\theta & 0 & 0 & 0 & 0 & 0 & 0 \\ -\sin\theta & \cos\theta & 0 & 0 & 0 & 0 & 0 & 0 \\ 0 & 0 & \cos\theta & \sin\theta & 0 & 0 & 0 & 0 \\ 0 & 0 & -\sin\theta & \cos\theta & 0 & 0 & 0 & 0 \\ 0 & 0 & 0 & 0 & \cos\theta & \sin\theta & 0 & 0 \\ 0 & 0 & 0 & 0 & -\sin\theta & \cos\theta & 0 & 0 \\ 0 & 0 & 0 & 0 & 0 & 0 & \cos\theta & \sin\theta \\ 0 & 0 & 0 & 0 & 0 & 0 & -\sin\theta & \cos\theta \end{bmatrix} \tag{A.13}$$

$$K_{abt} = \frac{t_t}{\delta_t} \quad (a = 5, 6; b = 7, 8), \tag{A.14a}$$

$$K_{abn} = \frac{t_n}{\delta_n} \quad (a = 5, 6; b = 7, 8) \tag{A.14b}$$

In Equation A.14, the normal and tangential separations are calculated from the displacement vector $\mathbf{U}\hat{}$ of the dummy nodes $5 - 6 - 7 - 8$. This procedure is shown

in Equation A.15.

$$\boldsymbol{\delta}_{\mathbf{n}} = \mathbf{L}_{\mathbf{n}}\mathbf{R}\mathbf{U}\hat{} \tag{A.15a}$$

$$\boldsymbol{\delta}_{\mathbf{t}} = \mathbf{L}_{\mathbf{t}}\mathbf{R}\mathbf{U}\hat{} \tag{A.15b}$$

where $\boldsymbol{\delta}_{\mathbf{n}}$ and $\boldsymbol{\delta}_{\mathbf{t}}$ are normal and tangential separation vectors, $\mathbf{L}_{\mathbf{t}}$ and are the matrices correlating separations with displacements in local coordinates. $\mathbf{L}_{\mathbf{t}}$ and $\mathbf{L}_{\mathbf{n}}$ are defined in Equation A.16.

$$\mathbf{L}_{\mathbf{n}} = \begin{bmatrix} -1 & 0 & 0 & 0 & 1 & 0 & 0 & 0 \\ 0 & 0 & -1 & 0 & 0 & 0 & 1 & 0 \end{bmatrix} \tag{A.16a}$$

$$\mathbf{L}_{\mathbf{t}} = \begin{bmatrix} 0 & -1 & 0 & 0 & 0 & 1 & 0 & 0 \\ 0 & 0 & 0 & -1 & 0 & 0 & 0 & 1 \end{bmatrix} \tag{A.16b}$$

Assembling the stiffness matrices and the nodal displacement and force vectors, the equations for the system as shown in Figure A.3 (b) are,

$$\mathbf{K} = \begin{bmatrix} \mathbf{K}^{**} & \mathbf{K}^{*\hat{}} \\ \mathbf{K}\hat{}^{*} & \mathbf{K}\hat{}\hat{} \end{bmatrix}, \mathbf{U} = \begin{bmatrix} \mathbf{U}^{*} \\ \mathbf{U}\hat{} \end{bmatrix}, \mathbf{F} = \begin{bmatrix} \mathbf{F}^{*} \\ \mathbf{F}\hat{} \end{bmatrix} \tag{A.17}$$

where, * stands for DOFs relative to the existing nodes before the crack initiation, $\hat{}$ stands for the DOFs associated to the dummy nodes inserted after the initiation. To be more specific, as illustrated in Figure A.3 (b), * represents DOFs relative to node 1, 2, 3, 4 and $\hat{}$ represents DOFs relative to node 5, 6, 7, 8. It should be pointed out that, since dummy nodes 5, 6, 7 and 8 are not exposed to the FEM solver, no external nodal forces are exerted on them, and hence $\mathbf{F}\hat{} = \{\mathbf{0}\}$.

The final step of the CDFE scheme is to perform static condensation to condense

the nodal displacements associated with the dummy nodes to generate an equivalent stiffness matrix and the right-hand side **RHS**. The static condensation is as in Equation A.18.

$$\mathbf{U\hat{}} = -(\mathbf{K\hat{}\hat{}})^{-1}\mathbf{K\hat{}^{*}U^{*}}, \tag{A.18a}$$

$$\mathbf{K_e^{eq}} = \mathbf{K^{**}} - \mathbf{K^{*}\hat{}(K\hat{}\hat{})^{-1}K\hat{}^{*}}, \tag{A.18b}$$

$$\mathbf{RHS} = \mathbf{K_e^{eq}U^{*}} - \mathbf{F_e^{ext}} \tag{A.18c}$$

After the static condensation, the equivalent stiffness matrix $\mathbf{K_e^{eq}}$ and **RHS** are obtained and can be provided back to the FEM solver with both implicit and explicit algorithms. In this appendix, explicit analysis is used due to the robustness of the method. CDFE has been implemented as the explicit user element subroutine VUEL linked to Abaqus. The input parameters of the CDFE VUEL subroutine include material properties, nodal coordinates, nodal displacement vector of the current time increment and the state variables inherited from the previous increment. The output variables include the **RHS** vector and updated state variables. The details of the implementation can be found in the flow chart of CDFE with arbitrary cracking in Figure A.4. In Figure A.4, the superscript (n) refers to the time increment n. Variables without this superscript are temporary and would not be passed back to the FEM solver. At the start of time increment n, the existing information includes the nodal coordinates $\mathbf{X}$, material properties E_{11}, E_{22}, ν_{12}, G_{12}, σ_C, τ_C, G_{IC} and G_{IIC}, current nodal displacement $\mathbf{U^{(n)}}$, cracking status '$cs^{(n-1)\prime}$, crack angle $\theta^{(n-1)}$, displacement vector of the dummy nodes $\mathbf{U\hat{}^{(n-1)}}$ and normal crack separation. The variable 'cs' indicates the crack status. If 'cs' is equal to 0, the element is pristine. If 'cs' is equal to 1, the crack has initiated but not fully propagated. If 'cs' is equal to 2, the element has failed. At the end of the increment, the right-hand side, updated

crack status '$cs^{(n)\prime}$', crack angle $\theta^{(n)}$, displacement vector of the dummy nodes $\mathbf{U}^{\hat{}\,\mathbf{(n)}}$ and normal separation $\boldsymbol{\delta}_{\mathbf{n}}^{\mathbf{(n)}}$ are output of the CDFE VUEL subroutine and passed back to the FEM solver.

A.3 CDFE for Composite Damage Analysis

Unlike CDFE for modeling the initiation and growth of arbitrary cracking, damage in composite material tends to follow well-defined crack angles. For example, as illustrated in Chapter II, fiber breaking is perpendicular to the fiber direction, matrix cracking is usually parallel with the fiber direction, and delamination usually takes place between the adjacent plies. Therefore, CDFE for meso-scale PFA of composite laminates does not require any damage initiation criterion to determine the crack angle. In this section, CDFE for the meso-scale PFA of composite laminates is introduced and a new inner-element discretization scheme and a novel mixed-mode cohesive formulation developed in [93] are implemented in CDFE.

The New Inner-element Discretization Scheme

As illustrated in Figure A.3, at the increment where crack initiation happens, additional DOFs are introduced into the CDFE FEM system. This introduction of additional DOFs would abruptly degrade the nominal stiffness of the element. Such an instantaneous stiffness change would cause a sudden change of the force vector. This local stiffness change has also been reported in [130].

To avoid this issue, and based on the fact that the crack angle is known a priori, in the enhanced CDFE, the DCZM element is existent along the fiber direction through the elemental centroid from the very beginning of the analysis. In this way, when the crack initiates, there would be no additional DOF introduced, but the separation between the crack surface starting to grow from zero. The new inner-element scheme of the enhanced CDFE is shown in Figure A.5.

INPUT: $\mathbf{X}$, $\mathbf{U}^{(n)}$, E_{11}, E_{22}, v_{12}, G_{12}, σ_C, τ_C, G_{IC}, G_{IIC}, $cs^{(n-1)}$, $\theta^{(n-1)}$, $\mathbf{U}^{\wedge(n-1)}$, $\boldsymbol{\delta}_n^{(n-1)}$

$\delta_{nC} = 2G_{IC}/\sigma_C$, $\delta_{tC} = 2G_{IIC}/\tau_C$

IF $cs^{(n-1)}==0$ **THEN**

$\mathbf{K}_e^{(n)} = \int_{\Omega_e} \mathbf{B}_e^{\mathrm{T}} \mathbf{D} \mathbf{B}_e \mathrm{d}V$

$\boldsymbol{\varepsilon}_e^{(n)} = \mathbf{B}_e \mathbf{U}_e^{(n)}$, $\boldsymbol{\sigma}_e^{(n)} = \mathbf{D}\boldsymbol{\varepsilon}_e^{(n)}$

acquire principal direction θ_p and normal pincipal stress σ_n

$\mathbf{RHS}_e^{(n)} = \mathbf{K}_e^{(n)}\mathbf{U}_e^{(n)} - \mathbf{F}_e^{ext(n)}$

$\mathbf{U}^{\wedge(n)} = \mathbf{U}^{\wedge(n-1)} = 0, \boldsymbol{\delta}_n^{(n)} = \boldsymbol{\delta}_n^{(n-1)} = \mathbf{0}$

IF $\sigma_n < \sigma_C$ **THEN**

$cs^{(n)} = 0,\ \theta^{(n)} = \theta^{(n-1)} = 0$

ELSE

$cs^{(n)} = 1,\ \theta^{(n)} = \theta_p$

ENDIF

ELSEIF $cs^{(n-1)}==1$ **THEN**

$\mathbf{K}_1 = \int_{\Omega_1} \mathbf{B}_1^{\mathrm{T}} \mathbf{D} \mathbf{B}_1 \mathrm{d}V$, $\mathbf{K}_2 = \int_{\Omega_2} \mathbf{B}_2^{\mathrm{T}} \mathbf{D} \mathbf{B}_2 \mathrm{d}V$

Determine K_{57n}, K_{57t}, K_{68n}, K_{68t} from equation (14)

Determine $\mathbf{K}_{\mathbf{DCZM}}$ from equation (12)

Assemble into global stiffness matrix $\mathbf{K} = \begin{bmatrix} \mathbf{K}^{**} & \mathbf{K}^{*\wedge} \\ \mathbf{K}^{\wedge *} & \mathbf{K}^{\wedge\wedge} \end{bmatrix}$

Static condensation : $\mathbf{K}_e^{eq(n)} = \mathbf{K}^{**} - \mathbf{K}^{*\wedge}(\mathbf{K}^{\wedge\wedge})^{-1}\mathbf{K}^{\wedge *}$

$\mathbf{RHS}_e^{(n)} = \mathbf{K}_e^{eq(n)}\mathbf{U}_e^{(n)} - \mathbf{F}_e^{ext(n)}$, $\mathbf{U}^{\wedge(n)} = -(\mathbf{K}^{\wedge\wedge})^{-1}\mathbf{K}^{\wedge *}\mathbf{U}^{(n)}$, $\boldsymbol{\delta}_n^{(n)} = \mathbf{L}_n \mathbf{R} \mathbf{U}^{\wedge(n)}$

IF $\boldsymbol{\delta}_n < \boldsymbol{\delta}_{nC}$ **THEN**

$cs^{(n)} = 1,\ \theta^{(n)} = \theta^{(n-1)}$

ELSE

$cs^{(n)} = 2,\ \theta^{(n)} = \theta^{(n-1)}$

ENDIF

ELSEIF $cs^{(n-1)}==2$ **THEN**

$\mathbf{K}_e^{(n)} = \int_{\Omega_e} \mathbf{B}_e^{\mathrm{T}} \mathbf{D} \mathbf{B}_e dV/10^{20}$

$\mathbf{RHS}_e^{(n)} = \mathbf{K}_e^{(n)}\mathbf{U}_e^{(n)} - \mathbf{F}_e^{ext(n)}$

ENDIF

OUTPUT: $\mathbf{RHS}_e^{(n)}$, $cs^{(n)}$, $\theta^{(n)}$, $\mathbf{U}^{\wedge(n)}$, $\boldsymbol{\delta}_n^{(n)}$

Figure A.4: Flow chart of the CDFE for arbitrary crack problems.

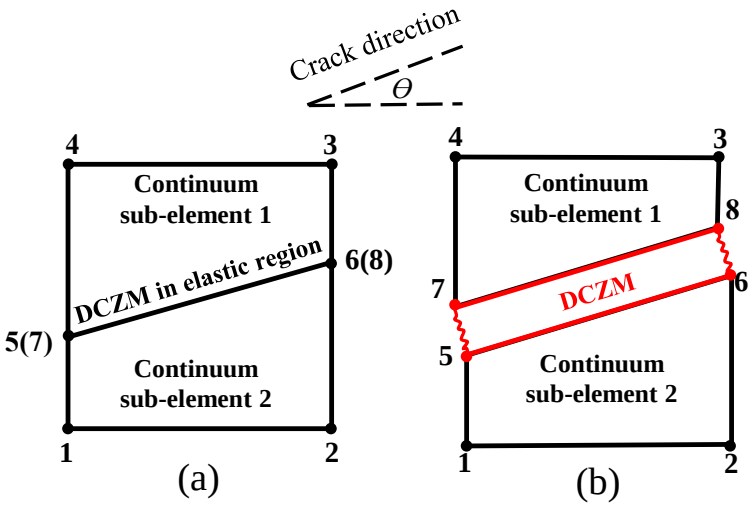

Figure A.5: Modified CDFE for composite damage analysis: (a)before initiation, (b)at and after initiation.

The Novel Mixed Mode Cohesive Formulation

For the CDFE model is discussed in this section, mode I and mode II damage is possible, such as transverse tensile cracking and in-plane shear cracking of matrix. Therefore, scenarios with mode mixity might be encountered. A popular failure criterion usually used is the first-order power law, as described in Equation A.19. In Equation A.19, G_I and G_{II} are dissipated energy of mode I and II.

$$\frac{G_I}{G_{IC}} + \frac{G_{II}}{G_{IIC}} \geq 1 \tag{A.19}$$

When Equation A.19 gets satisfied, there is no guarantee that the mode I and mode II tractions would have zero values. Therefore, the finite-value tractions would be forced to be zeros as the crack propagate. This would again lead to a instantaneous change in the force vector **RHS**. This instantaneous change would induce spurious numerical oscillations in the analysis and reduce the robustness and efficiency of the model. In addition, physically speaking, when a crack is propagated, the tractions on the newly created crack surfaces should be zero.

A novel mixed-mode cohesive formulation has been proposed in [93]. Compared to the traditional cohesive model based on Equation A.19, the novel mixed-mode

cohesive formulation does not require any more material properties while the tractions are guaranteed to vanish simultaneously and smoothly at crack propagation. This mixed-mode cohesive formulation has been integrated to the enhanced CDFE model to improve its behavior dealing with mixed-crack growth.

Mathematical Formulation

In enhanced CDFE for composite damage analyses, the DCZM element is existent inside the CDFE element from the start. The PVW framework for the enhanced CDFE before and after crack initiation is identical to Equation A.3.

Damage Evolution

This part will introduce the novel mixed-mode cohesive formulation. The input parameters for defining the formulation are σ_C, G_{IC}, τ_C, G_{IIC} and η. The formulation is illustrated in Figure A.6 and outlined according to Equations A.20 to A.24.

As seen in Equations A.20 to A.24, first, a scale factor β is calculated by stretching the mode II cohesive law to mode I, while keeping the stretched mode II critical separation equal the corresponding mode I value. The stretching is carried out in Equation A.20 and the critical strength and separation for the stretched mode II law are $\beta\tau_C$ and $\beta\tau_{nC}$ $(=\delta_{nC})$. With scaled traction-separation law, an effective separation δ, which is determined by Equation A.21, is used to obtain the effective tractions t_1 and t_2 from the scaled traction-separation laws. The calculation of the effective tractions is shown in Equation A.22 and A.23. The last step is to scale back the effective tractions to physical values, as shown in Equation A.24.

$$\beta = \frac{\delta_{nC}}{\delta_{tC}} \tag{A.20}$$

$$\delta = \sqrt{\delta_n^2 + (\beta\delta_t)^2} \tag{A.21}$$

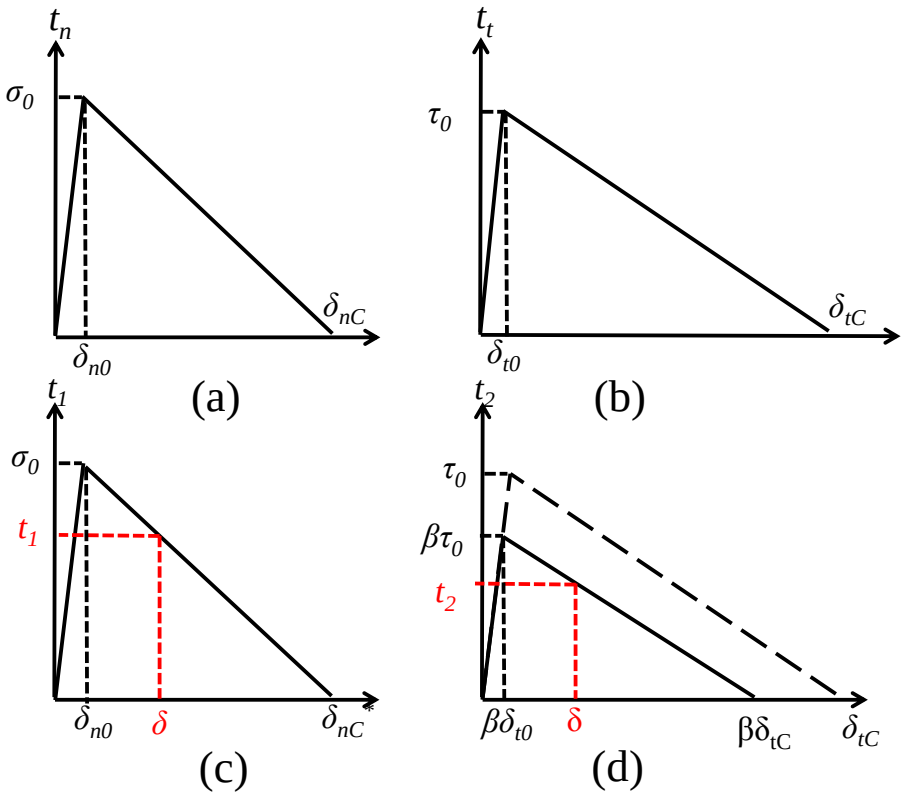

Figure A.6: (a) Mode I cohesive law (b) mode II cohesive law (c) scaled mode I cohesive law (d) scaled mode II cohesive law.

$$t_1(\delta) = \frac{\sigma_C}{\delta_{n0}}\delta \quad (\delta \leq \delta_{n0}), \tag{A.22a}$$

$$t_1(\delta) = \frac{\delta - \delta_{n0}}{\delta_{nC} - \delta_{n0}}\sigma_C \quad (\delta_{n0} \leq \delta < \delta_{nC}), \tag{A.22b}$$

$$t_1(\delta) = 0 \quad (\delta_{nC} < \delta) \tag{A.22c}$$

$$t_2(\delta) = \frac{\beta\tau_C}{\beta\delta_{t0}}\delta \quad (\delta \leq \beta\delta_{t0}), \tag{A.23a}$$

$$t_2(\delta) = \frac{\delta - \beta\delta_{t0}}{\beta\delta_{tC} - \beta\delta_{t0}}\beta\tau_C \quad (\beta\delta_{t0} \leq \delta < \beta\delta_{tC}), \tag{A.23b}$$

$$t_2(\delta) = 0 \quad (\beta\delta_{tC} < \delta) \tag{A.23c}$$

$$t_n(\delta_n, \delta_t) = t_1 \times \frac{\delta_n}{\delta}, \tag{A.24a}$$

$$t_t(\delta_n, \delta_t) = t_2 \times \frac{\delta_t}{\delta} \tag{A.24b}$$

Initiation Criterion

The initiation criterion for the novel mixed-mode cohesive formulation is Equation A.25, meaning that the effective separation is greater than the mode I separation corresponding to damage initiation or the stretched mode II critical separation. The equivalence of these two values is proved in Equation A.26.

$$\delta \geq \delta_{n0} \quad (or\ \delta \geq \beta\delta_{t0}) \tag{A.25}$$

$$\beta\delta_{t0} = \beta\eta\delta_{tC} = \eta\delta_{nC} = \delta_{n0} \tag{A.26}$$

Failure Criterion

The failure criterion of the mixed-mode cohesive formulation is that the effective separation being greater than the mode I separation corresponding to failure or the stretched mode II separation, as shown in Equation A.27. Due to the equivalence of the mode I value and the stretched mode II value, the progressive and simultaneous vanishing of the tractions is ensured.

$$\delta \geq \delta_{nC} \quad (or\ \delta \geq \beta\delta_{tC}) \tag{A.27}$$

FEM Formulation

Since the DCZM element is existent in the CDFE element throughout the analysis, the FEM formulation before and after the crack initiation is uniform, identical to Equations A.11 and A.12. The secant stiffness terms in $\mathbf{K_{DCZM}}$ are obtained from Equation A.14. The tractions are determined according to the mixed-mode cohesive formulation as in Equations A.22, A.23, and A.24.

After calculating the stiffness matrix $\mathbf{K_{DCZM}}$ of the DCZM element, the rest of the FEM procedure is identical to Equations A.13 to A.18. In Equation A.13, the crack angle θ is determined by the fiber angle of the lamina and the interface direction.

The flow chart of the enhanced CDFE for composite damage analysis is shown in Figure A.7. Like that shown in Figure A.4, the superscript (n) means at the time increment n. At the start of time increment n, the known information includes the nodal coordinates $\mathbf{X}$, material properties E_{11}, E_{22}, ν_{12}, G_{12}, σ_C, τ_C, G_{IC} and G_{IIC}, current nodal displacement $\mathbf{U^{(n)}}$, values from the previous increment including crack status $cs^{(n-1)}$, crack angle θ, displacement vector of the dummy nodes $\mathbf{U\hat{}^{(n-1)}}$ and normal, tangential and effective separations $\boldsymbol{\delta}_{\mathbf{n}}^{\mathbf{n-1}}$, $\boldsymbol{\delta}_{\mathbf{t}}^{\mathbf{n-1}}$, $\boldsymbol{\delta}^{\mathbf{n-1}}$. If cs (cracking status) is equal to 0, the element is still pristine. If cs is equal to 1, the crack has initiated in the element. If cs is equal to 2, the element has failed. At the end of time increment n, the right-hand side $\mathbf{RHS_e^{(n)}}$, updated crack status $cs^{(n)}$, displacement vector of the dummy nodes $\mathbf{U\hat{}^{(n)}}$ and normal, tangential and effective separations $\boldsymbol{\delta}_{\mathbf{n}}^{\mathbf{n}}$, $\boldsymbol{\delta}_{\mathbf{t}}^{\mathbf{n}}$, $\boldsymbol{\delta}^{\mathbf{n}}$ are output of the enhanced CDFE VUEL and are passed back to the FEM solver.

A.4 Applications

In this section, CDFE and enhanced CDFE are applied to the micro-scale and meso-scale damage analyses of composites. In the micromechanical damage growth case, the crack angle and path are not known beforehand and need to be determined according to Section A.2. In the meso-scale damage analysis case regarding the delamination toughness tests, the crack orientation is along the interface direction. Both

INPUT: $\mathbf{X}$, $\mathbf{U}^{(n)}$, E_{11}, E_{22}, v_{12}, G_{12}, σ_C, τ_C, G_{IC}, G_{IIC}, θ, $cs^{(n-1)}$, $\mathbf{U}^{\wedge(n-1)}$, $\boldsymbol{\delta}_n^{(n-1)}$, $\boldsymbol{\delta}_t^{(n-1)}$, $\boldsymbol{\delta}^{(n-1)}$

$\delta_{nC} = 2G_{IC}/\sigma_C$, $\delta_{tC} = 2G_{IIC}/\tau_C$, $\beta = \delta_{nC}/\delta_{tC}$

$\mathbf{K}_1 = \int_{\Omega_1} \mathbf{B}_1^{\mathrm{T}}\mathbf{D}\mathbf{B}_1 dV$, $\mathbf{K}_2 = \int_{\Omega_2} \mathbf{B}_2^{\mathrm{T}}\mathbf{D}\mathbf{B}_2 dV$

$\boldsymbol{\delta}^{(n-1)} = \sqrt{\left(\boldsymbol{\delta}_n^{(n-1)}\right)^2 + \left(\beta\boldsymbol{\delta}_t^{(n-1)}\right)^2}$

IF $cs^{(n-1)}==0$ **THEN**

Determine K_{57n}, K_{57t}, K_{68n}, K_{68t} from equation (14)

Determine $\mathbf{K}_{\mathbf{DCZM}}$ from equation (12)

Assemble into global stiffness matrix $\mathbf{K} = \begin{bmatrix} \mathbf{K}^{**} & \mathbf{K}^{*\wedge} \\ \mathbf{K}^{\wedge *} & \mathbf{K}^{\wedge\wedge} \end{bmatrix}$

Static condensation : $\mathbf{K}_e^{(n)} = \mathbf{K}^{**} - \mathbf{K}^{*\wedge}(\mathbf{K}^{\wedge\wedge})^{-1}\mathbf{K}^{\wedge *}$

$\mathbf{RHS}_e^{(n)} = \mathbf{K}_e^{(n)}\mathbf{U}_e^{(n)} - \mathbf{F}_e^{ext(n)}$, $\mathbf{U}^{\wedge(n)} = -(\mathbf{K}^{\wedge\wedge})^{-1}\mathbf{K}^{\wedge *}\mathbf{U}^{(n)}$

$\boldsymbol{\delta}_n^{(n)} = \mathbf{L}_n\mathbf{R}\mathbf{U}^{\wedge(n)}$, $\boldsymbol{\delta}_t^{(n)} = \mathbf{L}_t\mathbf{R}\mathbf{U}^{\wedge(n)}$, $\boldsymbol{\delta}^{(n)} = \sqrt{\left(\boldsymbol{\delta}_n^{(n)}\right)^2 + \left(\beta\boldsymbol{\delta}_t^{(n)}\right)^2}$

IF $\boldsymbol{\delta}^{(n)} < \boldsymbol{\delta}_{n0}$ **THEN**

$cs^{(n)} = 0$

ELSE

$cs^{(n)} = 1$

ENDIF

ELSEIF $cs^{(n-1)}==1$ **THEN**

Determine K_{57n}, K_{57t}, K_{68n}, K_{68t} from equation (14)

Determine $\mathbf{K}_{\mathbf{DCZM}}$ from equation (12)

Assemble into global stiffness matrix $\mathbf{K} = \begin{bmatrix} \mathbf{K}^{**} & \mathbf{K}^{*\wedge} \\ \mathbf{K}^{\wedge *} & \mathbf{K}^{\wedge\wedge} \end{bmatrix}$

Static condensation : $\mathbf{K}_e^{(n)} = \mathbf{K}^{**} - \mathbf{K}^{*\wedge}(\mathbf{K}^{\wedge\wedge})^{-1}\mathbf{K}^{\wedge *}$

$\mathbf{RHS}_e^{(n)} = \mathbf{K}_e^{(n)}\mathbf{U}_e^{(n)} - \mathbf{F}_e^{ext(n)}$, $\mathbf{U}^{\wedge(n)} = -(\mathbf{K}^{\wedge\wedge})^{-1}\mathbf{K}^{\wedge *}\mathbf{U}^{(n)}$

$\boldsymbol{\delta}_n^{(n)} = \mathbf{L}_n\mathbf{R}\mathbf{U}^{\wedge(n)}$, $\boldsymbol{\delta}_t^{(n)} = \mathbf{L}_t\mathbf{R}\mathbf{U}^{\wedge(n)}$, $\boldsymbol{\delta}^{(n)} = \sqrt{\left(\boldsymbol{\delta}_n^{(n)}\right)^2 + \left(\beta\boldsymbol{\delta}_t^{(n)}\right)^2}$

IF $\boldsymbol{\delta}^{(n)} < \boldsymbol{\delta}_{nC}$ **THEN**

$cs^{(n)} = 1$

ELSE

$cs^{(n)} = 2$

ENDIF

ELSEIF $cs^{(n-1)}==2$ **THEN**

$\mathbf{K}_e^{(n)} = \int_{\Omega_e} \mathbf{B}_e^{\mathrm{T}}\mathbf{D}\mathbf{B}_e dV / 10^{20}$

$\mathbf{RHS}_e^{(n)} = \mathbf{K}_e^{(n)}\mathbf{U}_e^{(n)} - \mathbf{F}_e^{ext(n)}$

ENDIF

OUTPUT: $\mathbf{RHS}_e^{(n)}$, $cs^{(n)}$, $\mathbf{U}^{\wedge(n)}$, $\boldsymbol{\delta}_n^{(n)}$, $\boldsymbol{\delta}_t^{(n)}$, $\boldsymbol{\delta}^{(n)}$

Figure A.7: Flow chart of the enhanced CDFE for composite damage analysis.

CDFE and enhanced CDFE are applied to the delamination toughness tests. The only difference between the CDFE and enhanced CDFE used for composite damage analysis is that the propagation of crack in CDFE is determined by the first-order power law (Equation A.19) while the crack propagation in enhanced CDFE is determined by the novel mixed-mode cohesive formulation.

A.4.1 Micromechanical Crack Growth

Micromechanical damage analysis of a representative volume element (RVE) with 13 randomly packed fiber is performed to demonstrate the capability of CDFE to tackle problems with arbitrary crack initiation and propagation. This RVE model follows the work reported in [13] and [135], where the micromechanical damage analyses were conducted using the framework of high-fidelity generalized method of cells (HFGMC) and the Carrera unified formulation (CUF) [136].

The size of the RVE studied is $21.25\ \mu m \times 21.25\ \mu m$. The material properties used for CDFE analyses are listed in Table A.1. Following [13], the assumption of plane strain is used and implemented in CDFE. The maximum principal stress criterion is used to determine the crack initiation and crack orientation inside each CDFE element. Periodic boundary condition (PBC) is applied to the RVE, as that in [13] and [135]. The PBC is as illustrated in Equation A.28, where the superscripts 1 and 2 correspond to the first and second node of a certain node pair. RF represents the reference node. The subscript i represents the i^{th} DOF of the node. However, it should be pointed out that whether PBC can be applied to the micromechanical damage analysis is still an open question.

$$u_i^1 - u_i^2 = u_i^{RF} \tag{A.28}$$

To perform sensitivity study of CDFE regarding mesh sizes and the types of the traction-separation laws, three meshes of the RVE are generated, as shown in Figure

Table A.1: Elastic and fracture properties of the glass fiber and epoxy matrix used in the RVE [13]

Property	Value	Property	Value
E_f (GPa)	74.0	G_m (GPa)	1.79
ν_f	0.2	σ_C^m (MPa)	0.0143
G_f (GPa)	30.8	τ_C^m (MPa)	0.0237
E_m (GPa)	4.65	G_{IC}^m (N/mm)	0.000563
ν_m	0.35	G_{IIC}^m (N/mm)	0.00385

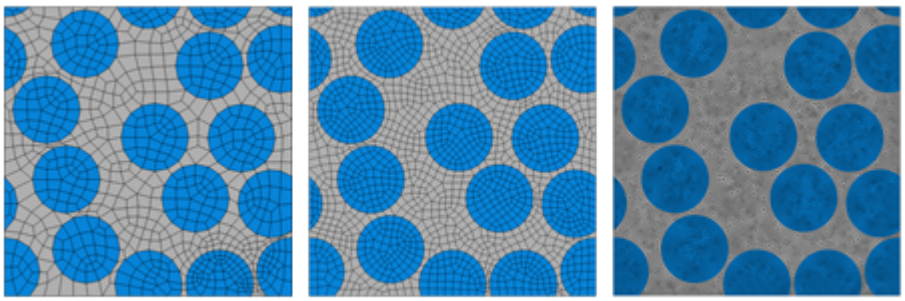

Figure A.8: Meshes of the RVE: (a) mesh 1, (b) mesh 2, and (c) mesh 3

A.8. In Figure A.8, the three meshes have various elemental sizes ranging from 1.0 μm to 0.2 μm. CDFE implemented with a bi-linear and an exponential traction-separation law are applied to these three meshes. The bi-linear traction-separation law is determined according to Equations A.6 and A.7. The exponential law follows Equation A.29. The required material parameters to define the exponential law are identical to that required for the bi-linear law. The comparison of the bi-linear and exponential law is shown in Figure A.9.

$$t_n(\delta_n) = \frac{\sigma_C}{\delta_{n0}}\delta_n \ (\delta_n \leq \delta_{n0}), \tag{A.29a}$$

$$t_n(\delta_n) = \sigma_C exp(\frac{-\sigma_C}{G_C}(\delta_n - \delta_{n0})) \ (\delta_{n0} \leq \delta_n \leq \delta_{nC}), \tag{A.29b}$$

$$t_n(\delta_n) = 0 \ (\delta_{nC} \leq \delta_n) \tag{A.29c}$$

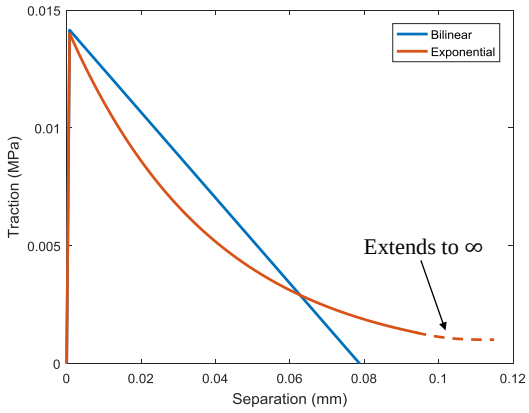

Figure A.9: Comparison of the bi-linear and exponential traction-separation laws

In the three meshes shown in Figure A.8, three types of elements are existent, including plane strain element with reduced integration (CPE4R) for the fiber, CDFE user elements for the matrix, and dummy elements for the visualization purpose. The dummy elements have extremely low stiffness values compared to the fiber and CDFE matrix elements such that no contribution is made from the dummy elements to the damage analysis. A nominal tensile strain of 0.004 along the global 2^{nd} direction (perpendicular to the fiber direction) is applied to the RVE.

The predicted displacement fields along the traverse loading direction of the three meshes after the failure of the RVE with the bi-linear and exponential traction-separation laws are shown in Figure A.10. From the figure, clear bands of displacement discontinuity are seen, implying the crack paths. Among the three meshes using the same traction-separation law, the crack paths are different. However, for the results using the same mesh but various traction-separation laws, the crack paths are essentially the same.

A more detailed and direct observation of the crack path can be found in Figure A.11. The plots in Figure A.11 were generated by plotting out the inserted dummy nodes. with the DCZM elements explicitly shown, the crack opening can be visualized. From Figure A.11, macroscopic cracks going through the RVE are seen. The

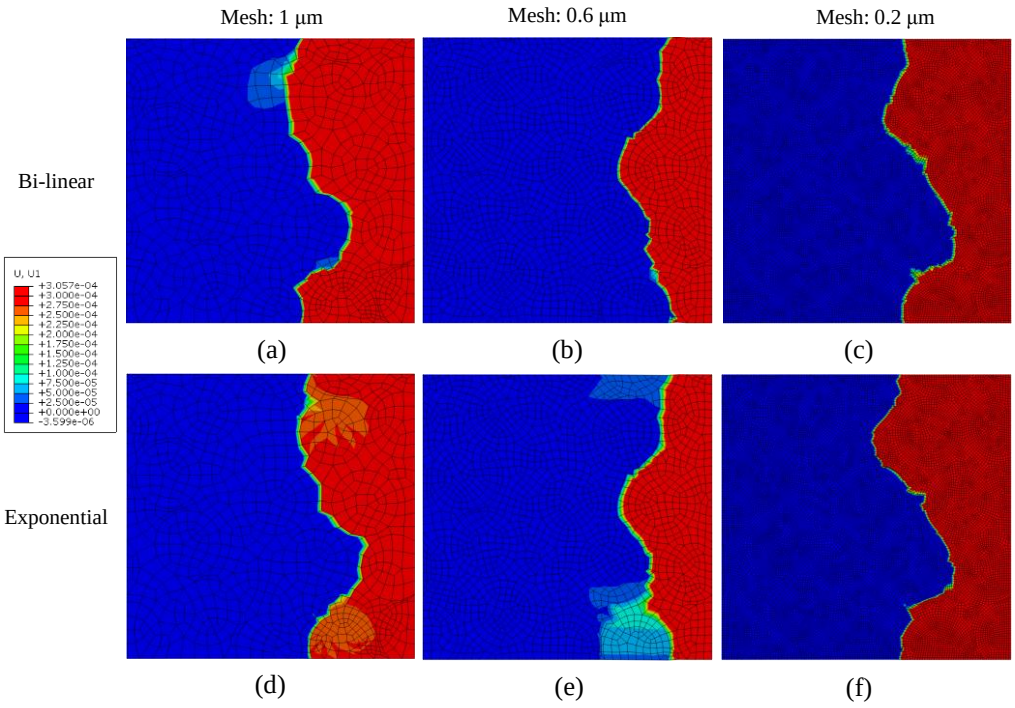

Figure A.10: Displacement fields of the RVE: (a) Mesh: 1.0 μm/Bi-linear, (b) Mesh: 0.6 μm/Bi-linear, (c) Mesh: 0.2 μm/Bi-linear,(d) Mesh: 1.0 μm/Exponential, (e) Mesh: 0.6 μm/Exponential and (e) Mesh: 0.2 μm/Exponential

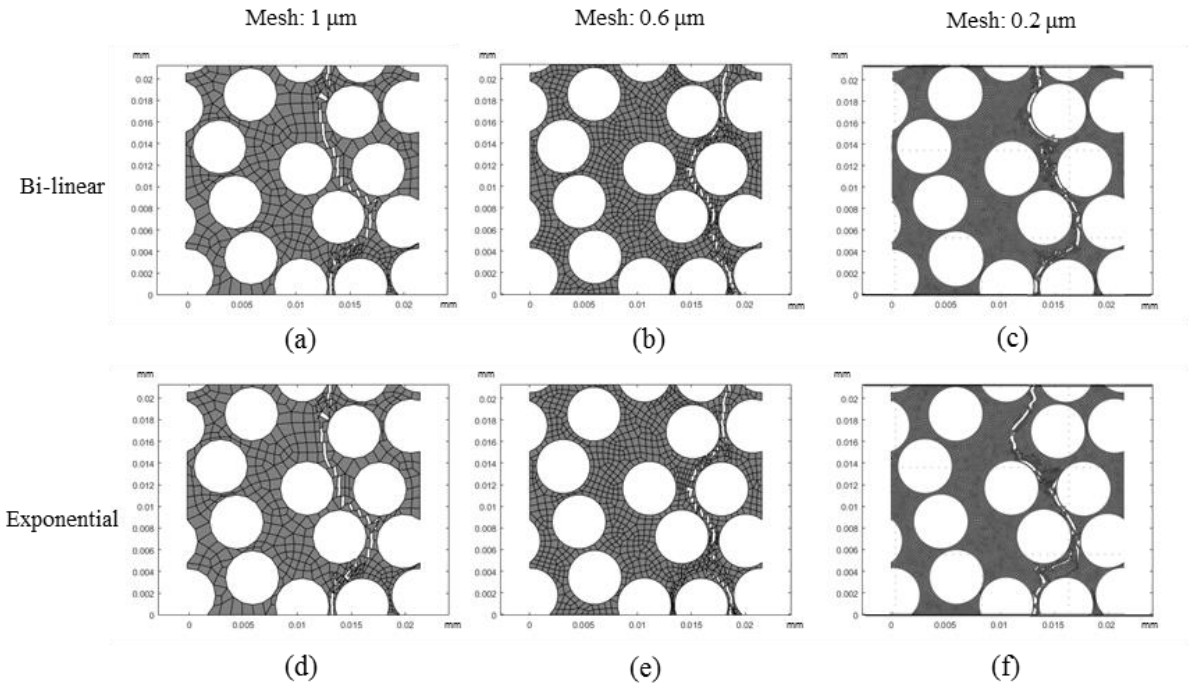

Figure A.11: Crack plots with dummy nodes of the RVE: (a) Mesh: 1.0 μm/Bi-linear, (b) Mesh: 0.6 μm/Bi-linear, (c) Mesh: 0.2 μm/Bi-linear,(d) Mesh: 1.0 μm/Exponential, (e) Mesh: 0.6 μm/Exponential and (e) Mesh: 0.2 μm/Exponential

macroscopic cracks are found to be formed by dummy cracks inside the cracked CDFE elements. At some locations, the dummy cracks inside the CDFE elements are quite continuous. However, at other locations, the continuity of the macroscopic cracks is interrupted by dummy cracks not aligning well.

The stress-strain responses of all the analyzed cases are shown in Figure A.12. The results obtained in this appendix agree well with that from [13]. Critical parameters including the initial stiffness, peak stress, and strain corresponding to failure are tabulated in Table A.2. In the table, the last column corresponds to the results in [13]. The other columns are the results obtained with CDFE using the three meshes and two traction-separation laws. Root-mean-square deviation (RMSE) and maximum error of the values are measured to investigate the variance of the data.

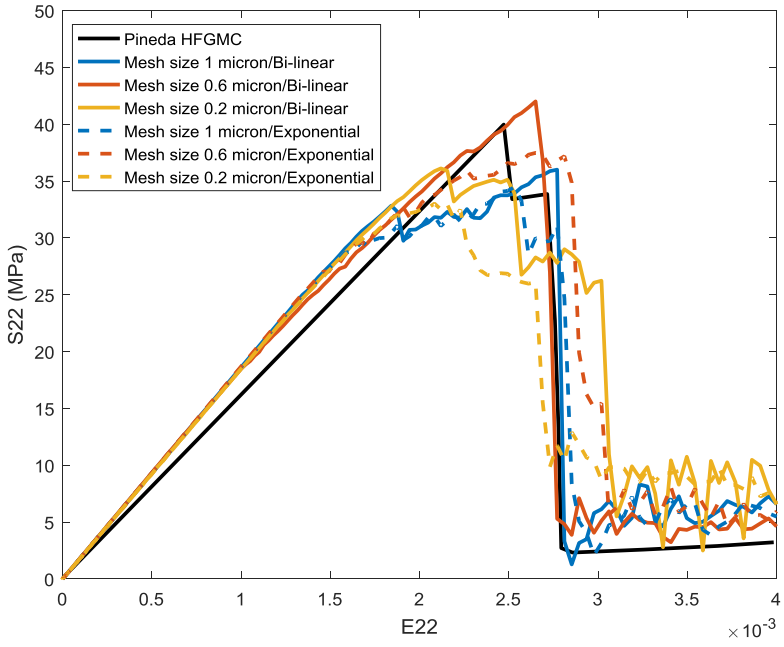

Figure A.12: Comparison of the stress strain curves obtained with CDFE and HFGMC

RMSEs for the three critical parameters are 8.9%, 11.4% and 4.8%. The maximum error for the parameters are 8.9%, 17.4% and 10.2%. Generally speaking, from Figure A.11 and Table A.2, the CDFE results agree well with the results obtained in [13].

The damage growth history is associated with the stress-strain curve in Figure A.13 for the case with the mesh size being 0.6 μm and the traction-separation law being bi-linear. From the figure. the damage initiation and growth is as illustrated as follows. First, before state (a), there is no dummy crack initiated in any of the

Table A.2: Comparison of the critical parameters

	CDFE						
	1 μm		0.6 μm		0.2 μm		
	Bi.	Exp.	Bi.	Exp.	Bi.	Exp.	
Ini. stiffness (GPa)	18.3	18.3	18.3	18.3	18.3	18.3	16.8
Peak load (MPa)	36.1	34.4	42.1	37.8	36.0	33.2	40.2
Failure strain	2.78e-3	2.82e-3	2.75e-3	2.86e-3	3.03e-3	2.67e-3	2.75e-3

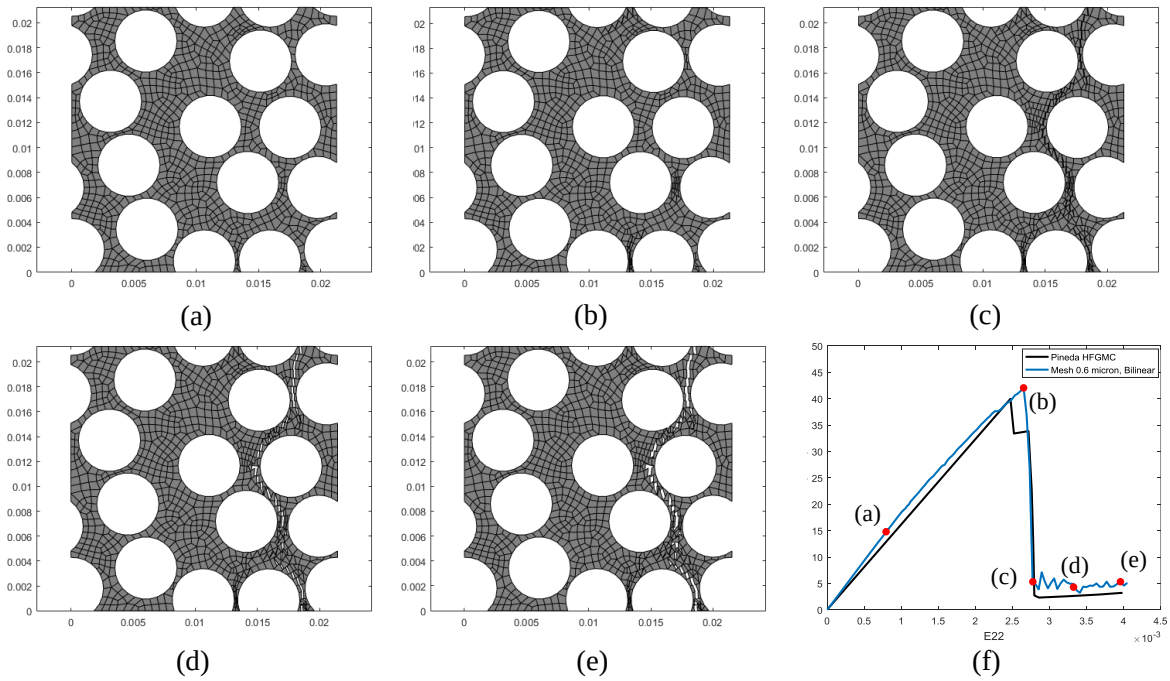

Figure A.13: Transverse crack growth in the RVE.

CDFE element. Also, as seen in Figure A.13 (f), before stage (a), the stress-strain curve is linear. Between stages (a) and (b), cracks initiate and open. However, the separation between the crack surfaces is barely visibly. The cracks initiate mostly at locations between closely packed fibers, where stress concentration is most likely to happen. Stage (b) as shown in Figure A.13 (b) corresponds to the peak point of the stress-strain curve displayed in Figure A.13 (f). Immediately after stage (b), a drastic stress drop is seen, corresponding the the connection of multiple cracks from stage (b) to stage (c). As seen in Figure A.13 (c), the macroscopic crack almost cut through the whole RVE, indicating the failure of the RVE. At stage (c), the cracks in the cracked CDFE elements align well with the macroscopic crack path. However, as seen in stages (d) and (e), some elements with interrupting cracks are seen.

Special attention is paid to an interrupting cracked CDFE element described in Figure A.13 and highlighted in Figure A.14. From Figure A.14 (c), the red frame represents the original shape of the element at the beginning of the analysis. At

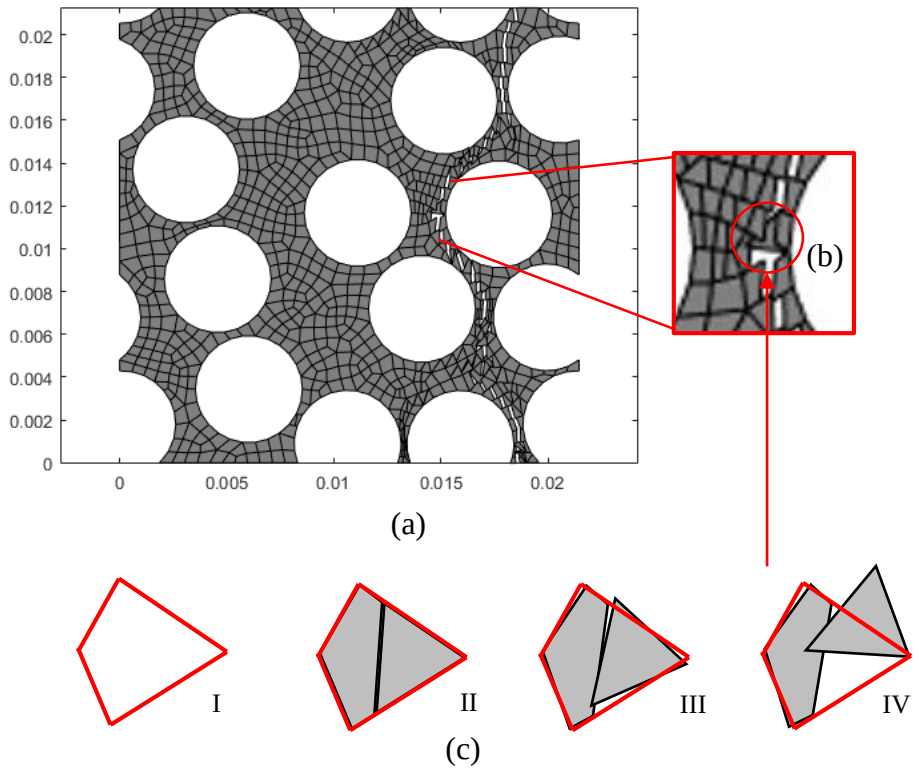

Figure A.14: Observation of the deformation of a CDFE element and its sub-elements.

stage I, no crack initiates. At stage (II), the crack initiates inside the CDFE element. From stage (II) to (IV), one of the two sub-elements shears out of the CDFE elemental boundary (the red frame) and induces the interruption of the continuity of macroscopic crack. Stages (I) and (II) correspond to points (a) and (b) in Figure A.13. Stages (III) and (IV) correspond to points (d) and (e) in Figure A.13. This shearing-out deformation of the sub-element is due to that fact that no constraint is applied to the CDFE elemental system to prevent the sub-elements from reaching into its neighbouring CDFE elements.

A.4.2 Delamination Toughness Tests

In Section A.4.1, the capability of CDFE to capture arbitrary crack initiation and growth has been demonstrated. This section will focus on the composite damage

analysis. Delamination toughness tests are modeled with CDFE and enhanced CDFE. The reason for studying the delamination toughness tests is that the crack orientation is well defined and mixed-mode cracking scenarios are possible.

Delamination toughness tests include the double cantilever beam bending (DCB) test for pure mode I cracking, the end notched flexure (ENF) test for mode II cracking, and the mixed mode bending (MMB) test for mixed-mode cracking. Benchmark results obtained with virtual crack closure technique (VCCT) technique exist for the delamination toughness tests [14]. CDFE results will be compared to the benchmark results from [14] in this section. It should be noticed that for the DCB (mode I) and ENF (mode II) tests, the results obtained with CDFE and enhanced CDFE are expected to be identical, since there is no mode mixity and the mixed-mode formulation implemented in enhanced CDFE would converge to single-mode formulation in CDFE. However, for the MMB (mixed-mode) tests, difference between the CDFE and enhanced CDFE results is expected.

DCB

The DCB test is illustrated in Figure A.15 (a). The geometry and material properties are from [14] and are listed in Tables A.3 and A.4. Since explicit algorithm was used for the analysis, material density ρ, mode I and mode II crack strengths are introduced from [137], s $\rho = 1.495 g/cm^3$, $\sigma_C = 50$ MPa, $\tau_C = 70$ MPa. The load-displacement curves predicted using CDFE and enhanced CDFE are compared to the benchmark results in Figure A.16. From Figure A.16, it is observed that in the pre-peak region, the initial stiffness values predicted by CDFE and enhanced CDFE agree very well with the benchmark results. The benchmark peak load is 62.0 N, while that obtained by CDFE and enhanced CDFE are 61.9 N. The error is 0.16%. In the post-peak region, both the CDFE and enhanced CDFE curves are oscillatory, which is the nature of explicit analyses. It is found that the CDFE and enhanced CDFE results are essentially identical, which is expected, since there is only mode I

Table A.3: Geometry parameters for the DCB case [14]

a	Initial crack length	30.5	mm
L	Half support distance	75.0	mm
h	Half thickness	1.5	mm
b	Out-of-plane width	25.0	mm

Table A.4: Material properties of T300/1076 [14]

E_{11}	139.4	GPa	$G_{12} = G_{13}$	4.6	GPa
$E_{22} = E_{33}$	10.16	GPa	G_{23}	3.54	GPa
$\nu_{12} = \nu_{13}$	0.3		G_{IC}	0.170	N/mm
ν_{13}	0.436		G_{IIC}	0.494	N/mm

cracking in the DCB test.

ENF

The ENF test is illustrated in Figure A.15 (b). The geometry and material properties are listed in Tables A.5 and A.6. The material density, mode I and II strengths are again from [137]. The load-displacement curves obtained with CDFE, enhanced CDFE are plotted in Figure A.17 against the benchmark results in [14]. As shown in the figure, the initial stiffnesses agree well. The peak loads obtained by CDFE and enhanced CDFE are 1381.0 N, while the benchmark solution is 1526.0 N. The error is 9.50%. In both the CDFE and enhanced CDFE curves, after the peak load, vertical drops of load are seen, which is the nature of explicit analyses. In the post-peak region, both the CDFE and enhanced CDFE curves show oscillations. However, the magnitude of the oscillations are of different magnitudes. The magnitude of the enhanced CDFE results seems to be slightly smaller than the CDFE results. This is due to two major factors. First, in the ENF modeling, a small extent of mode mixity is usually induced. Second, as illustrated in Section A.3, after crack initiation, dummy nodes are immediately introduced into CDFE, while for enhanced CDFE, the dummy nodes are always existent. The sudden stiffness degradation introduced by the introduction of dummy nodes in CDFE would induce spurious numerical oscillations which are avoided by enhanced CDFE.

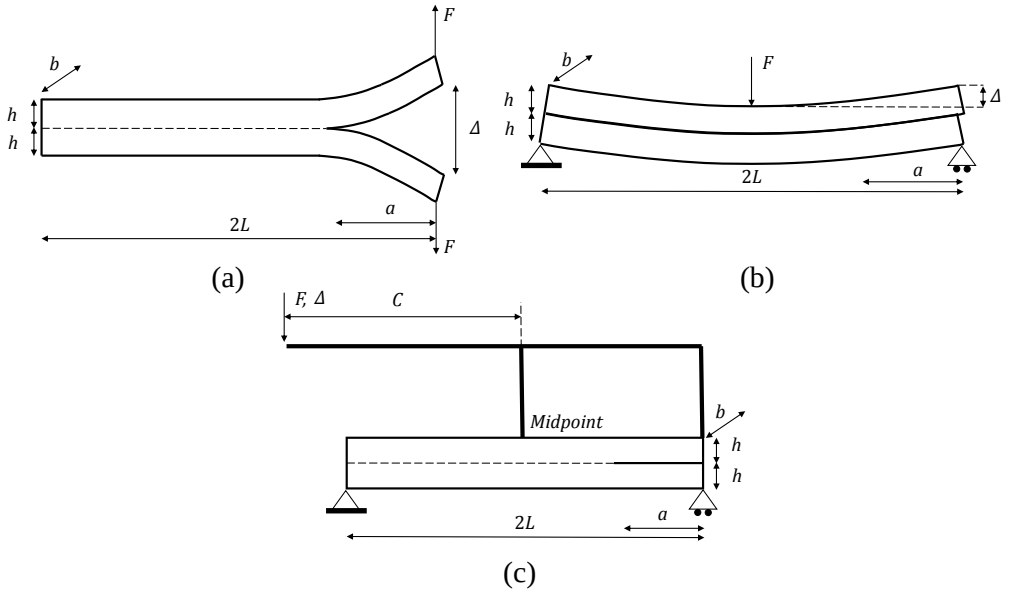

Figure A.15: Set-up for the delamination toughness tests: (a) DCB, (b) ENF and (c) MMB

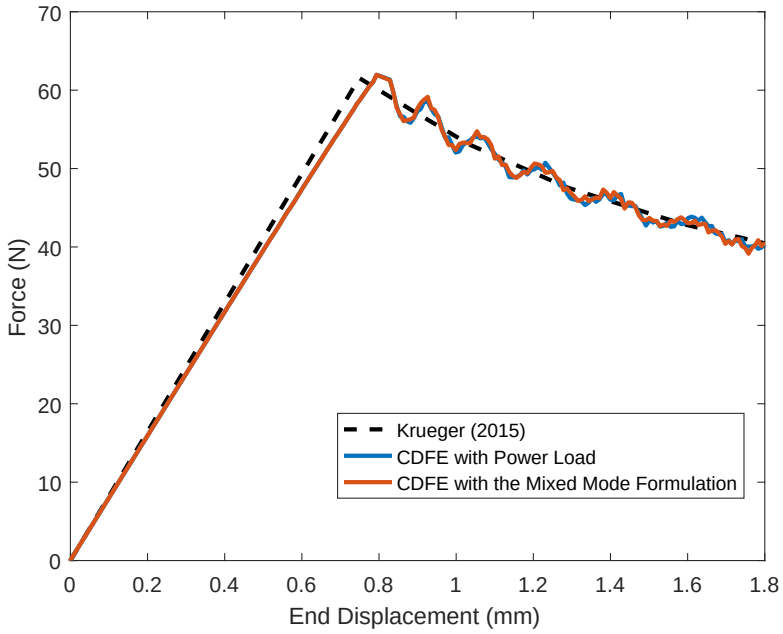

Figure A.16: Load-displacement curve of the DCB case

Table A.5: Geometry parameters for the ENF case [14]

a	Initial crack length	25.4	mm
L	Half support distance	50.8	mm
h	Half thickness	2.25	mm
b	Out-of-plane width	25.4	mm

Table A.6: Material properties of IM7/8552 [15]

E_{11}	161	GPa	$G_{12} = G_{13}$	5.2	GPa
$E_{22} = E_{33}$	11.38	GPa	G_{23}	3.9	GPa
$\nu_{12} = \nu_{13}$	0.32		G_{IC}	0.212	N/mm
ν_{13}	0.45		G_{IIC}	0.774	N/mm

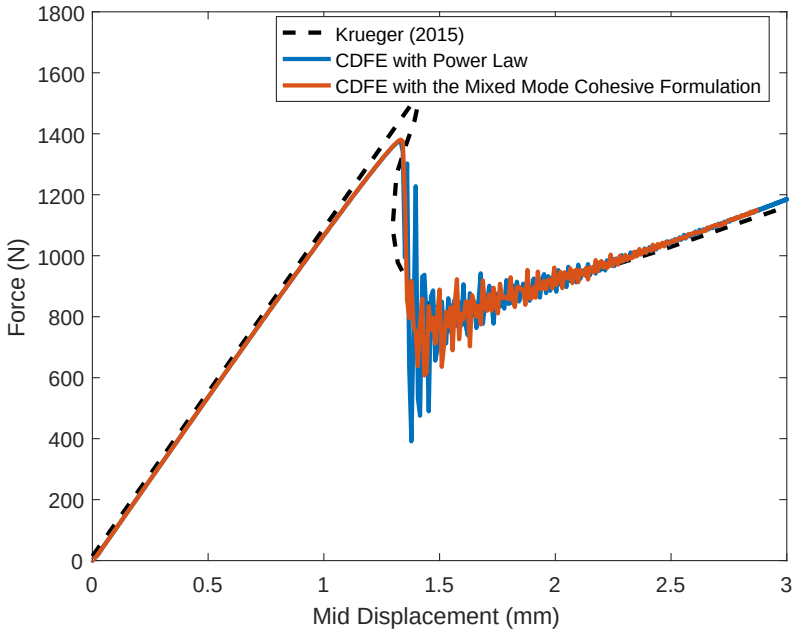

Figure A.17: Load-displacement curve of the ENF case

MMB

The MMB tests are illustrated in Figure A.15 (c). Three mixed-mode ratios have been studied, as that in [14]. The mixed-mode ratio is defined by $R = G_{II}/(G_I+G_{II})$. The relation between geometry and R can be found in the appendix of [138]. The geometry parameters and material properties can be found in Tables A.7 and A.6. Additional material properties including material density, mode I and mode II strengths are from [137]. The load-displacement curves obtained with CDFE and enhanced CDFE for the three mixed-mode ratios are plotted against the corresponding benchmark results from [14] in Figure A.18. For all the mixed-mode ratios, the initial stiffnesses predicted by CDFE and enhanced CDFE agree well with the benchmark values. The peak loads are listed in Table A.8. As seen in Table A.8, the maximum difference between the CDFE and enhanced CDFE predictions from the benchmark results is 5.45%, happening for the case with the mixed-mode ratio being 50%. Generally speaking, before the peak loads, the CDFE and enhanced CDFE results are identical. After the peak loads, CDFE results are more oscillatory than the enhanced CDFE results. As the case gets more inclined to a pure-mode case (R=20% and 80%), the differences in results obtained with CDFE and enhanced CDFE become less significant. This is due to the difference in the damage evolution laws implemented in the two methods. In CDFE, when the first-order power law as in Equation A.19, the tractions which might have finite values are forced to be zeros. In enhanced CDFE, the implementation of the novel mixed-mode cohesive formulation ensures that the tractions degrade to zeros simultaneously and progressively. Therefore, for a mixed-mode case, the enhanced CDFE results should be less oscillatory.

A.5 Summary and Conclusions

CDFE is a novel finite element scheme that seamlessly bridges continuum damage analysis and discrete damage analysis. Before the crack initiation, a CDFE element

Table A.7: Geometry parameters for the MMB cases [14]

a	Initial crack length	25.4	mm
L	Half support distance	50.8	mm
h	Half thickness	2.25	mm
b	Out-of-plane width	25.4	mm
c	Length of lever arm	R=20%: 92.9 R=50%: 41.3 R=80%: 27.3	mm

Table A.8: Load-displacement curve of three MMB cases

R	Benchmark (N)	CDFE (N)	Enhanced CDFE (N)	Max difference
20%	128.5	130.3	129.2	1.40%
50%	385.0	370.0	363.4	5.45%
80%	751.0	750.5	738.1	1.72%

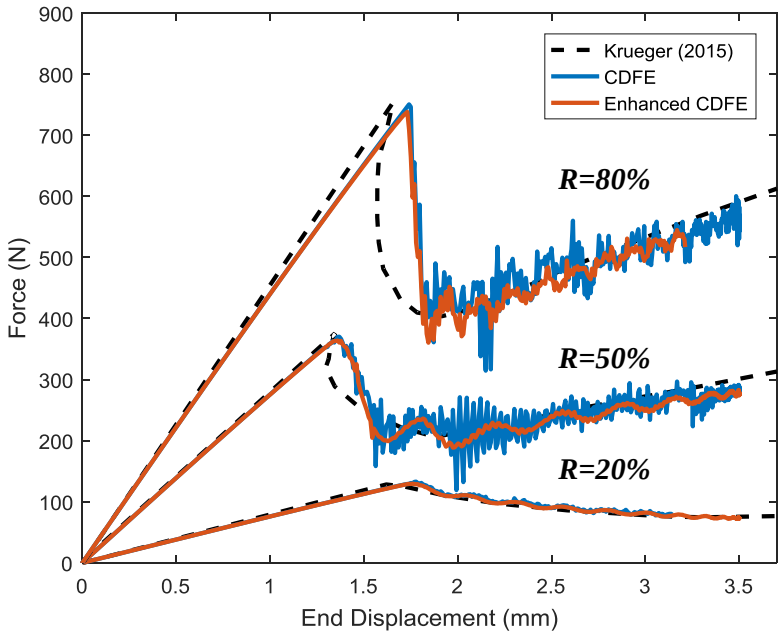

Figure A.18: Load-displacement curve of three MMB cases

is identical to a continuum element with elastic properties. After the crack initiation, a CDFE element is split into two elastic sub-elements connected by a DCZM cohesive element. CDFE has been developed and applied micro-scale and meso-scale PFA of composite materials in this appendix. Two categories of CDFE have been discussed and implemented. The first version is capable of predicting the initiation and growth of arbitrary cracking. The second version of CDFE is customized to perform meso-scale damage analysis of composites where the crack angle is usually known before the crack initiation. A novel mixed-mode cohesive formulation has been integrated into the second version of CDFE, and hence enhanced CDFE has been developed.

From the micromechanical PFA of a composite RVE, the first version of CDFE has been proved capable of predicting the initiation and growth of matrix cracks. The failing process of the RVE has been investigated, and the CDFE results show that, first, matrix cracks initiate at the locations where the fibers are closely packed. Then as the cracks develop and coalesce, the RVE fails with a drastic load drop. After the drastic load drop, some sub-elements are observed to shear out of the CDFE elemental boundaries. This phenomenon is caused by the fact that the current CDFE method does not enforce any crack tracking algorithm to ensure crack continuity.

The second version of CDFE and enhanced CDFE have been applied to model the delamination toughness tests, including a DCB, an ENF, and three MMB tests with various mixed-mode ratios. The CDFE results are compared to benchmark results reported in [14]. In general, the CDFE results agree very well with the benchmark results. Several differences are seen, such as the "snap-back" in the ENF test not being captured by CDFE or enhanced CDFE, which is due to the nature of explicit analyses. In addition, the CDFE and enhanced CDFE results are more oscillatory than the benchmark results, which is again due to the analyses being explicit. The major finding is that in the MMB cases, in the post-peak region, the enhanced CDFE results are less oscillatory than the CDFE result, proving that the implementation of

the novel mixed-mode cohesive formulation is effective.

APPENDIX B

3D EST Model with Damage Initiation Criteria based on the Mohr-Coulomb Model

B.1 Introduction

The Mohr-Coulomb (M-C) damage initiation criterion is widely used to describe matrix failure with considering frictional sliding. It assumes that the matrix damage initiation and propagation occur with a stress state as a certain combination of principal stresses. From experimental observations [36], composite materials fail in transverse (2 and 3 directions) compression by shearing along the failure plane oriented at an angle θ with respect the loading direction, as shown in Figure B.1. Figure B.1 (a) shows the fracture plane and the lamina local coordinate system 1-2-3. Figure B.1 (b) shows the fracture plane and the local coordinate system of the crack N-T-L.

The M-C criterion in its general form is defined as in Equation B.1.

$$|\tau_{cr}| \geq S_i + |\sigma_N| tan(\phi), (\sigma_N < 0) \tag{B.1}$$

where, τ_{cr} and σ_N are the shear and normal stresses on the fracture plane. S_i is the shear strength of the material. ϕ is the angle of friction, which is a material parame-

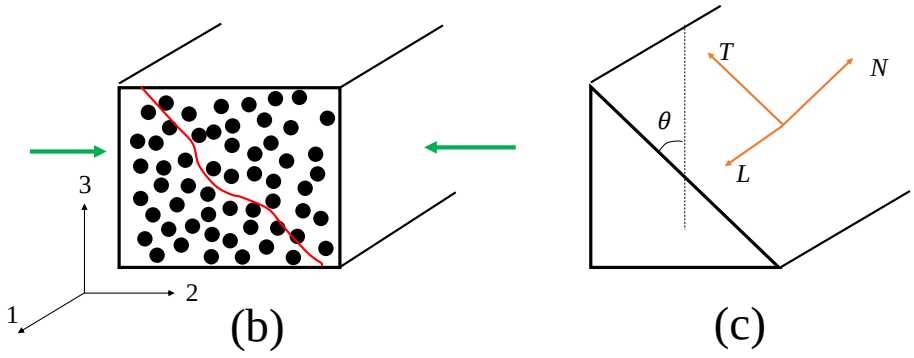

Figure B.1: The fracture plane of CFRP composites due to transverse compression: (a) an illustration of the fracture plane, and (b) the local coordinate system on the fracture plane.

ter measured from transverse compressive tests, related to the internal coefficient of friction μ as in Equation B.2.

$$\phi = tan^{-1}(\mu) \tag{B.2}$$

The relation between the crack plane θ and the angle of friction ϕ is as in Equation B.3.

$$2\theta = \phi + \frac{\pi}{2} \tag{B.3}$$

The M-C criterion can be illustrated better by the Mohr circle, as shown in Figure B.2. In Figure B.2, the green line is expressed by $\tau_{cr} = S_i + |\sigma_N| tan(\phi)$. Any stress state having its Mohr circle intersecting with the green line would satisfy the M-C criterion and the damage would initiate with respect to the crack plane at the crack angle θ [12, 139].

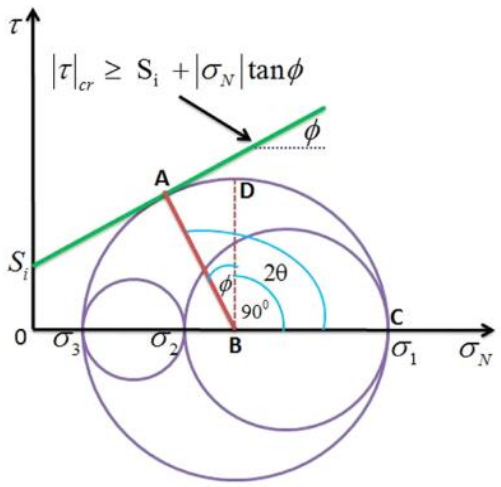

Figure B.2: The M-C criterion illustrated with a Mohr circle [12].

B.2 Implementing the M-C Criterion in 3D EST

B.2.1 M-C Criterion for Composites

The M-C criterion in 3D EST – where the 3D element is a homogenized transversely isotropic material, corresponds to describing transverse compressive failure when the normal stress σ_{NN} on the crack plane is compressive. When σ_{NN} is tensile, the second-order criterion similar to Equation 4.15 is still used, but in a stress-based form.

The pre-peak nonlinearity is still captured by ST in the lamina 1-2-3 coordinate system, as described in Section 4.2. For the matrix tensile damage initiation ($\sigma_{NN} > 0$), the quadratic criterion as shown in Equation B.4 is used.

$$(\frac{\sigma_{NN}}{\sigma_{22}^{ini,T}})^2 + (\frac{\tau_{NL}}{\tau_{12}^{ini}})^2 + (\frac{\tau_{NT}}{\tau_{23}^{ini}})^2 \geq 1, (\sigma_{NN} \geq 0) \tag{B.4}$$

In Equation B.4, $\sigma_{22}^{ini,T}$, τ_{12}^{ini}, and τ_{23}^{ini} are material strengths whose corresponding strain values are $\epsilon_{22}^{ini,T}$, γ_{12}^{ini}, and γ_{23}^{ini}, which have been illustrated in Chapter IV, as in Equation 4.15 and Equation 4.16.

For the matrix compressive damage initiation, the M-C criterion is adjusted using

Equation B.1. The modified M-C criterion sometimes is also referred to as the Puck and Schurmann criterion [86]. In this appendix, it is still referred to as the M-C criterion. The M-C criterion is Equation B.5.

$$(\frac{\tau_{NL}}{\tau_{12}^{ini} - \mu_L \sigma_{NN}})^2 + (\frac{\tau_{NT}}{\tau_{23}^{ini} - \mu_T \sigma_{NN}})^2 \geq 1, (\sigma_{NN} < 0) \tag{B.5}$$

Equation B.5 is adjusted using Equation B.1. The compressive normal stress serves as enhancing the matrix shear strengths due to the internal friction.

B.2.2 The Competing Algorithm to Determine the Fracture Angle

With a generic stress state $[\sigma_{11}, \sigma_{22}, \sigma_{33}, \tau_{23}, \tau_{13}, \tau_{12}]^T$, the fracture plane (fracture angle θ) needs to be determined based on if the stress state satisfies Equation B.4 or Equation B.5 first. A competing algorithm has been proposed to determine the fracture plane angle and if tensile or compressive matrix damage would initiate. At each time increment, the fracture angle θ is scanned from 0° to 180° with a certain interval, such as 1°. At each angle, Equations B.4 and B.5 are evaluated based on the stress state calculated at the end of the previous time increment. Once the tensile or compressive damage initiation criterion is satisfied, the crack angle θ is fixed and the post-peak degradation is performed on the fixed fracture plane. The flow chart of this algorithm is shown in Figure B.3. In Figure B.3, the coordinate transformation matrix is shown in Equation B.6. In Equation B.6, coordinate systems 1-2-3 and N-L-T are shown in Figure B.1.

$$\begin{bmatrix} cos(L,1) & cos(L,2) & cos(L,3) \\ cos(N,1) & cos(N,2) & cos(N,3) \\ cos(T,1) & cos(T,2) & cos(T,3) \end{bmatrix} \tag{B.6}$$

Since for laminated composites, the fracture plane would only rotate around the 1-axis in the 2-3 plane, the stress rotation matrix can be simplified as,

The Competing Algorithm for Matrix Tensile/Compressive Crack Initiation

At inc i, $\boldsymbol{\sigma^{i-1}}$ is known. $\theta = 0{:}1{:}180$
do j=1:length(θ)
    calculate coordinate transformation matrix $\boldsymbol{T(\theta(j))}$
    calculate transformed stress $\boldsymbol{\sigma_{cr}^{i-1} = T\sigma^{i-1}T^{T}}$
    calculate $f_{MT} = \left(\frac{\sigma_{NN}}{\sigma_{22}^{ini}}\right)^2 + \left(\frac{\tau_{NL}}{\tau_{12}^{ini}}\right)^2 + \left(\frac{\tau_{NT}}{\tau_{23}^{ini}}\right)^2$
    calculate $f_{MC} = \left(\frac{\tau_{NL}}{\tau_{12}^{ini} - \mu_L \sigma_{NN}}\right)^2 + \left(\frac{\tau_{NT}}{\tau_{23}^{ini} - \mu_T \sigma_{NN}}\right)^2$
    if $f_{MT} \geq 1$ then
        tensile initiation
        $\theta_{cr} = \theta(j)$
        break
    end if
    if $f_{MC} \geq 1$ then
        compressive initiation
        $\theta_{cr} = \theta(j)$
        break
    endif
    if tensile/compressive initiated then
        break
    endif
end do

Figure B.3: The competing algorithm to determine matrix tensile/compressive damage initiation and the fracture plane.

$$\sigma_{LL} = \sigma_{11} \tag{B.7a}$$

$$\tau_{NL} = \tau_{13} sin(\theta) + \tau_{12} cos(\theta) \tag{B.7b}$$

$$\tau_{LT} = \tau_{13} cos(\theta) - \tau_{12} sin(\theta) \tag{B.7c}$$

$$\sigma_{NN} = \sigma_{22} cos^2(\theta) + \sigma_{33} sin^2(\theta) + 2\tau_{23} sin(\theta) cos(\theta) \tag{B.7d}$$

$$\tau_{NT} = (\sigma_{33} - \sigma_{22}) sin(\theta) cos(\theta) + \tau_{23}(cos^2(\theta) - sin^2(\theta)) \tag{B.7e}$$

$$\sigma_{TT} = \sigma_{33} cos^2(\theta) + \sigma_{22} sin^2(\theta) - 2\tau_{23} sin(\theta) cos(\theta) \tag{B.7f}$$

Table B.1: Material properties of E-Glass/LY556 [16, 17].

$\sigma_{22}^{ini,T}$	$\sigma_{22}^{ini,C}$	τ_{12}^{ini}	θ_0
36 Mpa	138 MPa	61 MPa	53°

B.2.3 Application of the M-C Criterion

The M-C criterion following the flow chart shown in Figure B.3 is applied to the prediction of the damage initiation envelope of the material system E-Glass/LY556. The material parameters used are listed in Table B.1. In Table B.1, the value θ_0 is measured from uniaxial transverse compression tests. The strength τ_{23}^{ini} is calculated from $\sigma_{22}^{ini,C}$ and θ_0 based on Equation B.8. The internal frictional coefficients are calculated according to Equations B.9 and B.10.

$$\tau_{23}^{ini} = \frac{\sigma_{22}^{ini,C}}{2tan(\theta_0)} \tag{B.8}$$

$$\mu_T = -\frac{1}{tan(2\theta_0)} \tag{B.9}$$

$$\mu_L = \mu_L \frac{\tau_{12}^{ini}}{\tau_{23}^{ini}} \tag{B.10}$$

The predicted failure envelope of E-Glass/LY556 is compared to that reported in [16, 17], and plotted in Figure B.4. It should be noted that only plane stress states are considered in Figure B.4. From Figure B.4, it is seen that in the compressive failure region, the M-C criterion captures the failure envelope much better than the model only using the quadratic damage initiation criteria, as that implemented in 3D EST in Chapter IV. In the tensile failure region, both the M-C criterion and the quadratic based criterion perform well.

Once the fracture plane and fracture angle θ_{cr} are determined, the post-peak

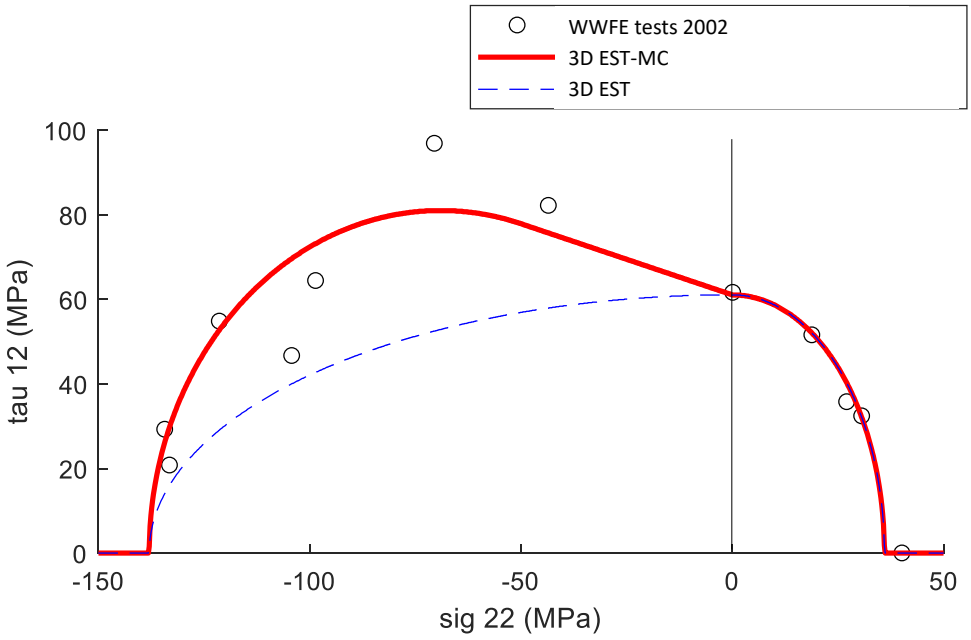

Figure B.4: Failure envelopes predicted by 3D EST-MC (with Mohr-Coulomb) and 3D EST.

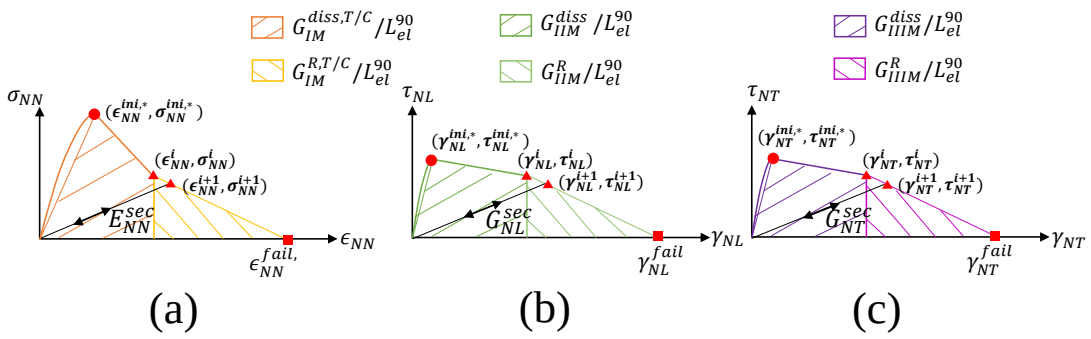

Figure B.5: Mixed-mode cohesive laws of 3D EST with the Mohr-Coulomb criterion: (a) mode I, (b) mode II, and (c) mode III.

degradation of all the stress components is performed with respect to θ_{cr}. The novel mixed-mode cohesive law proposed in [7] is still used in the local coordinate system of the fracture plane N-L-T. The mixed-mode cohesive laws for the NN (local mode I), NL (local mode II), and NT components (local mode III) are illustrated in Figure B.5. Since the theoretical background is identical to that described in Section 4.2.3 except for the coordinate transformation regarding the fracture angle θ_{cr}, specific equations will not be provided here for the conciseness of this appendix.

APPENDIX C

Program Architecture Diagram of EST

C.1 Program architecture diagram of EST

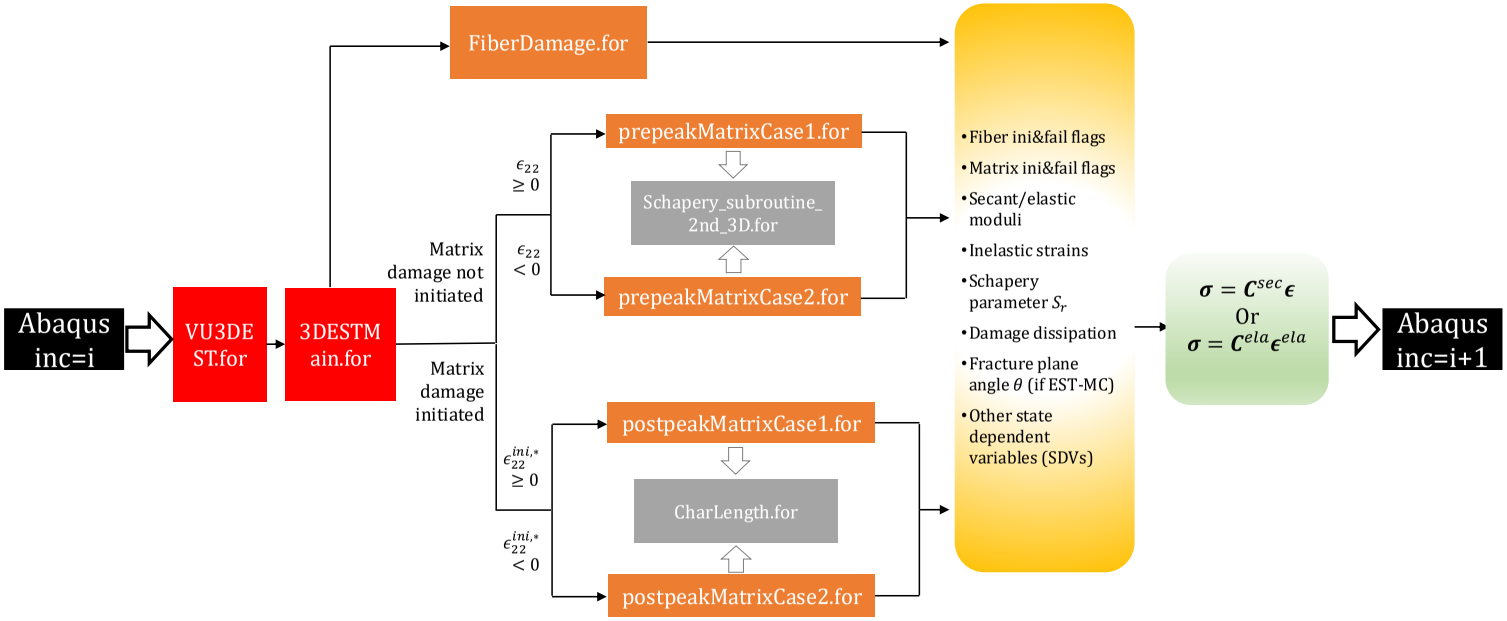

Figure C.1: Program architecture diagram of EST.

APPENDIX D

A Linear Elastic Semi-analytical Solution of Laminated Composites under LVI

The semi-analytical solution illustrated in this appendix follows the studies by Sun and Chattopadhyay [140]. The solution procedure in [140] has been re-derived here with more detail. A Matlab code has been developed based on a technical report by Chou et al. [141]. The original code was written in Fortran, as included in the [141]. The newly developed Matlab code has been applied to the cases reported in the panel size effect studies in Chapters II and V.

D.1 Formulation of the Problem

The LVI problem discussed in this dissertation can be simplified as a hemispherical impactor striking a simply supported rectangular composite laminate. The size of the laminate is dependent on the support lengths, instead of the sample size. A semi-analytical solution is developed in this appendix to solve the LVI responses of laminated composites based on the Kirchhoff–Love plate theory.

The simplified model is illustrated in Figure D.1. As seen in Figure D.1, the composite plate is simply supported. The length and width of the plate are a and b

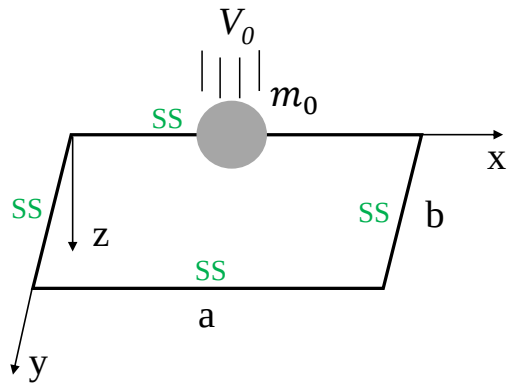

Figure D.1: The simplified LVI model.

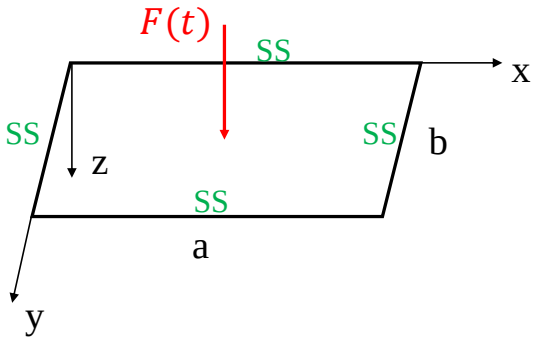

Figure D.2: EOMs of the composite plate.

respectively. Initial velocity V_0 is assigned to the impactor with a mass of m_0, similar to the prescribed boundary conditions of the FEM model.

The formulation of the semi-analytical solution is divided into three parts. First, the equations of motion (EOMs) of the composite plate will be introduced. Second, the EOMs of the impactor will be illustrated. Third, the contact interaction between the impactor and the plate will be outlined.

D.1.1 EOMs of the Composite Plate

For the EOMs of the plate, the problem can be simplified as a laminated composite plate under central point loading, as shown in Figure D.2. The governing equation of the plate under point loading is Equation D.1.

$$D_{11}\frac{\partial^4 w}{\partial x^4}+4D_{16}\frac{\partial^4 w}{\partial x^3\partial y}+2(D_{12}+2D_{66})\frac{\partial^4 w}{\partial x^2\partial y^2}+4D_{26}\frac{\partial^4 w}{\partial x\partial y^3}+D_{22}\frac{\partial^4 w}{\partial y^4}+\rho\frac{\partial^2 w}{\partial t^2}=q(x,y) \tag{D.1}$$

where, ρ is the areal mass of the plate. q is the pressure distributed on the top of the plate. For a centrally loaded plate, q is given by Equation D.2. In Equation D.2, F is the magnitude of the load and δ is the Dirac δ function.

$$q(x,y)=F\delta(\frac{a}{2},\frac{b}{2}) \tag{D.2}$$

The elastic potential of the plate is,

$$\begin{aligned} U=\frac{1}{2}\int_0^a\int_0^b [D_{11}(\frac{\partial^2 w}{\partial x^2})^2+2D_{12}\frac{\partial^2 w}{\partial x^2}\frac{\partial^2 w}{\partial y^2}+D_{22}(\frac{\partial^2 w}{\partial y^2})^2+4D_{66}(\frac{\partial^2 w}{\partial x\partial y})^2+ \\ 4D_{16}\frac{\partial^2 w}{\partial x^2}\frac{\partial^2 w}{\partial x\partial y}+4D_{26}\frac{\partial^2 w}{\partial y^2}\frac{\partial^2 w}{\partial x\partial y}]\,dxdy \end{aligned} \tag{D.3}$$

The work potential of the plate is,

$$W=\int_0^a\int_0^b [(q(x,y)-\rho\ddot{w})w(x,y)]\,dxdy \tag{D.4}$$

The total potential energy is,

$$\Pi=U-W \tag{D.5}$$

The displacement field $w(x,y,t)$ is approximated with a series of spatial shape functions $\phi_i(x,y)$ and a temporal function $A_i(t)$ as,

$$w(x,y)=\sum_{i=1}^{N}A_i(t)\phi_i(x,y) \tag{D.6}$$

According to the principle of minimum potential energy (PMPE) [142] expressed in Equation D.7, the EOMs of the plate can be derived as Equation D.8.

$$\frac{\partial \Pi}{\partial A_i} = 0 \tag{D.7}$$

$$[\mathbf{M}]\{\ddot{\mathbf{A}}\} + [\mathbf{K}]\{\mathbf{A}\} = \{\mathbf{Q}\} \tag{D.8}$$

In Equation D.8, $\mathbf{M}$ is the mass matrix, $\mathbf{K}$ is the stiffness matrix and $\mathbf{Q}$ is the force vector. These are;

$$\begin{aligned} K_{ij} = \int_0^a \int_0^b [&D_{11}\phi_i^{''}\phi_j^{''} + D_{22}\phi_i^{**}\phi_j^{**} + D_{12}(\phi_i^{**}\phi_j^{''} + \phi_i^{''}\phi_j^{**}) + 4D_{66}\phi_i^{*'}\phi_j^{*'} + \\ &2D_{16}(\phi_i^{''}\phi_j^{*'} + \phi_i^{*'}\phi_j^{''}) + 2D_{26}(\phi_i^{**}\phi_j^{*'} + \phi_i^{*'}\phi_j^{**})]dxdy \end{aligned} \tag{D.9}$$

$$M_{ij} = \int_0^a \int_0^b \rho\phi_i\phi_j dxdy \tag{D.10}$$

$$Q_i = \int_0^a \int_0^b q\phi_i dxdy \tag{D.11}$$

where, * means for $\frac{\partial()}{\partial x}$ and ' means for $\frac{\partial()}{\partial y}$.

For harmonic motion, assume that $A_i(t) = A_i e^{i\omega t}$:

$$(-\boldsymbol{\omega}^2[\mathbf{M}] + [\mathbf{K}])\{\mathbf{A}\} = \{\mathbf{0}\} \tag{D.12}$$

Equation D.12 is an eigenvalue problem.

By solving Equation D.12, a diagonal matrix of eigenvalues $[\boldsymbol{\omega}^2]$ and the modal matrix $[\mathbf{U}]$ (eigenvector) are obtained. Use the expansion theorem, the response is

described as a superposition of the normal modes in the form:

$$\mathbf{A(t)} = [\mathbf{U}]\{\boldsymbol{\eta}(t)\} \tag{D.13}$$

where $\{\boldsymbol{\eta}(t)\}$ is a column matrix consisting of a set of time-dependent generalized coordinates. And, the second-order time derivative of $\mathbf{A(t)}$ is:

$$\ddot{\mathbf{A}}(t) = [\mathbf{U}]\{\ddot{\boldsymbol{\eta}}(t)\} \tag{D.14}$$

Now Equation D.8 is cast into modal space:

$$[\mathbf{U}]^T[\mathbf{M}][\mathbf{U}]\{\ddot{\boldsymbol{\eta}}(t)\} + [\mathbf{U}]^T[\mathbf{K}][\mathbf{U}]\{\boldsymbol{\eta(t)}\} = [\mathbf{U}]^T\{\mathbf{Q}\} \tag{D.15}$$

in which,

$$[\mathbf{U}]^T[\mathbf{M}][\mathbf{U}] = [\mathbf{I}],\ [\mathbf{U}]^T[\mathbf{K}][\mathbf{U}] = [\boldsymbol{\omega}^2] \tag{D.16}$$

and therefore:

$$\{\ddot{\boldsymbol{\eta}}(t)\} + [\boldsymbol{\omega}^2]\{\boldsymbol{\eta}(t)\} = \{\mathbf{N}\},\ \{\mathbf{N}\} = [\mathbf{U}]^T\{\mathbf{Q}\} \tag{D.17}$$

Hence, with modal analysis, the discrete equations of motion are uncoupled into a series of uncoupled differential equations.

$$\ddot{\eta}_i(t) + \omega_i^2\eta_i(t) = N_i,\ i = 1, 2, 3...\infty \tag{D.18}$$

The uncoupled equations can be solved by using convolution integral:

$$\eta_i(t) = \frac{1}{\omega_i}\int_0^t N_i(\tau)sin(\omega_i(t-\tau))d\tau,\ i = 1, 2, 3...\infty \tag{D.19}$$

After obtaining the generalized coordinate vector $\{\boldsymbol{\eta}\}$, the coordinate vector is calculated with Equation D.13. To facilitate the calculation and programming, Equation D.13 and D.17 are expanded as:

$$N_i = \sum_{j=1}^{N} U_{ji} Q_j \tag{D.20}$$

$$A_i = \sum_{j=1}^{N} U_{ij} \eta_j \tag{D.21}$$

Combining Equations D.11, D.20, D.19, D.21 and D.6, the final version of the relation between the displacement field and load of the plate is:

$$\begin{aligned} w(x,y,t) = & \sum_{k=1}^{N} \phi_k(x,y) \\ & \{\sum_{i=1}^{N} U_{ki}[\frac{1}{\omega_i} \int_0^t (\sum_{j=1}^{N} U_{ji} \int_0^a \int_0^b q(x,y,\tau)\phi_j(x,y)dydx) sin(\omega_i(t-\tau))d\tau]\} \end{aligned} \tag{D.22}$$

Considering the plate being centrally loaded as in Equation D.2, Equation D.22 becomes,

$$w(x,y,t) = \sum_{k=1}^{N} \phi_k(x,y)\{\sum_{i=1}^{N} U_{ki}[\frac{1}{\omega_i}(\sum_{j=1}^{N} U_{ji}\phi_j(\frac{a}{2},\frac{b}{2}) \int_0^t F(\tau) sin(\omega_i(t-\tau))d\tau)]\} \tag{D.23}$$

D.1.2 EOMs of the Impactor

Denote the mass of the impactor as m_0, initial velocity as V_0, and displacement as w_0. The impactor is illustraeted in Figure D.3. The displacement of the impactor

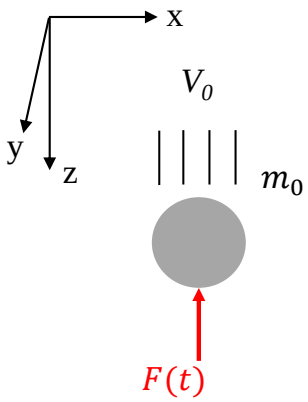

Figure D.3: EOMs of the impactor.

is,

$$w_0(t) = V_0 t - \frac{1}{m_0} \int_0^t \int_0^\tau F(\xi) d\xi d\tau \tag{D.24}$$

Denote the contact stiffness as k_c, the indentation as δ. The contact force is according to Hertz's contact law,

$$F = k_c \delta^{\frac{3}{2}} \ (\delta > 0) \tag{D.25a}$$

$$F = 0 \ (\delta \leq 0) \tag{D.25b}$$

where the contact stiffness k_c is calculated from the elastic moduli of the impactor and plate and discussed in detail in [143]. Indentation δ is simply a subtraction of the impactor displacement and the displacement at the center of the plate. The indentation is calculated as in Equation D.26 and illustrated in Figure D.4.

$$\delta(t) = w_0(t) - w(\frac{a}{2}, \frac{b}{2}, t) \tag{D.26}$$

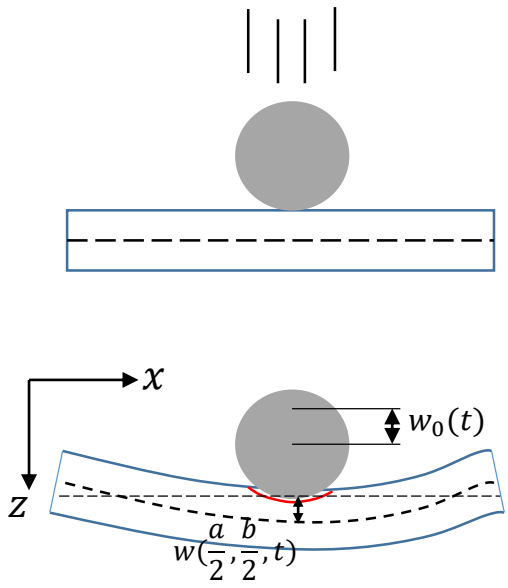

Figure D.4: Illustration of the indentation.

D.1.3 EOMs of the System

Combining Equation D.23, D.24, D.25a and D.26, the EOM for the system is:

$$[\frac{F(t)}{k_c}]^{\frac{2}{3}} = V_0 t - \frac{1}{m_0}\int_0^t\int_0^\tau F(\xi)d\xi d\tau - \sum_{k=1}^{N}\phi_k(\frac{a}{2},\frac{b}{2})\{\sum_{i=1}^{N}U_{ki}[\frac{1}{\omega_i}\sum_{j=1}^{N}U_{ji}\phi_j(\frac{a}{2},\frac{b}{2})\int_0^t F(\tau)sin(\omega_i(t-\tau))d\tau]\} \tag{D.27}$$

D.2 A Time Marching Algorithm for the Impact Analysis

The time marching algorithm outlined in this section follows the scheme described in [140].

Equation D.27 is an implicit nonlinear equation to be solved and therefore a closed-form analytical solution is not possible. A numerical method is adopted. The time span of analysis is divided into many small time increments with the time duration of Δt. During each time increment, the contact force is assumed to be constant. At

time $t = \mu\Delta t$, Equation D.27 becomes:

$$(\frac{F_\mu}{k_c})^{\frac{2}{3}} = V_0(\mu\Delta t) - \frac{1}{m_0}\sum_{\nu=1}^{\mu}\int_{(\nu-1)\Delta t}^{\nu\Delta t}(\int_{(\nu-1)\Delta t}^{\tau} F_\nu d\xi + V_{\nu-1})d\tau -$$
$$\sum_{k=1}^{N}\phi_k(\frac{a}{2},\frac{b}{2})\{\sum_{i=1}^{N}U_{ki}[\frac{1}{\omega_i}\sum_{j=1}^{N}U_{ji}\phi_j(\frac{a}{2},\frac{b}{2})(\sum_{\nu=1}^{\mu}\int_{(\nu-1)\Delta t}^{\mu\Delta t}F_\nu sin(\omega_i(\mu\Delta t-\tau))d\tau])\} \tag{D.28}$$

where $V_{\nu-1}$ is the velocity of impactor at the end of $(\nu-1)^{th}$ time increment.

Due to the contact force being piecewise constant, the temporal integral inside Equation D.27 can be simplified as,

$$(\frac{F_\mu}{k_c})^{\frac{2}{3}} = V_0(\mu\Delta t) - \frac{\Delta t^2}{m_0}\sum_{\nu=1}^{\mu}F_\nu(\mu-\nu+\frac{1}{2}) -$$
$$\sum_{k=1}^{N}\phi_k(\frac{a}{2},\frac{b}{2})\{\sum_{i=1}^{N}U_{ki}[\frac{1}{{\omega_i}^2}\sum_{j=1}^{N}U_{ji}\phi_j(\frac{a}{2},\frac{b}{2})\times \tag{D.29}$$
$$\sum_{\nu=1}^{\mu}(F_\nu cos(\omega_i((\mu-\nu)\Delta t)) - F_\nu cos(\omega_i(\mu-\nu+1)\Delta t))]\}$$

Equation D.29 is a nonlinear equation which can be solved with the Newton-Raphson method (N-R). At time $t = \zeta\Delta t$, the variables prior to $t = \zeta\Delta t$ is known, and therefore the summation of these variables in Equation D.29 is referred to as $(*)$ and Equation D.29 is simplified as:

$$(\frac{F_\zeta}{k_c})^{\frac{2}{3}} = V_0(\zeta\Delta t) + (*) - \frac{\Delta t^2}{m_0}\frac{1}{2}F_\zeta - \sum_{k=1}^{N}\phi_k(\frac{a}{2},\frac{b}{2})\times$$
$$\{\sum_{i=1}^{N}U_{ki}[\frac{1}{{\omega_i}^2}\sum_{j=1}^{N}U_{ji}\phi_j(\frac{a}{2},\frac{b}{2})\times \tag{D.30}$$
$$F_\zeta(cos(\omega_i((\mu-\zeta)\Delta t)) - cos(\omega_i(\mu-\zeta+1)\Delta t))]\}$$

Equation D.30 is solved with N-R at each time increment.

At the first increment, it is reasonable to make the initial guess of the contact force as in Equation D.31. This is based on the assumption that at the first small time increment, there is minimal displacement of the plate and therefore the indentation is only the value of the displacement of the impactor. This assumed value is just the initial guess from which the N-R iteration should be performed until a converged value is reached.

$$F_1 = k_c(V_0\Delta t)^{\frac{3}{2}} \tag{D.31}$$

D.2.1 Flow Chart

To solve the impact response on a laminated plate, the spatial shape function $\phi(x,y)$ needs to be specified. The first step of the program is to calculate the natural frequencies and modal matrix of the laminate based on Equation D.12. Then, initial guess of the contact force is obtained using Equation D.31. With the guessed value, N-R method is used to solve Equation D.30. The initially guessed contact force of every increment is from the converged value of the prior increment. To illustrate the solution procedure better, a flow chart is shown in Figure D.5.

```
Input: geometry data, material data, impactor data and solution data

• Calculate natural frequencies ω_i and modal matrix [U]

DO ν=1,NUMDT
  IF (ν .eq. 1) THEN
    Calculate initial guess of F_ν.
  ELSE
    WHILE (|F_{i+1}^{new} − F_{i+1}^{old}| < tol × F_{i+1}^{old})
      F_{i+1}^{old} = F_i
      Use Newton-Raphson to solve for F_{i+1}^{new}
    END
    F_{i+1}^{converged} = F_{i+1}^{new}
  END
  i=i+1
END
```

Figure D.5: Flow chart of the semi-analytical analysis.

D.3 Application of the Semi-analytical Method

In this appendix, the stacking sequence is taken as $[45/0/\text{-}45/90]_{3s}$ (L2 with 24 plies). The material system studied is IM7/977-3. The impactor's mass is 8.53 kg. Averaged ply thickness is 0.13 mm. The in-plane sizes of the plates are 139.7 mm × 88.9 mm, 127 mm × 127 mm, 304.8 mm × 304.8 mm. The in-plane sizes are according to the support lengths of the LVI test fixtures described in Chapter II. The impact energy levels are 25 J, 30 J, and 50 J. More details of the test parameters can be found in Table 2.2.

The first step is to choose shape functions. Double-sine functions are used in this appendix. Equation D.6 is now Equation D.32.

$$w(x,y,t) = A(t)\left(\sum_m \sum_n \sin(\frac{m\pi x}{a})\sin(\frac{n\pi y}{b})\right) \tag{D.32}$$

Then, with the chosen shape functions, analytical solution is obtained following the flowchart shown in Figure D.5. The results obtained experimentally, numerically with 2D EST, and analytically are plotted in Figures D.6 to D.8. It is seen from the figures that for all the in-plane sizes, the experimental results agree well with

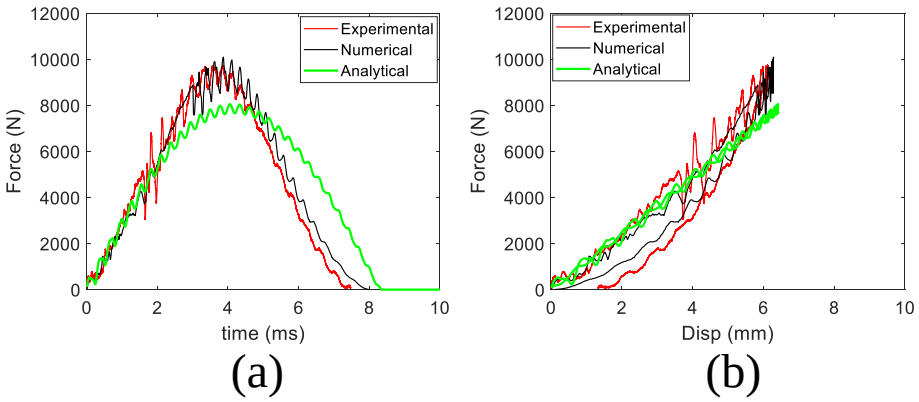

Figure D.6: Results comparison of 25 J impact on the L2-S-24 sample: (a) load-time response, (b) load-displacement response.

the numerical results. However, the agreement between the analytical solution to the other results gets worse as the in-plane size grows. Additionally, it is observed that, at the very initial parts of the curves, such as before displacement of 4 mm in Figure D.6 (b), 4 mm in Figure D.7 (b) and 6 mm in Figure D.8 (b), the analytical results are on top of the experimental and numerical results. However, as the displacement value increases, the curves start to deviate. For the experimental and numerical curves, a stiffening behavior is noticed. This stiffening behavior becomes more significant as the plate in-plane size increases. The stiffening behavior is believed to be the membrane effect caused by geometric nonlinearity, which is not considered in the current analytical solution.

To identify the effect caused by geometric nonlinearity, FEM modeling of a centrally and quasi-statically loaded quasi-isotropic laminate has been performed. For the efficiency of modeling, a static implicit algorithm of Abaqus was adopted. The FEM results are compared with experimental and analytical results in Figure D.9. From the figure, it is seen that initially, the FEM results with and without geometric nonlinearity are on top of each other. Then, as the displacement increases, the stiffening behavior as described in Figures D.6 to D.8 becomes pronounced. FEM analyses with geometric nonlinearity accounted for agree very well with the test re-

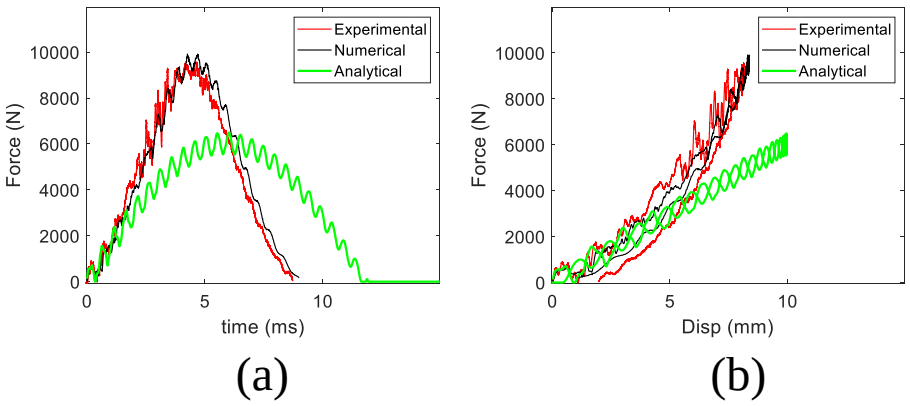

Figure D.7: Results comparison of 30 J impact on the L2-M-24 sample: (a) load-time response, (b) load-displacement response.

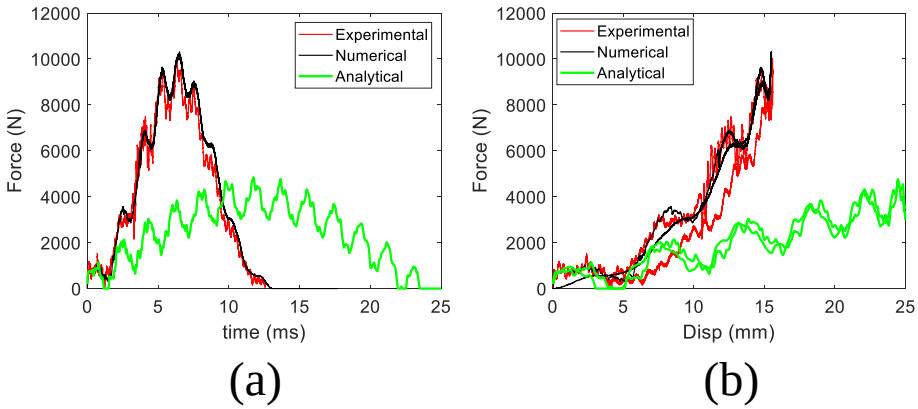

Figure D.8: Results comparison of 50 J impact on the L2-L-24 sample: (a) load-time response, (b) load-displacement response.

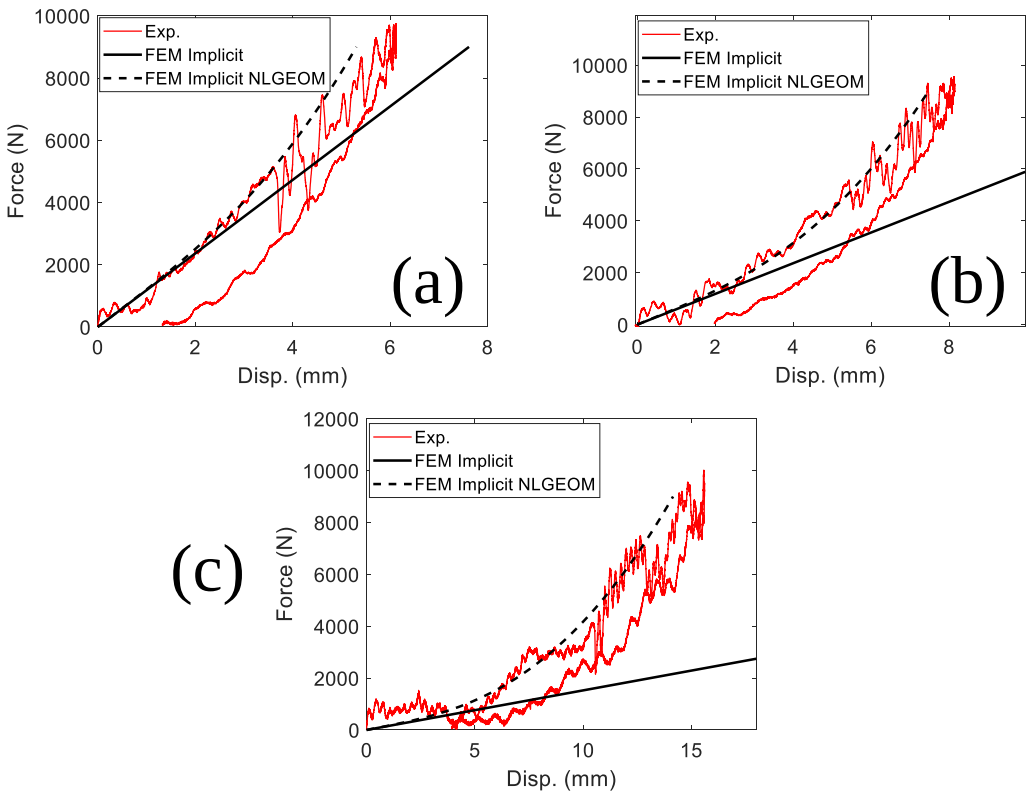

Figure D.9: Comparison of numerical analyses with and without geometric nonlinearity: (a) L2-S-24, (b) L2-M-24, and (c) L2-L-24.

sults. Therefore, in order to gain accurate analytical predictions of the LVI responses, geometric nonlinearity needs to be integrated in the current semi-analytical model. In other words, the currently used Kirchoff-Love plate theory should also include nonlinear kinematics [142].

APPENDIX E

Nondimensionalization of the LVI Load Responses

E.1 Nondimensionalization of the LVI Load Responses

LVI studies with the panel size effects have been reported in Section 2.4 and 5.3. It has been realized that the panel size significantly influences the load responses of the impacted samples. In this appendix, a nondimensionalization approach will be introduced to nondimensionalize the responses of the impacted panels with various sizes.

The nondimensionalization in this appendix follows the method introduced by Nemeth in [144], where the differential equation governing buckling of symmetrically laminated composite plates loaded in compression was presented in nondimensional form. In this appendix, the procedure in [144] will be followed. First, the governing equation of the bending of a laminated composite plate will be nondimensionalized. The governing equation is Equation E.1. It should be noticed that, compared to the governing equation provided in Appendix D, Equation E.1 has excluded the term $\rho\frac{\partial^2 w}{\partial t^2}$ to neglect the dynamic effect, since the nondimensionalization is performed only regarding the static response of the plate.

$$D_{11}\frac{\partial^4 w}{\partial x^4}+4D_{16}\frac{\partial^4 w}{\partial x^3\partial y}+2(D_{12}+2D_{66})\frac{\partial^4 w}{\partial x^2\partial y^2}+4D_{26}\frac{\partial^4 w}{\partial x\partial y^3}+D_{22}\frac{\partial^4 w}{\partial y^4}=q(x,y) \quad \text{(E.1)}$$

In [144], Nemeth introduced nondimensional parameters as in Equations E.2 to E.4.

$$\xi=\frac{x}{a} \quad \text{(E.2)}$$

$$\eta=\frac{y}{b} \quad \text{(E.3)}$$

$$\bar{w}=\frac{w}{\sqrt{ab}} \quad \text{(E.4)}$$

Substitute these nondimensional parameters into Equation E.1, the governing equation becomes,

$$\begin{aligned} D_{11}(\frac{b}{a})^2\frac{\partial^4 \bar{w}}{\partial \xi^4}+4D_{16}(\frac{b}{a})\frac{\partial^4 \bar{w}}{\partial \xi^3\partial \eta}+2(D_{12}+2D_{66})\frac{\partial^4 \bar{w}}{\partial \xi^2\partial \eta^2}+ \\ 4D_{26}(\frac{a}{b})\frac{\partial^4 \bar{w}}{\partial \xi\partial \eta^3}+D_{22}(\frac{a}{b})^2\frac{\partial^4 \bar{w}}{\partial \eta^4}=\sqrt{ab}^3 q(x,y) \end{aligned} \quad \text{(E.5)}$$

Divide both sides of Equation E.5 by $\sqrt{D_{11}D_{22}}$, then,

$$\begin{aligned} &\left(\frac{b}{a}(\frac{D_{11}}{D_{22}})^{0.25}\right)^2\frac{\partial^4 \bar{w}}{\partial \xi^4}+4\left[\frac{D_{16}}{(D_{11}^3D_{22})^{0.25}}\right]\left(\frac{b}{a}(\frac{D_{11}}{D_{22}})^{0.25}\right)\frac{\partial^4 \bar{w}}{\partial \xi^3\partial \eta}+ \\ &\frac{2(D_{12}+2D_{66})}{\sqrt{D_{11}D_{22}}}\frac{\partial^4 \bar{w}}{\partial \xi^2\partial \eta^2}+4\left[\frac{D_{26}}{(D_{22}^3D_{11})^{0.25}}\right]\left(\frac{a}{b}(\frac{D_{22}}{D_{11}})^{0.25}\right)\frac{\partial^4 \bar{w}}{\partial \xi\partial \eta^3}+ \\ &\left(\frac{a}{b}(\frac{D_{22}}{D_{11}})^{0.25}\right)^2\frac{\partial^4 \bar{w}}{\partial \eta^4}=\sqrt{ab}^3\frac{q(x,y)}{\sqrt{D_{11}D_{22}}} \end{aligned} \quad \text{(E.6)}$$

Again, use the nondimensional parameters in Nemeth's solution in [144], which are,

$$\alpha = \frac{b}{a}\left(\frac{D_{11}}{D_{22}}\right)^{0.25} \tag{E.7}$$

$$\beta = \frac{D_{12} + 2D_{66}}{\sqrt{D_{11}D_{22}}} \tag{E.8}$$

$$\gamma = \frac{D_{16}}{\left(D_{11}^3 D_{22}\right)^{0.25}} \tag{E.9}$$

$$\delta = \frac{D_{26}}{\left(D_{22}^3 D_{11}\right)^{0.25}} \tag{E.10}$$

Substituting Equations E.7 to E.10 into Equation E.1, the final nondimensional form of the governing equation is obtained,

$$\alpha^2\frac{\partial^4\bar{w}}{\partial\xi^4} + 4\alpha\gamma\frac{\partial^4\bar{w}}{\partial\xi^3\partial\eta} + 2\beta\frac{\partial^4\bar{w}}{\partial\xi^2\partial\eta^2} + 4(\frac{\delta}{\alpha})\frac{\partial^4\bar{w}}{\partial\xi\partial\eta^3} + (\frac{1}{\alpha})^2\frac{\partial^4\bar{w}}{\partial\eta^4} = \bar{q}(\xi,\eta) \tag{E.11}$$

In Equation E.11, γ and δ represent the contribution from D_{16} and D_{26}.

Therefore, finally, to nondimensionalize the LVI load responses, nondimensional terms $\bar{w} = \frac{w}{\sqrt{ab}}$ and $\bar{F} = \sqrt{\frac{ab}{D_{11}D_{22}}}F$ should be used. In Figure E.1, the load-displacement curves with dimensions and nondimensionalized are displayed. As shown in Figure E.1 (a), the initial stiffnesses vary significantly due to the difference in panel sizes. After the nondimensionalizing following $\bar{w} = \frac{w}{\sqrt{ab}}$ and $\bar{F} = \sqrt{\frac{ab}{D_{11}D_{22}}}F$, the initial stiffness agree well among the displayed cases. It should be pointed out that in Figure E.1 (b), after $\bar{w} > 0.015$, the stiffnesses vary again. This is not due to the panel size but due to the geometric nonlinearity as pointed out in Appendix D. In addition, due to the strong geometric nonlinearity in the L (330.2 mm $\times$ 330.2 mm)

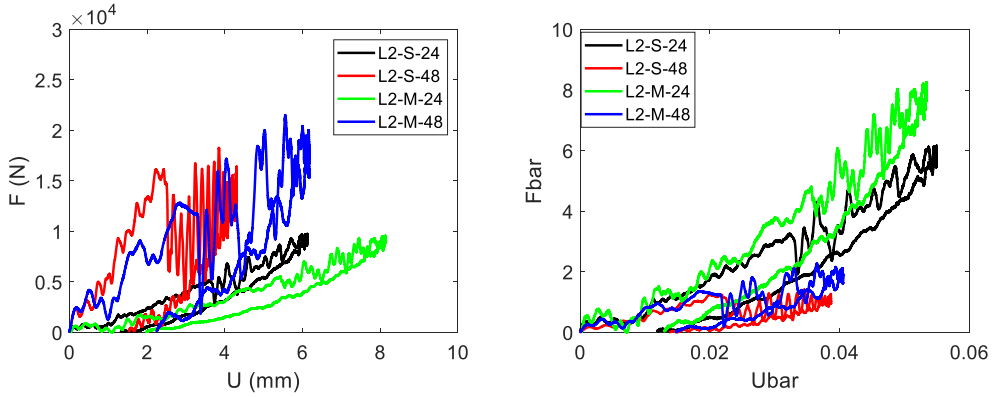

Figure E.1: Load-displacement responses of the L2-S/M-24/48 panels: (a) original data, and (b) nondimensionalized data.

samples, the LVI responses of the L samples are not included in Figure E.1.

In this appendix, a nondimensionalization approach for the LVI load responses have been proposed to present the load responses of the panel size effect studies in a nondimensional form. The approach is adopted from [144]. As shown in Figure E.1, the nondimensionalization is successful for the initial stiffness of composite plates of various sizes. However, the nondimensionalization in this appendix does not account for geometric nonlinearity or damage.

BIBLIOGRAPHY

BIBLIOGRAPHY

[1] Robin Olsson. Mass criterion for wave controlled impact response of composite plates. *Composites Part A: Applied Science and Manufacturing*, 31(8):879–887, 2000.

[2] Solver I Thorsson. Experimental and numerical investigation of fiber reinforced laminated composites subject to low-velocity impact. 2017.

[3] GAO Davies and R Olsson. Impact on composite structures. *The Aeronautical Journal*, 108(1089):541–563, 2004.

[4] Deepak Kumar Patel. *Developing a progressive damage and failure model for hybrid 3d woven textile composites using ncyl multiscale method*. PhD thesis, 2017.

[5] EV González, P Maimí, PP Camanho, A Turon, and JA Mayugo. Simulation of drop-weight impact and compression after impact tests on composite laminates. *Composite Structures*, 94(11):3364–3378, 2012.

[6] Ashith PK Joseph, Paul Davidson, and Anthony M Waas. Progressive damage and failure analysis of single lap shear and double lap shear bolted joints. *Composites Part A: Applied Science and Manufacturing*, 113:264–274, 2018.

[7] Ashith PK Joseph, Paul Davidson, and Anthony M Waas. Open hole and filled hole progressive damage and failure analysis of composite laminates with a countersunk hole. *Composite Structures*, 203:523–538, 2018.

[8] Y Shi, T Swait, and C Soutis. Modelling damage evolution in composite laminates subjected to low velocity impact. *Composite Structures*, 94(9):2902–2913, 2012.

[9] Jifeng Xu, Abe Askari, Olaf Weckner, and Stewart Silling. Peridynamic analysis of impact damage in composite laminates. *Journal of Aerospace Engineering*, 21(3):187–194, 2008.

[10] Farzad Pashmforoush, Mohamad Fotouhi, and Ahmed Aly Diaa Sarhan. Experimental–numerical study on minimizing impact induced damage in laminated composites under low-velocity impact. *Journal of Reinforced Plastics and Composites*, 37(3):155–165, 2018.

[11] Shiyao Lin and Anthony M Waas. Experimental and high-fidelity computational investigations on the low velocity impact damage of laminated composite materials. In *AIAA Scitech 2020 Forum*, page 0724, 2020.

[12] Deepak K Patel, Anthony M Waas, and Chian-Fong Yen. Compressive response of hybrid 3d woven textile composites (h3dwtcs): An experimentally validated computational model. *Journal of the Mechanics and Physics of Solids*, 122:381–405, 2019.

[13] Evan J Pineda, Brett A Bednarcyk, Anthony M Waas, and Steven M Arnold. Progressive failure of a unidirectional fiber-reinforced composite using the method of cells: discretization objective computational results. *International Journal of Solids and Structures*, 50(9):1203–1216, 2013.

[14] Ronald Krueger. A summary of benchmark examples to assess the performance of quasi-static delamination propagation prediction capabilities in finite element codes. *Journal of Composite Materials*, 49(26):3297–3316, 2015.

[15] Ronald Krueger. Development and application of benchmark examples for mixed-mode i/ii quasi-static delamination propagation predictions. 2012.

[16] P D Soden, M J Hinton, and AS Kaddour. Lamina properties, lay-up configurations and loading conditions for a range of fibre reinforced composite laminates. In *Failure criteria in fibre-reinforced-polymer composites*, pages 30–51. Elsevier, 2004.

[17] Carlos G Davila, Pedro P Camanho, and Cheryl A Rose. Failure criteria for frp laminates. *Journal of Composite materials*, 39(4):323–345, 2005.

[18] Serge Abrate. *Impact on composite structures*. Cambridge university press, 2005.

[19] ASTM D7136/D7136M-12. Standard test method for measuring the damage resistance of a fiber-reinforced polymer matrix composite to a drop-weight impact event, 2015.

[20] Mark Flores, David Mollenhauer, Vipul Runatunga, Timothy Beberniss, Daniel Rapking, and Mark Pankow. High-speed 3d digital image correlation of low-velocity impacts on composite plates. *Composites Part B: Engineering*, 131:153–164, 2017.

[21] Solver I Thorsson, Anthony M Waas, and Mostafa Rassaian. Low-velocity impact predictions of composite laminates using a continuum shell based modeling approach part a: Impact study. *International Journal of Solids and Structures*, 155:185–200, 2018.

[22] Shiyao Lin, Solver I Thorsson, and Anthony M Waas. Predicting the low velocity impact damage of a quasi-isotropic laminate using est. *Composite Structures*, page 112530, 2020.

[23] David Lu, Paul Davidson, Anthony M Waas, and Vipul Ranatunga. On the estimation of ply-by-ply information from ut scan of impacted composite panel. In *AIAA Scitech 2021 Forum*, page 1510, 2021.

[24] Solver I Thorsson, Akinori Yoshimura, Anthony M Waas, and Mostafa Rassaian. Prediction of low-velocity face-on impact response of composite laminates using high-fidelity finite element modeling techniques. In *57th AIAA/ASCE/AHS/ASC Structures, Structural Dynamics, and Materials Conference*, page 2184, 2016.

[25] Nicolas P Avdelidis, Darryl P Almond, A Dobbinson, BC Hawtin, Clemente Ibarra-Castanedo, and Xavier Maldague. Aircraft composites assessment by means of transient thermal ndt. *Progress in Aerospace Sciences*, 40(3):143–162, 2004.

[26] DJ Bull, SM Spearing, I Sinclair, and L Helfen. Three-dimensional assessment of low velocity impact damage in particle toughened composite laminates using micro-focus x-ray computed tomography and synchrotron radiation laminography. *Composites Part A: Applied Science and Manufacturing*, 52:62–69, 2013.

[27] ASTM D7137/D7137M-17. Standard test method for compressive residual strength properties of damaged polymer matrix composite plates, 2017.

[28] Jason Action and Mark Flores. Icme approach to compression strength after impact modeling. In *2018 AIAA/ASCE/AHS/ASC Structures, Structural Dynamics, and Materials Conference*, page 1899, 2018.

[29] Jason Action, Frank A Leone, and Nelson Vieira De Carvalho. Progressive damage analysis of a multi-stringer post-buckled panel. In *AIAA Scitech 2020 Forum*, page 1481, 2020.

[30] Christophe Bouvet, Samuel Rivallant, and Jean-Jacques Barrau. Low velocity impact modeling in composite laminates capturing permanent indentation. *Composites Science and Technology*, 72(16):1977–1988, 2012.

[31] Derek Hull and Yi Bing Shi. Damage mechanism characterization in composite damage tolerance investigations. *Composite Structures*, 23(2):99–120, 1993.

[32] Compressive response of hybrid 3D woven textile composites (H3DWTCs): An experimentally validated computational model, author=Patel, Deepak K and Waas, Anthony M and Yen, Chian-Fong. *Journal of the Mechanics and Physics of Solids*, 122:381–405, 2019.

[33] Deepak K Patel, Armanj D Hasanyan, and Anthony M Waas. N-layer concentric cylinder model (ncyl): an extended micromechanics-based multiscale model for nonlinear composites. *Acta Mechanica*, 228(1):275–306, 2017.

[34] Deepak K Patel and Anthony M Waas. Damage and failure modelling of hybrid three-dimensional textile composites: a mesh objective multi-scale approach. *Phil. Trans. R. Soc. A*, 374(2071):20160036, 2016.

[35] P Maimi, Pedro Ponces Camanho, JA Mayugo, and CG Davila. A continuum damage model for composite laminates: Part i–constitutive model. *Mechanics of Materials*, 39(10):897–908, 2007.

[36] Silvestre T Pinho, Carlos G Davila, Pedro P Camanho, Lorenzo Iannucci, and Paul Robinson. Failure models and criteria for frp under in-plane or three-dimensional stress states including shear non-linearity. 2005.

[37] R Gutkin, ST Pinho, P Robinson, and PT Curtis. Micro-mechanical modelling of shear-driven fibre compressive failure and of fibre kinking for failure envelope generation in cfrp laminates. *Composites Science and Technology*, 70(8):1214–1222, 2010.

[38] Evan J Pineda, Anthony M Waas, Brett A Bednarcyk, Craig S Collier, and Phillip W Yarrington. Progressive damage and failure modeling in notched laminated fiber reinforced composites. *International journal of fracture*, 158(2):125–143, 2009.

[39] Evan J Pineda and Anthony M Waas. Numerical implementation of a multiple-isv thermodynamically-based work potential theory for modeling progressive damage and failure in fiber-reinforced laminates. *International journal of fracture*, 182(1):93–122, 2013.

[40] Mark McElroy, Wade Jackson, Robin Olsson, Peter Hellström, Spyros Tsampas, and Mark Pankow. Interaction of delaminations and matrix cracks in a cfrp plate, part i: A test method for model validation. *Composites Part A: Applied Science and Manufacturing*, 103:314–326, 2017.

[41] Mark W McElroy, Renaud Gutkin, and Mark Pankow. Interaction of delaminations and matrix cracks in a cfrp plate, part ii: Simulation using an enriched shell finite element model. *Composites Part A: Applied Science and Manufacturing*, 103:252–262, 2017.

[42] Ashith PK Joseph, Paul Davidson, and Anthony M Waas. Intra-inter crack band model (i2cbm) for progressive damage and failure analysis of joints. In *58th AIAA/ASCE/AHS/ASC Structures, Structural Dynamics, and Materials Conference*, page 0200, 2017.

[43] Wei H Ng, Amit G Salvi, and Anthony M Waas. Characterization of the in-situ non-linear shear response of laminated fiber-reinforced composites. *Composites Science and Technology*, 70(7):1126–1134, 2010.

[44] CS Lopes, Sergio Sadaba, C Gonzalez, J Llorca, and PP Camanho. Physically-sound simulation of low-velocity impact on fiber reinforced laminates. *International Journal of Impact Engineering*, 92:3–17, 2016.

[45] Christophe Bouvet, Bruno Castanié, Matthieu Bizeul, and Jean-Jacques Barrau. Low velocity impact modelling in laminate composite panels with discrete interface elements. *International Journal of Solids and Structures*, 46(14-15):2809–2821, 2009.

[46] RA Schapery. Mechanical characterization and analysis of inelastic composite laminates with growing damage. *Mechanics of composite materials and structures*, pages 1–9, 1989.

[47] Solver I Thorsson, Anthony M Waas, Joseph Schaefer, Brian Justusson, and Salvatore Liguore. Effects of elevated loading rates on mode i fracture of composite laminates using a modified wedge-insert fracture method. *Composites Science and Technology*, 156:39–47, 2018.

[48] H Koerber, J Xavier, and PP Camanho. High strain rate characterisation of unidirectional carbon-epoxy im7-8552 in transverse compression and in-plane shear using digital image correlation. *Mechanics of Materials*, 42(11):1004–1019, 2010.

[49] DF Medina and JK Chen. Three-dimensional simulations of impact induced damage in composite structures using the parallelized sph method. *Composites Part A: Applied Science and Manufacturing*, 31(8):853–860, 2000.

[50] K Shintate and H Sekine. Numerical simulation of hypervelocity impacts of a projectile on laminated composite plate targets by means of improved sph method. *composites Part A: applied science and manufacturing*, 35(6):683–692, 2004.

[51] Stewart A Silling and Ebrahim Askari. A meshfree method based on the peridynamic model of solid mechanics. *Computers & structures*, 83(17-18):1526–1535, 2005.

[52] Wenke Hu, Youn Doh Ha, and Florin Bobaru. Peridynamic model for dynamic fracture in unidirectional fiber-reinforced composites. *Computer Methods in Applied Mechanics and Engineering*, 217:247–261, 2012.

[53] Chaoyang Sun and Zaixing Huang. Peridynamic simulation to impacting damage in composite laminate. *Composite Structures*, 138:335–341, 2016.

[54] Ik Hyeon Choi and Cheol Ho Lim. Low-velocity impact analysis of composite laminates using linearized contact law. *Composite structures*, 66(1-4):125–132, 2004.

[55] MH Malik and AFM Arif. Ann prediction model for composite plates against low velocity impact loads using finite element analysis. *Composite Structures*, 101:290–300, 2013.

[56] Eslam M Soliman, Michael P Sheyka, and Mahmoud Reda Taha. Low-velocity impact of thin woven carbon fabric composites incorporating multi-walled carbon nanotubes. *International Journal of Impact Engineering*, 47:39–47, 2012.

[57] Kuk Hyun Ji and Seung Jo Kim. Dynamic direct numerical simulation of woven composites for low-velocity impact. *Journal of Composite Materials*, 41(2):175–200, 2007.

[58] Xiaofei Lou, Hongneng Cai, Pengfei Yu, Fei Jiao, and Xuecheng Han. Failure analysis of composite laminate under low-velocity impact based on micromechanics of failure. *Composite Structures*, 163:238–247, 2017.

[59] Wooseok Ji, Sunil P Sringeri, Solver I Thorsson, Cyrus J Kosztowny, Anthony M Waas, Mostafa Rassaian, and Salvatore L Liguore. Face-on and edge-on impact response of composite laminates. In *56th AIAA/ASCE/AHS/ASC Structures, Structural Dynamics, and Materials Conference*, page 0956, 2015.

[60] Solver I Thorsson, Anthony M Waas, and Mostafa Rassaian. Low-velocity impact predictions of composite laminates using a continuum shell based modeling approach part b: Bvid impact and compression after impact. *International Journal of Solids and Structures*, 155:201–212, 2018.

[61] MV Donadon, L Iannucci, Brian G Falzon, JM Hodgkinson, and Sergio FM de Almeida. A progressive failure model for composite laminates subjected to low velocity impact damage. *Computers & Structures*, 86(11-12):1232–1252, 2008.

[62] CS Lopes, PP Camanho, Z Gurdal, P Maimi, and EV Gonzalez. Low-velocity impact damage on dispersed stacking sequence laminates. part ii: Numerical simulations. *Composites Science and Technology*, 69(7-8):937–947, 2009.

[63] Natthawat Hongkarnjanakul, Christophe Bouvet, and Samuel Rivallant. Validation of low velocity impact modelling on different stacking sequences of cfrp laminates and influence of fibre failure. *Composite Structures*, 106:549–559, 2013.

[64] De Xie and Anthony M Waas. Discrete cohesive zone model for mixed-mode fracture using finite element analysis. *Engineering fracture mechanics*, 73(13):1783–1796, 2006.

[65] Abaqus Version Simulia. 6.13 documentation. *Dassault systemes*, 2013.

[66] LS-DYNA Keyword User's Manual and I Volume. Version 971. *Livermore Software Technology Corporation*, 7374:354, 2007.

[67] Minh Hoang Nguyen and Anthony M Waas. A novel mode-dependent and probabilistic semi-discrete damage model for progressive failure analysis of composite laminates-part i: Meshing strategy and mixed-mode law. *Composites Part C: Open Access*, 3:100073, 2020.

[68] MV Donadon, L Iannucci, Brian G Falzon, JM Hodgkinson, and Sergio FM de Almeida. A progressive failure model for composite laminates subjected to low velocity impact damage. *Computers & Structures*, 86(11-12):1232–1252, 2008.

[69] Andrea Faggiani and BG Falzon. Predicting low-velocity impact damage on a stiffened composite panel. *Composites Part A: Applied Science and Manufacturing*, 41(6):737–749, 2010.

[70] Masaya Ebina, Akinori Yoshimura, Kenichi Sakaue, and Anthony M Waas. High fidelity simulation of low velocity impact behavior of cfrp laminate. *Composites Part A: Applied Science and Manufacturing*, 113:166–179, 2018.

[71] Zdeněk P Bažant and Byung H Oh. Crack band theory for fracture of concrete. *Matériaux et construction*, 16(3):155–177, 1983.

[72] Jan G Rots, P Nauta, GMA Kuster, and Johan Blaauwendraad. Smeared crack approach and fracture localization in concrete. *HERON, 30 (1), 1985*, 1985.

[73] Norman A Fleck and Dongquan Liu. Microbuckle initiation from a patch of large amplitude fibre waviness in a composite under compression and bending. *European Journal of Mechanics-A/Solids*, 20(1):23–37, 2001.

[74] Carl R Schultheisz and Anthony M Waas. Compressive failure of composites, part i: testing and micromechanical theories. *Progress in Aerospace Sciences*, 32(1):1–42, 1996.

[75] Yu Shi and Constantinos Soutis. A finite element analysis of impact damage in composite laminates. *The Aeronautical Journal*, 116(1186):1331–1347, 2012.

[76] Y Shi, C Pinna, and C Soutis. Modelling impact damage in composite laminates: a simulation of intra-and inter-laminar cracking. *Composite Structures*, 114:10–19, 2014.

[77] Yu Shi and Constantinos Soutis. Modelling low velocity impact induced damage in composite laminates. *Mechanics of Advanced Materials and Modern Processes*, 3(1):14, 2017.

[78] Zvi Hashin. Failure criteria for unidirectional fiber composites. *Journal of applied mechanics*, 47(2):329–334, 1980.

[79] Wei Tan, Brian G Falzon, Louis NS Chiu, and Mark Price. Predicting low velocity impact damage and compression-after-impact (cai) behaviour of composite laminates. *Composites Part A: Applied Science and Manufacturing*, 71:212–226, 2015.

[80] Albert Soto, EV González, Pere Maimí, F Martín De La Escalera, JR Sainz De Aja, and E Alvarez. Low velocity impact and compression after impact simulation of thin ply laminates. *Composites Part A: Applied Science and Manufacturing*, 109:413–427, 2018.

[81] EV González, P Maimí, E Martín-Santos, A Soto, P Cruz, F Martín de la Escalera, and JR Sainz de Aja. Simulating drop-weight impact and compression after impact tests on composite laminates using conventional shell finite elements. *International Journal of Solids and Structures*, 144:230–247, 2018.

[82] A Soto, EV González, P Maimí, JA Mayugo, PR Pasquali, and PP Camanho. A methodology to simulate low velocity impact and compression after impact in large composite stiffened panels. *Composite Structures*, 204:223–238, 2018.

[83] Samuel Rivallant, Christophe Bouvet, and Natthawat Hongkarnjanakul. Failure analysis of cfrp laminates subjected to compression after impact: Fe simulation using discrete interface elements. *Composites Part A: Applied Science and Manufacturing*, 55:83–93, 2013.

[84] Haris Ahmad Israr, Samuel Rivallant, and Jean-Jacques Barrau. Experimental investigation on mean crushing stress characterization of carbon–epoxy plies under compressive crushing mode. *Composite Structures*, 96:357–364, 2013.

[85] Alfred Puck and Helmut Schürmann. Failure analysis of frp laminates by means of physically based phenomenological models. *Composites Science and Technology*, 62(12-13):1633–1662, 2002.

[86] A Puck and H Schürmann. Failure analysis of frp laminates by means of physically based phenomenological models. In *Failure Criteria in Fibre-Reinforced-Polymer Composites*, pages 832–876. Elsevier, 2004.

[87] P Berbinau, C Soutis, P Goutas, and PT Curtis. Effect of off-axis ply orientation on 0-fibre microbuckling. *Composites Part A: Applied Science and Manufacturing*, 30(10):1197–1207, 1999.

[88] P Berbinau, C Soutis, and IA Guz. Compressive failure of 0 unidirectional carbon-fibre-reinforced plastic (cfrp) laminates by fibre microbuckling. *Composites Science and technology*, 59(9):1451–1455, 1999.

[89] NO Yokoyama, MV Donadon, and SFM De Almeida. A numerical study on the impact resistance of composite shells using an energy based failure model. *Composite Structures*, 93(1):142–152, 2010.

[90] Richard A Schapery. A theory of crack initiation and growth in viscoelastic media. *International Journal of Fracture*, 11(1):141–159, 1975.

[91] Shiyao Lin, Vipul Ranatunga, and Anthony M Waas. A comprehensive experimental and computational study on lvi induced damage of laminated composites. In *AIAA Scitech 2021 Forum*, page 1623, 2021.

[92] Pedro Ponces Camanho, C G Davila, and MF De Moura. Numerical simulation of mixed-mode progressive delamination in composite materials. *Journal of composite materials*, 37(16):1415–1438, 2003.

[93] Nhung Nguyen and Anthony M Waas. A novel mixed-mode cohesive formulation for crack growth analysis. *Composite structures*, 156:253–262, 2016.

[94] M L Benzeggagh and MJCS Kenane. Measurement of mixed-mode delamination fracture toughness of unidirectional glass/epoxy composites with mixed-mode bending apparatus. *Composites science and technology*, 56(4):439–449, 1996.

[95] Peter A Gustafson and Anthony M Waas. The influence of adhesive constitutive parameters in cohesive zone finite element models of adhesively bonded joints. *International Journal of Solids and Structures*, 46(10):2201–2215, 2009.

[96] Shiyao Lin and Anthony Waas. Micromechanical progressive failure analyses of composite materials using continuum decohesive finite element. In *Proceedings of the American Society for Composites—Thirty-third Technical Conference*, 2018.

[97] Shiyao Lin and Anthony M Waas. Using the continuum decohesive finite element for crack growth analysis in fiber reinforced composites. In *2018 AIAA/ASCE/AHS/ASC Structures, Structural Dynamics, and Materials Conference*, page 0731, 2018.

[98] Nhung Nguyen and Anthony M Waas. Continuum decohesive finite element modeling of in-plane fracture: Mesh-objectivity and sensitivity studies. AIAA/ASME/ASCE/AHS/ASC 58th Structures, Structural Dynamics, and Materials ..., 2017.

[99] Pavana Prabhakar and Anthony M Waas. A novel continuum-decohesive finite element for modeling in-plane fracture in fiber reinforced composites. *Composites Science and Technology*, 83:1–10, 2013.

[100] Richard W Macek and Stewart A Silling. Peridynamics via finite element analysis. *Finite Elements in Analysis and Design*, 43(15):1169–1178, 2007.

[101] Srujan K Rokkam, Quang T Truong, Max Gunzburger, and Kishan Goel. A peridynamics-fem approach for crack path prediction in fiber-reinforced composites. In *2018 AIAA/ASCE/AHS/ASC Structures, Structural Dynamics, and Materials Conference*, page 0651, 2018.

[102] Zdeněk P Bažant, Wen Luo, Viet T Chau, and Miguel A Bessa. Wave dispersion and basic concepts of peridynamics compared to classical nonlocal damage models. *Journal of Applied Mechanics*, 83(11), 2016.

[103] Minh Hoang Nguyen and Anthony M Waas. High-fidelity progressive failure analysis of the open hole tensile (oht) behavior of composite laminates with a novel semi-discrete method. In *AIAA Scitech 2021 Forum*, page 0312, 2021.

[104] S Metoui, E Pruliere, A Ammar, and F Dau. A reduced model to simulate the damage in composite laminates under low velocity impact. *Computers & Structures*, 199:34–45, 2018.

[105] Kuo Tian, Bo Wang, Yan Zhou, and Anthony M Waas. Proper-orthogonal-decomposition-based buckling analysis and optimization of hybrid fiber composite shells. *AIAA Journal*, 56(5):1723–1730, 2018.

[106] Paul Davidson and Anthony M Waas. Probabilistic defect analysis of fiber reinforced composites using kriging and support vector machine based surrogates. *Composite Structures*, 195:186–198, 2018.

[107] Shiyao Lin, Kuo Tian, and Anthony Waas. Prediction of delamination area of laminated composite under low velocity impact based on experimentally validated finite element modeling and machine learning methods. In *Proceedings of the American Society for Composites—Thirty-third Technical Conference*, 2018.

[108] MH Malik and AFM Arif. Ann prediction model for composite plates against low velocity impact loads using finite element analysis. *Composite Structures*, 101:290–300, 2013.

[109] JA Artero-Guerrero, J Pernas-Sanchez, J Martin-Montal, D Varas, and J López-Puente. The influence of laminate stacking sequence on ballistic limit using a combined experimental/fem/artificial neural networks (ann) methodology. *Composite Structures*, 183:299–308, 2018.

[110] B Yu, RS Bradley, C Soutis, PJ Hogg, and PJ Withers. 2d and 3d imaging of fatigue failure mechanisms of 3d woven composites. *Composites Part A: Applied Science and Manufacturing*, 77:37–49, 2015.

[111] OJ Nixon-Pearson and SR Hallett. An experimental investigation into quasi-static and fatigue damage development in bolted-hole specimens. *Composites Part B: Engineering*, 77:462–473, 2015.

[112] Ashith PK Joseph, Anthony M Waas, Wooseok Ji, Evan J Pineda, Salvatore L Liguore, and Steven P Wanthal. Progressive damage and failure prediction of open hole tension and open hole compression specimens. In *56th AIAA/ASCE/AHS/ASC Structures, Structural Dynamics, and Materials Conference*, page 0466, 2015.

[113] O Tanay Topac, Burak Gozluklu, Ercan Gurses, and Demirkan Coker. Experimental and computational study of the damage process in cfrp composite beams under low-velocity impact. *Composites Part A: Applied Science and Manufacturing*, 92:167–182, 2017.

[114] Solver I Thorsson, Jiawen Xie, Jaspar Marek, and Anthony M Waas. Matrix crack interacting with a delamination in an impacted sandwich composite beam. *Engineering Fracture Mechanics*, 163:476–486, 2016.

[115] Shiyao Lin, Paul Davidson, James Stieber, and Anthony Waas. Experimental and numerical investigation on the three point bending response of highly anisotropic composite beam. In *Proceedings of the American Society for Composites—Thirty-fourth Technical Conference*, 2019.

[116] James H Starnes Jr and Jerry G Williams. Failure characteristics of graphite-epoxy structural components loaded in compression. In *Mechanics of Composite Materials*, pages 283–306. Elsevier, 1983.

[117] ASTM International. Standard test method for in-plane shear response of polymer matrix composite materials by tensile test of a $\pm 45^{\circ}$ laminate, 2018.

[118] Minh Hoang Nguyen, Avinkrishnan A Vijayachandran, Paul Davidson, Damon Call, Dongyeon Lee, and Anthony M Waas. Effect of automated fiber placement (afp) manufacturing signature on mechanical performance of composite structures. *Composite Structures*, 228:111335, 2019.

[119] Jikui Zhang and Xiang Zhang. An efficient approach for predicting low-velocity impact force and damage in composite laminates. *Composite Structures*, 130:85–94, 2015.

[120] Michael J Bogdanor and Caglar Oskay. Prediction of progressive damage and strength of im7/977-3 composites using the eigendeformation-based homogenization approach: Static loading. *Journal of Composite Materials*, 51(10):1455–1472, 2017.

[121] Shiyao Lin and Anthony M Waas. Accelerating computational analyses of low velocity impact and compression after impact of laminated composite materials. *Composite Structures*, 260:113456, 2021.

[122] Matlab Documentation. The mathworks inc. *Natick, MA*, 2005.

[123] Nicolas Moës, John Dolbow, and Ted Belytschko. A finite element method for crack growth without remeshing. *International journal for numerical methods in engineering*, 46(1):131–150, 1999.

[124] Nicolas Moës and Ted Belytschko. Extended finite element method for cohesive crack growth. *Engineering fracture mechanics*, 69(7):813–833, 2002.

[125] Anita Hansbo and Peter Hansbo. A finite element method for the simulation of strong and weak discontinuities in solid mechanics. *Computer methods in applied mechanics and engineering*, 193(33-35):3523–3540, 2004.

[126] Siva Shankar Rudraraju, Amit Salvi, Krishna Garikipati, and Anthony Waas. Mixed mode in-plane fracture analysis of laminated fiber reinforced composites using the variational multiscale cohesive method. In *51st AIAA/ASME/ASCE/AHS/ASC Structures, Structural Dynamics, and Materials Conference 18th AIAA/ASME/AHS Adaptive Structures Conference 12th*, page 2860, 2010.

[127] Shiva Rudraraju, Amit Salvi, Krishna Garikipati, and Anthony M Waas. Predictions of crack propagation using a variational multiscale approach and its application to fracture in laminated fiber reinforced composites. *Composite Structures*, 94(11):3336–3346, 2012.

[128] Daosheng Ling, Qingda Yang, and Brian Cox. An augmented finite element method for modeling arbitrary discontinuities in composite materials. *International journal of fracture*, 156(1):53–73, 2009.

[129] W Liu, QD Yang, S Mohammadizadeh, XY Su, and DS Ling. An accurate and efficient augmented finite element method for arbitrary crack interactions. *Journal of Applied Mechanics*, 80(4):041033, 2013.

[130] W Liu, D Schesser, QD Yang, and DS Ling. A consistency-check based algorithm for element condensation in augmented finite element methods for fracture analysis. *Engineering Fracture Mechanics*, 139:78–97, 2015.

[131] BY Chen, ST Pinho, NV De Carvalho, PM Baiz, and TE Tay. A floating node method for the modelling of discontinuities in composites. *Engineering Fracture Mechanics*, 127:104–134, 2014.

[132] BY Chen, ST Pinho, NV De Carvalho, PM Baiz, and TE Tay. A floating node method for the modelling of discontinuities in composites. *Engineering Fracture Mechanics*, 127:104–134, 2014.

[133] BY Chen, TE Tay, ST Pinho, and VBC Tan. Modelling the tensile failure of composites with the floating node method. *Computer Methods in Applied Mechanics and Engineering*, 308:414–442, 2016.

[134] Pavana Prabhakar and Anthony M Waas. Micromechanical modeling to determine the compressive strength and failure mode interaction of multidirectional laminates. *Composites Part A: Applied Science and Manufacturing*, 50:11–21, 2013.

[135] Ibrahim Kaleel, Marco Petrolo, AM Waas, and Erasmo Carrera. Micromechanical progressive failure analysis of fiber-reinforced composite using refined beam models. *Journal of Applied Mechanics*, 85(2):021004, 2018.

[136] Erasmo Carrera, Maria Cinefra, Marco Petrolo, and Enrico Zappino. *Finite element analysis of structures through unified formulation*. John Wiley & Sons, 2014.

[137] Jiawen Xie, Anthony M Waas, and Mostafa Rassaian. Estimating the process zone length of fracture tests used in characterizing composites. *International Journal of Solids and Structures*, 100:111–126, 2016.

[138] Pedro P Camanho and Carlos G Dávila. Mixed-mode decohesion finite elements for the simulation of delamination in composite materials. 2002.

[139] Marianna Maiarù, Royan J D'Mello, and Anthony M Waas. Characterization of intralaminar strengths of virtually cured polymer matrix composites. *Composites Part B: Engineering*, 149:285–295, 2018.

[140] CT Sun and S Chattopadhyay. Dynamic response of anisotropic laminated plates under initial stress to impact of a mass. *Journal of applied mechanics*, 42(3):693–698, 1975.

[141] Pei C Chou, William J Flis, and Harry Miller. Certification of composite aircraft structures under impact, fatigue and environmental conditions. part 1-low speed impact of plates of composite materials. Technical report, DREXEL UNIV PHILADELPHIA PA, 1978.

[142] Y.C. Fung. *Foundations of Solid Mechanics*. Prentice-Hall, 1965.

[143] CT Sun and SH Yang. Contact law and impact responses of laminated composites. 1980.

[144] Michael P Nemeth. Importance of anisotropy on buckling of compression-loaded symmetriccomposite plates. *AIAA journal*, 24(11):1831–1835, 1986.